

65
165
300

4.3 LOAD-REJECTION OVERVOLTAGES

As indicated in Section 4.1, the stator winding of a high-voltage generator with minimum grounding ($X_0/X_1 = 3.0$) is subjected to higher levels of short-time overvoltages than is a conventional generator step-up transformer. In order to better define the expected short-time overvoltages of high-voltage generators, computer simulation studies have been performed for line-to-ground fault situations occurring near the generator terminals and accompanied by tripping of the generator breakers.

The system is modeled as a single high-voltage superconducting generator feeding an infinite bus through a transmission system equivalent impedance, as illustrated in Figure 4.3-1. The computer program utilized for the load-rejection calculations models only positive sequence networks, so fictitious transmission lines were added to simulate the zero and negative sequence circuits for a single line-to-ground fault. Closing switch B initiates the line-to-ground fault, and load rejection occurs when switch A is opened. Switch A could be located near the infinite bus at the far end of the transmission line, and the maximum overvoltage would then be a function of the transmission line length. The generator grounding reactance is selected to provide a generator X_0/X_d'' ratio of 3.0. The high-voltage superconducting generator is modeled with conventional synchronous machine theory using a single shell rotor (Refs. 4-3 and 4-4). The model equations and parameters are reviewed in Appendix H.

Two load-rejection cases are considered: case 1 is for a simple load-rejection tripout with no accompanying fault; case 2 is for a line-to-ground fault near the generator terminals accompanied by a load rejection. For both cases, the initial loading prior to the disturbance is $E_T = 1.05$ p.u., $P = 0.9$ p.u., and $Q = 0.35$ p.u. overexcited (p.f. = 0.93). The line-to-ground fault is applied at $t = 0$ and remains on. At $t = .067$ s (4 cycles) the generator main breaker is tripped.

For case 1, Figure 4.3-2 illustrates the overvoltage accompanying a simple load rejection with no fault. For case 2, Figures 4.3-3 and 4.3-4 illustrate the load-rejection overvoltage of an unfaulted phase for the case of a single line-to-ground fault remaining on Phase A. The maximum overvoltage is approximately 150% of normal line-to-ground voltage.

$$X'' = .229$$

Superconducting
Generator

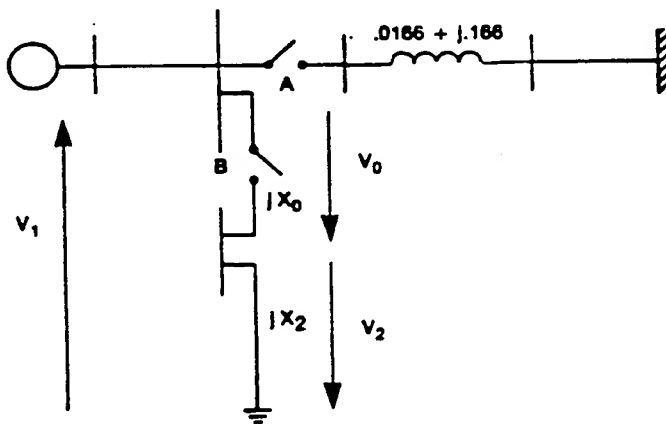


Figure 4.3-1. System Model for Load Rejection Studies

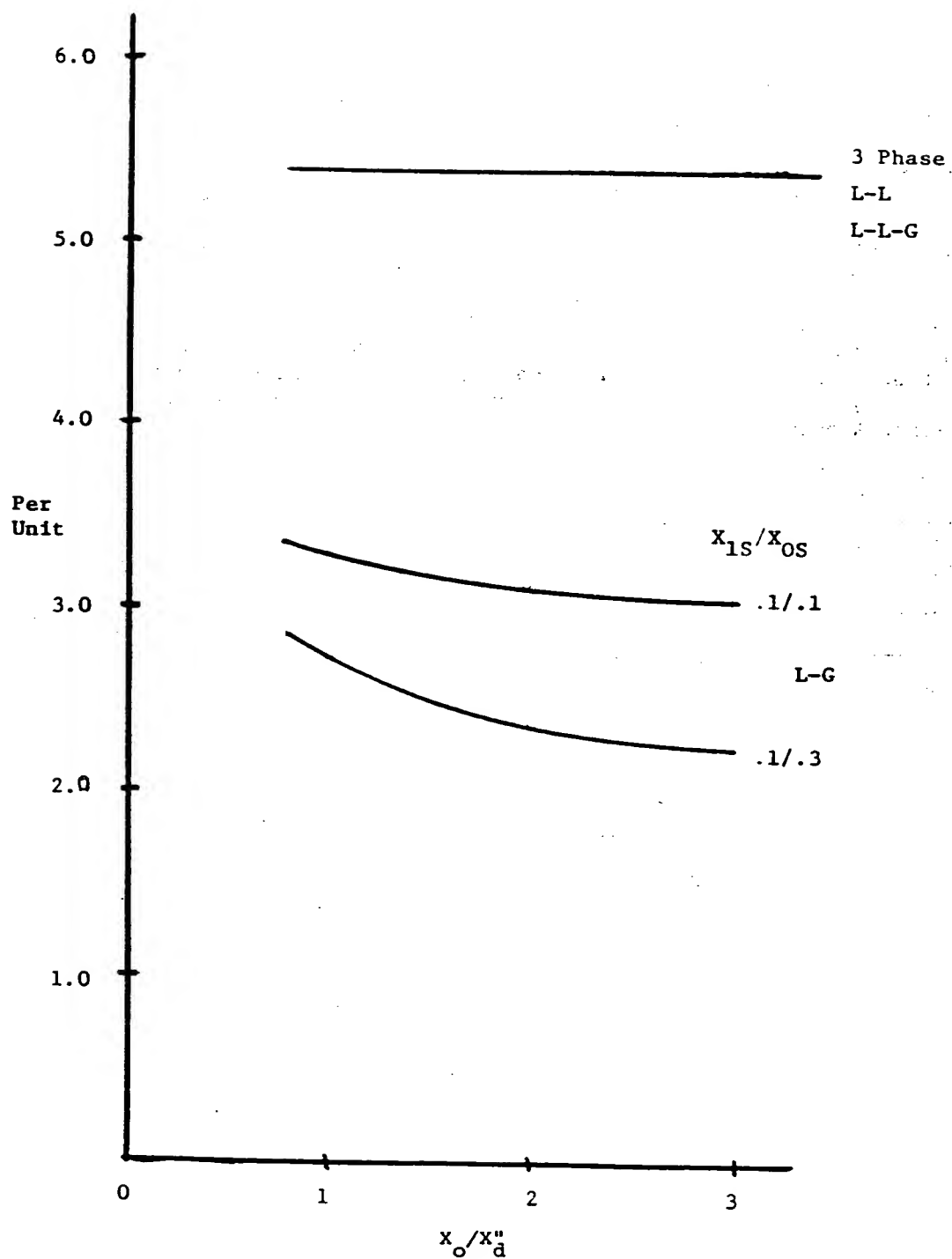


Figure 4.2-4. Fault Current Levels for Delta-Connected High-Voltage Generators

4.2.2 Fault Currents for Delta-Connected High-Voltage Generators

For the delta-connected high-voltage generator, grounding by means of some type of grounding transformer is assumed. A range of grounding effectiveness of the generator from $X_0/X_d'' = 0.8$ to 3.0 is considered. While a low ratio would appear to be economically unattractive because of the increased cost of the grounding transformers, it is included to permit evaluation of the benefit to the generator insulation requirements.

Figure 4.2-4 shows generator winding fault currents in per unit of normal winding current in the delta. The estimated short-time overvoltages on load rejection will be the same as those given in Figure 4.2-3 for the wye-connected generator.

Table 4.2-3 summarizes the fault current levels for delta-connected high-voltage generators. For line-to-ground faults, which predominate, the delta-connected generator experiences considerably lower current levels than the grounded wye-connected generator. The delta-connected generator experiences the same short circuit current for all types of phase-to-phase faults, as indicated by the table. This group of faults is not an insignificant number, and thus, the advantages of a delta-connected generator from the fault current standpoint are not as great as might be thought at first glance.

Table 4.2-3
FAULT CURRENT LEVELS FOR DELTA-CONNECTED
HIGH-VOLTAGE GENERATORS

Fault Type	Typical 30-Yr. Exp.	Fault Current (ac comp.)	
		$X_0/X_d'' = 3.0$	$X_0/X_d'' = 1.0$
L-G	146	3.1 p.u.	3.3 p.u.
L-L	34	5.4 p.u.	5.4 p.u.
L-L-G			
3-Phase			
Load-rejection over-voltage (with L-G fault)	Rare	1.6 p.u.	1.15 p.u.

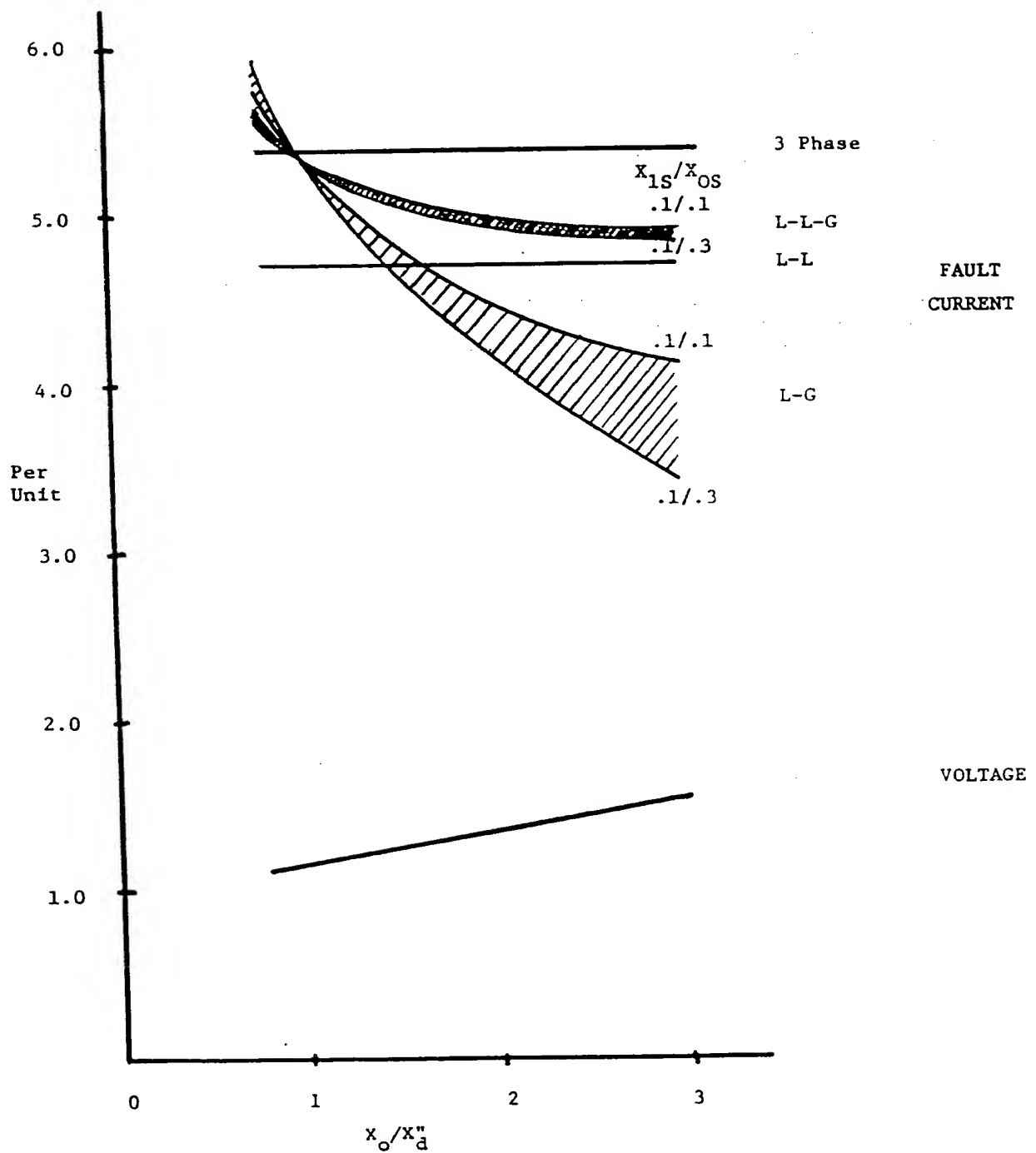


Figure 4.2-3. Fault Current Levels and Load Rejection Overvoltages for Wye-Connected High-Voltage Generators

The basic generator and system parameters for the fault calculations are listed in Table 4.2-1. Figure 4.2-3 shows generator fault current levels for close-in line-to-ground and multiphase faults. All of the fault currents plotted are the subtransient, symmetrical ac components and do not include the dc component of a fully offset wave, which may be present. While it is generally assumed that the line-to-ground fault currents will be the least severe, note that with a solidly grounded neutral the line-to-ground fault current exceeds the three-phase fault current.

Despite the higher fault currents with solid grounding, there is a compensating benefit in the form of lower short-time overvoltages associated with a terminal line-to-ground fault and load-rejection tripout of the unit. Figure 4.2-3 also shows the estimated load-rejection overvoltage levels as a function of the degree of grounding.

Table 4.2-2 summarizes the fault current levels for wye-connected high-voltage generators. It should be recognized that the 30-year exposure listed is simply a broad average around which there may be large perturbations. For example, during an unusual ice storm, a major generating station experienced the above "lifetime" exposure of nearby line-to-line faults in a single evening.

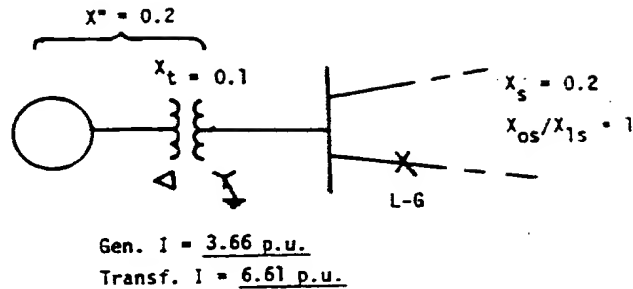
Table 4.2-1
BASIC DATA FOR FAULT CALCULATIONS

High-Voltage Generator:	
X_d''	= 0.20
X_d'	= 0.27
X_0	= 0.16 (Wye generator)
Initial loading $0.9 + j.31$ (0.95 p.f.), $E_T = 1.0$	
System: (per unit on generator kVA base)	
X_{1S}	= in range 0.1 to 0.8
X_{0S}/X_{1S}	= in range 1.0-3.0

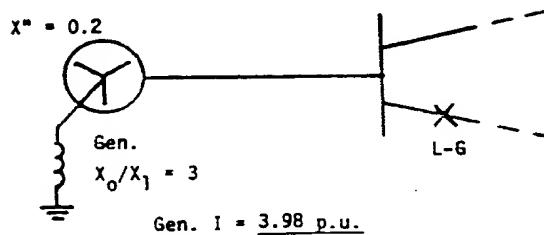
Table 4.2-2
**FAULT CURRENT LEVELS FOR WYE-CONNECTED
HIGH-VOLTAGE GENERATORS**

<u>Fault Type</u>	<u>Typical 30-Yr. Exp.</u>	<u>Fault Current (ac comp.)</u>	
		<u>$X_0/X_d'' = 3.0$</u>	<u>Neutral Solid Ground</u>
L-G	146	4.0 p.u.	6.0 p.u.
L-L	11	4.8 p.u.	4.8 p.u.
L-L-G	16	5.0 p.u.	5.6 p.u.
3-Phase	7	5.4 p.u.	5.4 p.u.
Load-rejection over- voltage (with L-G fault)	Rare	1.6 p.u.	1.15 p.u.

I. Conventional Unit



II. HV Generator - Wye



III. HV Generator - Delta

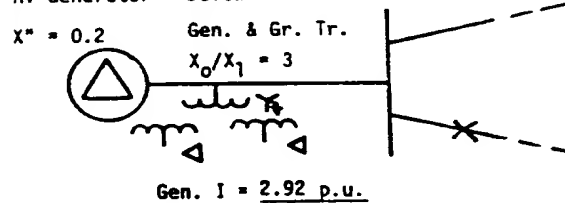


Figure 4.2-2. Generator Fault Currents (ac Component) for System Line-to-Ground Faults

For rough calibration purposes, assuming a four-line station and including faults within 50 miles of the station, the high-voltage generator would be exposed to the following 30-year duty:

- 146 L-G faults
- 11 L-L faults
- 16 L-L-G faults
- 7 Three-phase faults

Because of the preponderance of ground faults, the type of grounding employed is significant to the stator winding duties.

4.2.1 Fault Currents for Wye-Connected High-Voltage Generators

For the wye-connected generator, neutral grounding is assumed to vary from the extreme of connecting the neutral directly to ground to the utilization of a neutral reactor which provides a generator X_0/X_1 ratio as high as 3. As discussed in Section 4.1, grounding of at least this effectiveness should be provided for system considerations.

4.2 GENERATOR SHORT CIRCUIT CURRENTS

High-voltage generators have an inherent advantage over conventional generators in the design requirements for maximum short circuit forces because the currents for a three-phase fault at the generator terminals are smaller for the high-voltage generator. This attribute is illustrated in Figure 4.2-1 for generator systems possessing similar stability performance (presenting the same transient reactance to the transmission system).

On the other hand, depending on the winding type (wye or delta) and the degree of grounding, high-voltage generators may be subjected to greater short circuit forces than conventional generators for the more frequent transmission line-to-ground fault. One example is shown in Figure 4.2-2.

The most frequent fault conditions experienced by a generator are line-to-ground faults, comprising 80 to 90% or more of transmission line faults. Fortunately, they are generally the least severe of the fault types. Fault statistics vary widely with location, transmission voltage level, line construction, shielding practices, etc.; however, representative data for 345 kV are as follows:

• Fault frequency: 3 faults/100 mi/yr.

Distribution by fault type:

L-G	81%
L-L	6%
L-L-G	9%
3-Phase	4%

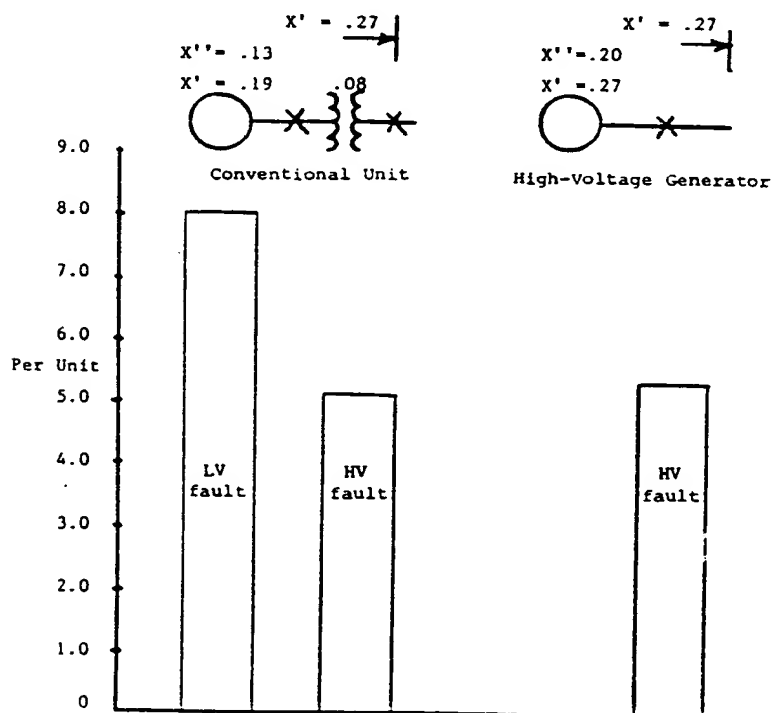


Figure 4.2-1. Three-Phase Fault Current Levels for Conventional and High-Voltage Generators

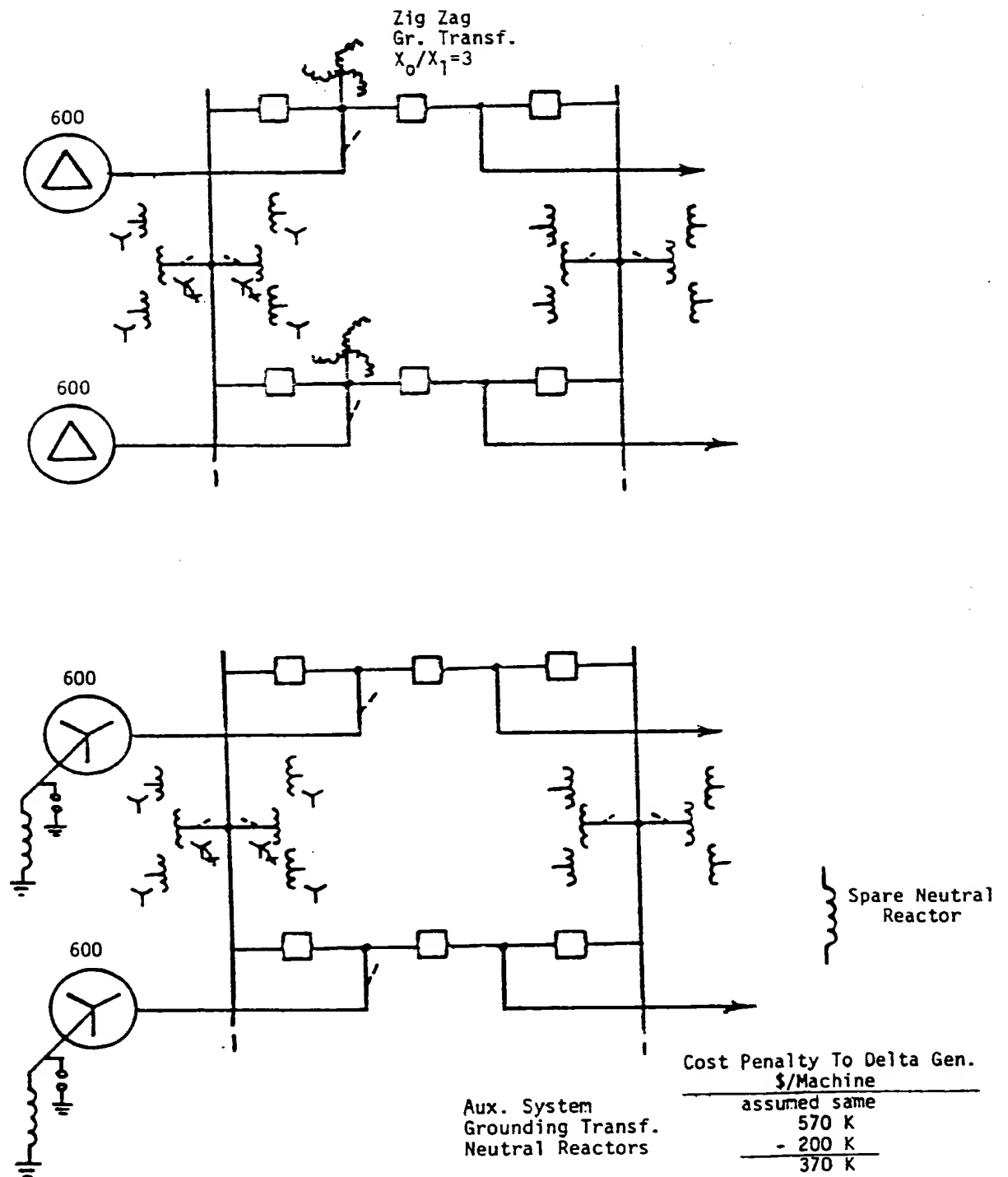


Figure 4.1-7. Cost Comparison for Separate Zig-Zag Transformer Grounding of Delta-Connected High-Voltage Generators

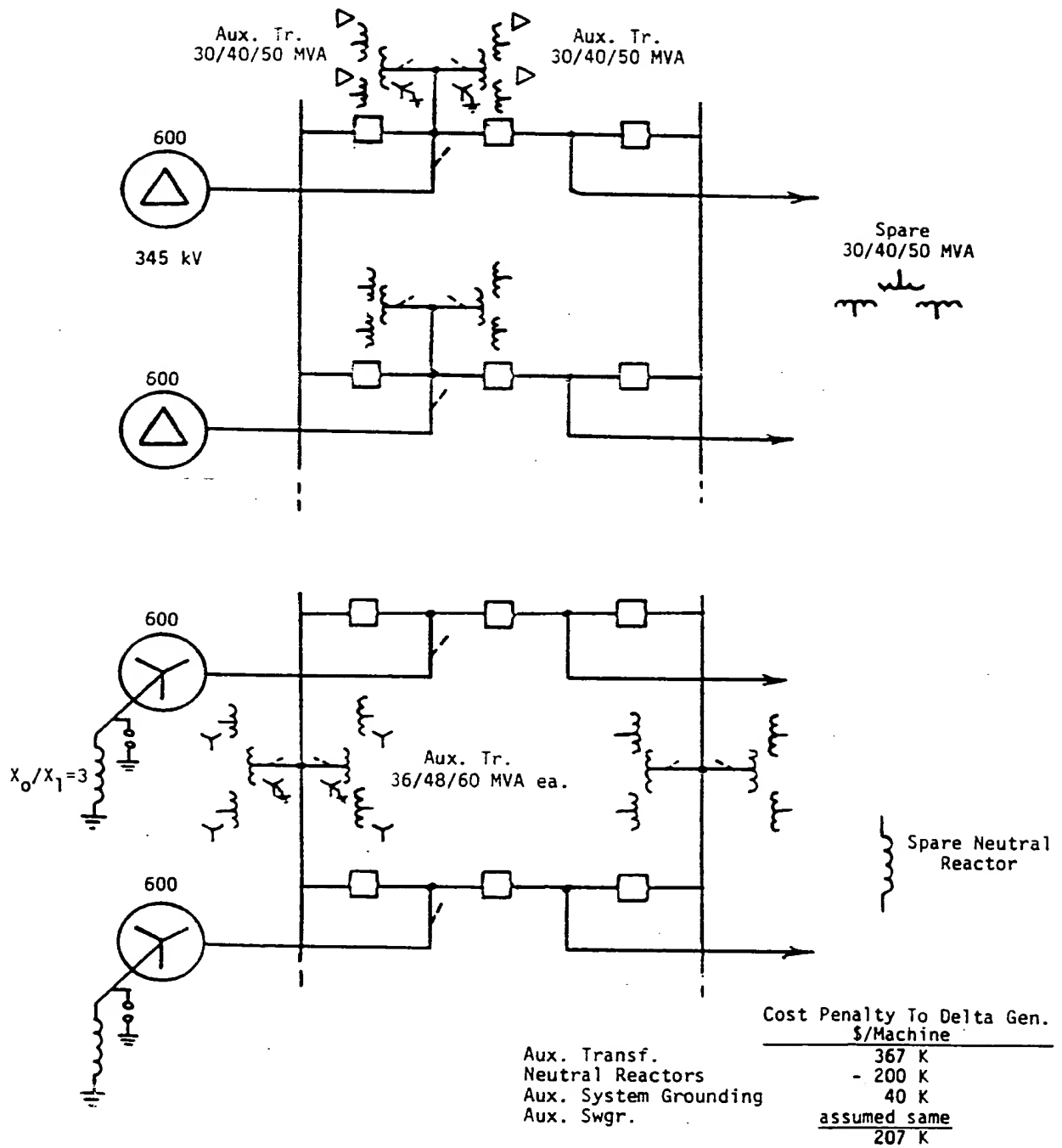


Figure 4.1-6. Cost Comparison for Auxiliary Transformer Grounding of Delta-Connected High-Voltage Generators

effect would be to produce lower short-time overvoltages at the expense of higher machine line-to-ground fault currents. The generator X_0/X_1 ratio cannot fall below a value of 1.0 if the line-to-ground fault current is not to exceed the three-phase fault current. Referring to Figure 4.1-1, it can be seen that reducing X_0/X_1 ratios substantially reduces the possible line-to-ground fault overvoltages. If the generator design studies indicate that this is a favorable trade-off direction to pursue, then lower X_0/X_1 ratios for the delta-connected high-voltage generator can be investigated. While of secondary importance, it can be noted that, in general, more effective grounding of the delta-connected high-voltage generator system will entail increased costs for the required grounding transformers whereas a similar action for the wye-connected generator will entail a decreased cost of the neutral reactor. There is, of course, no reason why solid grounding of a wye-connected generator neutral should not be considered, since this is the common practice for wye-connected step-up transformers. This would provide the maximum benefit from the standpoint of insulation design requirements.

The auxiliary transformers in Figure 4.1-5 are not required to provide grounding and are connected to the high-voltage main busses. If there were also a lower transmission-voltage bus in the station, it could be considered as an economical alternate for part of the auxiliary requirements. The auxiliary transformer backup requirements are provided by the forced cooled ratings, and no spare transformer is included.

4.1.3 Estimated Cost Penalties for the Delta-Connected Generator's Grounding Equipment

Since grounding of the delta-connected high-voltage generator involves special impedance auxiliary transformers, which in turn can effect the switchgear requirements, etc., a key element in the cost comparison must be the auxiliary system costs. This can become extremely involved when one considers the switchgear, the motor control center, the motor cost differences, and the wide variations in design philosophies. The general conclusions that can be stated are:

- Auxiliary system costs vary widely with specific plant circumstances and utility design philosophies. As a practical approach, one auxiliary system design which represents typical utility practice is considered.
- The delta and wye generator systems can reasonably use the same basic auxiliary system design, so the essential differences involve auxiliary transformer costs and the cost of spare capacity which may be included.

Estimated installed cost differences in station equipment for delta- and wye-connected high-voltage generators is summarized in Figures 4.1-6 and 4.1-7 for 600 MVA, 345 kV generators. Four arrangements are considered:

	Cost Penalty for Delta Generators \$/Machine (\$ thousands)
(1) Figure 4.1-6: Auxiliary transformer grounding of the delta generator	207
(2) Figure 4.1-7: Separate zig-zag grounding transformer for the delta generator	370
(3) Figure 4.1-6: Same as (1) except spare transformer and spare neutral reactor are omitted.	-10
(4) Figure 4.1-7: Same as (1) except wye generator neutral is solidly grounded	407

Comparison (1) would appear to be the one of most significance. Wide variations are possible, depending on particular station design assumptions.

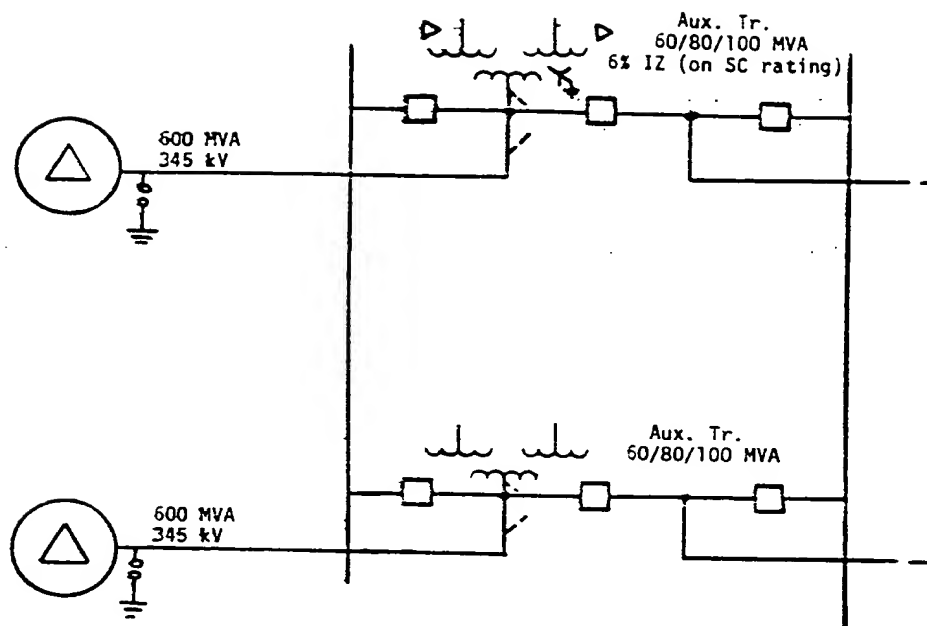


Figure 4.1-4. Station Arrangement and Grounding for Delta-Connected High-Voltage Generators

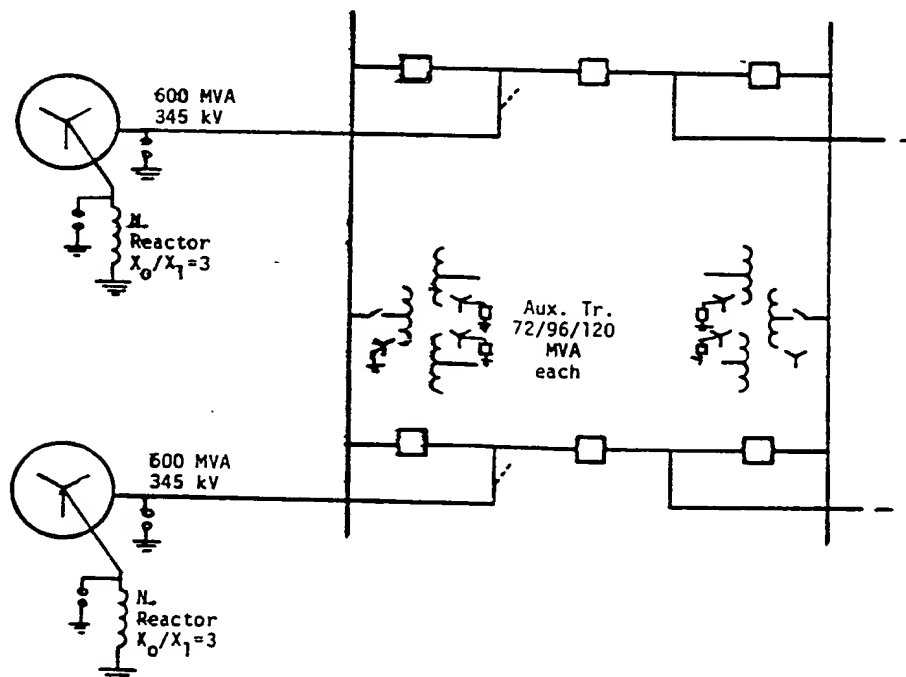


Figure 4.1-5. Station Arrangement and Grounding for Wye-Connected High-Voltage Generators

tem used in the high-voltage generator, these should be used in a final determination of insulation coordination. For the 765 kV rating, it should be noted that the indicated arrester does not have adequate withstand capability for the assumed 175% peak load-rejection voltage. At the present time, the arrester shown is the only rating available for the 765 kV voltage class; however, it is assumed that additional ratings with greater discharge capability will be obtainable when required so that an X_0/X_1 ratio of 3.0 can become sufficient for this voltage class.

4.1.2 Grounding Arrangements

Supplementary grounding for the station may be provided in a number of ways and can be influenced by the presence at the same station of a lower transmission-voltage bus. For the purposes of this study, a single transmission-voltage station consisting of two generating units is assumed. For the delta-connected generator, it is fundamental that the grounding remain connected to the machine at all times, rather than to one or more of the high-voltage bus sections. This is to provide grounding on startup prior to synchronizing and, more importantly, to maintain adequate grounding to limit voltage stresses during line-to-ground fault conditions coupled with load-rejection tripout of the generator.

The necessary grounding for the delta-connected generator may be provided by a separate zig-zag grounding bank for each unit; however, a more economical arrangement is illustrated in Figure 4.1-4, where the station auxiliary transformers are utilized as grounding banks in addition to their normal function. While this approach appears to be practical, several considerations which affect cost and/or operating procedures should be noted.

- The auxiliary transformers require lower than standard impedance to provide the minimum grounding criterion ($X_0/X_1 = 3.0$). This entails a cost penalty to these transformers of about 20%.
- To meet the transmission system grounding needs, the auxiliary transformer low-voltage winding connections should be delta connected. This requires separate small grounding transformers for auxiliary system grounding and produces a relatively insignificant cost addition.
- Since loss of an auxiliary transformer would shut down a machine for lack of grounding, a spare transformer should be provided and is included in the cost comparisons.
- From an operating standpoint during startup and shutdown, the arrangement of Figure 4.1-4 is basically the same as a typical conventional unit generator-transformer arrangement, which also has its major auxiliary supply transformer tied directly to the generator. The "startup" source in the case of the delta-connected high-voltage generator, however, is the auxiliary transformer of the second unit rather than a startup transformer permanently connected to one of the high-voltage busses. To maintain equivalent reliability of the auxiliary system, a delta machine on shutdown would need to have its own auxiliary transformer promptly reconnected to the bus. While this is a normal procedure, a permanently connected startup/shutdown auxiliary source is preferable. Such a source might be obtainable in connection with older conventional units at the site, or the spare auxiliary transformer referred to above could be utilized in this capacity.

The assumed full-load auxiliary requirements are 10% of the generator rating, i.e., 60 MVA for the 600 MVA unit shown in Figure 4.1-4. The 100 MVA forced cooled rating of the auxiliary transformer is intended to provide startup capability for another unit as well as 67% reserve capacity for outages within the auxiliary system.

A station arrangement for wye-connected high-voltage generators must be established to provide a basis for the cost comparisons of the grounding equipment. Figure 4.1-5 illustrates such an arrangement in which the grounding is provided by a reactor in the winding neutral, sized to provide an X_0/X_1 ratio of 3. For this arrangement, lower X_0/X_1 ratios could readily be provided, and the

the present dielectric test standards (Reference 4-1) indicate overvoltage test levels that are related to the basic impulse insulation levels (BIL). For example, for a 500 kV-rated transformer winding at 1300 kV BIL, the applied line-to-neutral overvoltage test potential is 575 kV, or about 80% of rated. These test levels are now in the process of change. Presently proposed standards (Reference 4-2) specify holding a lower test level (unrelated to BIL) of 150% of maximum rated line-to-neutral voltage for 1 hr. It is not clear that this adequately represents the higher short-time transient overvoltages which a high-voltage generator may experience on load rejection with a line-to-ground fault. As indicated previously, these overvoltages are related to the degree of grounding provided, i.e., the X_0/X_1 ratio. The dotted curve of Figure 4.1-1 shows estimated maximum overvoltages as a function of grounding effectiveness for the load-rejection type of voltage excursion illustrated in Figure 4.1-3. Load-rejection overvoltage studies which were performed for a 600 MVA, 345 kV high-voltage generator to substantiate these estimates are described in Section 4.3. Greater overvoltages are possible for contingencies in which a transmission line is connected to the machine during the load rejection. While such a contingency is unlikely, it should be noted that with the conventional generator/transformer arrangement the transformer saturation provides a clamping action which would be expected to limit maximum overvoltages to no more than 140%. Since the high-voltage superconducting generator would not possess this saturation characteristic, other protective means such as independent pole switching and redundancy in relaying assume greater importance.

The BIL levels required for the high-voltage generator depend on the rating of arresters which may be applied on the system. Limitations in the arrester ratings that can be applied depend in turn on the switching-surge and short-time overvoltage energy dissipation required. In this regard, a new type of arrester employing nonlinear zinc oxide elements provides major advantages in its ability to ride through the load-rejection overvoltage excursions which are critical to arrester application on the high-voltage generator. It is assumed that this type of arrester, which is now commercially available, would be utilized, and would permit application of high-voltage generator BILs as low as indicated in Table 4.1-1. In this table, the listed insulation test levels are those established for high-voltage transformer windings. If different values are assigned for the particular insulation sys-

Table 4.1-1
INSULATION COORDINATION

Generator Voltage Rating	Insulation Test Levels (kV)			Arrester Characteristics*			
	Full-Wave BIL	Chopped Wave	Switching Surge	Rated kV	Discharge Voltage 8×20 μ -Second Current Wave	Switching Surge Protection Level	Withstand Time at 175% of Generator L-N Rated V (seconds)
230 kV	750	865	620	264	(10 KA) 598	520	Over 60
345 kV	900	990	745	312	(10 KA) 707	615	10
500 kV	1300	1430	1080	444	(15 KA) 1043	874	8
765 kV	1800	1980	1500	588	(20 KA) 1418	1197	Under 1

*Based on GET-6460, *Application Guide for Tranquell Station Surge Arresters*.

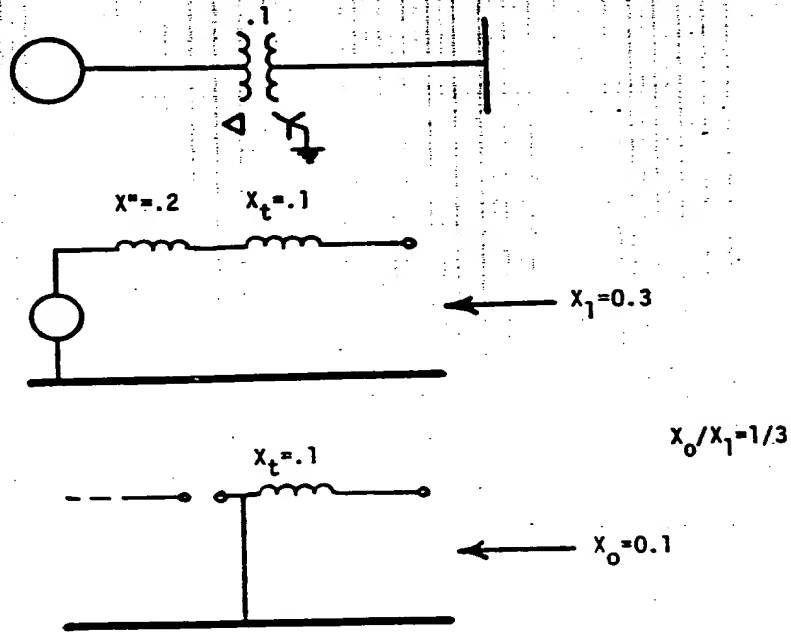


Figure 4.1-2. System Grounding of a Conventional Unit Generator-Transformer

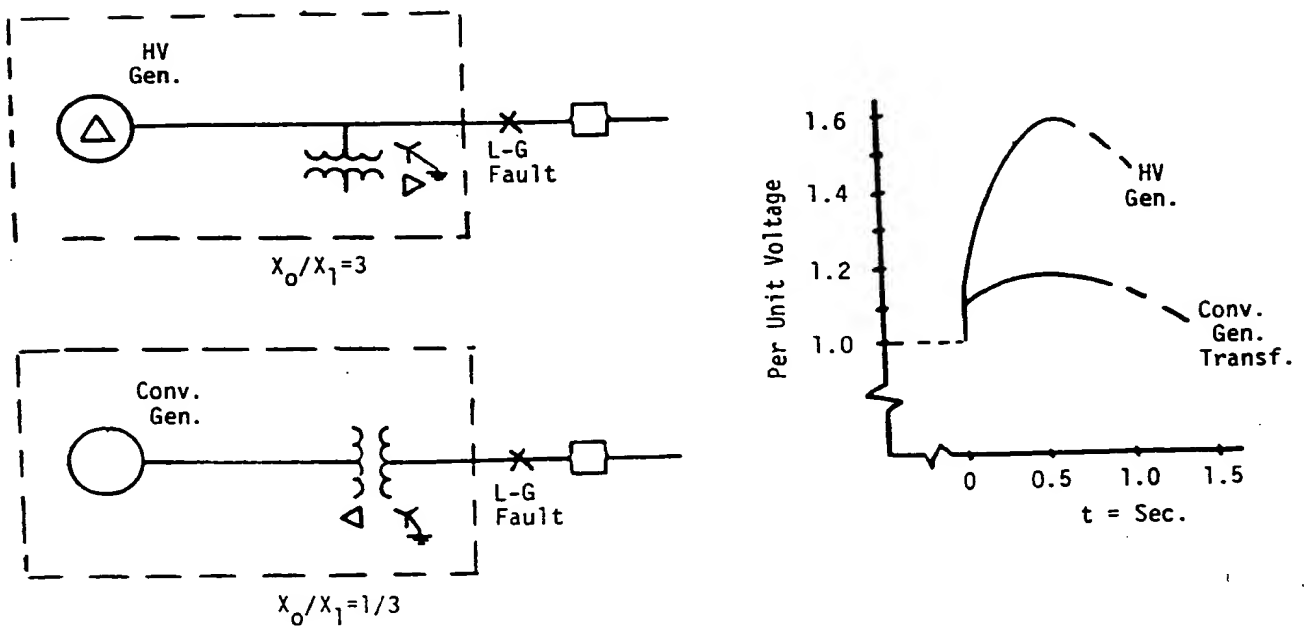


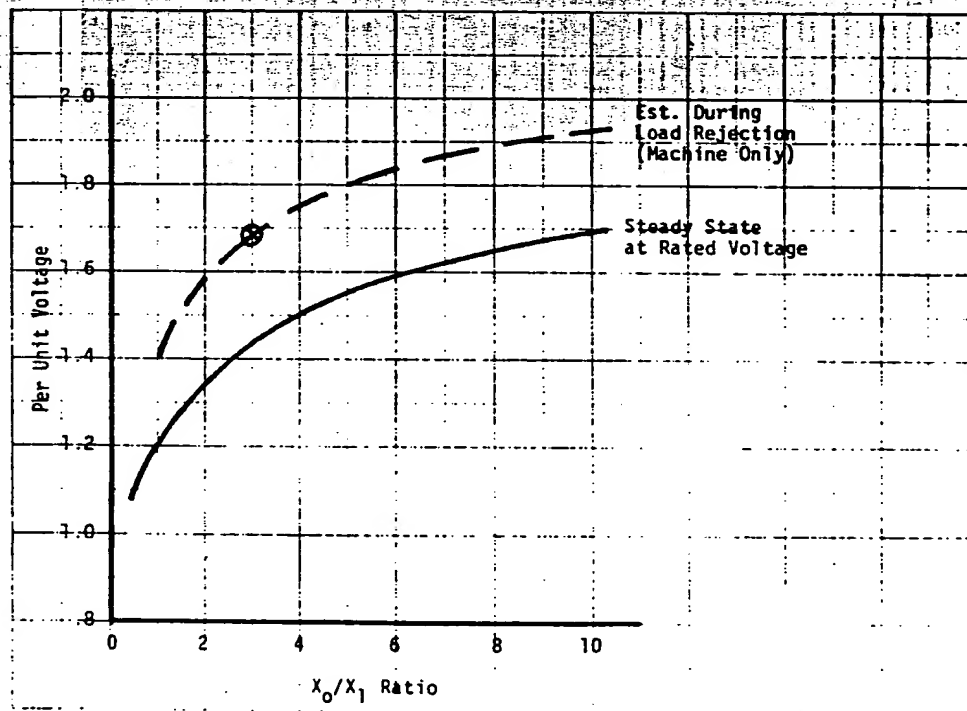
Figure 4.1-3. Load-Rejection Overvoltages

One relationship between grounding effectiveness and insulation requirements is shown by the solid curve of Figure 4.1-1, which illustrates the per unit voltage to ground on an unfaulted phase during a line-to-ground fault, neglecting switching transients or overvoltages from other causes. Greater overvoltages resulting from insufficient grounding require greater insulation requirements and consequent greater insulation costs.

As illustrated in Figure 4.1-2, very effective grounding in the conventional unit generator transformer system is easily accomplished through the grounded neutral of the transformer's Wye winding. The delta-connected high-voltage generator lacks such an easy means of grounding and must be grounded through auxiliary equipment. Although a trade-off between the cost of auxiliary grounding equipment and the cost of insulation requirements could be explored as a matter of academic interest, there are well-established industry standards that base transient switching capabilities on an assumption of an effectively grounded system defined by an X_0/X_1 ratio of 3.0 or less. It must be presumed that, at least in its initial establishment, the high-voltage generator should be compatible with present standards of system grounding. Therefore, the criteria used in this study require a minimum X_0/X_1 ratio of 3.

While an X_0/X_1 ratio of 3.0 meets the requirements of an effectively grounded system, it should be pointed out that this degree of grounding still allows higher insulation stresses to be experienced by the high-voltage generator during temporary overvoltages than are experienced by the high-voltage winding insulation of a main step-up transformer. This comparison is shown in Figure 4.1-3 for the case of a line-to-ground fault near the unit, accompanied by load rejection tripout of the unit.

These voltage excursions are in the range in which the commercial acceptance overvoltage test, or "hi-pot", is presently intended to test insulation capability. For high-voltage transformer windings,



⊗ Simulation Study Point

Figure 4.1-1. Overvoltage on the Unfaulted Phases During a Line-to-Ground Fault at the Generator Terminals

Section 4

POWER SYSTEM CONSIDERATIONS IN THE DESIGN OF HIGH-VOLTAGE GENERATORS

4.1 SYSTEM GROUNDING FOR DELTA-CONNECTED HIGH-VOLTAGE GENERATORS

Delta-connected winding arrangements for the monolith cylinder armature have been demonstrated in Section 2.1 to be beneficial in controlling voltage gradients affecting the armature's insulation system. The utilization of delta-connected armatures on the power system poses a number of difficulties, the foremost of which relates to the grounding of the transmission system. Although delta-connected generators have been supplied in the past, these were conventional voltage machines that were connected to the power system through delta-wye step-up transformers that provided the required transmission system grounding. The delta-connected high-voltage generator will require auxiliary equipment to provide minimum system grounding requirements, implying cost penalties for the utilization of the delta-connected armature.

4.1.1 System Grounding Requirements and Their Relation to Fault Overvoltages

All modern high-voltage transmission systems are designed on the basis of relatively solid grounding which limits the transient overvoltage levels encountered. Transient overvoltages occurring on the transmission system fall into several categories:

- Lightning impulses, which are characterized by very fast wavefront rise times (typically 1 μ s to the crest of the wave). These waves may be "chopped" as a result of insulator flashover, creating very steep front waves.
- Switching surges, which are characterized by 250-2500 μ s wavefront rise times.
- Temporary overvoltages, which are associated with generation load rejection, are of relatively long duration — measured in seconds. The highest voltage stresses to ground occur on unfaulted phases during a line-to-ground fault.

IEEE and ANSI Standards define dielectric test requirements for these categories of transients in terms of basic lightning impulse insulation level (BIL), chopped wave insulation level, switching impulse insulation level, and low-frequency phase-to-ground insulation level.

In general, the levels of system temporary overvoltages and switching surge overvoltages establish the lowest ratings of surge arresters which can be applied, and the surge arrester ratings then establish the insulation levels which will be protected.

The system grounding has a major influence on the temporary overvoltage and switching-surge levels and therefore on the equipment insulation strength required. The ratio of zero-sequence reactance to positive-sequence reactance (X_0/X_1 ratio) is a major parameter affecting transient voltage levels. Industry practice for many years has been to define an effectively grounded system as one having an X_0/X_1 ratio of 3.0 or less (with an R_0/X_1 not over 1.0). These criteria are generally met except under unusual circumstances. A unit generator-transformer, for example, will have an X_0/X_1 ratio viewed from the high-voltage bus of considerably less than 1.

Transmission lines exhibit an X_0/X_1 ratio of about 3.0 and transmission receiving end stations have grounding characteristics similar to generating stations. The net effect is that the overall X_0/X_1 ratios indicating the degree of grounding generally run between 0.5 and 3. Typically, the latter value would be approached at a generating station when all of the generating units with their respective step-up transformers are shut down. There is no local grounding in such a situation, but satisfactory grounding is provided through transmission-line connections to other grounded substations. This situation presents no difficulty in providing station surge protection. It should be recognized, however, that this situation is not comparable to the case where there are on-line, delta-connected high-voltage generators without local grounding. Here, the X_0/X_1 ratios would be much higher.

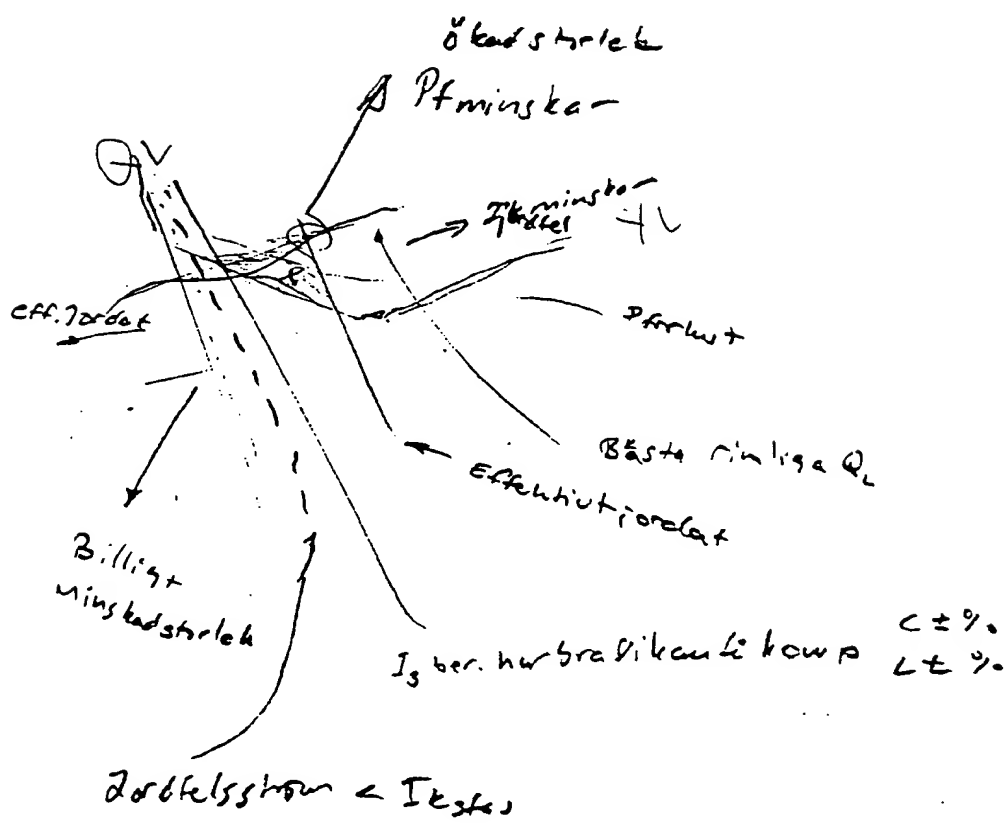


Table 3-1

CIRCUIT PARAMETERS OF SERIES-RESONANCE OVERVOLTAGE TEST FOR HIGH-VOLTAGE GENERATORS

High-Voltage Generator: 600 MVA, 345 kV, 1004 A, $X = 238.1 \Omega$	
	<u>240 Hz Test</u>
Generator Reactance	238.1 Ω
Required Line Current	1,673 A
Required Series Capacitance	2.8 μF
No. Capacitor Units per Phase	868 (28 series units, 31 parallel branches)
Total No. Capacitor Units	2,604
Total Capacitor Cost	\$1,117,116

sary to measure the winding reactance before the capacitor banks are sized. This is accomplished by exciting the generator winding directly with the high-frequency source and measuring the terminal voltages and currents. This measurement should be performed at the same frequency as the series-resonance test.

After the dielectric tests of the high-voltage generator have been completed, the complete stator and superconducting rotor can be initiated. These tests include no-load tests, short circuit heat run tests, rotor tests, and vibration tests, among others.

Although the generator winding is individually excited to twice-rated overvoltage, this voltage is cancelled by the capacitor bank, and the high-frequency generator appears to be operating in a short circuit condition, except for the voltage drop due to losses. Figure 3-3 illustrates the circuit for this test. The operating frequency is typically 240 Hz or 420 Hz. For a delta-connected generator winding, the test must be performed in three-phase, so that the nature of the winding voltage distribution may be duplicated. This requires three separate capacitor banks, one for each phase, with an attendant cost burden. The capacitor banks can be fabricated from standard rack-mounted distribution capacitors, although such an assembly may be corona-prone. Superior capacitor banks are fabricated from special capacitor units that are submersed in an oil-filled tank. Enough capacitor units must be connected in series to withstand the generator's twice-rated overvoltage, and enough branches of series connected units must be connected together in parallel to provide the required capacity. The high-frequency generator must be sized to handle the required line current and the circuit losses.

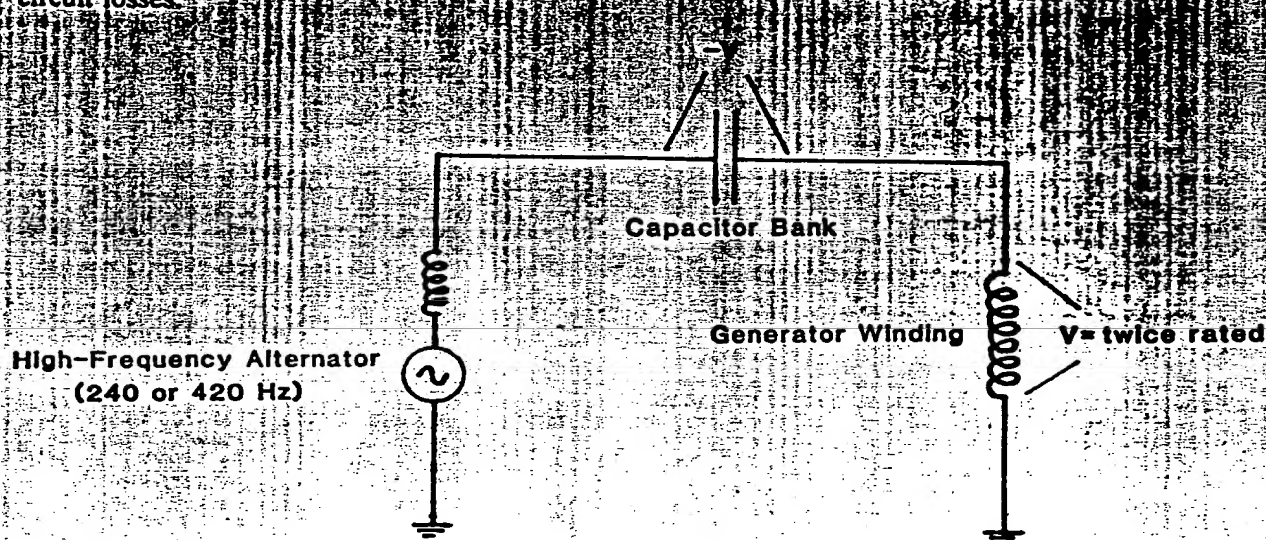


Figure 3-3. Series Resonance Circuit for the Overvoltage Test of High-Voltage Generators

Table 3-1 lists circuit parameters for two series-resonance overvoltage tests, one at 240 Hz and another at 420 Hz, for the 600 MVA, 345 kV high-voltage generator. The specifications for this generator are listed in the table. The ohmic value of reactance is listed in order to compare with the generator reactance at the higher frequencies, where it is seen that the reactance is proportional to the frequency. The required line current is the current required to obtain twice-rated voltage on the generator winding. At 240 Hz, the required line current is larger than the 60 Hz rated load current of the generator, although the winding could probably withstand such a current for the short time span of the test. The required series capacitance is proportional to the inverse square of the test frequency, so there is great motivation to utilize the 420 Hz test in order to reduce capacitor requirements. The capacitor bank arrangements are based upon a selected rack-mounted capacitor unit judged to be the most economical from which to assemble a large bank. This capacitor has a nominal rating of 14.4 kV and 200 kVAR (at 60 Hz). Its capacitance is $2.588 \mu\text{F}$ and it costs \$429. Twenty-eight capacitors must be connected in series to withstand the generator's twice-rated overvoltage of 400 kV line-to-ground, and several branches of these series-connected units are required to yield the necessary capacity.

A word of caution must be stated about the sizing of the capacitor banks. The series-resonance condition will be achieved only if the capacitor banks are exactly tuned to the reactance of the generator winding, and at the present time, the calculation accuracy of the reactance of air-gap windings is uncertain and therefore unsuitable for the accurate sizing of the capacitor banks. It is neces-

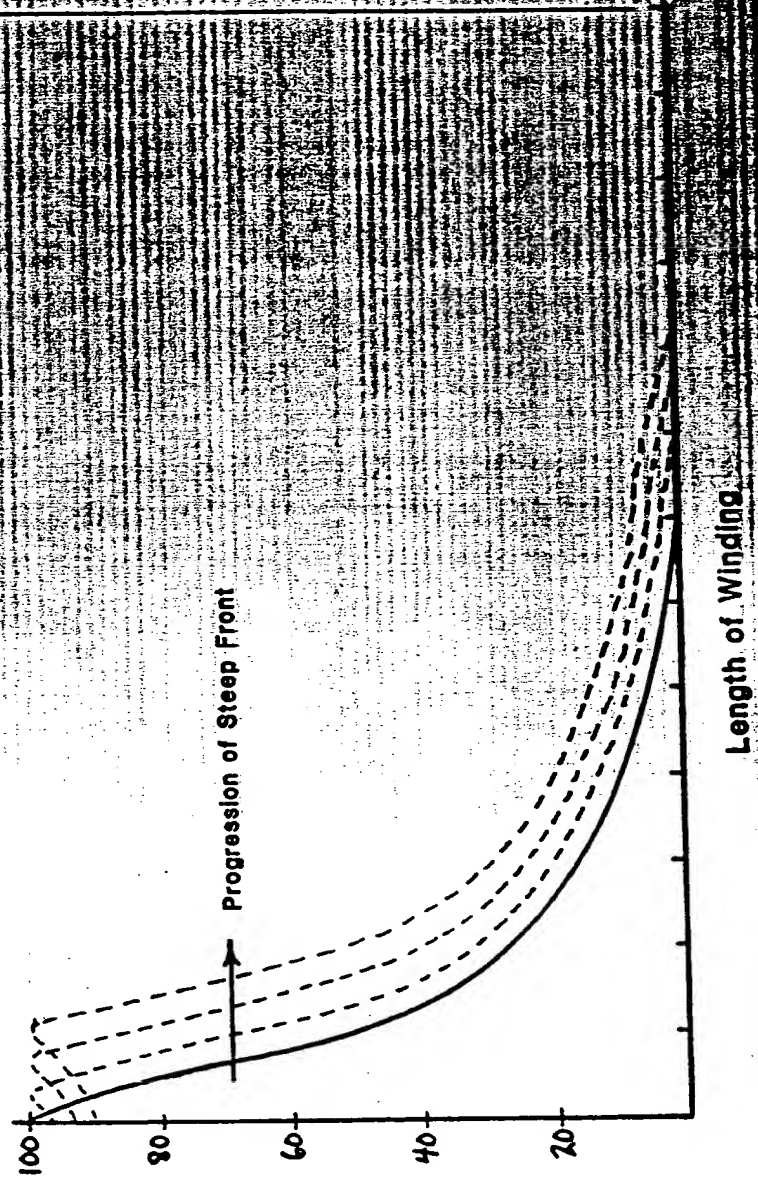
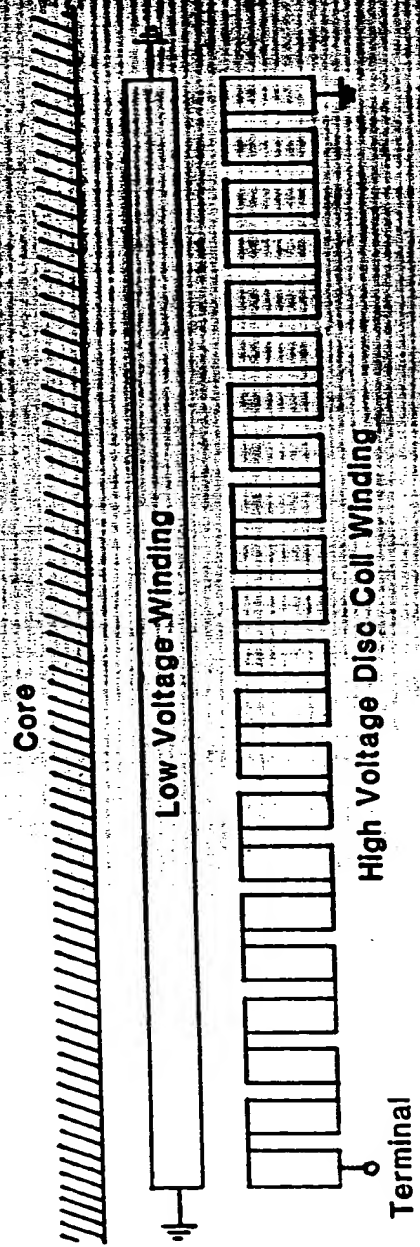


Figure 3-2. Voltage Distribution Within a Disc-Coil Transformer During Voltage Impulse

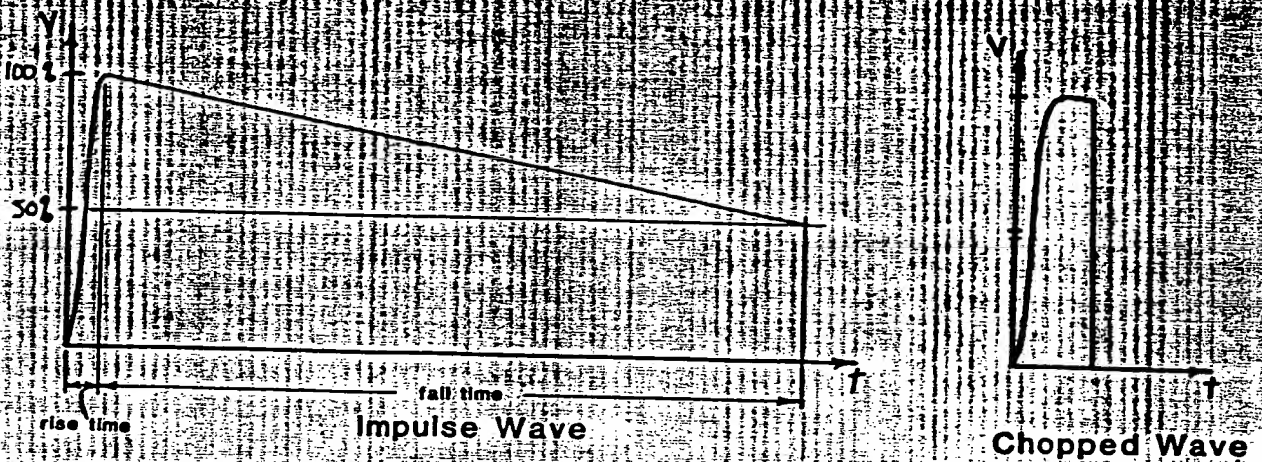


Figure 3-1. Impulse Waveforms

voltage distribution within a typical disc-coil transformer winding at the moment when the crest of the impulse has arrived at the winding terminal. The voltage falls rapidly progressing inward, producing large turn-to-turn voltages near the terminal of the winding. As time progresses, the steep-front of the voltage distribution travels toward the neutral and eventually reflects backward, so that all portions of the winding at some time during the application of the impulse experience large turn-to-turn voltages. The procedure for detecting dielectric faults from impulse testing is as follows: The waveform of the terminal current for a reduced magnitude impulse voltage is recorded. Current waveforms for full magnitude impulses are recorded and compared to the current waveform at reduced magnitude. Any differences are indicative of dielectric faults, and careful examination of the waveforms can often locate the proximity of the faults.

A variation of the impulse test, called a "chopped wave" test, is often performed, and its purpose is to simulate the effect of a lightning strike clipped by surge arresters. The test is performed with the same equipment and methods as the impulse test, only a spark gap is added to the terminal of the tested equipment and is set to flash over at a determined level. The spark gap forces the impulse wave to collapse almost immediately, and the effect is similar to superimposing upon a normal impulse wave of 1 μ s rise time a second, slightly delayed impulse of opposite polarity and extremely fast rise time. Figure 3-1 illustrates a chopped wave. The chopped wave produces in the transformer winding a steep-front voltage distribution of opposite and steeper slope than that produced by the normal impulse, with consequent larger turn-to-turn voltages.

The dielectric system of the high-voltage stator winding closely resembles that of a large power transformer, having conductors insulated with turn-to-turn insulation and thick oil-impregnated pressboard cylinders for the line-to-ground insulation. The operating environment of the high-voltage stator will also be similar to that of a transformer, particularly with respect to exposure to lightning strikes. Therefore, the recommended dielectric tests for the high-voltage stator are the same as those for a transformer, namely the overvoltage test and the impulse test. The impulse test can be performed in exactly the same manner as described earlier. For delta-connected windings, the winding phases must not be isolated during the impulse test, because the winding phase breaks will be overstressed. The impulse test can be performed by applying the impulse to one delta terminal with the other two delta terminals grounded, repeating the procedure to apply the impulse to the other terminals.

The overvoltage test must be performed in a somewhat different manner than that described for power transformers, because the high-voltage generator has no low-voltage winding with which to excite the high-voltage winding. Instead, an overvoltage test prescribed for large inductive reactors can be utilized, called a series-resonance test. A capacitor bank of such capacitive reactance as to exactly cancel the inductive reactance of the generator winding is connected in series with the generator, and the series combination is excited with a small, high-frequency motor-generator set.

Section

COMMERCIAL ACCEPTANCE TESTING

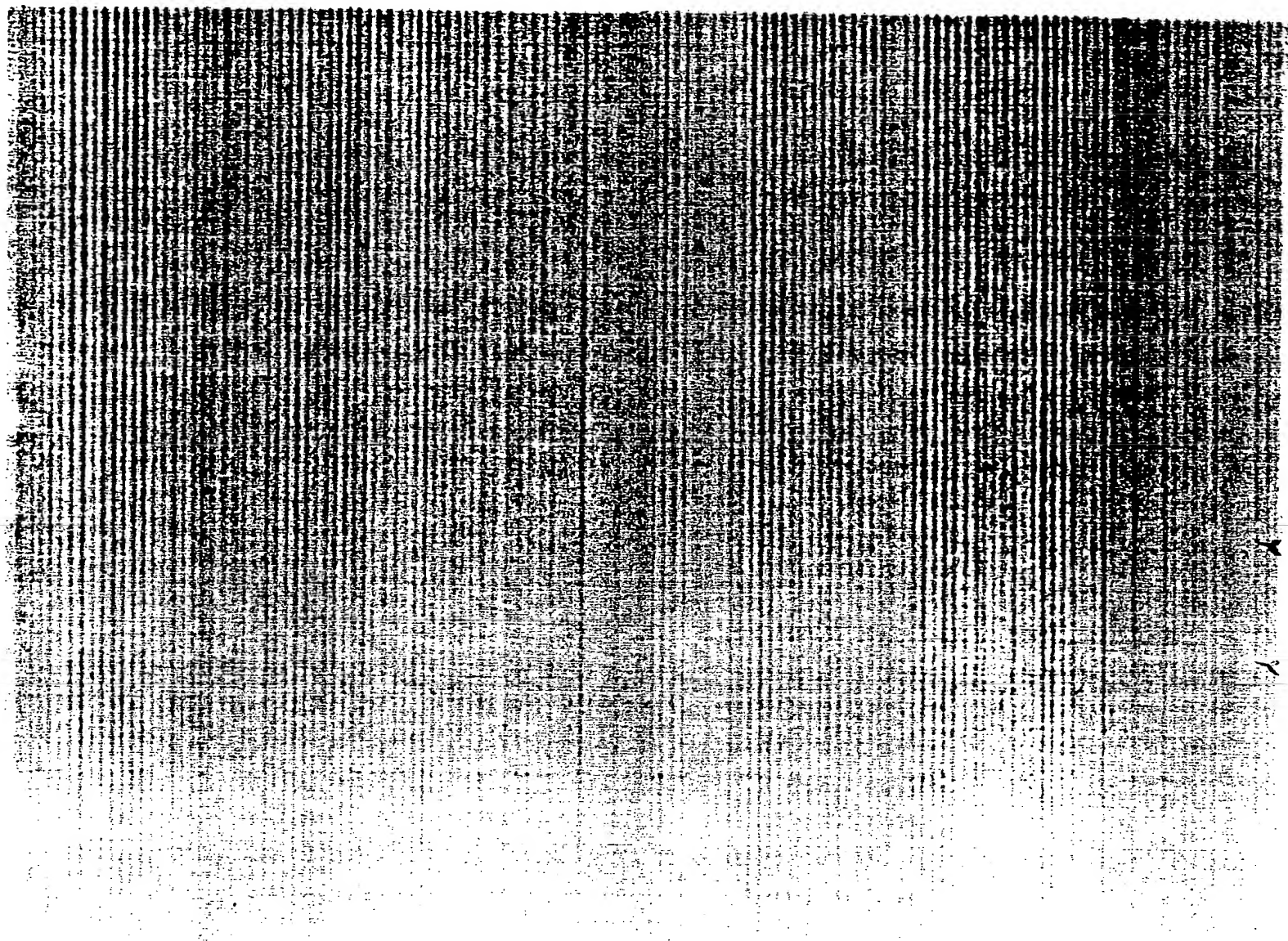
Commercial acceptance testing is performed on the dielectric systems of electrical generation and distribution equipment in order to guarantee that the apparatus contains no manufacturing flaws and will be able to perform in service according to a defined operating environment with a minimum likelihood of dielectric failure over the defined lifetime of the apparatus. The commercial acceptance tests must be tailored to each type of apparatus according to its design details and its defined operating environment, which can include likely overvoltages, range of temperature, and other specifications.

The conductors of a conventional turbine-generator are individually wrapped with line-to-ground insulation and an exterior grounding tape that encompasses all exterior surfaces of the insulation. The insulation of all conductors is tested for the same overvoltage criteria, even though only the conductors near the terminals of the wye-connected winding will receive any full overvoltage during the test. The grounding surfaces situated on all conductors allow insulation tests to be performed prior to the assembly of the conductors into the core. Subsequent insulation tests are performed at various stages of assembly, including completion of assembly. A typical insulation test is the application of approximately twice-rated voltage for one minute. The test apparatus consists of a single-phase variable voltage transformer which is reactively capable of testing an entire winding phase.

The dielectric configuration of a high-voltage power transformer is completely different from that of the conventional generator and consequently requires a different test procedure. The conductors of a transformer are wrapped with only turn-to-turn insulation. Oil-impregnated pressboard barriers, which form alternate layers of fluid and solid dielectric, serve as the line-to-ground insulation between the transformer coils and the grounded core and tank walls. Two different dielectric tests are performed on the transformer. One test is a twice-rated overvoltage test, and the other is an impulse test, which simulates the effects of a lightning strike and imposes very large turn-to-turn voltages. No tests can be performed until the transformer is completely assembled.

The objectives of the overvoltage test are to obtain a twice-rated voltage on the high-voltage winding and to hold it a specified amount of time (typically 7200 cycles). Partial discharges are measured during this test to determine if they fall within standards. Even if there is no breakdown during the overvoltage test, a high level of partial discharges indicates a dielectric fault that may considerably shorten the life of the transformer. The simplest way to obtain this overvoltage on the transformer high-voltage winding is not to impress it directly on the high-voltage winding but to induce it by exciting the low-voltage winding. For twice-rated overvoltage, at least 120 Hz excitation is required in order to avoid over-fluxing the core, although 240 Hz is more typically utilized. The required test apparatus is a small high-frequency motor-generator set.

The impulse test simulates the effects of a lightning strike on the transformer and is performed with a multistage impulse generator. This apparatus is comprised of column-mounted capacitor drums (each capacitor being a "stage") arranged with sphere gaps between the stages. The sphere gaps are adjusted to break down at a specified voltage. The capacitors are charged in parallel from an external dc source until such a level is reached that the sphere gaps flash over. The flashover of the gaps switches the capacitors in series, producing the high-voltage impulse. The level of the impulse crest is coordinated to the specified Basic Impulse Level (BIL) of the tested equipment. The BIL may be typically five times the operating voltage. Series and parallel resistances in the circuit of the impulse generator can be adjusted to control the waveshape of the impulse. The impulse waveshape is specified in terms of the rise time to the crest and the fall time to 50% of the crest voltage, as illustrated in Figure 3-1. A typical impulse has a rise time of $1 \mu s$ and a fall time of $50 \mu s$. The impulse does not distribute uniformly throughout the transformer winding, but tends to bunch up, producing large turn-to-turn voltages within the winding. Figure 3-2 illustrates the



METAL CO TEMPERATURE AND FLOW VELOCITY PROFILES

OUTER LAYER

TEMPERATURES

[illegible][illegible]

VELOCITIES					
	70.9	71.4	71.4	71.3	70.6
45° E	70.6	71.4	71.4	71.3	70.6
67.5					

OUTER LAYER

TEMPERATURES

[illegible]

LOCATION 7	LOCATION 8	LOCATION 9	LOCATION 10	LOCATION 11
58.0 67.7 61.2 70.1	63.5 72.4 65.9 74.8	68.8 77.7 71.2 80.6	73.8 82.7 76.2 85.6	78.8 87.7 81.2 90.6
74.1	76.7	79.2	81.7	84.2
61.1 71.5 63.7 74.1	66.3 76.7 68.0 79.3	71.8 81.2 73.5 84.9	76.8 86.2 78.5 91.9	81.8 91.2 83.5 97.9
74.8	79.5	82.2	84.9	87.5
61.8 72.8 64.5 75.6	67.2 78.3 69.0 81.1	73.7 84.8 76.4 88.5	78.7 89.8 81.4 94.9	83.8 94.9 86.6 100.0
77.6	80.4	83.2	86.0	88.8
61.9 73.2 64.7 76.0	67.3 78.4 69.1 81.2	73.8 84.9 76.5 89.2	78.8 89.9 81.6 94.9	83.9 95.0 87.7 100.0
77.8	80.7	83.5	86.3	89.1
61.9 73.2 64.7 76.0	67.5 78.6 69.2 81.3	74.0 85.1 76.7 89.8	79.0 90.1 81.8 94.9	84.1 95.2 87.9 100.0
77.6	80.4	83.2	86.0	88.8
61.8 72.8 64.5 75.6	67.2 78.3 69.0 81.1	73.7 84.8 76.4 88.5	78.7 89.8 81.4 94.9	83.8 94.9 86.6 100.0
77.6	80.4	83.2	86.0	88.8
61.1 71.5 63.7 74.1	66.3 76.7 68.0 79.3	71.8 81.2 73.5 84.9	76.8 86.2 78.5 91.9	81.8 91.2 83.5 97.9
74.1	76.7	79.2	81.7	84.2
58.0 67.7 61.2 70.1	63.5 72.4 65.9 74.8	68.8 77.7 71.2 80.6	73.8 82.7 76.2 85.6	78.8 87.7 81.2 90.6

VELCITILIS

Figure 2.10-5. 1200 MVA, 500 kV Winding Design Using Transil-Oil Coolant Concept

<p>HIGH VOLTAGE GENERATOR CONDUCTOR AND COILING DESIGN TRANSIL OIL COILANT</p> <p>1200 MVA, 500 KV, 0.9 PF WINDING CIRCUIT DELTA HELICAL WINDING 370 AMPS/SQ CM ARMATURE DENSITY 50 V/MIL INSULATION</p> <p>FIELD WINDING INNER RADIUS 11.0 IN FIELD WINDING OUTER RADIUS 14.0 IN ARMATURE BORE RADIUS 20.0 IN INNER LAYER INNER RADIUS 25.0 IN INNER LAYER OUTER RADIUS 26.5 IN OUTER LAYER INNER RADIUS 39.7 IN OUTER LAYER OUTER RADIUS 41.3 IN CORE INNER RADIUS 47.0 IN ACTIVE LENGTH 246.0 IN</p> <p>PERMANENT CURRENT CIRCUIT CURRENT 1305.6 AMPS RADIAL FLUX, INNER LAYER 400.0 TESLAS TANGENTIAL FLUX, INNER LAYER 0.75 TESLAS RADIAL FLUX, OUTER LAYER 0.48 TESLAS TANGENTIAL FLUX, OUTER LAYER 0.13 TESLAS</p> <p>INNER LAYER *****</p> <p>THERE ARE 204 TURNS PER PHASE BELT THE LAYER IS 7 CONDUCTORS HIGH THE CONDUCTOR AND HYDRAULIC LENGTH IS 260.4 IN THE HELIX ANGLE IS 16.1 DEGREES THE "SLOT WIDTH" IS 0.6306 IN</p> <p>CONDUCTOR SPECS:</p> <p>TYPE GRADE 18 NO. FILAMENTS HIGH 6 NO. FILAMENTS MIDE 11 BAR WIDTH 66 BAR HEIGHT 0.4752 IN COPPER AREA 0.2502 IN CURRENT DENSITY 4751.8 AMPS/SQ IN</p> <p>VERTICAL DIVIDER: THICKNESS 0.1644 IN VOLTAGE STRESS 75.6 V/MIL</p> <p>COILANT PASSAGE: WIDTH 0.4252 IN HEIGHT 0.0607 IN AREA 0.02501 SQ IN HYDRAULIC DIA 0.1062 IN</p>	<p>STAINLESS STEEL COILING TUBES:</p> <p>WALL THICKNESS 0.020 IN INSULATION THICKNESS 0.005 IN TUBE WIDTH 0.405 IN TUBE HEIGHT 0.101 IN LOSSES 1.022 W/IN</p> <p>CONDUCTOR LOSSES:</p> <p>DC LOSSES 1.463 W/IN AC LOSSES 0.094 W/IN TOTAL 2.557 W/IN</p> <p>COILING PERFORMANCE (AVERAGED):</p> <p>PRESSURE DROP (INPUT) 50.00 LBS/SQ IN COILANT INLET TEMP 45.00 DEGREES CENTIGRADE FLOW VELOCITY 70.12 IN/SEC TOTAL FLOW 947.5 GAL/MIN REYNOLDS NO. 706.7 COILANT OUTLET TEMP 61.23 DEGREES CENTIGRADE</p> <p>OUTER LAYER *****</p> <p>THERE ARE 204 TURNS PER PHASE BELT THE LAYER IS 7 CONDUCTORS HIGH THE CONDUCTOR AND HYDRAULIC LENGTH IS 277.0 IN THE HELIX ANGLE IS 27.4 DEGREES THE "SLOT WIDTH" IS 0.8969 IN</p> <p>CONDUCTOR SPECS:</p> <p>TYPE GRADE 16 NO. FILAMENTS HIGH 2 NO. FILAMENTS MIDE 14 BAR WIDTH 28 BAR HEIGHT 0.7546 IN COPPER AREA 0.1078 IN CURRENT DENSITY 7047.9 AMPS/SQ IN</p> <p>VERTICAL DIVIDER: THICKNESS 0.1423 IN VOLTAGE STRESS 87.5 V/MIL</p> <p>COILANT PASSAGE: WIDTH 0.6946 IN HEIGHT 0.0457 IN AREA 0.03173 SQ IN HYDRAULIC DIA 0.0857 IN</p>	<p>STAINLESS STEEL COILING TUBES:</p> <p>WALL THICKNESS 0.025 IN INSULATION THICKNESS 0.005 IN TUBE WIDTH 0.745 IN TUBE HEIGHT 0.066 IN LOSSES 1.327 W/IN</p> <p>CONDUCTOR LOSSES:</p> <p>DC LOSSES 2.208 W/IN AC LOSSES 0.270 W/IN TOTAL 2.478 W/IN</p> <p>COILING PERFORMANCE (AVERAGED):</p> <p>PRESSURE DROP (INPUT) 50.00 LBS/SQ IN COILANT INLET TEMP 45.00 DEGREES CENTIGRADE FLOW VELOCITY 70.12 IN/SEC TOTAL FLOW 947.5 GAL/MIN REYNOLDS NO. 446.2 COILANT OUTLET TEMP 71.18 DEGREES CENTIGRADE</p> <p>INSULATION *****</p> <p>INSULATION VOLUME 1184591.4 CUBIC INCHES PERCENT COILING AREA 0.1 COILING PASSAGE WIDTH 0.100 IN COILING PASSAGE HEIGHT 0.100 IN HYDRAULIC DIAMETER 0.1000 IN</p> <p>LOSSES DISSIPATION FACTOR 0.004 WATTS/CUBIC INCH 0.49 PERCENT</p> <p>COILING PERFORMANCE (AVERAGED):</p> <p>PRESSURE DROP (INPUT) 50.00 LBS/SQ IN COILANT INLET TEMP 45.00 DEGREES CENTIGRADE FLOW VELOCITY 75.47 IN/SEC TOTAL FLOW 94.4 GAL/MIN REYNOLDS NO. 626.1 COILANT OUTLET TEMP 45.51 DEGREES CENTIGRADE</p> <p>WINDING EFFICIENCY *****</p> <p>TOTAL CONDUCTOR LOSSES 2293.7 IN COILING TUBE LOSSES 1380.1 IN INSULATION LOSSES 9.3 IN LIQUID PUMPING LOSSES 36.8 IN TOTAL LOSSES 3726.4 IN</p> <p>EFFICIENCY DROP *****</p>
---	--	--

Figure 2.10-5. 1200 MVA, 500 kV Winding Design Using Transil Oil Coolant

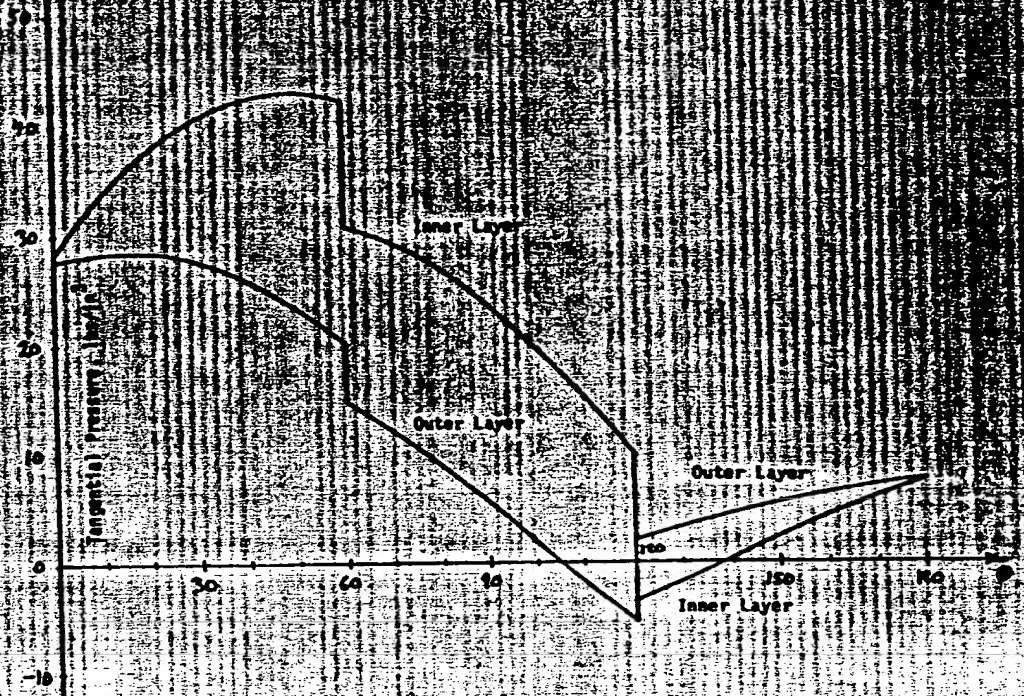


Figure 2.10-4. Tangential Winding Pressure on Three-Phase Short Circuit from Rated Voltage, 90° After Fault. 1200 MVA, 500 kV, $X'' = .215$

2.10.3 Conductor and Conductor Cooling Calculations

Conductor and conductor cooling calculations have been performed for a 1200 MVA, 500 kV monolith cylinder armature having helical coils. The cylinder dimensions were taken from Table 2.10-1 for the design having the 11 and 14 in. field winding radii. The technique and assumptions for performing the conductor and conductor cooling calculations are exactly the same as described in Section 2.6. The computer output for a winding design using transil oil coolant is contained in Figure 2.10-5. The required coolant flow is 1687 gal/min at a pressure drop of 50 psi. Both quantities are approximately double that required for the 600 MVA armature (891 gal/min and 22 psi, respectively).

Figure 2.10-2. Tangential Winding Pressure on Three-Phase Short-Circuit from Rated Voltage, 180° After Fault. 1200 MVA, 500 kV, $X'' = .215$

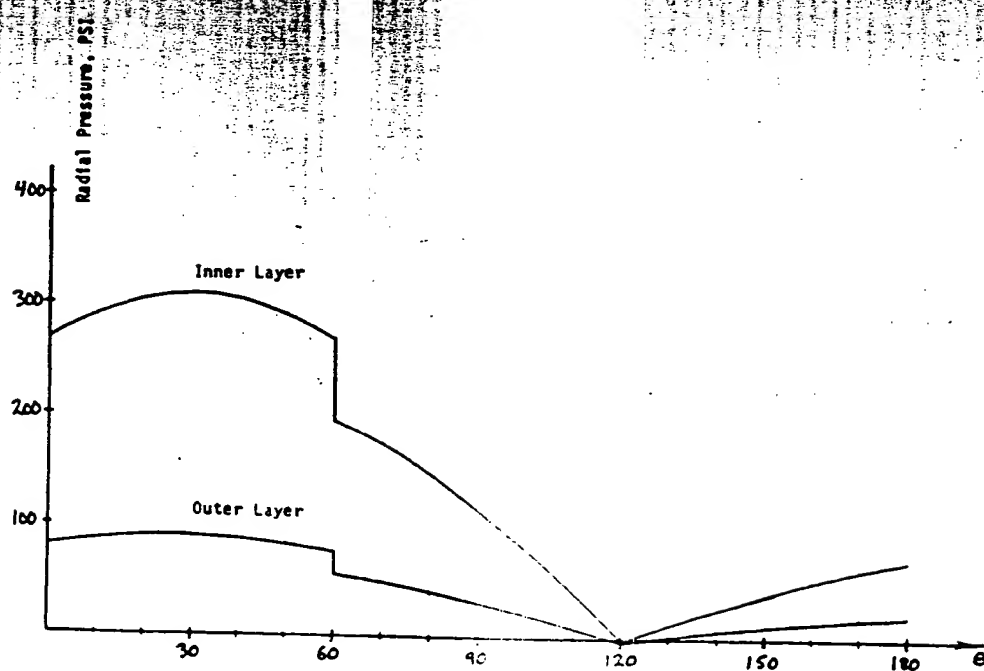


Figure 2.10-3. Radial Winding Pressure on Three-Phase Short Circuit from Rated Voltage, 90° After Fault. 1200 MVA, 500 kV, $X'' = .215$

The sizing radii of the helical coil armatures are approximately equal to those of the diamond coil armatures, but the helical coil armature active lengths are longer. However, when the end arms of the diamond coils are accounted, the overall lengths are approximately equal.

For both types of coils, the active lengths for the smaller rotor diameters are excessively long, and the designs with the larger rotor diameters are judged superior.

2.10.2 Winding Forces

Sudden short circuit winding forces have been calculated for a 1200 MVA, 500 kV monolith cylinder armature having diamond coils. The cylinder dimensions were taken from Table 2.10-1 for the design with the 11 and 14 in. field winding radii. The technique and assumptions for performing the winding force calculations are exactly the same as those described in Section 2.3. The winding force distributions are illustrated in Figures 2.10-1 through 2.10-4 and can be compared to Figures 2.3-5 through 2.3-8 of the 600 MVA, 345 kV monolith cylinder armature. The force distributions are similar in form and magnitude to those calculated for the 600 MVA armature, and it was felt unnecessary to perform mechanical stress calculations for the 1200 MVA armature, since the stress calculations for the 600 MVA armature appear low.

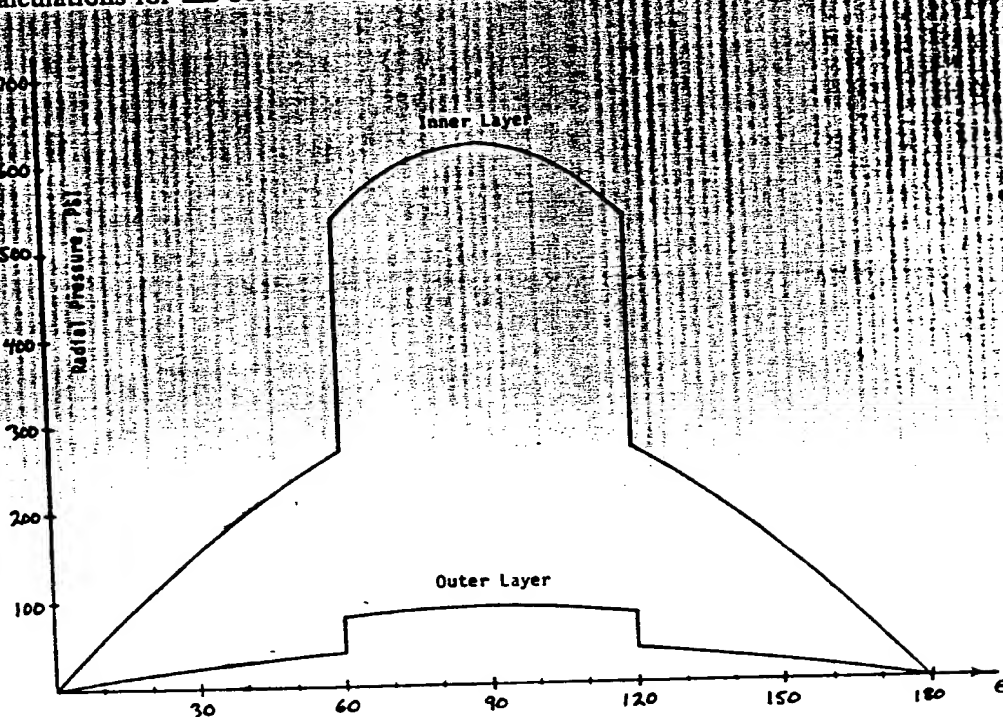


Figure 2.10-1. Radial Winding Pressure on Three-Phase Short Circuit from Rated Voltage, 180° After Fault. 1200 MVA, 500 kV, $X'' = .215$

2.10 DESIGN SUMMARY OF THE MONOLITH CYLINDER ARMATURE AT 1200 MVA, 500 kV

2.10.1 Sizing Studies

Computer sizing studies have been performed for a monolith cylinder armature with a rating of 1200 MVA and 500 kV. The technique and assumptions for performing these studies are exactly the same as described in Section 2.2. Table 2.10-1 contains a sizing study for helical coil windings and Table 2.10-2 contains a sizing study for diamond coil windings. Both studies were performed at an insulation dielectric stress of 50 kV/in.; greater values of dielectric stress were not attempted because the end-region electrical creepage becomes severe. For the same reason, 765 kV ratings were not attempted.

Table 2.10-1

HIGH VOLTAGE GENERATORS AT 1200 MVA, 500 kV HELICAL COIL WINDINGS 300 A/cm² CURRENT DENSITY, 50 kV/in. INSULATION STRESS

R ₁	R ₂	R ₃	R ₄	R ₅	R ₆	R ₇	R ₈	R ₉	R ₁₀	R ₁₁	L	X''	X'	X
7	10	12.5	13.5	15.0	20.8	22.4	33.9	35.0	40.7	51.6	752	0.244	0.272	0.295
8	11	13.5	15.5	17.0	22.8	24.5	36.0	37.2	42.9	55.8	556	0.240	0.272	0.297
9	12	14.5	16.5	18.0	23.8	25.7	37.3	38.5	44.3	59.5	408	0.240	0.271	0.299
10	13	15.5	17.5	19.0	24.8	26.9	38.5	39.9	45.7	63.3	310	0.239	0.271	0.301
11	14	16.5	18.5	20.0	25.8	28.1	39.7	41.3	47.0	67.2	246	0.240	0.272	0.305
12	15	17.5	20.5	22.0	27.8	30.2	41.7	43.4	49.2	71.6	210	0.238	0.272	0.305

- | | |
|--|--|
| R ₁ — field winding inside radius, in. | R ₉ — outer conductor layer outside radius, in. |
| R ₂ — field winding outside radius, in. | R ₁₀ — core inside radius, in. |
| R ₃ — shield inside radius, in. | R ₁₁ — core outside radius, in. |
| R ₄ — shield outside radius, in. | L — length, in. |
| R ₅ — armature inside radius, in. | X'' — subtransient reactance, p.u. |
| R ₆ — inner conductor layer inside radius, in. | X' — transient reactance, p.u. |
| R ₇ — inner conductor layer outside radius, in. | X — synchronous reactance, p.u. |
| R ₈ — outer conductor layer inside radius, in. | |

Table 2.10-2

HIGH-VOLTAGE GENERATORS AT 1200 MVA, 500 kV DIAMOND COIL WINDINGS 150 A/cm² CURRENT DENSITY, 50 kV/in. INSULATION STRESS

R ₁	R ₂	R ₃	R ₄	R ₅	R ₆	R ₇	R ₈	R ₉	R ₁₀	R ₁₁	L	X''	X'	X
7	10	12.5	14.5	16.0	21.8	24.4	36.0	37.6	43.4	53.5	575	.212	.270	.320
8	11	13.5	15.5	17.0	22.8	25.7	37.3	39.1	44.9	57.0	404	.214	.271	.325
9	12	14.5	17.5	19.0	24.8	27.8	39.3	41.3	47.1	61.1	314	.209	.270	.326
10	13	15.5	18.5	20.0	25.8	29.0	40.5	42.7	48.4	64.8	224	.210	.268	.327
11	14	16.5	19.5	21.0	27.8	31.0	42.5	44.7	50.5	69.0	194	.215	.268	.328
12	15	17.5	20.5	22.0	28.8	32.1	43.7	46.0	51.7	72.8	154	.217	.267	.329

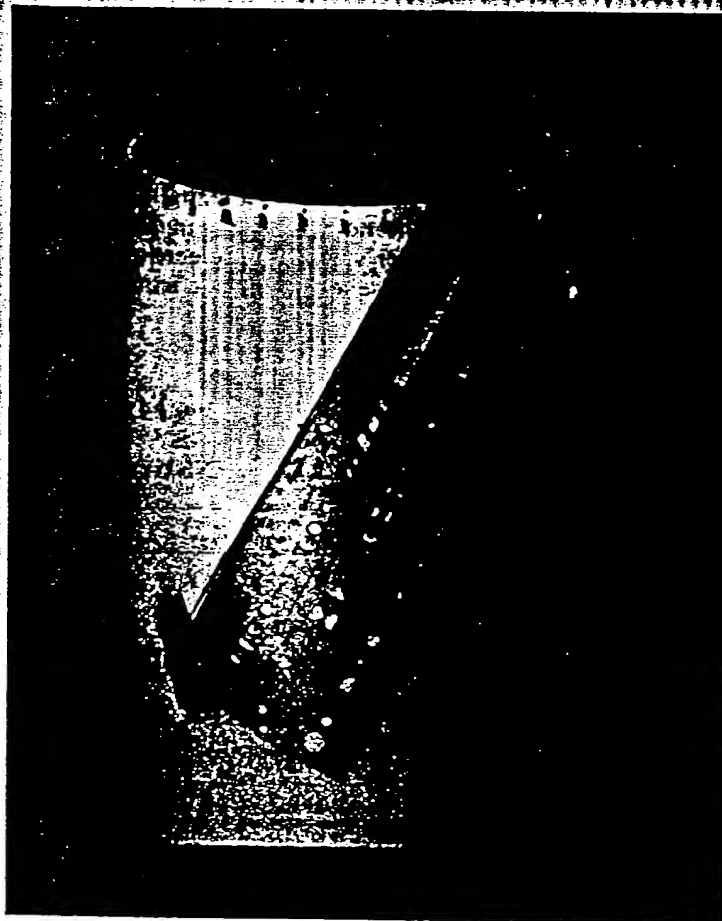


Figure 2.9-4. Fabrication of a Horizontal Divider

cylinder has been built on, the polygonal surface for the polygonal core-to-armature interface is machined. The completed armature is inserted into the frame and core assembly, followed by the attachment of terminal leads and frame-end parts. After the stator is completely sealed, the drying and oil impregnating can be performed.

The mechanical characteristics of pressboard with respect to its moisture content must be discussed. Pressboard supplied from the manufacturer has a 5% moisture content, which is the equilibrium condition with atmospheric humidity. After a transformer is assembled, prior to oil impregnation, it is dried to a moisture content of less than 0.5%. During this final drying, even the best of pressboards undergo a slight compression relaxation. In a transformer, the only concern is with the axial tightness of the coil assemblies; therefore, after drying is completed, the coil assemblies are retightened with the clamping mechanisms that have been provided for this purpose. However, no equally effective mechanisms exist for retightening such relaxation in a high-voltage armature; therefore, it may be desirable to predry the pressboard pieces before assembly. It would then be necessary to assemble the armature in a low-humidity controlled compartment, to prevent the pressboard from reabsorbing moisture from the atmosphere.

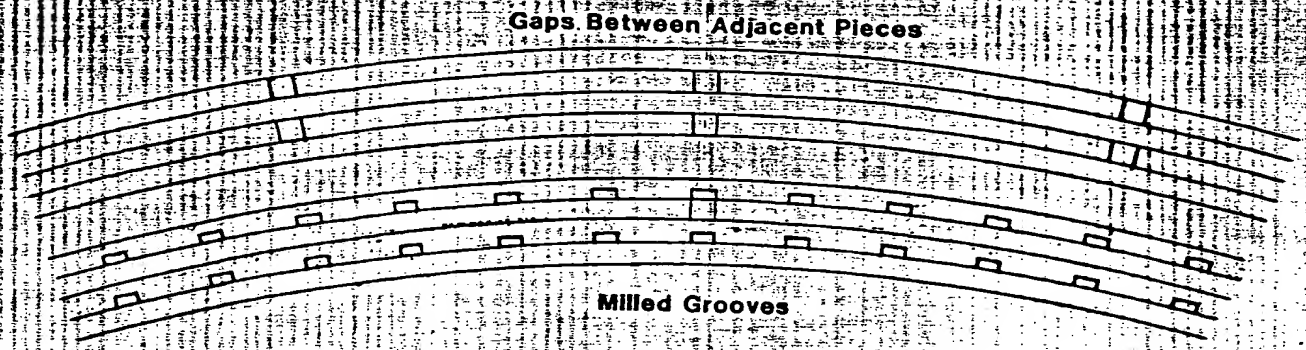


Figure 2.9-2. Axial Ventilation Passages in the Insulation Cylinders

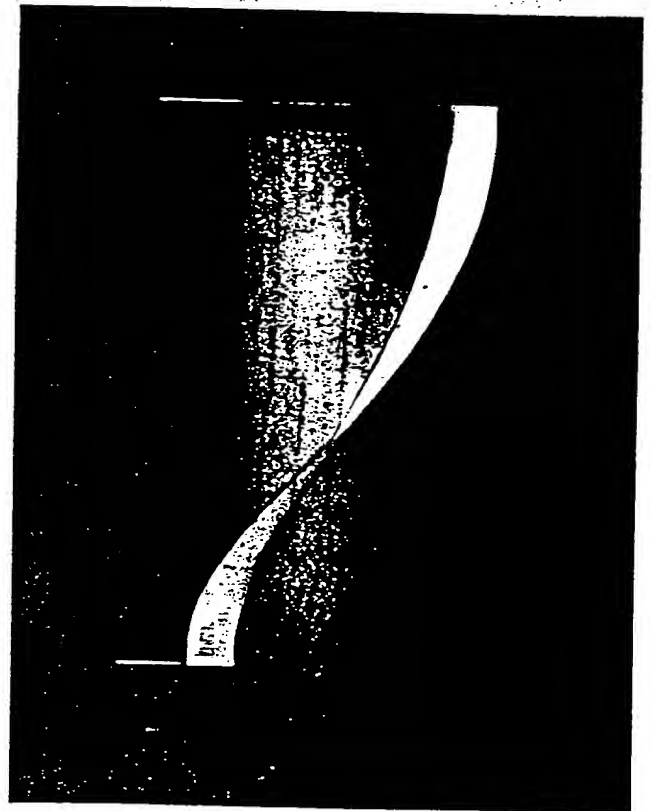
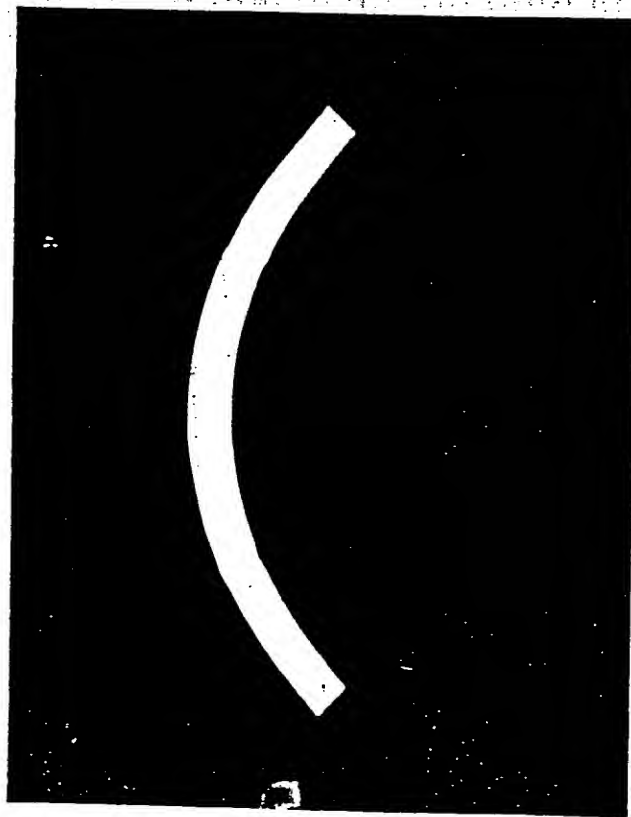


Figure 2.9-3. Fabrication of a Vertical Divider

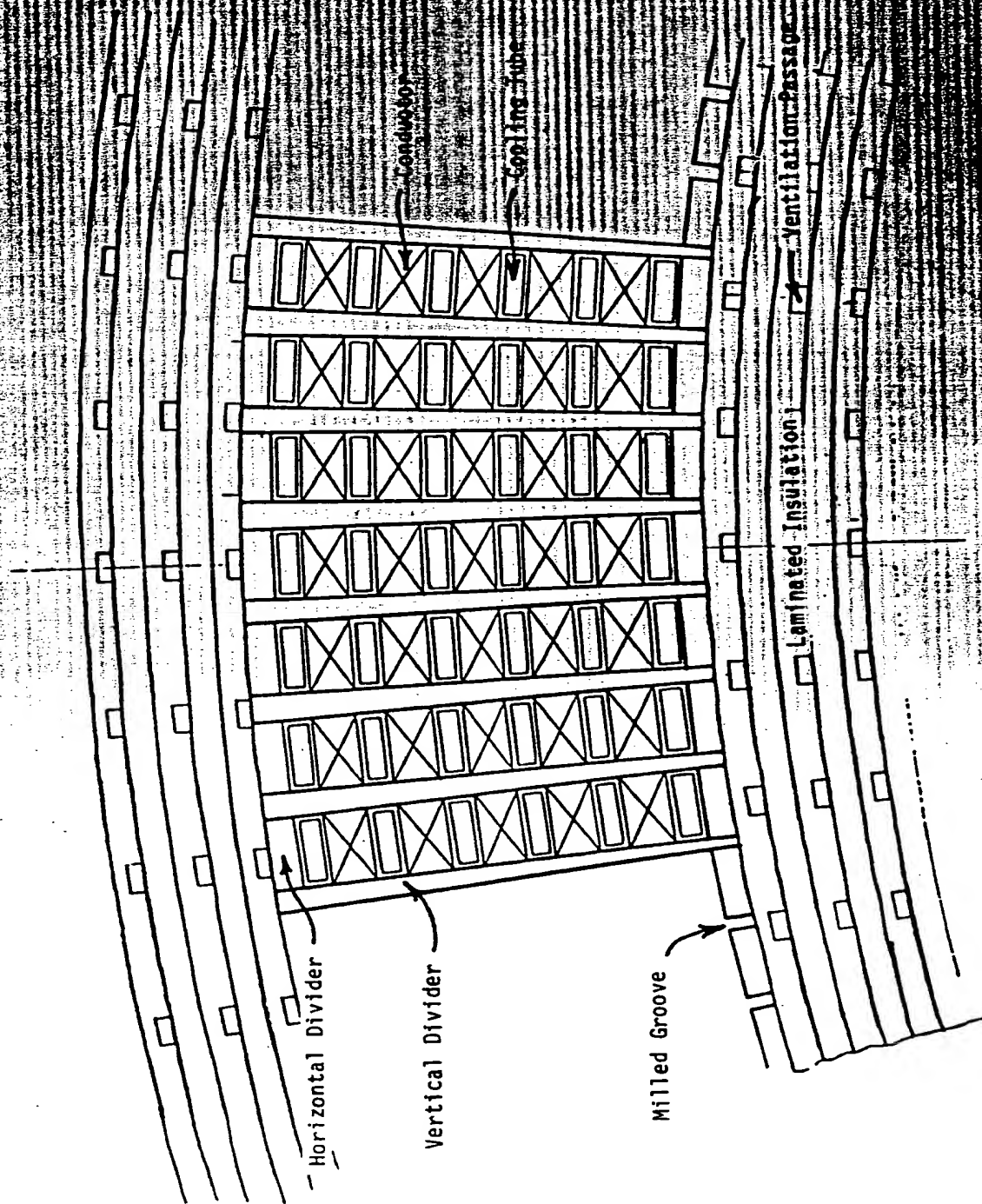


Figure 2.9-1. Laminated Construction of the Monolithic Cylinder Assembly

2.9 ARMATURE MANUFACTURE

The preferred insulation material for the monolith cylinder high-voltage armature is oil-impregnated pressboard, so the manufacture of the high-voltage armature will be similar to the manufacturing of a high-voltage step-up transformer. In the manufacture of a transformer, dry sheets of pressboard are fabricated into the necessary insulation parts that are assembled with the windings and core. The completed transformer assembly is then thoroughly dried to remove all possible moisture from the pressboard parts. Finally, the assembly is flooded with oil.

Pressboard is manufactured from pure and high-quality cellulose fiber. There are several grades of pressboard available from manufacturers, and the high-voltage armature would require the highest grade, referred to as "precompressed" pressboard. During the manufacture of this product, 2 to 3 in. buildups of wet deposited fiber layers are simultaneously subjected to heat and pressure during the pressing process. The heat press process improves the bonding of the fibers at the points where they touch, and the result is a pressboard with superior mechanical properties. The pressboard is available in thickness up to 0.315 in.

Structures as thick as the insulation cylinders of the monolith cylinder armature must be constructed from bonded pressboard laminations. Figure 2.9-1 illustrates a laminated construction for the monolith cylinder armature. The horizontal and vertical dividers that are incorporated in the conductor layers are also constructed of pressboard. There are two types of adhesive available for bonding the laminations. The preferred adhesive is a polyester resin, because it is waterless. However, the resulting adhesive layer is impermeable to oil, and oil impregnation must be accomplished tangentially through each individual pressboard lamination. The second adhesive, casein glue, provides an adhesive layer that is permeable to oil. This adhesive is water-based, and additional drying of the assembly is consequently required.

Axial ventilation passages must be provided in the laminated structure to facilitate drying and oil impregnating. The final drying process of a pressboard product involves creating a vacuum to draw water vapor from the interior of the pressboard through the ventilation passages. When the ventilation passages are numerous and closely spaced, the water vapor has less distance to travel and drying is accelerated. The axial ventilation passages facilitate oil impregnation in the same manner. Figure 2.9-2 illustrates two different configurations for the ventilation passages. In the first configuration, axial grooves are milled into the pressboard laminations prior to their assembly. In the second configuration, pressboard pieces of a peripherally short span are assembled with gaps appearing between adjacent pieces; these gaps serve as the axial ventilation passages.

The geometry of the horizontal and vertical dividers is complicated by their helical twist (since they follow the helical path of the conductors). Figure 2.9-3 demonstrates how the vertical dividers can be fabricated from arc-shaped pieces of pressboard that are twisted into the helix. The mathematical derivation of this fabrication is contained in Appendix G. Figure 2.9-4 demonstrates how the horizontal dividers can be fabricated from flat rectangular pieces of pressboard. If the required twisting to form these parts is beyond the capability of dry pressboard, the pressboard may be moistened slightly, bent to shape, and redried.

The monolith cylinder armature is constructed from the inside out, so the fiberglass-epoxy bore seal tube is constructed first by building it around a cylindrical mandril. The inner grounding surface is attached to the outer surface of the bore seal tube. The inner insulation cylinder is then constructed by laminating pressboard sheets one layer at a time. The vertical dividers extend above and below the confines of the conductor and cooling tube columns, so the vertical dividers of the inner conductor layer can be anchored to the inner insulation cylinder by milling grooves into the outer surface of inner insulation cylinder. The vertical dividers are placed into the grooves, and the columns of conductors and cooling tubes are placed between the vertical dividers. Adhesive is applied to all adjoining surfaces. Horizontal dividers are placed on top of the conductor columns to match the level of the vertical dividers. The center insulation cylinder can now be built on. The outer conductor layer is assembled in the same manner as described for the inner conductor layer, and the series loop connections are performed directly afterwards. After the outer insulation

HIGH VOLTAGE GENERATOR CORE COOLING DESIGN TRANSIL OIL COOLANT 400 KVA, 345 KV, 0.9 PF	
CORE DIMENSIONS	
CORE INNER RADIUS	37.9 INCHES
CORE OUTER RADIUS	55.4 INCHES
CORE LENGTH	173.0 INCHES
CORE WEIGHT	230873 LBS
CORE LOSSES	
FLUX DENSITY	1.5 TESLAS
LOSS DENSITY	0.176 WATTS/CUBIC INCH
TOTAL LOSSES	158.7 KW
COOLANT PASSAGES	
NUMBER	48
DIAMETER	0.340 INCHES
AREA	0.001 INCHES
COOLING PERFORMANCE	
PRESSURE DROP (INPUT)	22.0 LBS/SQ IN
COOLANT INLET TEMP	45.0 DEGREES CENTIGRADE
FLOW VELOCITY	123.8 IN/SEC
TOTAL FLOW	140.1 GAL/MIN
REYNOLDS NO.	4037.4
COOLANT OUTLET TEMP	55.8 DEGREES CENTIGRADE
CORE MAXIMUM TEMP	73.1 DEGREES CENTIGRADE

Figure 2.8-6. Core Cooling Performance

Reference

- 2.8-1. *Electrical Materials Handbook*, Allegheny Ludlum Steel Corporation, Pittsburgh, PA., page IX/3.

Enough uniformly distributed cooling passages should be specified to limit temperature rise in the core iron between the cooling passages. Forty-eight cooling passages will be specified in this design. This allows two radially distributed cooling passages to be aligned with each flat and each vertex of the twelve-sided core-to-armature interface illustrated in Figure 2.8-3. The temperature distribution within the core iron requires a field calculation that will not here be attempted, but crude approximations of the problem indicate that the temperature rises between the cooling passages are not more than a few degrees centigrade.

Figure 2.8-6 illustrates the computer output for the core cooling calculations. The core dimensions and weight are listed under the section entitled "Core Dimensions." The section "Core Losses" lists the core flux density, the loss density, and the total losses. The section "Coolant Passages" lists the number and dimensions of the cooling passages. The section "Cooling Performance" is initiated with listings of the pressure drop and coolant inlet temperature. The core coolant is fed from the same coolant flooded end region that supplies the armature cooling system, so these quantities are set equal to values used in an armature cooling calculation contained in Figure 2.6-1. The flow velocity, total flow, Reynolds number, and coolant outlet temperature are listed here. The core maximum temperature is the temperature of the cooling passage walls at the outlet. The flow velocity of this cooling design is rather high, and the core maximum temperature is lower than the allowable 90 °C. The Reynolds number is close to 4000, which is the lower boundary of fully turbulent flow. A better design could be performed by shrinking the cooling passage diameters to lower the flow velocity and raise the core temperature, but the Reynolds number would lower into the transition region where the flow and heat transfer properties are not well defined. A small testing program, however, could be initiated to determine the flow and heat transfer properties for promising cooling configurations.

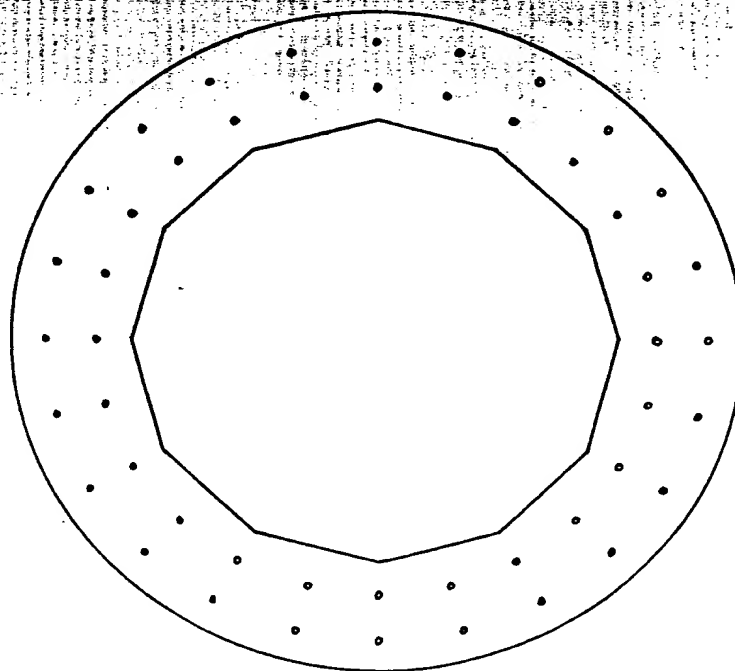


Figure 2.8-5. Placement of Core Cooling Passages

2.8.1 Core Cooling Design

The stator core of the high-voltage generator can be cooled by pumping coolant from the coolant flooded end regions through axial coolant passages that are formed from the cumulation of circular punchouts in the core laminations. The diametrical size of the core cooling passages is not limited, so it is possible to make the cooling passages large enough to allow turbulent flow of the transfer coolant. Heat transfer properties are enhanced by designing for turbulent instead of laminar coolant flow.

The equations and the technique for performing the cooling calculations are described in Section 2.6; it will not be necessary to repeat them here. The only difference between the core cooling and the armature winding cooling is that the cooling passages here are circular, so the hydraulic diameter specified in the equations is the same as the actual diameter.

The core losses can be calculated from material manufacturers' curves that relate core losses as a function of flux density. Figure 2.8-4, which was taken from Reference 2.8-1, illustrates a core loss curve for 14 mil grain-orientated silicon steel, a standard core lamination material.

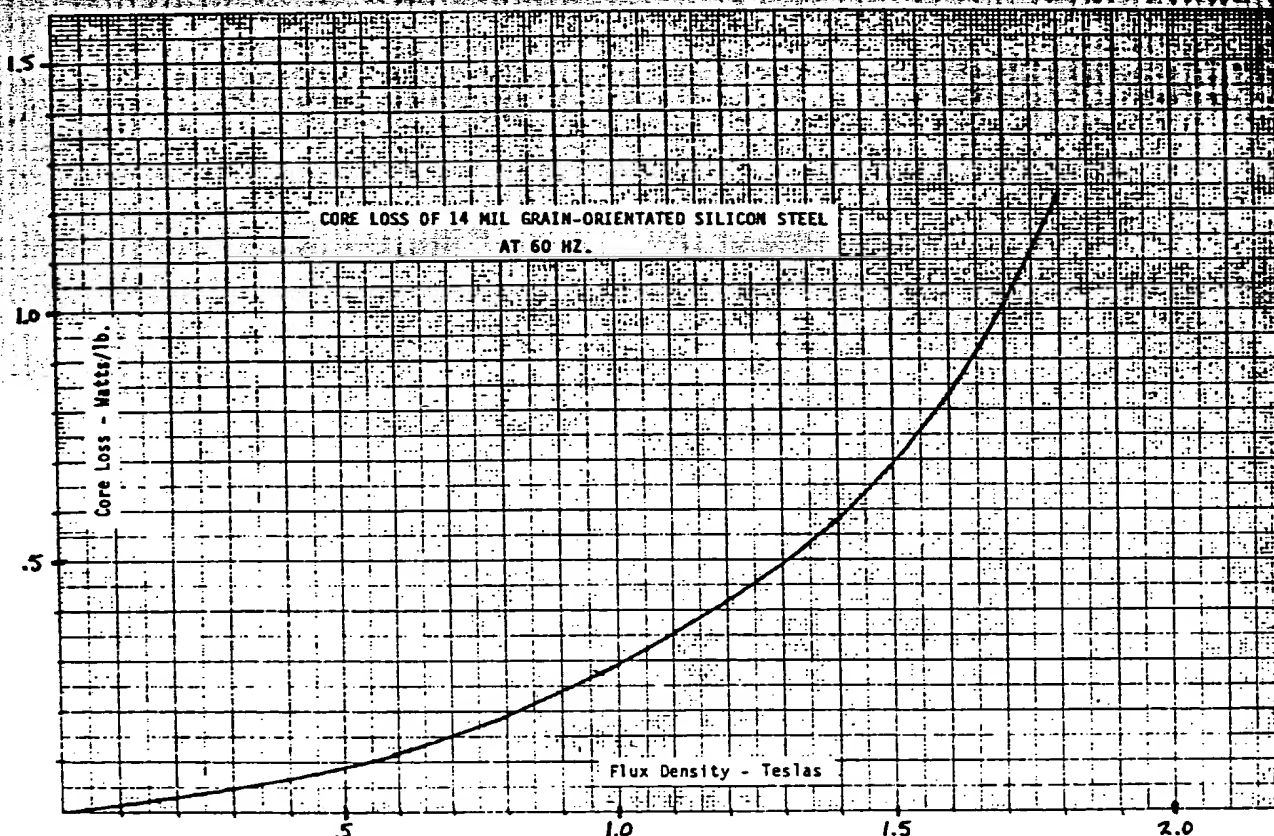


Figure 2.8-4. Core Loss of 14 Mil Grain-Orientated Silicon Steel at 60 Hz

Two methods of removing the rotor windage friction losses have been considered. The first system, illustrated in Figure 2.8-1, uses a rotor-mounted fan which would draw air from the main floor at the collector end of the generator and discharge the heated air at the turbine end of the generator. This approach will require air filters and sound suppression devices at each end of the generator. A potential problem with this cooling system is the large area of the armature inner surface that is exposed to air, raising the possibility of moisture migration through the armature inner surface and consequent contamination of the armature cooling fluid. This problem can be eliminated if the armature bore seal tube is made to be moisture impermeable. The second system reduces rotor windage losses by operating the rotor in a very low pressure (vacuum) environment. This system also eliminates any danger of moisture migration into the armature structure. Vacuum seals and pumps must be incorporated, along with a small liquid-cooled heat exchanger placed in the air gap to remove what little heat is generated in the vacuum atmosphere.

2.8.2 Core-To-Armature Clamping Mechanism

The polygonal core-to-armature interface is described in Section 2.4.2. The mechanical stress analysis performed in that section indicates that the concept is acceptable with respect to the mechanical stresses that are developed in the armature structure during armature sudden short circuit. The design details for implementing the polygonal core-to-armature interface must now be addressed.

The greatest difficulty in implementing this concept is providing and maintaining a tight fit between the armature structure and the core. Any looseness in this interface will allow vibrational motion and consequent chafing and erosion of the outer insulation cylinder of the armature structure. There is no difficulty in manufacturing and machining the components to the tolerances required to provide this tight fit, but a problem arises during assembly, since it may be very difficult to slide an armature structure into a core when there is such a close fit between the components. Such an assembly step will be required unless the core is built around the armature structure (an option that may compromise the structural integrity of the core and frame and may prohibit convenient disassembly of the armature structure from the core if it should become necessary).

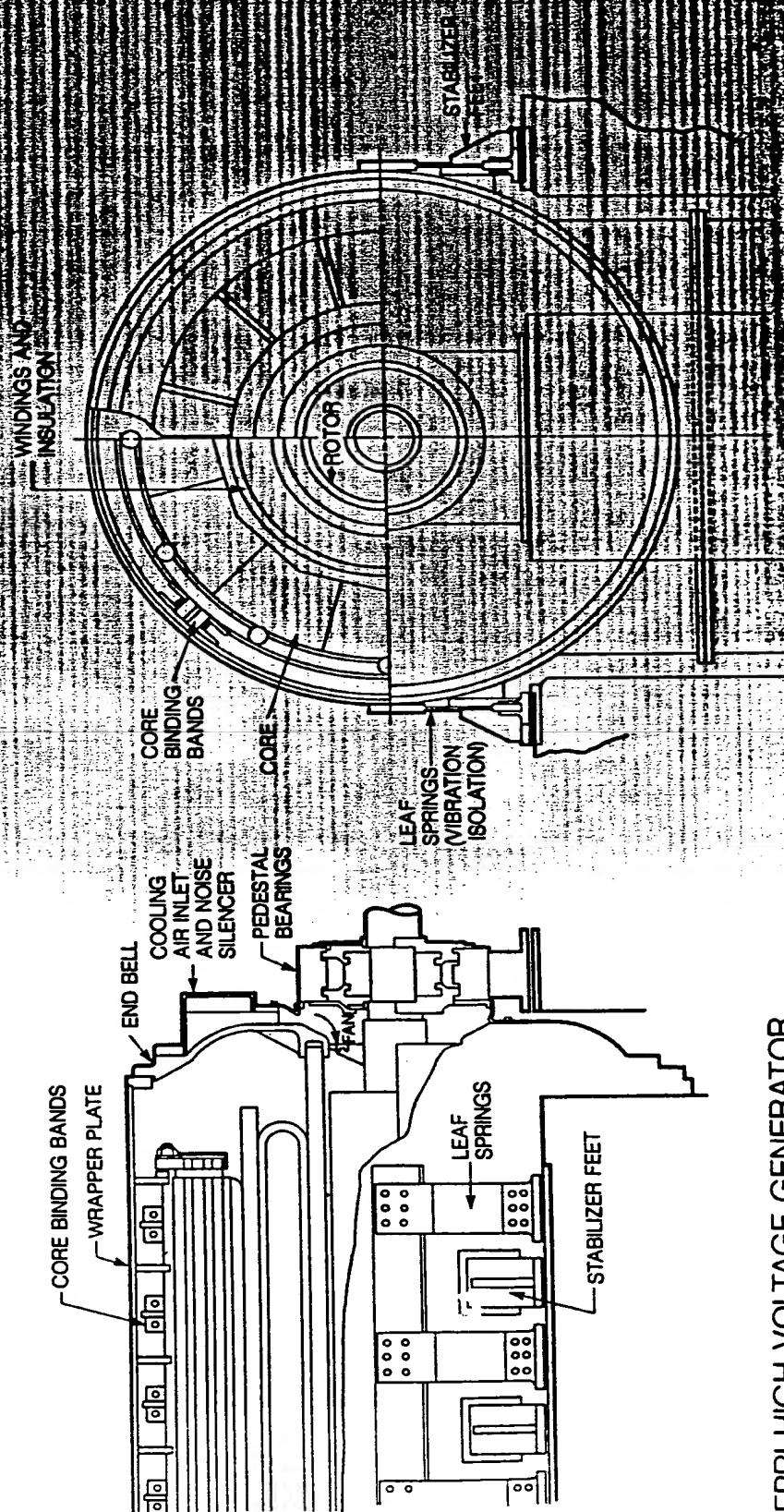
The design of the core-to-armature interface must allow for enough clearance at the interface to allow for an unencumbered insertion of the armature structure into the core. Tightening of the interface must come after the assembly. Figure 2.8-3 illustrates a concept for a tightening mechanism for the polygonal interface. Tightening bolts are placed between axial gaps in the core and are distributed around the entire periphery. The tips of the tightening bolts fit into a stainless steel pressure strip which distributes the tightening stresses from the bolts to the pressboard pressure blocks. The pressboard pressure blocks abut against the flats of the armature structure and have a triangular-shaped cross section that further distributes the tightening stresses to the armature structure. The guide blocks and threaded holding blocks of the tightening bolts are sandwiched between laminations and welded in place. Space blocks that are shaped like I-beams are incorporated into the sandwich to increase the axial compression rigidity of the assembly. The tightening assemblies are repeated at regular intervals in the axial direction. The metallic parts of the assembly should be made of stainless steel in order to limit eddy current heating.

The tightening mechanism allows retightening to be performed if the armature structure suffers compression relaxation.

at the frame outer surface. This design allows a significant reduction in the core-outer-surface frame-outer-surface distance as compared to that of conventional generators. It is estimated that a maximum core outer diameter of 142 in. could be accommodated with this design. The leaf springs are positioned on both sides of the frame and are attached to the frame at its vertical centerline. But because the leaf springs provide little restraint to gross horizontal motion, stabilizer feet are positioned on both sides of the frame to limit gross horizontal motion. The described leaf spring frame design has been used successfully in the past. Figure 2.8-2 is a photograph of one design used in the 1950's on multipiece generator frame designs. The leaf spring frame design depends on a solid connection between the frame and core to allow the frame to vibrate integrally with the core. Figure 2.8-1 illustrates a core-to-frame connection mechanism. The frame and keybars are manufactured as solidly welded assemblies. After the core is assembled into the frame, the keybars are tightened or compressed against the core by large heavy circumferential bands. These bands may have to be manufactured in three or four sections to provide the necessary compression forces over the full circumference of the frame and core. The radial vibration motion of the frame will follow that of the core, and 1.5 to 3.0 mils peak-to-peak vibration motion may be experienced. At these vibration amplitudes, audible noise levels may exceed acceptable noise standards. Thus, a noise suppression housing may be required to be placed around the complete generator. The high frame vibration levels will be transferred to the frame end bells, so it will be necessary to isolate the rotor bearings from the frame. This bearing isolation is accomplished by using separate pedestal bearings which are mounted directly to the foundation.



Figure 2.8-2. Application of a Leaf Spring Frame Design to a Conventional Generator



EPRI HIGH VOLTAGE GENERATOR

Figure 2.8-1. Leaf Spring Frame Design for the High-Voltage Generator

2.4 STATOR FRAME AND CORE DESIGN

2.4.1 Stator Frame Design

The stator frame design is critical to the successful performance of large steam-turbine-driven generators. In conventional hydrogen-cooled generators, the stator frame is required to perform the following functions:

- Isolate core vibration from the foundation
- Provide ventilation circuits for the hydrogen cooling gas
- Contain the required hydrogen pressure
- Incorporate rotor bearings in the end shields to minimize rotor bearing spans and bearing costs

Due to railroad shipping limitations, frame outside diameters are limited to approximately 13.5 ft. This railroad shipping limitation, along with the frame functional requirements, controls the magnetic dimensions of the largest size units that can be built today or in the future. For example, for present-day frame designs which incorporate single-piece economical frames, the core vibration isolation requirements of two-pole generators limit the core outside diameters to between 115 and 120 in. Greater core diameters require considerably different frame designs to provide the core vibration isolation requirements.

A review of the 600 MVA and 1200 MVA high-voltage generator sizing studies (Sections 2.7 and 2.10) shows that the designs which would most likely be selected to minimize rotor bearing spans and potentially high rotor bending stresses would have large outside diameters of 111.2 in. and 134.4 in., respectively. The 1200 MVA high-voltage generator core diameter is significantly greater than the presently anticipated maximum limit of 120 in. Thus, for at least the larger ratings, high-voltage superconducting generators will require new frame and core isolation designs. The new frame design will be required to perform the following functions:

- Isolate core vibration from the foundation and rotor bearings
- Contain the liquid cooling medium and provide cooling circuits for the core, winding, and insulation
- Ensure that air and moisture will not penetrate the frame or winding support system. Such penetration would contaminate the cooling medium and would cause premature electrical failure of the armature.
- Provide a shipping package which will not allow air and moisture penetration during transportation to the power station

The internal environment control functions are similar to those required by high-voltage step-up transformers.

A frame design concept which addresses these requirements is illustrated in Figure 2.8-1. The frame, end shields, and armature structure are assembled at the manufacturer's plant to provide a container which is as close to a hermetically sealed system as possible. Where shipping weights are not limiting, the cooling fluid would be left in the stator after the commercial acceptance tests have been performed and would be shipped with the frame. Where shipping limits would not allow the fluid to be shipped with the frame, dry air would be pumped into the frame for shipping to minimize moisture contamination. Upon arrival at the plant site, vacuum-heating cycles and new fluid filling operations would be required to condition the stator for startup.

Vibration isolation is accomplished in the following manner: the core is solidly connected to the frame and the vibrational motion of the frame follows the vibrational motion of the core. However, the outer surface of the frame can be designed at the diametrical location where it is known that the magnitude of the tangential vibrational motion will fall to zero. The frame is then attached to the foundation through vertical leaf springs that accommodate the remaining radial vibrational motion

The difference in the behavior of the surge voltage distributions for the 60 kVA armature and the 600 MVA armature is apparently due to the natural resonances of the windings. The resonances of the 60 kVA armature are at high frequencies (the lowest being about 10 MHz) and are excited only a small degree by the surge. The voltage therefore distributes uniformly over the length of the winding. The resonances of the 600 MVA armature are well below 1 MHz and are excited by the surge. This produces the surge-front propagation in the winding.

2.7.4 Insulation System Qualification

The ultimate goal of the surge voltage analysis is the qualification of the armature winding turn insulation system. For the monolith cylinder armature winding, the two portions of the turn-to-turn insulation system are the vertical dividers that separate columns of conductors and the insulation wrap placed around the cooling tubes that separate radially adjacent conductors (see Section 2.6).

The absolute magnitude of turn-to-turn voltages within a winding can be related to the specified Basic Impulse Level (BIL) for the voltage rating of the winding. For high-voltage transformers, the BIL for a 345 kV rating is 900 kV (BILs for other ratings can be found in Table 4.1-1). The minimum turn-to-turn insulation is required to withstand a voltage equal to the BIL multiplied by the ratio of maximum turn-to-turn voltage to uniform turn-to-turn voltage and divided by the number of series turns in the winding.

The vertical dividers in the 600 MVA, 345 kV monolith cylinder armature are required to withstand a voltage of

$$3.4 \times \frac{900}{53} = 57.7 \text{ kV}$$

The thicknesses of the vertical dividers (from Figure 2.6-11) are

0.79 in. inner layer

0.88 in. outer layer

and the dielectric stresses of the vertical dividers are

730 v/mil inner layer

657 v/mil outer layer

The stress and thickness coordinates for the vertical dividers can be entered onto Figure 2.1-7, which has a curve for the impulse strength of oil-impregnated pressboard. Both points are well within the criterion limit.

A similar exercise can be performed for the insulation wrap that is placed around the cooling tubes and which serves as a turn-to-turn insulation between radially adjacent conductors. It, too, is well qualified.

References

- 2.7-1. P.L. Conley, J.L. Kirtley, W.H. Hagman, and A.H. Ula, "Demonstration of a Helical Armature for a Superconducting Generator," *IEEE Transactions on Power Apparatus and Systems*, PAS-99, 4, pp. 1642-1649.

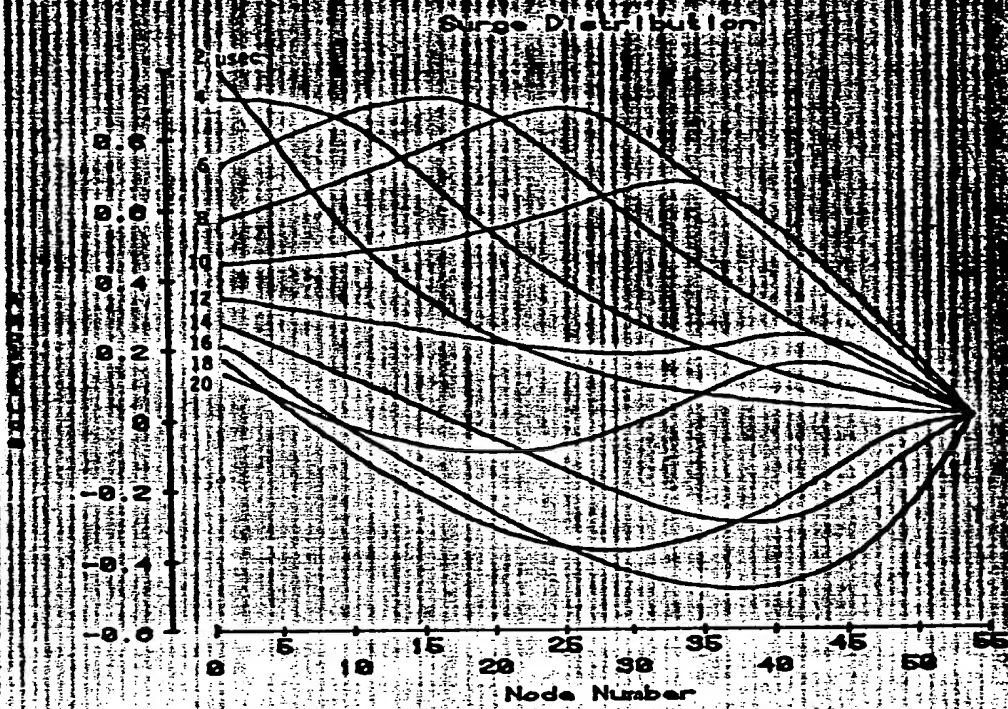


Figure 2.7-8. Calculated Surge Voltage Distributions for the 600 MVA Armature

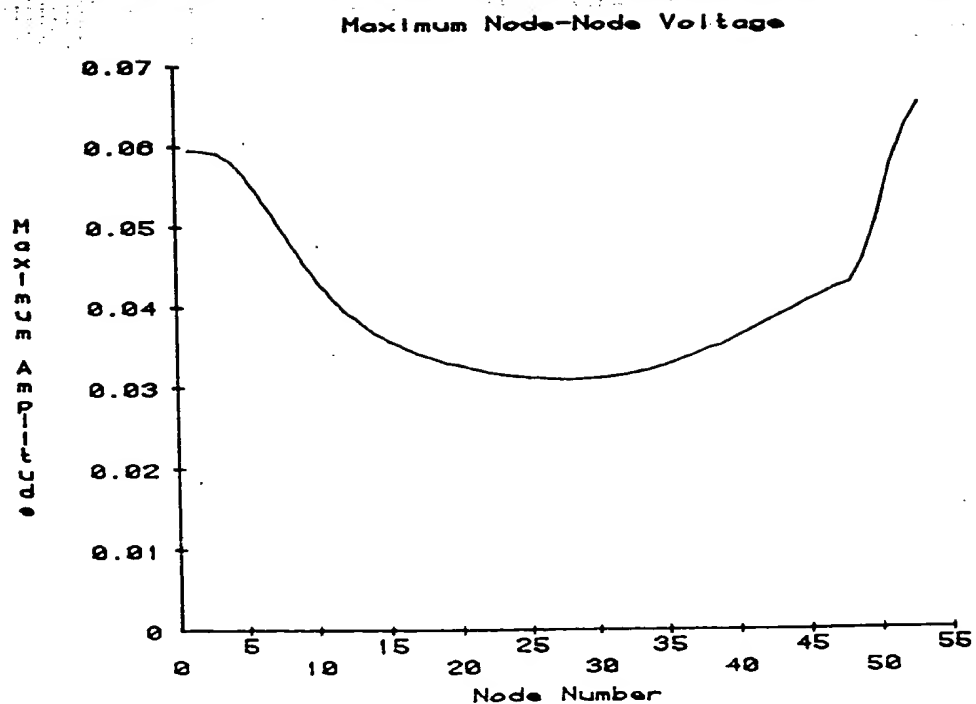


Figure 2.7-9. Maximum Turn-to-Turn Voltages for the 600 MVA Armature

illustrates oscilloscope traces of the voltage waveforms recorded during the experiment. The comparison between the calculated and measured waveforms is very good. It is apparent from the increasingly proportioned node voltage waveforms that the surge distributes fairly uniformly throughout the winding.

The surge voltage program is next applied to the 600 MVA, 345 kV helical coil monolithic cylinder armature whose dimensions are described in Figure 2.6-11. This armature has 371 series turns in each parallel circuit of a phase-belt. There are 7 conductors in each column and 53 columns in the circuit, so the circuit model has 54 nodes. Figure 2.7-7 illustrates the calculated voltage waveforms for the set of evenly distributed nodes labeled in the figure. The surge apparently does not distribute uniformly throughout the winding. The voltage distributions illustrated in Figure 2.7-8 will give the reader a better indication of the surge distribution in this winding. Here, the voltage distribution along the entire length of the winding is indicated for successive moments of time. The slope of the distributions indicates the severity of the turn-to-turn voltage along the length of the winding, and the steepest slope of each distribution indicates the location and magnitude of the largest turn-to-turn voltage for that moment of time. By examining the distributions for successive moments of time, it is possible to see the front of the surge propagate down the length of the winding and bounce off the end with opposite polarity. This behavior is similar to that experienced in high voltage step-up transformers. Figure 2.7-9 illustrates the maximum turn-to-turn voltage experienced at each location of the winding over the entire time span of the surge. The largest turn-to-turn voltages are found at the front and tail ends of the windings. The largest turn-to-turn voltages at the front end of the winding are experienced as the surge begins to propagate down the winding but the largest turn-to-turn voltages at the tail end of the winding are experienced when the surge bounces off the end with negative polarity. This phenomenon accounts for the apparent discontinuity in the curve at the tail end. The maximum turn-to-turn voltage (at the tail end) is indicated at a magnitude of .065. If the surge distributed uniformly in the winding, the maximum turn-to-turn voltage would be

$$\frac{1.00}{53} = .019$$

The maximum turn-to-turn voltage is therefore 3.4 times the turn-to-turn voltage of uniform distribution.

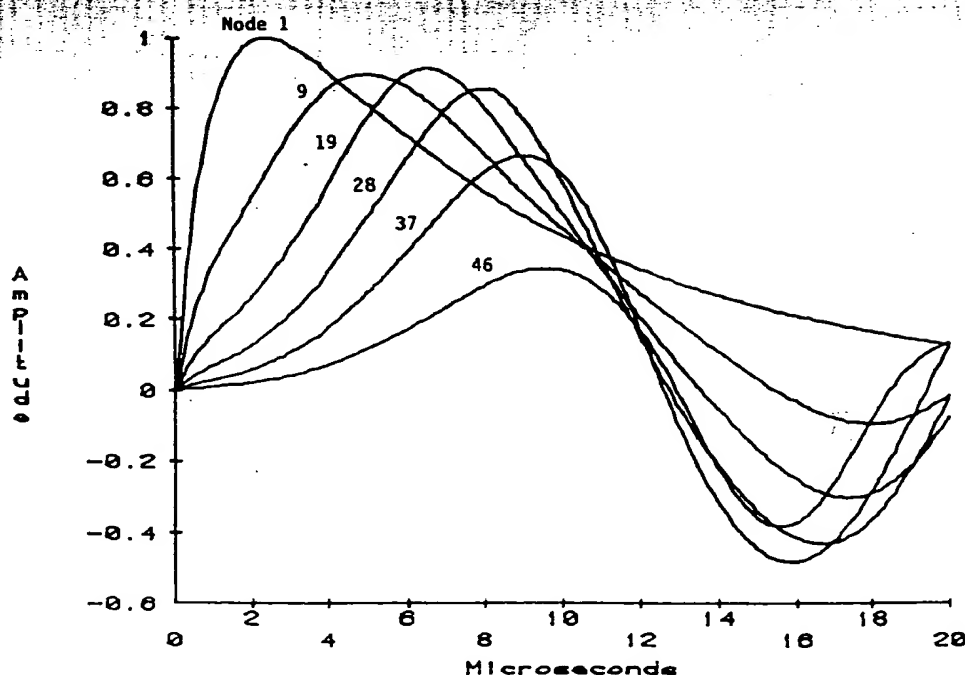


Figure 2.7-7. Calculated Surge Voltage Waveforms for the 600 MVA Armature

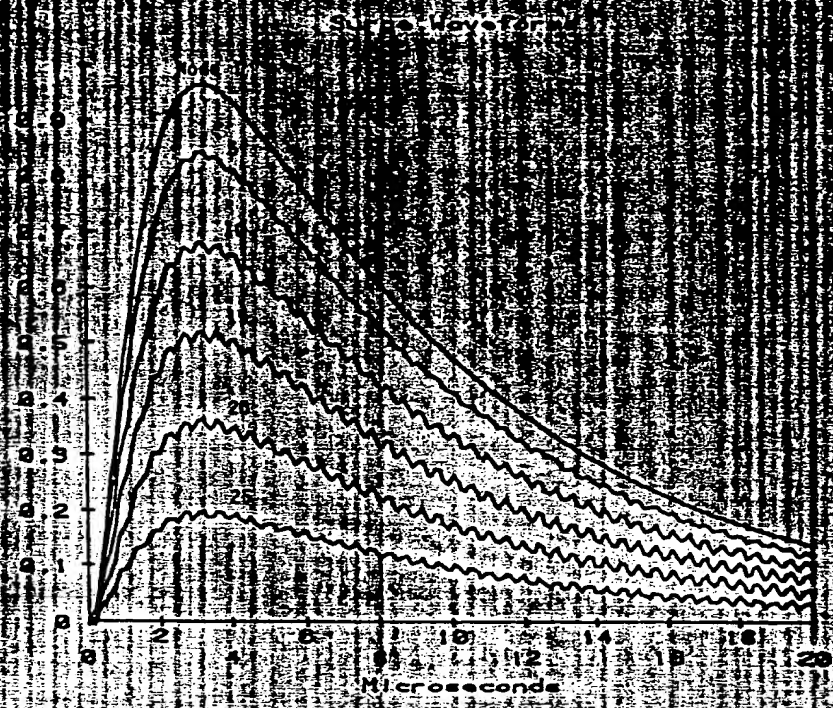


Figure 2.7-5. Calculated Surge Voltage Waveforms in the 60 kVA Armature

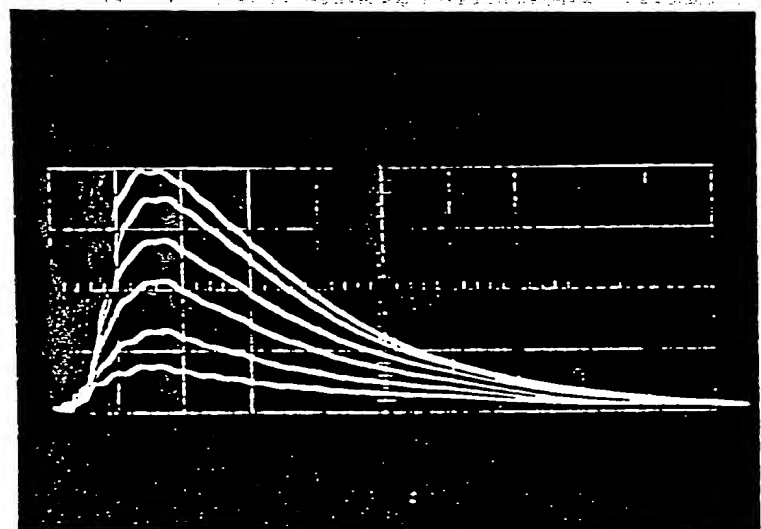


Figure 2.7-6. Measured Surge Voltage Waveforms in the 60 kVA Armature

This model assumes that the "leakage" inductance, L , between turns is the same for all turns and represents all interbranch coupling effects. The second element, L^* , represents self-inductance and is the same for all turns. This is a turn-based model; current at one of the nodes of this model is equivalent to the turn current in the actual armature.

Now if there are many turns with small leakage, the inductance will not vary much from one turn to the next. If L^* is the inductance at a given point, one cell of this ladder appears as shown in Figure 2.7-4.

Turn self-inductance is, then

$$L^* = \frac{1}{2} L + L = \frac{3}{2} L \quad (2.7-8)$$

Turn-to-turn mutual inductance is

$$M = \frac{1}{2} L \quad (2.7-9)$$

and the leakage element is

$$L = L^* - M \quad (2.7-10)$$

The two elements L and M can be calculated by using the magnetic field analyses in Appendix A. Inductive admittances can be computed easily: if all turns of the model are shorted to ground except for one that one has a flux imposed, currents appear in the branches. The currents are just the inductive admittances times the flux. For two turns, i and j , the reciprocal inductance elements are

$$b(i, j) = \begin{cases} \frac{1}{L} & \text{if } i - j = 1 \text{ or } n \\ \frac{2}{L} & \text{if } i - j = 2 \text{ or } n-1 \\ -\frac{1}{L} & \text{if } i - j = \pm 1 \\ 0 & \text{otherwise} \end{cases} \quad (2.7-11)$$

2.7.3 Surge Voltage Calculations

The surge voltage program was first applied to a small 60 kVA helical coil armature constructed several years ago by the Massachusetts Institute of Technology as a portion of their superconducting generator effort. This armature was tested with voltage surges, and the voltage distribution within the winding was recorded from equally distributed taps placed on the winding. The recorded voltage distributions allow a comparison with calculated voltage distributions from the surge voltage program.

This winding has 90 series-connected coils in a phase-belt, and the conductors are arranged 3 to a column, so there are 31 nodes in the winding model. Figure 2.7-5 illustrates the calculated voltage waveforms as a function of time for the evenly distributed nodes labeled in the figure. Figure 2.7-6

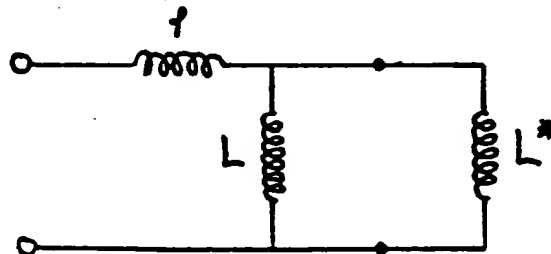


Figure 2.7-4. One Cell of the Ladder Model

and

$$I_{cs} = G_{ca} V_a + G_{cb} V_b + I_{cs} \quad (2.7-34)$$

Here, I_{ms} and I_{cs} are the inductive and capacitive portions of the history current.

It is necessary to partition both the inductive and capacitive admittance matrices to obtain G_{msa} , G_{msb} , G_{csa} and G_{csb} .

3. History currents for the next time step are

$$I_{ms} = I_{ms} + G_{msa} V_a + G_{msb} V_b \quad (2.7-35)$$

$$I_{cs} = I_{cs} + G_{csa} V_a + G_{csb} V_b \quad (2.7-36)$$

and

$$I_{cs} = I_{ms} + I_{cs} \quad (2.7-37)$$

4. Return to step 1.

This method requires initial values for the "history" currents. In the case of an initially quiescent system, however, all of the initial currents are zero.

Note that all of the matrices involved may be computed once before the start of the time-step process. The program will run quite fast, once started.

2.7.2-E Approximate Inductive-Admittances

Some difficulties were encountered when this program was initially utilized. The initial symptoms were those of numerical instability, as witnessed by its rapidly diverging answers. After some investigation, it was discovered that the problem was in the inverted inductance matrix. This matrix had elements which were both very large and which carried the wrong sign (corresponding to negative admittance elements).

It is believed that the reason for this difficulty is that the inductances of the system are very tightly coupled. Thus, the inductance matrix consists of elements which are nearly equal, and it is difficult to invert, being both nearly singular and ill conditioned. Furthermore, accuracy of the element values is critical.

Several attempts were made to resolve the difficulties arising from tight coupling. These included efforts to increase the accuracy of calculation of the inductance parameters, the use of transformation techniques, the use of high-precision arithmetic, and the use of different inversion techniques. The solution eventually adopted is the one which recognizes the very close coupling between branch elements. This solution, which is clearly approximate, gives good results and has the added advantage of avoiding one inversion.

To see how this technique works, assume that the armature may be represented by a ladder-type structure as shown in Figure 2.7-3.

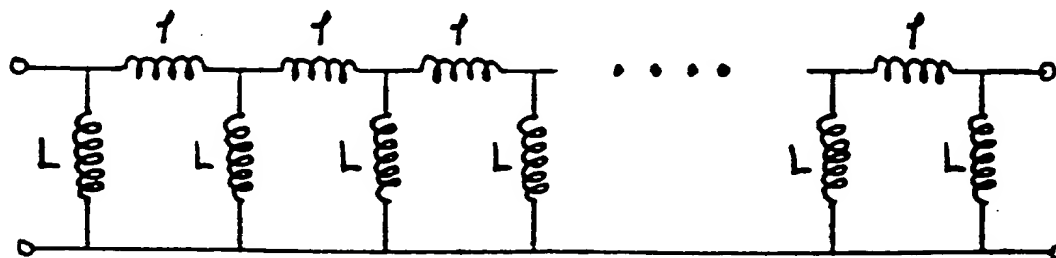


Figure 2.7-3. Ladder Model of Inductances

2.7.2-C Assembly Into a Complete System

If the assemblies of capacitance and coupled inductances are connected to a common set of nodes, the node currents will add:

$$\underline{I}_u = \underline{I}_{u1} + \underline{I}_{u2}$$

or

$$\underline{I}_u = \underline{G}_u \underline{V}_u + \underline{I}_{u1} + \underline{I}_{u2}$$

where

$$\underline{G}_u = \underline{G}_{u1} + \underline{G}_{u2}$$

In the armature windings, it is possible to classify nodes as being one of two types:

1. Driven, or terminal nodes
2. Undriven, or internal nodes.

In the undriven nodes, the node current is identically zero, because nothing but the capacitance and inductance elements are connected. It is, of course, the voltages at these nodes which is to be found.

It is possible to partition Equation 2.7-27 so that the internal nodes are grouped together:

$$\begin{bmatrix} \underline{G}_{aa} & \underline{G}_{ab} \\ \underline{G}_{ba} & \underline{G}_{bb} \end{bmatrix} \begin{bmatrix} \underline{V}_u \\ \underline{V}_k \end{bmatrix} + \begin{bmatrix} \underline{I}_{u1} + \underline{I}_{u2} \\ \underline{I}_k \end{bmatrix} = \begin{bmatrix} 0 \\ \underline{I}_k \end{bmatrix} \quad (2.7-29)$$

\underline{V}_u and \underline{V}_k represent voltages at the various "unknown voltage" (internal) and "known voltage" (terminal) nodes, respectively. The matrix \underline{G} has been partitioned into four submatrices: \underline{G}_{aa} and \underline{G}_{bb} are square and represent admittances within the unknown and known node groups, respectively. \underline{G}_{ab} and \underline{G}_{ba} are nonsquare and represent coupling between groups.

Splitting off the top part of Equation 2.7-29 gives

$$\underline{G}_{aa} \underline{V}_u + \underline{G}_{ab} \underline{V}_k + \underline{I}_u = 0, \quad (2.7-30)$$

where \underline{I}_u is the "unknown voltage" node portion of $\underline{I}_{u1} + \underline{I}_{u2}$. The unknown voltages are found from Equation 2.7-30 by inverting \underline{G}_{aa} and multiplying:

$$\underline{V}_u = -\underline{G}_{aa}^{-1} \underline{G}_{ab} \underline{V}_k - \underline{G}_{aa}^{-1} \underline{I}_u, \quad (2.7-31)$$

where

$$\underline{G}_g = -\underline{G}_{aa}^{-1} \underline{G}_{ab} \quad (2.7-32)$$

2.7.2-D Time-Step Solution

The recipe for the time-step solution is now given in the following steps.

1. Assuming that the history current \underline{I}_u is known, compute the unknown voltage \underline{V}_u using Equation 2.7-31
2. Since all voltages are now known, it is possible to compute, separately, the capacitive and inductive parts of the current by

$$\underline{I}_{nu} = \underline{G}_{naa} \underline{V}_u + \underline{G}_{nab} \underline{V}_k + \underline{I}_{nu} \quad (2.7-33)$$

Now assume that the branches are connected together into a network described by the node incidence matrix N in such a way that

$$I_n(t) = -N^T I_b(t) \quad (2.7-16)$$

and

$$V_n(t) = N^T V_b(t) \quad (2.7-17)$$

where the subscripts n and b refer to node- and branch- respectively. The node currents are the currents entering the nodes of the network, and the node voltages are the voltages from the work nodes to some datum node. By substituting Equations 2.7-16 and 2.7-17 into Equations 2.7-13 through 2.7-15, it is possible to derive

$$I_n(t) = G_{NL} V_n(t) + I_{nc}(t) \quad (2.7-18)$$

where

$$G_{NL} = N G_b N^T \quad (2.7-19)$$

and

$$I_{nc} = I_n(t - \Delta t) + G_{NL} V_n(t - \Delta t) \quad (2.7-20)$$

2.7.2-B Representation of Capacitive Elements

It is possible to formulate an equivalent to Equation 2.7-20 for capacitance elements directly. Start by assuming a capacitance matrix C which relates node currents to node voltages by

$$I_{nc} = C \frac{d}{dt} V_n \quad (2.7-21)$$

The capacitance matrix which satisfies this requirement is assembled according to the following rules:

1. The diagonal element corresponding to a node is the sum of all capacitances connected to that node.
2. Off-diagonal elements are the negatives of mutual capacitances between two nodes. That is, the entry C_{ij} is the negative of the directly connected capacitance connecting node i with node j .

Integration of Equation 2.7-21 with the use of the trapezoidal rule yields

$$G_C V_n(t) = G_C V_n(t - \Delta t) + I_{nc}(t) + I_{nc}(t - \Delta t) \quad (2.7-22)$$

where

$$G_C = \frac{2}{\Delta t} C \quad (2.7-23)$$

Equation 2.7-22 is easily manipulated to yield

$$I_{nc}(t) = G_C V_n(t) + I_{oc} \quad (2.7-24)$$

where

$$I_{oc} = -I_{nc}(t - \Delta t) - G_C V_n(t - \Delta t) \quad (2.7-25)$$

but since the DFT assumes, in effect, periodicity, this technique finds the response to a periodic chain of surges. It is possible for this chain to drive one of the low-frequency, high-Q resonances, giving an answer which is incorrect.

One further disadvantage of the frequency domain approach was the need to invert large matrices for each frequency point. The program was thus rather expensive to run.

The frequency response method was chosen initially because of the very large number of interconnected elements of the model. The argument that these would force the use of an impractically large model was incorrect because it was discovered how to build a trapezoidal-rule model on a nodal basis. As it turns out, the trapezoidal rule model is substantially less expensive to run than the frequency response model.

Because the frequency-response model did not produce valid results, it will not be discussed further.

In the formulation of the trapezoidal rule model, winding resistances are neglected. Doing so produces a major reduction in programming effort and a minor economy in computation. It is felt that the effect of neglecting resistance will be both minor and conservative. It should be minor, because, in the frequency range of interest, inductive impedances are large. It should be conservative because resistance would dampen the oscillations that are responsible for nonuniform voltage distributions.

2.7.2-A Representation of Coupled Inductors

Consider a set of coupled inductors representing the branches connecting the nodes of the armature winding model. The flux-current relationship is given by the matrix equation:

$$\underline{\lambda} = \underline{L} \underline{i}_l \quad (2.7-8)$$

where \underline{L} is the coupling matrix. Branch voltages are given by

$$\underline{v} = \frac{d}{dt} \underline{\lambda} \quad (2.7-9)$$

An expression for current may be found by integrating Equation 2.7-9, inverting Equation 2.7-8, and combining the results:

$$\underline{i}_l(t) - \underline{i}_l(t_0) = \underline{L}^{-1} \int_{t_0}^t \underline{v}(t) dt \quad (2.7-10)$$

Over a suitably short time interval,

$$\Delta t = t - t_0 \quad (2.7-11)$$

and it is possible to approximate Equation 2.7-10 by using the trapezoidal rule:

$$\underline{i}_l(t) = \underline{i}_l(t - \Delta t) + \frac{\Delta t}{2} \underline{L}^{-1} [\underline{v}(t) + \underline{v}(t - \Delta t)] \quad (2.7-12)$$

Thus, it is possible to determine current at some time t as a combination of current at a suitably recent point in time and voltages at two times. This may be formalized by recasting Equation 2.7-12 as

$$\underline{i}_l(t) = \underline{G}_L \underline{v}(t) + \underline{I}_0 \quad (2.7-13)$$

where the admittance matrix is

$$\underline{G}_L = \frac{\Delta t}{2} \underline{L}^{-1} \quad (2.7-14)$$

and the "history current" is

$$\underline{I}_0 = \underline{i}_l(t - \Delta t) + \underline{G}_L \underline{v}(t - \Delta t) \quad (2.7-15)$$

The self- and mutual-inductance terms are

$$L = \sum_n L_n \quad (2.7-4)$$

$$M_{m,l} = \sum_n L_n \cos(n(m-l)\gamma) \quad (2.7-5)$$

where L_{nl} is the n^{th} mutual harmonic component of inductance between conductors at radial locations l and l' , γ is the angular separation between adjacent columns, L is the fully developed self-inductance of each column, and $M_{m,l}$ is the mutual-inductance between columns m and l .

The inductive components can be calculated as described in Appendix F.

The surge voltage that is applied to the terminal of the armature winding is modeled by the mathematical expression

$$v(t) = A(e^{-\alpha t} - e^{-\beta t})u(t) \quad (2.7-6)$$

where $\beta > \alpha$. The parameter β controls the rise time and the parameter α controls the decay time. The parameters used in these studies are $\alpha = 1 \mu s$ and $\beta = 8 \mu s$.

In order that the magnitude of surge may be reconciled to 100% at its crest, the coefficient A is related to the exponential parameters α and β by

$$A = \frac{1}{e^{-\frac{\alpha}{\beta-\alpha} \log \frac{\beta}{\alpha}} - e^{-\frac{\beta}{\beta-\alpha} \log \frac{\beta}{\alpha}}} \quad (2.7-7)$$

2.7.2 Trapezoidal Rule Solution for Surge Voltage Distributions

The trapezoidal rule technique for time-step integration has been employed to solve for surge voltage distributions in armature windings. The considerations in the selection of this technique follow:

- The armature winding is a large and electrically complex system with a large number and wide range of natural frequencies.
- At least some of the natural frequencies of the armature winding have relatively low frequency and high Q.
- Despite the large number of elements in the armature winding model, it is possible to formulate a trapezoidal rule model which runs efficiently.

Trapezoidal rule integration is characterized by unconditional stability. Unlike some other time-step integration routines, trapezoidal rule integration is not unstable if the basic time step is longer than the period of one eigenfrequency. Of course the accuracy of such a solution can not be guaranteed, but the errors are generally characterizable as "filtering." That is, the selection of too long a time step results in losing high-frequency information. This is not a serious problem in this effort.

In the earlier stages of this study, a frequency domain approach was attempted. The frequency response of the system was calculated for each node and for a range of frequencies. This was multiplied by the Fourier transform of the surge waveform, which may be calculated analytically, to obtain the Discrete Fourier Transform (DFT) of the voltage waveform at each node. Finally, an inverse DFT was used to yield the voltage waveforms.

The problem with this technique is that the armature winding has several resonances with relatively low frequency and high Q. The use of a DFT implies the assumption of a signal that is periodic in time, with a period equal to the inverse of the frequency step. Of course the surge is not periodic,

Model order-reduction becomes necessary when the number of elements in the armature becomes excessive. First modeling efforts of the 60 kVA armature resulted in admittance matrices on the order of 60×60 elements. The 600 MVA armature has 371 turns per phase-belt, requiring a 372×372 admittance matrix, and computer processing time increases exponentially with the number of turns. Therefore, a reduced-order model which consolidates all of the conductors in a column is utilized. A column is the arrangement of conductors which are connected electrically in series and stacked radially one above each other (see Figure 2.6-2).

As it results, the reduced-order model has a structure which is somewhat simpler to use than that of the full model, because internal capacitances between radially adjacent conductors are ignored. The structure of the reduced-order model is illustrated in Figure 2.7-2.

Parallel-plate capacitance expressions are assumed to be sufficiently accurate for the capacitive elements. The capacitive elements in the reduced-order model can be evaluated from capacitive components as follows:

$$C_m = n_l C_1 \quad (2.7-1)$$

$$C_s = C_2 + C_3 + C_4 + C_5 \quad (2.7-2)$$

where

C_1 is the capacitance between peripherally adjacent conductors (calculated for the full turn length)

C_2 is the ground capacitance of the innermost conductor of the inner conductor layer

C_3 is the ground capacitance of the outermost conductor of the inner conductor layer, as viewed across the center and outer insulation cylinders.

C_4 is the ground capacitance of the innermost conductor of the outer conductor layer, as viewed across the center and inner insulation cylinders

C_5 is the ground capacitance of the outermost conductor of the outer conductor layer

n_l is the number of conductors in a column

In the reduced-order model, inductance is handled in the same way as in the full model except that there are fewer elements. In this case, a column inductance may be defined for each harmonic order n :

$$L_n = \sum_{i=1}^{n_l} \sum_{j=1}^{n_l} L_{i,j,n} \quad (2.7-3)$$

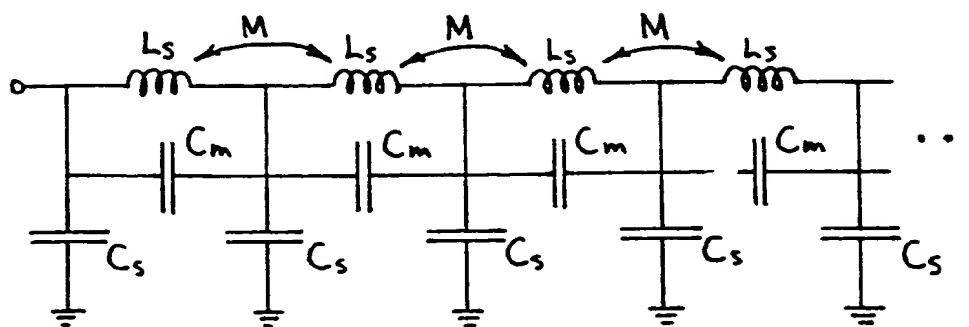


Figure 2.7-2. Reduced-Order Model Structure

2.7 SURGE VOLTAGE ANALYSIS

The high-voltage generator is connected directly to its transmission system and will be exposed to voltage surges from lightning strikes and switching activity in the same manner as high-voltage step-up transformers. Because voltage surges are known to produce large turn-to-turn voltages within the windings of step-up transformers, it is necessary to calculate the surge voltage distribution within the high-voltage generator to qualify its insulation system.

The theory of the time-step simulated surge voltage analysis is described. The analysis is applied to a small 60 kVA model armature (Ref. 2.7-1) and to the 600 MVA, 345 kV helical coil monophase cylinder armature described previously. The effect of the calculated turn-to-turn voltages on the insulation system is appraised from dielectric strength performance curves for oil-impregnated pressboard.

2.7.1 Armature Winding Representation

It should be possible to model the armature winding in a form similar to that shown in Figure 2.7-1. The nodes in this figure are arbitrarily chosen and might represent coil ends. Between these nodes are inductance elements, representing coil inductance. All of these elements will be coupled and so have mutual- as well as self-inductance. There will also be some series resistance, which may be included in the model. The capacitive elements will couple pairs of nodes together and will couple nodes to ground. These capacitive elements will appear between many different pairs of nodes, not just adjacent nodes; so it will probably be necessary to allow for a "full" capacitance matrix having capacitance elements between all pairs of nodes. If it is necessary to model dielectric loss, this can appear as conductances placed in parallel with the capacitive elements. Note that series resistance and shunt conductance may be frequency dependent.

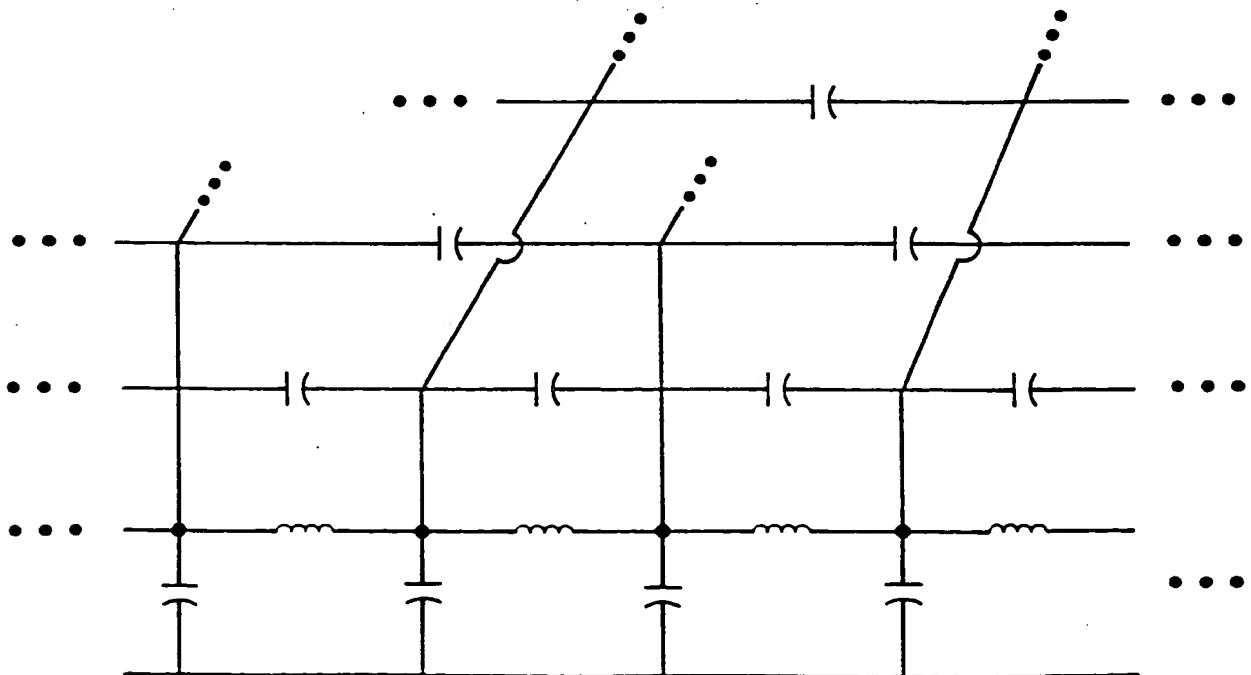


Figure 2.7-1. Lumped Parameter Circuit Model of an Armature Winding

DETAILED TEMPERATURE AND FLOW VELOCITY PROFILES

INNER LAYER

TEMPERATURES

[illegible]

VELOCITIES
12.3 44.9

OUTER LAYER

TEMPERATURES

LOCATION 1	LOCATION 2	LOCATION 3	LOCATION 4	LOCATION 5	LOCATION 6
45.0 52.1	46.0 54.1	48.9 56.2	50.8 58.2	52.6 60.3	54.8 62.1
45.0 59.0	61.3	63.5	65.8	68.0	70.3
45.0 54.7	47.5 57.1	49.9 59.5	52.4 61.9	54.8 64.3	57.2 66.7
60.6	63.2	65.7	68.2	70.7	73.8
45.0 55.3	47.6 57.0	50.2	52.7 63.0	55.2 65.5	57.8 68.1
61.0	63.6	66.3	68.9	71.5	74.1
45.0 55.4	47.6 58.0	50.2	52.6 63.3	55.2 65.9	58.0 68.5
61.1	63.7	66.4	69.0	71.6	74.2
45.0 55.4	47.6 58.0	50.2	52.6 63.3	55.2 65.9	58.0 68.5
61.0	63.6	66.3	68.9	71.5	74.1
45.0 55.3	47.6 57.8	50.2	52.6 63.0	55.2 65.5	57.8 68.1
60.6	63.2	65.7	68.2	70.7	73.2
45.0 54.7	47.5 57.1	49.9 59.5	52.4 61.9	54.8 64.3	57.2 66.7
61.3	63.5	65.8	68.0	70.3	72.6
45.0 52.1	46.0 54.1	48.9 56.2	50.8 58.2	52.6 60.3	54.8 62.1

LOCATION 6 LOCATION 4 LOCATION 5 LOCATION 1

[illegible]

VELOCITIES

Figure 2.6-16. Winding Design Using Cooling Tubes with Center Walls (Cont'd)

<p>HIGH VOLTAGE GENERATOR CONDUCTOR AND COILING DESIGN TRANSIL OIL COOLANT</p> <p>600 MVA, 345 KV, 0.9 PF DOUBLE CIRCUIT DELTA HELICAL WINDING 300 AMPS/50 CM ARMATURE DENSITY 50 V/MIL INSULATION</p> <p>FIELD WINDING INNER RADIUS 9.0 IN FIELD WINDING OUTER RADIUS 12.0 IN ARMATURE BORE RADIUS 18.0 IN INNER LAYER INNER RADIUS 22.0 IN INNER LAYER OUTER RADIUS 24.7 IN OUTER LAYER INNER RADIUS 32.1 IN OUTER LAYER OUTER RADIUS 37.0 IN CORE INNER RADIUS 173.0 IN ACTIVE LENGTH</p> <p>TERMINAL CURRENT 1004.1 AMPS CIRCUIT CURRENT 289.0 AMPS RADIAL FLUX, INNER LAYER 1.47 TESLAS TANGENTIAL FLUX, INNER LAYER 0.66 TESLAS RADIAL FLUX, OUTER LAYER 0.94 TESLAS TANGENTIAL FLUX, OUTER LAYER 0.13 TESLAS</p> <p>INNER LAYER *****</p> <p>THERE ARE 371 TURNS PER PHASE BELT THE LAYER IS 7 CONDUCTORS HIGH THE CONDUCTOR AND HYDRAULIC LENGTH IS 187.9 IN THE HELIX ANGLE IS 23.0 DEGREES THE "SLOT WIDTH" IS 0.4248 IN</p> <p>CONDUCTOR SPECS:</p> <p>WIRE GAUGE 18 NO. FILAMENTS HIGH 6 NO. FILAMENTS WIDE 8 NO. FILAMENTS 48 BAR WIDTH 0.3456 IN BAR HEIGHT 0.2592 IN COPPER AREA 0.06122 SQ IN CURRENT DENSITY 4734.6 AMPS/SQ IN</p> <p>VERTICAL DIVIDER:</p> <p>THICKNESS 0.0792 IN VOLTAGE STRESS 86.0 V/MIL</p> <p>CIVILIAN PASSAGES (THU PER TUBE):</p> <p>WIDTH 0.1046 IN HEIGHT 0.0492 IN AREA 0.00518 SQ IN HYDRAULIC DIA 0.0786 IN</p>	<p>STAINLESS STEEL COILING TUBES:</p> <p>WALL THICKNESS 0.024 IN INSULATION THICKNESS 0.005 IN TUBE WIDTH 0.461 IN TUBE HEIGHT 0.097 IN LOSSES 0.482 W/IN</p> <p>CONDUCTOR LOSSES:</p> <p>DC LOSSES 1.450 W/IN AC LOSSES 0.394 W/IN TOTAL 1.844 W/IN</p> <p>COILING PERFORMANCE (AVERAGED):</p> <p>PRESSURE DROP (INPUT) 28.00 LBS/SQ IN CIVILIAN INLET TEMP 45.00 DEGREES CENTIGRADE FLOW VELOCITY 33.97 IN/SEC TOTAL FLOW 429.8 GAL/MIN REYNOLDS NO. 301.6 CIVILIAN OUTLET TEMP 68.56 DEGREES CENTIGRADE</p> <p>INSULATION *****</p> <p>INSULATION VOLUME 471494.3 CUBIC INCHES PERCENT COILING AREA 0.1 COILING PASSAGE WIDTH 0.1000 IN HYDRAULIC DIAMETER 0.1000 IN</p> <p>LOSSES DISSIPATION FACTOR 0.004 WATTS/CUBIC INCH 0.40 PERCENT</p> <p>COILING PERFORMANCE (AVERAGED):</p> <p>PRESSURE DROP (INPUT) 28.00 LBS/SQ IN CIVILIAN INLET TEMP 45.00 DEGREES CENTIGRADE FLOW VELOCITY 40.04 IN/SEC TOTAL FLOW 42.5 GAL/MIN REYNOLDS NO. 496.0 CIVILIAN OUTLET TEMP 45.48 DEGREES CENTIGRADE</p> <p>WINDING EFFICIENCY *****</p> <p>CIVILIAN PASSAGES (THU PER TUBE):</p> <p>WIDTH 0.1378 IN HEIGHT 0.0407 IN AREA 0.00836 SQ IN HYDRAULIC DIA 0.0843 IN</p>	<p>STAINLESS STEEL COILING TUBES:</p> <p>WALL THICKNESS 0.020 IN INSULATION THICKNESS 0.005 IN TUBE WIDTH 0.536 IN TUBE HEIGHT 0.101 IN LOSSES 0.462 W/IN</p> <p>CONDUCTOR LOSSES:</p> <p>DC LOSSES 1.059 W/IN AC LOSSES 0.605 W/IN TOTAL 1.664 W/IN</p> <p>COILING PERFORMANCE (AVERAGED):</p> <p>PRESSURE DROP (INPUT) 28.00 LBS/SQ IN CIVILIAN INLET TEMP 45.00 DEGREES CENTIGRADE FLOW VELOCITY 44.10 IN/SEC TOTAL FLOW 487.5 GAL/MIN REYNOLDS NO. 390.6 CIVILIAN OUTLET TEMP 62.84 DEGREES CENTIGRADE</p> <p>OUTER LAYER *****</p> <p>THERE ARE 371 TURNS PER PHASE BELT THE LAYER IS 7 CONDUCTORS HIGH THE CONDUCTOR AND HYDRAULIC LENGTH IS 201.7 IN THE HELIX ANGLE IS 30.9 DEGREES THE "SLOT WIDTH" IS 0.5593 IN</p> <p>CONDUCTOR SPECS:</p> <p>WIRE GAUGE 14 NO. FILAMENTS HIGH 2 NO. FILAMENTS WIDE 7 NO. FILAMENTS 14 BAR WIDTH 0.4711 IN BAR HEIGHT 0.1346 IN COPPER AREA 0.04518 SQ IN CURRENT DENSITY 6415.7 AMPS/SQ IN</p> <p>VERTICAL DIVIDER:</p> <p>THICKNESS 0.0882 IN VOLTAGE STRESS 77.2 V/MIL</p> <p>TOTAL CONDUCTOR LOSSES 1523.9 KW COILING TUBE LOSSES 488.4 KW INSULATION LOSSES 2.1 KW LIQUID PUMPING LOSSES 11.7 KW TOTAL LOSSES 2006.1 KW EFFICIENCY DROP 0.372 PERCENT</p>
---	---	---

Figure 2.6-16. Winding Design Using Cooling Tubes with Center Walls

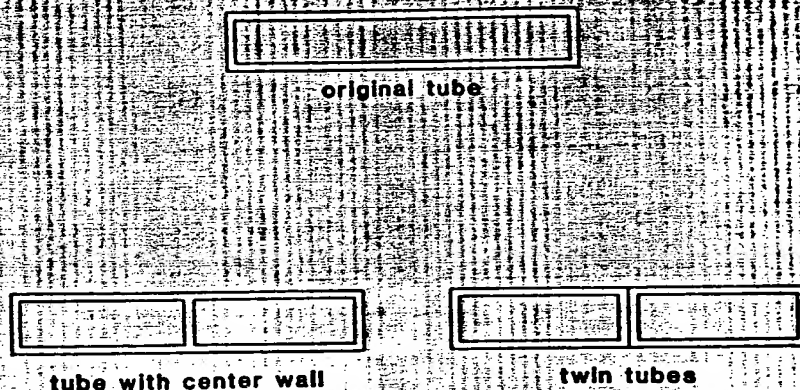


Figure 2.6-15. Substitute Cooling Tubes

coolant streams are not as short and wide, so the thermal resistances of convection are increased. However, each stream receives only half of the previous heat input, and the result is that the tube-wall-to-coolant temperature rise is not greatly affected. The coolant stream cross-sectional area is reduced by the amount of area that the center walls consume, while the coolant flow friction coefficient is reduced by the use of the more regular stream aspects. The overall effect of the employment of cooling tube center walls is that a slightly greater liquid pressure drop is required to maintain the hotspot temperature limitation. Figure 2.6-16 illustrates a cooling calculation for cooling tubes with center walls. The conductor and tube dimensions are exactly the same as those used in the calculations of Figure 2.6-11, except for the addition of the center walls. The required liquid pressure drop is 28.0 psi and the required flow is 918 gal/min, which compares to 22.0 psi and 891 gal/min, respectively, of the previous calculation. The tube wall bending stress is reduced to 25,000 psi.

In conclusion, transil oil appears to be the optimal cooling fluid from considerations of cooling performance, low cost, and dielectric experience. Only if the fire hazard of transil oil were overwhelmingly objectionable would there be any inclination to consider the other coolants.

References

- 2.6-1. S. Isobe et al., "Silicone Oil Filled Transformers and Its Silicon Oil Characteristics," *Proceedings of the IEEE 12th Electrical and Electronics Insulation Conference*, 1975, pp. 215-219.
- 2.6-2. Paul F. Ast, "Electrical Properties of Oil and Oil-Impregnated Pressboard at Temperatures up to 200 °C," *Proceedings of the IEEE 12th Electrical and Electronics Insulating Conference*, 1975, pp. 220-224.
- 2.6-3. *Engineering Notebook*, EHV Weidmann Industries, Inc., St. Johnsbury, Vermont.
- 2.6-4. Wm. Rohsenow, *Handbook of Heat Transfer*, McGraw-Hill, 1973.
- 2.6-5. D.S. Parasnis, "Electric and Thermal Conductivity of a Medium Containing Arrays of Spherical and Cylindrical Particles," *Nature*, Sept. 10, 1966, p. 1135.

DETAILED TEMPERATURE AND FLOW VELOCITY PROFILES										

3										

INNER LAYER										

TEMPERATURES										
LOCATION 1	LOCATION 2	LOCATION 3	LOCATION 4	LOCATION 5	LOCATION 6	LOCATION 1	LOCATION 2	LOCATION 3	LOCATION 4	LOCATION 5
45.0 59.9	46.0 60.8	47.0 61.8	47.9 62.9	48.9 63.9	49.9 65.0	45.0 54.0	46.8 55.9	48.6 57.8	50.4 59.8	52.3 61.7
71.8	72.9	74.1	75.2	76.4	77.6	61.2	63.3	65.4	67.5	69.7
45.0 64.8	46.3 67.3	47.6 68.8	48.8 70.9	50.1 71.4	51.4 71.1	45.0 57.1	47.3 59.3	49.6 61.6	51.9 63.8	54.2 66.1
75.0	76.3	77.6	78.9	80.2	81.5	63.2	65.5	67.8	70.2	72.6
45.0 66.1	46.4 67.5	47.7 68.8	49.1 70.2	50.4 71.5	51.8 72.8	45.0 57.9	47.4 60.3	49.8 62.7	52.3 65.1	54.7 67.5
75.3	76.5	77.8	79.0	80.3	81.7	63.7	66.1	68.6	71.1	73.6
45.0 66.4	46.4 67.8	47.7 69.2	49.1 70.6	50.5 71.9	51.9 73.3	45.0 58.1	47.5 60.5	49.9 63.0	52.4 65.5	54.8 68.0
75.0	77.3	78.7	80.1	81.5	82.9	63.7	66.1	68.6	71.1	73.6
45.0 66.4	46.4 67.8	47.7 69.2	49.1 70.6	50.5 71.9	51.9 73.3	45.0 57.9	47.4 60.3	49.8 62.7	52.3 65.1	54.7 67.5
75.3	77.6	78.9	80.2	81.5	82.8	63.2	65.5	67.8	70.2	72.6
45.0 66.1	46.4 67.5	47.7 68.8	49.1 70.2	50.4 71.5	51.8 72.8	45.0 57.1	47.3 59.3	49.6 61.6	51.9 63.8	54.2 66.1
75.0	76.3	77.6	78.9	80.2	81.5	61.2	63.3	65.4	67.5	69.7
45.0 64.8	46.3 67.3	47.6 68.8	48.8 70.9	50.1 71.4	51.4 71.1	45.0 54.0	46.8 55.9	48.6 57.8	50.4 59.8	52.3 61.7
71.8	72.9	74.1	75.2	76.4	77.6	61.2	63.3	65.4	67.5	69.7
45.0 59.9	46.0 60.8	47.0 61.8	47.9 62.9	48.9 63.9	49.9 65.0	61.2	63.3	65.4	67.5	69.7
71.8	72.9	74.1	75.2	76.4	77.6	61.2	63.3	65.4	67.5	69.7

OUTER LAYER										

TEMPERATURES										
LOCATION 1	LOCATION 2	LOCATION 3	LOCATION 4	LOCATION 5	LOCATION 6	LOCATION 7	LOCATION 8	LOCATION 9	LOCATION 10	LOCATION 11
45.0 54.0	46.8 55.9	48.6 57.8	50.4 59.8	52.3 61.7	54.1 63.7	56.0 65.7	57.9 67.6	59.8 69.6	61.8 71.7	63.7 73.7
71.8	72.9	74.1	75.2	76.4	77.6	73.9	76.1	78.3	80.4	82.6
45.0 57.1	47.3 59.3	49.6 61.6	51.9 63.8	54.2 66.1	56.4 68.3	58.7 70.6	61.0 72.9	63.2 75.1	65.5 77.4	67.8 79.7
75.0	76.3	77.6	78.9	80.2	81.5	77.3	79.7	82.1	84.5	86.8
45.0 57.9	47.4 60.3	49.8 62.7	52.3 65.1	54.7 67.5	57.1 70.0	59.5 72.4	62.0 74.8	64.4 77.2	66.8 79.7	69.2 82.1
76.1	78.5	80.9	83.3	85.7	88.1	78.5	81.0	83.5	86.0	88.5
45.0 58.1	47.5 60.5	49.9 63.0	52.4 65.5	54.8 68.0	57.3 70.5	59.8 72.9	62.3 75.4	64.7 77.9	67.2 80.4	69.7 82.9
76.3	78.7	81.1	83.5	85.9	88.3	78.8	81.3	83.8	86.3	88.8
45.0 58.1	47.5 60.5	49.9 63.0	52.4 65.5	54.8 68.0	57.3 70.5	59.8 72.9	62.3 75.4	64.7 77.9	67.2 80.4	69.7 82.9
76.3	78.7	81.1	83.5	85.9	88.3	78.8	81.3	83.8	86.3	88.8
45.0 57.9	47.4 60.3	49.8 62.7	52.3 65.1	54.7 67.5	57.1 70.0	59.5 72.4	62.0 74.8	64.4 77.2	66.8 79.7	69.2 82.1
76.1	78.5	80.9	83.3	85.7	88.1	78.5	81.0	83.5	86.0	88.5
45.0 57.1	47.3 59.3	49.6 61.6	51.9 63.8	54.2 66.1	56.4 68.3	58.7 70.6	61.0 72.9	63.2 75.1	65.5 77.4	67.8 79.7
75.0	76.3	77.6	78.9	80.2	81.5	77.3	79.7	82.1	84.5	86.8
45.0 54.0	46.8 55.9	48.6 57.8	50.4 59.8	52.3 61.7	54.1 63.7	56.0 65.7	57.9 67.6	59.8 69.6	61.8 71.7	63.7 73.7
71.8	72.9	74.1	75.2	76.4	77.6	73.9	76.1	78.3	80.4	82.6

VELOCITIES										
29.4	30.5	30.8	30.9	30.8	30.5	29.4	30.5	30.8	30.9	29.4

Figure 2.6-14. Winding Design with Silicone Oil Coolant (Cont'd)

<p>HIGH VOLTAGE GENERATOR CONDUCTOR AND COILING DESIGN SILICONE OIL COILANT</p> <p>600 MVA, 345 KV, 0.9 PF J00 AMPS/50 CM ARMATURE DENSITY 50 V/MIL INSULATION</p> <p>DIAPHRAGM CIRCUIT DELTA HELICAL WINDING</p> <p>FIELD WINDING INNER RADIUS 9.0 IN FIELD WINDING OUTER RADIUS 12.0 IN ARMATURE WIRE RADIUS 18.0 IN INNER LAYER INNER RADIUS 22.0 IN INNER LAYER OUTER RADIUS 24.9 IN OUTER LAYER INNER RADIUS 32.0 IN OUTER LAYER OUTER RADIUS 33.0 IN CORE INNER RADIUS 37.9 IN CORE OUTER RADIUS 173.0 IN ACTIVE LENGTH</p> <p>TERMINAL CURRENT 1004.1 AMPS CIRCUIT CURRENT 289.9 AMPS FIELD FLUX, INNER LAYER 1.46 TESLAS TANGENTIAL FLUX, INNER LAYER 0.65 TESLAS RADIAL FLUX, OUTER LAYER 0.94 TESLAS TANGENTIAL FLUX, OUTER LAYER 0.13 TESLAS</p> <p>INNER LAYER *****</p> <p>THERE ARE 371 TURNS PER PHASE BELT THE LAYER IS 7 CONDUCTORS HIGH THE CONDUCTOR AND HYDRAULIC LENGTH IS 188.0 IN THE HELIX ANGLE IS 23.1 DEGREES THE "SLOT WIDTH" IS 0.4263 IN</p> <p>CONDUCTOR SPECS:</p> <p>WIRE GAUGE 18 NO. FILAMENTS HIGH 6 NO. FILAMENTS WIDE 48 BAR WIDTH 0.3456 IN BAR HEIGHT 0.592 IN COPPER AREA 0.122 SQ IN CURRENT DENSITY 4234.6 AMPS/SQ IN</p> <p>VERTICAL DIVIDER:</p> <p>THICKNESS 0.0807 IN VOLTAGE STRESS 84.4 V/MIL</p> <p>COILANT PASSAGE:</p> <p>WIDTH 0.2956 IN HEIGHT 0.0607 IN AREA 0.01794 SQ IN HYDRAULIC DIA 0.1007 IN</p>	<p>STAINLESS STEEL COILING TUBES:</p> <p>WALL THICKNESS 0.023 IN INSULATION THICKNESS 0.005 IN TUBE WIDTH 0.461 IN TUBE HEIGHT 0.110 IN LOSSES 0.453 W/IN</p> <p>CONDUCTOR LOSSES:</p> <p>DC LOSSES 1.447 W/IN AC LOSSES 0.396 W/IN TOTAL 1.843 W/IN</p> <p>COILING PERFORMANCE (AVERAGED):</p> <p>PRESSURE DROP (INPUT) 90.00 LBS/SQ IN COILANT INLET TEMP 45.00 DEGREES CENTIGRADE FLOW VELOCITY 30.36 IN/SEC TOTAL FLOW 530.4 GAL/MIN REYNOLDS NO. 75.6 COILANT OUTLET TEMP 67.37 DEGREES CENTIGRADE</p> <p>INSULATION *****</p> <p>INSULATION VOLUME 462419.0 CUBIC INCHES PERCENT COILING AREA 0.1 COILING PASSAGE WIDTH 0.1000 IN COILING PASSAGE HEIGHT 0.1000 IN HYDRAULIC DIAMETER 0.1000 IN</p> <p>LOSSES 0.004 WATTS/CUBIC INCH DISSIPATION FACTOR 0.40 PERCENT</p> <p>COILING PERFORMANCE (AVERAGED):</p> <p>PRESSURE DROP (INPUT) 80.00 LBS/SQ IN COILANT INLET TEMP 45.00 DEGREES CENTIGRADE FLOW VELOCITY 34.38 IN/SEC TOTAL FLOW 23.9 GAL/MIN REYNOLDS NO. 65.2 COILANT OUTLET TEMP 45.96 DEGREES CENTIGRADE</p> <p>WINDING EFFICIENCY *****</p> <p>TOTAL CONDUCTOR LOSSES 1518.2 KW COILING TUBE LOSSES 454.1 KW INSULATION LOSSES 2.1 KW LIQUID PUMPING LOSSES 48.0 KW TOTAL LOSSES 2022.5 KW EFFICIENCY DROP 0.375 PERCENT</p>	<p>STAINLESS STEEL COILING TUBES:</p> <p>WALL THICKNESS 0.020 IN INSULATION THICKNESS 0.005 IN TUBE WIDTH 0.136 IN TUBE HEIGHT 0.101 IN LOSSES 0.407 W/IN</p> <p>CONDUCTOR LOSSES:</p> <p>DC LOSSES 1.077 W/IN AC LOSSES 0.595 W/IN TOTAL 1.672 W/IN</p> <p>COILING PERFORMANCE (AVERAGED):</p> <p>PRESSURE DROP (INPUT) 9.00 LBS/SQ IN COILANT INLET TEMP 45.00 DEGREES CENTIGRADE FLOW VELOCITY 30.41 IN/SEC TOTAL FLOW 360.5 GAL/MIN REYNOLDS NO. 4942.4 COILANT OUTLET TEMP 72.80 DEGREES CENTIGRADE</p> <p>OUTER LAYER *****</p> <p>THERE ARE 371 TURNS PER PHASE BELT THE LAYER IS 7 CONDUCTORS HIGH THE CONDUCTOR AND HYDRAULIC LENGTH IS 201.7 IN THE HELIX ANGLE IS 30.9 DEGREES THE "SLOT WIDTH" IS 0.5593 IN</p> <p>CONDUCTOR SPECS:</p> <p>WIRE GAUGE 14 NO. FILAMENTS HIGH 2 NO. FILAMENTS WIDE 7 BAR WIDTH 0.4711 IN BAR HEIGHT 0.1346 IN COPPER AREA 0.04518 SQ IN CURRENT DENSITY 6415.7 AMPS/SQ IN</p> <p>VERTICAL DIVIDER:</p> <p>THICKNESS 0.0882 IN VOLTAGE STRESS 77.2 V/MIL</p> <p>COILANT PASSAGE:</p> <p>WIDTH 0.4151 IN HEIGHT 0.0637 IN AREA 0.02645 SQ IN HYDRAULIC DIA 0.1105 IN</p>	<p>STAINLESS STEEL COILING TUBES:</p> <p>WALL THICKNESS 0.023 IN INSULATION THICKNESS 0.005 IN TUBE WIDTH 0.461 IN TUBE HEIGHT 0.110 IN LOSSES 0.453 W/IN</p> <p>CONDUCTOR LOSSES:</p> <p>DC LOSSES 1.447 W/IN AC LOSSES 0.396 W/IN TOTAL 1.843 W/IN</p> <p>COILING PERFORMANCE (AVERAGED):</p> <p>PRESSURE DROP (INPUT) 90.00 LBS/SQ IN COILANT INLET TEMP 45.00 DEGREES CENTIGRADE FLOW VELOCITY 30.36 IN/SEC TOTAL FLOW 530.4 GAL/MIN REYNOLDS NO. 75.6 COILANT OUTLET TEMP 67.37 DEGREES CENTIGRADE</p> <p>INSULATION *****</p> <p>INSULATION VOLUME 462419.0 CUBIC INCHES PERCENT COILING AREA 0.1 COILING PASSAGE WIDTH 0.1000 IN COILING PASSAGE HEIGHT 0.1000 IN HYDRAULIC DIAMETER 0.1000 IN</p> <p>LOSSES 0.004 WATTS/CUBIC INCH DISSIPATION FACTOR 0.40 PERCENT</p> <p>COILING PERFORMANCE (AVERAGED):</p> <p>PRESSURE DROP (INPUT) 80.00 LBS/SQ IN COILANT INLET TEMP 45.00 DEGREES CENTIGRADE FLOW VELOCITY 34.38 IN/SEC TOTAL FLOW 23.9 GAL/MIN REYNOLDS NO. 65.2 COILANT OUTLET TEMP 45.96 DEGREES CENTIGRADE</p> <p>WINDING EFFICIENCY *****</p> <p>TOTAL CONDUCTOR LOSSES 1518.2 KW COILING TUBE LOSSES 454.1 KW INSULATION LOSSES 2.1 KW LIQUID PUMPING LOSSES 48.0 KW TOTAL LOSSES 2022.5 KW EFFICIENCY DROP 0.375 PERCENT</p>
---	---	--	---

Figure 2.6-14. Winding Design with Silicone Oil Coolant

DETAILED TEMPERATURE AND FLOW VELOCITY PROFILES

INNER LAYER

TEMPERATURES

LOCATION 1	LOCATION 2	LOCATION 3	LOCATION 4	LOCATION 5	LOCATION 6
45.0 47.1	46.0 49.0	51.1 50.9	53.1 53.0	55.2 55.1	57.4 57.4
57.0 57.0	59.5 59.5	62.0 62.0	64.5 64.5	67.0 67.0	69.5 69.5
45.0 48.2	48.0 51.2	51.0 54.1	53.9 57.0	56.8 59.9	59.7 62.7
57.7 57.7	60.7 60.7	63.7 63.7	66.8 66.8	69.7 69.7	72.7 72.7
45.0 48.3	48.1 51.4	51.2 54.5	54.3 57.6	60.6 60.4	63.7 63.3
57.7 57.7	60.8 60.8	63.9 63.9	67.1 67.1	70.2 70.2	73.3 73.3
45.0 48.3	48.1 51.4	51.2 54.5	54.3 57.6	60.6 60.5	63.9 63.9
57.7 57.7	60.8 60.8	64.0 64.0	67.1 67.1	70.2 70.2	73.4 73.4
45.0 48.3	48.1 51.4	51.2 54.5	54.3 57.6	60.6 60.5	63.9 63.9
57.7 57.7	60.8 60.8	63.9 63.9	67.1 67.1	70.2 70.2	73.3 73.3
45.0 48.3	48.1 51.4	51.2 54.5	54.3 57.6	60.6 60.4	63.7 63.7
57.7 57.7	60.7 60.7	63.7 63.7	66.8 66.8	69.7 69.7	72.7 72.7
45.0 48.2	48.0 51.2	51.0 54.1	53.9 57.0	56.8 59.9	59.7 62.7
57.0 57.0	59.5 59.5	62.0 62.0	64.5 64.5	67.0 67.0	69.5 69.5
45.0 47.1	46.0 49.0	48.9 51.1	50.9 53.1	53.0 55.2	55.1 57.4

LOCATION 7	LOCATION 8	LOCATION 9	LOCATION 10	LOCATION 11
57.2 59.6	61.8 61.8	64.0 64.0	66.3 66.3	68.5 68.5
72.1 72.1	74.6 74.6	77.1 77.1	79.7 79.7	82.2 82.2
62.5 65.5	65.3 68.3	68.1 71.1	70.9 73.9	73.7 76.6
75.7 75.7	78.7 78.7	81.6 81.6	84.5 84.5	87.5 87.5
63.5 66.8	66.5 69.6	69.6 72.9	72.6 75.9	75.7 79.0
76.4 76.4	79.6 79.6	82.7 82.7	85.8 85.8	88.9 88.9
61.6 67.0	66.7 70.1	69.9 73.2	73.0 76.3	76.1 79.5
76.5 76.5	79.7 79.7	82.9 82.9	86.0 86.0	89.2 89.2
63.6 67.0	66.7 70.1	69.9 73.2	73.0 76.3	76.1 79.5
76.4 76.4	79.6 79.6	82.7 82.7	85.8 85.8	88.9 88.9
63.5 66.8	66.5 69.6	69.6 72.9	72.6 75.9	75.7 79.0
75.7 75.7	78.7 78.7	81.6 81.6	84.5 84.5	87.5 87.5
62.5 65.5	65.3 68.3	68.1 71.1	70.9 73.9	73.7 76.6
72.1 72.1	74.6 74.6	77.1 77.1	79.7 79.7	82.2 82.2
57.2 59.6	59.4 61.8	61.6 64.0	63.8 66.3	66.1 68.5

ALL VELOCITIES ARE 30.4

OUTER LAYER

TEMPERATURES

LOCATION 1	LOCATION 2	LOCATION 3	LOCATION 4	LOCATION 5	LOCATION 6
45.0 46.9	47.2 49.2	49.6 51.6	52.0 54.1	54.6 56.7	57.2 59.4
52.9 52.9	55.8 55.8	58.7 58.7	61.6 61.6	64.5 64.5	67.5 67.5
45.0 47.9	48.4 51.2	51.8 54.5	55.1 57.7	58.3 61.0	61.5 64.2
53.5 53.5	57.0 57.0	60.4 60.4	63.8 63.8	67.2 67.2	70.6 70.6
45.0 47.9	48.5 51.5	52.1 55.0	55.6 58.5	59.1 62.1	65.6 65.6
53.5 53.5	57.1 57.1	60.7 60.7	64.3 64.3	67.9 67.9	71.5 71.5
45.0 48.0	48.6 51.5	52.1 55.1	58.7 59.3	62.3 62.3	65.9 65.9
53.5 53.5	57.1 57.1	60.8 60.8	64.4 64.4	68.0 68.0	71.7 71.7
45.0 48.0	48.6 51.5	52.1 55.1	58.7 59.3	62.3 62.3	65.9 65.9
53.5 53.5	57.1 57.1	60.7 60.7	64.3 64.3	67.9 67.9	71.5 71.5
45.0 47.9	48.5 51.5	52.1 55.0	55.6 58.5	59.1 62.1	65.6 65.6
53.5 53.5	57.0 57.0	60.4 60.4	63.8 63.8	67.2 67.2	70.6 70.6
45.0 47.9	48.4 51.2	51.8 54.5	55.1 57.7	58.3 61.0	61.5 64.2
52.9 52.9	55.8 55.8	59.7 59.7	61.6 61.6	64.5 64.5	67.5 67.5
45.0 46.9	47.2 49.2	49.6 51.6	52.0 54.1	54.6 56.7	57.2 59.4

LOCATION 7	LOCATION 8	LOCATION 9	LOCATION 10	LOCATION 11
59.8 62.1	62.5 64.8	65.3 67.6	68.0 70.4	70.9 73.2
70.5 70.5	73.5 73.5	76.5 76.5	79.5 79.5	82.6 82.6
64.7 67.3	67.9 70.5	71.1 73.7	74.3 76.9	77.5 80.1
74.0 74.0	77.4 77.4	80.8 80.8	84.1 84.1	87.5 87.5
66.1 69.1	69.6 72.5	73.1 76.0	76.6 79.5	80.1 83.0
75.1 75.1	78.7 78.7	82.3 82.3	85.9 85.9	89.5 89.5
66.5 69.5	70.1 73.1	73.7 76.7	77.3 80.3	80.9 83.9
75.3 75.3	79.0 79.0	82.6 82.6	86.3 86.3	89.9 89.9
66.5 69.5	70.1 73.1	73.7 76.7	77.3 80.3	80.9 83.9
75.1 75.1	78.7 78.7	82.3 82.3	85.9 85.9	89.5 89.5
66.1 69.1	69.6 72.5	73.1 76.0	76.6 79.5	80.1 83.0
74.0 74.0	77.4 77.4	80.8 80.8	84.1 84.1	87.5 87.5
64.7 67.3	67.9 70.5	71.1 73.7	74.3 76.9	77.5 80.1
70.5 70.5	73.5 73.5	76.5 76.5	79.5 79.5	82.6 82.6
59.8 62.1	62.5 64.8	65.3 67.6	68.0 70.4	70.9 73.2

ALL VELOCITIES ARE 27.4

Figure 2.6-13. Winding Design with Freon Coolant (Cont'd)

<p>HIGH VOLTAGE GENERATOR CONDUCTOR AND COWLING DESIGN FREON COWLING</p> <p>600 MVA, 345 KV, 0.9 PF 10000 AMP/50 CM ARMATURE DENSITY 50 V/IN INSULATION</p> <p>FIELD WINDING INNER RADIUS FIELD WINDING OUTER RADIUS ARMATURE DRIVE RADIUS INNER LAYER INNER RADIUS INNER LAYER OUTER RADIUS OUTER LAYER INNER RADIUS OUTER LAYER OUTER RADIUS CORE INNER RADIUS ACTIVE LENGTH</p> <p>1004.1 AMPS 2009.0 AMPS 1.47 TESLAS 0.66 TESLAS 0.94 TESLAS 0.13 TESLAS</p> <p>INNER LAYER *****</p> <p>THERE ARE 371 TURNS PER PHASE BELT THE LAYER IS 7 CONDUCTORS HIGH THE CONDUCTOR AND HYDRAULIC LENGTH IS 187.0 IN THE HELIX ANGLE IS 23.0 DEGREES THE "SLOT WIDTH" IS 0.424 IN</p> <p>CONDUCTOR SPECS:</p> <p>WIRE GAUGE 18 NO. FILAMENTS HIGH 6 NO. FILAMENTS WIDE 8 NO. FILAMENTS 48 WIRE WIDTH 0.1458 IN WIRE HEIGHT 0.2592 IN COPPER AREA 0.0603 SQ IN CURRENT DENSITY 311.7 AMP/IN</p> <p>VELOCITY IN/IN/SEC 0.0002 IN</p> <p>THICKNESS 0.0002 IN VOLTAGE STRESS 36.0 V/IN</p>	<p>COWLING PASSAGE:</p> <p>WIDTH 0.2056 IN HEIGHT 0.0607 IN AREA 0.01794 SQ IN HYDRAULIC DIA 0.1007 IN</p> <p>STAINLESS STEEL COWLING TUBES:</p> <p>WALL THICKNESS 0.020 IN INSULATION THICKNESS 0.005 IN TUBE WIDTH 0.136 IN TUBE HEIGHT 0.101 IN LOSSES 0.407 W/IN</p> <p>CONDUCTOR LOSSES:</p> <p>DC LOSSES 1.077 W/IN AC LOSSES 0.595 W/IN TOTAL 1.672 W/IN</p> <p>COWLING PERFORMANCE (AVERAGED):</p> <p>PRESSURE DROP (INPUT) 9.00 LBS/50 IN COWLING INLET TEMP 45.00 DEGREES CENTIGRADE FLOW VELOCITY 30.41 IN/SEC TOTAL FLOW 360.5 GAL/MIN REYNOLDS NO. 4942.4 COWLING OUTLET TEMP 72.80 DEGREES CENTIGRADE</p> <p>OUTER LAYER *****</p> <p>THERE ARE 371 TURNS PER PHASE BELT THE LAYER IS 7 CONDUCTORS HIGH THE CONDUCTOR AND HYDRAULIC LENGTH IS 201.7 IN THE HELIX ANGLE IS 30.9 DEGREES THE "SLOT WIDTH" IS 0.5593 IN</p> <p>CONDUCTOR SPECS:</p> <p>WIRE GAUGE 14 NO. FILAMENTS HIGH 2 NO. FILAMENTS WIDE 7 NO. FILAMENTS 14 WIRE WIDTH 0.1400 IN WIRE HEIGHT 0.1350 IN COPPER AREA 0.0650 SQ IN CURRENT DENSITY 315.7 AMP/IN</p> <p>VELOCITY IN/IN/SEC 0.0002 IN</p> <p>THICKNESS 0.0002 IN VOLTAGE STRESS 77.2 V/IN</p>	<p>COWLING PASSAGE:</p> <p>WIDTH 0.4131 IN HEIGHT 0.0492 IN AREA 0.02033 SQ IN HYDRAULIC DIA 0.0960 IN</p> <p>STAINLESS STEEL COWLING TUBES:</p> <p>WALL THICKNESS 0.024 IN INSULATION THICKNESS 0.005 IN TUBE WIDTH 0.461 IN TUBE HEIGHT 0.097 IN LOSSES 0.439 W/IN</p> <p>CONDUCTOR LOSSES:</p> <p>DC LOSSES 1.471 W/IN AC LOSSES 0.386 W/IN TOTAL 1.859 W/IN</p> <p>COWLING PERFORMANCE (AVERAGED):</p> <p>PRESSURE DROP (INPUT) 9.00 LBS/50 IN COWLING INLET TEMP 45.00 DEGREES CENTIGRADE FLOW VELOCITY 27.43 IN/SEC TOTAL FLOW 368.5 GAL/MIN REYNOLDS NO. 3894.0 COWLING OUTLET TEMP 77.24 DEGREES CENTIGRADE</p> <p>WINDING EFFICIENCY *****</p> <p>TOTAL CONDUCTOR LOSSES 1534.3 KW COWLING TUBE LOSSES 419.8 KW LIQUID PUMPING LOSSES 2.9 KW TOTAL LOSSES 1957.0 KW EFFICIENCY DROP 0.362 PERCENT</p>
--	---	--

Figure 2.6-13. Winding Design with Freon Coolant

20 mils. The cooling tube interior height should not be less than 50 mils. The pressure drop should not exceed 60 psi. Filaments of 18 AWG are necessary for the inner layer conductors, while filaments of 16 AWG or 14 AWG will suffice for the outer layer conductors.

It required placing seven conductors high in a column to minimize the thermal resistances sufficiently. Twenty-two psi pressure drop is then required to circulate enough coolant to limit the hotspots. The hotspot of the inner layer is 89.6 °C and that of the outer layer is 88.0 °C. The coolant outlet temperatures of the inner layer range from 58.9 °C to 63.9 °C, encompassing the 62.2 °C coolant outlet temperature calculated earlier by the averaged method. The coolant stream flow velocities of the inner layer range from 39.7 in./s to 42.5 in./s, encompassing the 41.5 in./s flow velocity calculated earlier by the averaged method. The same agreement is also found for these quantities calculated for the outer layer. Considering the good agreement between the cooling performance quantities determined by both the averaged method and the ladder thermal circuit method, it is safe to assume that the other quantities calculated by the averaged method are fairly accurate. The Reynolds numbers indicate that the flows are indeed laminar. The inner layer requires 492 gal/min of coolant, and the outer layer requires 399 gal/min, for a total of 891 gal/min. This amount of flow is considerably larger than that required by a 600 MVA conventional generator, but it is hardly surprising, considering that the allowed hotspot temperatures are much lower and that transil oil is an inferior coolant compared to water. This amount of flow is, however, perfectly within the practice of large power transformers.

The heating of the cylinder insulations is indeed minimal, judging from the low coolant outlet temperature and low flow calculated for the insulation. One may be tempted to eliminate the insulation cooling passages altogether; however, such axial passages will be required to facilitate the drying and impregnating of the insulation. Also, the use of cooling passages will guarantee that there will be no thermal runaway, a phenomenon relating to the rising dissipation factor accompanying rising temperature.

Figure 2.6-13 contains a calculation using Freon 113 coolant. The same design dimensions that were used for the calculation with transil oil coolant are retained. The calculations, however, may be no more accurate than the coolant properties on which they are based. (The stated cooling properties of Freon 113 were measured at 30 °C, without any temperature relationship.) The greatest advantage in using Freon is that the flow conditions are turbulent, and the convection heat transfer is greatly improved. This allows the flow to be decreased while maintaining the same hotspot temperature. The combined flow of the inner and outer conductor layers is 728 gal/min and the pressure drop is 9.0 psi. The flow and pressure drop for the transil oil calculation are 891 gal/min and 20 psi, respectively. The flow reduction for Freon is certainly not spectacular, and when one considers the greater expense and required pressurization, the option of using Freon may not be as attractive as using transil oil. Also, the dielectric experience with Freon is limited.

Figure 2.6-14 contains a calculation using silicone oil coolant. The viscosity of silicone oil is greater than that of transil oil while the heat capacity of silicone oil is less, and the two combine to produce inferior cooling performance. The required flow is 1355 gal/min with a pressure drop of 80 psi! Clearly, more cooling cross-sectional area is needed, requiring a larger machine size, or a silicone oil having a lower viscosity than that identified in Reference 2.6-1 would be needed.

It was mentioned earlier that a reduction in the equivalent thermal resistance of convection is obtained by utilizing cooling tubes of a very short and wide aspect. Such cooling tubes will suffer increased eddy current losses, but, more importantly, the bending stresses of the horizontal walls of the cooling tubes will become excessive. The maximum radial winding pressure during sudden short circuit was calculated to be 608 psi compressive at the location of the inner conductor layer (see Section 2.4.2). This pressure produces a 114,000 psi bending stress in the horizontal walls of the cooling tubes, and the yield strength of stainless steel is only 35,000 psi. The preferred solution for this problem is to utilize cooling tubes having center walls or to utilize smaller twin tubes placed side-by-side. Both concepts are illustrated in Figure 2.6-15. These tube configurations lower the bending stresses by shortening the beam span over which the pressure is applied. The effect of these tube configurations on the cooling performance is minor. The aspects of the individual

The machine losses are summed together under "Winding Efficiency." The components of losses need no explanation except for the liquid pumping losses, which are merely the frictional losses of the fluid flow. The efficiency drop is the total losses divided by the power rating of the machine.

Finally, the detailed temperature and flow calculations performed by the laddered thermal circuit method are listed as "Detailed Temperature and Flow Velocity Profiles." All coolant stream temperatures, cooling tube temperatures, and conductor midline temperatures are listed for each location, and the individual coolant stream flow velocities are also given. The legend for interpreting the temperature listings is on Figure 2.6-12.

The ultimate criterion for the design of the winding and its cooling is that no winding temperature should greatly exceed 90 °C. The winding hotspot will be found at the conductor midline of the center conductor of the stack at location 11. There are three methods for limiting the hotspot: one, reduce the generated losses of the conductor and cooling tube; two, reduce the temperature rise from the coolant stream to the conductor midline; and three, reduce the coolant temperature rise from inlet to outlet. Reducing generated losses can be accomplished by reducing eddy current

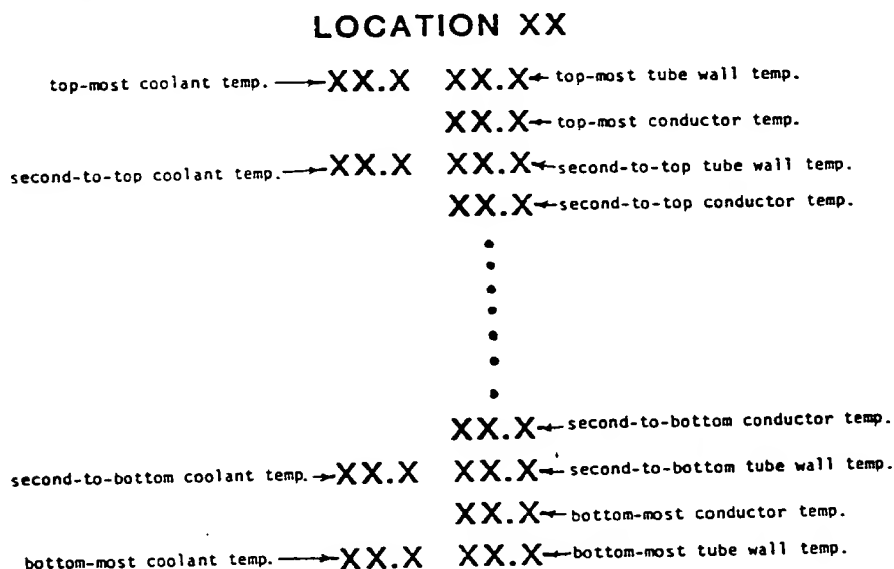


Figure 2.6-12. Interpretation of Temperature Profile Listings

losses or reducing I^2R losses or both. Eddy current losses can be limited by using very small filaments in the conductors, and this technique is particularly important for the conductors of the inner layer where the magnetic flux is intense. Reducing I^2R losses must be accomplished by increasing the copper cross-sectional area, but there may be space restrictions preventing such an increase. Also, the added copper increases the eddy current losses so that a situation of diminished returns is realized. Reducing the coolant temperature rise from inlet to outlet is accomplished by increasing the flow, a technique that is contrary to minimizing pumping capacity. The most effective technique for limiting hotspots is to reduce the coolant stream to conductor midline temperature rise by reducing the thermal resistances. The thermal resistance of the conductor half may be reduced by utilizing short and wide conductor configurations. The equivalent thermal resistance of convection in the coolant stream is also reduced by employing a short and wide configuration of the cooling tube. With the conductor layer height and number of turns already specified, increasing the aspect ratios of the conductors and cooling tubes is accomplished by increasing the number of conductors stacked in a column. The winding design being discussed uses seven conductors in a column. It is important, however, that the aspect ratios not be excessive since the conductors and cooling tubes will become unwieldy. Also, the cooling tube eddy current losses will become excessive.

Several recommended design constraints should be followed. The electrical stress on the vertical divider should not exceed 100 V/mil. The cooling tube wall thickness should not be less than

<p>HIGH VOLTAGE GENERATOR CONDUCTOR AND COILING DESIGN TRANSIL OIL COOLANT</p> <p>600 MVA, 345 KV, 0.9 PF 300 AMPS/50 CM AMPATURE DENSITY 50 V/MIL INSULATION</p> <p>FIELD WINDING INNER RADIUS 9.0 IN FIELD WINDING OUTER RADIUS 12.0 IN ARMATURE WIRE RADIUS 18.0 IN INNER LAYER INNER RADIUS 22.0 IN INNER LAYER OUTER RADIUS 24.7 IN OUTER LAYER INNER RADIUS 32.1 IN OUTER LAYER OUTER RADIUS 33.9 IN CORE INNER RADIUS 37.9 IN ACTIVE LENGTH 173.0 IN</p> <p>TERMINAL CURRENT 1004.1 AMPS CIRCUIT CURRENT 289.9 AMPS RADIAL FLUX, INNER LAYER 1.47 TESLAS TANGENTIAL FLUX, INNER LAYER 0.66 TESLAS RADIAL FLUX, OUTER LAYER 0.94 TESLAS TANGENTIAL FLUX, OUTER LAYER 0.13 TESLAS</p> <p>INNER LAYER =====</p> <p>THERE ARE 371 TURNS PER PHASE BELT THE LAYER IS 7 CONDUCTORS HIGH THE CONDUCTOR AND HYDRAULIC LENGTH IS 187.9 IN THE HELIX ANGLE IS 23.0 DEGREES THE "SLOT WIDTH" IS 0.4248 IN</p> <p>CONDUCTOR SPECS:</p> <p>WIRE GAUGE 18 NO. FILAMENTS HIGH 6 NO. FILAMENTS WIDE 48 BAR WIDTH 0.3456 IN BAR HEIGHT 0.2592 IN COPPER AREA 0.06122 SQ IN CURRENT DENSITY 4734.6 AMPS/SQ IN</p> <p>VERTICAL DIVIDER:</p> <p>THICKNESS 0.0792 IN VOLTAGE STRESS 86.0 V/MIL</p> <p>COILANT PASSAGE:</p> <p>WIDTH 0.2056 IN HEIGHT 0.0607 IN AREA 0.01794 SQ IN HYDRAULIC DIA 0.1007 IN</p>	<p>STAINLESS STEEL COILING TUBES:</p> <p>WALL THICKNESS 0.020 IN INSULATION THICKNESS 0.005 IN TUBE WIDTH 0.336 IN TUBE HEIGHT 0.101 IN LOSSES 0.409 W/IN</p> <p>CONDUCTOR LOSSES:</p> <p>DC LOSSES 1.058 W/IN AC LOSSES 0.604 W/IN TOTAL 1.664 W/IN</p> <p>COILING PERFORMANCE (AVERAGED):</p> <p>PRESSURE DROP (INPUT) 22.00 LBS/SQ IN COILANT INLET TEMP 45.00 DEGREES CENTIGRADE FLOW VELOCITY 41.53 IN/SEC TOTAL FLOW 492.3 GAL/MIN REYNOLDS NO. 435.9 COILANT OUTLET TEMP 62.18 DEGREES CENTIGRADE</p> <p>OUTER LAYER =====</p> <p>THERE ARE 371 TURNS PER PHASE BELT THE LAYER IS 7 CONDUCTORS HIGH THE CONDUCTOR AND HYDRAULIC LENGTH IS 201.7 IN THE HELIX ANGLE IS 30.9 DEGREES THE "SLOT WIDTH" IS 0.5593 IN</p> <p>CONDUCTOR SPECS:</p> <p>WIRE GAUGE 14 NO. FILAMENTS HIGH 2 NO. FILAMENTS WIDE 7 BAR WIDTH 0.4711 IN BAR HEIGHT 0.1346 IN COPPER AREA 0.04518 SQ IN CURRENT DENSITY 6415.7 AMPS/SQ IN</p> <p>VERTICAL DIVIDER:</p> <p>THICKNESS 0.0882 IN VOLTAGE STRESS 77.2 V/MIL</p> <p>COILANT PASSAGE:</p> <p>WIDTH 0.4131 IN HEIGHT 0.0492 IN AREA 0.02033 SQ IN HYDRAULIC DIA 0.0880 IN</p>	<p>STAINLESS STEEL COILING TUBES:</p> <p>WALL THICKNESS 0.024 IN INSULATION THICKNESS 0.005 IN TUBE WIDTH 0.461 IN TUBE HEIGHT 0.097 IN LOSSES 0.440 W/IN</p> <p>CONDUCTOR LOSSES:</p> <p>DC LOSSES 1.453 W/IN AC LOSSES 0.393 W/IN TOTAL 1.846 W/IN</p> <p>COILING PERFORMANCE (AVERAGED):</p> <p>PRESSURE DROP (INPUT) 22.00 LBS/SQ IN COILANT INLET TEMP 45.00 DEGREES CENTIGRADE FLOW VELOCITY 39.69 IN/SEC TOTAL FLOW 308.9 GAL/MIN REYNOLDS NO. 300.1 COILANT OUTLET TEMP 69.87 DEGREES CENTIGRADE</p> <p>INSULATION =====</p> <p>INSULATION VOLUME 471494.3 CUBIC INCHES PERCENT COILING AREA 0.1 COILING PASSAGE WIDTH 0.1000 IN HYDRAULIC DIAMETER 0.1000 IN</p> <p>LOSSES DISSSIPATION FACTOR 0.014 MATTS/CUBIC INCH 0.40 PERCENT</p> <p>COILING PERFORMANCE (AVERAGED):</p> <p>PRESSURE DROP (INPUT) 22.00 LBS/SQ IN COILANT INLET TEMP 45.00 DEGREES CENTIGRADE FLOW VELOCITY 47.26 IN/SEC TOTAL FLOW 331.5 GAL/MIN REYNOLDS NO. 391.2 COILANT OUTLET TEMP 45.60 DEGREES CENTIGRADE</p> <p>WINDING EFFICIENCY =====</p> <p>TOTAL CONDUCTOR LOSSES 1524.8 KW COILING TUBE LOSSES 421.6 KW INSULATION LOSSES 2.1 KW LIQUID PUMPING LOSSES 8.8 KW TOTAL LOSSES 1957.3 KW EFFICIENCY DROP 0.362 PERCENT</p>
---	--	---

Figure 2.6-11. Winding Design with Transil Oil Coolant

tube temperatures now both known, the heat input to each coolant stream can be calculated. The coolant stream temperature-rises over the length of the first segment can be calculated from a formula similar to Equation 2.6-5, finally arriving at the coolant stream temperatures at location 2. These now become the coolant temperature inputs to the thermal circuit at location 2, allowing the thermal circuit at location 2 to be solved. This ladder sequence of thermal circuit calculations and coolant rise calculations proceeds until the end of the winding is reached (location 11).

The calculation ladder just described constitutes but one iteration of the entire temperature calculation process. At the first iteration, all coolant stream viscosities and all metallic electrical resistivities are calculated at 45 °C. For subsequent iterations, the coolant viscosity of each coolant stream is calculated at the coolant stream temperature at location 6 of the previous iteration, and the metallic electrical resistivities of all nodes at all locations are calculated at the nodal temperatures calculated in the previous iteration. The iterations are continued until convergence of each coolant stream outlet temperature (temperature at location 11) is obtained.

The aforementioned equations and calculation procedures have been incorporated into computer programs to allow for rapid calculations and rapid adjustment of design parameters. Calculations have been performed for the 600 MVA, 345 kV helical coil winding, high-voltage generator whose basic dimensions were calculated in Section 2.2.2. This machine has insulation rated at 50 V/mil and has a 300 A/cm² overall armature current density. Calculations have been performed with the utilization of each of the three identified coolants.

Figure 2.6-11 shows the computer output for a design using transil oil coolant. The output begins with a listing of the cylinder radii and active length (as taken from the sizing studies). This is followed by a listing of the terminal current, circuit current, and calculations of the magnetic flux densities at the inner and outer conductor layers. Next, a large set of calculations is repeated for both the inner and outer conductor layers and is tabulated under the respective headings "Inner Layer" and "Outer Layer." These sets contain conductor dimensions, conductor filament compositions, cooling tube dimensions, averaged cooling performance (assuming equal distribution of the losses into the coolant streams), and the losses under these conditions. These sets provide a generalized view of the winding performance. The detailed cooling and temperature calculations of the ladder thermal circuit method are contained in a later section. The generalized set begins with a listing of the number of turns per phase belt, the number of conductors stacked in a column, the conductor and hydraulic length (which is longer than the axial active length due to the helix geometry), the helix angle, and the "slot-width" (the distance between adjacent conductor columns). The subsection "Conductor Specs" describes the filament wire gauge, the filament arrangement, the conductor external dimensions, the copper area, and the copper current density. The subsection "Vertical Divider" describes the thickness of the divider and the voltage stress due to the voltage that appears between peripherally adjacent conductors. The subsection "Coolant Passage" describes the dimensions of the cooling tube interior, its area, and the hydraulic diameter. The subsection "Stainless Steel Cooling Tubes" describes the wall thickness of the tubes, the thickness of the insulation wrap, the external dimensions of the tubes, and the tubes' eddy current losses. The subsection "Conductor Losses" describes the I^2R losses (dc losses) and the eddy current losses (ac losses) of the conductors. The subsection "Cooling Performance (Averaged)" describes the cooling performance under the assumption that the losses are equally distributed into the coolant streams. The pressure drop and coolant inlet temperature are input. The flow velocity, total flow-volume rate of the entire winding layer, Reynolds number, and coolant outlet temperature are shown.

After the averaged cooling calculation set is repeated for the outer layer, a set of calculations devoted to the cylinder insulations is listed under the heading "Insulation." First, the total insulation volume is listed. The percent cooling area is the proportion of the insulation cylinders' cross-sectional area that is devoted to cooling passages. The dimensions of individual cooling passages follow. The losses are calculated on a per-unit-volume basis and the dissipation factor of the insulation is given. The same set of averaged cooling calculations described for the winding layers is listed next.

tor and cooling tube; temperature nodes for each conductor, cooling tube, and coolant stream; and the appropriate thermal resistances to link them together. The temperature nodes marked "TCP" are coolant stream average temperatures and these temperatures are input for the circuit solution. At location 1, for instance, the coolant average temperature for all tubes is the coolant inlet temperature of 45 °C (the industry standard for turbine-generator cooling systems). The coolant temperature nodes are linked to the cooling tube temperature nodes by resistors marked "RS". These are the equivalent thermal resistances of convection, and are defined by

$$\text{resistance of convection ("RS")} = \frac{1}{hS}$$

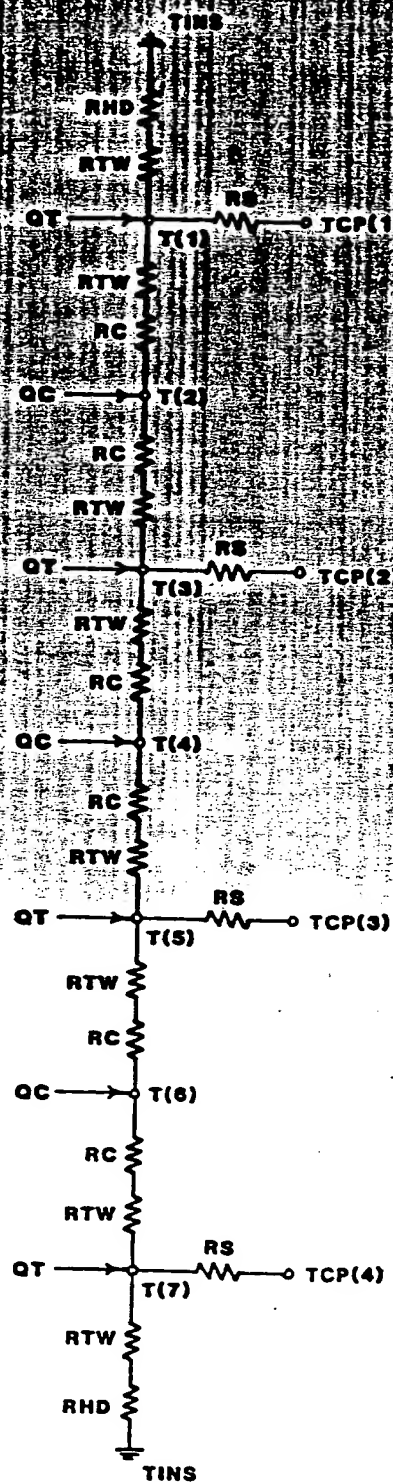
from the convection temperature drop equation (2.6-13). Values of RS are determined from the modified Nusselt number relationships, Figure 2.6-8, or Equation 2.6-16. The entire cooling tube wall is assumed to be at a uniform temperature, implying negligible thermal resistance and allowing it to be modeled as a single temperature node. Each cooling tube node has a heat input, marked "QT", which represents the cooling tube eddy current losses. The cooling tube nodes are linked to the conductor midline nodes by thermal resistances marked "RTW", representing the thermal resistance of the cooling tube insulation wrap, and "RC", representing the thermal resistance of a conductor-half. Each conductor midline node has a heat input marked "QC", which represents the conductor I²R losses and eddy current losses. At this point, the reader may note a discrepancy in that the losses of the conductor are uniformly generated over the cross-section of the conductor and are not nodally injected, as the model represents. The model would therefore calculate a conductor edge to conductor midline temperature rise that is too large. This assertion is absolutely correct; however, Appendix D demonstrates that the correct temperature rise can be calculated if the conductor-half thermal resistance is reduced by exactly one-half from its actual value. The thermal conductivity of the conductor must be estimated from graphs (Ref. 2.6-5) relating this quantity to the thermal conductivity of the filament insulation and the amount of metal in the cross-section of the conductor. A value of 5.5 times the filament insulation thermal conductivity is used in this model. The thermal conductivities of the various materials in the winding are listed in Table 2.6-3. The top and bottommost cooling tube temperature nodes are joined to thermal resistances marked "RHD", which represent the pressboard horizontal dividers. The RHD resistances are in turn connected to grounded temperature nodes marked "TINS". These represent the temperature of the cylinder insulations. The heating of the cylinder insulation is so minimal that these temperatures are kept at 45 °C over the entire length of the winding; hence their grounded representation.

Table 2.6-3
THERMAL CONDUCTIVITIES OF THE WINDING MATERIALS

Filament Insulation	.0056	$\frac{\text{watts}}{\text{in } ^\circ\text{C}}$
Conductors	.0308	
Oil-Impregnated Pressboard (Cooling Tube Insulation Wrap, Horizontal Dividers)	.0028	
Stainless Steel Cooling Tubes	assumed infinite	

The inputs to the described thermal circuit are the resistance values, the heat inputs, and the coolant stream temperatures. The resistance values and heat inputs are calculated on a per-unit-length basis. The circuit is solved for the temperatures of the cooling tubes and the conductor midlines, and the formulation to produce this solution is described in Appendix E.

The thermal circuit at location 1 is calculated first, with the coolant stream temperatures of all tubes set at the coolant inlet temperature of 45 °C. The circuit is solved to produce the cooling tube temperatures and the conductor midline temperatures. With the coolant stream temperatures and cool-



LEGEND

- RHD - RESISTANCE OF HORIZONTAL DIVIDER
- RTW - RESISTANCE OF COOLING TUBE INSULATION WRAP
- RC - RESISTANCE OF CONDUCTOR HALF
- RS - EQUIVALENT RESISTANCE OF CONVECTION SURFACE RISE
- QC - CONDUCTOR HEAT INPUT
- QT - COOLING TUBE HEAT INPUT
- T() - TEMPERATURE OF COOLING TUBE, ODD ARGUMENT
- TEMPERATURE OF CONDUCTOR CENTER, EVEN ARGUMENT
- TCP() - COOLANT TEMPERATURE
- TINS - TEMPERATURE OF CYLINDER INSULATION (45° C)

Figure 2.6-10. Thermal Resistance Circuit for the Calculation of Winding Component Temperatures

illustrated in graphical form in Figure 2.6-8. The modified Nusselt number for turbulent flow, also derived from Reference 2.6-4, is the empirical formula

$$N_1 = .023 N_2^3 \left[\frac{\mu C_p}{k} \right]^{.4} \left[\frac{2 + \alpha + \frac{1}{\alpha}}{3} \right] \quad (2.6-16)$$

The thermal conductivities of the considered coolants are contained in Table 2.6-2.

The internal temperatures of the monolith cylinder winding are calculated as follows: a winding layer is axially divided into 10 segments, and temperature calculations are performed at the interfaces of the segments, called *locations*. The locations are numbered from 1 at the coolant inlet to 11 at the coolant outlet, as illustrated in Figure 2.6-9. At each location, a thermal resistance circuit similar to Figure 2.6-10 is solved. The thermal resistance circuit contains heat inputs for each conduc-

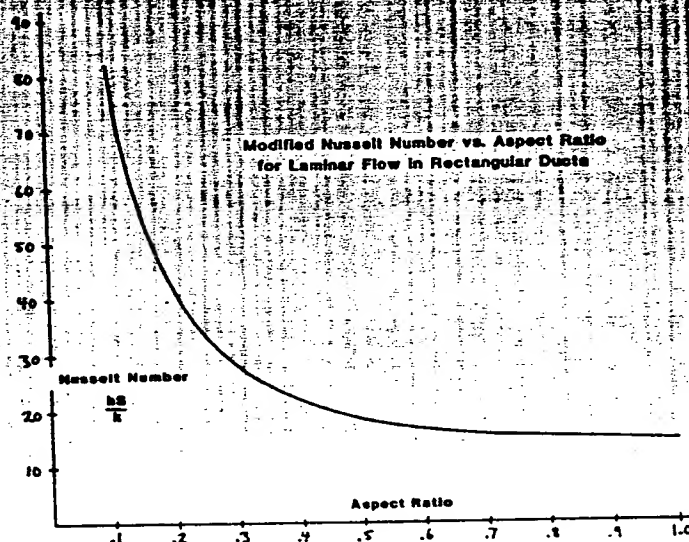


Figure 2.6-8. Modified Nusselt Number vs. Aspect Ratio for Laminar Flow in Rectangular Ducts

Table 2.6-2

COOLANT THERMAL CONDUCTIVITIES

Freon 113	Transil Oil	Silicone Oil
.00191 $\frac{\text{watts}}{\text{in } ^\circ\text{C}}$.00340	.00383

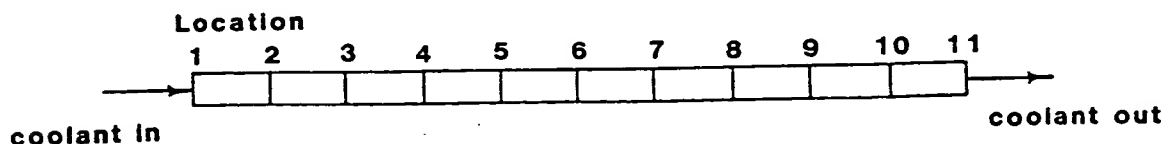


Figure 2.6-9. Segmentation of Winding for Cooling Calculations

not likely to be point locations but rather peripherally extending isotherms that penetrate the vertical dividers. Therefore, if pressboard is used as the vertical divider material, the conductor hotspots must be limited to 90 °C, even though the temperature limitation of the conductor insulation enamel is much higher.

The two mechanisms of heat transfer that are involved in the cooling of the monolith cylinder winding are thermal conduction and forced convection in internal ducts. Thermal conduction describes directional heat transfer through a volumetric media. In the monolith cylinder winding, the thermal conduction is from the conductor midline going into the cooling tube wall. The model for the thermal conduction process in the monolith cylinder winding assumes that the temperatures are axially and peripherally invariant. The expression for the temperature drop of thermal conduction is

$$\Delta T = Q \frac{l}{kw} \text{ } ^\circ\text{C} \quad (2.6-12)$$

where Q = heat flow per unit of winding length, watts/in.

l = length of heat flow path, in.

w = width of the heat flow path, in.

k = thermal conductivity, watts/(in. °C)

The thermal conduction path in the monolith cylinder winding consists of three series portions: the conductor half, the cooling tube insulation wrap, and the cooling tube wall.

The process of forced convection in internal ducts describes the heat transfer mechanism from the cooling tube wall to the flowing coolant. Although the process is quite complicated, it is desired to be able to describe the process in a simple relationship similar to Equation 2.6-12:

$$\Delta T = Q \frac{1}{hS} \text{ } ^\circ\text{C} \quad (2.6-13)$$

where h = convection coefficient, watts/(in.² °C)

S = internal perimeter of tube, in.

ΔT is the temperature difference between the tube wall and the coolant average temperature. The major problem with Equation 2.6-12 is determining a single numerical value of convection coefficient that describes the complicated process of heat transfer in forced convection. The results differ for turbulent and laminar flow. Heat transfer theory shows that the convection coefficient, tube hydraulic diameter, and coolant thermal conductivity are intimately related with a quantity called the Nusselt number:

$$N_d = \frac{hD}{K} \quad (2.6-14)$$

A single numerical value of Nusselt number can be analytically determined for laminar flow in a circular tube. For other situations (laminar flow in a rectangular tube or turbulent flow in any tube), Nusselt numbers are empirically determined. For laminar flow in rectangular tubes, the Nusselt number is a function of the aspect ratio of the tube only, while for turbulent flow, the Nusselt number is a function of the Reynolds number and of coolant properties. The Nusselt number can be made to relate to the temperature drop Equation 2.6-13 if the hydraulic diameter, D , can be replaced by the tube perimeter, S . Therefore, this discussion defines a modified Nusselt number as

$$N'_d = \frac{hS}{K} = N_d(2 + \alpha + \frac{1}{\alpha}) \quad (2.6-15)$$

where α is the rectangular tube aspect ratio.

The numerator of the modified Nusselt number is identical to the denominator of the temperature drop equation, and calculation manipulations are consequently facilitated. The modified Nusselt number for laminar flow, derived from Reference 2.6-4, is a function of aspect ratio only, and is il-

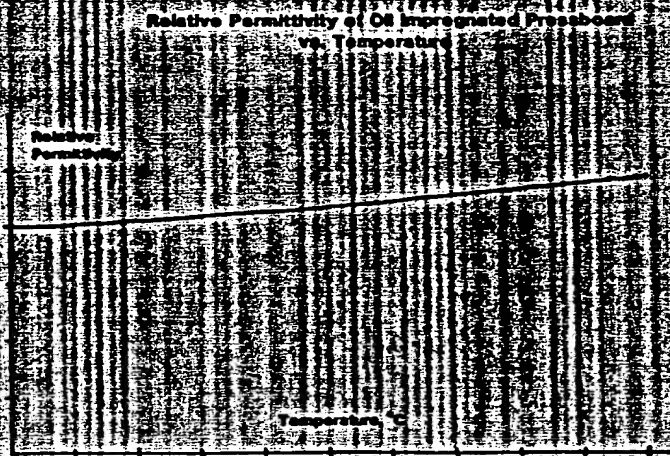


Figure 2.6-6. Relative Permittivity of Oil-Impregnated Pressboard vs. Temperature

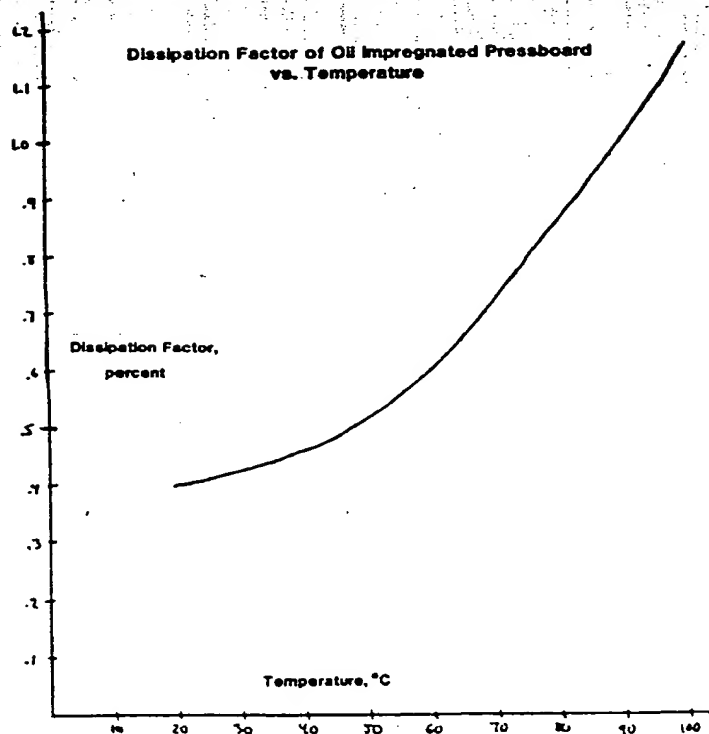


Figure 2.6-7. Dissipation Factor of Oil-Impregnated Pressboard vs. Temperature

temperature is the same as the inlet temperature (45 °C). The iterations are continued until convergence of the temperature rise is achieved.

The conductor losses are temperature dependent due to the temperature dependence of the electrical resistivities. An expression for the resistivity of copper is

$$\rho_{cu} = 1.594 + 0.006797 T \times 10^{-8} \Omega \cdot m \quad (2.6-6)$$

where T is degrees centigrade. An expression for the resistivity of stainless steel is

$$\rho_{ss} = .72 + 0.072 T \times 10^{-8} \Omega \cdot m \quad (2.6-7)$$

The I^2R loss of a copper filament is

$$W = I^2 \rho_{cu} \frac{L}{\pi r^2} \quad (2.6-8)$$

where I = filament current, amps

L = length, m

r = filament radius, m

The eddy current loss of a copper filament is

$$W = \frac{\pi}{8} \frac{\omega^2}{\rho_{cu}} L r^4 (B_r^2 + B_\theta^2) \quad (2.6-9)$$

where ω = angular electrical frequency, rad/s

B_r = maximum radial flux density, T

B_θ = maximum tangential flux density, T

The eddy current loss of a rectangular stainless steel cooling tube is

$$W = \omega^2 \frac{L}{24\rho_{ss}} \left[B_r^2 (hw^3 - h'w'^3) + B_\theta^2 (wh^3 - w'h'^3) \right] \quad (2.6-10)$$

where h = tube height, m

w = tube width, m

h' = internal height, m

w' = internal width, m

The effect of increasing temperature is to increase the electrical resistivities, resulting in increased I^2R losses and reduced eddy current losses.

Cooling calculations can also be performed for the insulation cylinders. The insulation cylinders have rectangular cooling passages which are regularly interspersed throughout the insulation cross-section, run axially from end to end, and connect with the end-region fluid reservoirs. The losses per unit volume within the insulation are

$$W = \omega \epsilon \epsilon_o E^2 \tan \delta \frac{W}{m^3} \quad (2.6-11)$$

where ϵ = relative permittivity

ϵ_o = permittivity of free space, $8.85 \times 10^{-12} F/m$

E = electric field strength, V/m

$\tan \delta$ = dissipation factor

The insulation cooling calculations are performed for oil-impregnated pressboard. The relative permittivity and dissipation factor of this material are temperature dependent, and curves for these properties are contained in Figures 2.6-6 and 2.6-7 (Refs. 2.6-2 and 2.6-3).

The calculation of internal hotspot temperatures is necessary to ensure that the temperature limitations of the involved electrical insulation materials are not compromised. Pressboard insulation in particular is sensitive and will begin to suffer mechanical and electrical degradation at temperatures above 90 °C. The hotspot locations in the winding configuration will be at the conductor centers, but owing to the mechanism of heat transfer specific to this winding configuration, the hotspots are

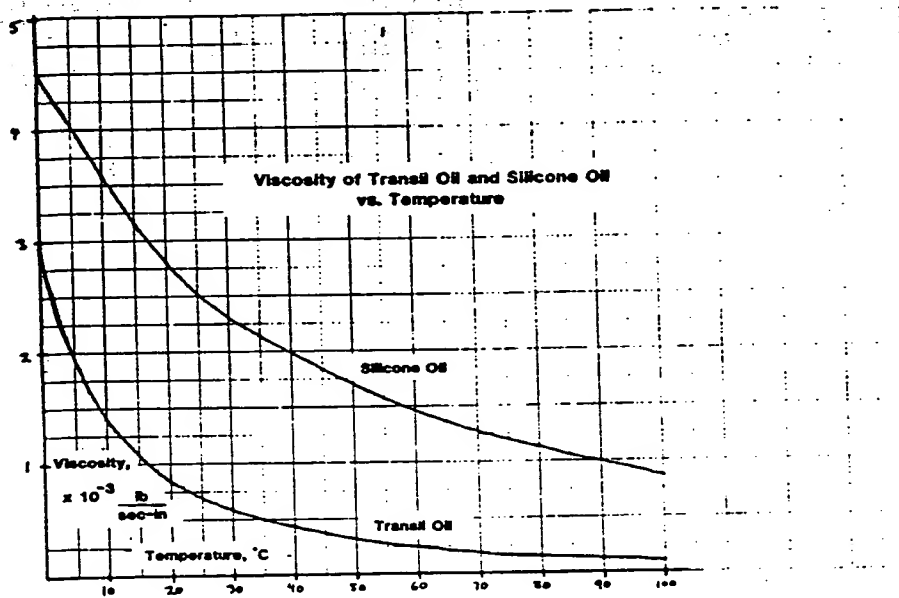


Figure 2.6-4. Viscosity of Transil Oil and Silicone Oil vs. Temperature

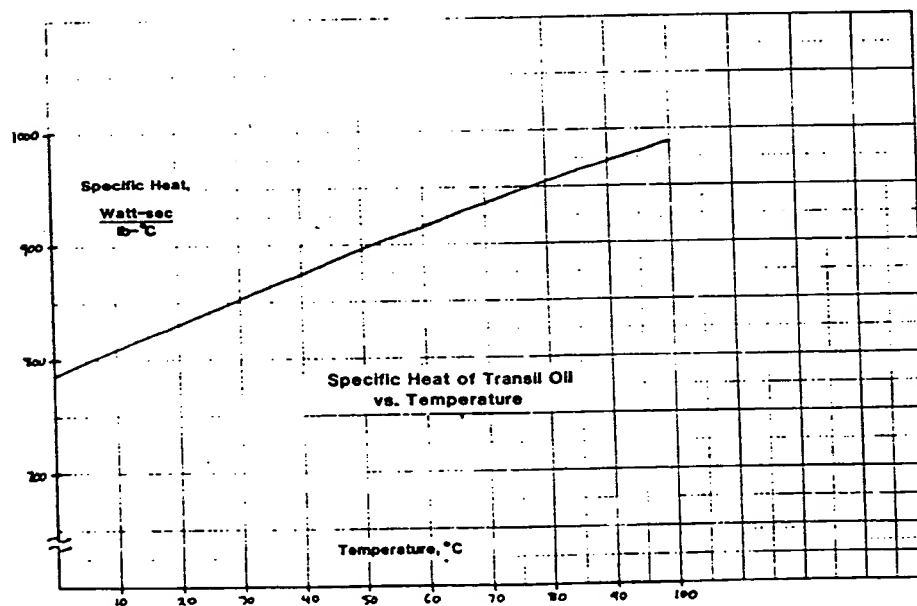


Figure 2.6-5. Specific Heat of Transil Oil vs. Temperature

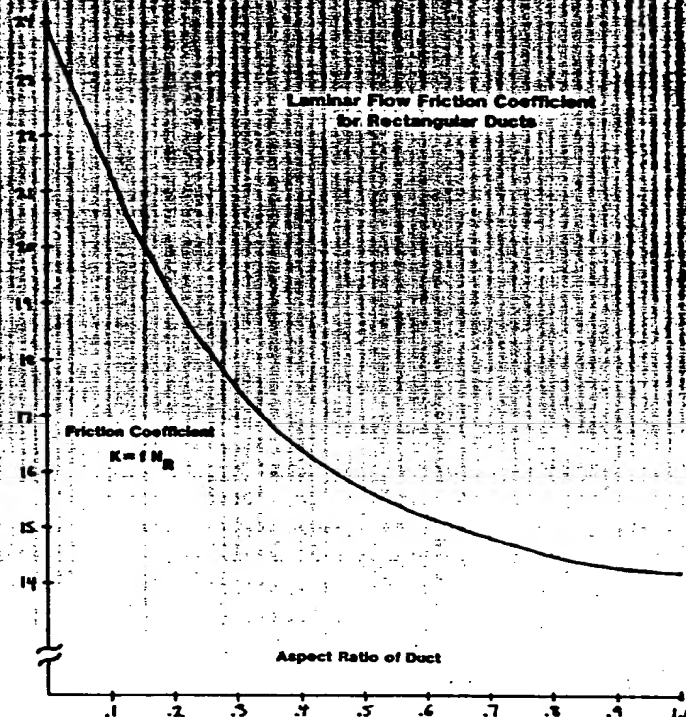


Figure 2.6-3. Laminar Flow Friction Coefficient for Rectangular Ducts

Table 2.6-1
COOLANT PROPERTIES

	Freon 113	Transil Oil	Silicone Oil
Density $\left[\frac{\text{lb}}{\text{in.}^3} \right]$	0.056	0.0303	0.0347
Viscosity $\left[\frac{\text{lb}}{\text{s-in.}} \right]$	3.47×10^{-5}	Fig. 2.6-4	Fig. 2.6-4
Specific Heat $\left[\frac{\text{watt-s}}{\text{lb-}^\circ\text{C}} \right]$	413.8	Fig. 2.6-5	668.2
Flow Condition	turbulent	laminar	laminar

dence of transil oil and silicone oil deserves comment, because as these fluids warm up their viscosity decreases, thereby increasing their cooling performance. This viscosity temperature dependence also poses a problem with respect to the cooling calculations. The coolant is heated as it travels down the coolant passage, and, correspondingly, its viscosity decreases as it travels down the passage. But the flow velocity must be constant over the length of the coolant passage, so according to Equation 2.6-4, there must be an equivalent single value of viscosity for the entire length. This enigma is accommodated in an iterative cooling calculation procedure which determines the viscosity at the coolant passage mid-temperature of the previous iteration. At the first iteration, the mid-

where

- ΔP = pressure drop, psi
- g = acceleration of gravity, 386.4 in./s²
- D = hydraulic diameter, in.
- f = friction factor
- L = length, in.
- ρ = density, lb/in.³

The hydraulic diameter of a rectangular duct is four times the cross-sectional area divided by the perimeter. The friction factor of a duct can vary with the flow condition. The flow condition is determined by the Reynolds number

$$N_R = \frac{\rho V D}{\mu} \quad (2.6-2)$$

where μ = viscosity, $\frac{\text{lb}}{\text{s} \cdot \text{in.}}$

The flow condition is completely laminar for a Reynolds number under 1500 and completely turbulent for a Reynolds number above 4000. When the flow condition is turbulent, the friction factor is related to the roughness of the duct walls and the size of the duct. Charts exist for determining the turbulent flow friction factor for a few common pipe materials, but, in other cases, estimates must be used. Theoretically, there is a maximum possible turbulent flow friction factor of 0.018, which is used when required in these calculations. Using the maximum friction factor leads to conservative calculations, although it is felt that such calculations will not be too far away from the actual turbulent flow conditions, based on the experience of fluid flow calculations of conventional generators. When the flow condition is laminar, the friction factor is based only on the duct dimensions and the Reynolds number:

$$f = \frac{K}{N_R} \quad (2.6-3)$$

where the friction coefficient, K , is based only on the aspect ratio of the duct, as illustrated in Figure 2.6-3. When Equations 2.6-2 and 2.6-3 are combined into Equation 2.6-1, the following flow velocity equation which is convenient for laminar flow conditions results:

$$V = \frac{\Delta P g D^2}{2 \mu K L} \frac{\text{in.}}{s} \quad (2.6-4)$$

If the laminar flow friction factor is of any interest, it can be calculated after determining the flow velocity. It is good practice to calculate the Reynolds number, to check that the flow condition is indeed laminar.

After completing its course through the winding, the temperature rise of the coolant is

$$\Delta T = \frac{W}{C_p V A \rho} \quad ^\circ\text{C}, \quad (2.6-5)$$

where W = heat input per cooling passage, watts

C_p = specific heat of the coolant, $\frac{\text{watt} \cdot \text{s}}{(\text{lb} \cdot ^\circ\text{C})}$

A = cross-sectional area of the coolant passage, in.²

The heat input is comprised of the conductor I^2R losses, the conductor eddy current losses, and the cooling tube eddy current losses.

For coolant passage dimensions which are typical for the described winding configuration, the flow condition of Freon 113 is turbulent, while that of transil oil and of silicone oil is laminar. The coolant properties of these substances are contained in Table 2.6-1, which refers to property versus temperature curves where they exist (Figures 2.6-4 and 2.6-5). The viscosity temperature depen-

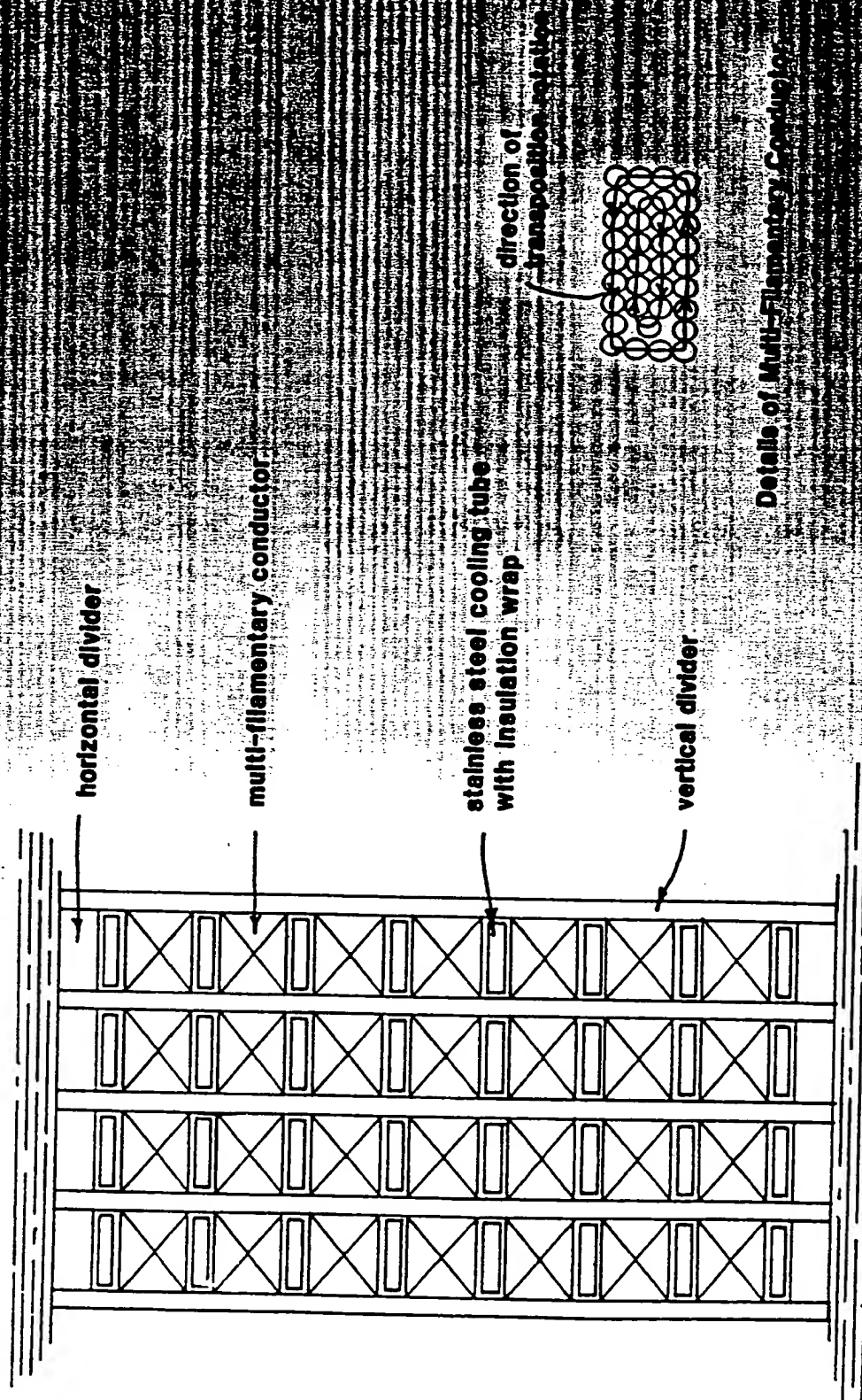


Figure 2.6-2. Components of the Monolith Cylindrical Conductor

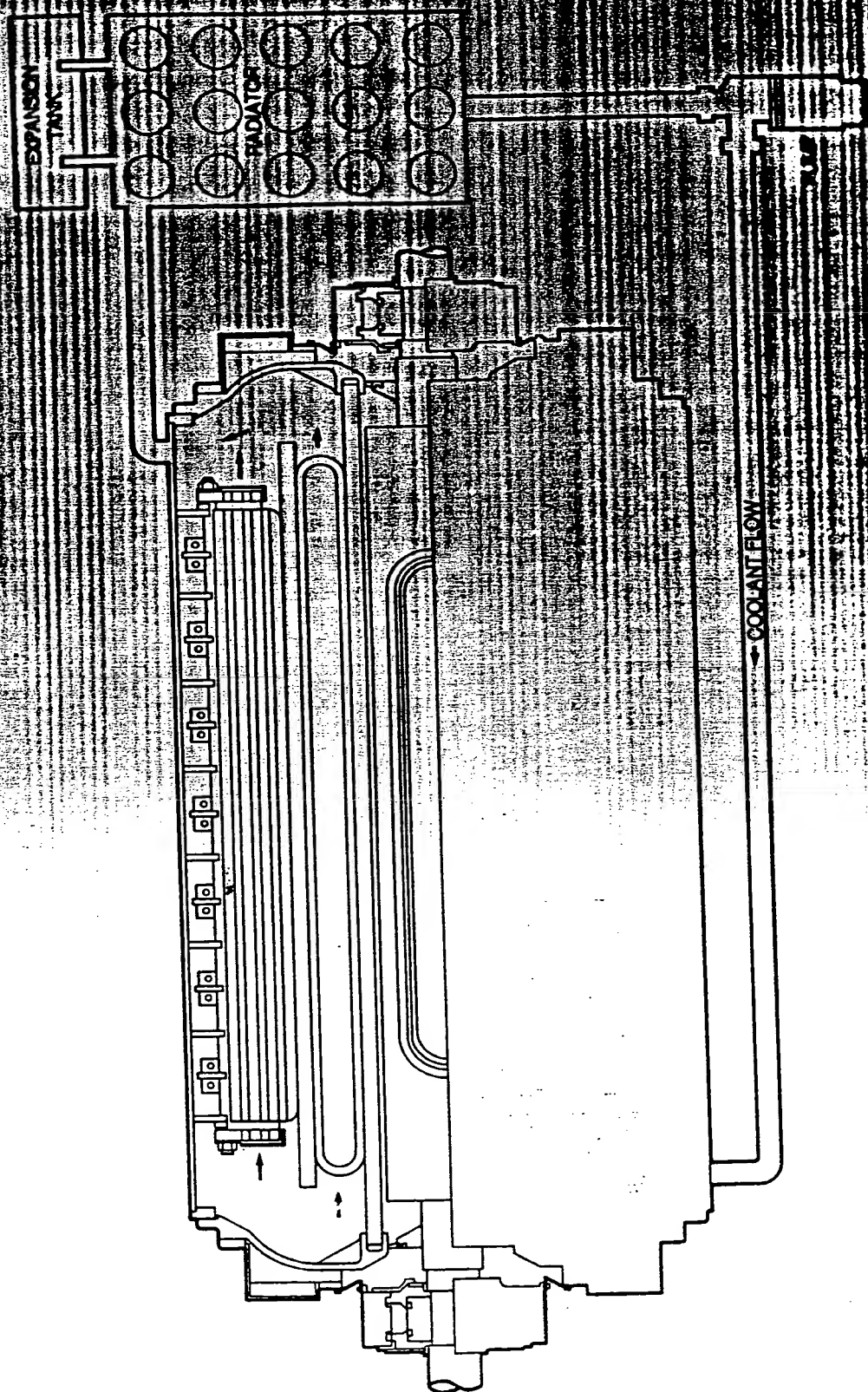


Figure 2.6-1. Cooling Scheme for the Monolith Cylinder Head
Flooded End Region Coolant Header

2.6 CONDUCTOR AND CONDUCTOR COOLING DESIGN

The general cooling scheme for a monolith cylinder high-voltage stator winding has been described earlier and will be briefly reviewed. It is desired to avoid the use of coolant connection hoses due to the hundreds of hoses and hose connections that would be required. Therefore, it is envisioned that the entire winding end region would be flooded with coolant which would be pumped through the winding coolant passages via access ports in the vicinity of the winding series loops. It is necessary for the coolant to be a dielectric fluid, since the coolant would be electrically stressed over portions of the cooling path. The general cooling scheme is illustrated in Figure 2.6-1.

This section describes the detailed design of the coolant passages and the conductors. Performance calculations are made for the conductor losses, coolant flows, temperature rises, and other quantities. Hotspot temperatures are limited to 90°C to minimize pressboard degradation, and the calculations will show that the required coolant flow is considerably larger than that required for water-cooled conventional generators, although it is within the realm of coolant flows for transformers. Designs are performed for each of the three identified coolants: transil oil, silicone oil, and Freon 113. Freon is a slightly better coolant than transil oil, while silicone oil is a poor coolant.

Transil oil is the classical high-voltage dielectric and cooling fluid that has been in use for decades. Transil oil's shortcoming is in its flammability, and owners of equipment using transil oil usually insist on outdoor locations for the equipment. PCB oil was developed to eliminate the flammability problem, but PCB oil has in recent times been outlawed due to its toxicity. Silicone oil has recently been developed to replace PCB oil as a low-flammable fluid. It can be manufactured in a large range of viscosities, with the highest viscosity having the lowest flammability, and vice versa. A particular grade of silicon oil identified as having suitable nonflammability is several times more viscous than transil oil (Ref. 2.6-1). Silicone oil is considerably more expensive than transil oil. Lastly, Freon 113, a fluorocarbon fluid manufactured by DuPont, is nonflammable and of low viscosity. However, Freon 113 has a low boiling point (47.6 °C) and would require pressurization in order to be used in machinery at the higher temperatures that are typical of electrical equipment. There are other fluorocarbons that have higher boiling points, but they are considerably more expensive than Freon 113, which is itself considerably more expensive than transil oil.

The configuration of conductors and cooling tubes within the winding layer is illustrated in Figure 2.6-2. Individual conductors and cooling tubes are alternately stacked in a column, and there is always one more cooling tube than conductor in the column, so that the column may be flanked by cooling tubes at both the top and bottom. The conductor and cooling tube columns are sandwiched between vertical dividers, which serve as mechanical support and as electrical insulation between peripherally adjacent conductors. The tops and bottoms of the vertical dividers may be extended into the cylinder insulations in order to serve as barriers to peripherally directed electrical creepage, as described in Section 2.5.2. All adjacent surfaces in the winding layer assembly are bonded. The conductors are comprised of transposed copper filaments (14, 16, or 18 AWG enamel-coated magnet wire) formed in a rectangular configuration. The filaments may be organized into concentric layers having opposite transposition directions. The cooling tubes should be wrapped with turn-to-turn insulation in order to prevent radially adjacent conductors from having contact through the tube. In order to reduce eddy current losses in the cooling tubes, stainless steel is the preferred material, being nonmagnetic and having a high electrical resistivity. The cooling tubes are not electrically connected and are merely terminated at the ends of the winding.

The cooling passages of the inner and outer winding layers are fed from the same fluid reservoir at one end of the machine and both discharge into a similar reservoir at the other end of the machine, so the fluid flow pressure drop will be the same for both the inner and outer layers. Therefore, it is convenient to formulate the fluid-flow equations with the pressure drop as input. The flow velocity of the coolant is

$$V = \sqrt{\frac{\Delta P g D}{2 f L \rho}} \frac{\text{in.}}{s} \quad (2.6-1)$$

The problem of phase-belt creepage impacts upon the winding in two separate regions, at the end turns (series loops) and within the body of the armature. The most important impact is upon the series loops. The series loops are in contact with the transil oil coolant region, and the creepage criterion has determined that the peripheral phase-belt creepage along the surface of the series loops is excessive. Section 2.5.1 describes a solution where baffles are inserted between peripherally adjacent series loops and Figure 2.5-12 illustrates the construction. Peripheral phase-belt creepage will be easier to control within the body of the winding, since bonding of the conductor layers to the insulation cylinders will eliminate fluid film dielectric boundaries at the interfaces. Unfortunately, it is quite possible for cracks to develop at these boundaries due to winding short circuit forces or thermal expansion forces. Transil oil saturated in the pressboard insulation cylinders will fill such cracks, averting the creation of critically deleterious air voids. If the crack is not too long, the creepage along the fluid film boundary in the crack will not exceed a critical level (a short path can withstand a creepage stress that will fail on a long path). For longer cracks, it is possible to extend vertical creepage baffles into the insulation cylinders for the purpose of lengthening the creepage path, as illustrated in Figure 2.5-14. The creepage baffles also double as the vertical dividers placed between columns of conductors for mechanical support.

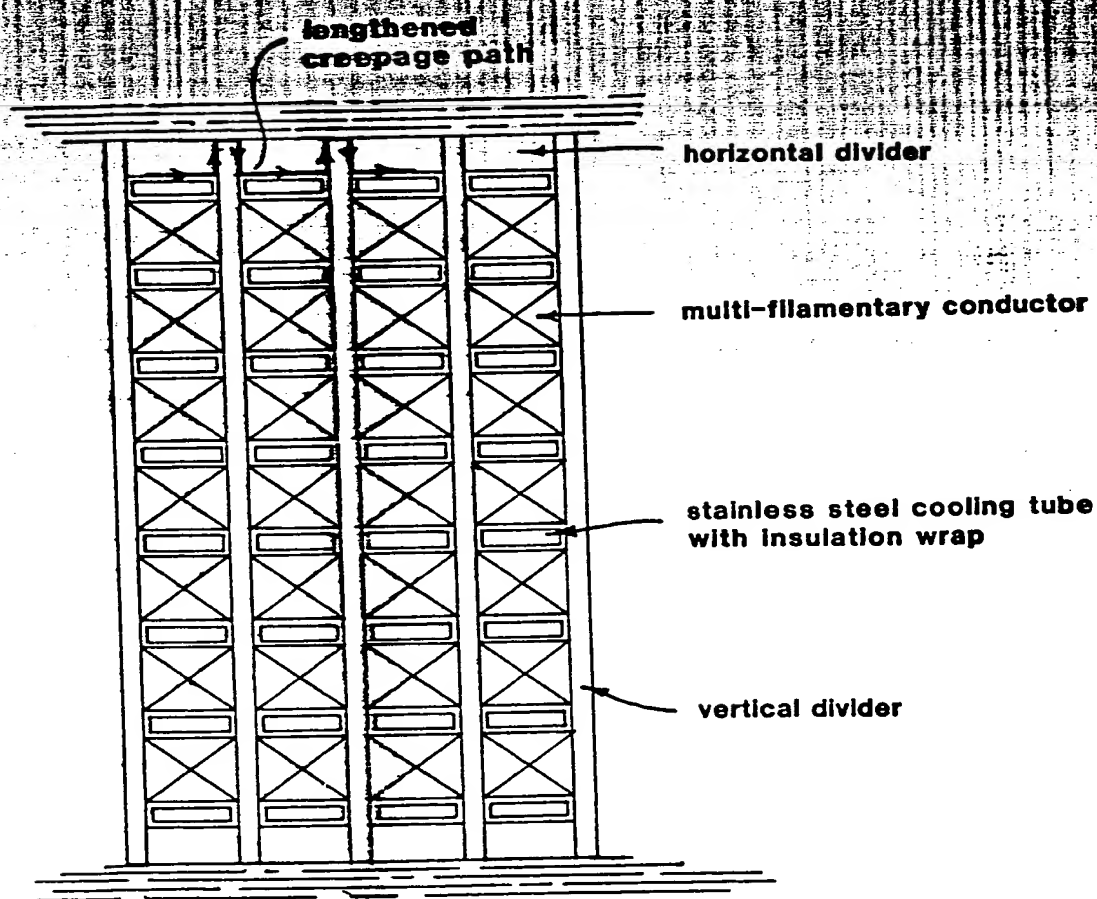


Figure 2.5-14. Vertical Dividers Used as Peripheral Creepage Baffles

2.5.2 Electrical Creepage Analysis of the Phase-Belt Design

The voltage difference developed across opposite sides of a phase belt in a high-voltage transformer may be large enough to create a critical creepage situation along the breadth of the phase belt, depending on the magnitude of the voltage and the peripheral span of the phase belt. Some winding arrangements are more vulnerable than others with respect to this problem, as discussed in Section 2.3.1.

The magnitude of a particular winding arrangement's phase belt creepage can be quantified by performing a creepage criterion similar to that described in Section 2.5.1. Such a criterion, as applied to the 60° phase-belt, two-circuit delta winding, is illustrated in Figure 2.5-13. Delta windings, having no grounded conductors within the winding, produce rotating patterns of voltage distribution. It is advisable to search beyond the physical environs of the phase belt (a 60° span in this case) for critical creepage situations. Here, creepage plots are calculated for a 90° span of the winding for several instances of time. The maximum excursion of the plots above the gray area quantifies the critical creepage value, and for this winding it turns out to be the line-to-line voltage divided by the span of the 60° phase belt, a quantity confirming intuition.

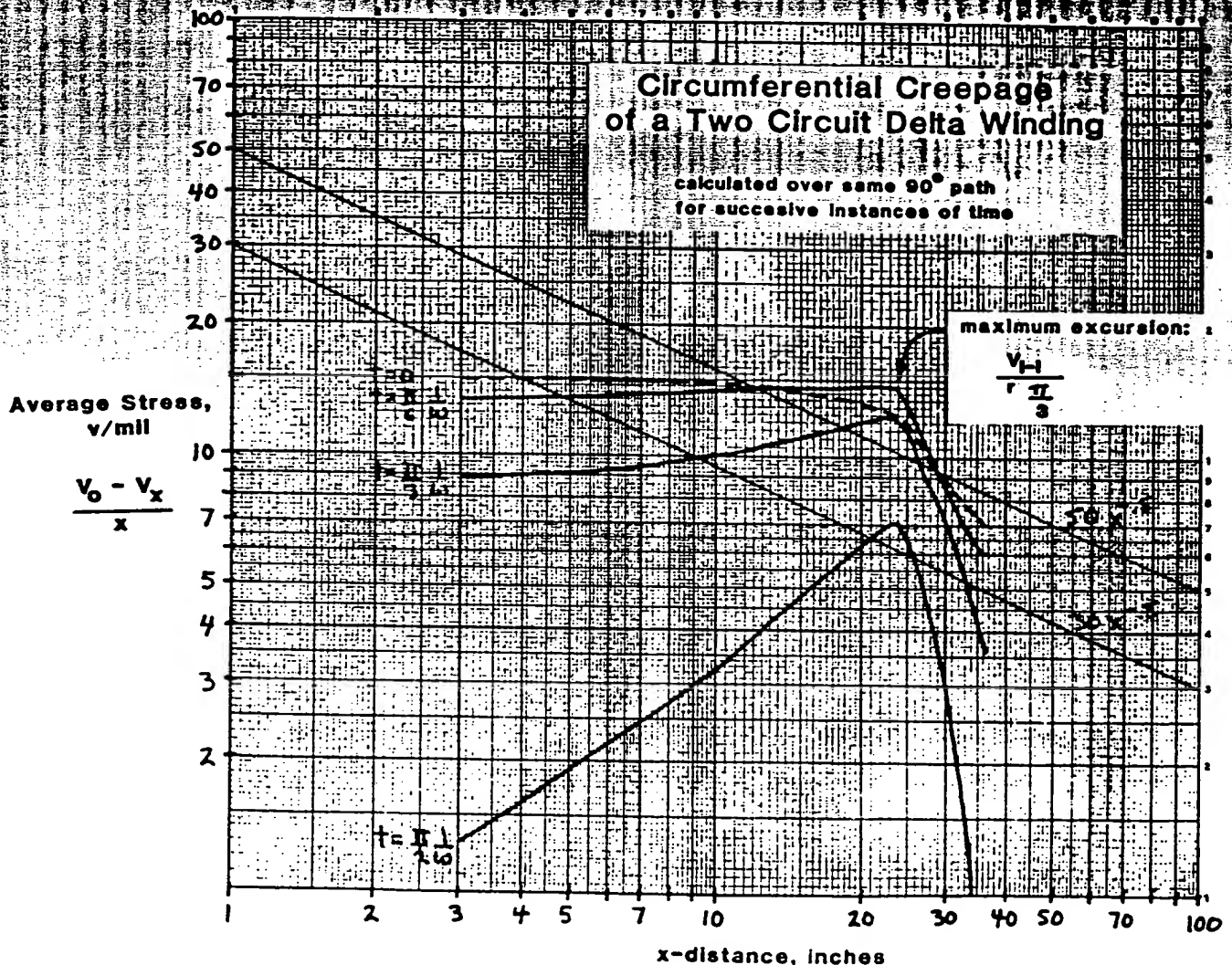


Figure 2.5-13. Peripheral Creepage of the 60° Phase-Belt Two-Circuit Delta-Connected Winding Calculated Over the Same 90° Path for Successive Instances of Time

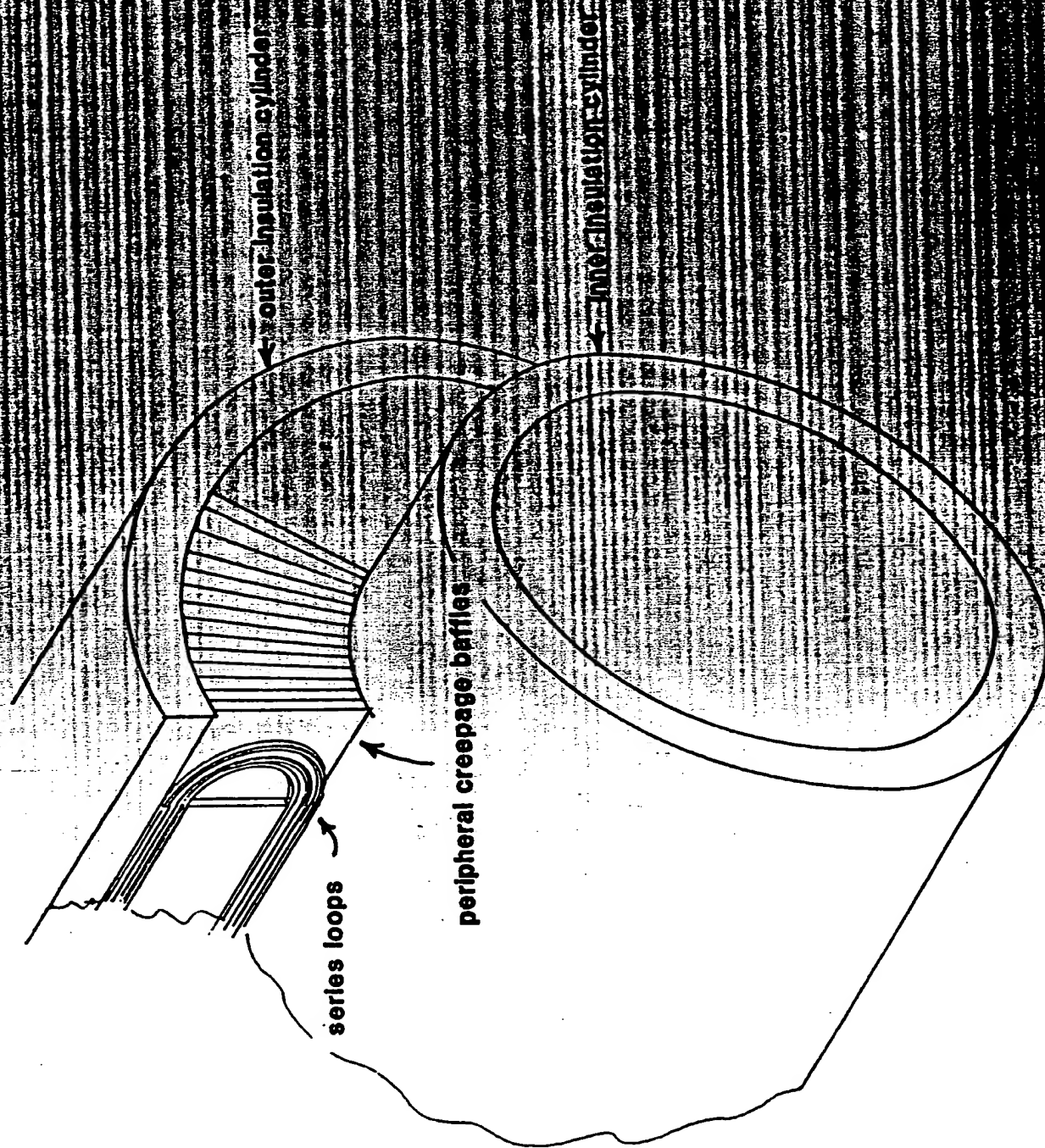


Figure 2.5-12. Peripheral Creepage Barrier in the Motor Winding

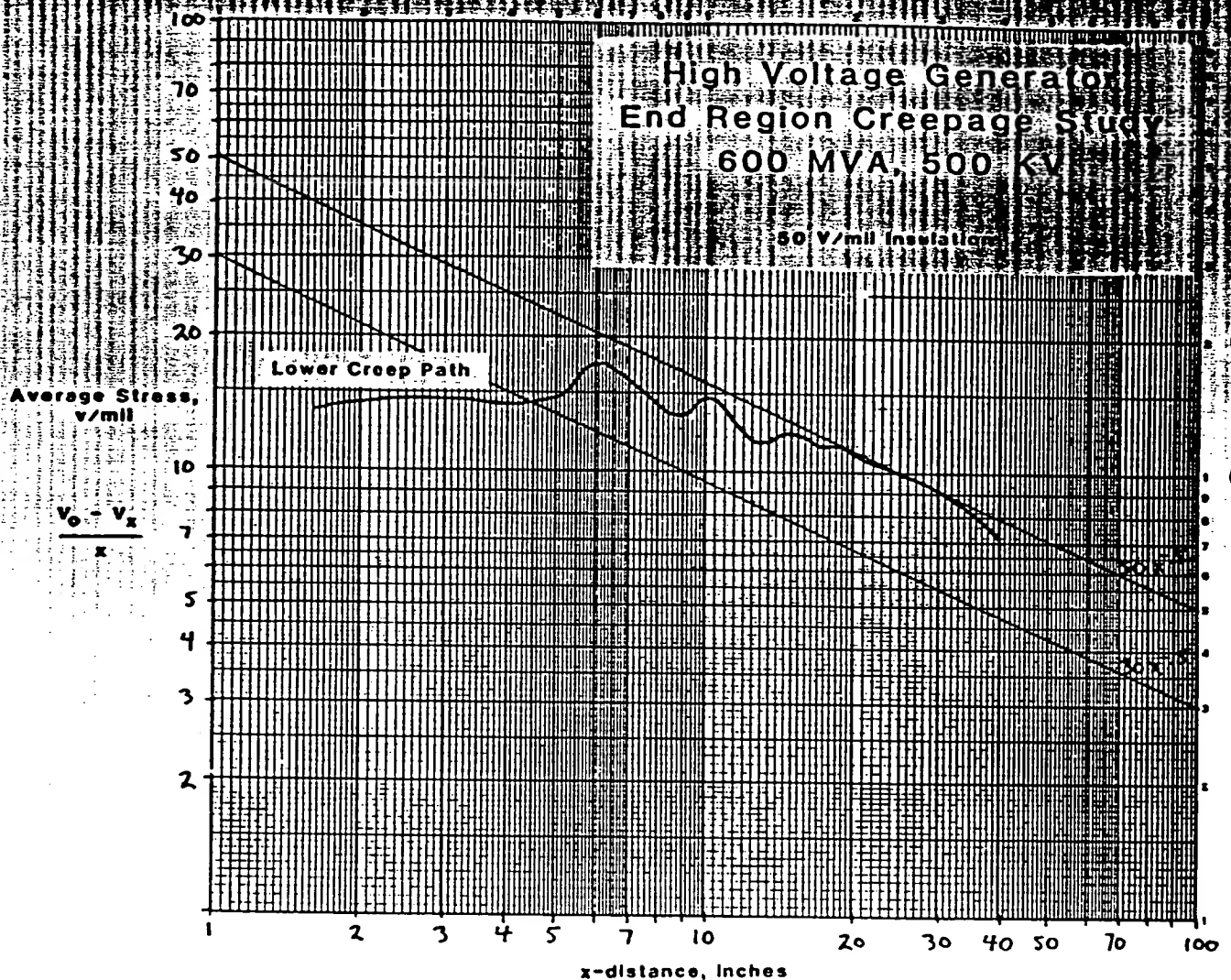


Figure 2.5-11. Creepage Plots for the 600 MVA, 500 kV Monolith Cylinder End Region (Case #3)

An important conclusion to be drawn from these exercises is that the end-region axial creepage situation has a limiting effect upon the allowable design stress of the insulation cylinders. It is found that higher insulation design stresses (producing thinner insulation cylinders) greatly increase the axial creepage stresses. If it was difficult to design an end region at a 500 kV rating with 50 V/mil insulation, it may be impossible to design an end region for a 500 kV rating with 75 V/mil insulation. Similarly, a 765 kV rating would have to use much less than a 50 V/mil insulation design stress.

The design of the monolith cylinder end region must also consider peripherally directed electrical creepages. This type of creepage results from the peripheral variation of voltage at the series loops and is similar to the phase belt creepage discussed in Section 2.5.2. The solution to this problem is the placement of baffles between peripherally adjacent series loops, as illustrated in Figure 2.5-12. These baffles extend axially beyond the series loops to a location where the magnitude of the peripheral creepage is no longer critical. This location may be found by calculating the maximum allowable peripheral creepage stress and then locating its position with the aid of a finite element electric-field solution.

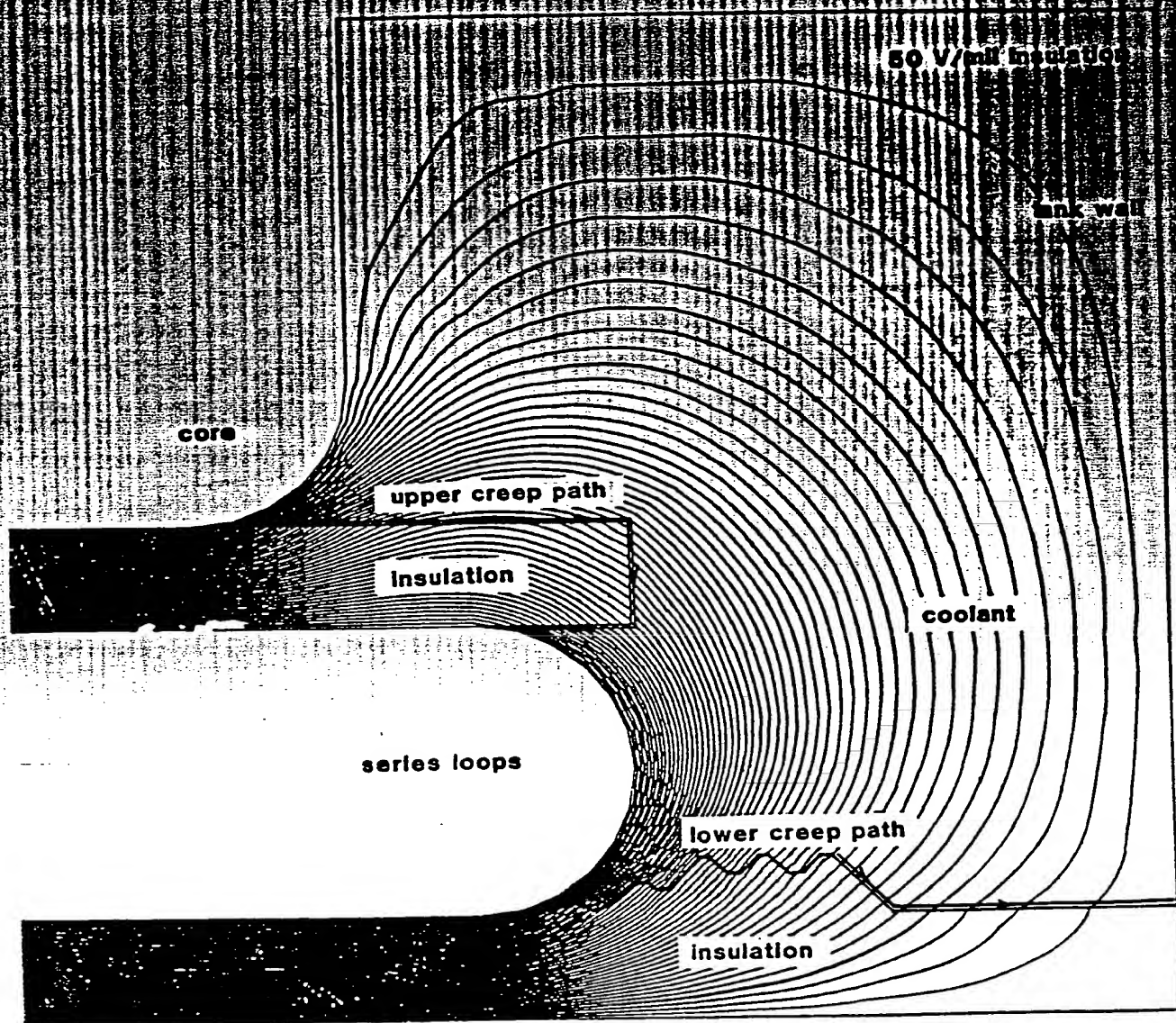


Figure 2.5-10. Electrostatic Field Solution of a 600 MVA, 500 kV Monolith Cylinder End Region (Case #3)

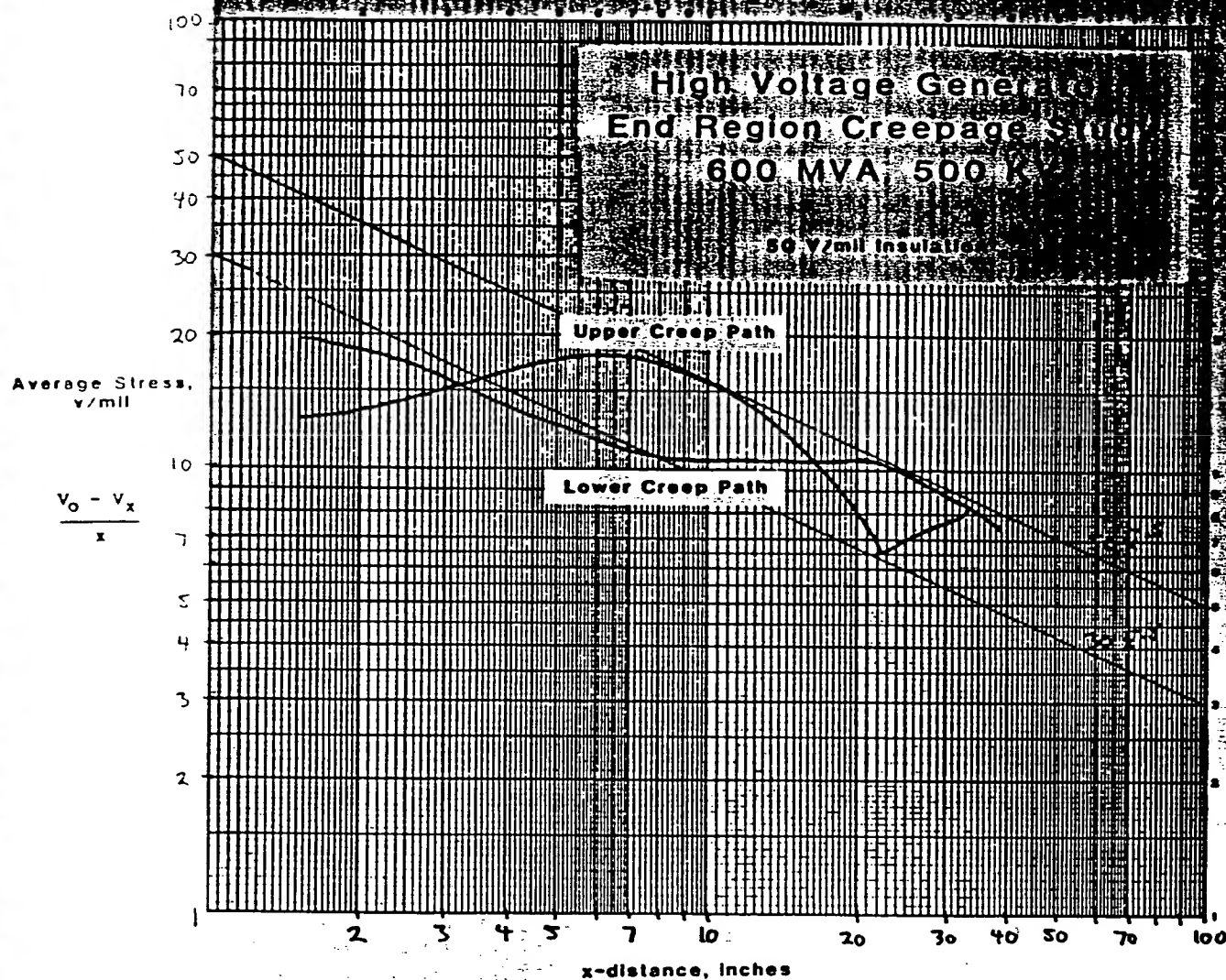


Figure 2.5-9. Creepage Plots for the 600 MVA, 500 kV Monolith Cylinder End Region (Case #2)

Figure 2.5-10 illustrates a refined creepage mound containing convoluted surfaces. The philosophy of this mound is similar to the previous one in that it contains surfaces parallel to the series loop contour. The wavy shape of this creepage path is preferable to the smoother shape of the previous mound. Figure 2.5-11 illustrates the creepage plot of this design.

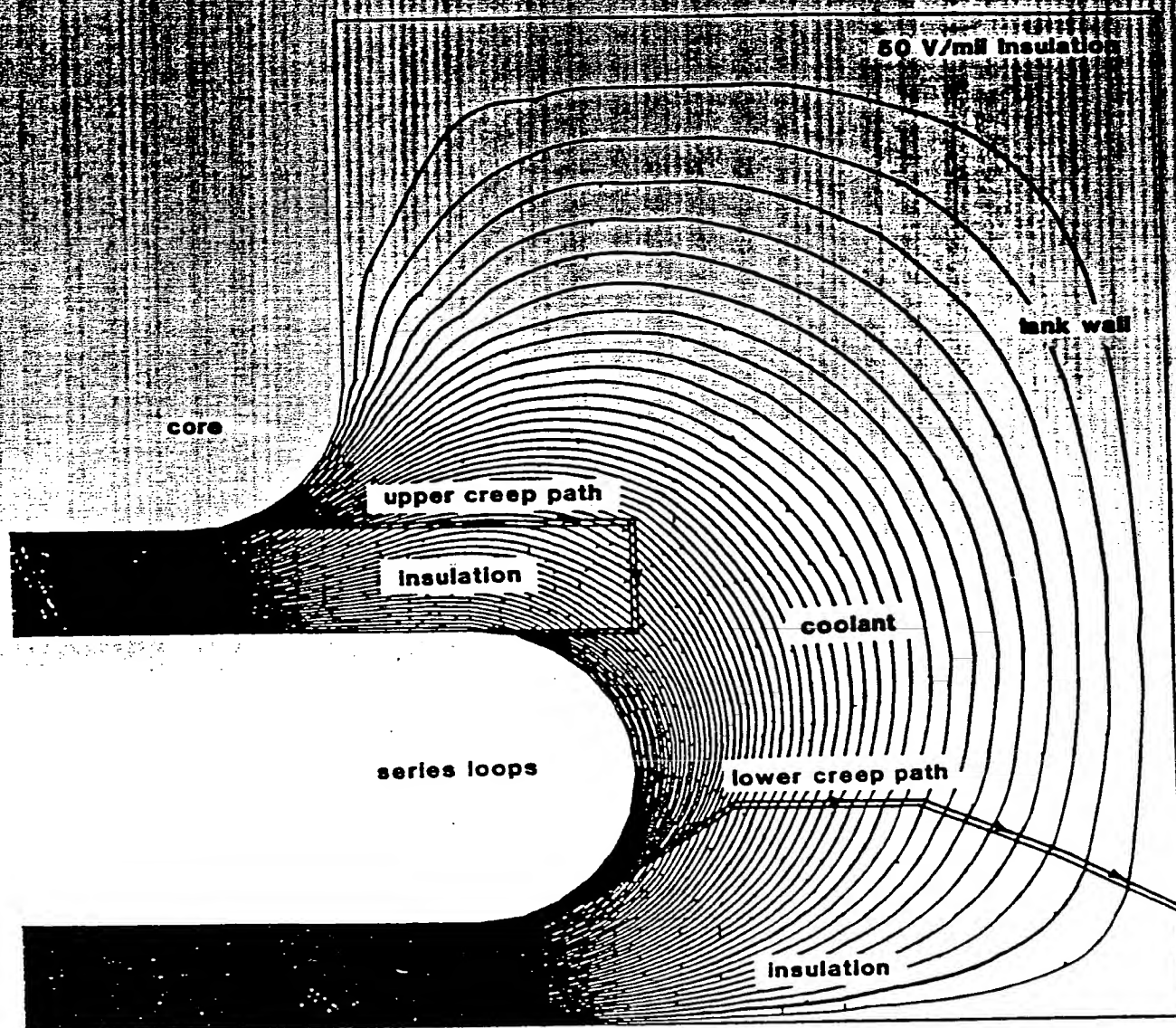


Figure 2.5-8. Electrostatic Field Solution of a 600 MVA, 500 kV Monolith Cylinder End Region (Case #2)

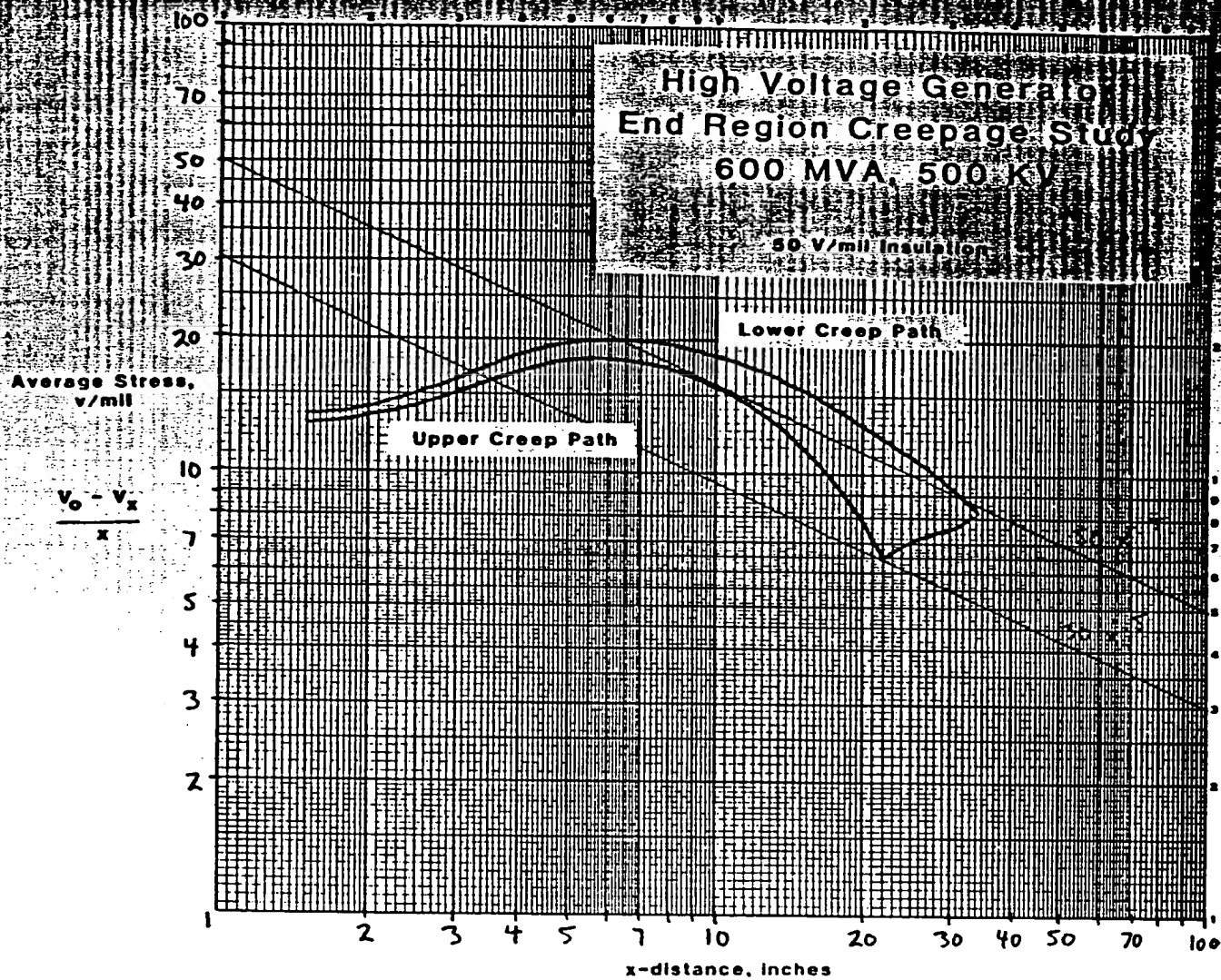


Figure 2.5-7. Creepage Plots for the 600 MVA, 500 kV Monolith Cylinder End Region (Case #1)

A crude innovation is illustrated in Figure 2.5-8, where a large mound of insulation is added to the inner insulation cylinder in the end region. The shape of this mound near the series loops is such that the surface is nearly parallel to the series loops and local equipotential lines. The effect of this surface is to bring the creepage plot of the lower creepage path into the gray area, as illustrated in Figure 2.5-9.

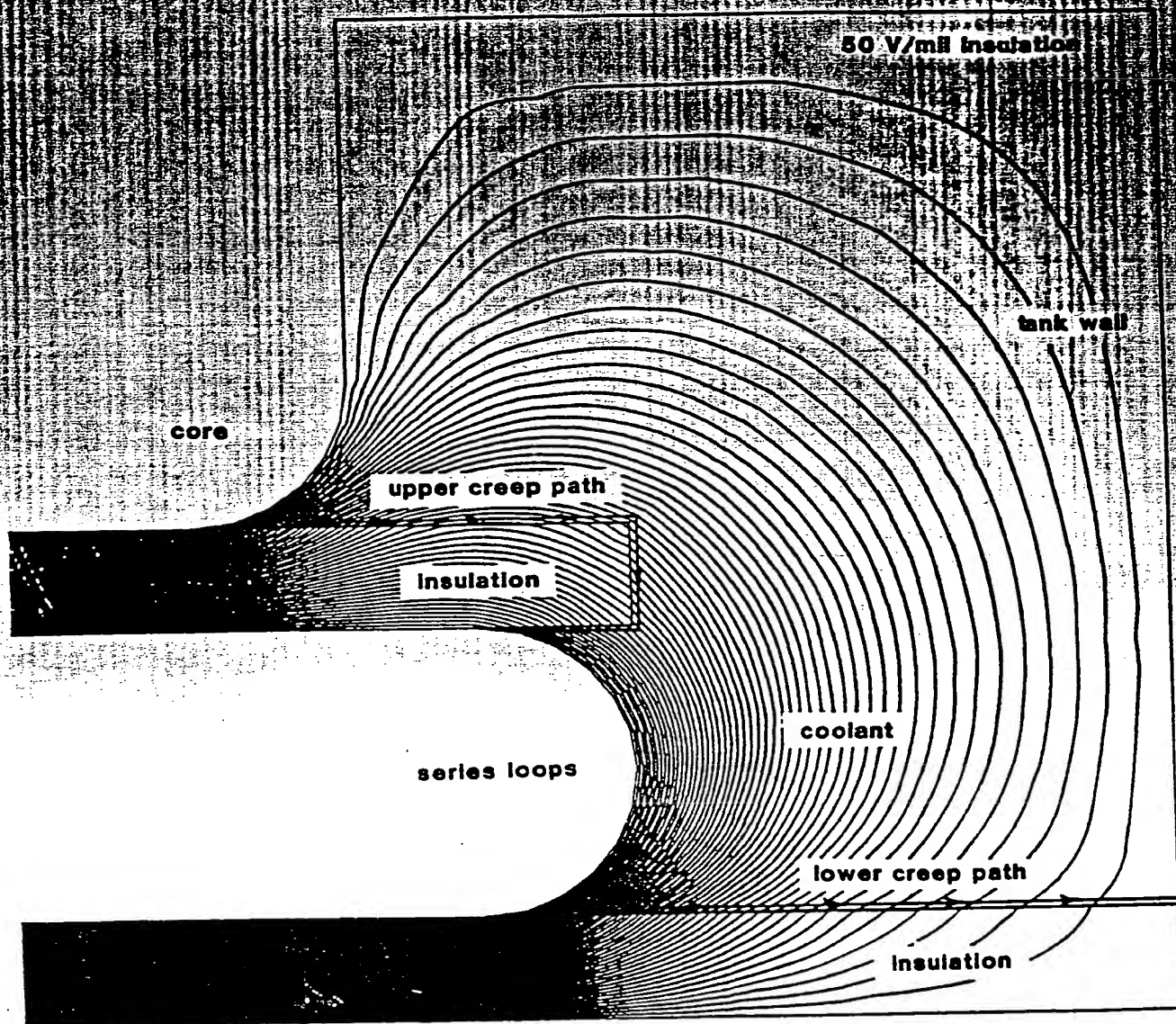


Figure 2.5-6. Electrostatic Field Solution of a 600 MVA, 500 kV Monolith Cylinder End Region (Case #1)

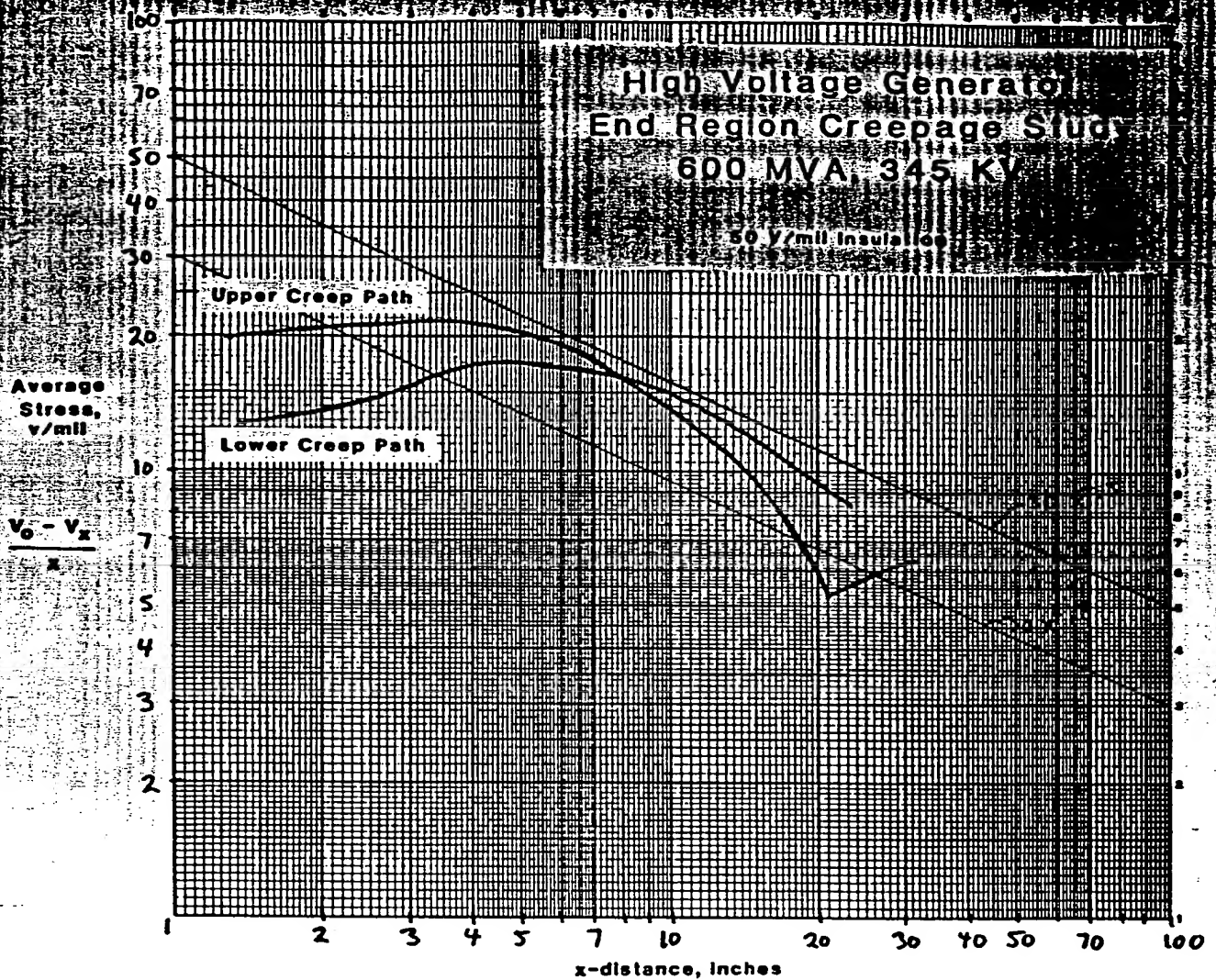


Figure 2.5-5. Creepage Plots for the 600 MVA, 345 kV Monolith Cylinder End Region with Rounded Contours

Designing the end region of a 600 MVA, 500 kV monolith cylinder armature without using less than 50 V/mil insulation cylinder stress provides a greater challenge. Figure 2.5-6 illustrates the field solution for an end region with these specifications. The radial dimensions are from the sizing studies of Section 2.2. Figure 2.5-6 is not to scale with Figure 2.5-4. Figure 2.5-7 illustrates the creepage plots for this design. The upper creepage plot is barely confined within the gray area, while the lower creepage plot is well above the gray area. Further innovations will be required to qualify a design at this rating.

The easiest remedy to implement is the rounded profiling of the core and series loops. Figure 2.5-4 illustrates the field solution for the 600 MVA, 345 kV monolith cylinder armature with the rounded core and series loops incorporated. Figure 2.5-5 illustrates the creepage plots for both the upper and lower creepage paths. Both plots are now contained within the gray area.

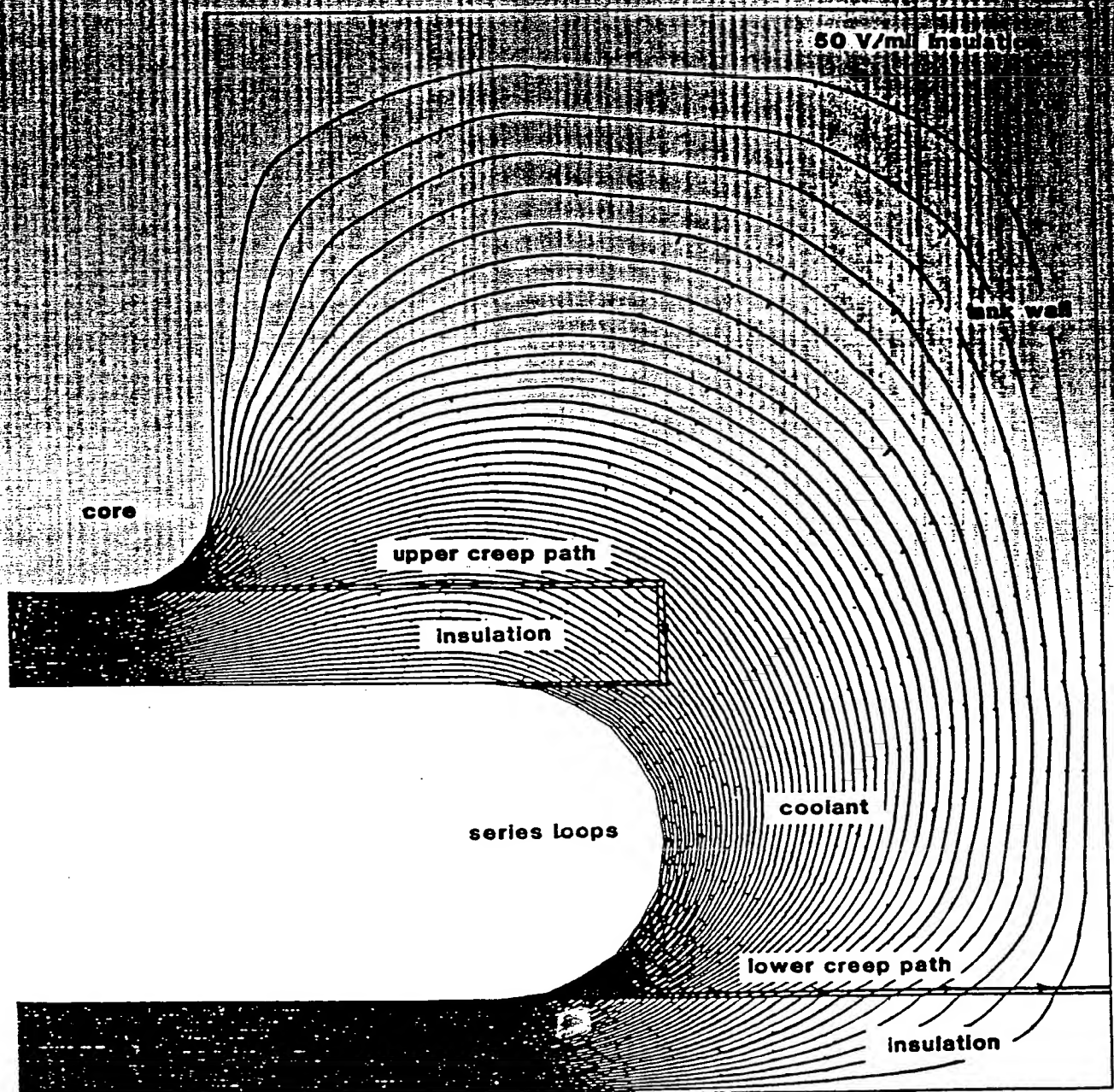


Figure 2.5-4. Electrostatic Field Solution of a 600 MVA, 345 kV Monolith Cylinder End Region with Rounded Contours

The creepage plots for the upper creepage path are illustrated in Figure 2.5-3. The creepage plot for 50 V/mil insulators is barely within the gray area, while the creepage plot for the 75 V/mil insulators is above the gray area.

When a critical creepage situation is determined for a particular design, as is certainly the case for the aforementioned example, there are several remedies available. One obvious remedy is to merely increase the thickness of the insulation cylinders (decreasing the insulation cylinder stress), although this increases the size of the machine. The surfaces of the insulation cylinders can be convoluted at critical locations to increase the length of the creepage paths. The profiles of the core end and series loops can be roundly contoured in such a way as to reduce the stress at the insulation cylinders. Stress grading by means of conductive coatings is a possibility, although transformer designers have not had much success with this method.

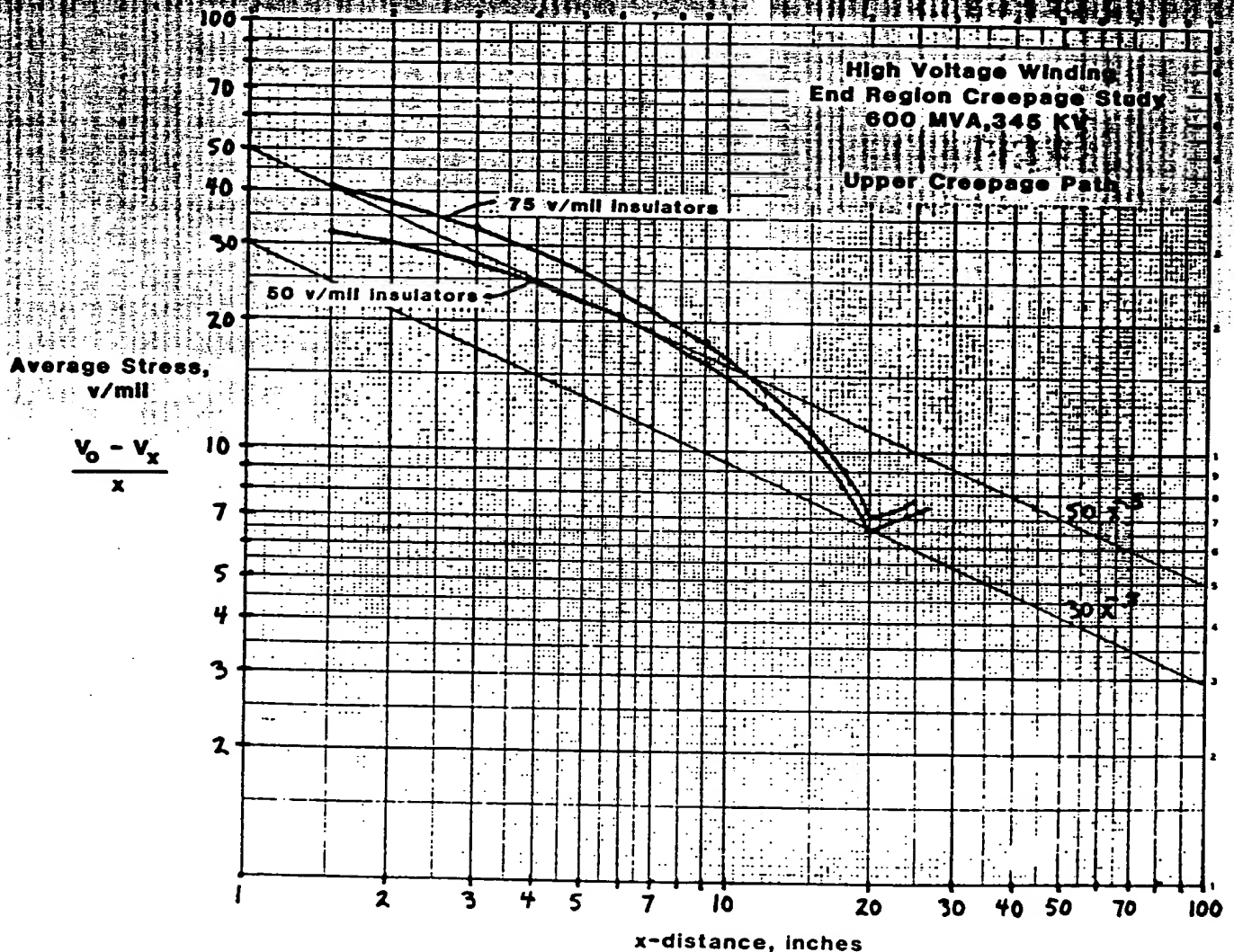


Figure 2.5-3. Creepage Plots of the Upper Creepage Path for the 600 MVA, 345 kV Monolith Cylinder End Region

perimposing on the plot a "gray area" defined by the lines $50 x^{-1/5}$ and $30 x^{-1/5}$. If any portion of the plotted line falls above the gray area, there is a great probability of creepage failure. If the plotted line lies entirely below the gray area, there is a minimal probability of creepage failure. This criterion was developed from test data produced by the General Electric Generator Department. It is not the best criterion available, since the best criteria are the proprietary possessions of high voltage transformer designers. The method of application is similar, however, and is presented to illustrate the method and its application to creepage path design.

As seen in Figure 2.5-2, creepage plots of the lower creepage path for both the 75 V/mil insulation and 50 V/mil insulation lie above the gray area, and as expected, the plot for the 75 V/mil insulation is higher than the plot for the 50 V/mil insulation. The effect of the longer 27 in. extension is not to change the front part of the plot, but to extend the back part of the plot, as depicted by the dotted line. These creepage plots confirm the earlier statement that creepage stress is more strongly dependent on insulation cylinder thickness than on axial extension distance.

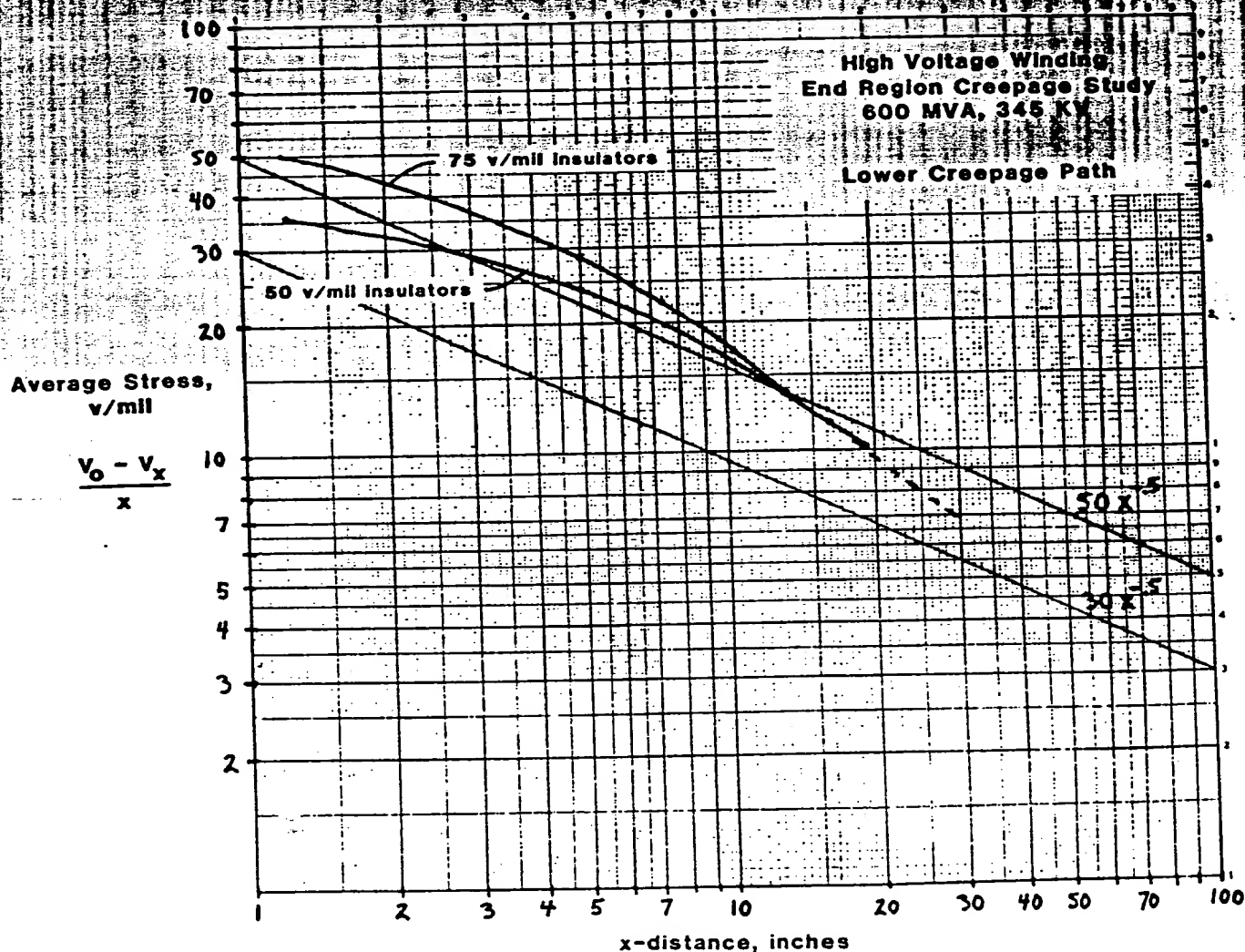


Figure 2.5-2. Creepage Plots of the Lower Creepage Path for the 600 MVA, 345 kV Monolith Cylinder End Region

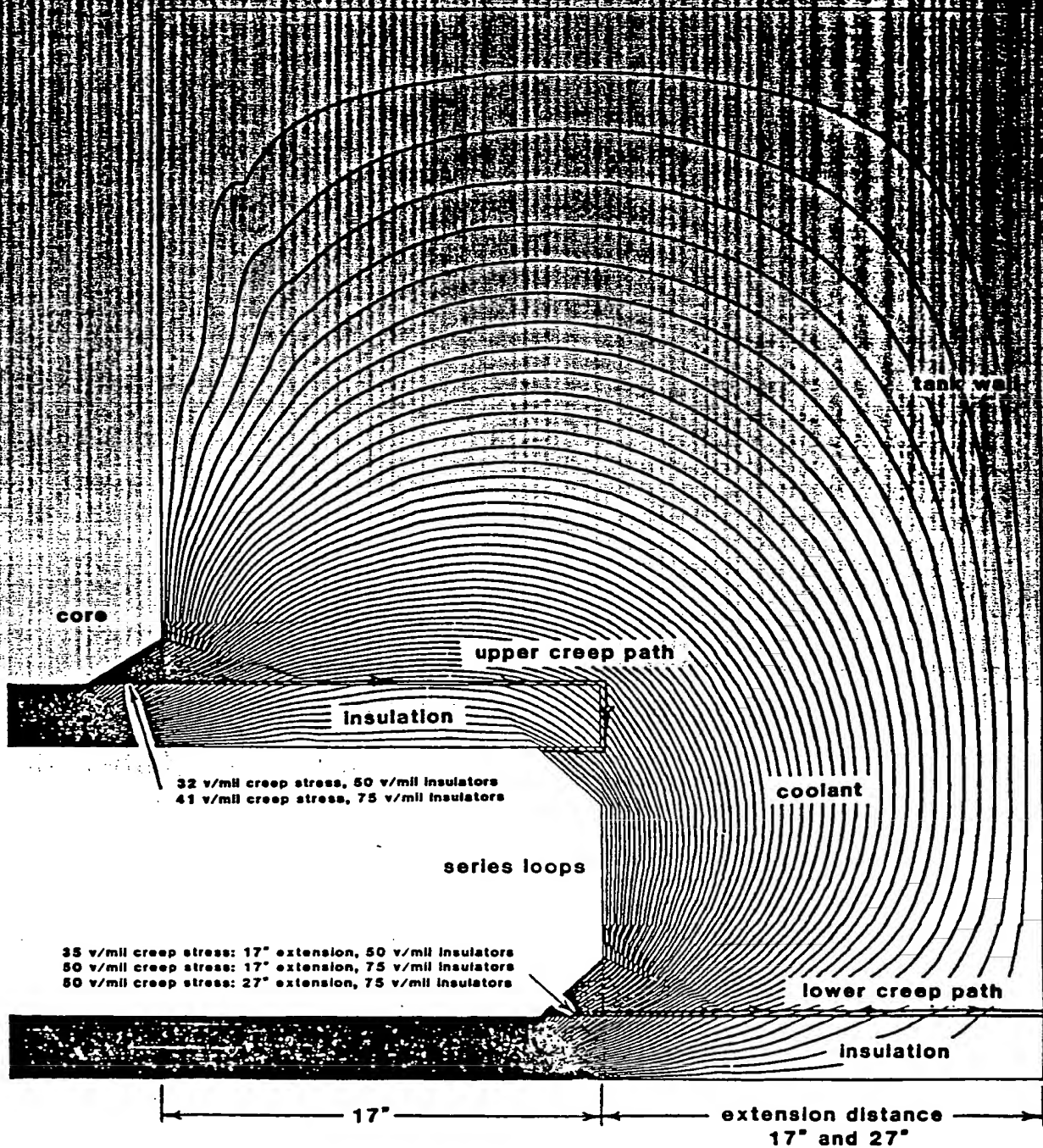


Figure 2.5-1. Electrostatic Field Solution of a 600 MVA, 345 kV Monolith Cylinder End Region

2.5 ELECTRICAL CREEPAGE ANALYSIS

2.5.1 Electrical Creepage Analysis of the End-Region Design

The end regions of a monolith cylinder high-voltage armature present a number of opportunities for electrical creepage failures, which are flashovers running along dielectric boundaries (usually solid-to-fluid boundaries or solid-to-air boundaries). Creepage failures can occur from the conductors to grounded frame parts along the surfaces of the insulation cylinders in the axial direction and from conductor to conductor along the surface of the series loops in the peripheral direction. Determination of a critical creepage situation requires the union of two separate calculation processes. First, the electrostatic field solution for the particular end-region geometry is performed so that the electrical stresses along the dielectric boundaries can be established. Second, the application of mathematically associated criteria to the calculated electric stresses determines if the creepage situation is critical. The criteria are still a developing art, and the best are the proprietary possessions of high-voltage step-up transformer designers.

The electrostatic field solution of an armature end region is easily performed by finite element analysis. Figure 2.5-1 illustrates such a solution of a crude end-region geometry for a 600 MVA, 345 kV monolith cylinder armature whose radial dimensions were determined in the sizing studies of Section 2.2. The field solution is illustrated in the radial-axial plane, and radial-axial cross-sections of the inner insulation cylinder, outer insulation cylinder, and coolant region are visible, along with outlines of the winding series loops, core, and tank wall. The finite element analysis accounts for the cylindrical nature of the geometry; the finite element model is actually an annulus being viewed in a radial-axial cross-section. The insulation cylinders and coolant regions are given dielectric constants of 4.5 and 2.2, respectively, corresponding to a dielectric system of pressboard and transil oil. The outline of the series loops is placed at line-to-ground potential, and the outlines of the core, tank wall, and inner surface of the inner insulation cylinder are placed at ground potential. The lines illustrated in the field solution are lines of constant potential, and the electric field vectors must be visualized normally to these lines. The finite element analysis allows the potentials and field to possess a sinusoidal variation in the peripheral direction. Most two-pole winding arrangements produce a twice-per-revolution variation of the potentials and field.

Three different calculations were performed for slight variations in the geometry of Figure 2.5-1. The first calculation utilizes 50 V/mil insulation cylinders and a 17 in. extension from the series loops to the tank wall. The second calculation utilizes 75 V/mil insulation cylinders, which have the effect of shrinking the radial dimensions. Axial dimensions were kept the same. The third calculation utilizes 75 V/mil insulation cylinders with the extension distance increased to 27 in. Two creepage paths are defined: the upper creepage path, extending from the core to the series loops along the outer insulation cylinder, and the lower creepage path, extending from the series loops to the tank wall along the inner insulation cylinder. The highest creepage stresses are seen to be located near the core on the upper creepage path and near the series loops on the lower creepage path. High creepage stresses at such locations can initiate a creepage failure along the entire length of the creepage path. Numerical values of these creepage stresses are contained within Figure 2.5-1. The effect of going from 50 V/mil insulation to 75 V/mil insulation is to increase the creepage stress at both locations. Increasing the extension distance does not affect the creepage stress at the lower creepage path. The creepage stresses are apparently a strong function of the insulation cylinder thickness and a weak function of the axial extension.

A criterion of the creepage stress along a creepage path can be performed by plotting the average creepage stress as a function of path distance on log-log paper. The average creepage stress is defined as

$$\frac{V_o - V_x}{x}$$

where V_o is the voltage at the path start and V_x is the voltage at distance x along the creepage path. Such a plot is illustrated in Figure 2.5-2 for the lower creepage path. The criterion is applied by su-

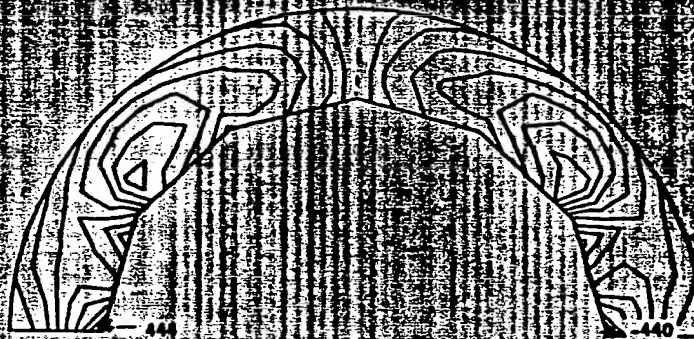


Figure 2.4-33. Contour Plot of the r - θ Shear Stress in the Core, 180° after Sudden Short Circuit, High-Modulus Polygonal Interface

Table 2.4-2

STRESSES OCCURRING AT 180° AFTER SUDDEN SHORT CIRCUIT

Stress	Figure No.	Max, psi	Min, psi	Stress Line Increment, psi
Radial Stress, Armature Structure	2.4-28	74	-608	40
Radial Stress, Core	2.4-29	361	-566	50
Peripheral Stress, Armature Structure	2.4-30	866	-303	80
Peripheral Stress, Core	2.4-31	2938	-1672	250
r - θ Shear Stress, Armature Structure	2.4-32	184	-177	20
r - θ Shear Stress, Core	2.4-33	444	-440	50

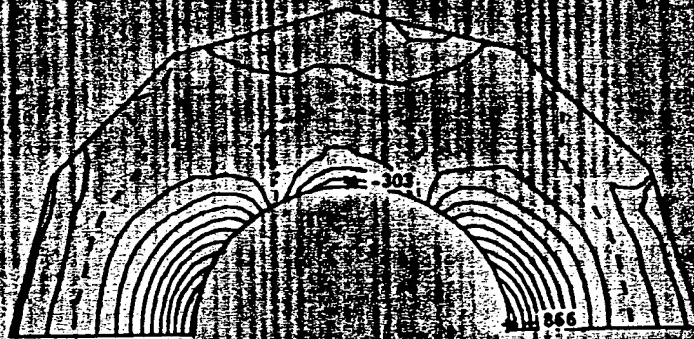


Figure 2.4-30. Contour Plot of the Peripheral Stress in the Armature Structure, 180° after Sudden Short Circuit, High-Modulus Polygonal Interface

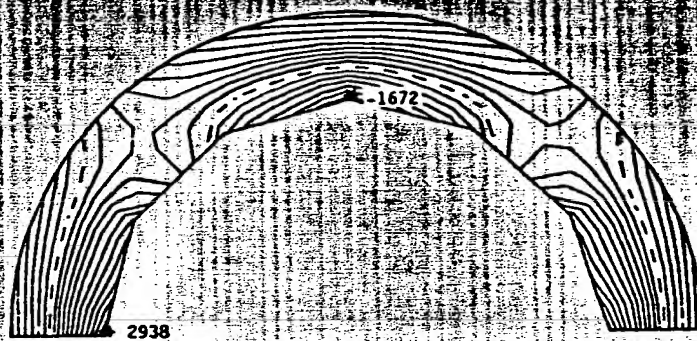


Figure 2.4-31. Contour Plot of the Peripheral Stress in the Core, 180° after Sudden Short Circuit, High-Modulus Polygonal Interface

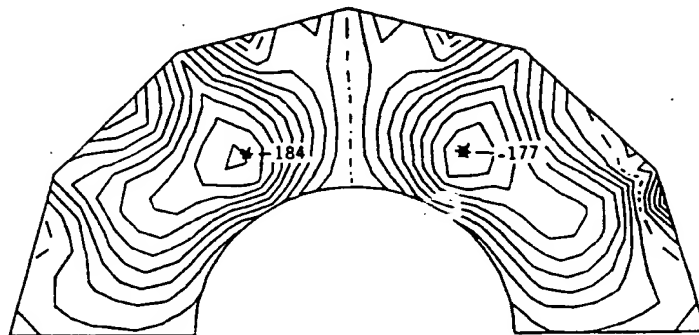


Figure 2.4-32. Contour Plot of the r - θ Shear Stress in the Armature Structure, 180° after Sudden Short Circuit, High-Modulus Polygonal Interface

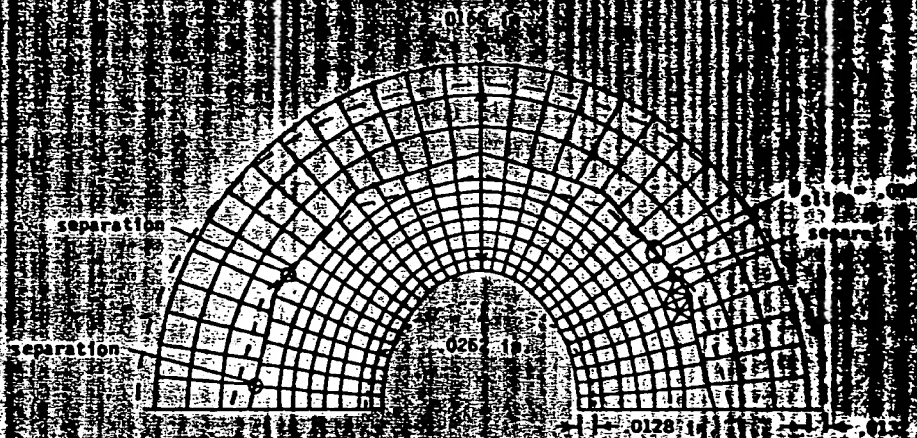


Figure 2.4-27. Deflection of the Armature Structure and Core, 180° after Sudden Short Circuit, High-Modulus Polygonal Interface

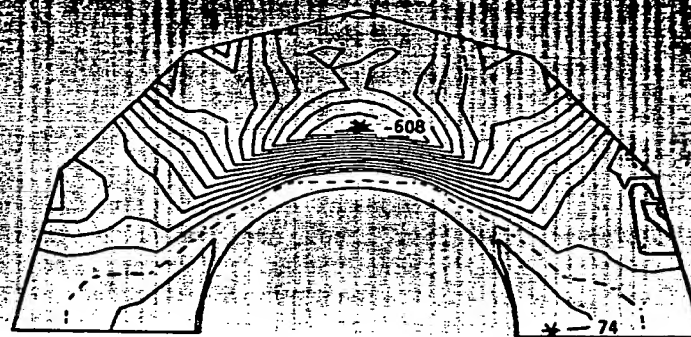


Figure 2.4-28. Contour Plot of the Radial Stress in the Armature Structure, 180° after Sudden Short Circuit, High-Modulus Polygonal Interface

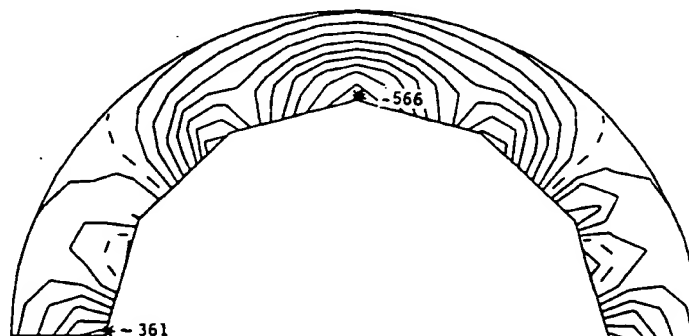


Figure 2.4-29. Contour Plot of the Radial Stress in the Core, 180° after Sudden Short Circuit, High-Modulus Polygonal Interface

Table 2.4-2

STRESSES OCCURRING AT 90° AFTER SUDDEN SHORT CIRCUIT

Stress	Figure No.	Max. psi	Min. psi	Stress Line Increment, psi
Radial Stress, Armature Structure	2.4-21	41	-1009	80
Radial Stress, Core	2.4-22	165	-868	80
Peripheral Stress, Armature Structure	2.4-23	223	-855	80
Peripheral Stress, Core	2.4-24	2004	-625	150
r- θ Shear Stress, Armature Structure	2.4-25	361	-675	80
r- θ Shear Stress, Core	2.4-26	308	-300	40

Figure 2.4-27 illustrates exaggerated deflections of the armature structure and core with the high modulus interface at 180° after sudden short circuit. Only half of the geometry is modeled in this figure because of the symmetry of the winding loading. At the armature inner surface, the maximum outward deflection is .0262 in. and the maximum inward deflection is .0128 in. At the core outer surface, the maximum outward deflection is .0166 in. and the maximum inward deflection is .0132 in. The interface separates at the several locations indicated in the figure, and there is also sliding motion at the interface at locations where the radial lines are discontinuous. The maximum sliding motion is .0088 in. The stresses produced in the armature structure and core at 180° after the fault are presented in Figures 2.4-28 through 2.4-33. Table 2.4-2 summarizes the information presented in these figures.

Many of the stresses are somewhat higher than those calculated for the perfectly bonded interface, and it is not surprising to find many of the stress maximums located right at the boundary of the polygonal interface. However, all calculated stresses are well within the stated mechanical properties of pressboard (Table 2.1-2).

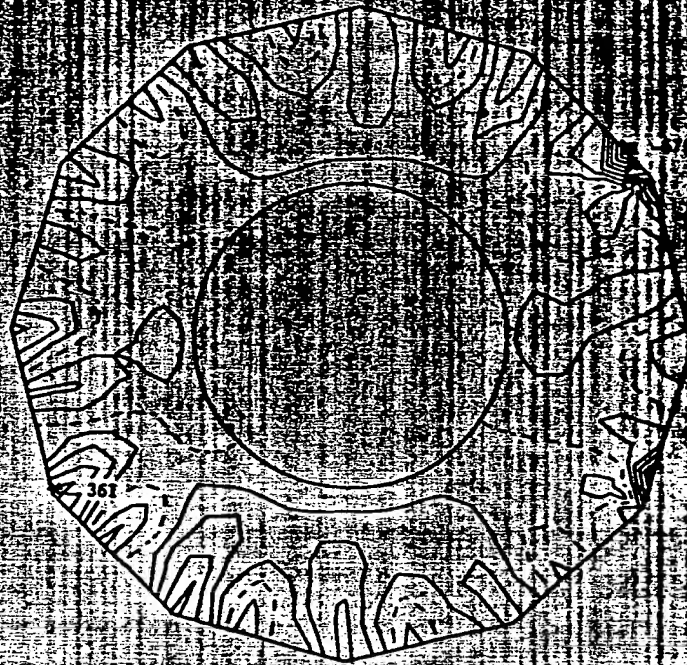


Figure 2.4-25. Contour Plot of the r - θ Shear Stress in the Armature Structure, 90° after Sudden Short Circuit, High-Modulus Polygonal Interface

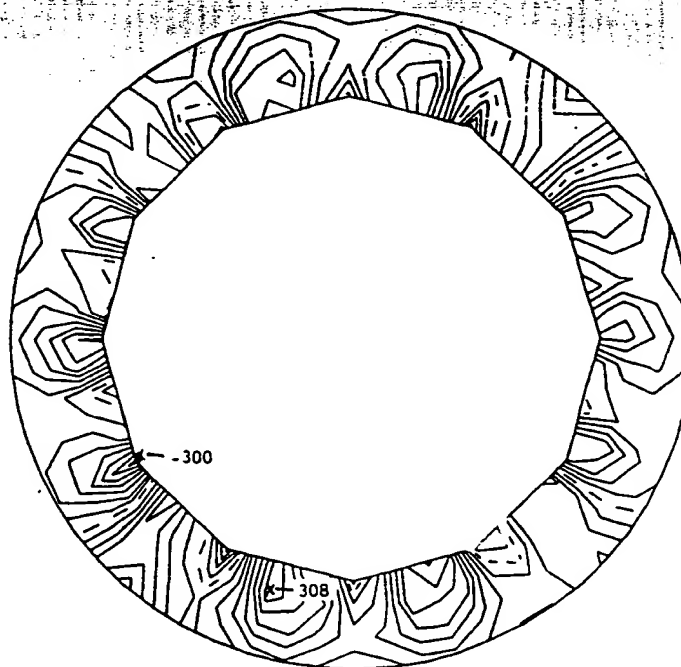


Figure 2.4-26. Contour Plot of the r - θ Shear Stress in the Core, 90° after Sudden Short Circuit, High-Modulus Polygonal Interface

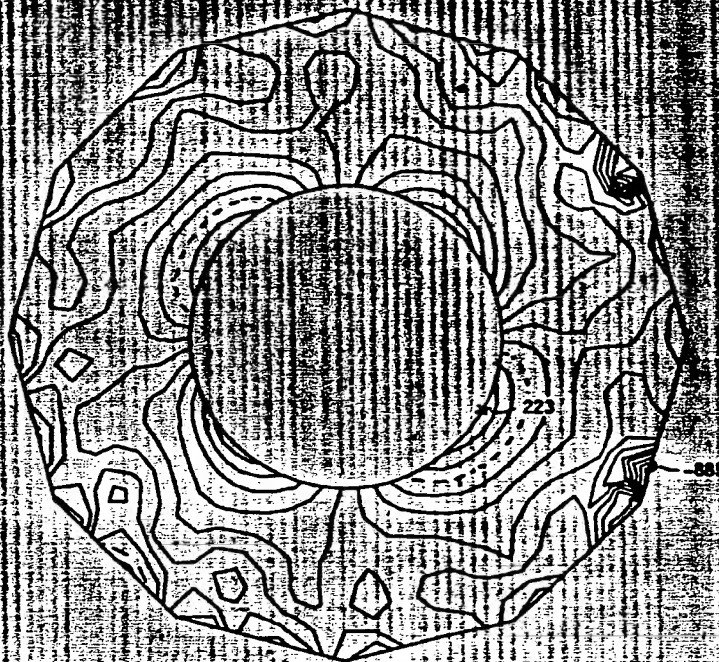


Figure 2.4-23. Contour Plot of the Peripheral Stress in the Armature Structure, 90° after Sudden Short Circuit, High-Modulus Polygonal Interface

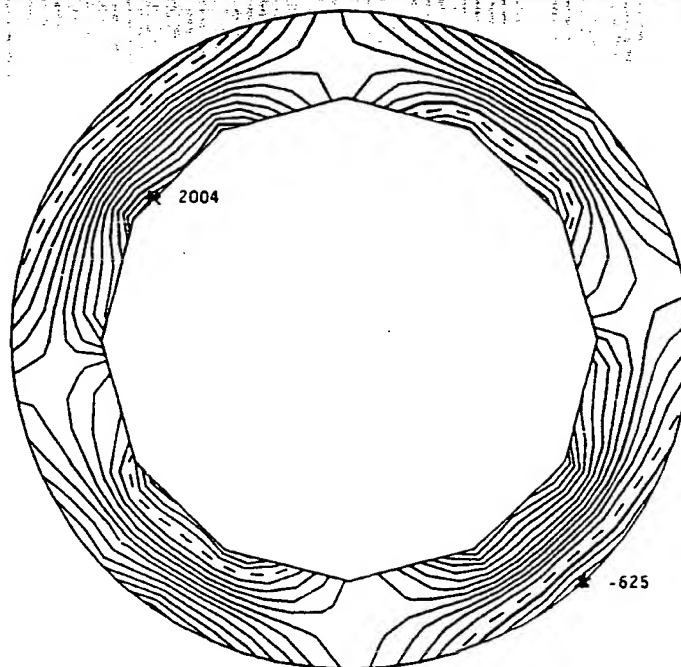


Figure 2.4-24. Contour Plot of the Peripheral Stress in the Core, 90° after Sudden Short Circuit, High-Modulus Polygonal Interface

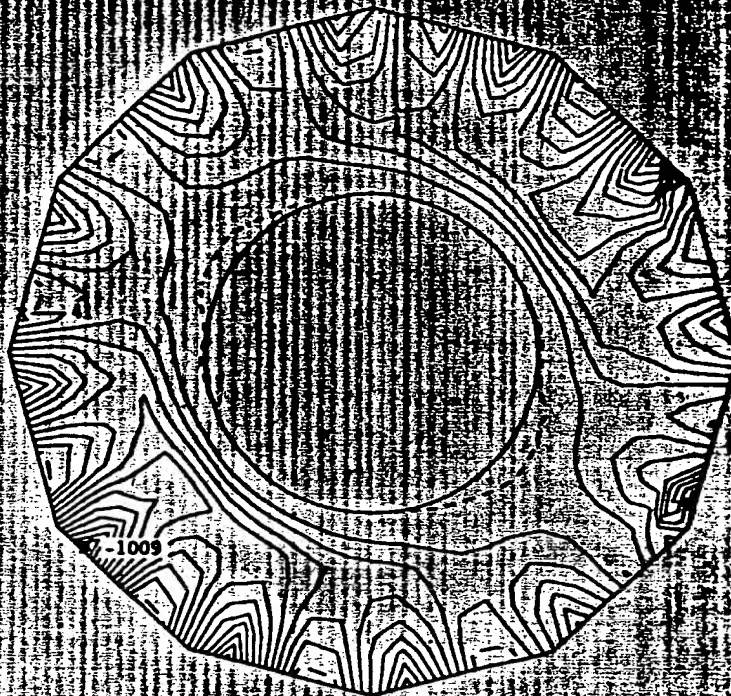


Figure 2.4-21. Contour Plot of the Radial Stress in the Armature Structure, 90° after Sudden Short Circuit, High-Modulus Polygonal Interface

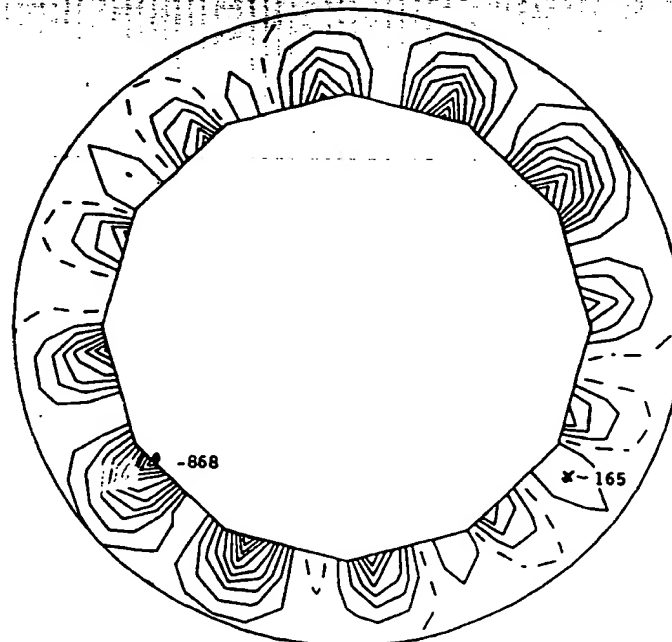


Figure 2.4-22. Contour Plot of the Radial Stress in the Core, 90° after Sudden Short Circuit, High-Modulus Polygonal Interface

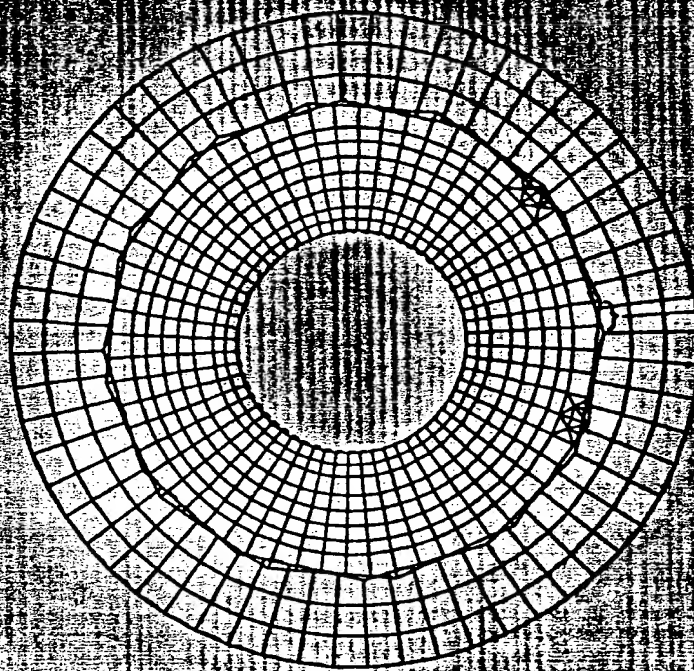


Figure 2.4-19. Deflection of the Armature Structure and Core, 90° after Sudden Short Circuit, Low-Modulus Polygonal Interface

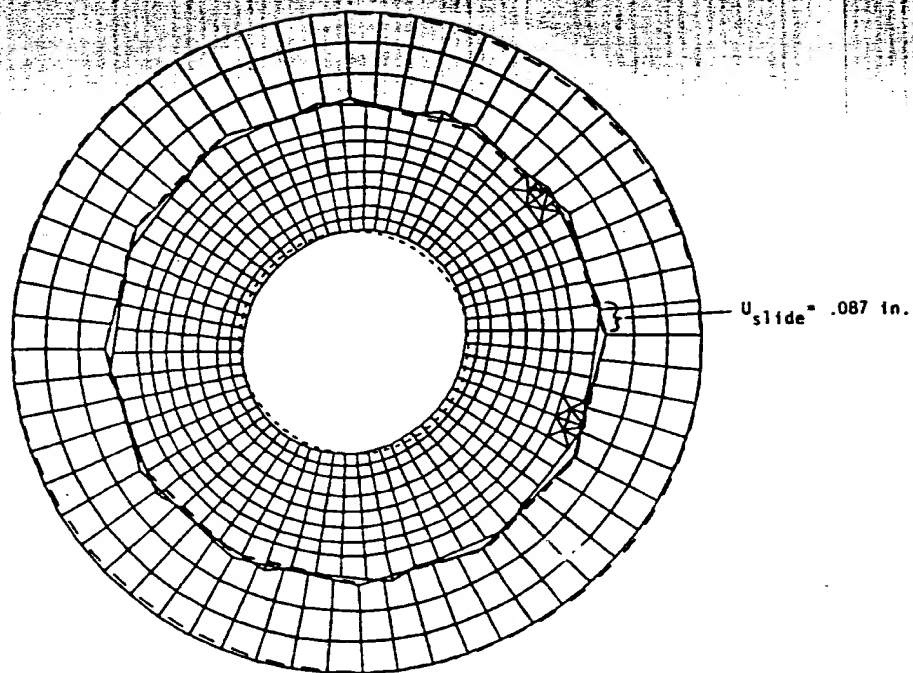


Figure 2.4-20. Deflection of the Armature Structure and Core, 90° after Sudden Short Circuit, High-Modulus Polygonal Interface

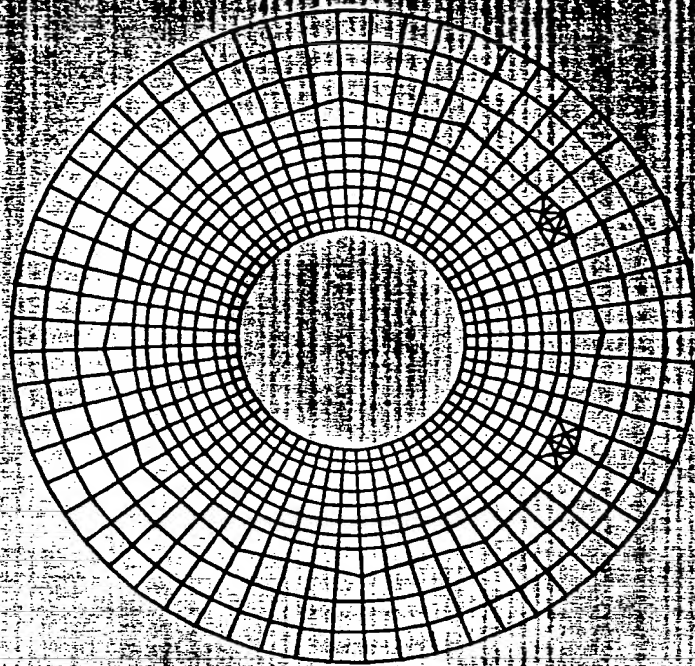


Figure 2.4-18. Finite Element Model of the Armature Structure and Core with Polygonal Interface

The first case uses a modulus of 1000 psi. This case can be visualized as having an unbonded 0.060 in.-thick piece of rubber inserted between the armature structure and the core. The second case uses an interface modulus equal to that of the core, 17×10^6 psi. This case can be visualized as having the armature structure inserted into the core with a line-to-line fit at the interface.

Figure 2.4-19 illustrates exaggerated deflections of the armature structure and core with the low modulus interface at 90° after sudden short circuit. The armature structure has twisted considerably and the elements at the interface appear to be interfering with each other. The elements do not actually interfere, and the illusion is due to the deflection magnitude being scaled to a considerably greater value than that to which the geometry is scaled. Tangential sliding of the armature structure, however, is indeed present and is of the alarmingly great magnitude of .447 in. Such a great deflection would surely damage the rubber in the interface, so this design approach must be judged to be undesirable. Further discussion of this design will not be presented.

Figure 2.4-20 illustrates exaggerated deflections of the armature structure and core with the high modulus interface at 90° after sudden short circuit. The sliding motion at the interface here is only .087 in. The interface also separates at the trailing sides of the vertices. The stresses produced in the armature structure and core at 90° after the fault are presented in Figures 2.4-21 through 2.4-26. Since a material and physical discontinuity occurs at the polygonal boundary, accurate stress contour plots can be obtained only by displaying the armature structure separately from the core. Table 2.4-1 summarizes the information presented in these figures.

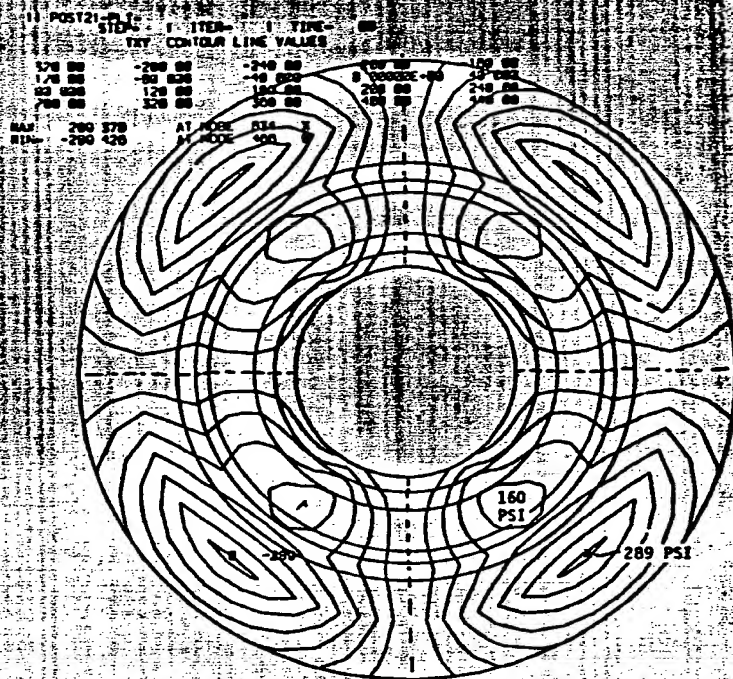


Figure 2.4-17. Contour Plot of the r - θ Shear Stress, Low-Modulus Insulation, 180° after Sudden Short Circuit

2.4.2 Mechanical Stress Analysis of the Polygonal Core-to-Armature Interface

A polygonal-shaped core-to-armature interface has been proposed as a practicable means of containing the armature structure within the core without resorting to the bonded core-to-armature interface described in the previous section. An unbonded interface would allow for an easier assembly of the armature into the core and would allow for later disassembly if it should become necessary. Motion of the armature structure within the core is constrained by interference at the flats of the polygonal interface.

Figure 2.4-18 illustrates the finite element model of the armature structure and core with a polygonal interface. The armature structure extends from the inner diameter to the polygonal boundary. The core extends from the polygonal boundary to the outer diameter. Additional elements are added at a couple of the vertices for increased stress resolution. The modulus of the core is 17×10^6 psi and the moduli of the insulation cylinders and the conductor cylinders is 1×10^6 psi.

In modeling the interface between the armature structure and the core, a special element has been used which can transmit only compressive forces across the interface. The element will not prevent the interface from separating, nor will it transmit a shear force across the interface; therefore, the polygonal geometry of the interface is the only means by which the winding is immobilized, similar to a nut within a socket. The element used at the polygonal interface is one for which a length, cross-sectional area, and modulus can be specified. The radial length of the interface is 0.060 in. Two different modulus cases for the interface elements are analyzed.

It has been seen that the largest deflections and stresses were experienced at 180° after a sudden short circuit. In the interest of exploring the effects of different insulation properties, this particular calculation was repeated for an insulation modulus representative of pressboard (1×10^6 psi). Figure 2.4-14 illustrates exaggerated armature structure deflections, which are approximately doubled from the same case with the high modulus insulation. Figure 2.4-15 illustrates a contour plot of the peripheral stress. The maximum tensile stress has increased in magnitude and has moved in location from the inner insulation cylinder to the core. The maximum compressive stress has increased in magnitude but has remained in the same location in the core. The largest peripheral tensile stress in the insulation and conductor region is about 600 psi, a decrease from the high modulus calculation. Figure 2.4-16 is a contour plot of the radial stress, and it looks very similar to the high modulus calculation. The maximum compressive stress has increased slightly and remains in the same location, and the maximum tensile stress has decreased slightly and has moved from the inner conductor layer to the core. Figure 2.4-17 is a contour plot of the $r-\theta$ shear stress, and it looks somewhat similar to the high modulus calculation. The maximum shear stress has increased slightly and has moved from the middle insulation cylinder to the core. The largest shear stress within the insulation and conductor region is about 160 psi, a decrease from the high modulus calculation. The overall effect of the lower modulus insulation has been to decrease the stresses in the insulation and conductor regions, at the expense of larger deflections. All calculated mechanical stresses appear to be well within the stated mechanical properties of pressboard (Table 2.1-2).

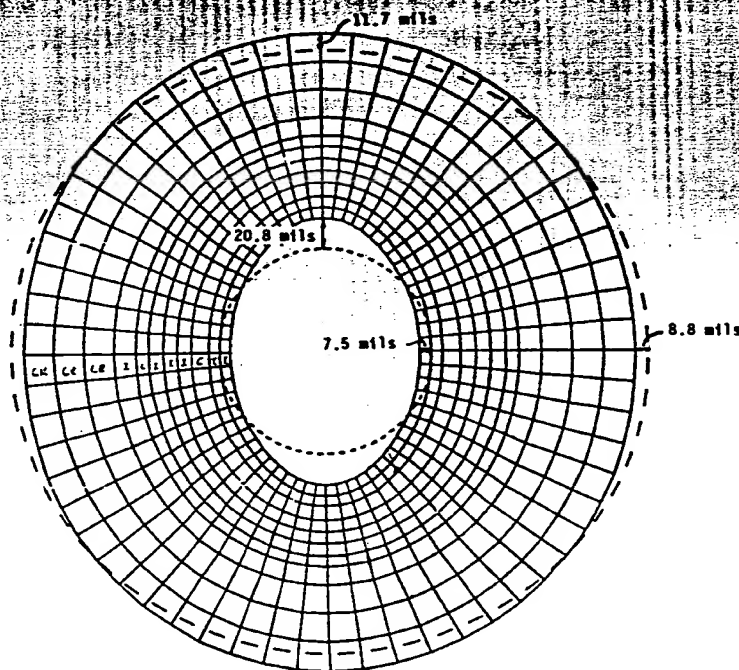


Figure 2.4-14. Deflection of the Armature Structure and Core, Low-Modulus Insulation, 180° after Sudden Short Circuit

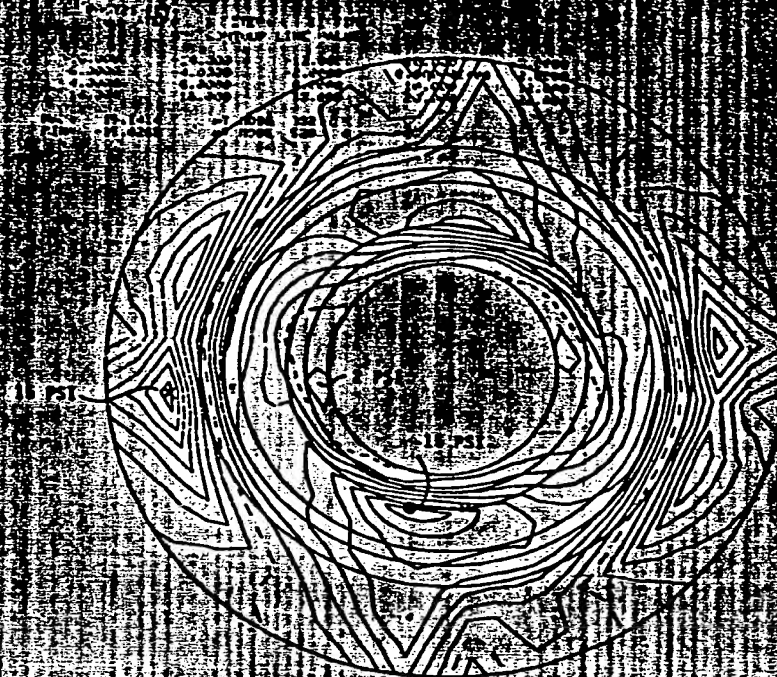


Figure 2.4-12. Contour Plot of the Radial Stress, Rated Load

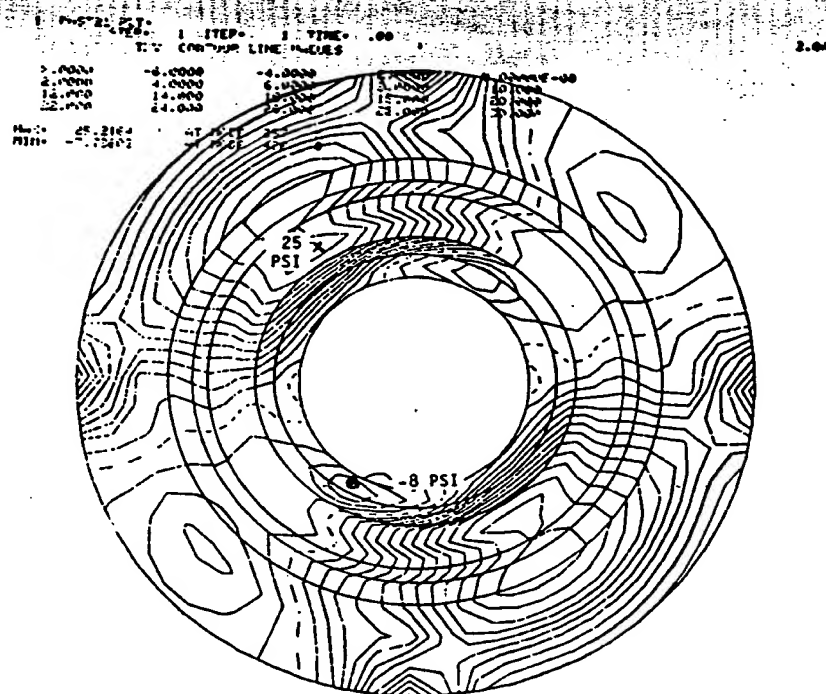


Figure 2.4-13. Contour Plot of the $r-\theta$ Shear Stress, Rated Load

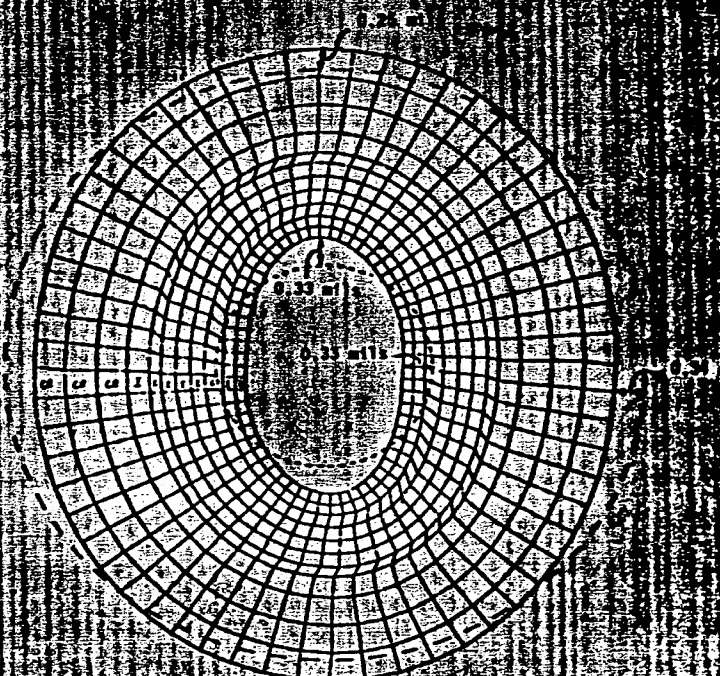


Figure 2.4-10. Deflection of the Armature Structure and the Core, Rated Load

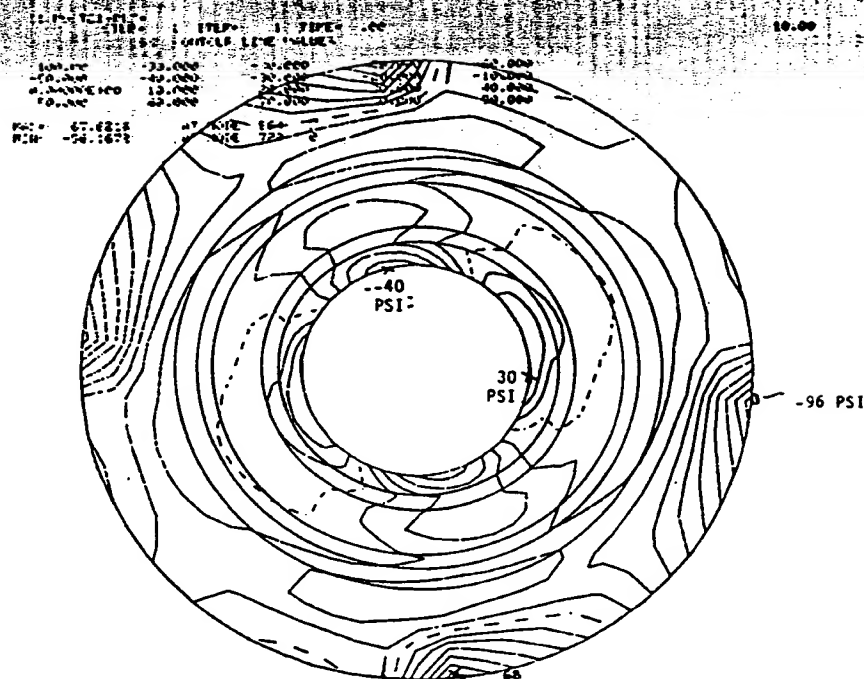


Figure 2.4-11. Contour Plot of the Peripheral Stress, Rated Load

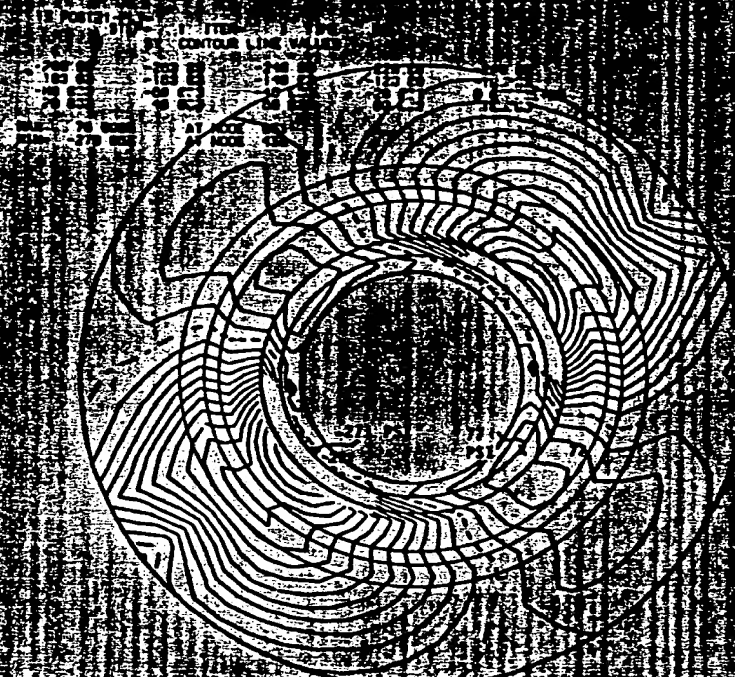


Figure 2.4-8. Contour Plot of the Radial Stress, 90° after Sudden Short Circuit

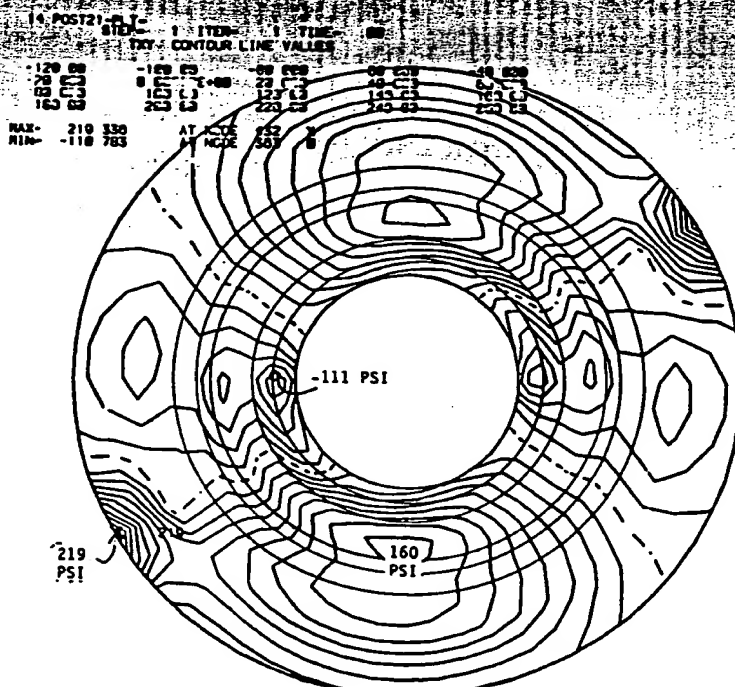


Figure 2.4-9. Contour Plot of the $r-\theta$ Shear Stress, 90° after Sudden Short Circuit

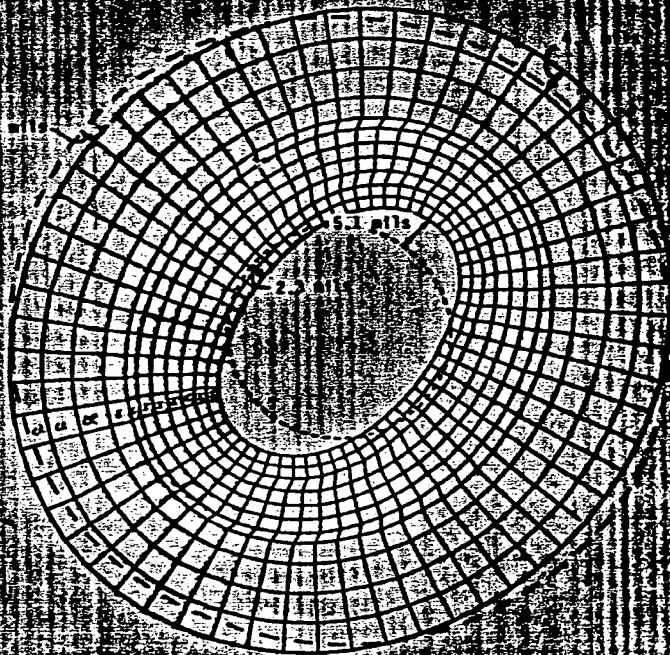


Figure 2.4-6. Deflection of the Armature Structure and Core, 90° after Sudden Short Circuit

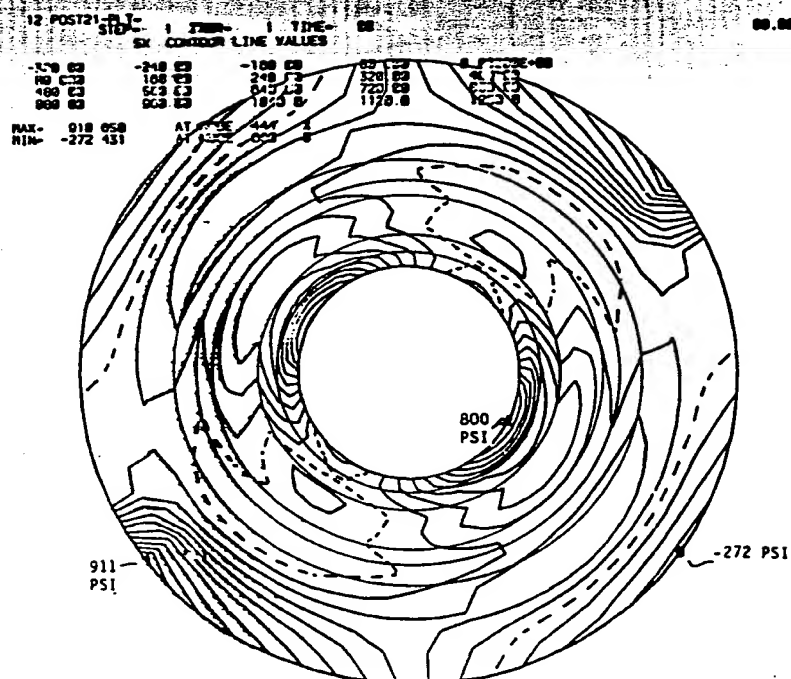


Figure 2.4-7. Contour Plot of the Peripheral Stress, 90° after Sudden Short Circuit

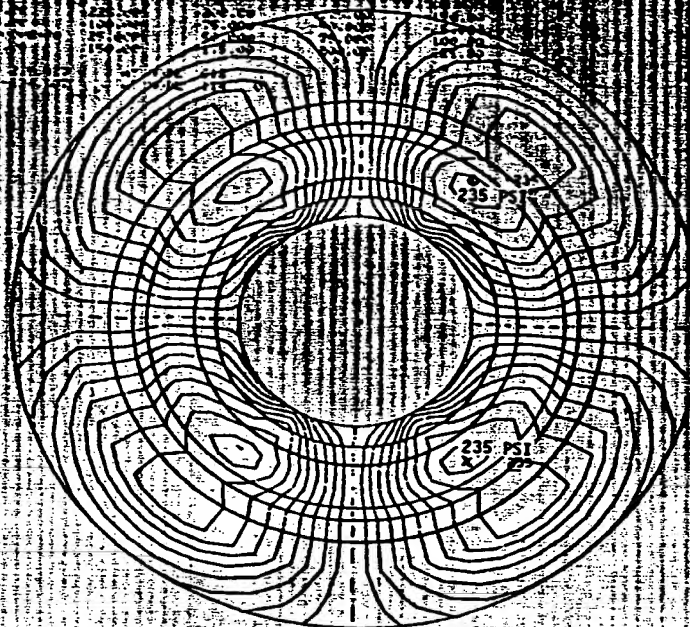
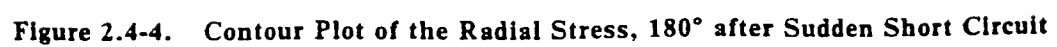


Figure 2.4-5. Contour Plot of the r - θ Shear Stress, 180° after Sudden Short Circuit

The next calculation to be discussed is the condition of sudden short circuit 90° after the fault. This condition has the largest tangential loading on the winding. The radial loading is also large, but not as great as exists at 180° after the fault. Figure 2.4-6 illustrates exaggerated deflections of the armature structure. As might be expected, the deflections are smaller than the case at 180° after the fault. The outward deflections are larger than the inward deflections, indicating the presence of a hoop strain. The peripheral stress and radial stress are illustrated in Figures 2.4-7 and 2.4-8, respectively, and the stresses are lower than those found at 180° after the fault. The same can be said for the r - θ shear stress illustrated in Figure 2.4-9, where it is seen that the largest shear stress within the conductor and insulation region is about 160 psi. Therefore, although the condition of sudden short circuit at 90° after the fault has the largest tangential loading of the winding, the largest shear stresses are produced by the greater deflections of the armature structure at 180° after the fault.

Figure 2.4-10 is an exaggerated illustration of the armature structure deflections under rated load. The deflections are expectedly very low. The outward deflection is equal to the inward deflection at the armature structure inner surface, while at the core outer surface, the inward deflection is greater than the outward deflection. This is due to the compressive hoop strain caused by the core inner surface pressure, which dominates over the outward tensile hoop strain of the winding pressure. It is only at the rated load condition that the core inner surface pressure is anywhere comparable to the winding forces. Contour plots of the peripheral stress, radial stress, and r - θ shear stress are contained in Figures 2.4-11, 12, and 13, respectively. The stresses are also very small.



The first calculation to be discussed is the condition of sudden short circuit 180° after the fault. Figure 2.4-2 illustrates exaggerated deflections of the armature structure and core, with the dotted lines indicating the undeflected positions. At the armature structure inner surface, the maximum outward deflection is 10.3 mils and the maximum inward deflection is 4.2 mils. At the core outer surface, the maximum outward deflection is 6.1 mils and the maximum inward deflection is 4.2 mils. The reason that the outward deflections are greater than the inward deflections can be explained from the nature of the force distribution. The largest force component is the radial winding force, which is approximately equivalent to the form

$$F_R = F_m \cos^2 \theta = \frac{F_m}{2} + \frac{F_m}{2} \cos 2\theta$$

The nonvarying component produces a tensile hoop strain of constant outward deflection around the periphery while the $\cos 2\theta$ term produces an ovalization strain of sinusoidal variation around the periphery. The ovalization strain adds to the hoop strain at the maximum outward deflection and subtracts from the hoop strain at maximum inward deflection, thus explaining the difference between maximum outward deflection and inward deflection. Figure 2.4-3 is a contour plot of the peripheral stress. Values of the stresses at the contour lines are listed in the figure and minimum and maximum points are marked. The dotted line is the contour of zero stress. The maximum peripheral stress is 1512 psi tensile in the inner insulation cylinder. The minimum peripheral stress (maximum compressive) is 445 psi in the core. Figure 2.4-4 is a contour plot of the radial stress. Both the maximum tensile stress of 131 psi and maximum compressive stress of 561 psi occur in the inner conductor layer. Figure 2.4-5 is a contour plot of the $r-\theta$ shear stress. This is considered to be an important quantity because it is in such an orientation as to delaminate the insulation cylinders or the conductor to insulation bonds. The maximum shear stress of 235 psi is found in the center insulation cylinder, although a shear stress of 200 psi is found all the way from the inner conductor layer to the core.

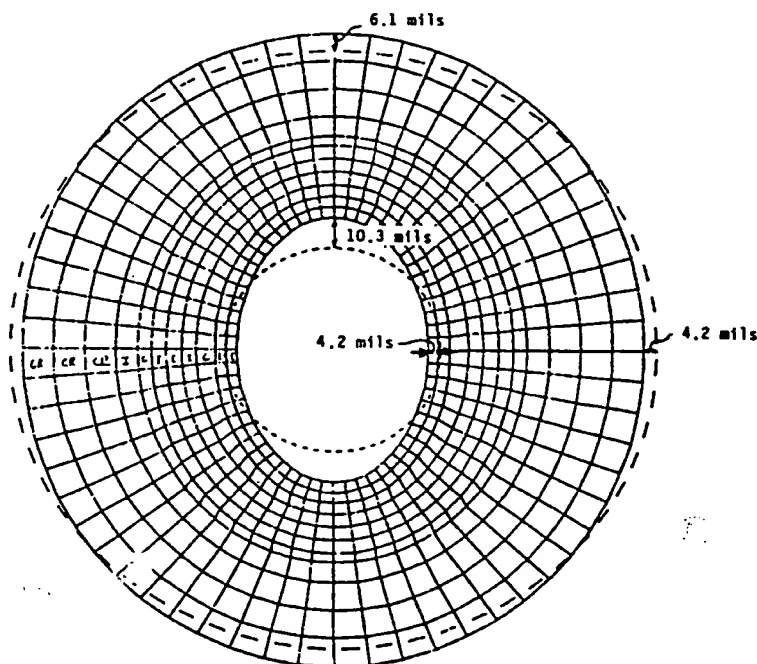


Figure 2.4-2. Deflection of the Armature Structure and Core, 180° after Sudden Short Circuit

2.4 MECHANICAL STRESS ANALYSIS

2.4.1 Mechanical Stress Analysis of the Perfectly Bonded Core-to-Armature Interface

The ultimate goal of the force calculations performed in Section 2.3 is the determination of the mechanical stresses within the armature structure, so that the required material properties of the insulation cylinders and conductor-to-insulation bonds can be determined. Owing to the complexity of the problem and the complicated force distributions, it seemed to be a task well suited for a mechanical finite element analysis package called ANSYS. The mechanical stress calculations were performed on the same machine for which the winding forces were calculated, a 600 MVA 245 kV diamond coil armature having its straight sections extending over the entire magnetic active length. Such a winding geometry allows for a two-dimensional analysis. Two different insulation materials, fiberglass-epoxy and pressboard, are modeled, and the calculated stresses show that pressboard insulation, which had been thought to be too mechanically weak for the application, is well qualified. The geometry of the armature structure and core is modeled by dividing the annular cross section into many trapezoidal elements, as illustrated in Figure 2.4-1. The peripheral span of each element is 6° . The material annuli are assumed to be intimately bonded with each other, and the material properties are contained in Figure 2.4-1. The modulus of the insulation cylinders is representative of fiberglass-epoxy material which was thought to be necessary for the insulation cylinders at the time the calculations were performed. Later calculations in this section utilize a modulus representative of pressboard. The pressure distributions are loaded into the model by specifying radial and tangential surface pressures on the faces of the elements of the conductor layers, as well as radial pressures on the core inner surface. The finite element analysis returns numerical calculations of deflections, radial stress, peripheral stress, and $r-\theta$ shear stress.

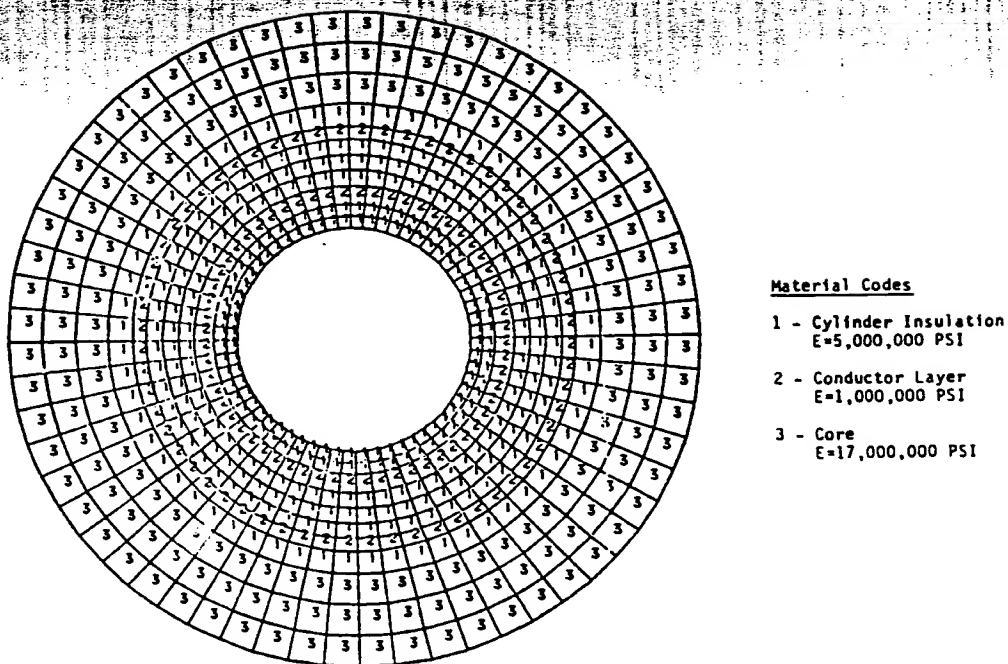


Figure 2.4-1. Finite Element Model of the Armature Structure and Core

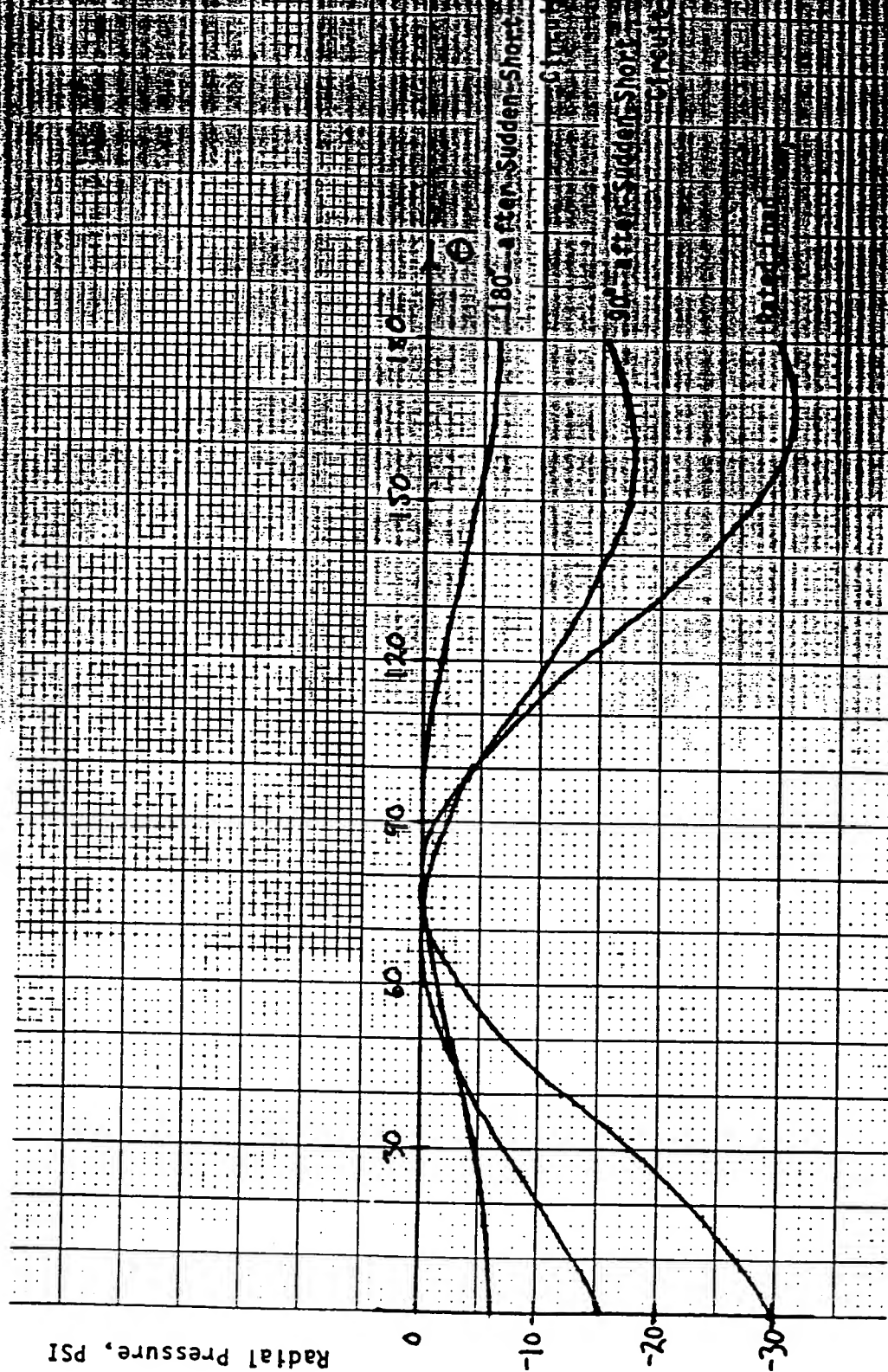


Figure 2.3-9. Core Inner Surface Pressure, 600 MVA, 145 kV Reactor Core

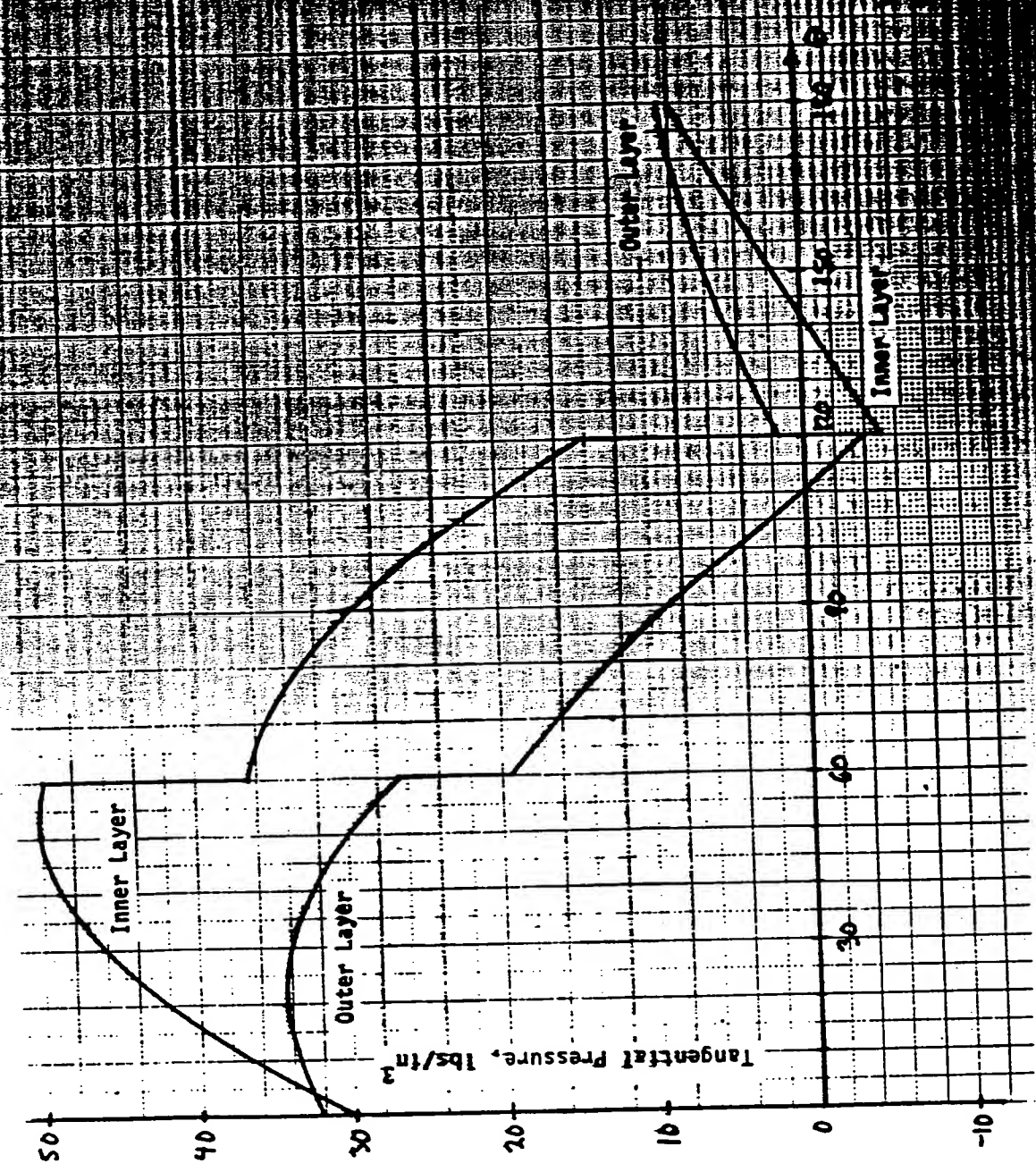


Figure 2.3-8. Tangential Winding Pressure on Three-Phase Sheet Steel with Inner Layer of Insulation
90° after Fault; 600 MVA, 345 kV, $X'' = 0.20$

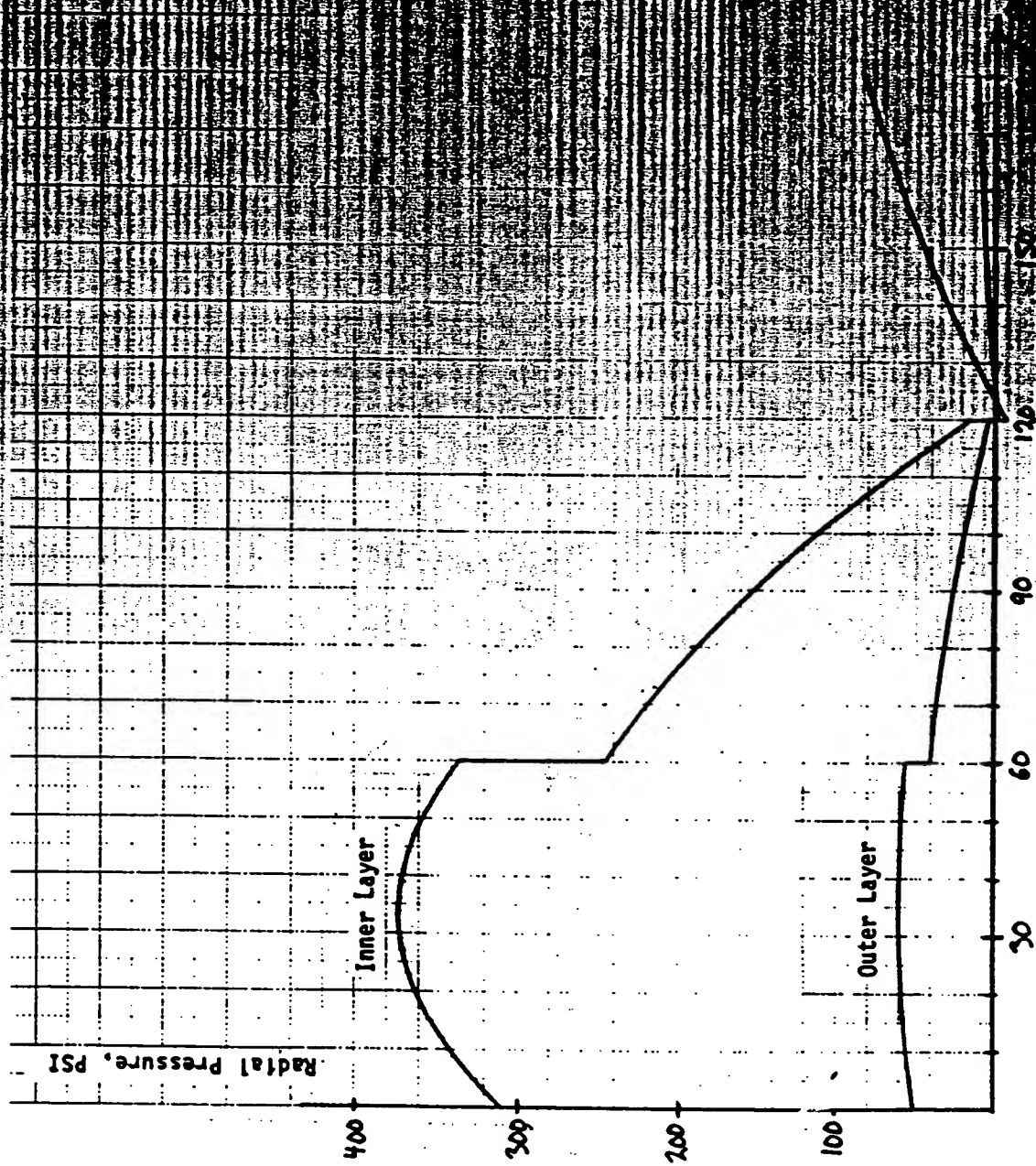


Figure 2.3-7. Radial Winding Pressure on Three-Phase Short Circuit from Faulted Phase after Fault; 600 MVA, 345 kV, $X'' = 0.20$

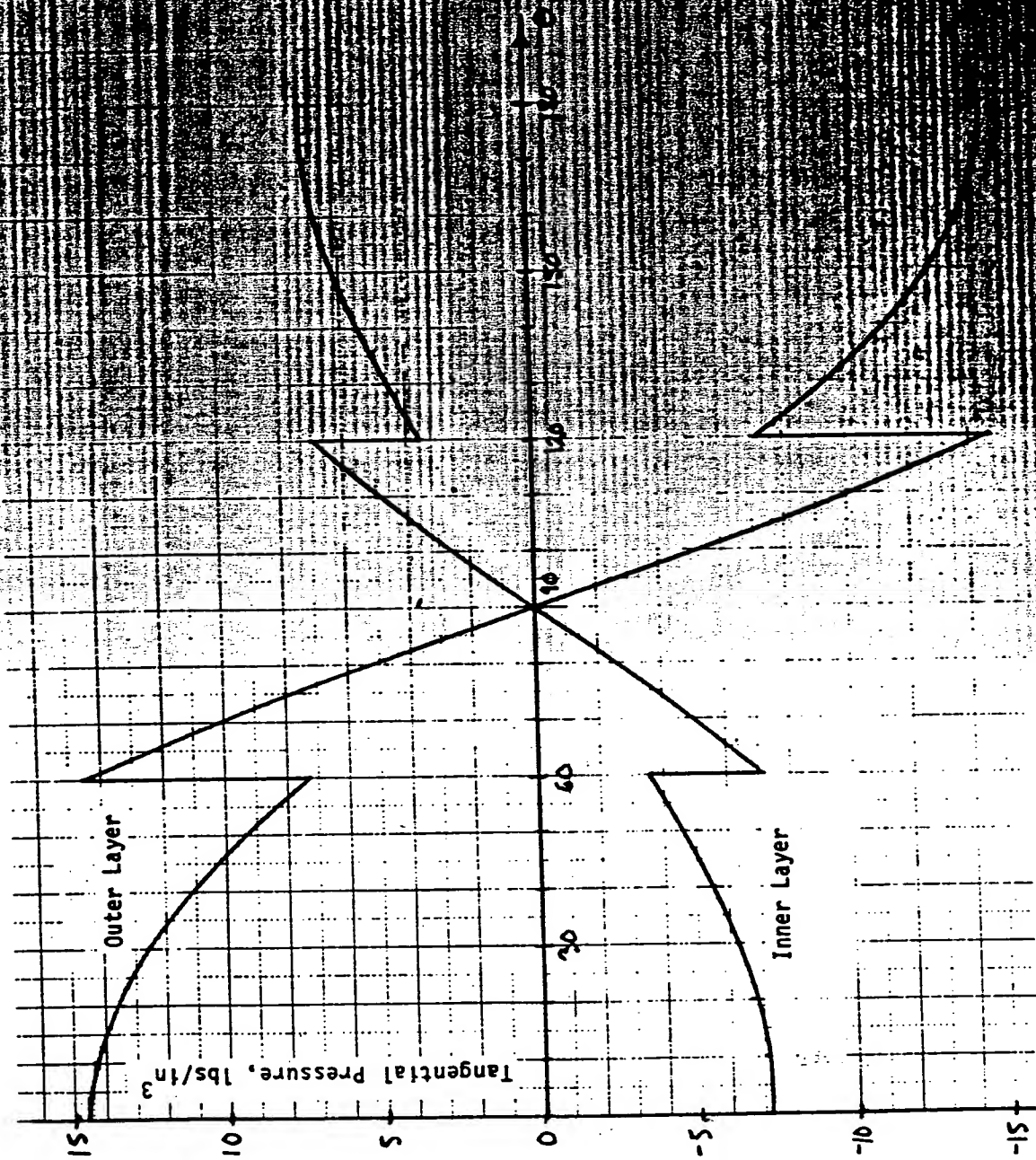


Figure 2.3-6. Tangential Winding Pressure on Three-Phase Short Circuit Bus at 180° after Fault; 600 MVA, 345 kV, $X'' = 0.20$

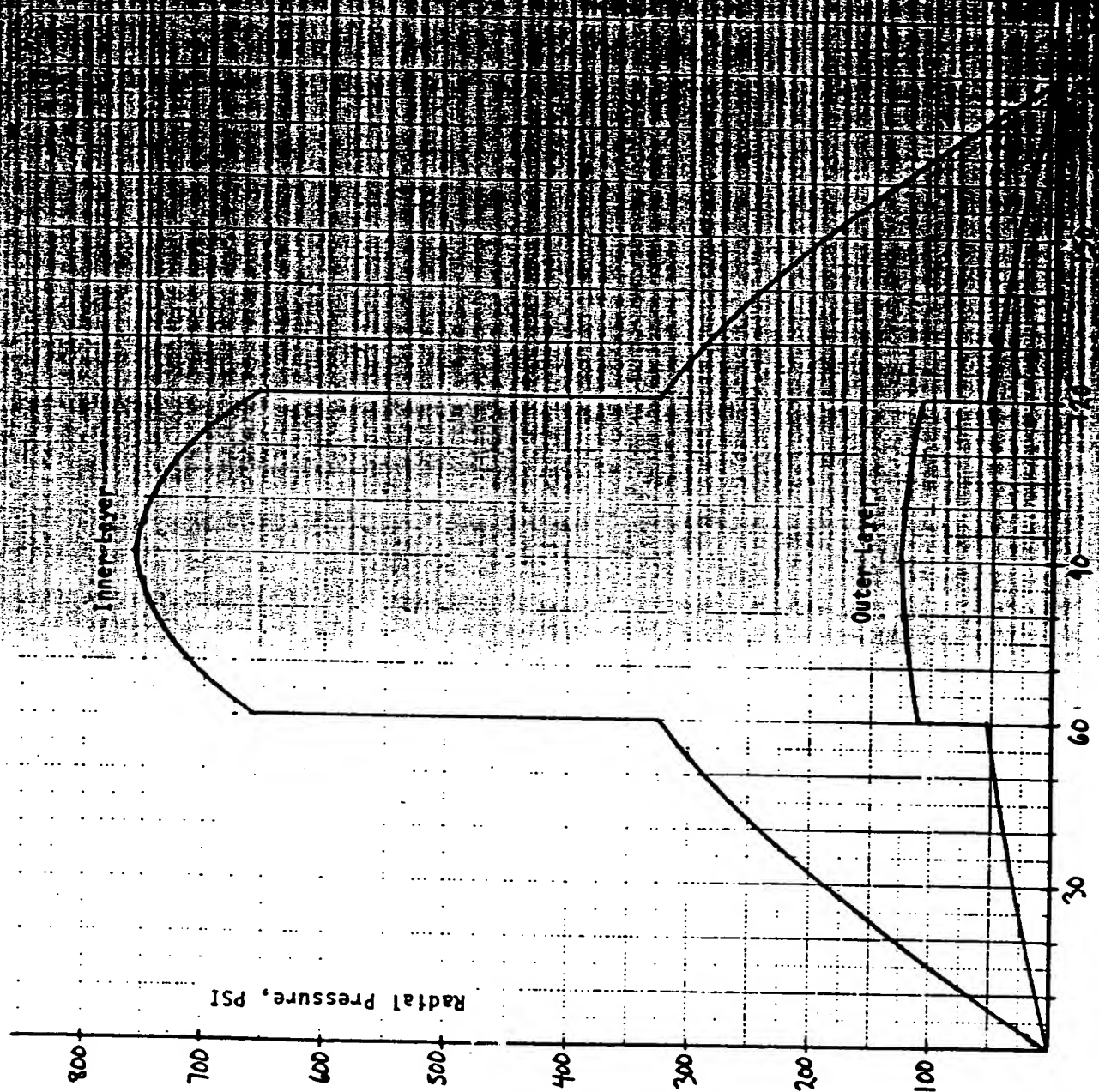


Figure 2.3-5. Radial Winding Pressure on Three-Phase Spurt Winding Motor after Fault; 600 MVA, 345 kV, $X'' = 0.20$

The magnetic field produced by the dc component of the armature current is identical to Equation 2.3-5. The field winding is shielded from transients by the rotor shield, so its magnetic field is unaltered and is specified by Equation 2.3-4. The total magnetic field is the superposition of three components of field: the rotating armature field, the stationary armature field, and the rotor field. At 180° after the moment of fault, the two armature fields are aligned with each other while being directly opposed by the rotor field. The total magnetic field is

$$\begin{aligned} \vec{B} &= \vec{a}_r (2B_{AR} - B_{FR}) \cos \theta \\ &= \vec{a}_\theta (2B_{A\theta} - B_{F\theta}) \sin \theta \end{aligned} \quad (2.3-6)$$

The forces existing at 90° after the fault may also be of interest, since it is expected that maximum torsional loading of the armature winding exists at this moment. The total magnetic field at 90° after the fault is

$$\begin{aligned} \vec{B} &= \vec{a}_r [B_{AR} \cos \theta + B_{AR} \cos(\theta + 90^\circ) + B_{FR} \cos(\theta - 90^\circ)] \\ &= \vec{a}_\theta [B_{A\theta} \sin \theta + B_{A\theta} \sin(\theta + 90^\circ) + B_{F\theta} \sin(\theta - 90^\circ)] \end{aligned} \quad (2.3-7)$$

The force distributions at 180° after the moment of fault are illustrated in Figures 2.3-5 and 2.3-6. The force distributions at 90° after the moment of fault are illustrated in Figures 2.3-7 and 2.3-8. The origin of the peripheral coordinate ($\theta = 0$) corresponds to the magnetic axis of one of the phases. The magnetic axis of the field winding was aligned with the origin at the moment of fault.

In addition to the winding forces, the core experiences a force of attraction from the radial component of flux at the core inner surface. The expression for this inward pressure is derived in Reference 2.3-1, and is

$$\bar{P} = -\vec{a}_r \frac{1}{2} \frac{B_R^2}{\mu_o}, \quad (2.3-8)$$

where B_R is the total radial flux density at the core inner surface. The core pressure distributions for 180° after sudden short circuit, 90° after sudden short circuit, and rated load are illustrated in Figure 2.3-9.

References

- 2.3-1. M.V.K. Chari and T.R. Haller, "Steady State and Short Circuit Force Analysis on the Stator Windings of a Superconducting Generator," Paper F79 624-8, IEEE PES Summer Meeting, 1979.

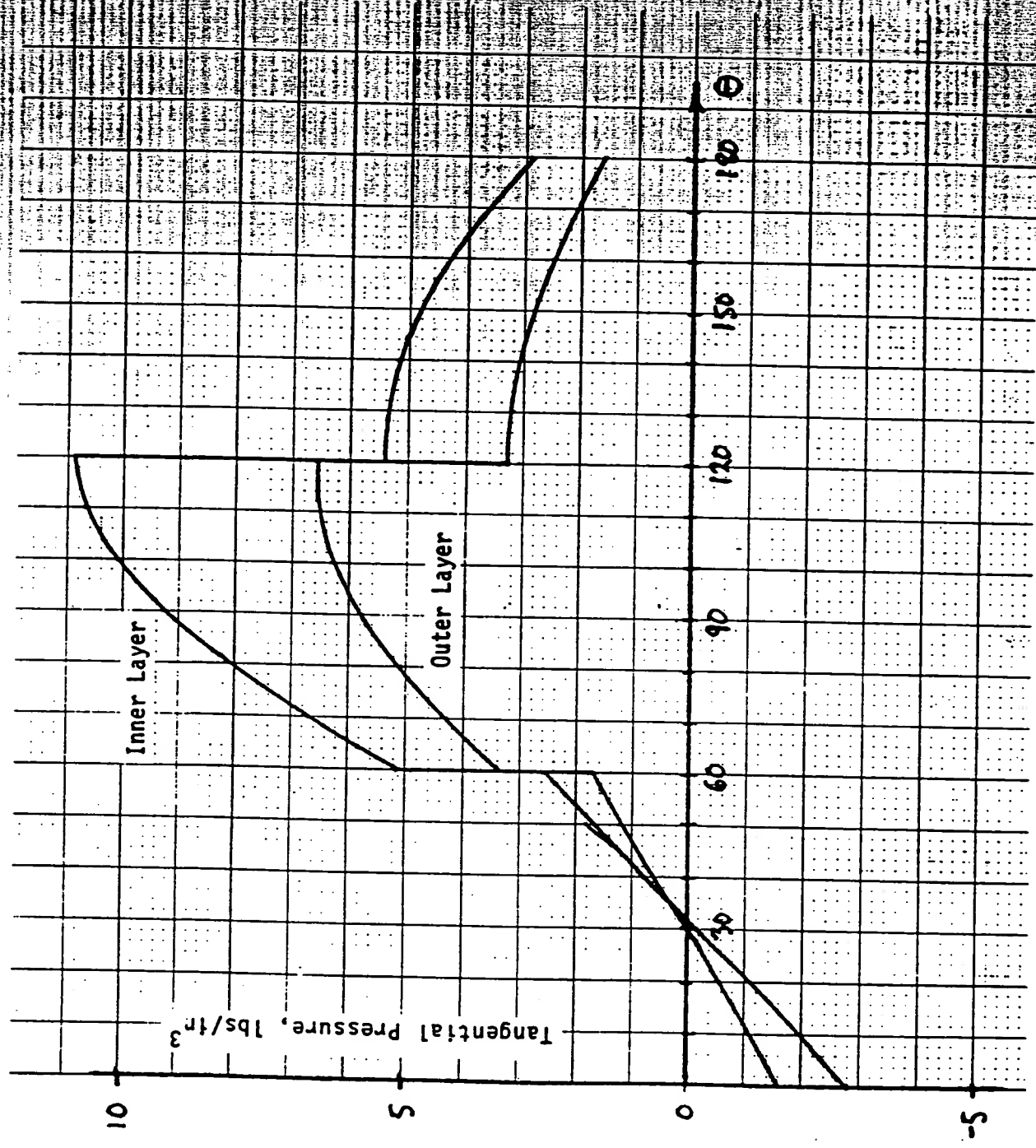


Figure 2.3-4. Tangential Winding Pressure at Rated Load: 600 MVA, 345 kV, 0.9 pf

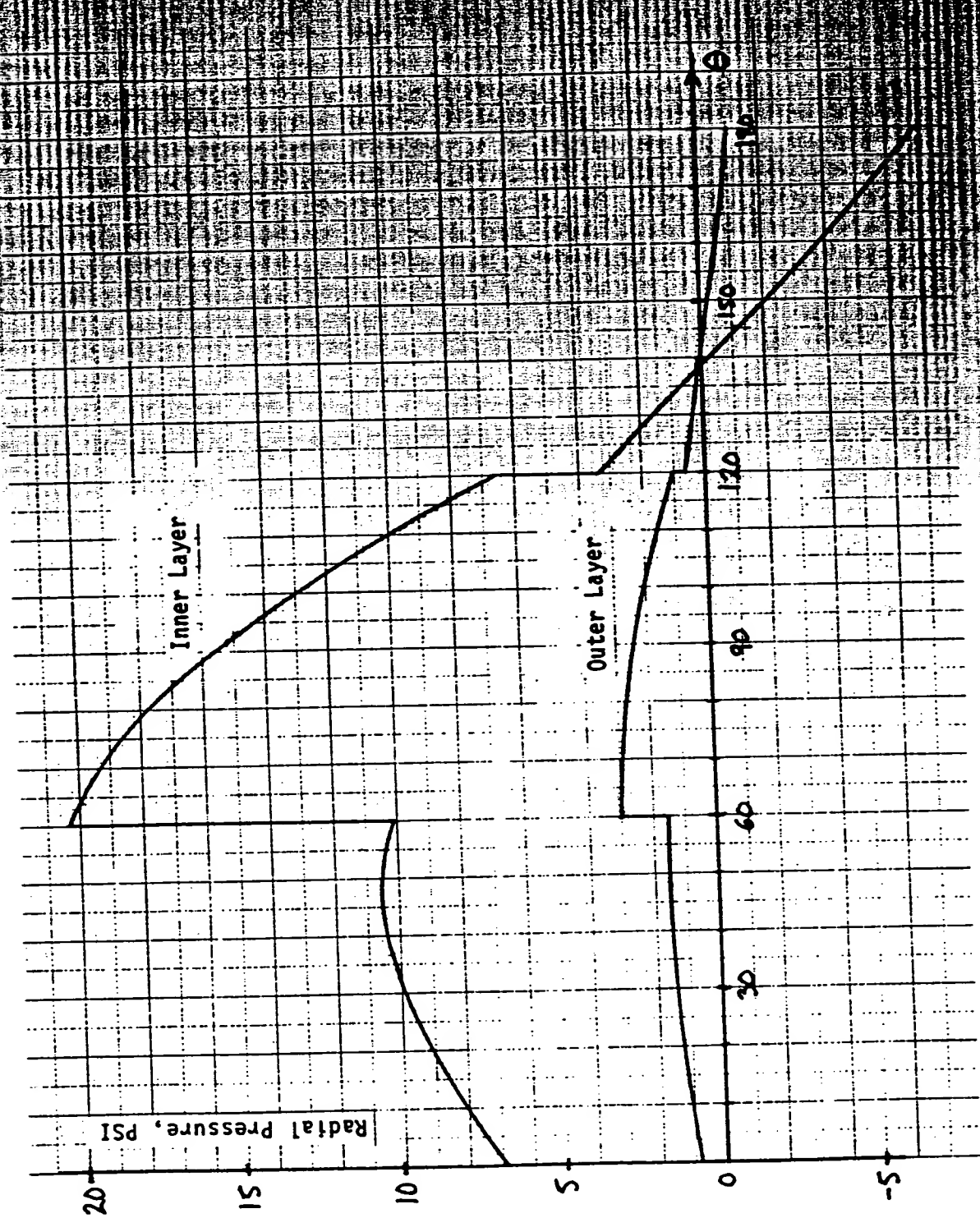


Figure 2.3-3. Radial Winding Pressure at Rated Load: 600 MVA, 345 kV, 12.5 ft.

The expression for the rotor flux density is applicable for all three regions:

$$\begin{aligned} \bar{B}_r = & \frac{1}{r} \frac{\sqrt{3}}{2\pi} \left[J_A r (r_o^2 - r_i^2) \left(\frac{1}{r_o^2} - \frac{1}{r^2} \right) \cos \theta \right. \\ & \left. - \bar{a}_\theta \frac{\sqrt{3}}{2\pi} \mu_o J_A r (r_o^2 - r_i^2) \left(\frac{1}{r_o^2} - \frac{1}{r^2} \right) \sin \theta \right] \quad r > r_o \end{aligned} \quad (2.3-4)$$

The flux expressions are evaluated at radii $r = r_i$ and $r = r_o$, superimposed according to Equation 2.3-2 and cross multiplied with the instantaneous phase-belt currents to produce the force distributions illustrated in Figures 2.3-3 and 2.3-4. The radial force is given as a force per unit area, as per Equation 2.3-1, but the tangential force is converted to a force per unit volume by dividing the tangential component of Equation 2.3-1 by the conductor layer height. The force distributions are illustrated over only 180° since they repeat over the next 180°. The discontinuities arise from the different values of currents in adjacent phase belts. The origin of the peripheral coordinate ($\theta = 0$) corresponds to the magnetic axis of a phase having maximum instantaneous current.

A three-phase fault from rated open-circuit voltage at the generator terminals will cause abnormally large armature currents and consequent large forces on the armature winding. It is well known that the armature fault currents contain both dc and ac components, owing to the requirement that the armature current cannot change instantaneously at the moment of fault. The ac component of current produces a rotating magnetic field, while the dc component of current produces a stationary magnetic field of equal magnitude. The two fields oppose each other at the moment of fault, and assist each other at 180° after the fault.

To evaluate the magnetic field created by the armature winding, it is necessary to consider the effect of eddy currents in the rotor electromagnetic shield on the magnetic field. If the shield is modeled as a perfect conductor that does not allow penetration of the magnetic field below its surface, a boundary condition is imposed where $B_R = 0$ at the shield surface, and equations for the armature magnetic field are derived accordingly. Therefore, the magnetic field produced by the ac component of armature current, neglecting time decrements, is:

$$\begin{aligned} \bar{B}_A = & \bar{a}_r \frac{3}{\pi\sqrt{2}} \mu_o \frac{J_A}{X''} \left[(r_{i2} - r_{i1}) \left(\frac{r_i^2 + r_c^2}{r_s^2 + r_c^2} \right) + (r_{o2} - r_{o1}) \left(\frac{r_o^2 + r_c^2}{r_s^2 + r_c^2} \right) \right] \left(1 - \frac{r_s^2}{r^2} \right) \cos \theta \\ & - \bar{a}_\theta \frac{3}{\pi\sqrt{2}} \mu_o \frac{J_A}{X''} \left[(r_{i2} - r_{i1}) \left(\frac{r_i^2 + r_c^2}{r_s^2 + r_c^2} \right) + (r_{o2} - r_{o1}) \left(\frac{r_o^2 + r_c^2}{r_s^2 + r_c^2} \right) \right] \left(1 + \frac{r_s^2}{r^2} \right) \sin \theta \quad r_s < r < r_i \\ = & \bar{a}_r \frac{3}{\pi\sqrt{2}} \mu_o \frac{J_A}{X''} \left[(r_{i2} - r_{i1}) \left(\frac{r_i^2 - r_s^2}{r_s^2 + r_c^2} \right) \left(1 + \frac{r_c^2}{r^2} \right) + (r_{o2} - r_{o1}) \left(\frac{r_o^2 + r_c^2}{r_s^2 + r_c^2} \right) \left(1 - \frac{r_s^2}{r^2} \right) \right] \cos \theta \\ & - \bar{a}_\theta \frac{3}{\pi\sqrt{2}} \mu_o \frac{J_A}{X''} \left[(r_{i2} - r_{i1}) \left(\frac{r_i^2 - r_s^2}{r_s^2 + r_c^2} \right) \left(1 - \frac{r_c^2}{r^2} \right) + (r_{o2} - r_{o1}) \left(\frac{r_o^2 + r_c^2}{r_s^2 + r_c^2} \right) \left(1 + \frac{r_s^2}{r^2} \right) \right] \sin \theta \quad r_i < r < r_o \\ = & \bar{a}_r \frac{3}{\pi\sqrt{2}} \mu_o \frac{J_A}{X''} \left[(r_{i2} - r_{i1}) \left(\frac{r_i^2 - r_s^2}{r_s^2 + r_c^2} \right) + (r_{o2} - r_{o1}) \left(\frac{r_o^2 - r_s^2}{r_s^2 + r_c^2} \right) \right] \left(1 + \frac{r_c^2}{r^2} \right) \cos \theta \\ & - \bar{a}_\theta \frac{3}{\pi\sqrt{2}} \mu_o \frac{J_A}{X''} \left[(r_{i2} - r_{i1}) \left(\frac{r_i^2 - r_s^2}{r_s^2 + r_c^2} \right) + (r_{o2} - r_{o1}) \left(\frac{r_o^2 - r_s^2}{r_s^2 + r_c^2} \right) \right] \left(1 - \frac{r_c^2}{r^2} \right) \sin \theta \quad r_o < r < r_c \end{aligned}$$

(2.3-5)

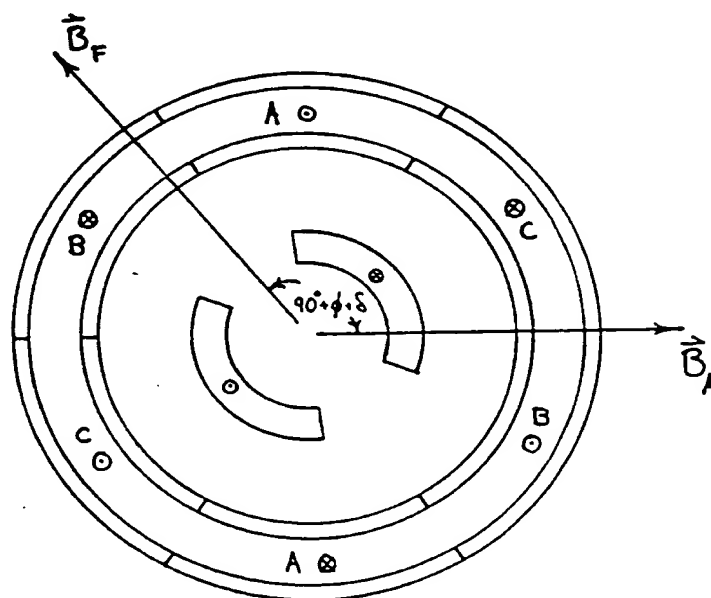
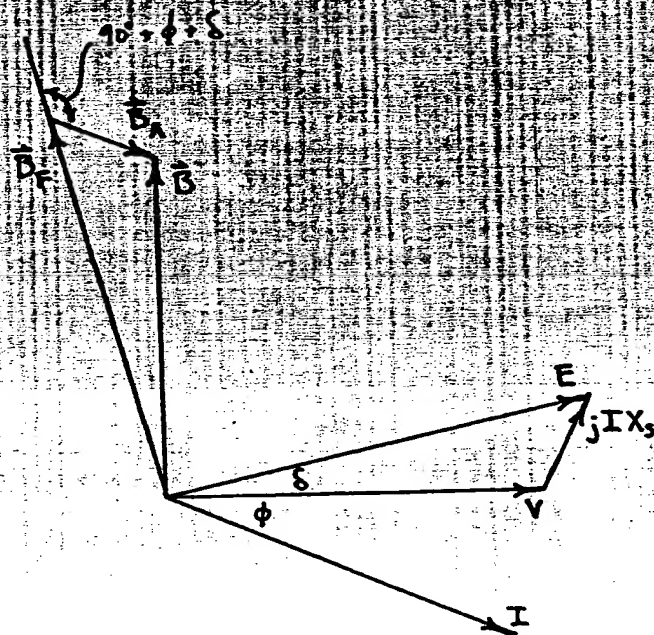


Figure 2.3-2. Angular Relation of Stator and Rotor Fluxes Under Load Operation

$$\begin{aligned}
 & -\frac{\rho_0}{a_0} \frac{3}{\pi\sqrt{2}} \mu_0 J_A \left\{ (r_{i2} - r_{i1}) \left(\frac{r_i^2}{r_c^2} - \frac{r_i^2}{r_f^2} \right) + (r_{o2} - r_{o1}) \left(\frac{r_i^2 + r_o^2}{r_c^2} \right) \right\} \sin \theta \quad r_i < r < r_o \\
 & -\frac{\rho_0}{a_0} \frac{3}{\pi\sqrt{2}} \mu_0 J_A \left\{ (r_{i2} - r_{i1}) \left(\frac{r_i^2}{r_c^2} + \frac{r_i^2}{r_f^2} \right) + (r_{o2} - r_{o1}) \left(\frac{r_o^2}{r_c^2} + \frac{r_o^2}{r_f^2} \right) \right\} \cos \theta \\
 & -\frac{\rho_0}{a_0} \frac{3}{\pi\sqrt{2}} \mu_0 J_A \left\{ (r_{i2} - r_{i1}) \left(\frac{r_i^2}{r_c^2} - \frac{r_i^2}{r_f^2} \right) + (r_{o2} - r_{o1}) \left(\frac{r_o^2}{r_c^2} - \frac{r_o^2}{r_f^2} \right) \right\} \sin \theta \quad r_o < r < r_c
 \end{aligned}$$

Core

(2.3-3)

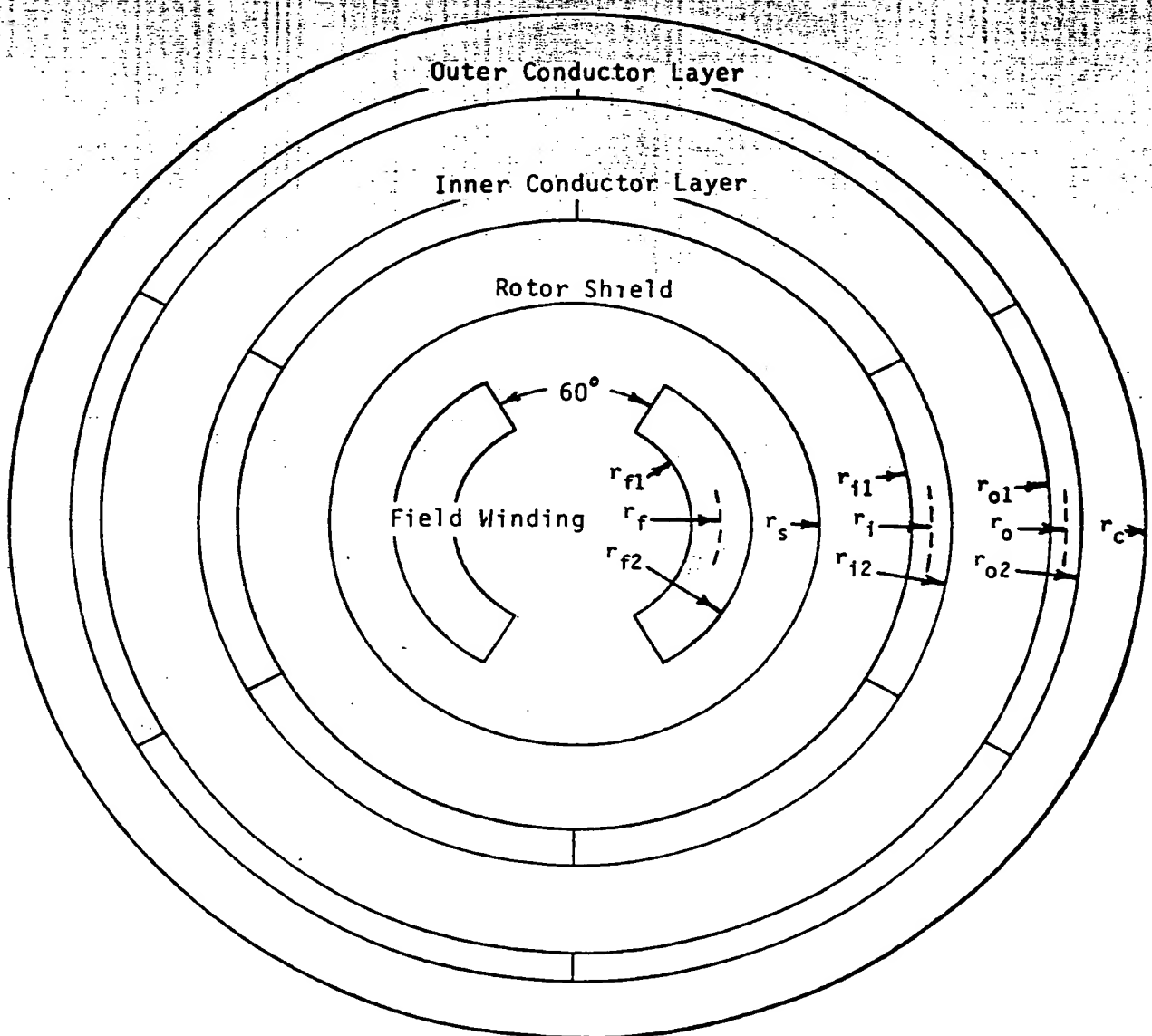


Figure 2.3-1. Cross-Sectional Geometry and Terminology of a Monolith Cylinder Armature and Superconducting Rotor

Table 2.3-1

DIMENSIONS OF THE 600 MVA, 345 kV DIAMOND COIL ARMATURE HIGH-VOLTAGE GENERATOR

J_A	= rms armature current density at rated load = 1.5×10^6 A/m ²
J_F	= field winding current density = 1×10^8 A/m ²
r_{f1}	= field winding inner radius = 9 in., 0.2286 m
r_{f2}	= field winding outer radius = 12 in., 0.3048 m
r_f	= field winding average radius = 10.5 in., 0.2667 m
r_s	= rotor shield outer radius = 17.5 in., 0.4445 m
r_{i1}	= inner radius of inner conductor layer = 23.0 in., 0.5842 m
r_{i2}	= outer radius of inner conductor layer = 26.2 in., 0.6655 m
r_i	= average radius of inner conductor layer = 24.6 in., 0.6248 m
r_{o1}	= inner radius of outer conductor layer = 34.1 in., 0.8661 m
r_{o2}	= outer radius of outer conductor layer = 36.4 in., 0.9246 m
r_o	= average radius of outer conductor layer = 35.3 in., 0.8954 m
r_c	= core inner radius = 40.4 in., 1.0262 m
X_s	= synchronous reactance = 0.33 pu
X''	= subtransient reactance = 0.20 pu

During steady state operation, the armature flux rotates in synchronism with the rotor flux, and the two can be superimposed according to the angular relationship between the two. This angular relationship is easily determined from a phasor diagram of voltages and currents, as illustrated in Figure 2.3-2, and it is seen that the armature flux lags behind the rotor flux by an angle of $90 + \phi + \delta$. Therefore, the superposition of the rotor and armature flux is

$$\begin{aligned} \vec{B} = \vec{a}_r \left[B_{FR} \cos \theta + B_{AR} \cos(\theta + 90 + \phi + \delta) \right] \\ - \vec{a}_\theta \left[B_{F\theta} \sin \theta + B_{A\theta} \sin(\theta + 90 + \phi + \delta) \right] \end{aligned} \quad (2.3-2)$$

The armature and rotor flux distributions are derived from solutions of Laplace's equation in cylindrical geometries. For the armature-produced flux, there are separate expressions for the region inside the inner conductor layer, the region between the two conductor layers, and the region between the outer conductor layer and the core. They are:

$$\begin{aligned} \vec{B}_A = \vec{a}_r \frac{3}{\pi\sqrt{2}} \mu_o J_A \left[(r_{i2} - r_{i1}) \left(\frac{r_c^2 + r_i^2}{r_c^2} \right) + (r_{o2} - r_{o1}) \left(\frac{r_c^2 + r_o^2}{r_c^2} \right) \right] \cos \theta \\ - \vec{a}_\theta \frac{3}{\pi\sqrt{2}} \mu_o J_A \left[(r_{i2} - r_{i1}) \left(\frac{r_c^2 + r_i^2}{r_c^2} \right) + (r_{o2} - r_{o1}) \left(\frac{r_c^2 + r_o^2}{r_c^2} \right) \right] \sin \theta \quad r < r_i \\ = \vec{a}_r \frac{3}{\pi\sqrt{2}} \mu_o J_A \left[(r_{i2} - r_{i1}) \left(\frac{r_i^2}{r_c^2} + \frac{r_i^2}{r^2} \right) + (r_{o2} - r_{o1}) \left(\frac{r_c^2 + r_o^2}{r_c^2} \right) \right] \cos \theta \end{aligned}$$

2.3 WINDING FORCES

In conventional turbine-generator constructions, the load reaction torque and sudden short circuit torques and forces are largely absorbed by the iron teeth of the stator core. The conductors are shielded from the air-gap flux by the iron teeth and experience only a small force due to cross-slot leakage flux. The conductors are firmly anchored in the iron slots by wedging systems that are effective in limiting vibration.

The conductors in a high-voltage monolith cylinder air-gap winding are fully exposed to the air-gap flux and must absorb full load torque and sudden short circuit forces. Severe mechanical duties are imposed on the insulation cylinders, which must be able to transmit the forces from the conductors to the core and frame without excessive vibration or deflections. The mechanical stresses within the armature structure must be within the yield limits of the involved materials, with adequate margin. Of particular importance are shear stresses wanting to delaminate conductor layer to insulation cylinder bonds or the laminations within a laminarily built insulation cylinder.

The winding forces under both load and sudden short circuit conditions are to be calculated for the 600 MVA, 345 kV diamond coil armature. The winding has its straight sections over the entire flux producing length. The force calculations follow closely the technique of Reference 2.3-1, and are later used to calculate mechanical stresses within the armature structure by finite element techniques.

Diamond coils having straight sections over the entire magnetic active length are specified so that a two-dimensional analysis can be performed. The assumptions to the two-dimensional analysis are:

1. The six armature phase-belt currents and the field current are axially directed and are represented by thin sheets of uniform current sheet density.
2. The magnetic field is two-dimensional, having radial and tangential components, and curvature effects are accounted for by solving the field problem in a cylindrical geometry.
3. The iron core is perfectly magnetic and the rotor shield is perfectly conducting (in transients).
4. Only the fundamental harmonic components of the magnetic field are used for computing the forces.
5. End effects are neglected.

The sample generator for which the forces are to be calculated is the 600 MVA, 345 kV diamond coil armature machine produced by the sizing studies of Section 2.2. The dimensions and parameters of the generator are listed in Table 2.3-1, and Figure 2.3-1 illustrates the terminology.

The winding pressure is calculated from the Lorenz force expression

$$\begin{aligned}\bar{P} &= \bar{J} \times \bar{B} \\ &= -\bar{a}_r J_z B_\theta + \bar{a}_\theta J_z B_r \quad \text{N/m}^2,\end{aligned}\tag{2.3-1}$$

where J_z = axially directed current sheet density, A/m

B_r = total radial flux density, teslas

B_θ = total peripheral flux density, teslas

The armature windings are modeled as current sheets lying at the average radius of each conductor layer, and sheet current densities are obtained from volumetric current densities by multiplying by the thickness of the conductor layer. Since the tangential flux density is discontinuous across a current sheet, the average value of the tangential flux densities on both sides of the current sheet is used in Equation 2.3-1.

Tab. 1

BEST HIGH-VOLTAGE GENERATORS HELICAL COILS 300 A/cm ² CURRENT DENSITY	THE 600 MVA RATING IGS INSULATION STRESS
--	--

kV	<u>R₁</u>	<u>R₂</u>	<u>R₃</u>	<u>R₄</u>	<u>R₅</u>	<u>R₆</u>	<u>R₇</u>	<u>R₁₀</u>	<u>R₁₁</u>	<u>L</u>	<u>X''</u>	<u>X'</u>	<u>X</u>
345	9	12	14.5	16.5	18	22.0	24.3	37.9	55.6	173	.239	.272	.301
500	9	12	14.5	16.5	18	23.8	25.7	44.3	59.5	217	.244	.271	.295

References

- 2.2-1. J.L. Kirtley, "Basic Formulas for Air-Cooled Synchronous Machines," Paper 71CP155-PWR, IEEE Power Engineering Society Winter Meeting, January 1971.
- 2.2-2. T.A. Keim, "Fractional Pitch Coils in Synchronous Machines," Paper A 800 47-1, IEEE Power Engineering Society Winter Meeting, January 1980.
- 2.2-3. A.F. Anderson, et al., "Analysis of Helical Winding Winding with Particular Reference to Superconducting A.C. Generators," IEEE Transactions 127, Pt. C., 3, pp. 129-144.
- 2.2-4. S.D. Umans, et al., "Three-Dimensional Analysis of Superconducting Generators," IEEE Transactions on Power Apparatus and Systems PAS-98, 6, pp. 2055-2063.

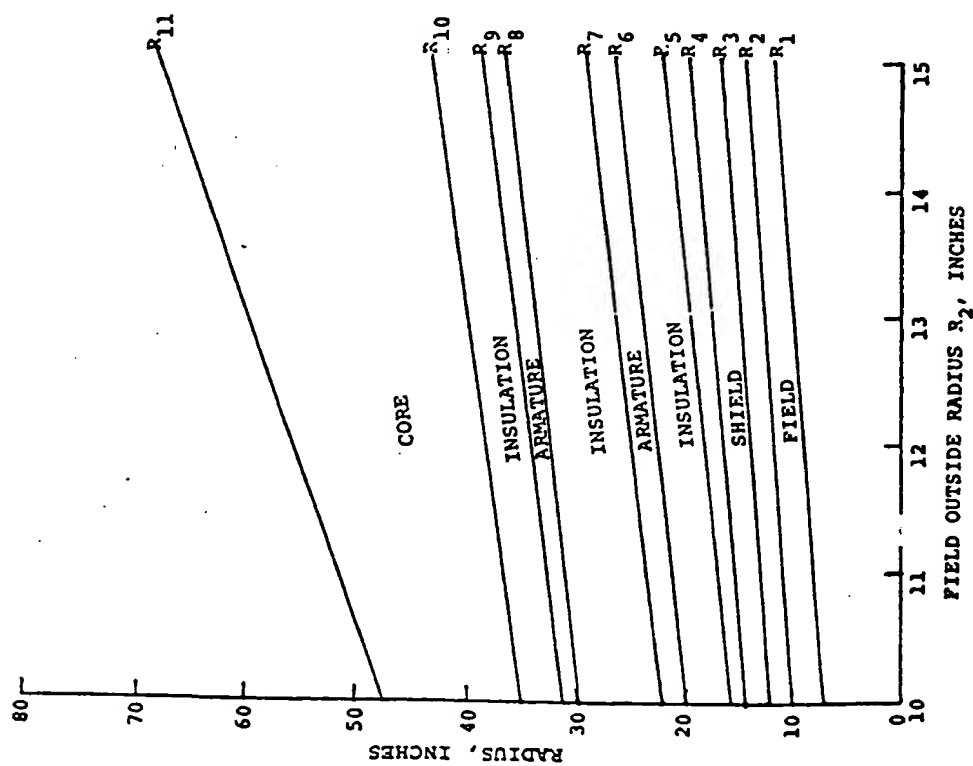


Figure 2.2-5. Radial Dimensions for the 600 MVA, 345 kV High-Voltage Generator with Helical Coil Windings

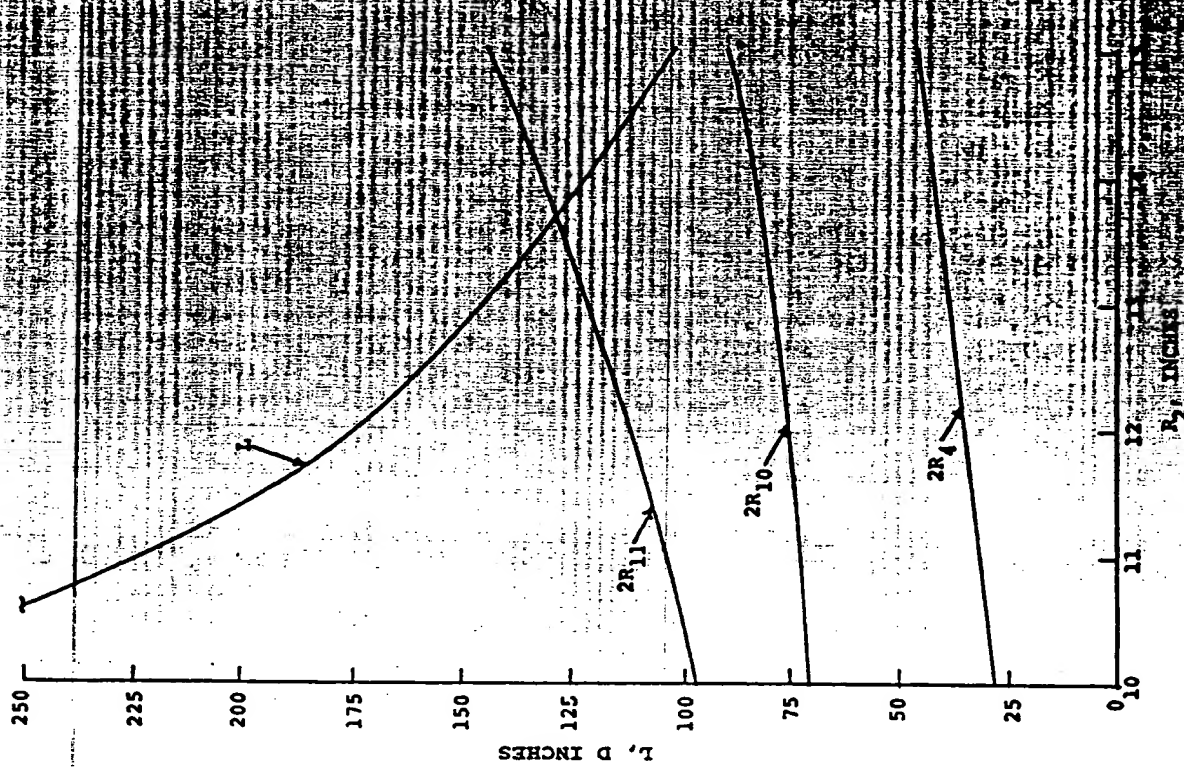


Figure 2.2-6. Length at Diameter for the 600 MVA, 345 kV High-Voltage Generator with Helical Coil Windings

This problem was addressed in a paper by Umans, et al. (Ref. 2.2-4) in developing a three-dimensional machine model. Without resorting to the complexity of their model, the following scheme was used. In the calculation of the self-inductances of the field winding and the shielding system, the straight winding calculations were retained. The self-inductance of the armature winding was calculated using the helical winding representation; the thickness of the winding was represented by a weighted sum of current sheet representations, since finite-thickness helical winding formulae are intractable. The mutual coupling of the field winding to the shielding system was computed by using the straight winding inductance formulae. The coupling of the field winding and shield to the armature is most readily accomplished by representing them all as helical windings. These two straight windings are represented as a number of layers of coincident counter-spiralling helical windings for the purpose of the calculation. In order to account for the fact that the straight windings produce an axially distributed radial flux pattern (square wave) which is different from that produced by the helical winding (a half sinusoid), the results are multiplied by the corrective factor $4/\pi$. This factor was chosen since the fundamental component of a square wave has an amplitude $4/\pi$ times as large as the square wave amplitude. No corrections for the end-turn effects are made in any of the helical winding formulae, as there is not enough experience with these windings to justify a correction. It has been assumed that the iron core covers the entire length of the helical winding.

The specified armature current density for the helical coil armature sizing studies will be the current density in direction of the conductor helices. The numerical value of this current density can be specified to greater values than were indicated for the diamond coil armature sizing studies. The geometry of the diamond coil requires that spaces appear between peripherally adjacent coils in the straight sections, even when the end arms are packed tightly (see Appendix B). Helical coils can be packed tightly throughout their entire length, so there are no spaces to detract from the applied current density.

Machine sizing investigations for the helical coil armature machines showed a general trend that helical coil armature machines have approximately the same radial dimensions as the diamond coil armature machines but have longer armature lengths than the diamond coil armature machines. This result is in accord with the magnetic coupling behavior of the helical winding. These trends are noted in Figures 2.2-5 and 2.2-6, which are similar to Figures 2.2-1 and 2.2-2 of the diamond coil armature sizing studies.

Best designs for the 600 MVA helical coil armature machine at two different voltage ratings are shown in Table 2.2-4. These can be compared to the 600 MVA entries in Table 2.2-2 for the diamond coil armature machines. Again, it can be seen that the helical coil armatures are longer than the diamond coil armatures, while the radii are about the same.

In comparing the helical coil armatures to the diamond coil armatures, one must qualify the active lengths which are specified. For the helical coil armature, the active length is the full helix length, while for the diamond coil armature, the active length is the length of the coil straight sections. The diamond coil winding has end arms of considerable length (on the order of the outer conductor layer diameter), while the helical coil armature has only the additional end length of the series loops connections. Further, it is possible to reduce the straight length of the field winding in the helical coil armature design without changing the overall machine performance or dimensions significantly; this is due to the small coupling near the winding ends. A suitably modified version of the sizing program showed that it is possible to reduce the field winding straight length by a distance equal to the outer diameter of the field winding without any significant damage to machine specifications. Thus, the helical coil winding begins to look more favorable than the diamond coil winding when viewed in terms of overall machine size.

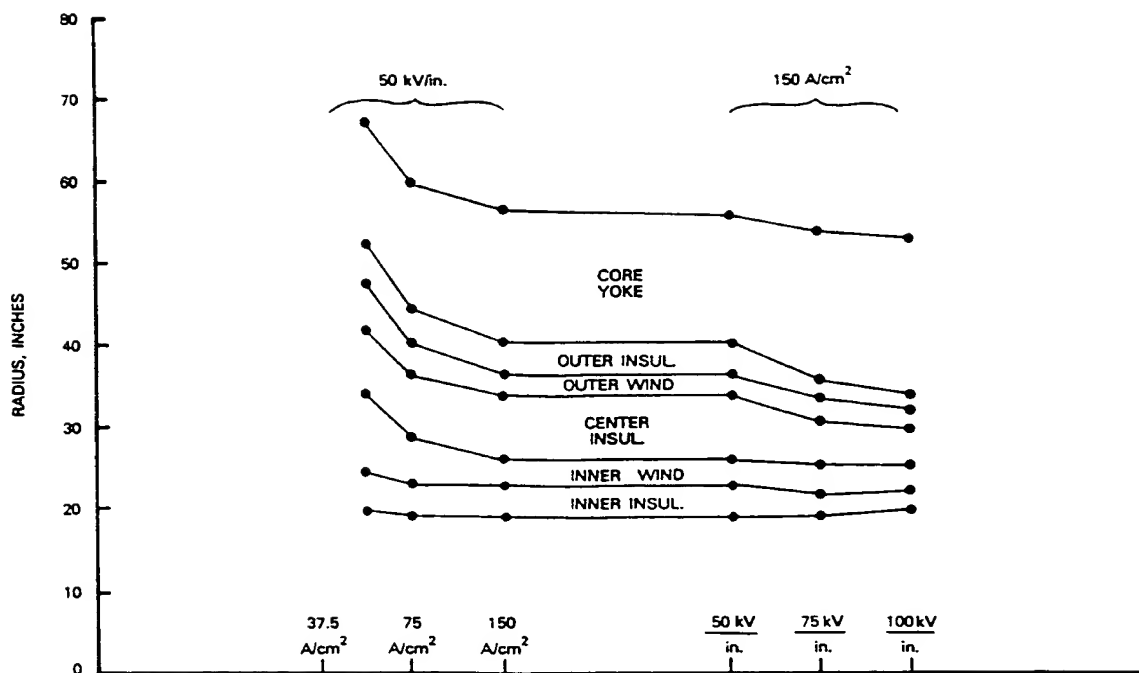


Figure 2.2-4. The Effect of Varying Armature Current Density and Insulation Dielectric Stress in the 600 MVA, 345 kV High-Voltage Generator

The results for increasing insulation dielectric stress show an interesting effect. The increase from 50 to 75 kV/in. shows a significant reduction in machine volume; a further increase from 75 to 100 kV/in. shows a much smaller reduction. Some part of this effect may be due to the fact that the insulation thickness, which is a variable which directly influences machine size, is the inverse of the dielectric strength (i.e., the first increment represents a 33% reduction in insulation thickness, but the second represents only a further 25% reduction). A further part of the observed effect is due to the discrete step sizes incorporated in the program. In going from the 75 kV/in. to the 100 kV/in. dielectric stress, the armature inside radius R_5 increases an entire inch. The increase is necessary because the smaller machine would have unacceptable shield stresses. This increase affects all the dimensions outside R_5 . If the program incremented dimensions in smaller steps, more change would be observed between the 75 kV/in. and 100 kV/in. cases. Finally, part of the effect observed represents the fundamental non-linearity of the problem. Even at zero insulation thickness, a finite machine volume is required. The effect of insulation thickness on machine design should not be significant until insulation volume becomes significant with respect to that of other components.

2.2.2 Sizing Studies for Helical Coil Armatures

The helical coil armature produces a magnetic field which is inherently three dimensional, unlike the conventional diamond coil armature. For the purpose of calculating the magnetic fields and the associated inductances, an armature model based upon an infinitely long helical structure can be used with acceptable accuracy, as indicated by References 2.2-2 and 2.2-3. This model was adapted to the sizing study computer program to allow comparative studies of the helical coil armature designs.

The computer model of the helical coil armature presented a number of difficulties in the calculation of machine reactances. The major difficulty arises in the calculation of the coupling of the field and shielding system to the armature, since the field and solid shield are modeled as *straight* windings of infinite length. It was unclear, at first, how a consistent marriage of the two approaches could be achieved.

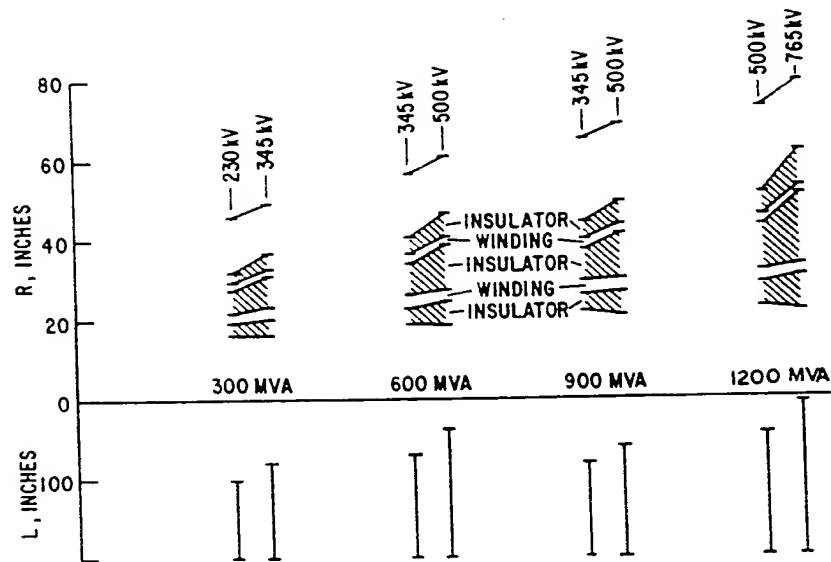


Figure 2.2-3. High-Voltage Generators of Varying Ratings

Table 2.2-3 and Figure 2.2-4 present the results of varying the armature current density and insulation dielectric stress in the 600 MVA, 345 kV rating. Each case represents a machine selected from a table of possibilities in the partially subjective manner described earlier. The effect of reduced current density is a substantial increase in machine volume. The radius increases for the lowest current density design are somewhat larger than might be expected if all variables were changed smoothly, rather than in steps, because a field winding radius one full inch larger was selected for this design. The length for this case is correspondingly lower. Note that the current density was changed in a geometric, rather than arithmetic, progression.

Table 2.2-3

**600 MVA, 345 kV HIGH-VOLTAGE GENERATORS
DIAMOND COIL WINDINGS
ARMATURE CURRENT DENSITY AND INSULATION DIELECTRIC STRESS VARIED**

$J_a, a/cm^2$	$W, kV/in.$	R_1	R_2	R_3	R_4	R_5	R_6	R_7	R_8	R_9	R_{10}	R_{11}	L	X''	X'	X
37.5	50	10	13	15.5	18.5	20	24.0	34.1	42.1	48.6	52.6	67.8	146	.22	.27	.31
75	50	9	12	14.5	17.5	19	23.0	28.7	36.6	40.4	44.4	59.4	153	.21	.27	.32
150	50	9	12	14.5	17.5	19	23.0	26.2	34.1	36.4	40.4	56.7	131	.20	.27	.33
150	75	9	12	14.5	17.5	19	21.7	25.3	30.6	33.2	35.9	54.2	108	.20	.27	.34
150	100	9	12	14.5	17.5	20	22.0	25.5	29.5	32.2	34.2	53.4	104	.19	.27	.34

Note: Headings $R_1 - X$ are identical to those listed in Table 2.2-1

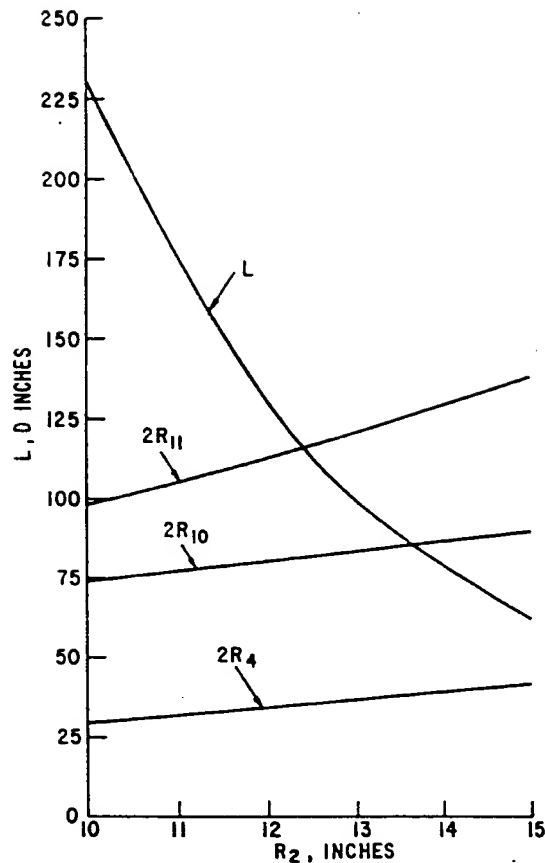


Figure 2.2-2. Length at Diameter for the 600 MVA, 345 kV High-Voltage Generator with Diamond Coil Windings

Table 2.2-2 and Figure 2.2-3 summarize these designs. No surprising trends are revealed. The outside radius of the 1200 MVA, 765 kV design exceeds even the generous self-imposed limit discussed above, but a machine with a one inch smaller field winding is excessively long. Significantly higher ratings may require higher dielectric working stresses, special assembly or shipping methods, relaxed reactance requirement, or some other means of extending the art.

Table 2.2-2

**BEST HIGH-VOLTAGE GENERATORS OF EACH RATING
DIAMOND COIL WINDINGS
150 A/cm² CURRENT DENSITY, 50 kV/in. INSULATION STRESS**

MVA	KV	R ₁	R ₂	R ₃	R ₄	R ₅	R ₆	R ₇	R ₈	R ₉	R ₁₀	R ₁₁	L	X''	X'	X
300	230	7	10	12.5	14.5	16	18.7	21.8	27.1	29.3	31.9	45.5	99	.20	.27	.33
300	345	7	10	12.5	14.5	16	20.0	22.7	30.7	32.5	36.5	48.4	120	.21	.27	.32
600	345	9	12	14.5	17.5	19	23.0	26.2	34.1	36.4	40.4	56.7	131	.20	.27	.33
600	500	9	12	14.5	16.5	19	24.8	27.5	39.1	40.9	46.7	60.9	162	.22	.27	.32
900	345	11	14	16.5	20.5	22	26.0	29.5	37.5	40.0	44.0	65.2	119	.20	.27	.34
900	500	11	14	16.5	19.5	21	26.8	30.0	41.6	43.8	49.5	68.4	140	.22	.27	.33
1200	500	12	15	17.5	21.5	23	28.8	32.1	43.7	46.0	51.7	72.8	154	.21	.27	.33
1200	765	12	15	17.5	20.5	22	30.8	33.7	51.4	53.2	62.0	79.7	194	.23	.27	.32

Note: Headings R₁ - X are identical to those listed in Table 2.2-1.

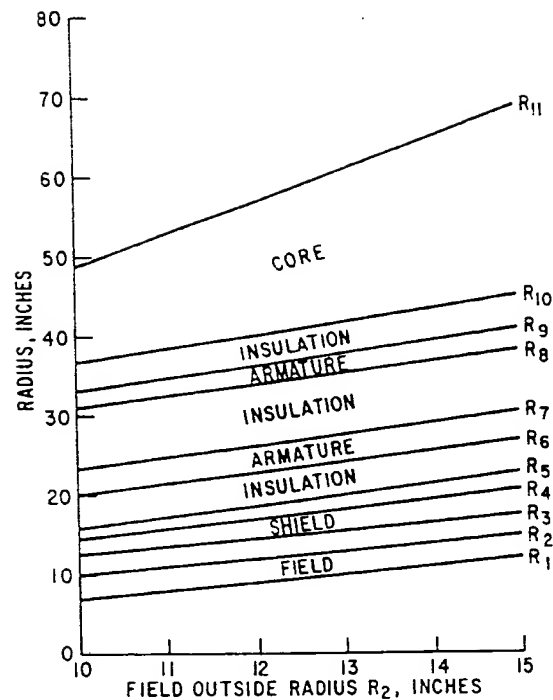


Figure 2.2-1. Radial Dimensions for the 600 MVA, 345kV High-Voltage Generator with Diamond Coil Windings

Figure 2.2-2 shows the variation of active length as a function of R_2 . To provide insight into the changing proportions, several significant *diameters* are plotted on the same scale. The rotor outside diameter is $2R_4$. It can be seen that the rotor ranges from very long and thin (perhaps too long and thin for acceptable rotor dynamics) to very short and squat. The core outside diameter is $2R_{11}$. The overall machine is seen to have a length-to-diameter ratio of less than one for large values of R_2 .

The core inside diameter is $2R_{10}$. The relation of this number to the length of the machine is significant in determining the validity of assumptions underlying the electromagnetic analysis. The model assumes $R_{10}/L \ll 1$. As this ratio approaches 1, the accuracy of the basic formulation diminishes. For the case represented in Figure 2.2-2, results for values of R_2 greater than 12 in. are suspect. These comments do not imply that short, squat machines are or are not unattractive designs. However, the existing methodology cannot make a reliable assessment. Analytical representation of three-dimensional magnetic fields is required to permit the true merits of these designs to be assessed.

Table 2.2-1 shows that when machines of different radius R_2 are held to constant transient reactance; the other reactances do not vary much with R_2 . This observation holds for the whole range of ratings, although the values which the subtransient and synchronous reactances assume do vary from case to case.

For each voltage and power rating, one "best" machine has been selected from a table like Table 2.2-1. The selection is to some extent subjective. Long, low-diameter rotors have been avoided. Core outside diameters have been kept within reason by imposing an arbitrary cutoff of 156 in. A stator this large is at the limits of that which can be shipped by railway; a smaller limit may be more appropriate. The ratio of core inside diameter to length has also been considered. The designs selected are from the upper end of the range over which the two-dimensional analysis is thought to be applicable.

Table 2.2-1 is a sizing study for the 600 MVA, 345 kV rating and is typical of tables prepared for each combination of rating and voltage. The independent variable in this case is the field winding outside radius R_2 . Field winding thickness, field-winding-to-shield spacing, shield-to-armature spacing, and the thicknesses of the insulation cylinders are all fixed for all machines in the table. The table entries are the dimensions of the shortest machines having acceptable shield stresses. (They are also the machines with the smallest armature inside radius and acceptable shield stresses.) Figure 2.2-1 presents the same information as Table 2.2-1 with smooth lines drawn between the points.

Table 2.2-1
HIGH-VOLTAGE GENERATORS AT 600 MVA, 345 kV
DIAMOND COIL WINDINGS
150 A/cm² CURRENT DENSITY, 50 kV/in. INSULATION STRESS

R_1	R_2	R_3	R_4	R_5	R_6	R_7	R_8	R_9	R_{10}	R_{11}	L	X''	X'	X
7	10	12.5	14.5	16	20	23.0	30.9	32.9	36.9	48.7	232	.20	.27	.33
8	11	13.5	16.5	18	22	25.0	33.0	35.0	39.0	52.9	177	.20	.27	.33
9	12	14.5	17.5	19	23	26.2	34.1	36.4	40.4	56.7	131	.20	.27	.33
10	13	15.5	18.5	20	24	27.3	35.3	37.7	41.6	60.6	99	.21	.27	.33
11	14	16.5	19.5	22	26	29.2	37.2	39.5	43.5	65.0	80	.22	.27	.33
12	15	17.5	21.5	23	27	30.3	38.3	40.7	44.7	69.0	62	.21	.27	.33

R_1 - field winding inside radius, in.	R_7 - inner conductor layer outside radius, in.
R_2 - field winding outside radius, in.	R_8 - outer conductor layer inside radius, in.
R_3 - shield inside radius, in.	R_9 - outer conductor layer outside radius, in.
R_4 - shield outside radius, in.	R_{10} - core inside radius, in.
R_5 - armature inside radius, in.	R_{11} - core outside radius, in.
R_6 - inner conductor layer inside radius, in.	L - Length, in.
	X'' - subtransient reactance, p.u.
	X' - transient reactance, p.u.
	X - synchronous reactance, p.u.

The required shield thickness increases substantially as R_2 increases, ranging from 2 to 4 in. in the example shown. This increase is typical. It should be noted that the program steps dimensions in one-inch increments. As a result, the most precise statement that can be made is that shield thickness varies from between 1 and 2 in. for small R_2 to between 3 and 4 in. for larger R_2 . The minimum shield thickness requirement for any R_2 is substantially less than for low-voltage superconducting generators, so some of the shield forging availability problems anticipated for those machines may be alleviated. The reduced shield thickness requirement is in part due to larger reactances than those proposed for low-voltage machines and in part due to decreased magnetic coupling owed to the large insulation volume.

Surprisingly, armature thickness varies only slightly over the range of R_2 , and Figure 2.2-1 shows many essentially parallel lines. The greatest trend observable in Figure 2.2-1 is in the core outside radius R_{11} . This radius increases substantially faster than its inside radius R_{10} . Core thickness is calculated by determining the total flux incident on the core and then providing a sufficient thickness for the same flux to flow in the core without exceeding 1.5 tesla flux density in the core. The core thickness varies from 28% to 42% of mean radius in Table 2.2-1, implying a substantial variation in core ring-mode stiffness. If the ring-mode stiffnesses are inadequate, thicker cores than those described here may be required.

The program accommodates shield design indirectly. The shield inside radius is determined by adding to the field winding outside radius a small allowance for a radiation shield and torque tube. The armature inside radius is stepped through a range of values. The appropriate winding thicknesses and machine length are determined for each armature inside radius. For each armature inside radius, the shield thickness is stepped through a range of values limited by the armature inside radius. For each shield thickness, the peak stress under short circuit conditions is computed by combining magnetic and centrifugal loads. The results are printed. Selection of a design with satisfactory shield stresses is performed by hand.

Any or all of the parameters described above can be varied systematically to determine the impact on overall machine size and configuration.

To keep the volume of work manageable, it is wise to concentrate on the effect of certain variables, holding others constant at representative values. Terminal voltage, insulation dielectric stress, and output MVA rating are of special interest to this study. Therefore, these factors will be independent variables in this study.

In many parametric studies, including this one, the relation between length and diameter is of interest. Length is a dependent variable in this formulation, so field winding diameter is used as an independent variable.

Field winding parameters other than diameter have not been varied. A well-designed superconducting coil, in the size ranges to be considered, will conservatively operate at an overall current density of about $10,000 \text{ A/cm}^2$ in ambient magnetic fields of 6 to 7 tesla. An annular field winding, according to the equations used, will generate a maximum flux density of about 6.5 tesla in the winding if its thickness is about 3 in. Although field winding current density and winding thickness could have been traded against one another at constant field, or at constant short sample margin, the effect of such trade-offs is not expected to be materially different for high-voltage superconducting generators than from that for other superconducting generators.

For similar reasons, the clearance between the field winding and the electromagnetic shield inside surface was not varied. A 2 1/2-in. total was allowed for the coil housings and plates, the torque tube, and the radiation shield.

For most work, the current density over the annular regions devoted to the conductor layers has been maintained at the value of 150 A/cm^2 , which has proved appropriate in previous work with low-voltage superconducting generators. However, a brief look at the effect of this parameter was performed, in recognition of the possibility of a low packing factor in high-voltage windings.

Transient reactance is a parameter with a significant effect on machine size (lower reactances produce larger machines). However, the benefits of reduced reactance accrue not to the design of the generator but to the power system as a whole. To completely evaluate this effect would require analysis beyond the scope of this program. These parametric studies have been performed for transient reactance $X_d' = 0.27$.

Both the stress occurring in the electromagnetic shield following sudden short circuit and the maximum value of that stress depend on the material of the shield. This study assumes a shield material with a density of 0.29 lb/in.^3 , a modulus of $30 \times 10^6 \text{ psi}$, and an allowable stress of 120,000 psi. These values are typical of several iron- or nickel-base high-strength alloys.

The principal results of this study are basic dimensions for machines of the following ratings: 300 MVA, 230 and 345 kV; 600 MVA, 345 and 500 kV; 900 MVA, 345 and 500 kV; and 1200 MVA, 500 and 750 kV, all at 0.9 power factor. These results are obtained for an insulation stress of 50 kV/in. The effect of varying the armature current density and insulation stress have been investigated for the 600 MVA, 345 kV rating.

2.2 SIZING STUDIES

2.2.1 Sizing Studies for Diamond Coil Armatures

Calculations of machine dimensions and parameters were performed for machines having diamond coil windings with the straight sections extending over the field winding active length. The basic equations used in calculating the machine parameters for diamond coil windings are those reported in Reference 2.2-1. These equations have been in common use for some time, and have been derived from two-dimensional polar coordinate solutions of the magnetic field equations. Corrections for end winding effects are made in the form of additive corrections to the inductances. The equations model the machine in terms of annular regions of field winding and armature winding to which an overall current density is assigned. The equations have explicit provisions for an annular space between the armature winding and core, and between the armature winding and rotor. Space between layers of the armature winding can be incorporated by modeling the armature winding as two concentric single-layer armature windings connected in series. Reference 2.2-2 presents equations with sufficient generality to do this.

The results which are reported here have been obtained from a computer program containing such a model. The program computes dimensions for a family of machines of a given power rating and transient reactance.

Power rating and transient reactance are parameters of prime importance to this program formulation because the program iterates armature thickness and machine length to achieve the required reactance and rating. To find the appropriate armature thickness and length, many other parameters besides rating and length must of course be specified. These parameters include field winding radius, thickness, and current density, inner conductor layer inside radius, outer conductor layer inside radius, conductor layer current density and iron core inside radius. The program requires explicit selection of the field winding parameters and a radius for the inner surface of the innermost insulation cylinder. In addition, a voltage rating and insulation dielectric stress must be specified. The program then determines the required insulation cylinder thicknesses and spaces the conductor layers and the core inside radius appropriately. The thicknesses of the conductor layers are not equal, but both layers are assumed to operate at the same current density, so there is only one independent conductor layer thickness variable.

For a given set of these parameters, the program first iterates the length to achieve the required output, and then adjusts armature thickness, etc., in the direction required to obtain the required transient reactance. The entire process is repeated until a length and armature thickness which result in both required rating and reactance are determined.

Nothing in the foregoing has discussed space requirements for rotor shielding. The space required for rotor shielding is an important part of the spacing between field and armature windings, but once that spacing has been determined, rating and transient reactance for the geometry can be determined without further reference to rotor shielding.

The outer electromagnetic shield is the largest member of the rotor shielding system. The principal requirement on this member is that it be strong enough to survive the combination of centrifugal and magnetic loads imposed on sudden short circuit. The magnitude of the sudden short circuit load is determined by the design of the other components of the generator. From considerations of rating and reactance alone, the closest possible field-to-armature spacing results in the most compact design, but very thin shields do not have the strength to withstand the high crushing loads when the armature experiences a sudden short circuit.

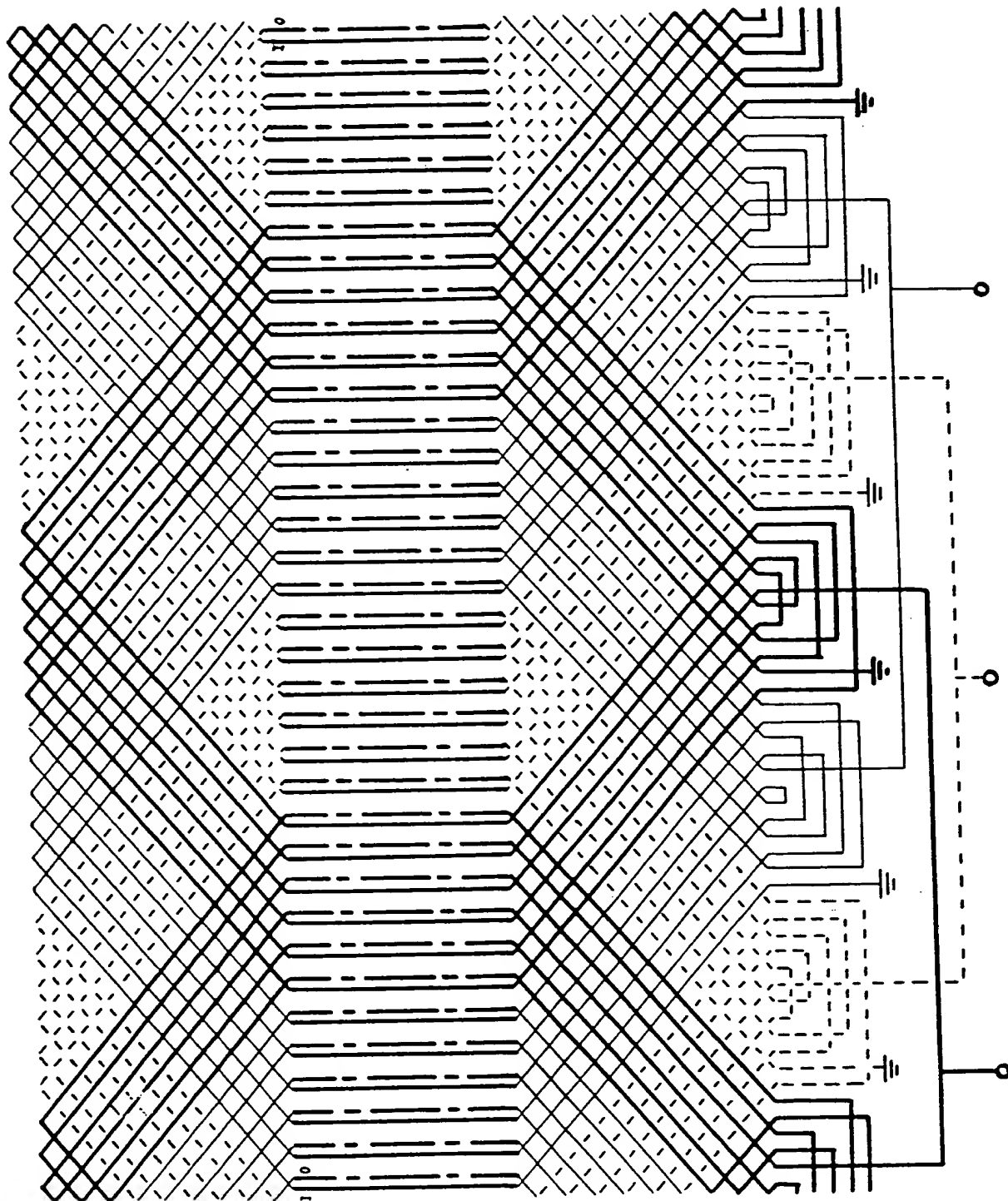


Figure 2.1-18. Winding Diagram of the 60° Phase-Belt Two-Circuit Graded-Wye Winding

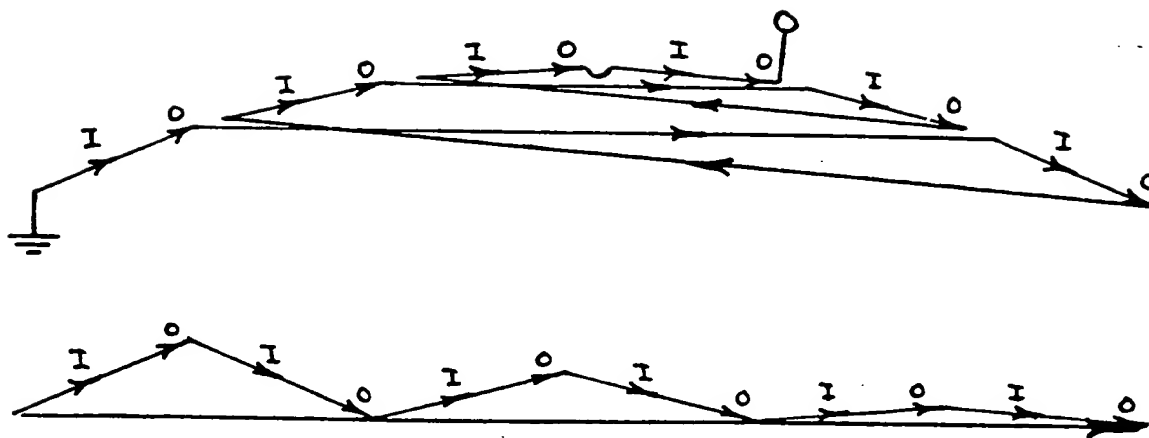


Figure 2.1-17. Circle Phasor Diagram of the 60° Phase-Belt Two-Circuit Graded-Wye Winding

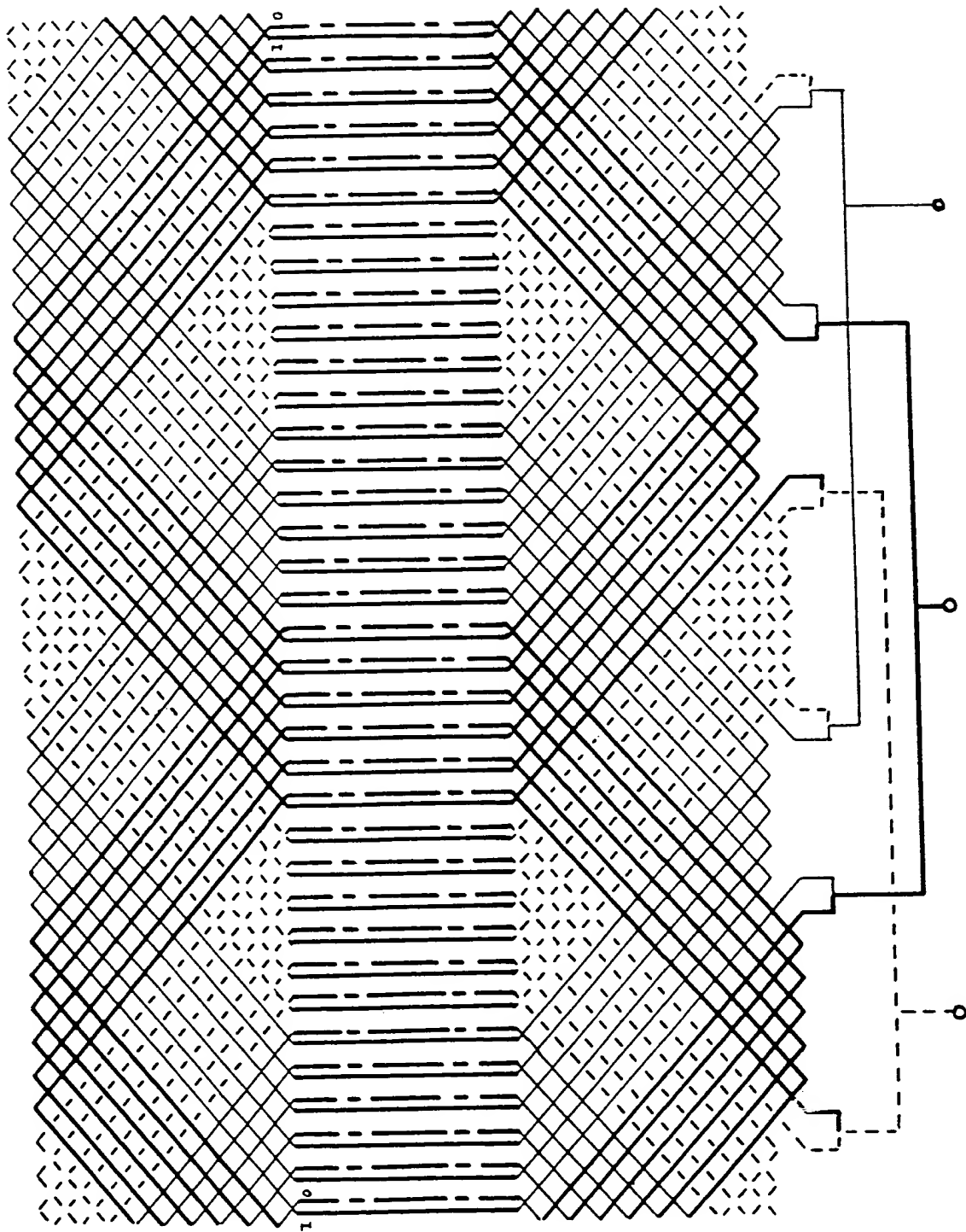


Figure 2.1-16. Winding Diagram of the 60° Phase-Belt Two-Circuit Delta-Connected Winding

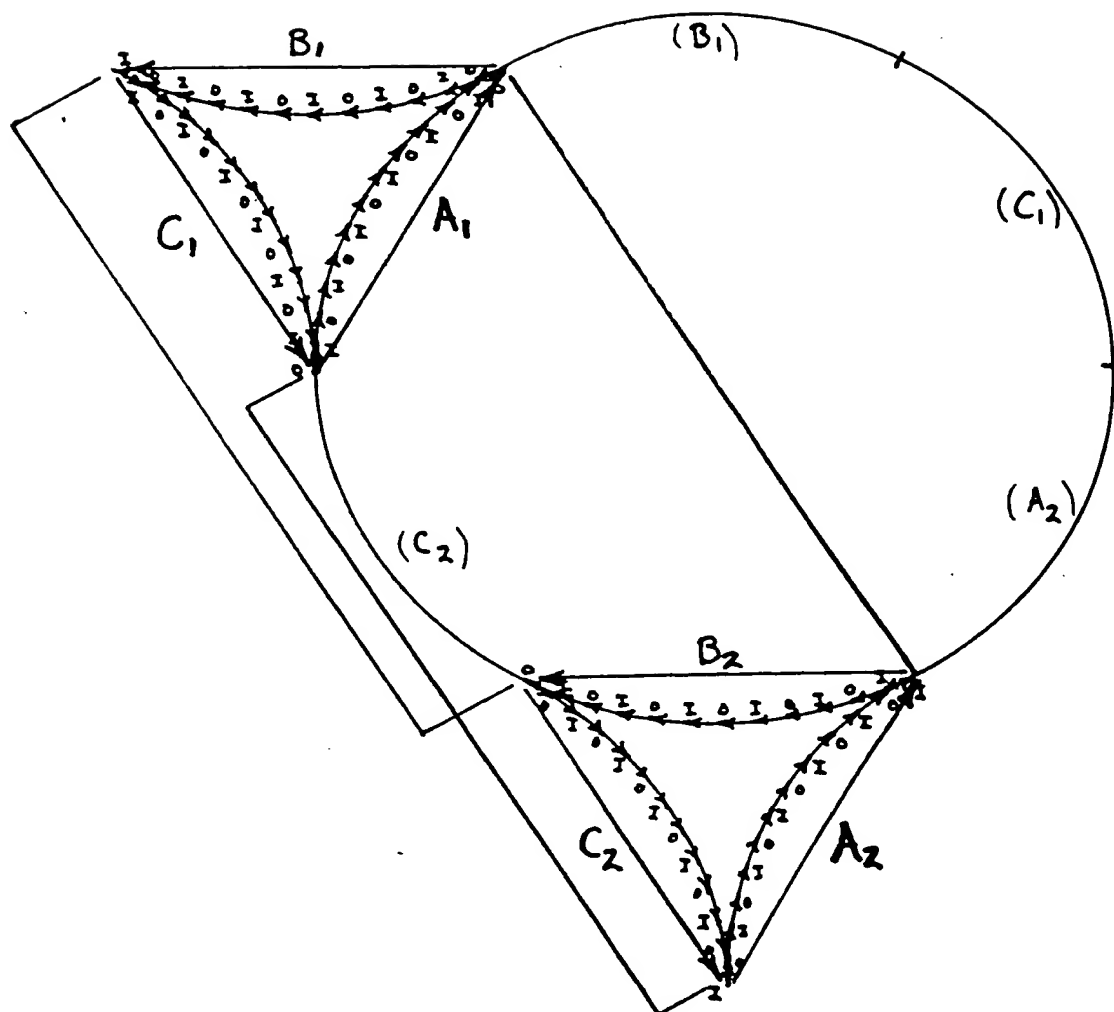


Figure 2.1-15. Circle Phasor Diagram of the 60° Phase-Belt Two-Circuit Delta-Connected Winding

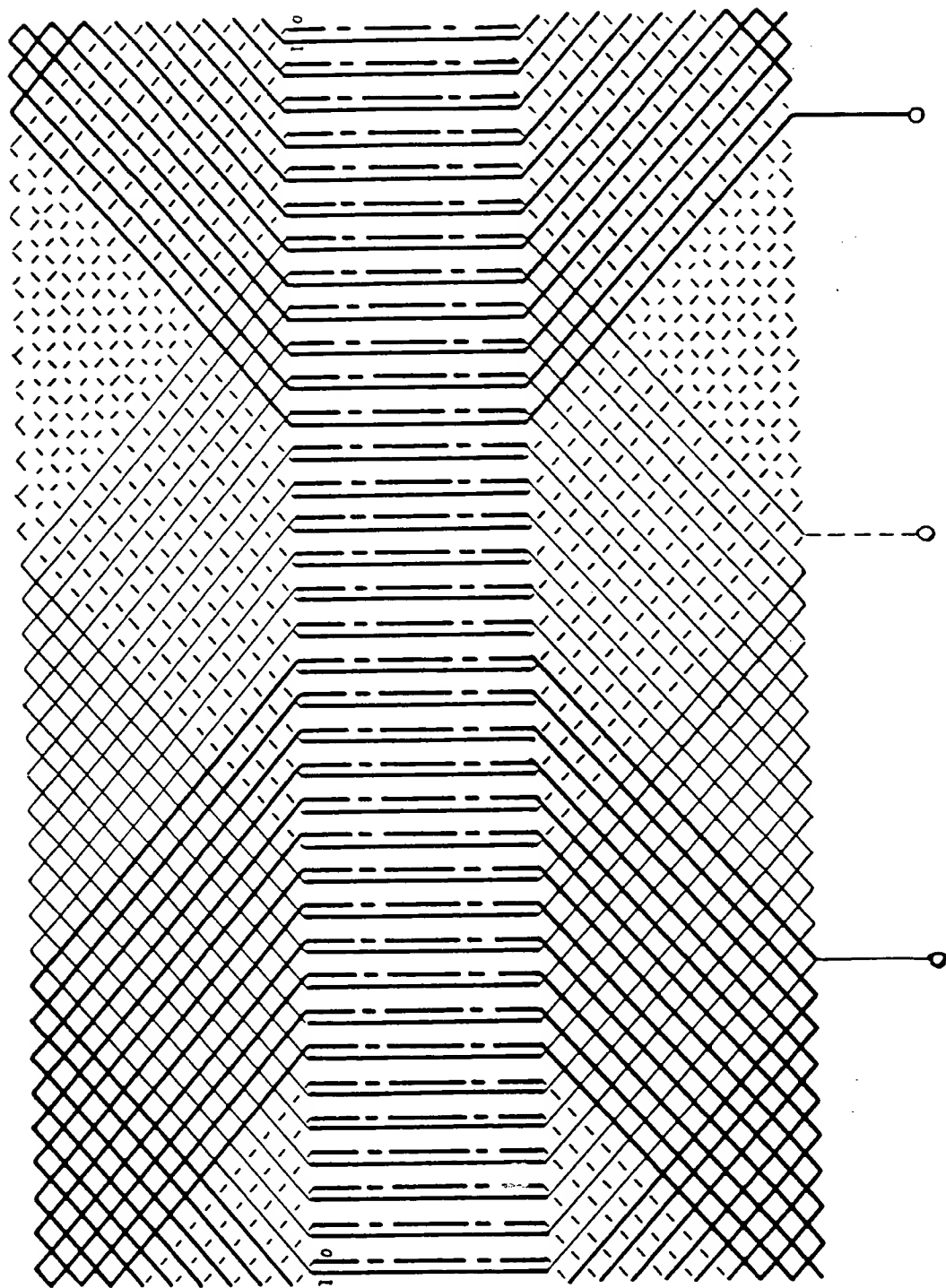


Figure 2.1-14. Winding Diagram of the 120° Phase-Belt Single-Circuit Delta-Connected Winding

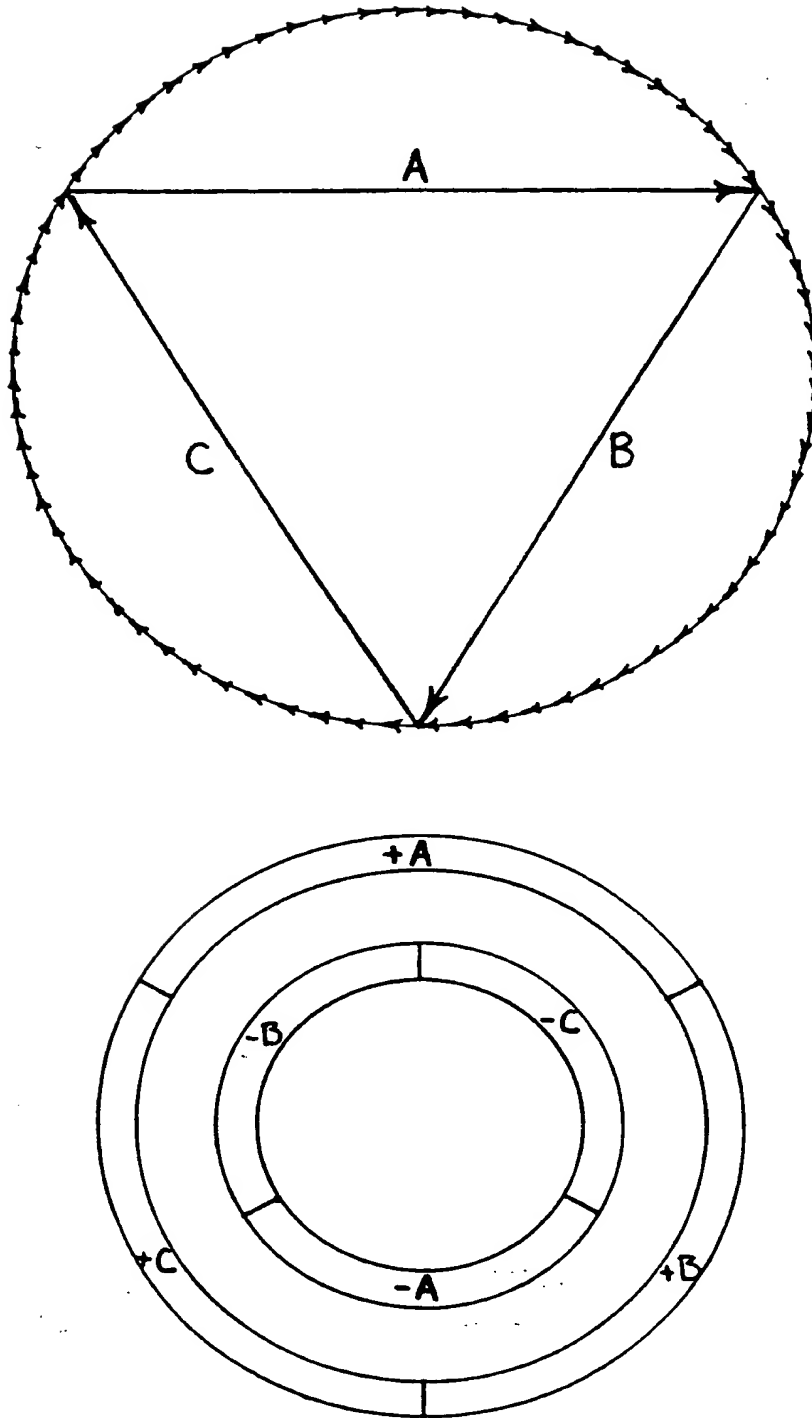


Figure 2.1-13. Circle Phasor Diagram of the 120° Phase-Belt Single-Circuit Delta-Connected Winding

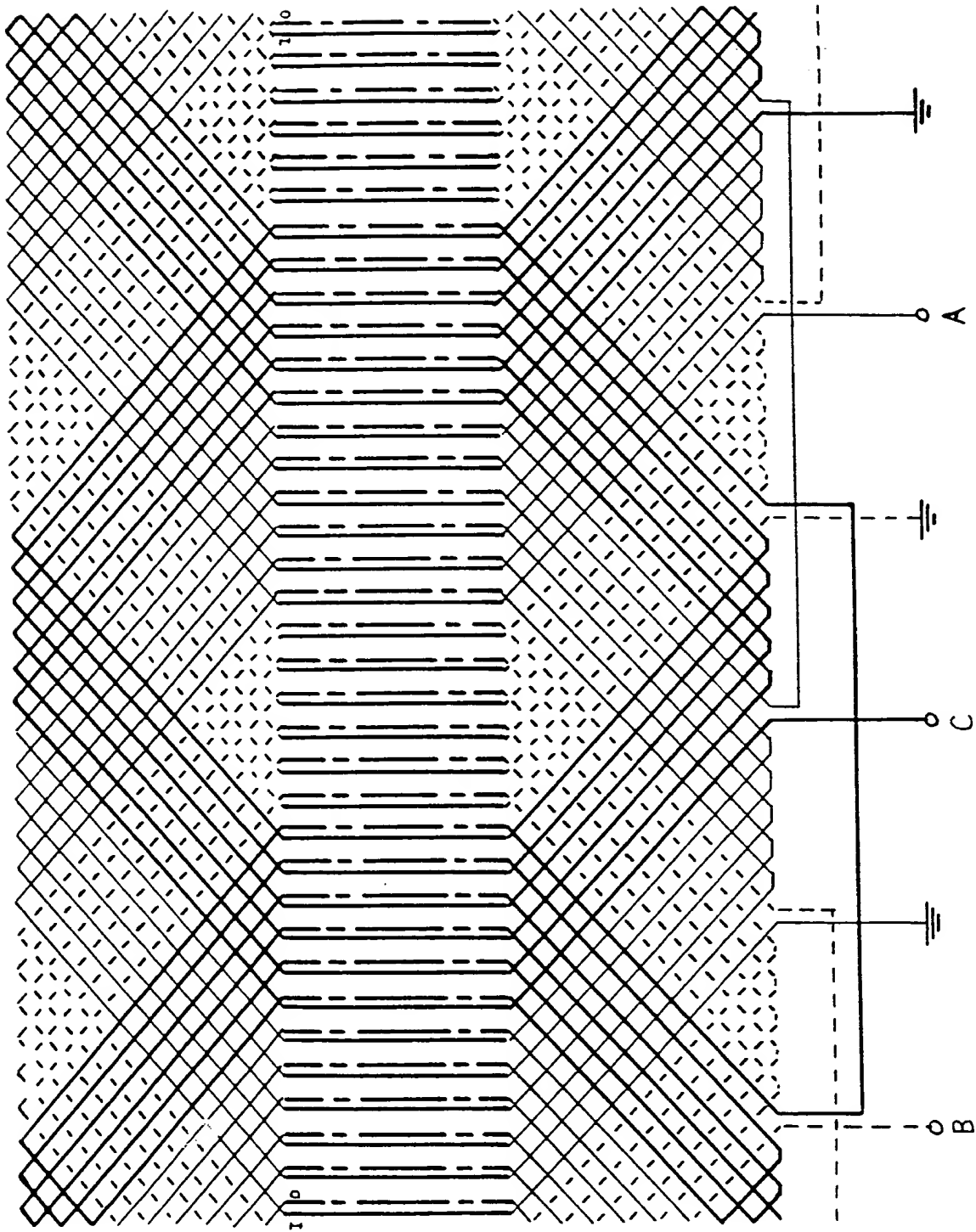


Figure 2.1-12. Winding Diagram of the Classical 60° Phase-Belt Single-Circuit Wye-Connected Winding

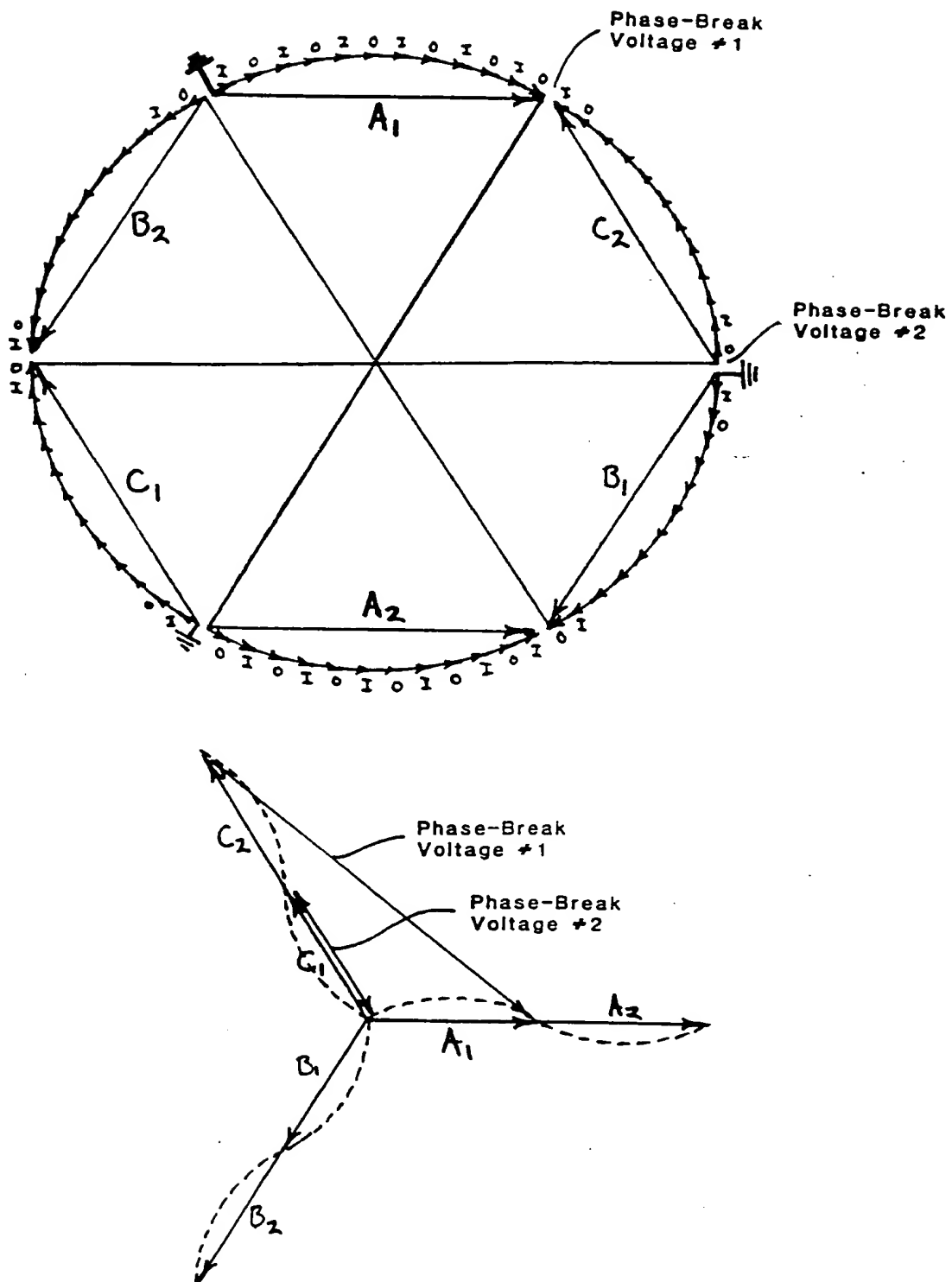


Figure 2.1-11. Circle Phasor Diagram of the Classical 60° Phase-Belt Single-Circuit Wye-Connected Winding

many turns as the high-voltage winding, the coil jumper system is certain to be cumbersome. The phase-belt creepage stress is the highest yet encountered:

$$E_{pb} = \frac{V_{l-g}}{\frac{\pi}{6}r} = 1.910 \frac{V_{l-g}}{r} \quad (2.1-4)$$

This winding arrangement can also be performed with 120° phase belts, although such a winding will produce the same rotor vibratory forces that the 120° phase-belt delta winding produces.

The preferred winding arrangement for the monolith cylinder high-voltage armature is the 60° phase-belt two-circuit delta connection, from considerations of electrical configuration, magnetic symmetry, and practicability of manufacture.

References

- 2.1-1. J.S. Ross, A.F. Anderson, and R.B. Macnab, *Alternating Current Dynamo-Electric Machine Windings*, British Patent #1395152, May 1975.
- 2.1-2. P.L. Conley, J.L. Kirtley, W.H. Hagman, A.H. Ula, "Demonstration of a Helical Armature for a Superconducting Generator," *IEEE Transactions on Power Apparatus and Systems*, PAS-99, 4, pp. 1642-1649.
- 2.1-3. H.P. Moser, *Transformerboard*, an engineering information publication of EHV Weidmann, Inc., St. Johnsbury, Vt.
- 2.1-4. T. Bratoljic, *Delta-Connected, Two-Layer, Three-Phase Winding for an Electrical Machine*, U.S. Patent 4,200,817, April 1980.

phase belts, and this is indicated in Figure 2.1-13 by the phase-belt phasors spanning 120° portions of the phasor circle. The voltage difference between adjacent conductors anywhere in a conductor layer is no more than a few coil voltages, and large phase break voltages are nowhere to be found. The phase-belt creepage stress for this winding is low compared to windings to be discussed shortly.

$$E_{pb} = \frac{V_{l-l}}{\frac{2}{3}\pi r} = .827 \frac{V_{l-g}}{r} \quad (2.1-2)$$

This winding might seem at first glance to be ideal for the high-voltage generator, except for one annoying difficulty: the magnetic flux distribution produced by the 120° phase belts contains even harmonics which produce rotor vibratory forces. Appendix C analyzes this phenomenon and concludes that although the even harmonic content of the flux can be reduced, it cannot be entirely eliminated. The magnitude of the resulting rotor vibrations is difficult to quantify and may be dependent on resonance conditions. The philosophy of prudence excludes this winding arrangement for consideration for the high-voltage generator.

A 60° phase-belt two-circuit delta connection was developed by the Massachusetts Institute of Technology for application to their superconducting generator effort (Refs. 2.1-2 and 2.1-4). Figure 2.1-15 illustrates a circle phasor diagram for this winding and Figure 2.1-16 illustrates the winding diagram. This winding utilizes a novel phase joint connection to eliminate large phase break voltages. Consider the phase belt labeled A₁ on Figure 2.1-15. The last conductor of this phase belt, a conductor on the outer layer, is joined to the neighboring *outer* layer conductor of the adjacent phase, marked B₁. This causes phase-belt B₁ to be wound in the reverse sense, and the phase belt labeled B₁ on Figure 2.1-15 is therefore depicted as being reversed from its original position on the circle phasor diagram. The same type of connection is performed on the inner layer conductors at the junction of phases B₁ and C₁; this causes the direction of phase C₁ to be restored to its original direction. The phase belt labeled C₁ on Figure 2.1-15 is therefore depicted in its original direction although it is shifted from its original position on the circle phasor diagram. The connection of the phase belts in this manner has produced a closed delta out of phase-belts A₁, B₁, and C₁, and has eliminated any large phase break voltages. The phase joint connection scheme is continued for phase-belts A₂, B₂, and C₂, producing direction reversals for phases A₂ and C₂. A second closed delta is formed from phases A₂, B₂, and C₂, and this delta is paralleled with the first delta, as is depicted with the parallel connections indicated on Figure 2.1-15.

The phase-belt creepage stress for the 60° phase-belt delta connection is

$$E_{pb} = \frac{V_{l-l}}{\frac{\pi}{3}r} = 1.654 \frac{V_{l-g}}{r} \quad (2.1-3)$$

The phase-belt creepage stress for this winding is considerably larger than that for the other windings and may require special engineering treatment. Section 2.5.2 discusses this topic in greater detail.

A special 60° phase-belt two-circuit graded wye connection eliminates large phase break voltages through the liberal application of coil jumpers. Figure 2.1-17 illustrates the circle phasor diagram for this winding, and Figure 2.1-18 illustrates the winding diagram. If the edge-most coil on the left side of the phase belt is connected to ground, it is in turn connected to the edge-most coil on the right side of the phase-belt through a coil jumper. The edge-most right side coil is connected to the second-to-edge coil on the left side of the phase belt, and the second-to-edge left-side coil is subsequently connected to the second-to-edge coil on the right side of the phase belt. This process is repeated, back and forth, until the center of the phase belt is reached, and the last coil to be connected becomes the high-voltage terminal. The other phase belts are connected in a similar manner. The result of these connections is that the edges of all phase belts are at or near ground potential and the voltage is graded from the edges to the center of the phase belts. It requires a considerable number of coil jumpers to perform these connections, and for a winding requiring as

The classical 60° phase-belt single-circuit wye connection is an example of a winding arrangement that produces large phase break voltages. Figure 2.1-11 illustrates a phasor diagram for this winding and Figure 2.1-12 illustrates the winding diagram. The top diagram of Figure 2.1-11 shows the circular arrangement of individual conductor voltage phasors in their order around the periphery of the armature. Individual conductor phasors are labeled "I" and "O" to indicate their location on the inner and outer conductor layers, respectively. Sixty-degree spans of the conductor phasors are grouped into phase belts, as indicated by the longer phasors appearing as chords of the circles. Each phase belt phasor is labeled "A", "B", or "C" with respect to its phase identification and is subscripted "1", or "2" to indicate its location close to ground or close to terminal, respectively. Ground points, terminal points, and phase-belt connections are also indicated on the diagram. The phase break voltages will be the voltages appearing at the physical junctions of the phase belts indicated on the circle diagram. For example, phase break voltages are indicated at the junction of the head of A_1 and the head of C_2 and the junction of the tail of C_2 and the tail of B_1 . In the bottom diagram of Figure 2.1-11, the circle diagram phasors are rearranged into the conventional wye arrangement of phasors. It is here that the magnitudes of the phase break voltages are revealed. The phase break voltage indicated at the junction of the head of A_1 and the head of C_2 is now seen to be a phasor stretching from the terminal of phase C to the midpoint of phase A. The magnitude of this phasor is 1.32 times line-to-ground voltage. The phase break voltage indicated at the junction of the tail of C_2 and the tail of B_1 is a phasor stretching from the neutral to the phase C midpoint. The magnitude of this phasor is 0.5 times line-to-ground voltage. The other phase break voltages are identical to the two identified above.

The phase-belt creepage stress for the single-circuit wye connection is the voltage appearing across the breadth of the phase belt divided by the span of the phase belt (as measured from a line perpendicular to the conductors). The phase-belt span will vary according to the coil type and to the location in the winding. The phase-belt span is greatest in the straight sections of a diamond coil but decreases in the end arms of a diamond coil or in helical coils. The voltage across the span of the phase belt for the 60° phase-belt single-circuit wye connection is 0.5 times line-to-ground voltage. The phase-belt creepage stress at the straight sections of a diamond coil is

$$E_{pb} = \frac{0.5 V_{l-g}}{\frac{\pi r}{3}} = 0.477 \frac{V_{l-g}}{r} \quad (2.1-1)$$

where r = winding radius.

The phase belt creepage stress will be somewhat higher for a helical winding.

The maximum voltage appearing across the center insulation cylinder is not necessarily found at the center of the winding (the straight sections of a diamond-coil winding or the axial center of a helical coil winding). In the case of the 60° phase-belt single-circuit wye connection, the maximum voltage across the center insulation cylinder is line-to-line voltage and is located at certain criss-crosses in the end arms of a diamond coil winding or at certain off-axial-center criss-crosses of a helical coil winding. The maximum voltage across the center insulation cylinder for any winding connection is no less than line-to-line voltage and no more than twice line-to-ground voltage.

The classical 60° phase-belt two-circuit wye connection also has large phase break voltages. One phase break voltage is zero and the other is line-to-line voltage. The classical 60° phase-belt delta connections also have large phase break voltages. The elimination of these large phase break voltages has required the invention of completely new winding arrangements, called *voltage gradient controlled windings*; the more important of these windings will be described presently.

The 120° phase-belt single-circuit delta connection is the paragon of simplicity. The coils of this winding are continuously connected around the periphery of armature. This is allowed because the phasor sum of all coil voltage phasors is zero, as illustrated in the circle phasor diagram of Figure 2.1-13. The terminals are made by tapping the series loops at three locations 120° apart, as illustrated in the winding diagram of Figure 2.1-14. This produces a delta winding having 120°

All air must be purged from the cooling system, and thermal expansion of the coolant in the resulting closed system is accommodated by an elastic bladder in the expansion tank. A water-cooled heat exchanger is precluded by the danger of moisture contamination of the coolant through a cracked heat exchanger tube.

In order to reduce the likelihood of dielectric failures, the greatest attention must be paid to the control of internal voltage gradients within the armature. Dielectric failures are described as being either puncture failures, which are flashovers directly through a dielectric medium, or creepage failures, which are flashovers along a boundary of two different dielectric media. The control of voltage gradients is accomplished either by electrical configuration (winding arrangements that produce small voltage differences between adjacent conductors) or by physical configuration (placing of thick dielectrics at critical locations or shaping of dielectric contours). The insulation cylinders of the monolith cylinder armature are examples of the control of voltage gradients by physical configuration, since the cylinders are thick dielectrics placed in between the large voltages appearing across the two conductor layers and across the conductor layers and the grounding surfaces.

Control of voltage gradients by electrical configuration is found to be important with respect to the problem of phase break voltages. A phase break voltage is defined as the voltage appearing between adjacent conductors of adjacent phase belts. Some winding arrangements produce large phase break voltages, and in a monolith cylinder high-voltage winding it would be necessary to insert thick dielectric barriers in between the phase belts (Figure 2.1-10). This in no way solves the problem, since there is now a path for creepage failure at the boundary between the phase break insulation and the insulation cylinder. The solution for this problem lies in the utilization of winding arrangements that produce small phase break voltages.

Another problem of somewhat less concern is the possibility of creepage failures across the entire breadth of a phase belt along the boundary of the conductor layer and the insulation cylinder. The magnitude of this phase belt creepage is a function of the winding arrangement.

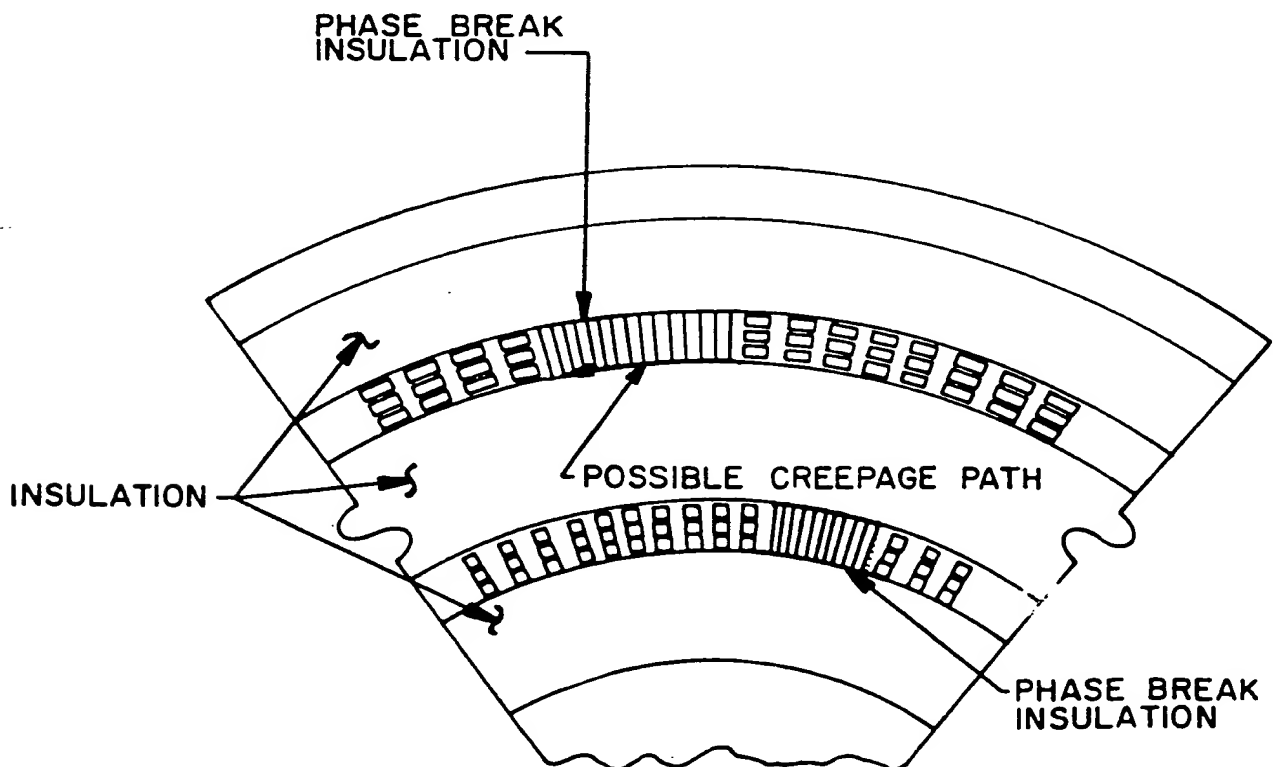


Figure 2.1-10. Phase Break Insulation for Windings with Large Phase Break Voltages

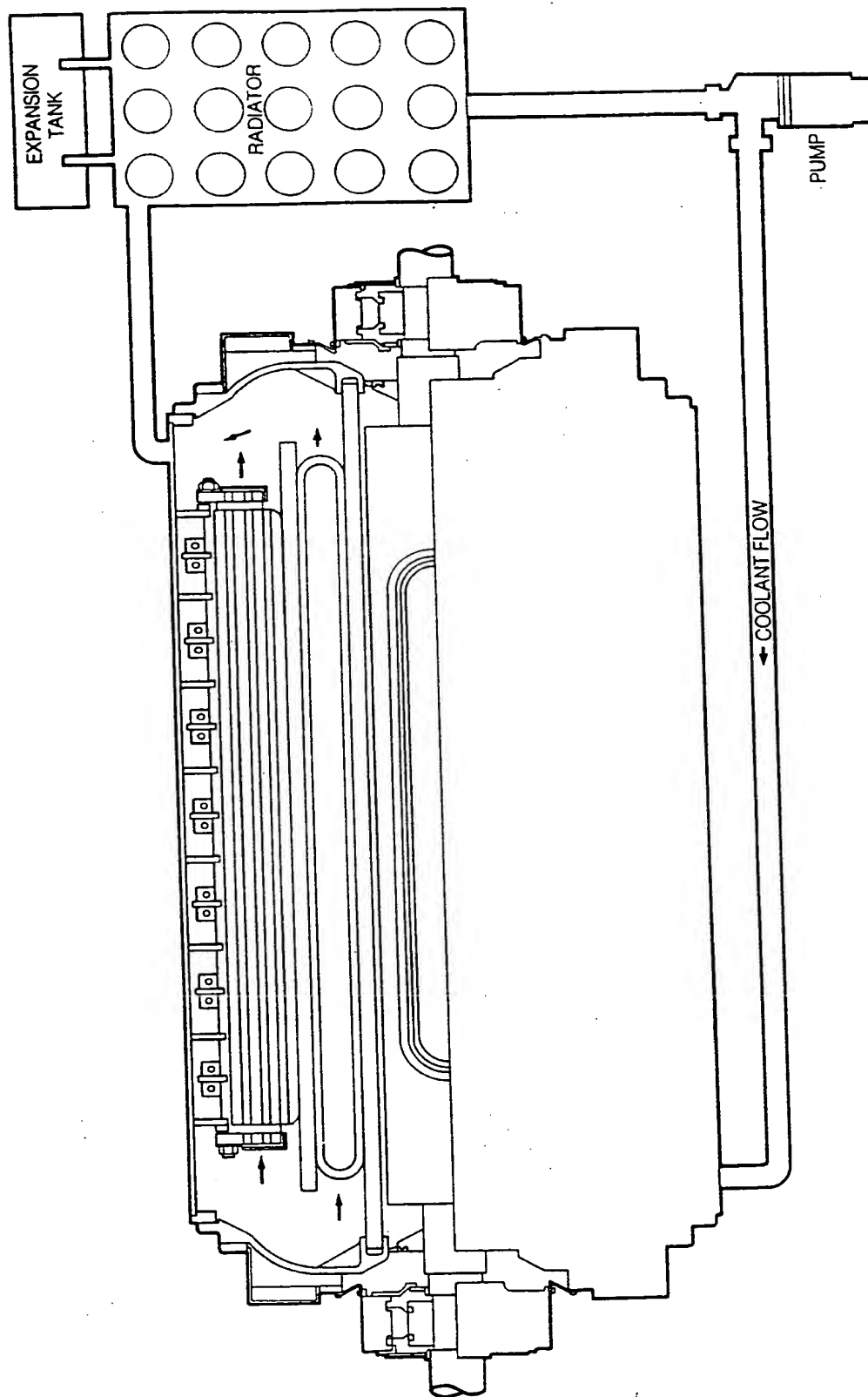


Figure 2.1-9. Cooling Scheme for the High-Voltage Armature (Illustrating Flooded End Regions)

Table 2.1-2
STATED MECHANICAL PROPERTIES OF OIL-IMPREGNATED
HIGH-DENSITY PRESSBOARD

Average Tensile Strength	~15,000 psi
Average Shear Strength	~14,500 psi
Average Modulus of Elasticity	~1,800,000 psi

The use of oil-impregnated insulation will necessitate the placement of a bore seal tube at the interior of the armature, so that oil can be prevented from seeping into the bore. The bore seal tube can be made of any oil-impermeable material, and a tube constructed of filament wrapped fiberglass-epoxy is a likely candidate. Figure 2.1-8 is a detailed cross-section of the monolith cylinder armature and illustrates the placement of the bore seal tube. The inner grounding surface is placed in between the bore seal tube and the inner insulation cylinder to isolate the bore seal tube from electrical stress. It is not necessary to provide a sealing tube in between the armature and the core since the core and frame are themselves completely filled with dielectric fluid.

Figure 2.1-9 illustrates a radial-axial cross-section of the high-voltage generator and its cooling scheme. It is desired to avoid the use of coolant connection hoses because of the thousands of hoses and hose connections that would be required. Therefore, it is envisioned that the entire stator end regions would be flooded with coolant that would be pumped through the winding coolant passages via access ports in the vicinity of the winding series loops. The coolant will be electrically stressed over portions of the coolant path, so it is necessary for the coolant to be a dielectric fluid. (The same fluid used as the insulation impregnant is convenient.) The core can be cooled from the end region coolant header through axial passages cumulated from holes prepunched in the core laminations. The insulation cylinders can also be cooled from the end region coolant header through axial passages provided in the cylinders during the assembly of the pressboard sheets. The external cooling equipment is of the type used by large step-up transformers, and the main heat exchanger is a fan-cooled radiator. The external cooling equipment and the entire stator casing must be hermetically sealed to prevent the coolant from absorbing moisture from atmospheric humidity.

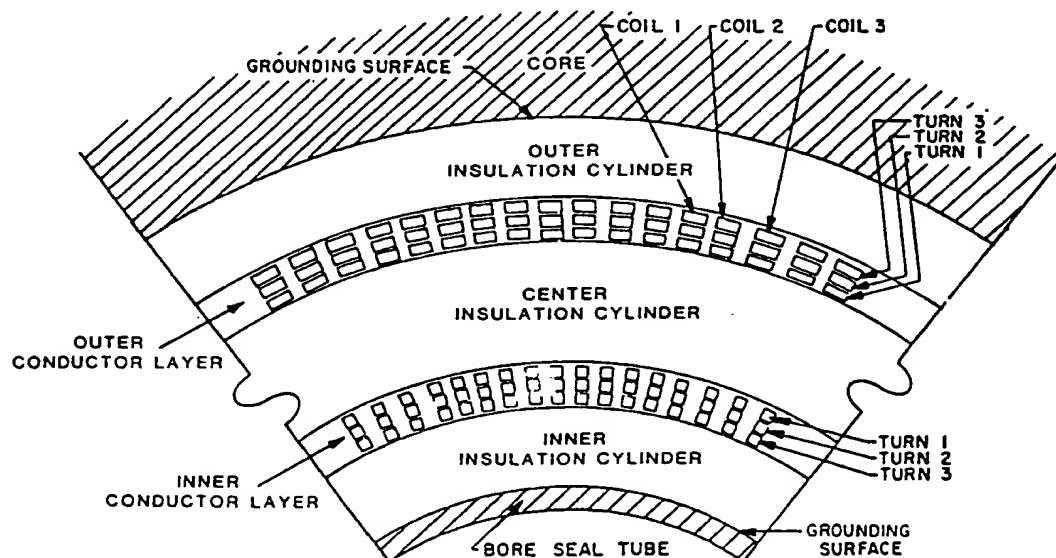


Figure 2.1-8. Components of the Monolith Cylinder Armature

plastic laminates such as fiberglass-epoxy. A fiberglass-epoxy insulation is made from fiberglass cloth laminations or fiberglass filament wraps that are saturated with epoxy and baked hard. No plastic laminate can be manufactured entirely free of voids without resorting to extreme vacuum and pressure techniques. The voids in a plastic laminate result in slow but progressive damage caused by ionization in the voids at operating stress. A more important consideration, however, is the possible formation of cracks within the armature due to winding forces or thermal expansion forces. A small crack that develops in an armature constructed from plastic laminate insulation may rapidly lead to a dielectric failure. In an armature constructed from fluid impregnated pressboard, any small cracks will be filled with the dielectric fluid and rapid dielectric failure will thus be averted. This is the primary reason for selecting pressboard as the preferred insulating material. The technology for pressboard impregnated with transil oil is well-established, and the selection of this combination for the insulation would greatly reduce the amount of development effort required for a high-voltage stator winding. Figure 2.1-7 illustrates the partial discharge inception field strength of oil-impregnated pressboard for both impulse voltage and power frequency voltage (Ref. 2.1-3). The mechanical properties of oil-impregnated pressboard appear to be adequate, and Table 2.1-2 lists average measured mechanical properties of a pressboard grade having the greatest density and mechanical strength (from Ref. 2.1-3).

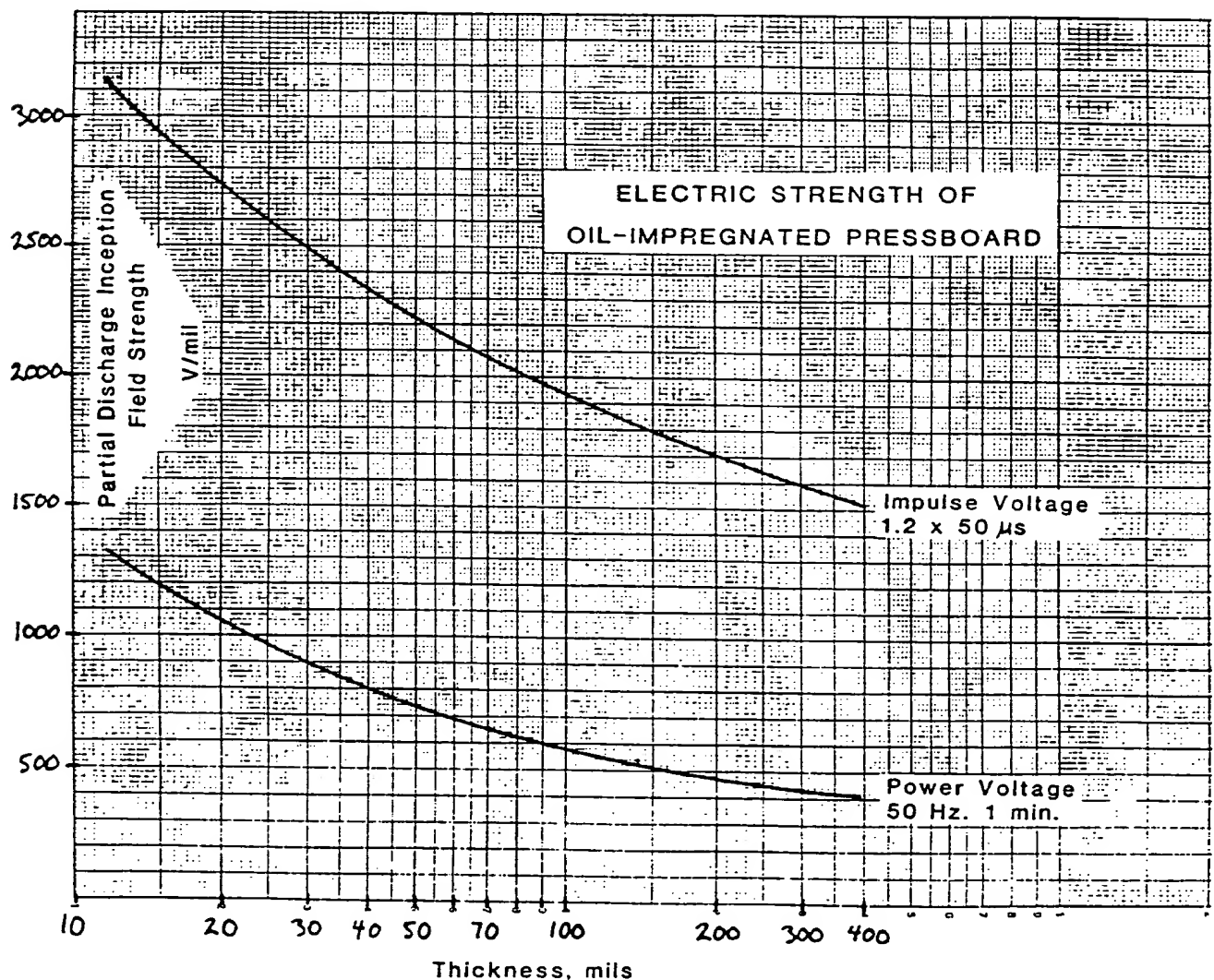


Figure 2.1-7. Electric Strength of Oil-Impregnated Pressboard

strengths of up to 200 V/mil, it would be imprudent to design new demonstration machines at anything greater than 50 V/mil dielectric strength. The dielectric strengths of all insulating materials decrease with increasing thickness, and since there have never been any tests of materials in the thicknesses required for the high-voltage winding, it is not known if dielectric strengths approach an asymptotic lower limit when such thicknesses are obtained or if they decrease to impractical values. It is felt that a dielectric strength of 50 V/mil is a conservative design value, and the machine designs contained in later sections of this report assume that the insulation is capable of this strength. Section 2.2 describes machine sizing studies for the monolith cylinder high-voltage generator.

Table 2.1-1
REQUIRED INSULATION CYLINDER THICKNESSES FOR VARIOUS
VOLTAGE RATINGS AND DIELECTRIC STRENGTHS

	Dielectric Strengths		
	50 V/mil	100 V/mil	200 V/mil
<u>230 kV Rating</u>			
line-to-ground insulation cylinder	2.65"	1.32"	.66"
line-to-line insulation cylinder	4.60"	2.30"	1.15"
<u>345 kV Rating</u>			
line-to-ground insulation cylinder	3.98"	1.99"	1.00"
line-to-line insulation cylinder	6.90"	3.45"	1.73"
<u>500 kV Rating</u>			
line-to-ground insulation cylinder	5.77"	2.89"	1.44"
line-to-line insulation cylinder	10.00"	5.00"	2.50"
<u>765 kV Rating</u>			
line-to-ground insulation cylinder	8.83"	4.42"	2.21"
line-to-line insulation cylinder	15.30"	7.65"	3.83"

The thick insulation builds required for the monolith cylinder high-voltage armature preclude the use of anything but a superconducting rotor winding, since only the superconducting rotor is capable of exciting such great non-magnetic reluctances. The machine sizing studies of Section 2.2 include superconducting rotor windings for all calculations.

The dielectric material for the insulation cylinders must not only possess suitable dielectric strength and life but also must possess adequate mechanical strength. The insulation cylinders are required to transmit radial and tangential winding loads to the core and frame and must withstand large bending and shear stresses caused by armature ovalization deflections exhibited during sudden short circuit. Solid dielectric materials suitable for the insulation cylinders may be grouped into two categories: fluid impregnated pressboard and dry-type dielectrics. Pressboard is a hard, stiff material that is heat pressed from moist cellulose pulp into sheets ranging up to 0.25-inch thickness. The pressboard sheets can be formed and laminated into the insulation cylinders, and the finished armature winding is later impregnated with a dielectric fluid such as transil oil, Freon,* or silicone oil. The dielectric fluid fills all voids in the pressboard, and the result is an exemplary insulating material that has been in-use for decades by the transformer industry. Dry-type insulations can include

* E.I. DuPont DeNemours Co., Inc.

Grounding surfaces must be provided in the armature to control the electric field distribution at critical locations. It is particularly important to place a grounding surface on the inner surface of the inner insulation cylinder in order to prevent a flashover from the inner conductor layer to the grounded rotor body. A grounding surface can be constructed from thin stainless steel wires placed around the entire periphery of the surface and orientated in the axial direction. The wires are connected by a loop at one end but not the other (Figure 2.1-6). In this manner, no closed loops are formed and the losses of the grounding surface are limited to eddy current losses within individual wires. The wires must be placed close enough together to eliminate electric stress concentrations from individual wires. If the wires are not closely spaced, the wire cage can be coated with a semi-conductive paint which will also serve to eliminate the electric stress concentrations. The inner surface of the core can serve as the grounding surface for the outer insulation cylinder, although a wire cage grounding surface can be provided here if it is felt that void-free contact between the core and outer insulation cylinder cannot be assured.

The inner and outer insulation cylinders must be thick enough to withstand the line-to-ground voltages that appear between the outer conductor layer and the core inner surface and between the inner conductor layer and the inner grounding surface. The center insulation cylinder must be thick enough to withstand the line-to-line voltage that appears between the two conductor layers. (This can be twice line-to-ground voltage in some winding connection schemes.) The dielectric strength of the insulation plays a crucial role in determining the overall machine dimensions, since a great portion of the radial build-up of the armature will be consumed by the insulation cylinders. Table 2.1-1 lists required insulation cylinder thicknesses for various machine voltage ratings and dielectric strengths. Insulation requirements will become quite large with the lower dielectric strengths (the 345 kV rating at 50 V/mil dielectric strength, for instance, requires nearly 15 inches of just insulation). When the radial build-ups of the conductor layers and the core and frame are added, a machine of large external dimensions is realized. Although Table 2.1-1 describes dielectric

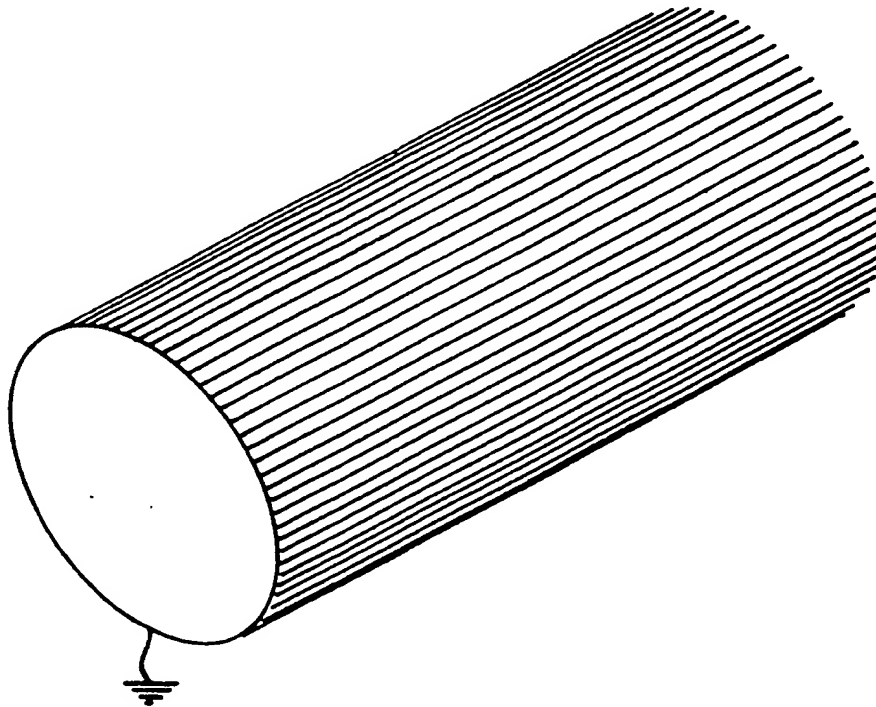


Figure 2.1-6. Wire Cage Grounding Surface

One or two thousand conductors may be required in each conductor layer cylinder, and it will be necessary to stack conductors one above each other in columns to avoid conductors of excessively tall and thin proportions. Figure 2.1-1, for instance, illustrates three conductors stacked in each column in the conductor layer cylinders. The conductors of the inner and outer conductor layer cylinders can be connected at the series loops in such a manner as to produce a nested series loop system (Figure 2.1-4). Here it is seen that the outermost conductor of the inner layer is connected to the innermost conductor of the outer layer, the innermost conductor of the inner layer is connected to the outermost conductor of the outer layer, and so on. Figure 2.1-5 illustrates a similar nested series loop and coil jumper system for the connection end of the winding.

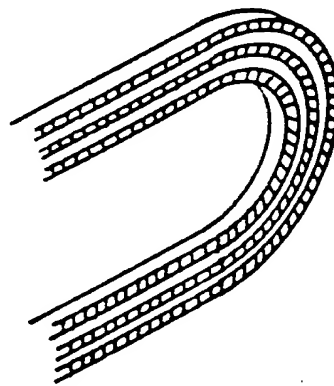


Figure 2.1-4. Non-Connection-End Series Loop Nest

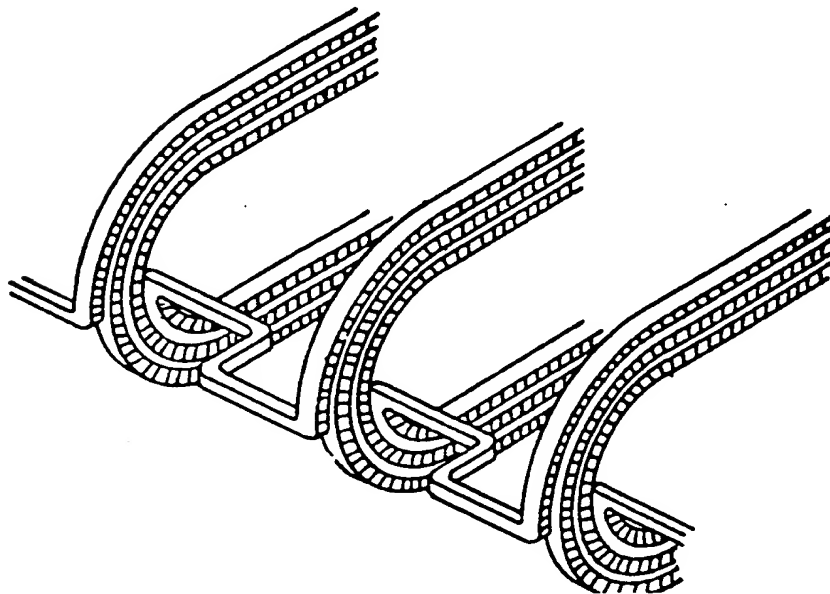


Figure 2.1-5. Connection-End Series Loop Nest and Coil Jumper System (Expanded in Horizontal Direction)

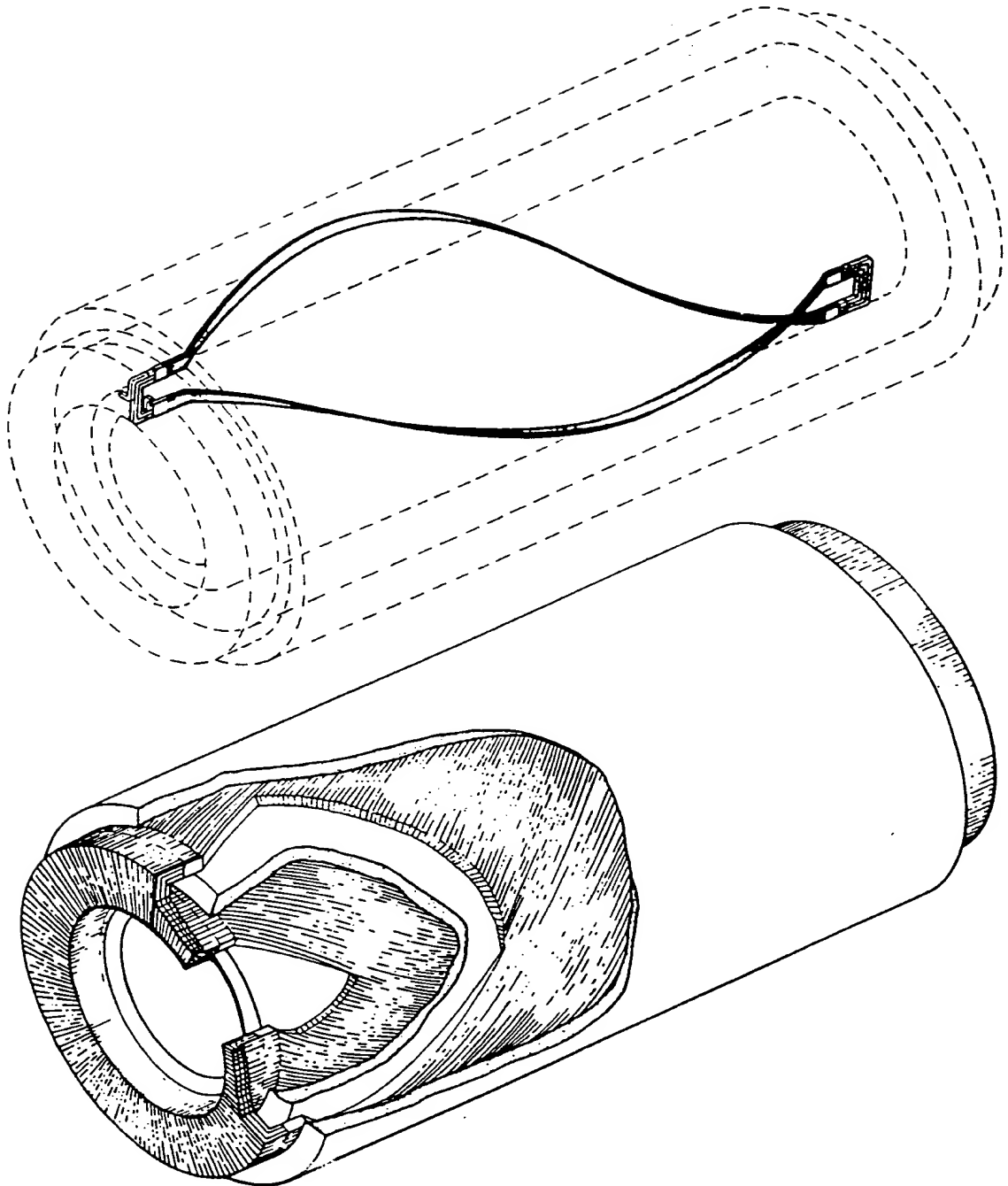


Figure 2.1-3. Monolith Cylinder Armature with Helical Coils

ure 2.1-3 illustrates the fully helical coil shape, where the conductor twists 180° peripherally from end to end (Refs. 2.1-1 and 2.1-2). Variations of these shapes are also possible: for instance, the end arms of the diamond coil can be brought well within the active magnetic zone. The fully helical coil shape is equivalent to a diamond coil having no straight sections. An optimization process is implied in the coil shape selection; because while a diamond coil with short straight sections links less magnetic flux, it is possible to pack more such coils within the periphery of the conductor cylinders. Appendix B describes the theory behind the coil shape selection and concludes that the fully helical coil shape is close to optimal.

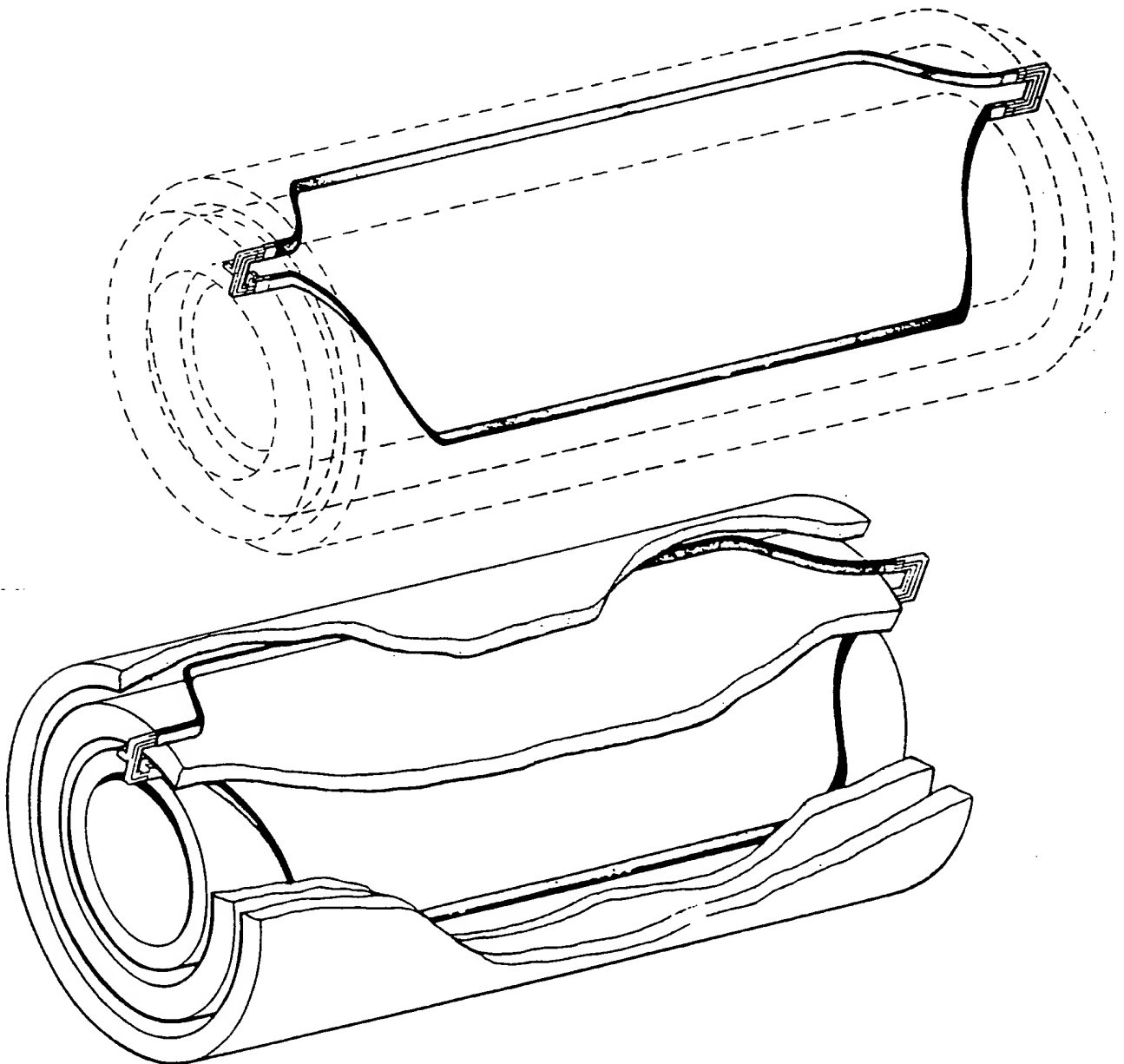


Figure 2.1-2. Monolith Cylinder Armature with Diamond Coils

Section 2

PRIMARY APPROACH—MONOLITH CYLINDER ARMATURE

2.1 ARMATURE TOPOLOGY AND WINDING ARRANGEMENTS

The monolith cylinder armature is appropriately named for its concentric cylinder construction having separate cylinders devoted to electrical insulation and electrical conductors. The monolith cylinder armature utilizes geometrical simplicities and symmetries to produce an armature that is dimensionally compact and straightforward to manufacture by virtue of its many identical components and repeatable assembly sequences.

Figure 2.1-1 illustrates a cross-section of the monolith cylinder armature in its most elementary form. Two cylinders of conductors are encapsulated by three cylinders of insulation, and the entire structure is fastened to a toothless iron core. A slotted iron core is precluded by the great number of conductors required to reach transmission level voltages. The inner and outer insulation cylinders must be thick enough to withstand line-to-ground voltage while the center insulation cylinder must be thick enough to withstand line-to-line voltage. Each conductor layer cylinder can contain from one to two thousand individual conductors. The conductors lie on the same radius throughout their entire length and do not flare into a cone at the ends, as do the conductors of a conventional turbine-generator.

Since the conductors are not confined in iron teeth, the coil shape can assume a variety of forms. Figure 2.1-2 illustrates the familiar straight coil with helix end arms (diamond coil), and Fig-

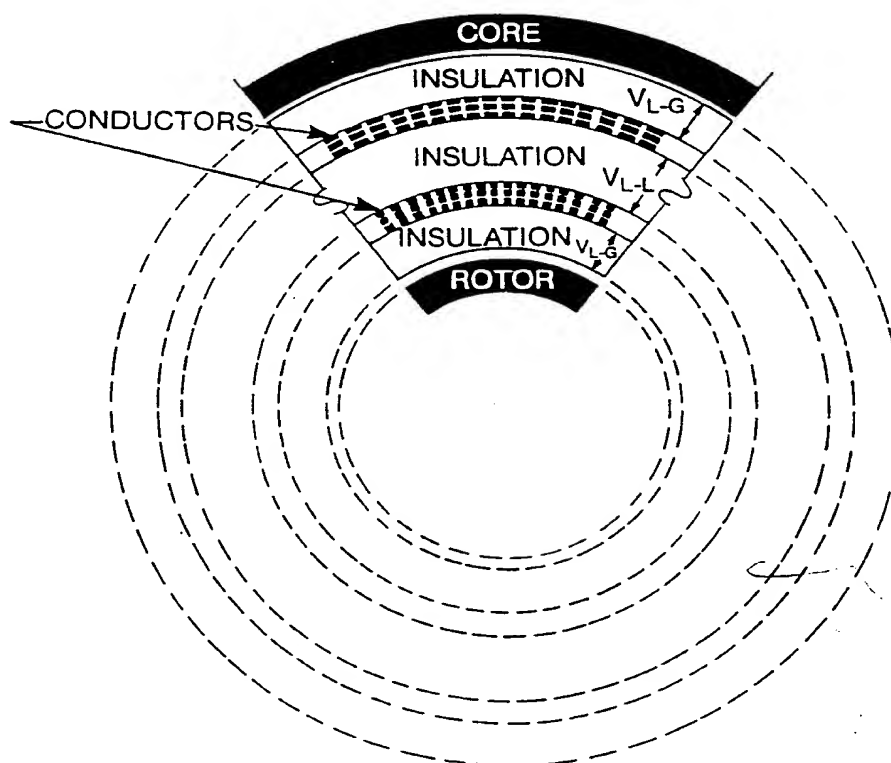


Figure 2.1-1. Cross-Section of a Monolith Cylinder Armature

pressboard. If these tests proved encouraging, mockup winding tests would be performed to confirm whether the analytically calculated non-uniform creepage stress limits are valid. Following the insulation testing program, the construction of a demonstration high-voltage generator model using an existing model superconducting rotor would be the next logical development program.

1.9 SUBJECT INVENTIONS

In the course of this contract, only one contractor's invention disclosure letter was submitted to the contracting officer:

- A novel wye-connected winding arrangement that provides smooth circumferential voltage grading and eliminates large phase break voltages was submitted as an invention. This winding arrangement is accomplished by the use of special end-winding connections. The smooth voltage grading allows high material utilization, and the wye-connection is preferable for the power systems interrelation. This winding arrangement is applicable to both monolith cylinder armatures and taped integral-insulated phase belt armatures, although neither application was selected as the preferable design for the high-voltage stator winding.

The selection of the monolith cylinder armature as the primary design approach reduced the potential for new patentable ideas. The monolith cylinder concept has already been studied and publicized by several specialists in the field. The detailed studies in this report on the monolith cylinder armature describe a number of component designs which are probably patentable. Techniques of reducing electrical creepage stresses in the body and in the end regions are examples of these ideas. Disclosure letters were not submitted since it was concluded that the ideas fall within the state-of-the-art of transformer technology. Publication of these and other patentable ideas in this report will provide the industry with the required patent protection.

References

- 1-1. General Electric Co., *Superconducting Generator Design*, EPRI Research Project RP 429-2, Final Report, Dec. 1977.

- Integral-insulated phase-belt armature — taped system
- Integral-insulated phase-belt armature — coaxial system

The results of these studies and the results of the studies on the monolith cylinder armature provided the information necessary to make a rational decision as to which design concept has the best potential of being proven technically and economically feasible. As stated earlier in this report, the monolith cylinder armature was selected as the primary design approach.

1.6 ECONOMIC ANALYSIS OF SUPERCONDUCTING GENERATORS

Section 6 describes economic analyses comparing the cost benefits of low-voltage and high-voltage superconducting generator development programs. The economic comparisons incorporate a number of possible business scenarios during a 35 year period from 1986 through 2020. Each scenario includes the following data:

- Anticipated electrical growth rate
- Estimated yearly generating capacity additions
- Introduction rate of low-voltage or high-voltage superconducting generators
- Penetration rate of the superconducting generators
- Estimated yearly development costs (1985 dollars)
- High, average, and low savings estimates based on capital cost differences and operating cost savings resulting from improved efficiencies (1985 dollars)

Present worth values, breakeven years, and rates of return on invested development funds are calculated by using the data for each scenario and applying the appropriate interest rate formulas. The studies indicate that both the low-voltage and high-voltage superconducting generator development programs should provide financial benefits to the industry. As measured by present worth values, the high-voltage generator benefits are significantly larger than the low-voltage generator benefits. However, rates of return and breakeven years for high-voltage generators are not significantly better than for low-voltage generators.

1.7 FINAL DESIGN RECOMMENDATION

Section 7 presents a summary of the monolith cylinder high-voltage superconducting generator design. This design was selected from several design concepts as the approach which has the best potential of proving to be technically and economically feasible. Many of the results from the analytical studies throughout this report are summarized, and the advantages and limitations of this design are also discussed.

All of the other conceptual designs are reviewed, and the justification for selecting the monolith cylinder armature over the other designs is discussed.

1.8 RECOMMENDATION FOR FOLLOW-ON EFFORT

The general conclusion of this report is that follow-on effort to develop high-voltage superconducting generators should be deferred until the feasibility of superconducting rotors has been established. When superconducting rotors are shown to be economical to manufacture and are shown to operate with satisfactory reliability and availability, a re-evaluation of the high-voltage generator concept should be made. One of the first considerations should be to establish whether the insulation systems proposed in this report are practical.

Section 8 outlines a minimal hardware development program that will provide the insulation characteristics of the very thick insulations required for the monolith cylinder armature. The program would be initiated with electrical puncture and creepage tests under uniform field stresses for press-board impregnated with transil oil. The same tests could also be performed for Freon impregnated

1.4 POWER SYSTEM CONSIDERATIONS

Section 4 describes the power system considerations for the high voltage generator. Since the high-voltage generator is connected directly to the high-voltage transmission network, the transient voltage and current levels which the machine will be subjected to are of particular interest. One of the most important system interface considerations relates to the ability to provide adequate transmission system grounding. This determines allowable surge arrester ratings and thus the necessary basic insulation requirements of the high-voltage stator winding as well as that of all of the other high-voltage components (lines, circuit breakers, etc.) At conventional generating stations, transmission system grounding is provided by the step-up transformer. At a high-voltage generator station, other means must be employed. For the delta-connected high-voltage generator determined to be the preferable design, the station auxiliary transformers can be arranged to provide system grounding. The grounding thus provided permits the same basic insulation level (BIL) to be applied to the high-voltage stator and the other station high-voltage components as is normally applied at conventional stations.

Fault current levels for various types of transmission line and terminal faults are calculated for the high-voltage generator. In general, the per unit winding fault current levels for the high-voltage generator are comparable to those of a conventional generator. These fault currents are also generally lower than the fault current levels experienced by the high voltage winding of a step-up transformer for transmission line faults.

The high-voltage generator shaft torsional duties accompanying transmission line faults and normal line reclosing can be excessive and may require special mechanical design considerations. These torsional considerations arise out of the low inertia of the superconducting rotor and would be characteristic of either low-voltage or high-voltage superconducting generators.

For protective relaying, many of the conventional relays are directly applicable to the high-voltage generator. One area requiring development will be that of providing fiber optic transmitted current transformer signals for split-phase differential protection of the windings. The basic technology for this high-voltage electronic current measurement requires only adaptation to this specific application.

A natural replacement for the conventional isolated phase bus will be SF₆ gas-insulated high-voltage buswork which has been developed for the interconnection of high-voltage transformers and other station high-voltage components. The high-voltage bushings for the high-voltage generator would be expected to be similar to transformer bushings for gas-insulated bus installations.

The phenomenon of Subsynchronous Resonance (SSR) is more affected by torsional dynamics than generator electrical dynamics. The mechanical design provisions that need to be made to make superconducting generators adequate for normal line switching duties should also provide adequate SSR performance.

The lower reactance brought about by the elimination of the step-up transformer enhances the transient stability characteristics of the high-voltage generator, despite the lower rotor inertia. An improvement on the order of 2 cycles in critical clearing time was found for a comparison example between conventional and high-voltage units. This is a rather substantial difference and is comparable to or greater than that attainable by the addition of a very high performance excitation system on a conventional unit.

1.5 SECONDARY APPROACHES

Section 5 describes the studies performed on the following secondary high-voltage generator design concepts:

- Spiral pancake armature
- Salient-pole stator

Electrical creepage situations within the armature body and at the armature end regions are evaluated. The electrical creepage at the armature end regions is strongly controlled by the thickness of the insulation cylinders. Generator voltage ratings greater than 500 kV may not be possible because of the excessively thick insulation cylinders required to control the end region electrical creepage.

Conductor and conductor cooling designs are described for three proposed dielectric fluid coolants: transil oil, Freon 113, and silicone oil. The conductors are comprised of braided copper filaments and are cooled through stainless steel cooling tubes that are interspersed throughout the winding. Cooling performance is evaluated in terms of allowable temperature rises, coolant flow, and coolant pressure, among other quantities.

Large turn-to-turn voltages that are produced by voltage surges such as lightning strikes are calculated. The surge voltage distribution within the high-voltage generator is similar to that experienced by high-voltage step-up transformers. The calculations are used to qualify the armature turn insulation.

A conceptual stator frame design that will accommodate larger diameter cores than do present conventional frame designs is described. Such a frame will be important in implementing high-voltage generators because of the large magnetic dimensions of high-voltage generators. The stator frame will be required to be hermetically sealed to guard against moisture contamination of the high-voltage insulation.

The design studies performed in this section strongly suggest that the monolith cylinder armature is technically feasible. However, this conclusion is based on the results of analytical models which have not yet been fully calibrated. Also, a few potential problems which could not be modeled and analyzed — such as the effects of thermal expansion forces and the effects of long-term insulation shrinkage — were not addressed. Therefore, the final assessment on technical feasibility will require extensive model testing and operating experience.

1.3 COMMERCIAL ACCEPTANCE TESTING

Section 3 describes the methods and equipment required to test the integrity of the high-voltage stator winding insulation system. Insulation testing is emphasized in this section because the insulation tests are significantly different than those presently required for low-voltage generators, while the electromagnetic and mechanical tests can be essentially the same. The tests and test procedures outlined in IEEE Standard 115 "Test Procedure for Synchronous Machines," should generally apply with the exception of the stator winding insulation testing references.

The dielectric system of the high-voltage generator is similar to that of a high-voltage step-up transformer, and the operating environment is also similar, particularly with respect to exposure to lightning strikes and switching surges. Therefore, the recommended insulation tests for the high-voltage generator are the same as those for a transformer, namely the impulse test and the overvoltage test. The impulse test simulates the effects of lightning strikes and switching surges. The overvoltage test holds a twice-rated voltage on the winding for a specified short amount of time (typically 7200 cycles).

The impulse test can be performed in almost the same manner as performed on transformers and will use the same testing equipment. The overvoltage test will be similar to that prescribed for large inductive reactors and is called a series-resonance test. This test has capacitor banks connected in series with the generator winding. The circuit is driven with a small high-frequency (240 or 420 Hz) motor-generator set. When the capacitive reactance is tuned to the generator reactance, the voltage across the generator winding is cancelled by the voltage across the capacitor bank, and the high-frequency alternator appears to be operating in short-circuit, except for a voltage drop due to circuit losses. The high-frequency excitation limits core overfluxing and reduces the circuit current required to achieve twice-rated voltage on the generator winding. For a delta-connected high voltage generator, this test must be performed in three-phase, tripling the cost of the test equipment. The high-frequency motor-generator set must supply all circuit losses and may have to be as large or larger than any such set built to date.

ducting generators are technically feasible. The time scale of the development program will be long and the development costs will be high. Due to the high premium assigned to reliability and availability, the industry will probably require backup conventional generators for the first few low-voltage and high-voltage superconducting generators, in case the reliability and availability of these early designs prove to be poorer than can be economically justified.

1.1.9 General Prognosis

The results of this study to assess the potential industry benefits of a high-voltage generator development program suggest that a prudent course of action would be to defer further development effort until on-going low-voltage superconducting generator programs have better defined the technical feasibility of superconducting rotors. Successful superconducting rotors are a prerequisite to the high-voltage generator concept and any development effort for high-voltage generators could be wasted if superconducting rotors do not perform satisfactorily.

Although the economic studies show that a high-voltage generator development program has the potential for providing a large present worth economic value, the higher anticipated development costs results in a rate of return on development costs of almost the same as a low-voltage superconducting generator development program. Since the risk of encountering a critical problem on high-voltage generators is greater than on low-voltage generators, it appears appropriate, at this time, to concentrate exclusively on low-voltage superconducting generator technology.

Following the successful development of superconducting rotors in low-voltage generator applications, it would be appropriate to again assess the potential economic advantages of high-voltage generators. The reassessment study would have the advantage of having more reliable development costs and savings estimates to better define the long-term economic benefits to the industry. The reassessment would also gain from the technical knowledge obtained from experience with low-voltage superconducting generator air-gap windings.

1.2 PRIMARY APPROACH: MONOLITH CYLINDER ARMATURE

Section 2 presents the design studies performed on the monolith cylinder armature to assess the technical feasibility of the design concept and to determine acceptable engineering criteria. Several of the studies explore potentially critical problems and identify modified component designs which resolve the problems. Other studies explore component modifications that produce design optimization. Methods of calculating mechanical and electrical stresses within the armature are presented, and the calculated stresses are evaluated in terms of required material specifications and machine design limits.

New winding arrangements that produce smooth circumferential voltage grading and eliminate large phase break voltages are evaluated. Such winding arrangements are necessary to eliminate destructively large electrical creepage and puncture stresses. A novel delta-connected winding is selected as the preferred winding arrangement. Different winding coil shapes are also evaluated.

Generator sizing studies which describe the sensitivity of generator dimensions to variations in rotor diameter, armature winding current density, average insulation dielectric stress, and terminal voltage are performed. The large insulation volume in a high-voltage armature produces large magnetic dimensions which may limit the maximum ratings that can be shipped. The calculated magnetic dimensions are very sensitive to changes in voltage rating or insulation dielectric stress, both of which affect the insulation volume.

The sizing studies are used to select best designs for 600 MVA, 345 kV and 1200 MVA, 500 kV units. Detailed component designs are performed for both selected ratings, and operating performance is evaluated.

Stator winding forces during sudden short circuit and normal operating conditions are calculated. The stator winding forces are in turn used to calculate mechanical stress levels within the armature structure in order to establish the mechanical requirements of the insulation material. The calculated mechanical stresses appear to be low and are well within the limitations of the proposed oil-impregnated pressboard insulation material.

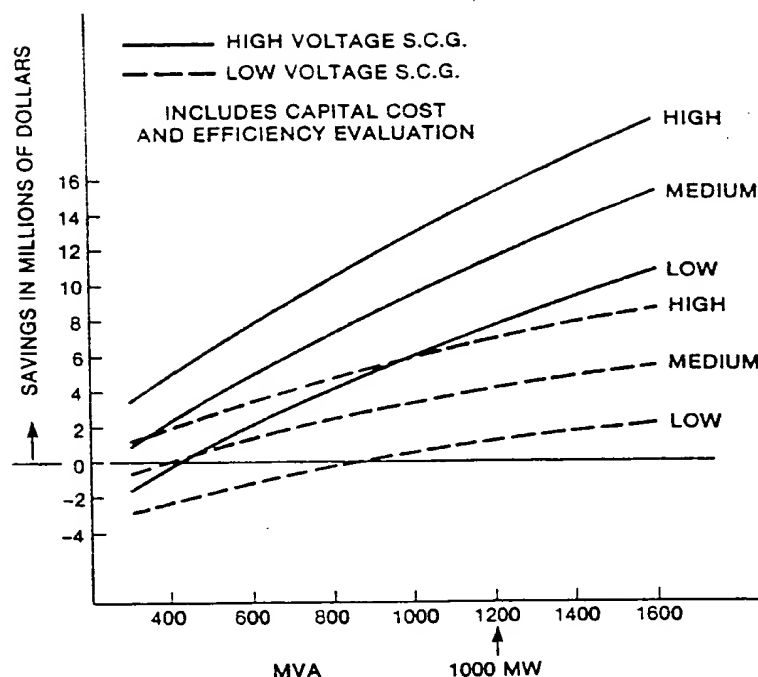


Figure 1-6. Potential User's Savings for Superconducting Generators

- Economic analysis sensitivity studies accounting for a number of different electrical growth rate, cost savings, and development cost scenarios over a thirty five year period (1986-2020) provided a wide range of potential economic savings to the electrical industry for both the low-voltage and high-voltage superconducting generator development programs. The results are, as might be expected, very sensitive to all the variables, and the reader should review the data and judge the merits of the rationale used to produce the variables. Two similar electrical growth rate scenarios using average unit cost savings estimates provided a present worth savings (1985 dollars) of 144 million dollars for the low-voltage superconducting generator development program and 375 million dollars for the high-voltage superconducting generator development program. The breakeven years were 2011 and 2010 respectively. Rates of return on development costs were 11% and 13% respectively.

1.1.8 Technical Assessment

High-voltage superconducting generator concepts represent radical departures in design and construction from the concepts used in low-voltage superconducting generators, since the stator windings will be significantly different than what is used in low-voltage superconducting generators. Although the high-voltage stator windings will use many of the known high-voltage step-up transformer technologies, the winding support system and the electrical stresses on the insulation system are different from any known similar applications. Preliminary designs and analyses presented in this report have uncovered and solved a great number of potential design problems. However, final assurance of commercial feasibility will depend on operating experience with machines of at least the mid-range of commercial ratings.

Since operating experience on large superconducting generators can not be obtained by a natural evolution of larger and larger ratings, as has been the case with conventional generators, a series of rapidly escalating rating sizes will be required to prove that low-voltage or high-voltage supercon-

tors mainly as a result of the very low field losses inherent in the superconducting field design. Efficiency improvements of 0.5% for both low-voltage and high-voltage superconducting generators over conventional generators were used in the economic analyses to calculate first cost operating savings.

1.1.6 Power System Considerations

Power system studies for high-voltage superconducting generators connected directly to transmission lines arrived at the following conclusions:

- Acceptable power station arrangements can be devised using either wye- or delta-connected armature windings. However, modified and somewhat more expensive auxiliary equipment will be required to provide acceptable system grounding.
- Generator winding voltage excursions experienced during line-to-ground faults, load rejections, and impulse conditions will be as high or higher than what is presently experienced in high-voltage step-up transformers. Thus, commercial acceptance testing techniques similar to those required for step-up transformers will be required for high-voltage generators.
- Satisfactory generator relay protection can be devised. However, due to the high-voltage environment in which some of the current transformers are required to operate, new electronic current transformers must be developed.
- The low inertia superconducting rotors required in high-voltage generators produce the same potential problems that have been identified in low-voltage superconducting generators: High shaft torsional duties will occur during system faults and transmission line reclosing, and turbine-generator rotor overspeed control will be more difficult than that for conventional generators. The optimal solutions to these problems and the possible cost penalties to resolve them have not been fully defined. Due to the inability of assigning these cost penalties, they were not included in the economic analyses. Thus, from this area of concern, the economic analyses results may be considered optimistic.
- Stability studies suggest that high-voltage superconducting generators will provide improved steady-state and transient stability performance as compared to conventional units. Transient stability studies show a potential 2 cycle improvement in critical clearing time. With these improved stability characteristics, it could be speculated that the use of superconducting generators could significantly reduce the utility industry's cost of transmission line installation. These savings would result by eliminating the need for a new or extra transmission line on an expanding utility system which would have marginal stability with conventional generator critical clearing time characteristics. Due to the difficulty of assessing how many new transmission lines could be eliminated over the next 35 years if superconducting generators were used, no potential cost savings for transmission line elimination were included in the economic analyses. From this area of concern, the economic analyses may be considered pessimistic.

1.1.7 Economic Analysis

Comparative economic evaluations of conventional generators, low-voltage superconducting generators, and high-voltage superconducting generators provided the following conclusions:

- Estimated utility first cost savings (1985 dollars) for low-voltage and high-voltage superconducting generators compared with conventional generators are shown in Figure 1-6. The cost savings reflect estimated capital cost differences and evaluated lower operating costs resulting from projected improved efficiencies. The use of high, average, and low savings estimates account for the uncertainties in identifying the material and labor costs which will be required to provide mature generator designs. The estimated savings for high-voltage generators are greater than for low-voltage generators, reflecting the additional cost savings produced by eliminating the capital cost of the transformer and the transformer electrical losses.

1.1.4 Generator Size Relationships

The active volume relationships of low-voltage and high-voltage superconducting generators with conventional generators are shown in Table 1-1. To provide direct comparisons between helical coil winding high-voltage generators, which have no end-winding overhangs, and diamond coil winding conventional and low-voltage superconducting generators, which have considerable end-winding overhangs, the active volumes listed in Table 1-1 are based on total winding lengths that include overhangs where applicable.

Based on these data for 600 MVA generators, the low-voltage superconducting generator is 30 to 40% smaller than a conventional generator. The 345 kV high-voltage generator is 25 to 30% larger than the low-voltage superconducting generator. The 500 kV high-voltage generator is 80 to 85% larger than the low-voltage superconducting generator and is 22% larger than the conventional generator. These size relationships reflect the poorer electrical coupling between the rotor and stator windings because of the large insulation volumes required for the high-voltage generator. The larger unit sizes required for high-voltage generators will limit the maximum generator rating which can be designed and shipped in an economical frame construction. This limit may detract from the long-term benefits of the high-voltage generator concept.

1.1.5 Generator Electrical Losses

Calculated electrical losses of high-voltage superconducting generators are of the same order of magnitude as those calculated for low-voltage superconducting generators. The electrical losses of both superconducting generator approaches are significantly less than those of conventional genera-

Table 1-1
ACTIVE VOLUME RELATIONSHIPS
600 MVA GENERATORS

Generator Design	Core Diameter Inches	Total Winding Length Inches	$D^2L \times 10^6$	Per Unit
Conventional (22 kV) Diamond Coil Winding	—	—	2.52	1.0
L-V Superconducting (24 kV) $X_d' = 0.2$ Diamond Coil Winding 150 A/cm ² Current Density	105	153	1.69	0.67
H-V Superconducting (345 kV) $X_d' = 0.27$ Helical Coil Winding 300 A/cm ² Current Density	111.2	173	2.14	0.85
H-V Superconducting (500 kV) $X_d' = 0.27$ Helical Coil Winding 300 A/cm ² Current Density	119	217	3.07	1.22
<ul style="list-style-type: none"> • Superconducting Generator Designs Use 50 V/mil Insulation Stress • Total Winding Lengths Include Diamond Coil End-Winding Overhangs. 				

connected winding arrangement is employed to provide a smooth electrical voltage grading throughout the winding so that high electrical stress concentrations can be eliminated.

Figure 1-5 illustrates a radial-axial cross-section of the monolith cylinder armature and its cooling scheme. The stator end regions are flooded with a dielectric fluid that is pumped through axial cooling passages in the winding, core, and insulation cylinders. The dielectric fluid, which can be either transil oil or Freon fluoro carbon fluid, also serves to control electrical stresses in the armature end regions. The external cooling equipment is of the type used by large step-up transformers, and the main heat exchanger is a fan-cooled radiator. The external cooling equipment and the entire stator casing must be hermetically sealed to prevent the dielectric fluid coolant from absorbing moisture from atmospheric humidity. Rotor windage losses are removed by pumping air from the ambience through the bore.

1.1.3 Insulation System

Based on an extensive review of high-voltage insulation technology and the identification of the electrical creepage and puncture stresses that will be experienced in the high-voltage generator, it has been concluded that present-day high-voltage transformer technology must be employed for both insulating materials and dielectric design. The dielectric-fluid-impregnated cellulose press-board insulation system appears to be the only insulation system that will guarantee long-term operation at the high electrical creepage and puncture stresses identified in the high-voltage generator. The fluid impregnation ensures that all voids resulting from assembly operations and cracks resulting from winding forces or thermal expansion forces will be filled with dielectric fluid. Thus, incipient electrical insulation damage due to ionization in voids will be minimized.

The considerable transformer industry experience with transil oil makes it the preferred dielectric fluid impregnant. However, Freon may be utilized instead if the fire hazard of transil oil within the power station machine hall is considered objectionable. The dielectric experience with a Freon impregnant is minimal and extensive dielectric testing would be required to support its application.

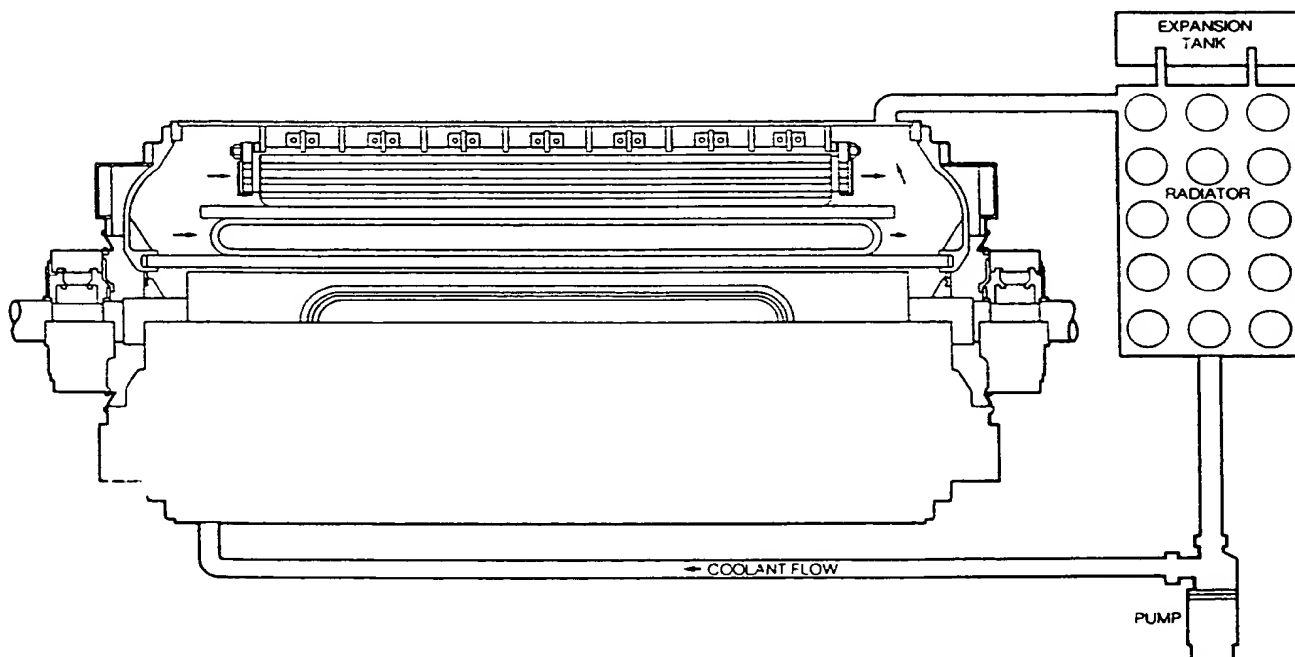


Figure 1-5. Cooling Scheme for the Monolith Cylinder Armature

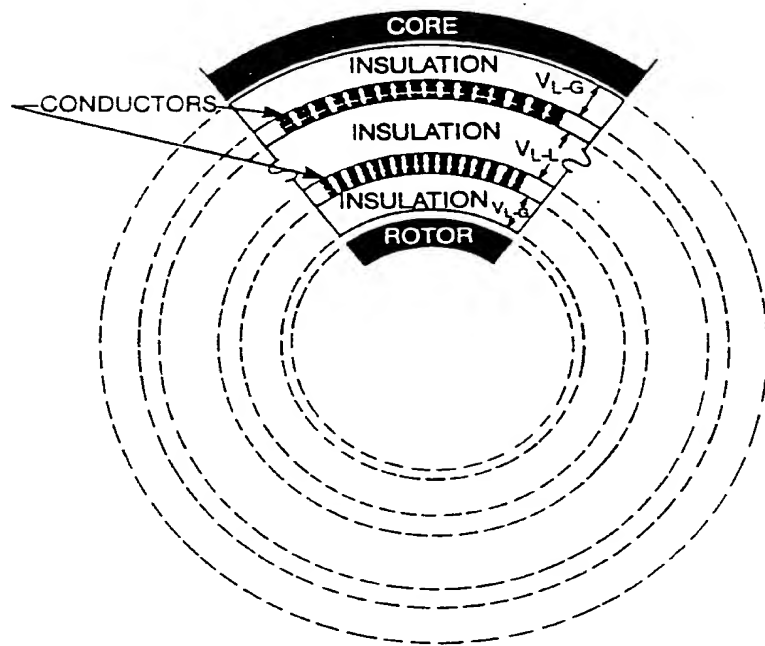


Figure 1-3. Cross-Section of the Monolith Cylinder Armature

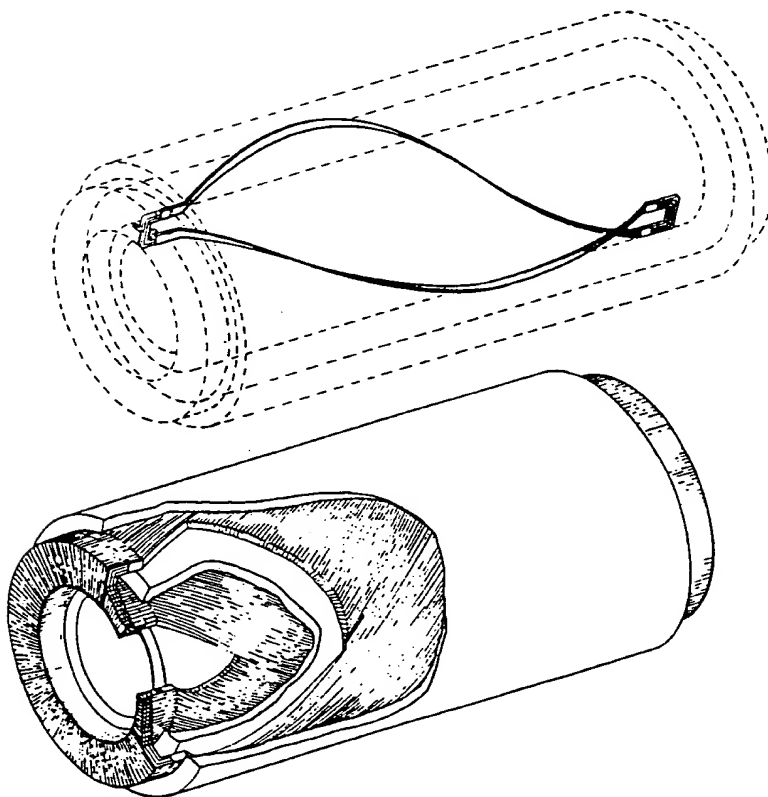
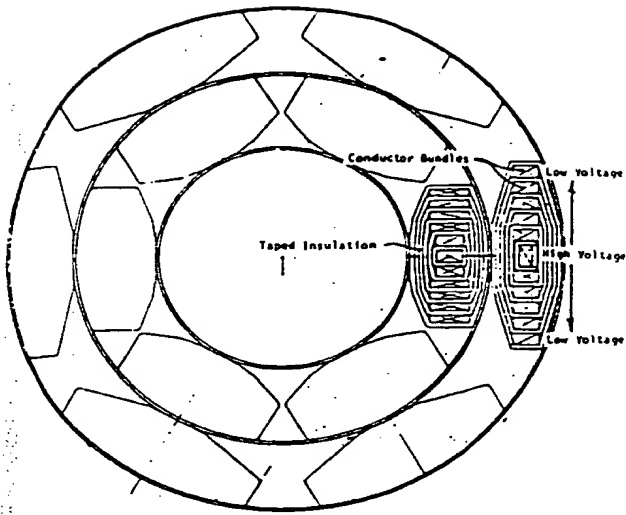
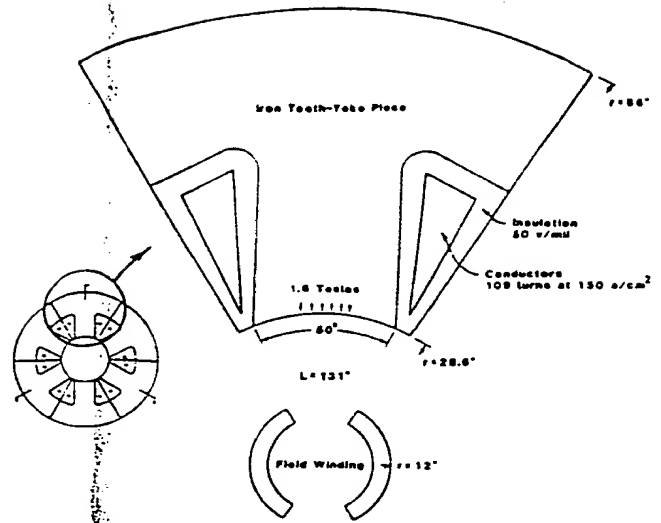


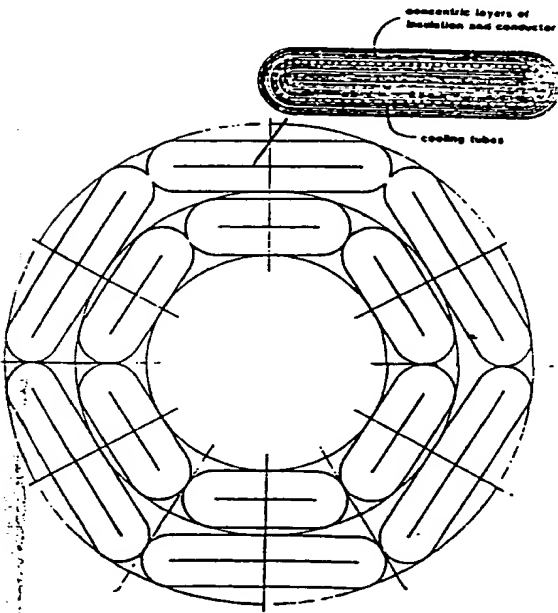
Figure 1-4. Fully Helical Winding for the Monolith Cylinder Armature



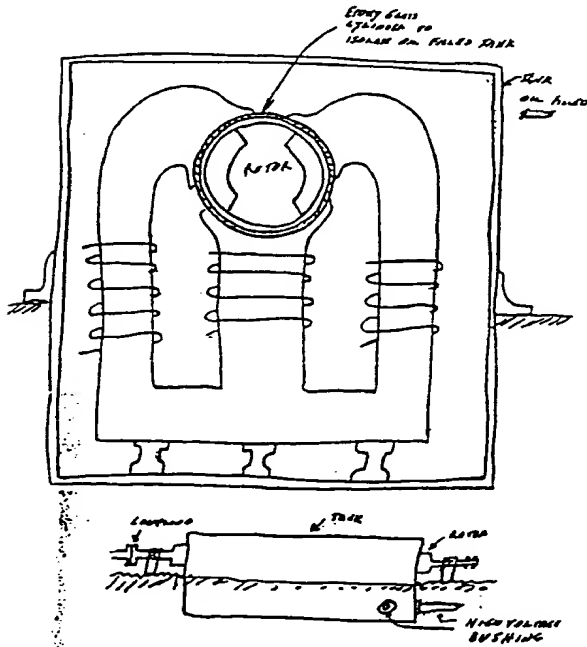
Integral-Insulated Phase Belt Armature
Taped System



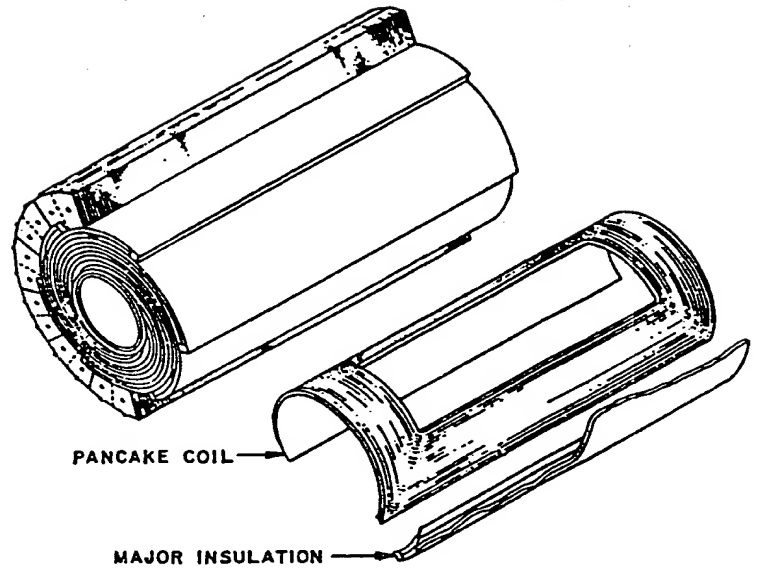
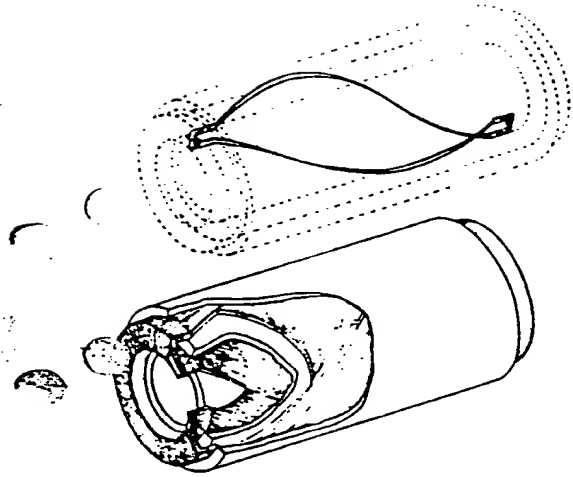
Salient Pole Stator
(six magnetic poles)



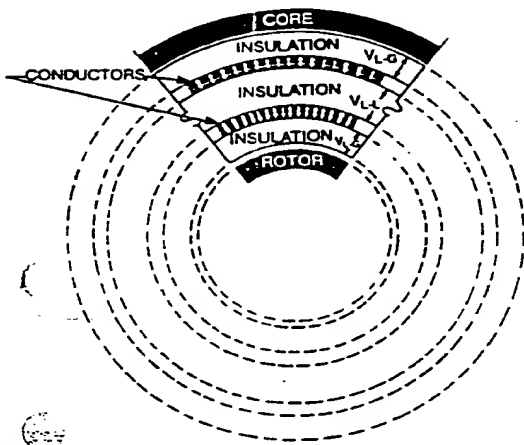
Integral-Insulated Phase Belt Armature
Coaxial System



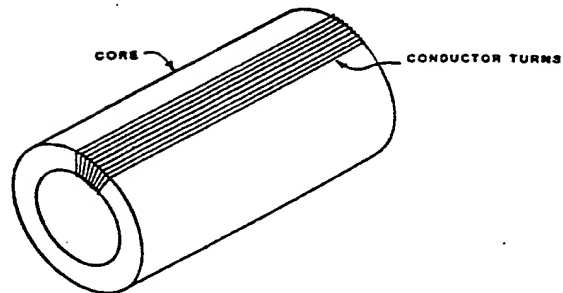
Salient Pole Stator
(three magnetic poles)



Spiral Pancake Armature



Monolith Cylinder Armature



Toroidal Armature

Figure 1-2. High-Voltage Generator Conceptual Designs.

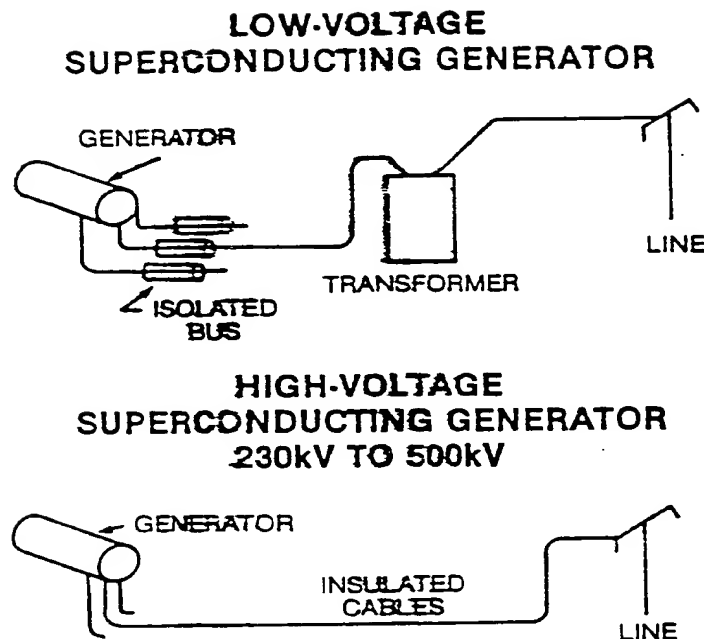


Figure 1-1. Connection of Generators to Transmission Lines with and without Step-up Transformers

valuable background for the technical and economical studies performed for the high-voltage superconducting generator. Many electromagnetic models and computer programs developed for the low-voltage superconducting generator were utilized for the high-voltage superconducting generator.

1.1 PRINCIPAL CONCLUSIONS

1.1.1 Primary Design Approach Selected

A large number of novel high-voltage generator conceptual designs were revealed during the study. Figure 1-2 displays the basic conceptual designs which were identified, and many variations of these designs were also identified. As a result of the design evaluations of the advantages, disadvantages and potentially critical problems of each design, it was concluded that the monolith cylinder armature has the best potential of being proven technically and economically feasible.

Detailed design analyses performed on monolith cylinder armature designs at 600 MVA, 345 kV and 1200 MVA, 500 kV ratings revealed a number of potentially critical technical problems. Analytical studies of each problem area indicated that there are viable solutions for all of the identified problems, but the maximum practical voltage was established to be 500 kV, since higher voltage ratings (765 kV and greater) would require uneconomically large unit sizes.

1.1.2 Description of the Monolith Cylinder Armature

The complete design details of the monolith cylinder armature are described in the various sections of this report, but a brief description of the armature will be provided here. Figure 1-3 illustrates a cross-section of the monolith cylinder armature in its most elementary form. Two cylinders of conductors are encapsulated by three cylinders of insulation, and the entire structure is fastened to a toothless iron core. The insulation cylinders must be thick enough to withstand the line-to-line and line-to-ground voltages imposed upon them. Each conductor layer cylinder can contain from one to two thousand individual conductors. Figure 1-4 illustrates the fully helical coil construction. The gently curving shape of these coils allows dense conductor packing and eliminates mechanical stress concentrations that can result from coil bends in other types of coil shapes. A novel delta-

Section 1

SUMMARY

Technical research and development efforts performed by the General Electric Company for the Electrical Power Research Institute under contract RP 1716 "High-Voltage Stator Winding Development" are described in this document. The goals of this research project were (1) to develop conceptual designs of large steam-turbine generators that can be connected to transmission systems without step-up transformers (Figure 1-1) and (2) to assess their technical and economical feasibility. The motivation for the development of such generators is to eliminate the purchase cost of the high-voltage step-up transformer and the operational cost of its losses. The general objectives of this research program were to—

- Review the technical literature (Appendix A) to identify all published conceptual designs of generators which can be operated at transmission-level voltages (230 kV and greater)
- Propose new conceptual designs for high-voltage generators
- Perform preliminary design studies of each conceptual design to identify critical problems and to propose possible resolutions
- Perform an evaluation program to select the conceptual design having the greatest potential of being proven technically and economically feasible
- Perform as detailed a design study as possible on the selected primary conceptual design to identify its physical characteristics and limitations. Design studies were performed for two-pole units of 600 MVA, 345 kV and 1200 MVA, 500 kV ratings
- Evaluate the power system implications of high-voltage generators
- Provide a comparative economic evaluation of conventional generators, low-voltage superconducting generators, and high-voltage generators
- Identify possible follow-on development effort based on an assessment of the technical feasibility of high-voltage generators and the magnitude of their potential benefit to the electric utility industry.

The concept of developing transmission-level-voltage generators has evolved, in part, from the extensive domestic and worldwide effort being performed to demonstrate the technical feasibility of superconducting generator rotors and their economic benefits to the electric utility industry. The successful development of superconducting rotors provides a unique opportunity to seriously consider designing generators at present-day transmission-level voltages, since the large excitation capability of the superconducting field makes it possible to employ air-gap armature windings having sufficient insulation thicknesses to support the transmission-level-voltage electrical stresses. The successful high-voltage generator would eliminate the capital cost of the step-up transformer and the operational cost of its electrical losses, and rough cost savings estimates indicate that these can amount to between 10 and 14 million dollars for a 1000 MVA unit. These cost savings are in addition to those associated with the superconducting rotor's elimination of the field electrical losses. The cost savings, however, must be weighed against the development costs of high-voltage superconducting generators, and the results of economical analyses performed in this study will indicate if follow-on development efforts are warranted.

This technical study was primarily directed at exploring the high-voltage stator winding concept. No significant effort was devoted to upgrade the designs of superconducting rotors and low-voltage air-gap armature windings. However, the General Electric Company's involvement with the EPRI sponsored development of low-voltage superconducting generators (Reference 1-1) provided in-

TABLES (Cont'd)

Table		Page
4.10-1	Reactance and Inertia Data for Transient Stability Studies	4-32
5.1-1	Best Spiral Pancake Armatures at 600 MVA 300 A/cm ² Maximum Current Density	5-7
5.2-1	600 MVA, 345 kV Salient-Pole Stator with Superconducting Rotor	5-14
5.2-2	Economic Comparison of the Salient-Pole Stator with the Monolith Cylinder Stator and a Conventional Generator 600 MVA	5-16
6.1-1	Economic Analysis Approach	6-2
6.2-1	Economic Study for Low-Voltage Superconducting Generators (1985 Dollars)	6-4
6.2-2	Economic Study for High-Voltage Superconducting Generators (1985 Dollars)	6-5
6.3-1	Average Added Equipment Capacity	6-8
6.4-1	Value to Users — Low-Voltage S.C.G. over Conventional Generators 1985 Dollars — \$1270/kW Efficiency Evaluation	6-10
6.4-2	Value to Users — High-Voltage S.C.G. over Conventional Generators 1985 Dollars — \$1270/kW Efficiency Evaluation	6-11
6.5-1	Development Cost Estimates Low-Voltage S.C.G.	6-13
C-1	Magnetic Flux Magnitudes (teslas)	C-7
C-2	Dimensions of a 1200 MVA — 500 kV High-Voltage Generator	C-7
C-3	Numerical Values of Magnetic Flux Magnitudes (teslas)	C-8
C-4	Force Magnitudes	C-8
C-5	Magnetic Flux Magnitudes for the Modified Winding (teslas)	C-10
C-6	Numerical Values of Magnetic Flux Magnitudes for the Modified Winding (teslas)	C-10
C-7	Force Magnitudes for the Modified Winding	C-10
J-1	Heat Rate Justified Investment	J-4

TABLES

Table		Page
1-1	Active Volume Relationships 600 MVA Generators	1-7
2.1-1	Required Insulation Cylinder Thicknesses for Various Voltage Ratings and Dielectric Strengths	2-6
2.1-2	Stated Mechanical Properties of Oil-Impregnated High-Density Pressboard	2-8
2.2-1	High-Voltage Generators at 600 MVA, 345 kV Diamond Coil Windings 150 A/cm ² Current Density, 50 kV/in. Insulation Stress	2-24
2.2-2	Best High-Voltage Generators of Each Rating Diamond Coil Windings 150 A/cm ² Current Density, 50 kV/in. Insulation Stress	2-26
2.2-3	600 MVA, 345 kV High-Voltage Generators Diamond Coil Windings Armature Current Density and Insulation Dielectric Stress Varied	2-27
2.2-4	Best High-Voltage Generators of the 600 MVA Rating Helical Coil Windings 300 A/cm ² Current Density, 50 kV/in. Insulation Stress	2-31
2.3-1	Dimensions of the 600 MVA, 345 kV Diamond Coil Armature High-Voltage Generator	2-33
2.4-1	Stresses Occurring at 90° After Sudden Short Circuit	2-61
2.4-2	Stresses Occurring at 180° After Sudden Short Circuit	2-64
2.6-1	Coolant Properties	2-84
2.6-2	Coolant Thermal Conductivities	2-89
2.6-3	Thermal Conductivities of the Winding Materials	2-91
2.10-1	High Voltage Generators at 1200 MVA, 500 kV Helical Coil Windings 300 A/cm ² Current Density, 50 kV/in. Insulation Stress	2-128
2.10-2	High Voltage Generators at 1200 MVA, 500 kV Diamond Coil Windings 150 A/cm ² Current Density, 50 kV/in. Insulation Stress	2-128
3-1	Circuit Parameters of Series-Resonance Overvoltage Tests for High-Voltage Generators	3-5
4.1-1	Insulation Coordination	4-4
4.2-1	Basic Data for Fault Calculations	4-12
4.2-2	Fault Current Levels for Wye-Connected High-Voltage Generators	4-12
4.2-3	Fault Current Levels for Delta-Connected High-Voltage Generators	4-14
4.3-1	Effect of External Field Resistance R_F	4-18
4.8-1	Peak Shaft Torques	4-29

100

1. The first part of the report is a general introduction to the subject of the study. It discusses the importance of the study and the objectives of the research. It also mentions the scope of the study and the limitations of the study.

2. The second part of the report is a literature review. It discusses the previous studies on the subject of the study. It also mentions the gaps in the literature and the need for the study.

3. The third part of the report is a methodology section. It discusses the research design, the data collection methods, and the data analysis methods. It also mentions the ethical considerations of the study.

4. The fourth part of the report is a results section. It discusses the findings of the study. It also mentions the statistical analysis of the data and the interpretation of the results.

5. The fifth part of the report is a conclusion section. It discusses the conclusions of the study. It also mentions the implications of the study and the recommendations for future research.

6. The sixth part of the report is a bibliography. It lists the references used in the study. It also mentions the sources of the data and the materials used in the study.

7. The seventh part of the report is an appendix. It contains the raw data of the study. It also mentions the supplementary materials used in the study.

8. The eighth part of the report is a glossary. It defines the terms used in the study. It also mentions the abbreviations used in the study.

9. The ninth part of the report is a list of figures. It lists the figures used in the study. It also mentions the captions of the figures.

ILLUSTRATIONS (Cont'd)

Figure		Page
5.4-3	Comparison of Two-Layer and Single-Layer Coaxial Integral-Insulated Phase-Belt Windings	5-23
6.2-1	Typical Sensitivity Study for Variations in Development Costs and Savings Estimates	6-6
6.4-1	High, Average, and Low Cost Differentials of Superconducting Generators over Conventional Generators	6-9
6.4-2	Potential User Savings (1985 Dollars) of Superconducting Generators over Conventional Generators	6-12
8.2-1	Low- and High-Voltage Model Superconducting Generators	8-4
B-1	Coil Shape Terminology	B-1
B-2	Illustration of Coil Packing	B-2
B-3	Variation of Rating with End Arm Length and Overhang Length for Fully Pitched Coils with Constant Bar Dimensions and Constant Current Density; $r = 25$ in., $L_s = 100$ in.	B-3
C-1	Cross-Section of a 120° Phase-Belt Winding	C-1
C-2	Flux Distribution of a 120° Phase-Belt Winding	C-3
C-3	Pressure Distributions Producing Offsetting Forces	C-5
C-4	Modified 120° Phase-Belt Winding	C-9
D-1	Field and Circuit Models of a Heat Generating Solid	D-2
E-1	Thermal Circuit Diagram	E-2
F-1	Coil Labeling of a Two-Circuit Winding	F-1
F-2	Developed View of Helical Coils	F-2
F-3	Radii Terminology of the Helical Armature	F-3
G-1	Concentric Helices Formed from Concentric Arcs	G-1

ILLUSTRATIONS (Cont'd)

Figure		Page
4.10-1	Comparison of Critical Clearing Times for High-Voltage and Conventional Generators	4-33
5.1-1	Spiral Pancake Armature Illustrating Pancake Coils	5-1
5.1-2	Cross-Section of a High-Voltage Spiral Pancake Armature	5-2
5.1-3	Winding Pattern of a Two-Layered Pancake Coil	5-3
5.1-4	Details of a High-Voltage Spiral Pancake Armature	5-4
5.1-5	Model of a Spiral Pancake Armature	5-5
5.1-6	Determination of Current Density for the Spiral Pancake Model	5-6
5.1-7	Insulation Wedge Separating Pancake Coil Layers	5-6
5.1-8	Size Comparison of Monolith Cylinder and Spiral Pancake Armatures	5-8
5.1-9	600 MVA, 345 kV Monolith Cylinder Armature, to Scale with Figure 5.1-5	5-8
5.1-10	Electrostatic Study Region of the High-Voltage Spiral Pancake Armature	5-9
5.1-11	Electrostatic Field Solution of the High-Voltage Spiral Pancake Armature	5-10
5.1-12	Spiral Pancake Electrostatic Stress Riser	5-11
5.1-13	Creepage Criterion Plot of the High-Voltage Spiral Pancake Armature	5-12
5.1-14	Creepage Baffles for the High-Voltage Spiral Pancake Armature	5-12
5.2-1	Rough Design of a Salient-Pole Stator	5-13
5.2-2	Division of Salient-Pole Stator Flux into Two Portions (a) Flux Producing Gap Inductance L_g and (b) Flux Producing Leakage Inductance L_l	5-15
5.3-1	Cross-Section of an Integral-Insulated Phase-Belt Armature with Taped Insulation	5-17
5.3-2	End Connections for the Integral-Insulated Phase-Belt Armature with Taped Insulation	5-19
5.3-3	Model of the End Connections for the Integral-Insulated Phase-Belt Armature with Taped Insulation	5-20
5.4-1	Cross-Section of an Integral-Insulated Phase-Belt Armature with Coaxial Phase-Belts	5-21
5.4-2	End-Region Connections of the Coaxial Integral-Insulated Phase-Belt Armature	5-22

ILLUSTRATIONS (Cont'd)

Figure		Page
4.1-5	Station Arrangement and Grounding for Wye-Connected High-Voltage Generators	4-6
4.1-6	Cost Comparison for Auxiliary Transformer Grounding of Delta-Connected High-Voltage Generators	4-8
4.1-7	Cost Comparison for Separate Zig-Zag Transformer Grounding of Delta-Connected High-Voltage Generators	4-9
4.2-1	Three-Phase Fault Current Levels for Conventional and High-Voltage Generators	4-10
4.2-2	Generator Fault Currents (ac Component) for System Line-to-Ground Faults	4-11
4.2-3	Fault Current Levels and Load Rejection Overvoltages for Wye-Connected High-Voltage Generators	4-13
4.2-4	Fault Current Levels for Delta-Connected High-Voltage Generators	4-15
4.3-1	System Model for Load Rejection Studies	4-16
4.3-2	High-Voltage Generator Load Rejection Without Fault, $R_F = 1.5 \Omega$	4-17
4.3-3	High-Voltage Generator Load Rejection with Line-to-Ground Fault on Phase A, $R_F = 1.5 \Omega$	4-17
4.3-4	High-Voltage Generator Load Rejection with Line-to-Ground Fault on Phase A (Expanded Time Scale)	4-18
4.3-5	High-Voltage Generator Load Rejection with Line-to-Ground Fault on Phase A, $R_F = .75 \Omega$	4-19
4.4-1	Fault Current Duties for the High-Voltage Generator Auxiliary Transformers	4-20
4.6-1	Gas-Insulated Buswork for the High-Voltage Generator	4-21
4.7-1	Arrangements of Circuit Leads and Current Transformers for the Protection of the Delta-Connected High-Voltage Armature Winding	4-23
4.7-2	Protection Arrangement for the Single-Delta Circuit-Lead Configuration	4-25
4.7-3	Protection Arrangement for the Double-Delta Circuit-Lead Configuration	4-26
4.7-4	Air-Core Current Transformers and Internally Mounted Relaying Electronics for Split-Phase Protection	4-27
4.8-1	Fault Torque on the Turbine-to-Generator Shaft for a 892 MVA Turbine Connected to the High-Voltage Generator	4-30
4.8-2	Fault Torque on the Turbine-to-Generator Shaft for a 815 MVA Turbine Connected to the High-Voltage Generator	4-30
4.8-3	Fault Torque on the Turbine-to-Generator Shaft for a 690 MVA Turbine Connected to the High-Voltage Generator	4-31

ILLUSTRATIONS (Cont'd)

Figure		Page
2.7-8	Calculated Surge Voltage Distributions for the 600 MVA Armature	2-114
2.7-9	Maximum Turn-to-Turn Voltages for the 600 MVA Armature	2-114
2.8-1	Leaf Spring Frame Design for the High-Voltage Generator	2-117
2.8-2	Application of a Leaf Spring Frame Design to a Conventional Generator	2-118
2.8-3	Clamping Mechanism for the Polygonal Core-to-Armature Interface	2-120
2.8-4	Core Loss of 14 Mil Grain-Orientated Silicon Steel at 60 Hz	2-121
2.8-5	Placement of Core Cooling Passages	2-122
2.8-6	Core Cooling Performance	2-123
2.9-1	Laminated Construction of the Monolith Cylinder Armature	2-125
2.9-2	Axial Ventilation Passages in the Insulation Cylinders	2-126
2.9-3	Fabrication of a Vertical Divider	2-126
2.9-4	Fabrication of a Horizontal Divider	2-127
2.10-1	Radial Winding Pressure on Three-Phase Short Circuit from Rated Voltage, 180° After Fault. 1200 MVA, 500 kV, $X''=.215$	2-129
2.10-2	Tangential Winding Pressure on Three-Phase Short-Circuit from Rated Voltage, 180° After Fault. 1200 MVA, 500 kV, $X''=.215$	2-130
2.10-3	Radial Winding Pressure on Three-Phase Short Circuit from Rated Voltage, 90° After Fault. 1200 MVA, 500 kV, $X''=.215$	2-130
2.10-4	Tangential Winding Pressure on Three-Phase Short Circuit from Rated Voltage, 90° After Fault. 1200 MVA, 500 kV, $X''=.215$	2-131
2.10-5	1200 MVA, 500 kV Winding Design Using Transil Oil Coolant	2-132
3-1	Impulse Waveforms	3-2
3-2	Voltage Distribution Within a Disc-Coil Transformer During Voltage Impulse	3-3
3-3	Series Resonance Circuit for the Overvoltage Test of High-Voltage Generators	3-4
4.1-1	Overvoltage on the Unfaulted Phases During a Line-to-Ground Fault at the Generator Terminals	4-2
4.1-2	System Grounding of a Conventional Unit Generator-Transformer	4-3
4.1-3	Load-Rejection Overvoltages	4-3
4.1-4	Station Arrangement and Grounding for Delta-Connected High-Voltage Generators	4-6

ILLUSTRATIONS (Cont'd)

Figure		Page
2.5-10	Electrostatic Field Solution of a 600 MVA, 500 kV Monolith Cylinder End Region (Case #3)	2-75
2.5-11	Creepage Plots for the 600 MVA, 500 kV Monolith Cylinder End Region (Case #3)	2-76
2.5-12	Peripheral Creepage Baffles in the Monolith Cylinder End Region	2-77
2.5-13	Peripheral Creepage of the 60° Phase-Belt Two-Circuit Delta-Connected Winding Calculated Over the Same 90° Path for Successive Instances of Time	2-78
2.5-14	Vertical Dividers Used as Peripheral Creepage Baffles	2-79
2.6-1	Cooling Scheme for the Monolith Cylinder High-Voltage Generator (Illustrating Flooded End Region Coolant Header)	2-81
2.6-2	Components of the Monolith Cylinder Conductor Layer	2-82
2.6-3	Laminar Flow Friction Coefficient for Rectangular Ducts	2-84
2.6-4	Viscosity of Transil Oil and Silicone Oil vs. Temperature	2-85
2.6-5	Specific Heat of Transil Oil vs. Temperature	2-85
2.6-6	Relative Permittivity of Oil-Impregnated Pressboard vs. Temperature	2-87
2.6-7	Dissipation Factor of Oil-Impregnated Pressboard vs. Temperature	2-87
2.6-8	Modified Nusselt Number vs. Aspect Ratio for Laminar Flow in Rectangular Ducts	2-89
2.6-9	Segmentation of Winding for Cooling Calculations	2-89
2.6-10	Thermal Resistance Circuit for the Calculation of Winding Component Temperatures	2-90
2.6-11	Winding Design with Transil Oil Coolant	2-93
2.6-12	Interpretation of Temperature Profile Listings	2-95
2.6-13	Winding Design with Freon Coolant	2-97
2.6-14	Winding Design with Silicone Oil Coolant	2-99
2.6-15	Substitute Cooling Tubes	2-101
2.6-16	Winding Design Using Cooling Tubes with Center Walls	2-102
2.7-1	Lumped Parameter Circuit Model of an Armature Winding	2-104
2.7-2	Reduced-Order Model Structure	2-105
2.7-3	Ladder Model of Inductances	2-110
2.7-4	One Cell of the Ladder Model	2-111
2.7-5	Calculated Surge Voltage Waveforms in the 60 kVA Armature	2-112
2.7-6	Measured Surge Voltage Waveforms in the 60 kVA Armature	2-112
2.7-7	Calculated Surge Voltage Waveforms for the 600 MVA Armature	2-113

ILLUSTRATIONS (cont'd)

Figure		Page
2.4-26	Contour Plot of the $r-\theta$ Shear Stress, 90° after Sudden Short Circuit Polygonal Interface	2-60
2.4-27	Deflection of the Armature Structure, 180° after Sudden Short Circuit Polygonal Interface	2-62
2.4-28	Contour Plot of the Radial Stress Structure, 180° after Sudden Short Circuit, High-Modulus Polygonal Interface	2-62
2.4-29	Contour Plot of the Radial Stress Structure, 180° after Sudden Short Circuit Polygonal Interface	2-62
2.4-30	Contour Plot of the Peripheral Stress Armature Structure, 180° after Sudden Short Circuit, High-Modulus Polygonal Interface	2-63
2.4-31	Contour Plot of the Peripheral Stress Core, 180° after Sudden Short Circuit Polygonal Interface	2-63
2.4-32	Contour Plot of the $r-\theta$ Shear Stress Armature Structure, 180° after Sudden Short Circuit, High-Modulus Polygonal Interface	2-63
2.4-33	Contour Plot of the $r-\theta$ Shear Stress Core, 180° after Sudden Short Circuit, High-Modulus Polygonal Interface	2-64
2.5-1	Electrostatic Field Solution of a 345 kV Monolith Cylinder End Region	2-66
2.5-2	Creepage Plots of the Lower Creepage Region for the 600 MVA, 345 kV Monolith Cylinder End Region	2-67
2.5-3	Creepage Plots of the Upper Creepage Region for the 600 MVA, 345 kV Monolith Cylinder End Region	2-68
2.5-4	Electrostatic Field Solution of a 345 kV Monolith Cylinder End Region Contours	2-69
2.5-5	Creepage Plots for the 600 MVA Monolith Cylinder End Region with Round Edges	2-70
2.5-6	Electrostatic Field Solution of a 345 kV Monolith Cylinder End Region	2-71
2.5-7	Creepage Plots for the 600 MVA Monolith Cylinder End Region (Case #1)	2-72
2.5-8	Electrostatic Field Solution of a 345 kV Monolith Cylinder End Region	2-73
2.5-9	Creepage Plots for the 600 MVA Monolith Cylinder End Region (Case #2)	2-74

ILLUSTRATIONS (Cont'd)

Figure		Page
2.4-7	Contour Plot of the Peripheral Stress, 90° after Sudden Short Circuit	2-49
2.4-8	Contour Plot of the Radial Stress, 90° after Sudden Short Circuit	2-50
2.4-9	Contour Plot of the $r-\theta$ Shear Stress, 90° after Sudden Short Circuit	2-50
2.4-10	Deflection of the Armature Structure and the Core, Rated Load	2-51
2.4-11	Contour Plot of the Peripheral Stress, Rated Load	2-51
2.4-12	Contour Plot of the Radial Stress, Rated Load	2-52
2.4-13	Contour Plot of the $r-\theta$ Shear Stress, Rated Load	2-52
2.4-14	Deflection of the Armature Structure and Core, Low-Modulus Insulation, 180° after Sudden Short Circuit	2-53
2.4-15	Contour Plot of the Peripheral Stress, Low-Modulus Insulation, 180° after Sudden Short Circuit	2-54
2.4-16	Contour Plot of the Radial Stress, Low-Modulus Insulation, 180° after Sudden Short Circuit	2-54
2.4-17	Contour Plot of the $r-\theta$ Shear Stress, Low-Modulus Insulation, 180° after Sudden Short Circuit	2-55
2.4-18	Finite Element Model of the Armature Structure and Core with Polygonal Interface	2-56
2.4-19	Deflection of the Armature Structure and Core, 90° after Sudden Short Circuit, Low-Modulus Polygonal Interface	2-57
2.4-20	Deflection of the Armature Structure and Core, 90° after Sudden Short Circuit, High-Modulus Polygonal Interface	2-57
2.4-21	Contour Plot of the Radial Stress in the Armature Structure, 90° after Sudden Short Circuit, High-Modulus Polygonal Interface	2-58
2.4-22	Contour Plot of the Radial Stress in the Core, 90° after Sudden Short Circuit, High-Modulus Polygonal Interface	2-58
2.4-23	Contour Plot of the Peripheral Stress in the Armature Structure, 90° after Sudden Short Circuit, High-Modulus Polygonal Interface	2-59
2.4-24	Contour Plot of the Peripheral Stress in the Core, 90° after Sudden Short Circuit, High-Modulus Polygonal Interface	2-59
2.4-25	Contour Plot of the $r-\theta$ Shear Stress in the Armature Structure, 90° after Sudden Short Circuit, High-Modulus Polygonal Interface	2-60

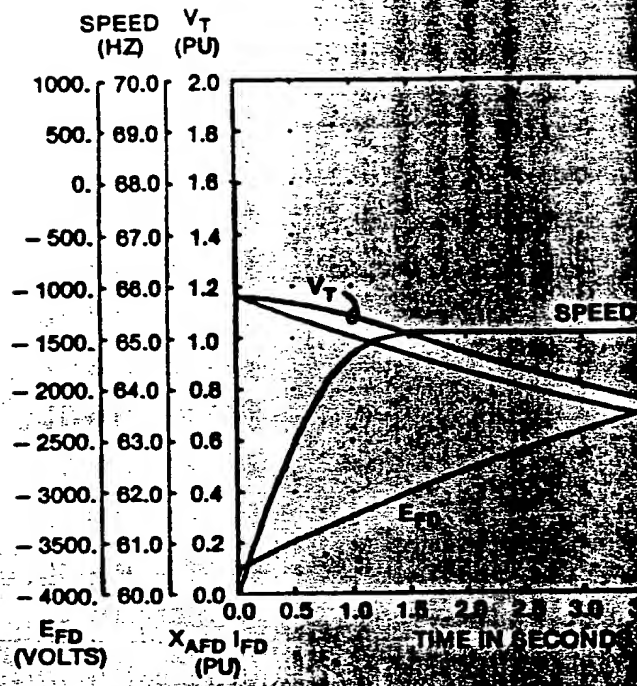


Figure 4.3-2. High-Voltage Generator Load Rejection With $R_f = 1.5 \Omega$

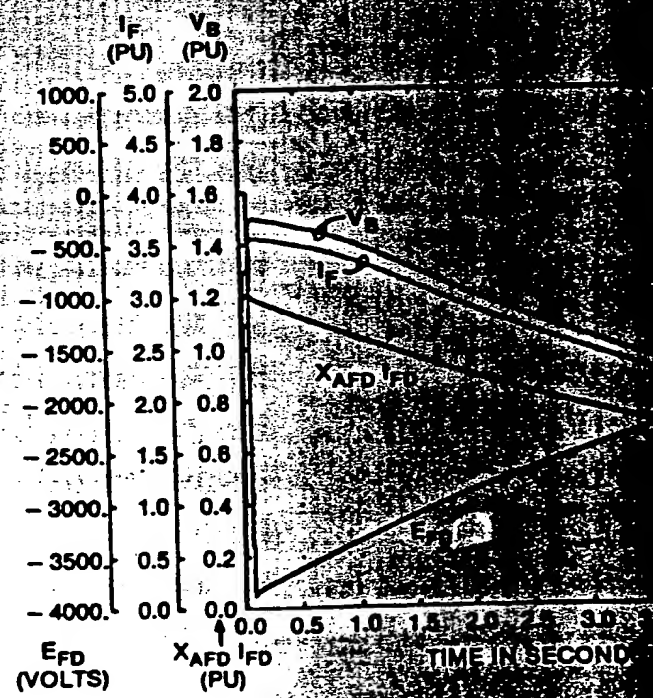


Figure 4.3-3. High-Voltage Generator Load Rejection with Fault on Phase A, $R_f = 1.5 \Omega$

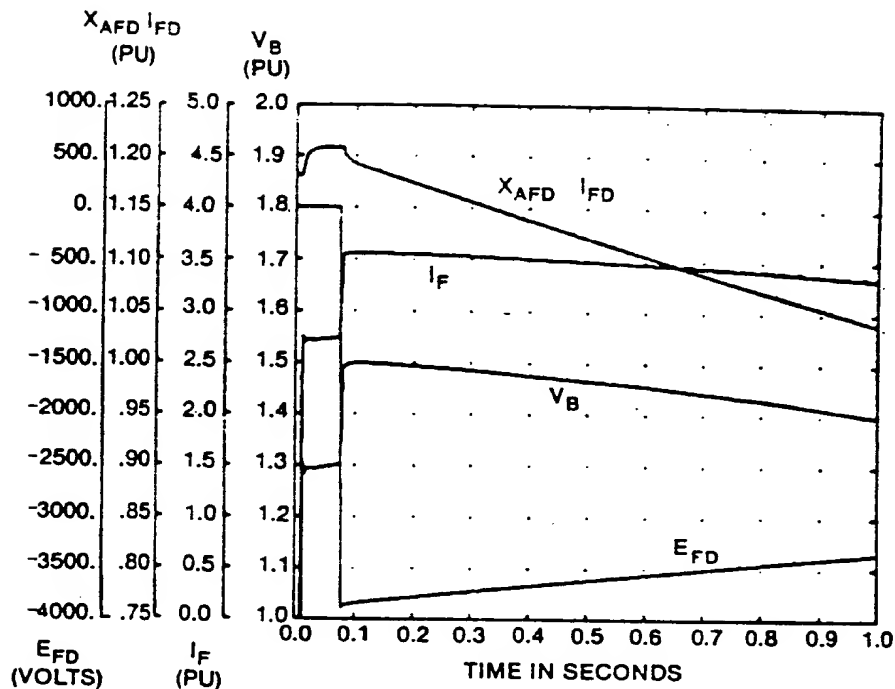


Figure 4.3-4. High-Voltage Generator Load Rejection with Line-to-Ground Fault on Phase A (Expanded Time Scale)

The degree of overvoltage that is experienced is influenced by the de-excitation speed that can be employed. The limits of the de-excitation speed depend on the maximum short-time field voltages which can be tolerated. In both of the studied load rejection cases, the field is de-excited at $t = .067$ s by switching a 1.5Ω resistor across the field. This causes approximately 4000 V to appear on the superconducting field, which Reference 4-5 judges to be a reasonable maximum. In order to explore the effect of de-excitation rate on short-time overvoltages, a range of discharge resistor values was considered. The results given in Table 4.3-1 indicate a negligible effect on the peak voltage, although the time of decay is directly affected. Figure 4.3-5 illustrates the initial load rejection profile with a 0.75Ω discharge resistor.

Table 4.3-1
EFFECT OF EXTERNAL FIELD RESISTANCE R_F

R_F	Max. V_B	Max. E_{fd}	T_F
.75 Ω	1.514 pu	1942. V	13.5 s
1.5	1.50	3882.	6.8
3.0	1.496	7758.	3.4

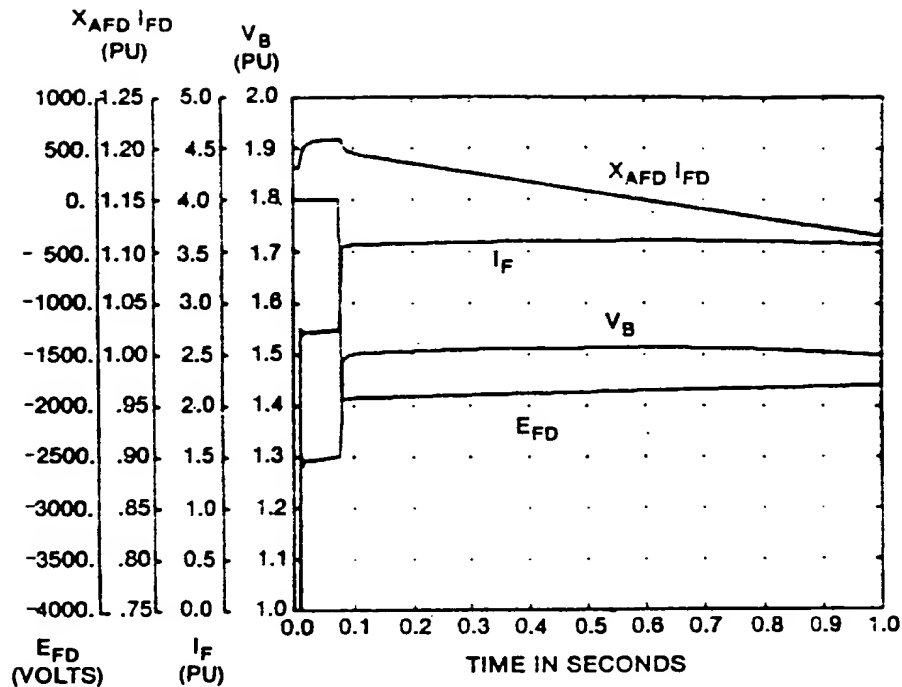


Figure 4.3-5. High-Voltage Generator Load Rejection with Line-to-Ground Fault on Phase A, $R_F = .75 \Omega$

4.4 GROUNDING TRANSFORMER SHORT-TIME FAULT CURRENT REQUIREMENTS

Grounding for the delta-connected high-voltage generator is accomplished with the unit auxiliary transformers, which in their role as grounding transformers must also carry substantial short-time ground fault currents. The severest fault condition would be like the load rejection cases studied in Section 4.3, where a permanent line-to-ground fault is assumed and the fault current decays at a rate that is a function of the machine time constants. While such duty is unique insofar as grounding duty is considered, the long-time fault current decrement duty on the auxiliary transformers is not. Reference 4-6 discusses the through-fault current decrements which a typical unit auxiliary transformer must withstand. As a basis of comparison, the per unit transformer winding current for the high-voltage generator fault conditions illustrated in Figures 4.3-3 and 4.3-5 are plotted on Figure 4.4-1 together with typical fault current duties derived in Reference 4-6. It is apparent that even with the 0.75Ω field winding discharge resistor, the short-time duty for the high-voltage generator auxiliary transformers is not excessive.

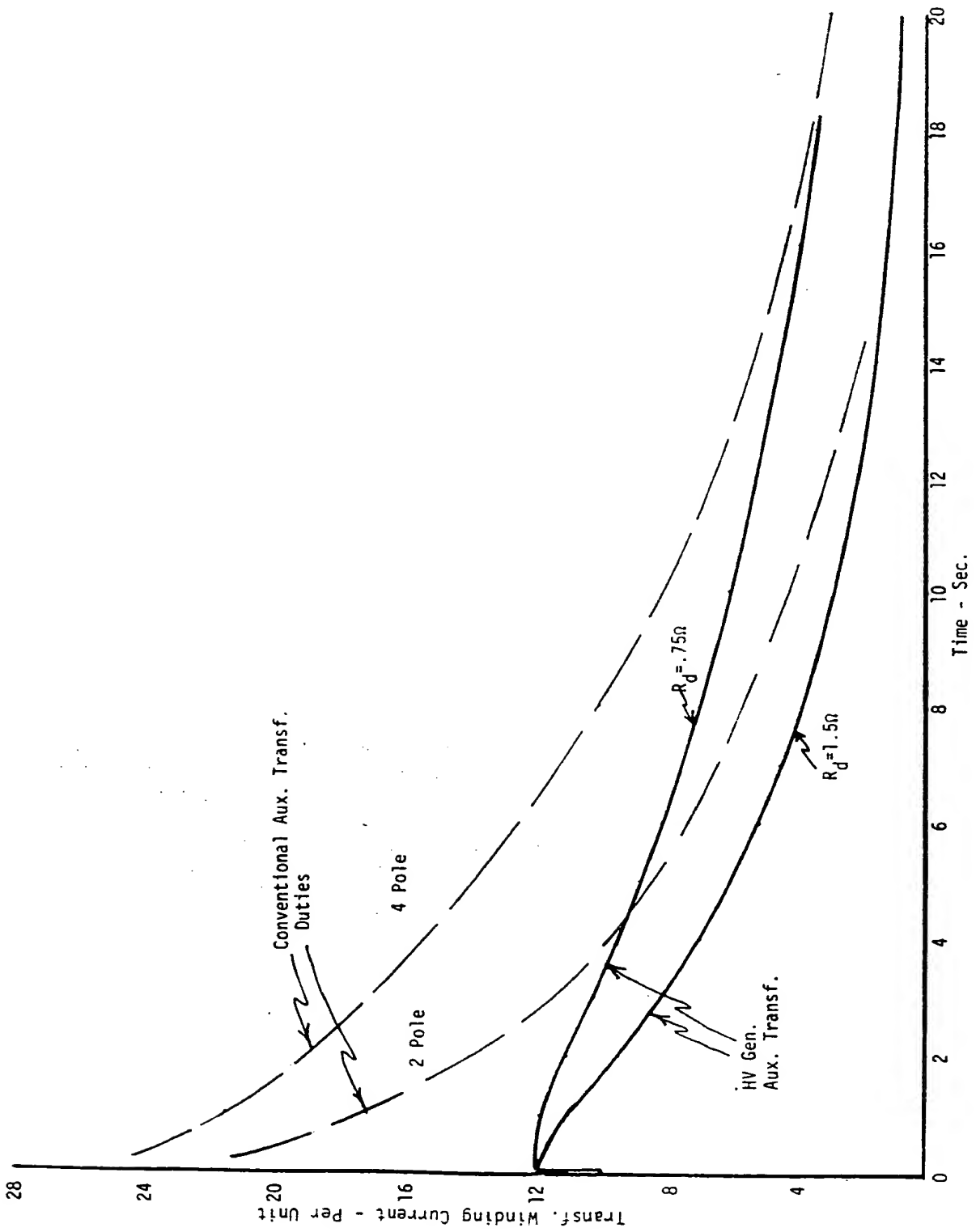


Figure 4.4-1. Fault Current Duties for the High-Voltage Generator Auxiliary Transformers

4.5 LINE RELAYING CONSIDERATIONS

The influence of the degree of system grounding provided at the generating station on the ability of the line relays to operate correctly for line-to-ground faults was investigated. Effective line relaying is provided with negative sequence current quantities, so this should not be a factor in considering delta-connected high-voltage generators and the degree of grounding provided.

4.6 GENERATOR LEADS

The main leads of the high-voltage generator will require no major development, since they will utilize either SF₆ gas-insulated buswork or high-voltage cable. There is much 345 kV cable experience but little experience at higher transmission voltages. The gas-insulated bus is available for all transmission voltages.

Cable connection to the switchyard would be made without intermediate taps because auxiliary transformer, surge arrester, etc., connections could be made in the high-voltage switchyard. Gas-insulated buswork could provide a little more flexibility in equipment location. Figure 4.6-1 illustrates one arrangement schematically.

The overall physical dimensions of gas-insulated bus containment is not significantly different in diameter than the isolated phase bus of a conventional unit. The inner current-carrying conductor of the gas-insulated system carries far less current, but it must be designed for control of much higher voltage stresses. Any cost difference between high-voltage generator buswork and conventional generator buswork will be relatively small and will not be a significant factor in the economic appraisal of the high-voltage generator.

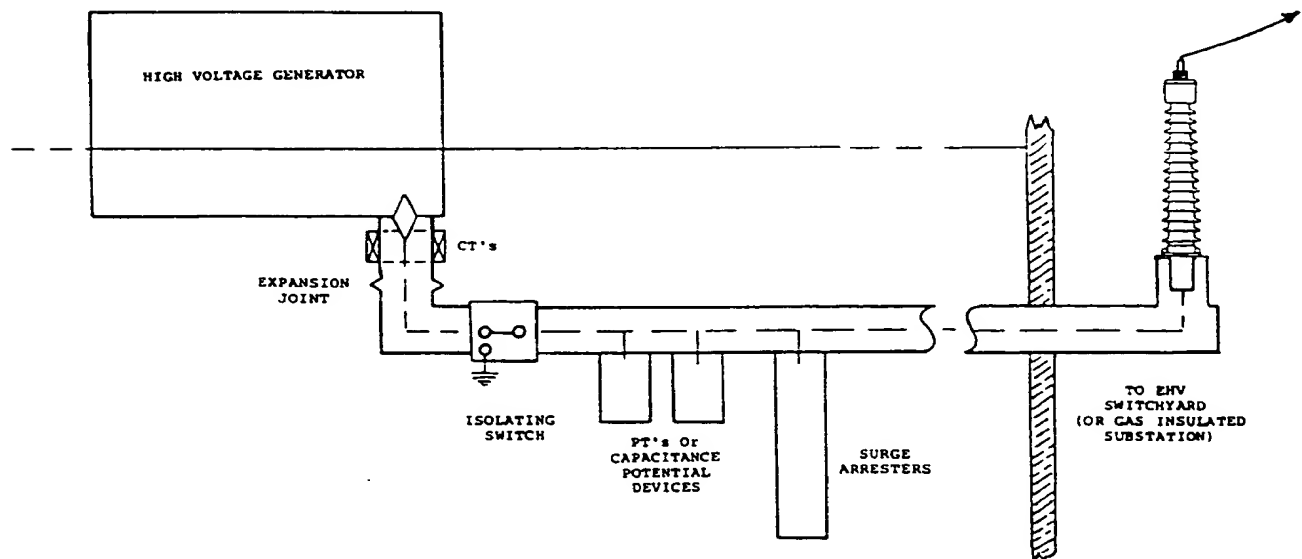


Figure 4.6-1. Gas-Insulated Buswork for the High-Voltage Generator

4.7 PROTECTION OF HIGH-VOLTAGE GENERATORS

The preferred winding arrangement for the high-voltage armature is the 60° phase-belt, two-circuit delta arrangement illustrated in Figures 2.1-15 and 2.1-16. In determining the protection for this type of winding, two arrangements of the circuit leads are considered, as shown in Figure 4.7-1.

The arrangement illustrated in Figure 4.7-1A is labeled the *single-delta arrangement* because the two circuits of each phase are paralleled internally and only one set of delta connections is required. The two phase leads of each phase are brought out through high-voltage bushings and the delta connections are performed externally. Current transformers (CTs) are placed in each circuit and in the high-voltage bushings. Additional CTs are shown in the generator leads.

The arrangement illustrated in Figure 4.7-1B is labeled the *double-delta arrangement* because two separate delta connections are performed internally from the two sets of circuits. Leads from each delta junction are exited through high-voltage bushings and the deltas are paralleled externally. This arrangement is the most natural to the winding and requires the least amount of internal lead-work. CTs are placed in the bushings and in the generator leads.

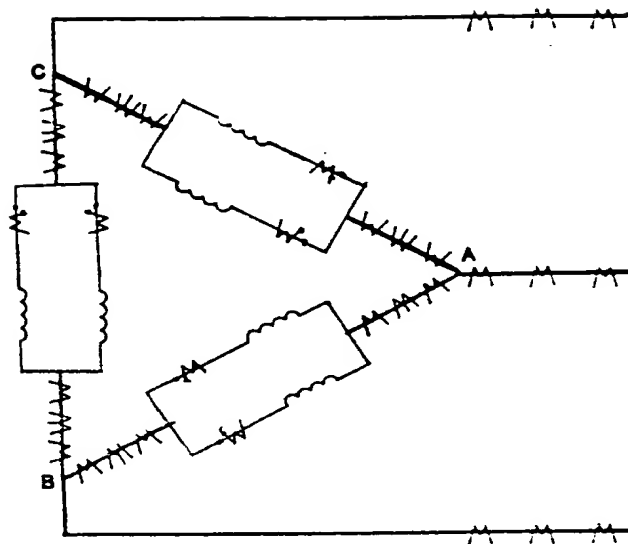
While in each arrangement there are three CTs in each bushing and three CTs in each lead, only four CTs per phase are actually required for protection purposes. It should be noted that the CTs in the generator leads are free-standing high-voltage CTs.

4.7.1 Protection Arrangements

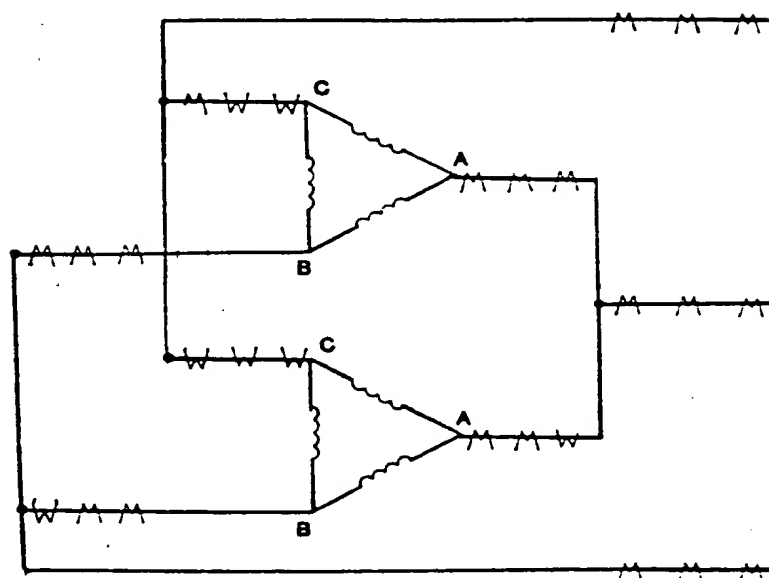
Figures 4.7-2 and 4.7-3 illustrate the proposed protection arrangements for the two circuit-lead configurations. These arrangements provide fault protection for both the stator and the rotor and protection for abnormal operating conditions. For purposes of clarity, only one phase of the stator fault protection is shown.

Protection is provided for the following conditions:

Device Number	Protection
21	Impedance relay for backup protection for uncleared system phase faults.
21G	Impedance relay for backup protection for faults in the generator and generator leads
32	Reverse power relay for antimotoring protection
40	Impedance relays for detection of loss of excitation
46	Negative sequence overcurrent relay for the detection of unbalanced currents
51TN	Time overcurrent relay for backup protection for uncleared system ground faults
59VHZ	Volts/hertz relay for overexcitation protection
60	Voltage balance relay for detecting a blown fuse in the potential transformer circuits
64F	Voltage relay for detecting ground faults in the field
78	Impedance relay scheme for detecting a loss of synchronism
81	Under frequency relay to detect prolonged operation at reduced frequencies
87B	Differential relay. In Figure 4.7-2, this relay provides backup protection for generator faults and primary protection for the leads from the generator to the circuit breakers. In Figure 4.7-3, this relay provides only primary protection for the leads from the generator to the circuit breakers.



(A) Single-Delta Configuration



(B) Double-Delta Configuration

Figure 4.7-1. Arrangements of Circuit Leads and Current Transformers for the Protection of the Delta-Connected High-Voltage Armature Winding

- 87G1 Split phase differential relay. In Figure 4.7-2, this relay is primarily intended for the detection of stator turn and ground faults. In Figure 4.7-3, this relay provides protection for turn faults, multiphase faults, and ground faults in the stator.
- 87G2 Differential relay for the detection of phase and ground faults in the generator
- 87GN Zero sequence current differential relay for the detection of ground faults in the generator and generator leads

For the most part, it appears that devices 21, 32, 40, 46, 51TN, 59, 60, 64F, 78, and 81 will provide the same degree of generator protection for either circuit-lead configuration, and the protection provided would be essentially the same as for present-day conventional generators. On the other hand, there is some difference in the sensitivity and coverage provided for stator fault protection between the two circuit-lead configurations. Therefore, the fault protection for the single-delta and double-delta configurations will be discussed in more detail.

4.7.2 Fault Protection for the Single-Delta Configuration

The protection arrangement shown in Figure 4.7-2 provides the same degree of sensitive and comprehensive protection as that provided on present-day wye-connected conventional generators. In fact, the ground fault sensitivity may even be greater.

The primary protection for the stator windings is provided by devices 87G1 and 87G2. As mentioned previously, device 87G1 is a split-phase differential relay which provides stator turn fault and ground fault protection. The sensitivity of this protection is dependent on the amount of current unbalance between the two circuits in each phase, because the relay will have to be set above the level of any circulating current caused by circuit magnetic unbalance. While there is no turn fault short circuit current data available for the generator being considered, some previous work performed by the Massachusetts Institute of Technology on a similar type of generator indicates that, assuming no initial unbalance, a conventional differential relay would be able to detect a turn fault having as much as a .01 Ω fault resistance.

The current transformers for the split-phase protection must be placed internally and are therefore prevented by space restrictions from being conventional-bushing-type CTs. Low-voltage air-core current transformers utilizing internally mounted relaying electronics for a fiber-optic alarm-signal transmission could be easily substituted. Figure 4.7-4 illustrates one such possible arrangement. Development work would be required for the specific application; however, the basic technology is well established and is described in References 4-7 and 4-8.

Fault pressure relays widely used for transformer internal fault detection should be applicable to the high-voltage generator. It should also be possible to provide sensitive incipient fault detection through the use of gas detection and/or gas analysis devices presently used on power transformers. Potential faults in the stator may start as localized hot spots in the stator winding. Such faults will generate small amounts of gas which can be detected by a gas detector relay or through a microprocessor-based oil monitor. The gas detector relay is a simple float-type of device which accumulates any gas generated in the stator. When a given amount of gas is accumulated, the relay will sound an alarm. The gas can then be analyzed to determine the existence of an incipient fault. Concentrations of certain gases indicate dielectric degradation, arcing, corona, or hot spots. The microprocessor-based oil monitor provides a sophisticated method for measuring concentrations of dissolved gases in oil. This equipment can be programmed to extract oil samples at preset time intervals and then determine the concentration of nine different gases through chromatographic analysis. The data is stored and displayed in bar chart form on a paper chart recorder. Again, the concentration of certain gases would indicate an incipient fault in the unit. Additional development work would be required to study the adaptability of transformer fault pressure relays or gas analysis devices to the high-voltage generator.

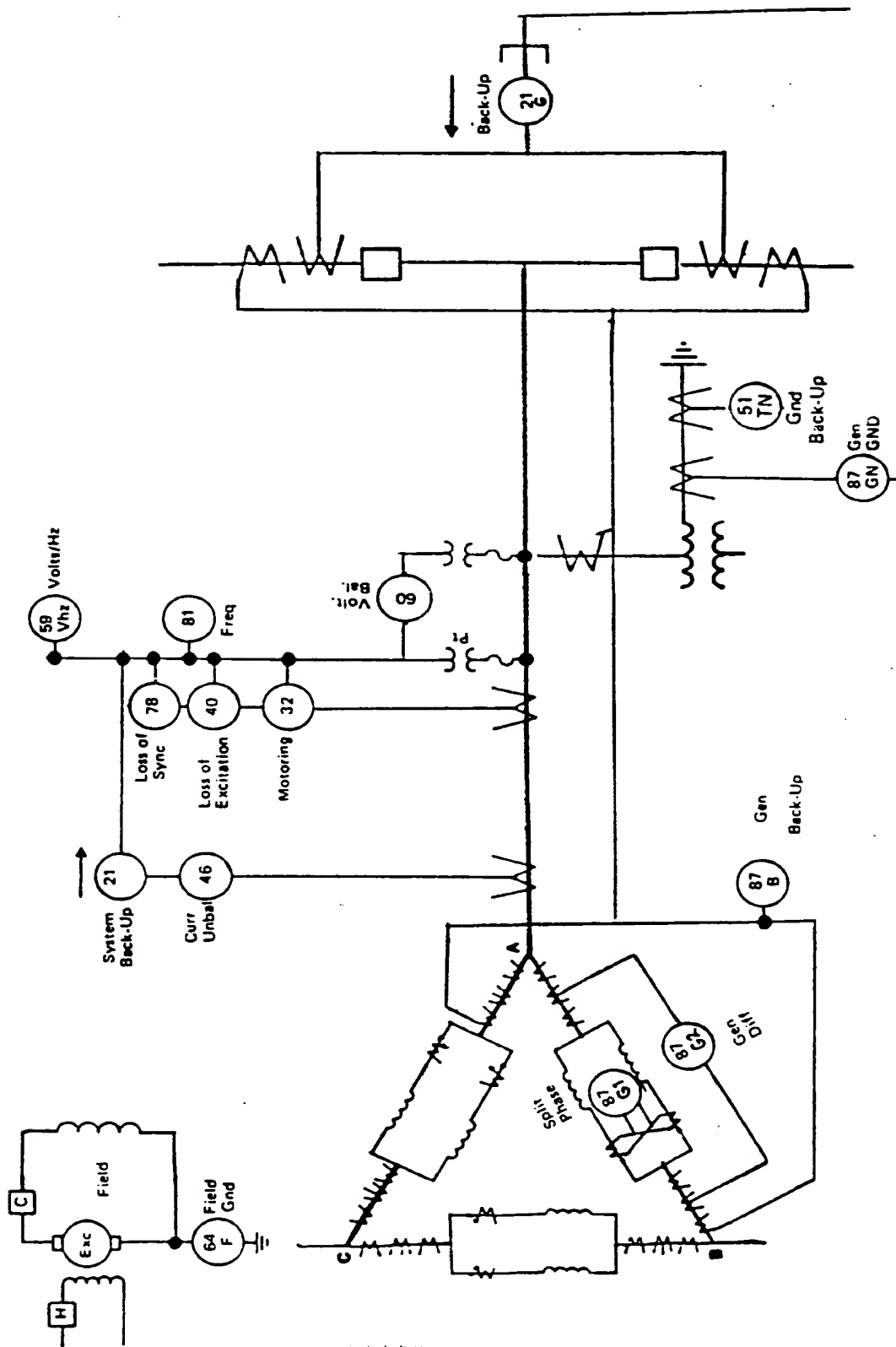


Figure 4.7-2. Protection Arrangement for the Single-Delta Circuit-Lead Configuration

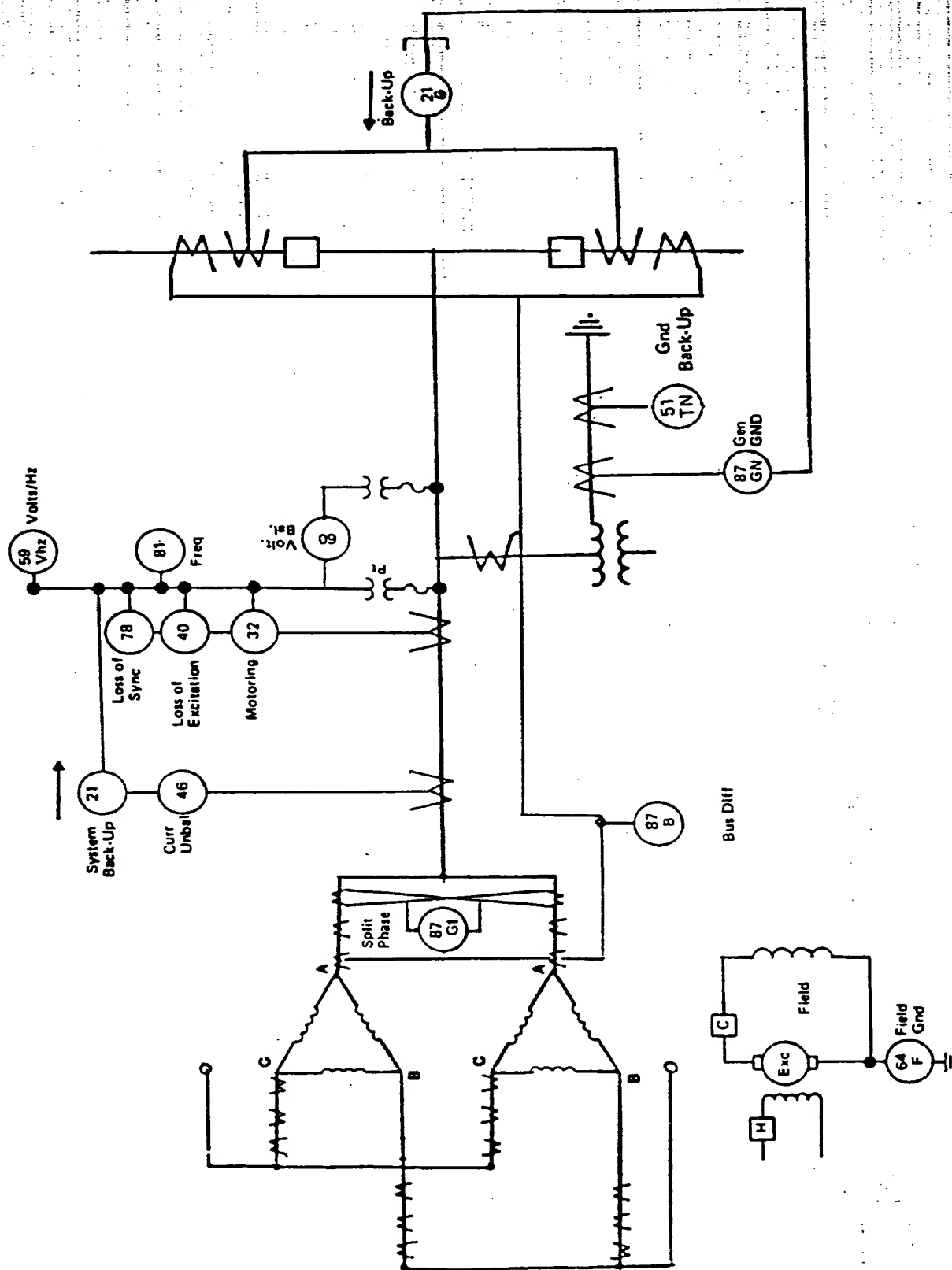


Figure 4.7-3. Protection Arrangement for the Double-Delta Circuit-Lead Configuration

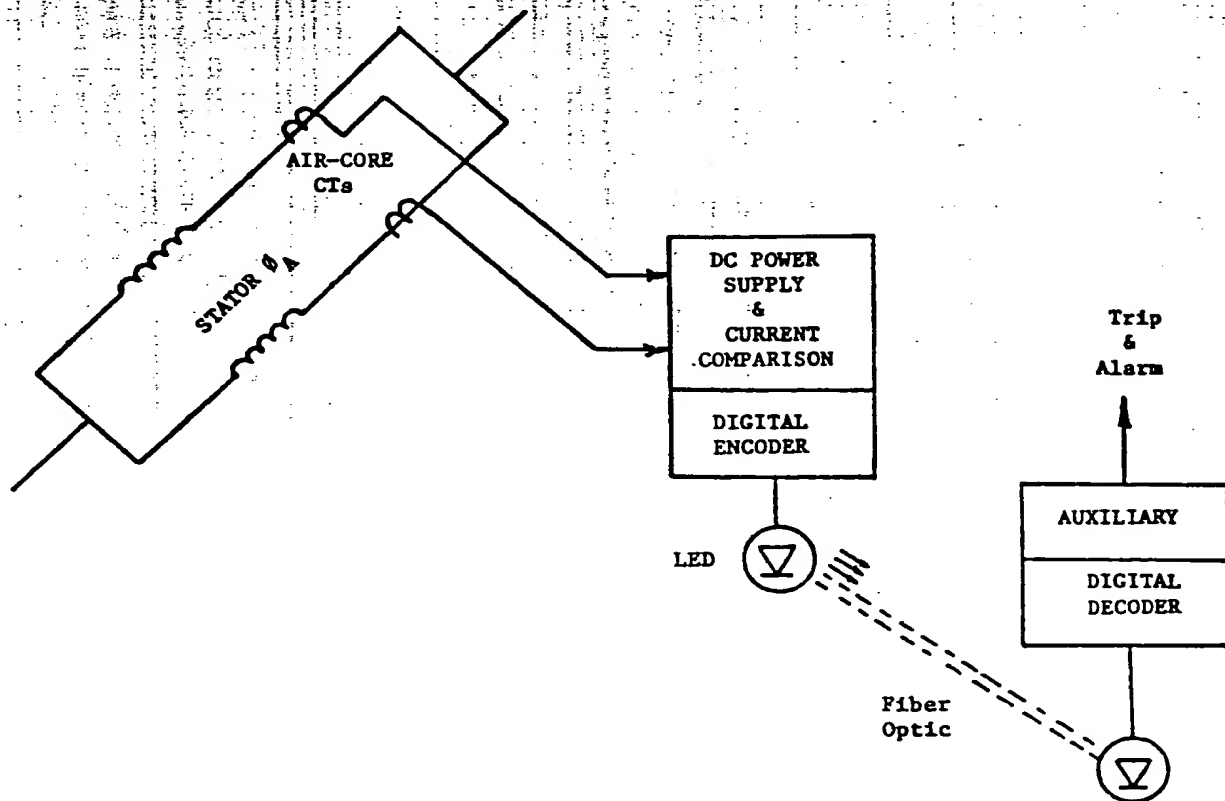


Figure 4.7-4. Air-Core Current Transformers and Internally Mounted Relaying Electronics for Split-Phase Protection

Device 87G2 is a conventional generator differential relay that provides phase-to-phase fault, three-phase fault, and ground fault protection for the stator winding. This type of protection has a 0.2 A pickup under no-load conditions and a 0.5 A pickup under full-load conditions. According to fault calculations made by MIT, it is possible that this protection could detect a phase-to-phase fault with as much as a 100 Ω fault resistance. While there is no data available on ground fault current magnitudes, it is likely that both device 87G1 and device 87G2 could detect these faults anywhere in the winding. The operating times of both types of protection is from 1 to 2 cycles.

Device 87B is a high-speed bus differential relay which is capable of detecting both phase and ground faults in the generator and the generator leads. This relay can provide more sensitive protection than a standard generator differential relay.

The combination of devices 87G1, 87G2, and 87B provides overlapping high-speed primary and backup protection for the generator.

Backup protection for the generator leads and additional backup for the generator are provided by devices 21G, 87GN, and 51TN.

Device 21G, an impedance relay which is connected to "look" into the generator, provides backup protection for phase faults. Time delay will have to be used with this relay in order to prevent possible misoperations due to stable swings.

Device 87GN is connected in a zero sequence current differential scheme and is used to detect ground faults in the generator zone. Time delay may have to be used with this relay to prevent operation on external faults.

While device 51TN is a system fault backup relay, it will also provide time-delayed backup for the generator.

In general, the fault protection illustrated in Figure 4.7-2 is equal to or better than that presently provided on conventional generators. Preliminary calculations indicate that fault currents for ground faults anywhere in the stator windings can be several times full-load current. If this is the case, it would be possible to protect 100% of the winding for ground faults. Such protection is difficult to achieve in the conventional wye-connected generator with a high-impedance grounded neutral.

4.7.3 Fault Protection for the Double-Delta Configuration

Figure 4.7-3 illustrates the protection arrangement for the double-delta configuration. In general, the fault protection for the double-delta configuration is not as sensitive or comprehensive as for the single-delta arrangement. With CTs only available at the terminals of each delta, it is only possible to provide one high-speed protective zone for the detection of turn faults, phase faults, and ground faults in the stator windings.

As shown in Figure 4.7-3, split-phase differential scheme 87G1 is used for winding fault protection. Again, the sensitivity of the turn fault protection is dependent on the unbalance between circuits. However, in this case, the relay will see the unbalance between the circuits of two phases. For example, the Phase A relay will see the unbalance between the circuits in the (A-B) and (A-C) phases. Depending on how these currents add up, the circulating current could be higher or lower than in the single-delta configuration. Another factor which affects the sensitivity is the fact that the currents being compared include currents from two phases. For example, for a turn fault in winding (A-B), the current in the CTs includes the phasor addition of the current from winding (A-C). Assuming no initial unbalance and using the data from the MIT study, the relay will only detect a turn fault with zero fault resistance. In the single-delta configuration, it was possible to detect a turn fault with as much as a 0.01Ω fault resistance. For phase-to-phase faults between windings, this scheme would detect a fault with as much as a 100Ω fault resistance. This scheme should also be able to detect ground faults anywhere in the winding.

It should be noted that it is possible for two relays to operate for a fault involving one phase. For example, for faults involving winding (A-B), the relays in the (A) and (B) phases will see the unbalance caused by the fault.

For backup protection, the high-speed split-phase differential scheme could be duplicated in each phase by using the spare CTs in the leads from the delta windings. This approach would provide two high-speed zones of protection for the stator windings. This duplicate scheme is not shown in Figure 4.7-3. Otherwise, impedance relay 21G will provide backup for phase faults, while differential relay 87GN and time overcurrent relay 51TN will provide backup for ground faults. There would be time delay associated with the operation of devices 21G, 87GN, and 51TN.

The leads from the generator to the circuit breakers would be protected by a high-speed bus differential relay 87B, while backup for faults in this area would be provided by devices 21G, 87GN, and 51TN.

4.8 SHAFT TORSIONAL DUTIES

The torsional duty of the high-voltage generator must be investigated because the high-voltage generator's direct connection to the power system and its low-inertia superconducting rotor will exacerbate the effects of power system faults on the torsional duty of its shaft system. The elimination of the reactance of the step-up transformer increases the level of fault currents and the consequent torque on the generator rotor. The reduced superconducting rotor inertia, which is some 25% to 35% that of a conventional generator rotor, allows greater torsional acceleration of the superconducting rotor and consequent greater torsional stress on the generator-to-turbine shaft.

ANSI standards for turbine-generator design call for the generator to withstand the effects of a terminal three-phase sudden short circuit within the generator's short-time thermal rating. This definition has been embraced for the mechanical torsional duty associated with the short circuit and represents one basis for sizing the shaft journal sections.

Since the early seventies, it has been understood that cleared faults out on the power system can produce much more severe torsional duty than does the standard terminal fault. This more severe disturbance results from the clearing process applying additional shock before the response to the initial disturbance (fault application) has subsided. The degree of the additional duty is strongly dependent on the torsional dynamics of the turbine-generator shaft system, the duration of the fault with respect to the period of torsional oscillations, and the impedance between the generator and the fault.

The torsional duty for the 600 MVA, 345 kV high-voltage generator was evaluated for the conditions of a three-phase fault applied immediately adjacent to the generator terminals and cleared in a manner to achieve the greatest torsional shock. These evaluations were performed for three different turbine designs (892 MVA, 815 MVA, and 690 MVA) that were coupled to the high-voltage generator. Torsional duties were also calculated for conventional generators coupled to the same turbines and are used as a basis of comparison for the high-voltage generator. For evaluation purposes, the high-voltage generator replaced the conventional generator without making any changes to the turbine-generator shaft stiffnesses. All calculations were performed for faults at the generator terminals. The model and data associated with the turbine-generator designs are contained in Appendix I.

The torsional responses of the turbine-to-generator shaft are displayed in Figures 4.8-1 to 4.8-3 for the three different turbines. The peak shaft torques for all shafts are listed in Table 4.8-1, with the turbine-to-generator shaft labeled as shaft 4-5. The turbine-to-generator shaft torques for the high-voltage generator are nearly four to six times that calculated for the conventional units. These increased torsional duties are strictly due to the lower rotor inertia of the high-voltage generator and are to be expected from simple physical reasoning. If the generator rotor inertia is very small compared to the turbine inertia, a fault torque placed on the generator rotor will be resisted only by the generator inertia, since the turbine will resemble an infinite inertia.

The shaft-torque comparisons would appear even worse if a transformer reactance was included in the calculations for the conventional units (modeling a fault on the transmission lines near the

Table 4.8-1
PEAK SHAFT TORQUES
(average of positive and negative peaks)

Shaft	Conventional Generator Peak Torque (p.u.)			High-Voltage Generator Peak Torque (p.u.)		
	892	815	690 MVA	892	815	690 MVA
1-2	NA	.3	NS	.7	.8	NS
2-3	NA	.4	1.4	.8	1.1	1.3
3-4	1.4	1.0	1.7	2.1	2.5	3.0
*4-5	1.9	1.3	NA	7.4	7.3	7.0
5-6	.2	.1	.1	.43	.33	.3

*LP turbine-to-generator rotor shaft

NS = No shaft

NA = Data not available

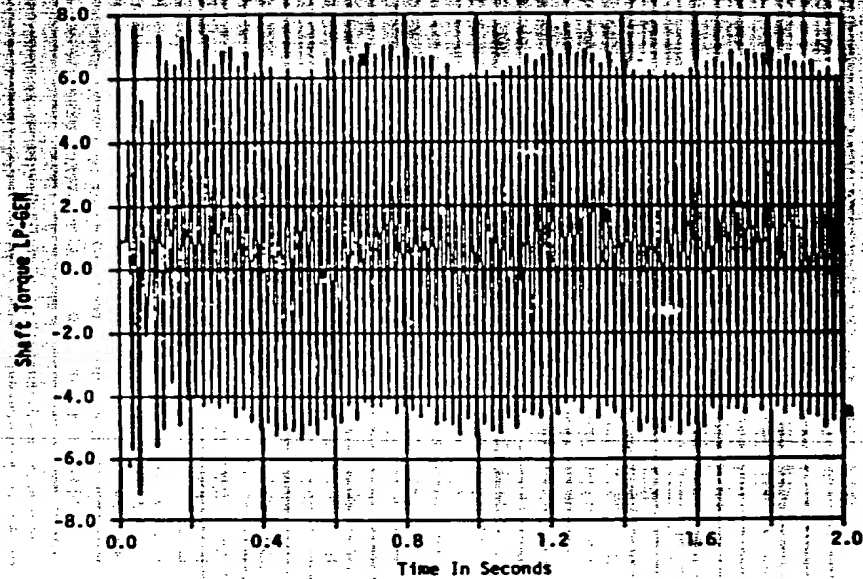


Figure 4.8-1. Fault Torque on the Turbine-to-Generator Shaft for a 892 MVA Turbine Connected to the High-Voltage Generator

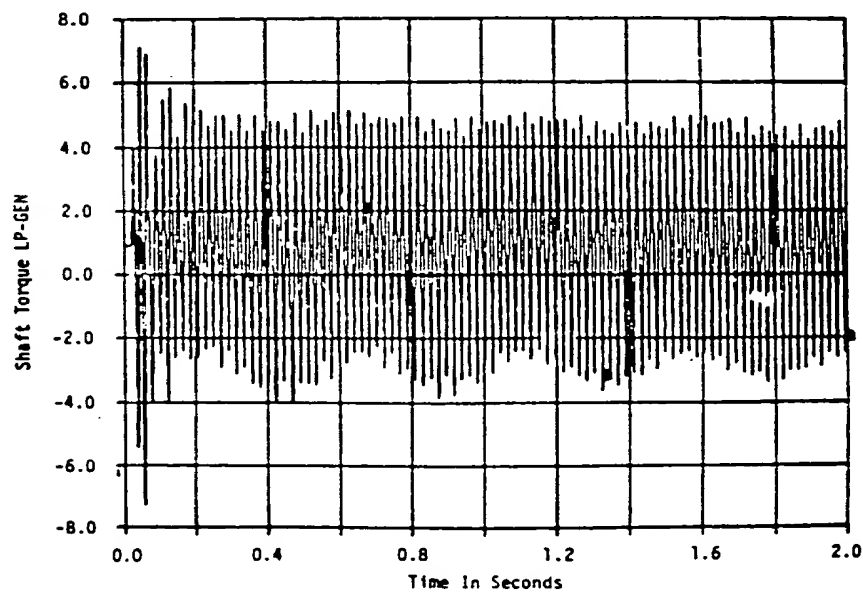


Figure 4.8-2. Fault Torque on the Turbine-to-Generator Shaft for a 815 MVA Turbine Connected to the High-Voltage Generator

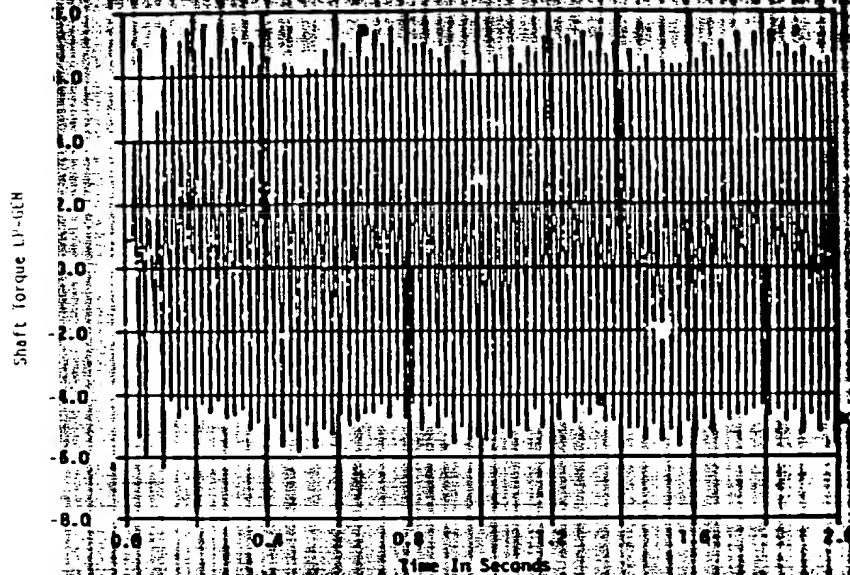


Figure 4.8-3. Fault Torque on the Turbine-to-Generator Shaft for a 690 MVA Turbine Connected to the High-Voltage Generator

transformer). The transformer reactance would reduce the fault currents and the applied fault torque on the conventional generator rotors.

The conclusion to be drawn from these studies is that the turbine-to-generator shaft of the high-voltage generator will have to be considerably strengthened.

4.9 SUBSYNCHRONOUS RESONANCE CONSIDERATIONS

The phenomenon of Subsynchronous Resonance (SSR) describes the interaction between the torsional and electrical dynamics of synchronous generators with a series capacitor compensated power system. The generator electrical and torsional dynamic parameters are important to the severity of possible SSR effects and are a legitimate concern in the evaluation of the high-voltage generator.

The three components of SSR phenomena are:

1. Induction generator effect
2. Torsional interaction
3. Transient shaft torque amplification

The induction generator effect concerns the appearance of a generator negative resistance to the subsynchronous stator current. If the negative component of resistance exceeds the positive resistance components of the positive sequence network at or below the resonant frequency of the system, subsequent electrical responses will be unstable. The magnitude of the negative resistance is proportional to the generator negative sequence resistance and therefore affords a basis for design comparison. Any design effect that reduces generator rotor resistance will reduce negative sequence resistance. The absence of iron in the superconducting rotor of the high-voltage generator produces a natural reduction in the rotor resistances; therefore, a high-voltage generator would be of benefit in reducing the SSR induction generator effect.

The torsional interaction component of SSR phenomena is more affected by torsional dynamics than generator electrical dynamics. Therefore, just as the shaft torsional duty for faults was worse for the high-voltage generator (see Section 4.8), so will the SSR torsional interaction also be worse.

In general, the contribution of the torsional dynamics to SSR torsional interaction is proportional to the contribution of the generator rotor in the torsional vibration behaviour of the whole turbine-generator. The reduced inertia of the superconducting rotor will increase this contribution in some modes of vibration. The mechanical design corrections that improve normal fault-caused torsional duty, such as reduced turbine-to-generator shaft section stiffness, will also suffice to improve the SSR torsional interaction performance.

4.10 TRANSIENT STABILITY

The very low synchronous reactance of the high-voltage generator with its superconducting rotor tends to enhance both its steady state and transient stability characteristics, while its lower rotor inertia tends to degrade its transient stability characteristics. A brief study was made to compare critical clearing times for the 600 MVA, 345 kV high-voltage generator and a conventional unit of the same MVA rating. The generators are modeled with the synchronous machinery equations described in Appendix H. Reactance and inertia data for the two 600 MVA machines are contained in Table 4.10-1.

The power system model uses a single equivalent reactance connected to an infinite bus. The post-fault reactance is twice the prefault reactance for all cases.

Figure 4.10-1 shows the results for a range of system reactances. A two-cycle improvement in critical clearing time is indicated for the high-voltage generator. This is a rather substantial improvement and is comparable to or greater than that attainable by the addition of a very high performance excitation system on a conventional unit.

Table 4.10-1

REACTANCE AND INERTIA DATA FOR TRANSIENT STABILITY STUDIES

	High-Voltage Generator	Conventional Generator
X_d	.299	1.88
X_{dv}	.266	.28
X_{dv}	.228	.20
$X_{transf.}$	None	.10
H	2.0	2.5
Excitation	Fixed E_{fd}	0.5 Response ratio

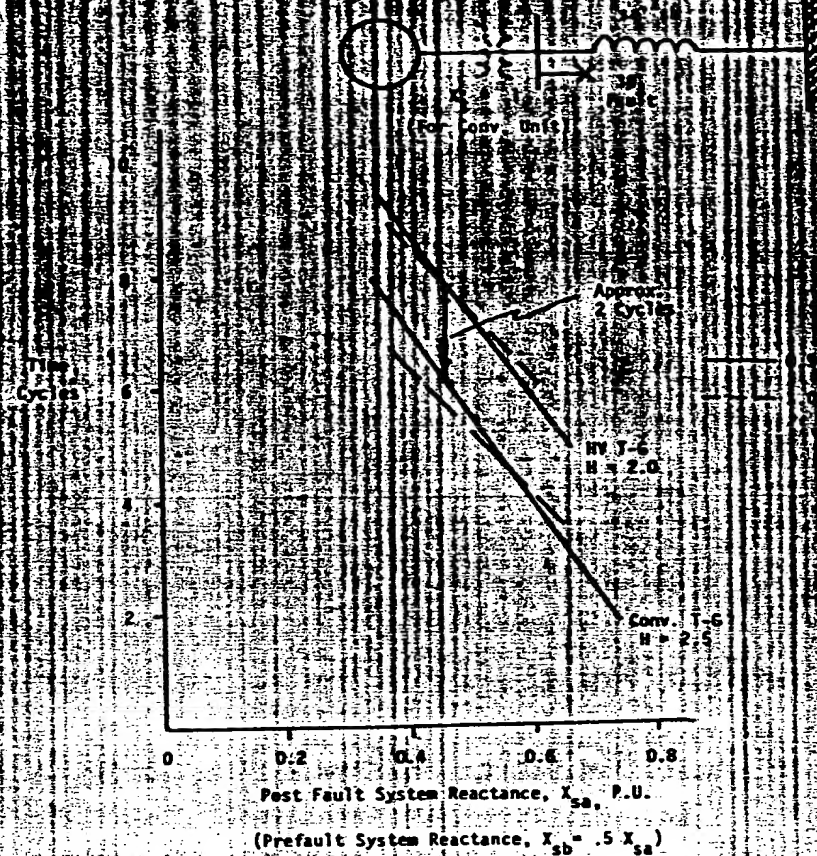
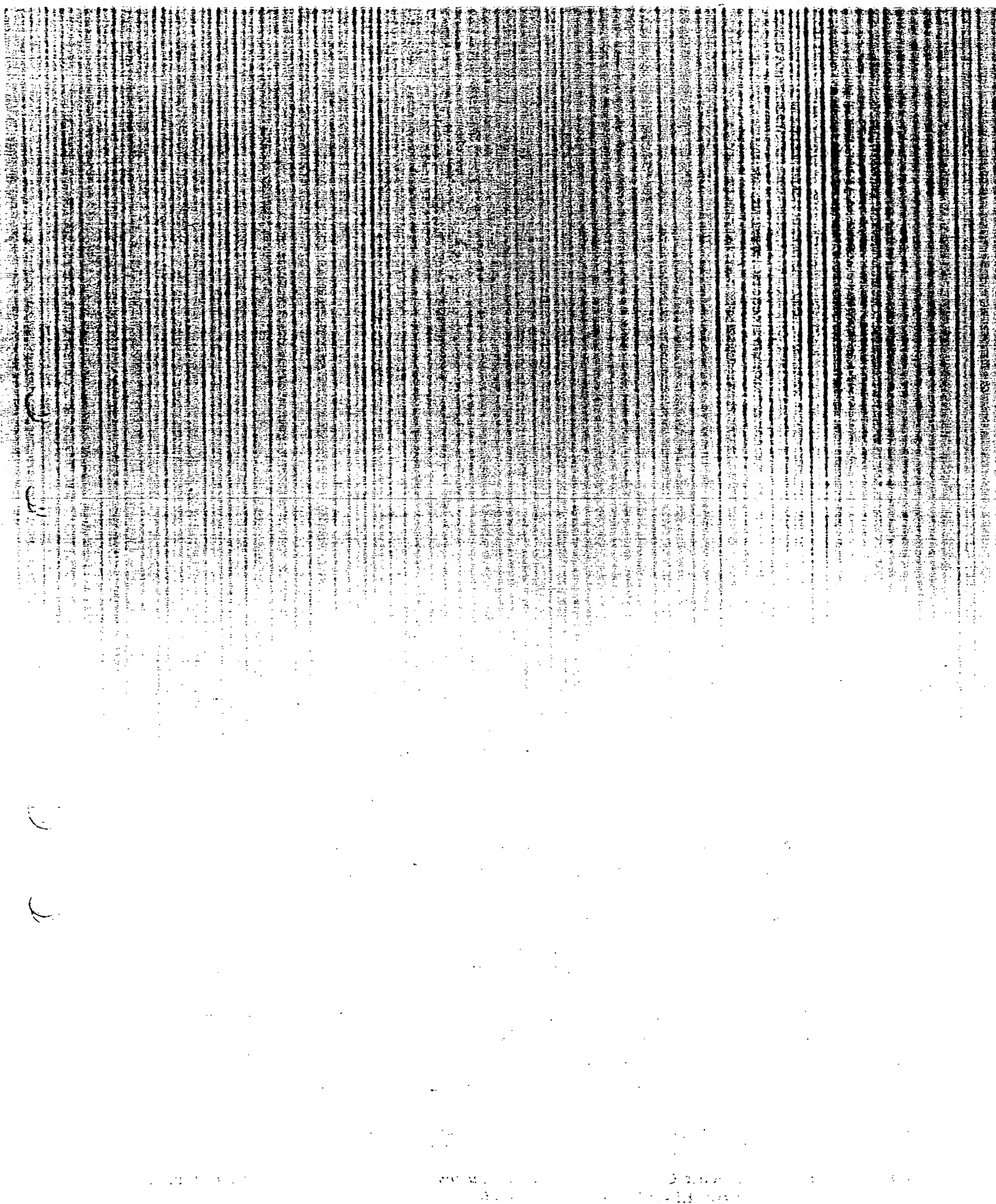


Figure 4.10-1. Comparison of Critical Clearing Times for High-Voltage and Conventional Generators

References

- 4-1. IEEE Std. 462-1973, *General Requirements for Distribution, Power and Regulating Transformers*.
- 4-2. IEEE Std. 262B-1977, *Trial-Use Dielectric Test Requirements for Power Transformers for Operation on Effectively Grounded Systems 345 kV and Above*.
- 4-3. C. Concordia, Chapter 2, *Synchronous Machines*, Wiley, 1951.
- 4-4. General Electric Company, *Superconducting Generator Design*, Final Technical Report, EPRI Contract RP 429-2, December 1977, Vol. 2, Appendix A, "Electromagnetic Shield Analysis."
- 4-5. S.H. Minnich, et al., *Design Studies of Superconducting Generators* 1978 Applied Superconductivity Conference, Pittsburgh, Pa., Sept. 1978.
- 4-6. M.L. Crenshaw, E.T. Jauch, and R.L. Winchester, "Fault Current Decrements and Duties on Unit-Connected Generators and Transformers", paper presented at the 40th American Power Conference, Chicago, Ill, April 24-26, 1978.
- 4-7. General Electric Company, *Electronic Current Transducer (ECT) for High-Voltage DC Lines*, Final Report, EPRI Contract EL-1343, February 1980.
- 4-8. Westinghouse Electric Corporation, *Electronic Current Transducer for EHV Circuits*, Final Report, EPRI Contract EL-1611, November, 1980.



Section 5

SECONDARY APPROACHES

The monolith cylinder armature described in Section 2 was one of many concepts proposed for the high-voltage stator winding, but it proved to be the only one considered technically and economically feasible. This section describes a few of the more important secondary approaches; the reasons for their technical and economical impracticability are documented.

5.1 SPIRAL PANCAKE ARMATURE

5.1.1 Armature Topology

The spiral pancake armature has been proposed in both low-voltage and high-voltage forms for superconducting generators (Refs. 5-1 and 5-2), although only the high-voltage form will be discussed here. Figure 5.1-1 illustrates how this armature is assembled from preformed multiterminal racetrack or pancake coils, each of which serves as a phase belt. Six such pancake coils are interleaved with major insulation blankets and assembled into a toothless core. The pancake coils and insulation blankets are arranged in a spiral fashion when viewed in cross-section, as illustrated in Figure 5.1-2. This spiral arrangement allows all pancake coils to be identical and to lie upon the same average radius, providing magnetic and electric symmetry (non-spiral arrangements of pancake coils require that the coils of different phases lie on different radii, producing magnetic dissymmetry). A bore seal tube is located at the interior of the armature structure for the purpose of sealing the armature from the rotor and air gap.

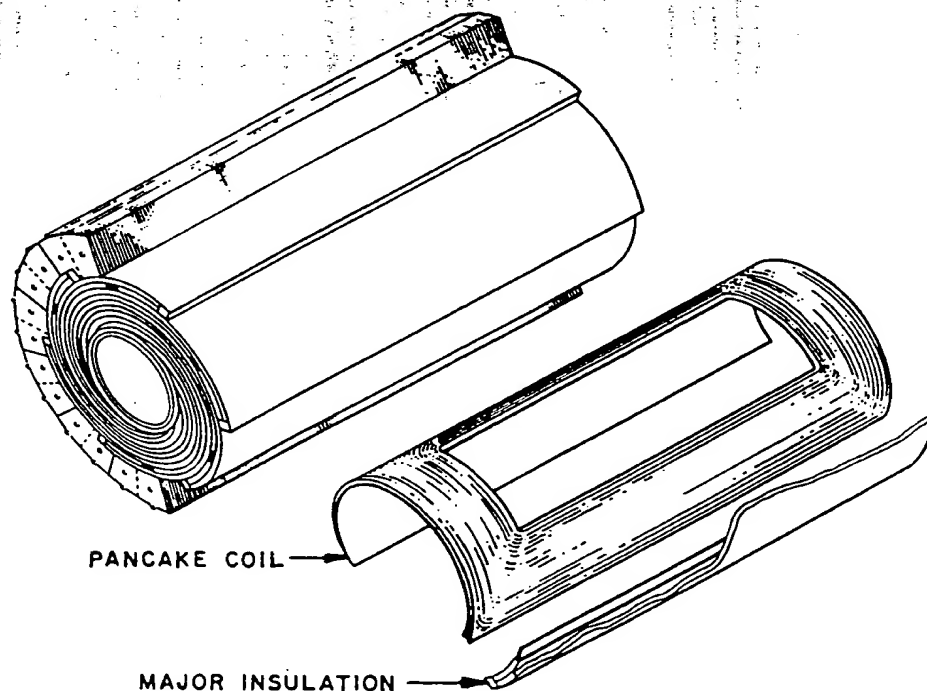


Figure 5.1-1. Spiral Pancake Armature Illustrating Pancake Coils

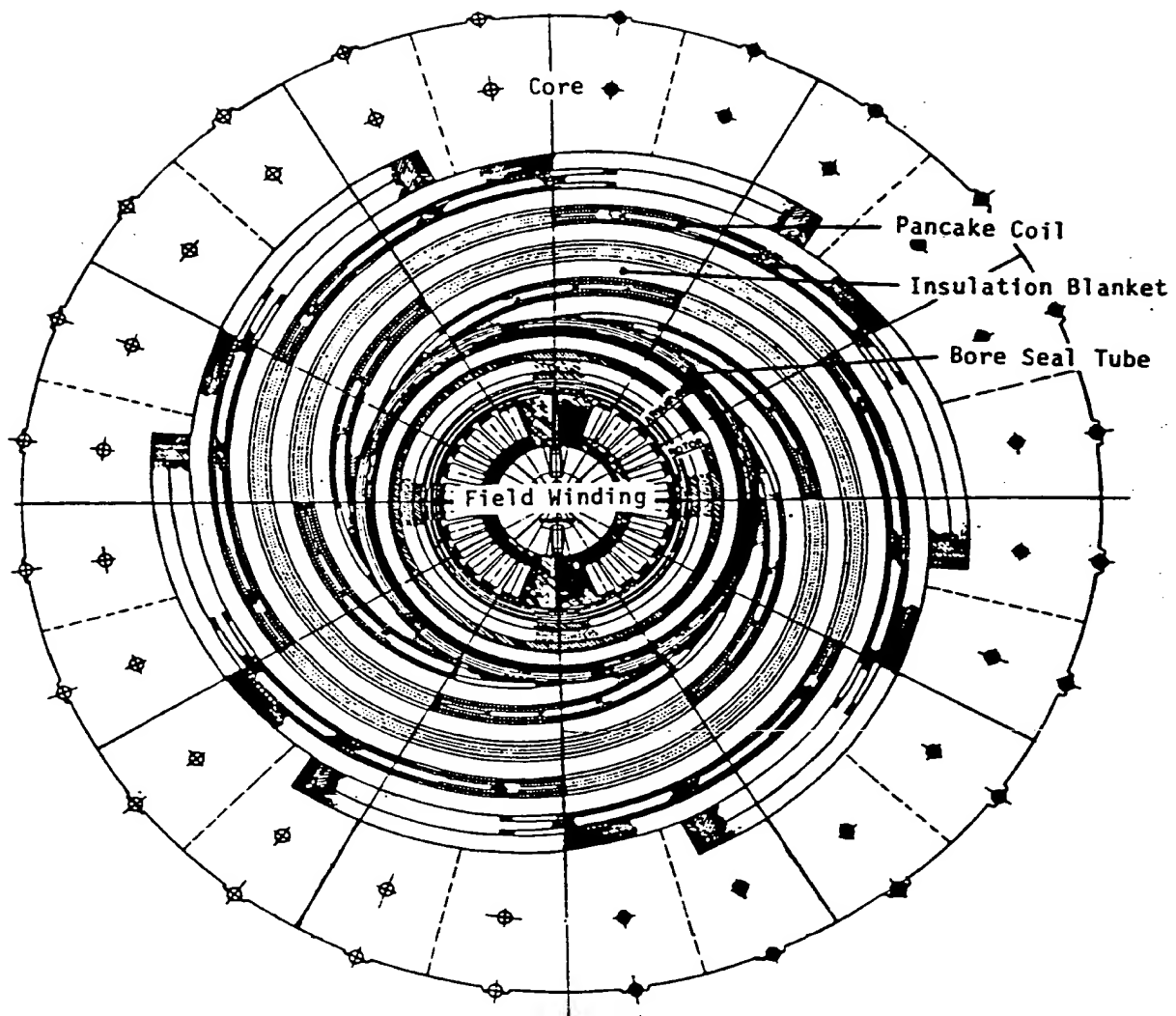


Figure 5.1-2. Cross-Section of a High-Voltage Spiral Pancake Armature

Individual pancake coils are wound in two layers, with the conductors being wound from the outside inward on the first layer and inside outward on the second layer, as illustrated in Figure 5.1-3. Winding the coils in this manner allows the coil leads to be exited on peripherally opposite sides of the pancake coil (a single layered coil must have a lead running from the interior of the coil across the breadth of the coil in the end region, producing an irregular region of electric stress). The voltage in a two-layer pancake coil builds up in the same manner that it is wound. Therefore, the voltage difference between the two layers of the coil is zero in the center and builds to a maximum at the edge of the coil. This voltage difference requires a wedge-shaped piece of insulation to be placed between the two layers, as illustrated in Figure 5.1-4. Each layer of the pancake coil can be wound from a continuous length of braided conductor, minimizing conductor connections.

The intended winding connection for the spiral pancake armature is a single-circuit wye. Section 2.1 discusses how wye connections produce large voltage differences at the phase breaks, and the spiral pancake winding is not immune to this effect. The spiral arrangement of the pancake coils, however, skews the coil sides so that the phase break voltages become orientated in the radial

direction (as opposed to the peripheral direction in the monolith cylinder armature). The thick insulation blankets interleaved between the pancake coils are then sized to withstand the magnitude of the phase break voltages. Figure 5.1-4 illustrates the location of the phase breaks in a spiral pancake armature. The pancake coils can be wound and arranged in such a manner that the largest phase break voltage is 1.15 times line-to-ground voltage (the magnitude of a phasor stretching from the terminal of one phase to the quarter-point of another). All of the insulation blankets should therefore be sized to withstand 1.15 times line-to-ground voltage. Also, the bore seal tube is required to withstand .5 times line-to-ground voltage.

One may now begin to acquire an intuition that the spiral pancake armature is not as space-effective as the monolith cylinder armature. The radial build-up of the insulation blankets and bore seal tube amounts to 6.25 times line-to-ground voltage, as opposed to 3.73 times line-to-ground voltage for the radial build-up of the insulation cylinders of the monolith cylinder armature. The pancake coils are devoid of conductors in their centers and must be filled with an unproductive insulation. Computer sizing studies for the spiral pancake armature, described in Section 5.1.2, will confirm the intuition.

The electric stresses at the phase breaks will be studied in more detail in Section 5.1.3, and it will be shown that merely shifting the orientation of the phase break voltage does not eliminate all of the problems associated with large phase break voltages.

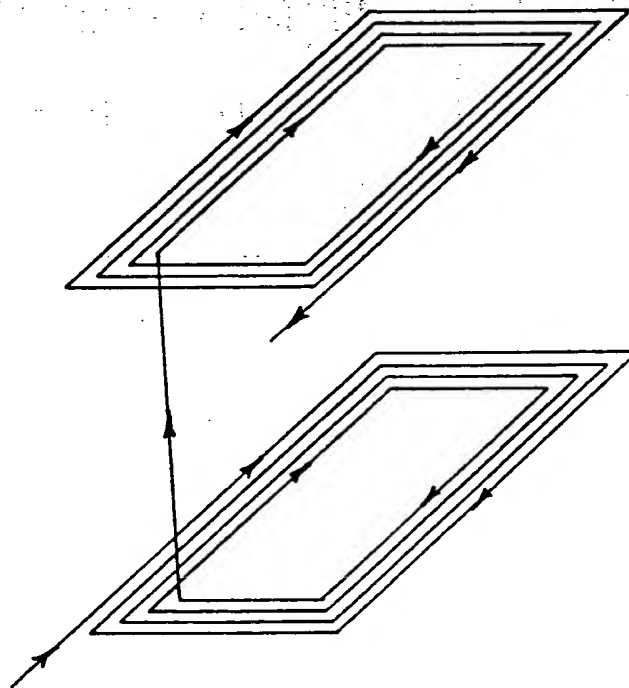


Figure 5.1-3. Winding Pattern of a Two-Layered Pancake Coil

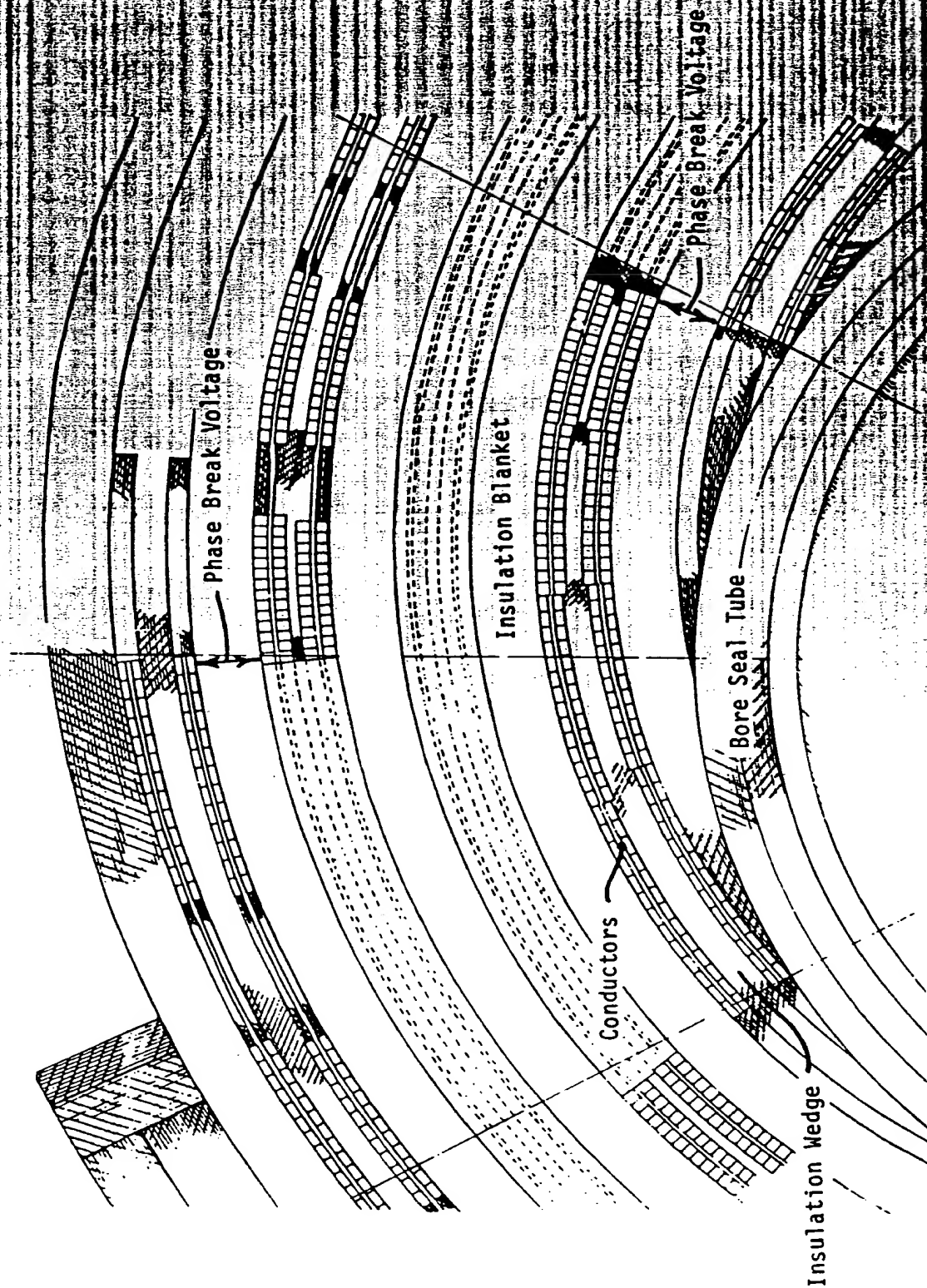


Figure 5.1-4. Details of a High-Voltage Spiral Pancake Insulator

5.1.2 Sizing Study

Magnetic analysis of spiral pancake armatures is not a widely practiced art. The basic procedures to follow and the general results to be expected are similar to those for the monolith cylinder sizing studies. Expenditure of the effort required to formulate all the necessary geometry-specific equations can be justified only if a detailed design is to be carried out. However, with modest effort, spiral pancake armatures can be approximately characterized, at least in terms of their overall armature dimensions and space factors, in a manner which permits them to be represented by the existing two-dimensional computer program described in Section 2.2.1.

The cross-section of a spiral pancake armature can be divided into annular regions which correspond directly to those in a monolith cylinder magnetic model, as shown in Figure 5.1-5. The innermost annulus, which corresponds to the bore seal tube, contains only insulation. The second annulus from the center is bounded by the inner and outermost conductors of the inner lying coil sides of the pancake coils. The actual conductors within the annulus are distributed in the spiral fashion. A large amount of insulation must be necessarily included within this annulus, and the packing factor of copper within this annulus is consequently much lower than the copper packing factor within the corresponding winding annulus of the monolith cylinder model. This lowered packing factor affects only the current density to be entered into the model and does not affect the validity of the model. The phases are concentrated into 60° sectors. Between the outermost conductors of the inner lying coil sides and the innermost conductors of the outer lying coil sides, there is an annulus containing only insulation, corresponding to the center insulation cylinder of the monolith cylinder model. The outer winding annulus and outermost insulation annulus correspond to the monolith cylinder model in the same manner as described previously for the other annuli.

Therefore, to obtain a two-dimensional magnetic representation of a spiral pancake armature, all that is required are reasonable means to assign thicknesses to the various annuli and current densities to the annuli containing conductors.

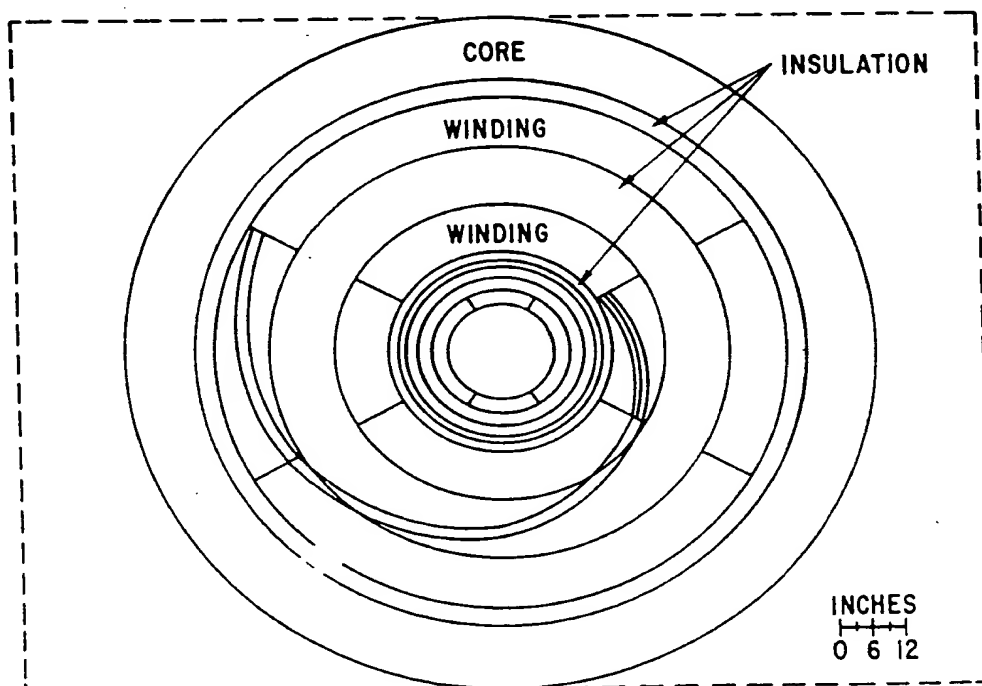


Figure 5.1-5. Model of a Spiral Pancake Armature, 600 MVA, 345 kV

The logical independent variables to characterize a spiral pancake armature are the insulation blanket thickness and the pancake coil thickness. These can readily be related to the corresponding annulus thicknesses by simple geometric relationships. To get a simplified result readily comparable to monolith cylinder designs, the cosine of the angle between the normal to the pancakes and the radial may be neglected. With this assumption, the thickness of each of the two winding annuli is the thickness of an insulation blanket plus twice the thickness of a pancake coil. The thickness of the center insulation annulus is thickness of an insulation blanket plus the thickness of one pancake coil. The thickness of the outermost insulation annulus is the thickness of one insulation blanket. The thickness of the innermost insulation annulus is the thickness of the bore seal tube. The insulation blankets must be thick enough to withstand 1.15 times line-to-ground voltage and the bore seal tube must be thick enough to withstand .5 times line-to-ground voltage.

The winding annuli in the monolith cylinder model are assumed to work at a constant current density. In the spiral pancake model, the winding annulus current densities are computed by estimating ampere turns for the actual winding and spreading them uniformly over the winding annulus. Estimation of the ampere turns is further simplified by averaging the variation in radius of the pancake coil side over the region of the winding annulus. That is, the coil side is presumed for calculation of ampere turns to be a sector of the winding annulus at the mid-radius of the winding annulus, as illustrated in Figure 5.1-6.

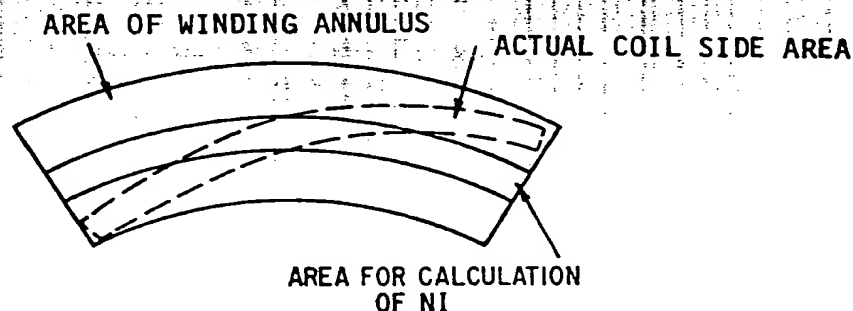


Figure 5.1-6. Determination of Current Density for the Spiral Pancake Model

The two-layer construction of the pancake coils produces a voltage difference of one-half line-to-ground voltage between the two layers at the outer edge of the pancake coil. This voltage difference decreases approximately linearly to zero, going inward to the center of the coil. This voltage distribution requires a wedge-shaped area of insulation to be placed between the two layers, as illustrated in the developed view of Figure 5.1-7. The insulation wedge implies that there must be a minimum pancake coil thickness equal to the thickness of the insulation wedge at the outside edge of the coil. In a minimum-thickness pancake coil, half of the coil side area would be devoted to the insulation wedge and the other half would be devoted to conductors.

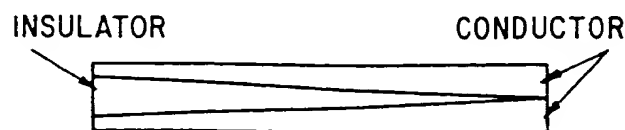


Figure 5.1-7. Insulation Wedge Separating Pancake Coil Layers

The fact that there is a non-zero minimum pancake coil thickness implies that there is a non-zero minimum conductor area. If this conductor area is presumed to work at a stated current density, this implies a minimum number of armature ampere turns. If this minimum is greater than the number the computer model requires to achieve the specific rating and reactance, the program will not converge to a solution. To circumvent this difficulty, the solution algorithm has been slightly modified. Iterations are performed with an auxiliary parameter. If the auxiliary parameter is greater than the minimum pancake coil thickness, it is treated as this thickness. Total armature ampere turns are determined from the armature current density and the approximate area of the pancake, with due allowance for the triangular-shaped insulation area. If the auxiliary parameter is less than the minimum thickness, armature dimensions are determined by using the minimum thickness and ampere turns are determined by subtracting the insulation wedge area from a gross coil-side area determined by multiplying the arc length and the auxiliary variable, and then multiplying this term by the current density. The result is that ampere-turns can become zero for positive values of the auxiliary variable. This result permits the program to find a solution. The area defined by this calculation has no physical significance; the definition has been selected so that ampere-turns will be a continuous function of the auxiliary parameter. Values of the auxiliary parameter less than the minimum thickness can be interpreted to mean that the current density in the conductor portion of the pancake coil is less than the specified value. The specified current density may then be interpreted as a maximum value.

Because the program does not explicitly account for the insulation wedge in the coil side, the copper portion of the remaining area may be presumed to be high relative to that for monolith cylinder windings. A current density of 300 A/cm² has been assumed for these studies.

The modifications just described have been incorporated into a sizing program similar to that described in Section 2.2.1. This program has been used to size 600 MVA machines at 345 and 500 kV. Designs are produced for insulation dielectric stresses of 100, 75, and 50 kV/in. The end correction algorithm used is the same as that used for monolith cylinder armatures. There is no formal justification for this selection, but in view of the relatively low length-to-diameter ratios being encountered in this study, some representation of the finite length effects is required. It is presumed that spiral pancake armatures and monolith cylinder armatures of similar proportions have similar end leakages. This presumption may well lead to comparisons favorable to spiral pancake armatures, because no allowance is made for additional core iron over the ends. The results are summarized in Table 5.1-1.

Figure 5.1-8 compares monolith cylinder and spiral pancake armatures as a function of insulation thickness requirements. For every insulation thickness, the spiral pancake armature is larger. The increased sensitivity of the spiral pancake armature to insulation thickness is characterized by the generally steeper slopes. In addition, the spiral pancake armatures are longer than the corresponding monolith cylinder armatures. The 600 MVA spiral pancake armature at 50 kV/in. insulation stress is approaching limits both in diameter and length.

Table 5.1-1

BEST SPIRAL PANCAKE ARMATURES AT 600 MVA
300 A/cm² MAXIMUM CURRENT DENSITY

kV	kV/in.	R ₁	R ₂	R ₃	R ₄	R ₅	R ₆	R ₇	R ₈	R ₉	R ₁₀	R ₁₁	L	X"	X'	X
345	100	9	12	14.5	17.5	19	20.0	26.8	33.6	40.4	42.4	57.9	128	.20	.27	.34
345	75	9	12	14.5	17.5	19	20.3	27.9	36.3	43.9	46.6	60.8	146	.21	.27	.33
500	100	9	12	14.5	17.5	19	20.4	28.3	37.3	45.2	48.0	61.8	154	.21	.27	.32
500	75	9	12	14.5	16.5	18	19.9	29.3	40.6	50.0	53.9	66.2	171	.22	.27	.32
345	50	9	12	14.5	16.5	18	20.0	29.5	41.2	50.7	54.7	66.9	174	.22	.27	.32
500	50	9	12	14.5	16.5	18	20.9	33.3	49.5	61.9	67.7	77.5	234	.24	.27	.31

Note: Headings R₁ - X are identical to those listed in Table 2.2-1

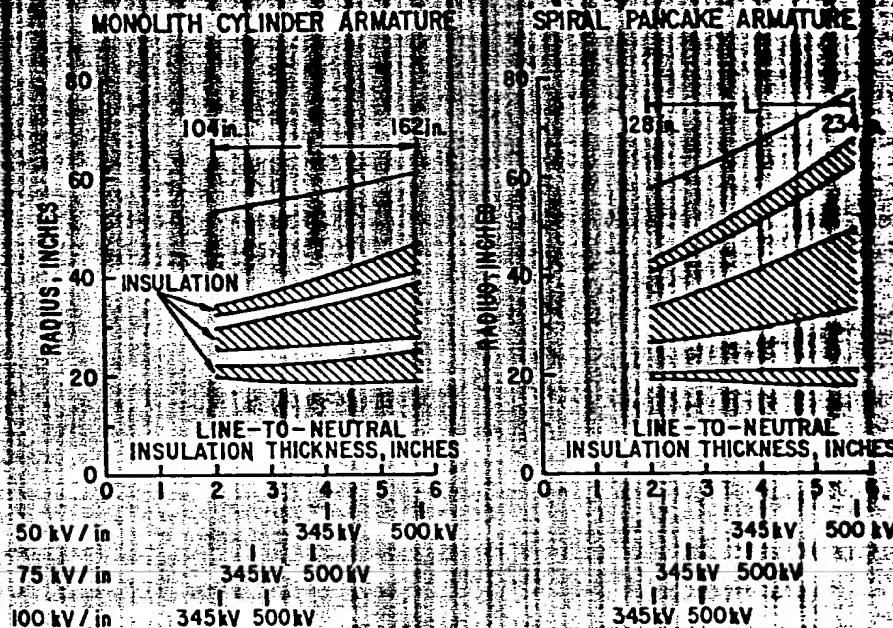


Figure 5.1-8. Size Comparison of Monolith Cylinder and Spiral Pancake Armatures

Figure 5.1-5 is drawn to proportion for the 345 kV, 50 kV/in. design. For comparison, Figure 5.1-9 is the corresponding monolith cylinder armature drawn to the same scale. In addition to the increased armature volume, note that the spiral pancake armature has a thinner, larger diameter core. It may be necessary to increase the core thickness to provide structural stiffness.

In conclusion, based on the study assumptions, the spiral pancake armature configuration has a poor space utilization that requires significantly larger machine dimensions.

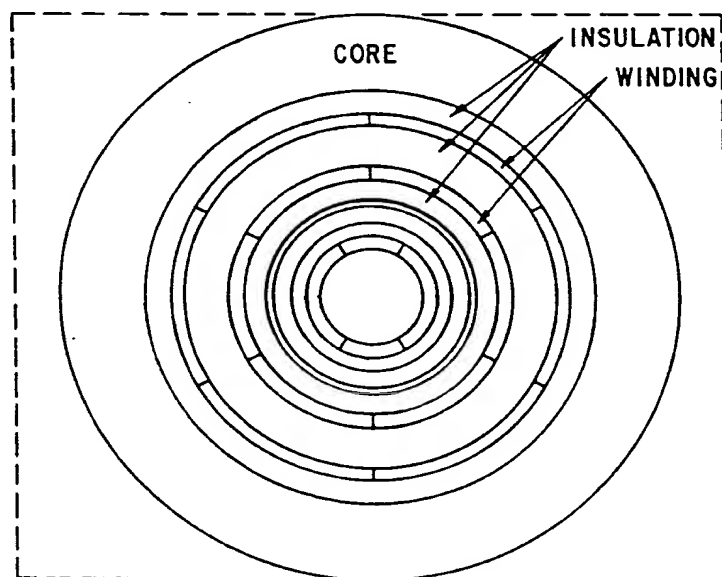


Figure 5.1-9. 600 MVA, 345 kV Monolith Cylinder Armature, to Scale with Figure 5.1-5

5.1.3 Phase Break Electrical Stresses

The intended winding connection for the spiral pancake armature is a single-circuit wye. Section 2.1 describes how wye connections produce large voltages between adjacent conductors at the phase breaks. In a monolith cylinder armature, the phase break voltage appears peripherally within the conductor layer and creates an intolerable electrical creepage situation at the phase break. In a spiral pancake armature, the spiral arrangement of the pancake coils skews the coil sides in such a manner that the phase break voltages become orientated in the radial direction. The thick insulation blankets that are interleaved between the pancake coils are sized to handle this voltage, assuming that the electric stresses at the phase break are evenly graded and oriented normally to the insulation blankets. Figure 5.1-4 illustrates the locations of the phase breaks. The insulation wedges that separate the top and bottom layers of the pancake coils are extended well past the edges of the pancake coils in order to provide long creepage paths from the coil edges to grounded surfaces such as the core. Figure 5.1-4 also illustrates the insulation wedges.

It was decided to further explore the electrical creepage situation existing at the boundary of a blanket insulation and the extension of a pancake coil insulation wedge. A finite element electrostatics program was used to calculate the electrostatic field. Figure 5.1-10 illustrates the region of study, which includes the bore seal tube, an insulation blanket, an insulation wedge, and borders of the inner surface of one pancake coil and the edge of another. The finite element calculation of the electrostatic field is illustrated in Figure 5.1-11, which shows lines of constant potential. Lines of electric stress are normal to the lines of constant potential. The pancake coil captured at its edge has line-to-ground voltage at the top layer and one-half line-to-ground voltage at the bottom layer. The pancake coil exposing its inner surface is of a different phase, and the voltage at this surface varies from ground to negative one-eighth line-to-ground voltage at the moment of time that the calculation is made. The inner surface of the bore seal tube is at ground. The dimensions of the

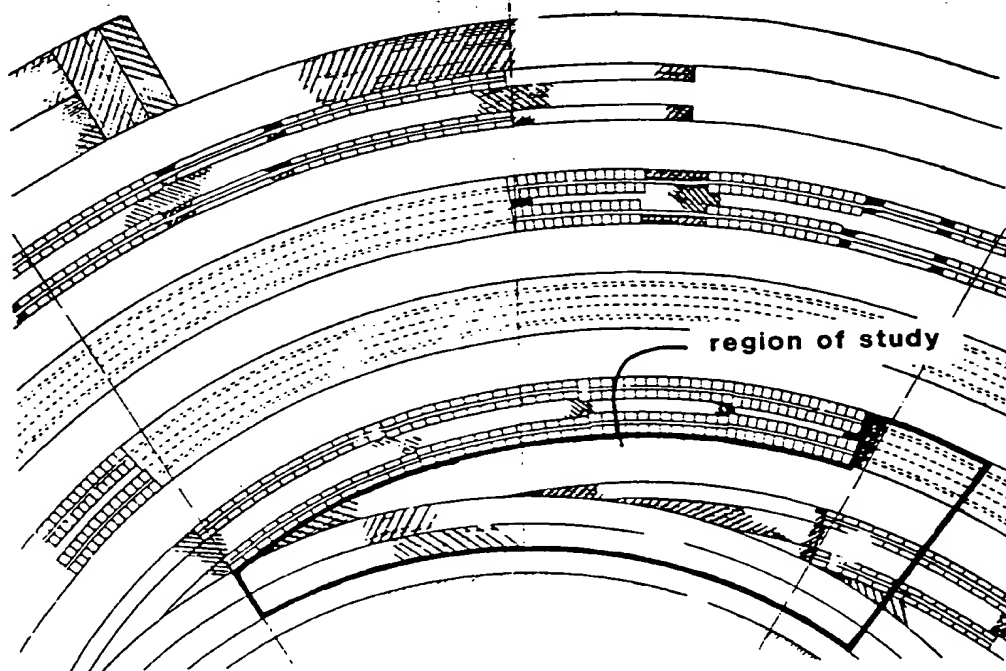
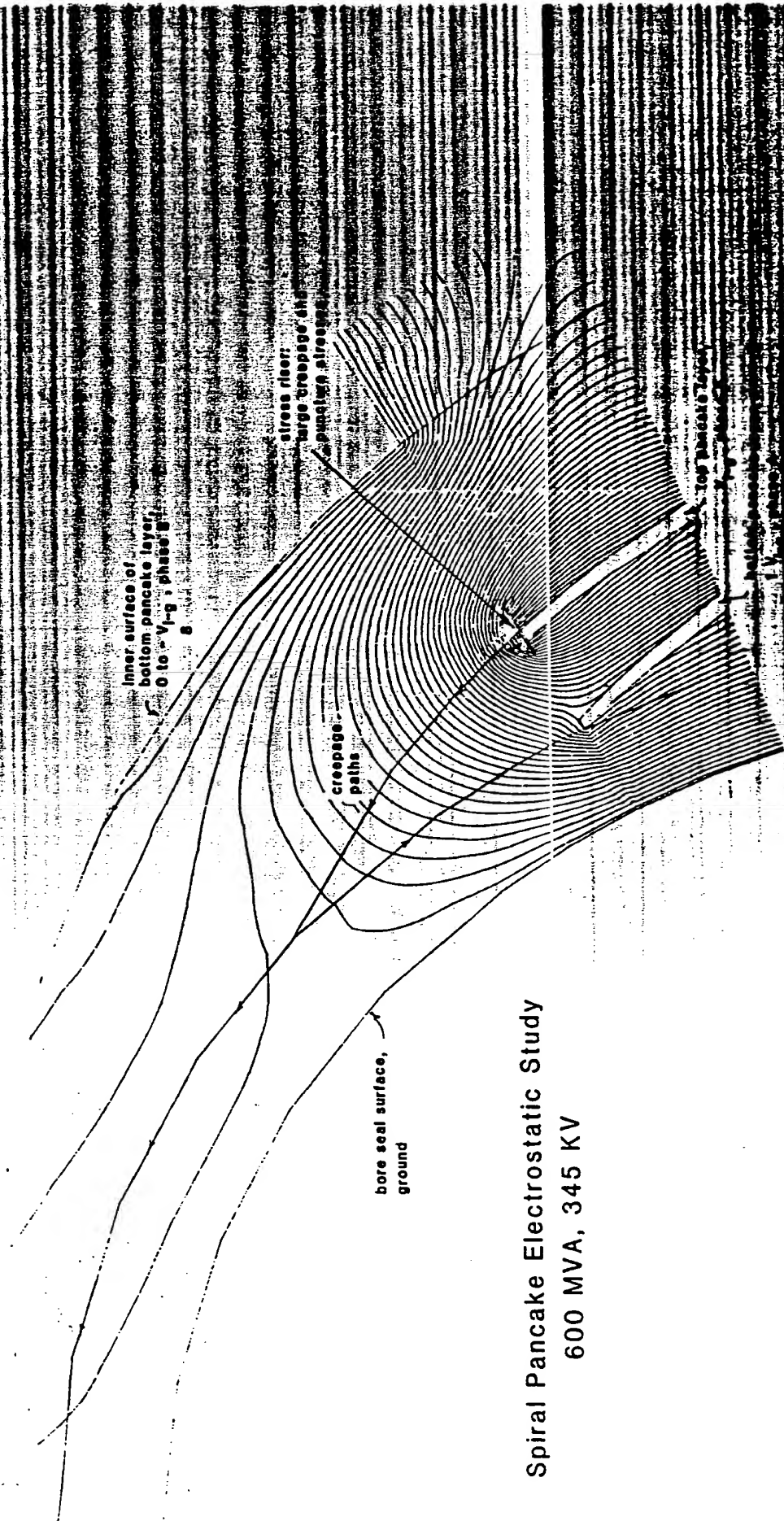


Figure 5.1-10. Electrostatic Study Region of the High-Voltage Spiral Pancake Armature



Spiral Pancake Electrostatic Study
600 MVA, 345 KV

Figure 5.1-11. Electrostatic Field Solution of the High Voltage Spiral Pancake Capacitor

region are taken from the computer sizing study for the 600 MVA, 345 kV rating with the insulation designed for 50 kV/in. dielectric stress. Examination of Figure 5.1-10 reveals the presence of a large stress riser at the edge of the top pancake layer. The stresses in the proximity of the stress riser are neither uniformly graded or oriented normally to the insulations. Figure 5.1-12 is an enlargement of the stress riser. The maximum puncture stress is about 140 V/mil, nearly three times the 50 V/mil design value. The creepage stress at the boundary of the insulation blanket and the insulation wedge extension is 140 V/mil near the edge of the pancake coil. Figure 5.1-13 illustrates a creepage criterion plot for this creepage path. (Creepage criterion plots are described in Section 2.5 for electrical creepage along oil and pressboard interfaces.) The creepage plot is well above the gray area for a long distance, starting very close to the coil edge. The interface of the insulation blanket and the insulation wedge would, therefore, require bonding in order to seal the interface. However, there is the problem of small cracks that may develop at the interface due to winding forces or thermal expansion forces. Even though such cracks would fill with oil from the surrounding impregnated pressboard, the smallest cracks would be subjected to discharging, judging from the distance and magnitude of the creepage criterion plot excursion.

Solutions to such stress riser problems are found in transformer technology, where systems of interlocking baffles are incorporated at stress riser locations. Figure 5.1-14 illustrates such a system applied at the edge of a pancake coil. The interlocking parts greatly increase the length of the creepage path in the proximity of the stress riser, and the lines of electric stress are normally oriented to the parts. Such baffle systems would be incorporated at all locations of stress risers within the armature. The baffle systems must span the entire length of the armature winding and must incorporate curved sections that fit at the end windings.

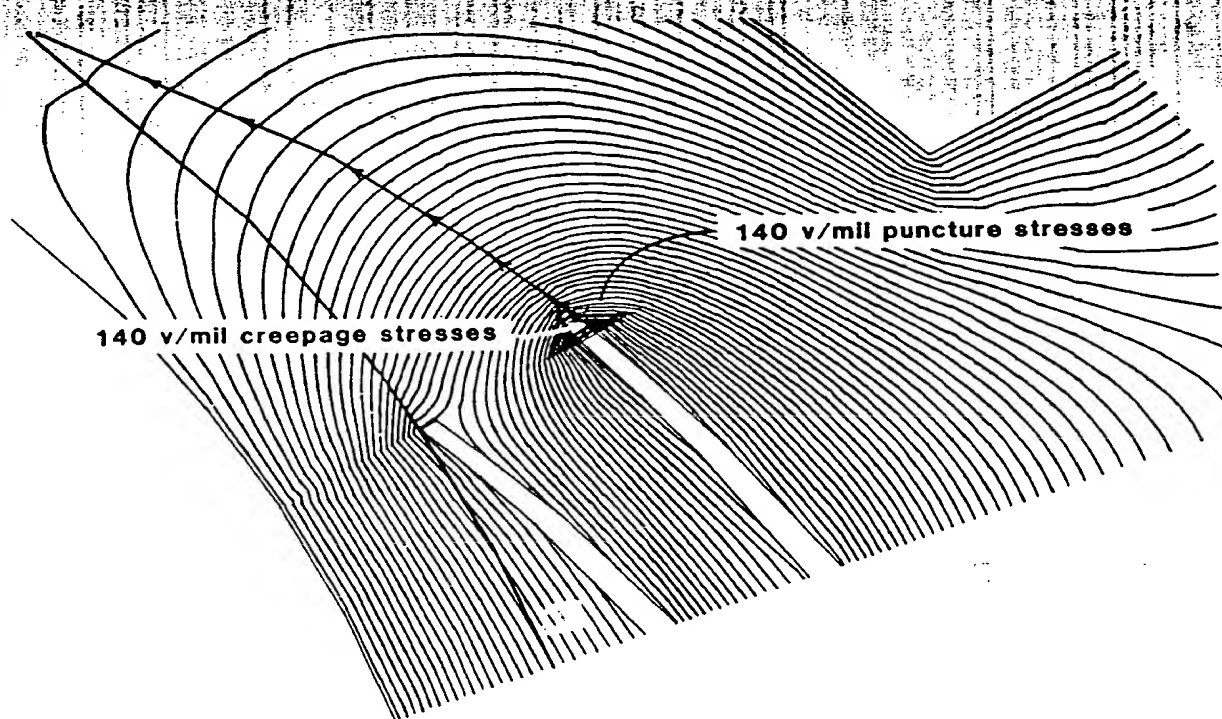


Figure 5.1-12. Spiral Pancake Electrostatic Stress Riser

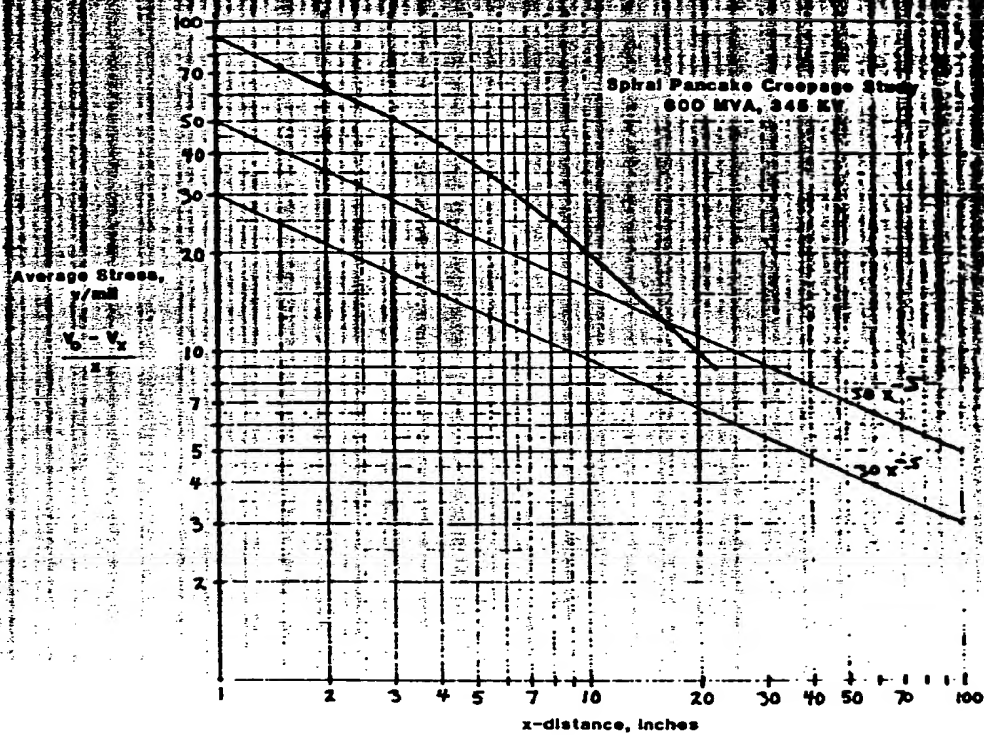


Figure 5.1-13. Creepage Criterion Plot of the High-Voltage Spiral Pancake Armature

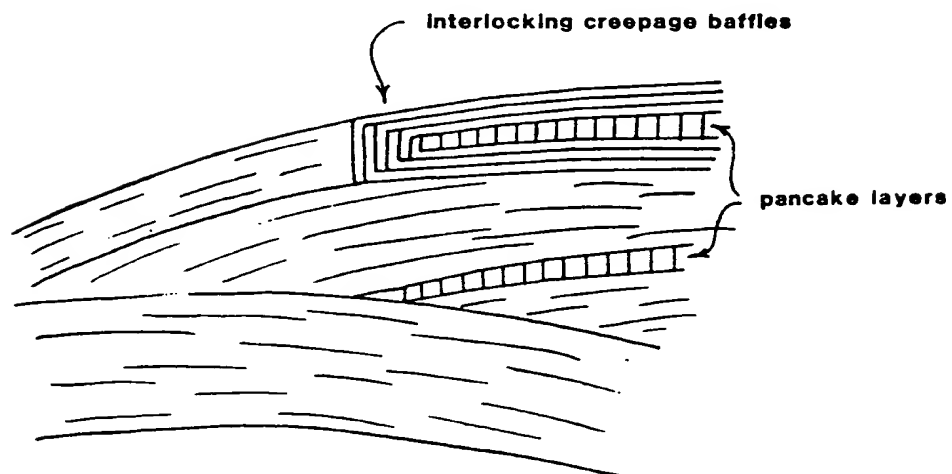
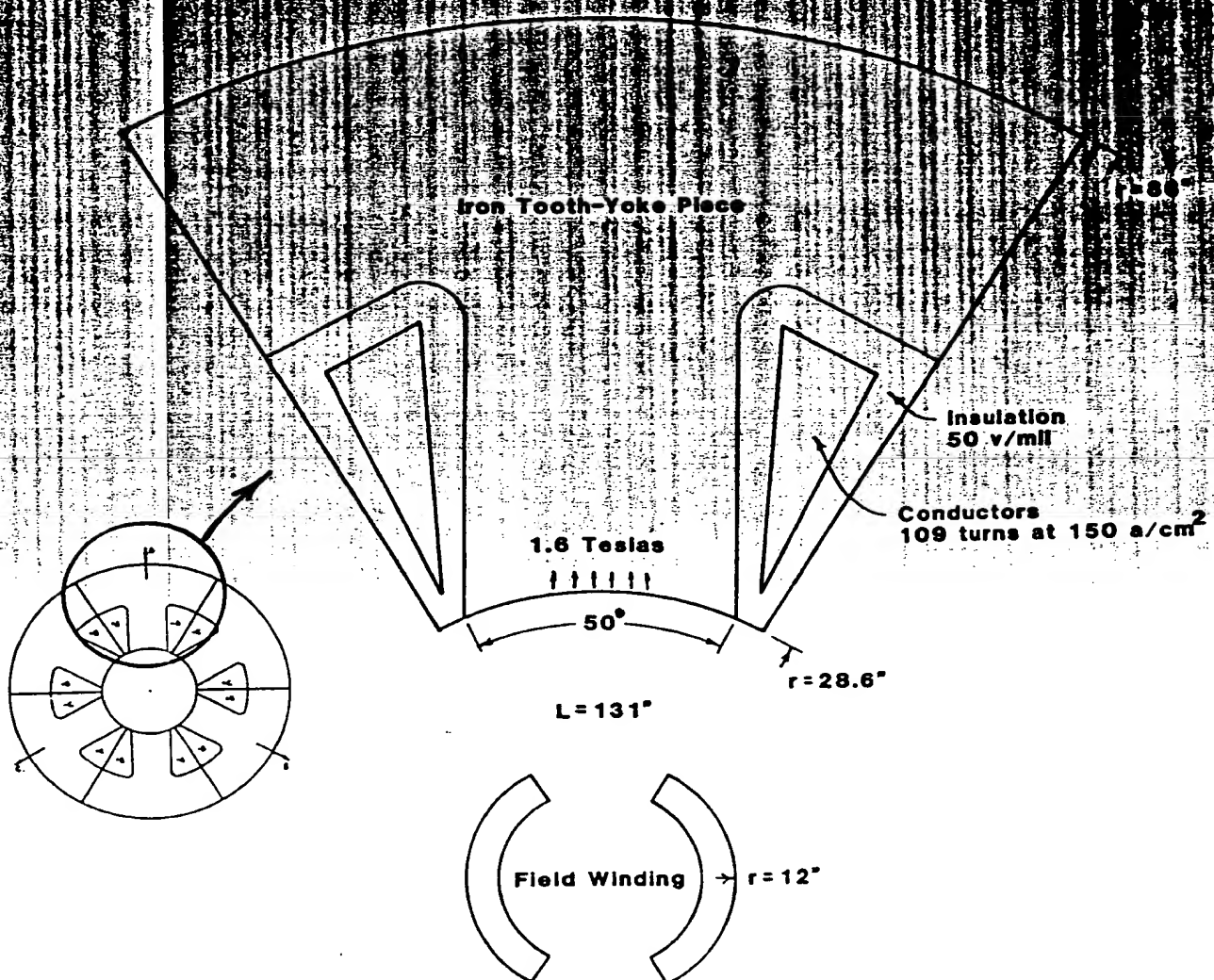


Figure 5.1-14. Creepage Baffles for the High-Voltage Spiral Pancake Armature

5.2 SALIENT POLE STATOR

An intriguing stator configuration which utilizes concentrated coils is illustrated in Figure 5.2-1. It is called variously a *salient-pole* stator or a *six-tooth* stator. The concentrated coils are wound about projecting iron-pole pieces, or "teeth," in a fashion closely reminiscent of transformer technology. Each concentrated coil and pole piece can be built as a separate module. Six such modules are assembled to form a complete stator, with each concentrated coil serving as a phase belt. Each concentrated coil is effectively short-pitched at 60° . The connection of the coils would be a simple circuit wye.



Salient Pole Stator 600 MVA, 345 KV

Figure 5.2-1. Rough Design of a Salient-Pole Stator

The advantages of the six-tooth stator are mostly mechanical in nature, owing to its dissociation with mechanical problems inherent in air-gap windings. The projecting iron teeth serve as a firm mechanical anchor for the winding. The projecting iron teeth also tend to isolate the winding from the air-gap flux so that most stator forces and torques are transmitted directly through the teeth (instead of through the conductors and insulation, as is the situation for an air-gap winding). There would be no diametrical limitations due to shipping considerations, since the modules could be shipped separately and be assembled on-site.

The six-tooth stator requires an electrical and magnetic evaluation in order to determine its competitiveness with other designs that have been studied. A rough design was executed at a 600 MVA, 345 kV rating, the same rating at which the computer sizing studies for the monolith cylinder and spiral pancake armatures were performed. The design of the six-tooth stator utilizes the same rotor as the design of the monolith cylinder armature.

The first step in roughing a design for the six-tooth stator is to size the dimensions of the tooth. The peripheral span of the tooth at the inside radius is limited to 50° out of a possible 60° in order to limit the amount of leakage flux which crosses from tooth to tooth. The inside radius of the tooth is adjusted to limit the rotor-produced flux density within the tooth to 1.6 T. The total flux within the tooth is calculated, after which the number of turns required around each tooth is calculated (using a single-circuit wye connection). The conductors must be packed into the wedge-shaped area between the tooth and the module edge. The overall current density of the conductor region is assumed to be 150 A/cm^2 , and the conductor region is entirely wrapped by a layer of insulation at 50 V/mil dielectric stress. The insulation is built for one-half line-to-ground voltage at the closest radial location of the conductor package and is increasingly built to full line-to-ground at the furthest radial location. The sizing of the conductor and insulation package determines the inner radius of the yoke. The outer radius of the yoke is sized to limit the yoke flux density to 1.6 T. The design dimensions of the six-tooth stator are contained in Table 5.2-1.

Table 5.2-1
600 MVA, 345 kV SALIENT-POLE STATOR
WITH SUPERCONDUCTING ROTOR

Voltage	345 kV
Current	1004 A
Connection	Wye
Turns/Phase	218
Armature Current Density	150 A/cm^2 , 967 A/in.^2
Tooth Inner Radius	28.6 in.
Core Outer Radius	86 in.
Core Length	131 in.
Field Winding Inner Radius	9 in.
Field Winding Outer Radius	12 in.
Field Current Density	$1 \times 10^8 \text{ A/m}^2$
Field Turns	1418
L_{ff}	4.15 H
L_{af}	0.2496 H
L_g	0.0867 H
L_l	0.2688 H
$X_{\text{synch}} = \omega(L_g + L_l/2)$	83.4Ω , .420 pu
$X' = \omega(L_g + L_l/2 - \frac{3}{2} \frac{L_{af}^2}{L_{ff}})$	74.9Ω , .377 pu

The reactances of the six-tooth stator can be determined from a rather assumptive division of the single-phase inductance into two portions, as illustrated in Figure 5.2-2. The gap inductance, L_g , is due to flux crossing the air-gap from tooth to tooth of similar phases. This flux does not link the other phases. The leakage inductance, L_l , is due to flux crossing the conductor packages from tooth to tooth of neighboring phases. This flux links the adjacent phases with an opposite polarity as found in conventional machines or air-gap windings with large-pitch coils. With the flux portioned and idealized to geometrically simple paths, the inductances L_g and L_l are calculated from reluctance and turn linkage summations. The single-phase reactance is

$$X = \omega (L_g + L_l)$$

The three-phase or synchronous reactance can be shown to be

$$X_{\text{sync}} = \omega (L_g + \frac{L_l}{2})$$

The three-phase transient reactance can be shown to be

$$X' = \omega (L_g + \frac{L_l}{2} - \frac{3}{2} \frac{L_{af}^2}{L_{ff}})$$

Numerical values of the inductances and reactances are contained in Table 5.2-1. It is not surprising to find the leakage inductance to be larger than the gap inductance. The reactances turn out to be somewhat larger than desired but could no doubt be adjusted with a sizing program, if the six-tooth stator is judged to be promising enough to justify preparing one.

Comparing the dimensions calculated for the salient-pole stator to the dimensions calculated for the monolith cylinder stator indicates that the six-tooth stator is a huge machine requiring an enormous amount of stator iron. This requires a proportional increase in the materials cost of the machine. Perhaps even more important are the large core losses in a machine requiring so much core iron.

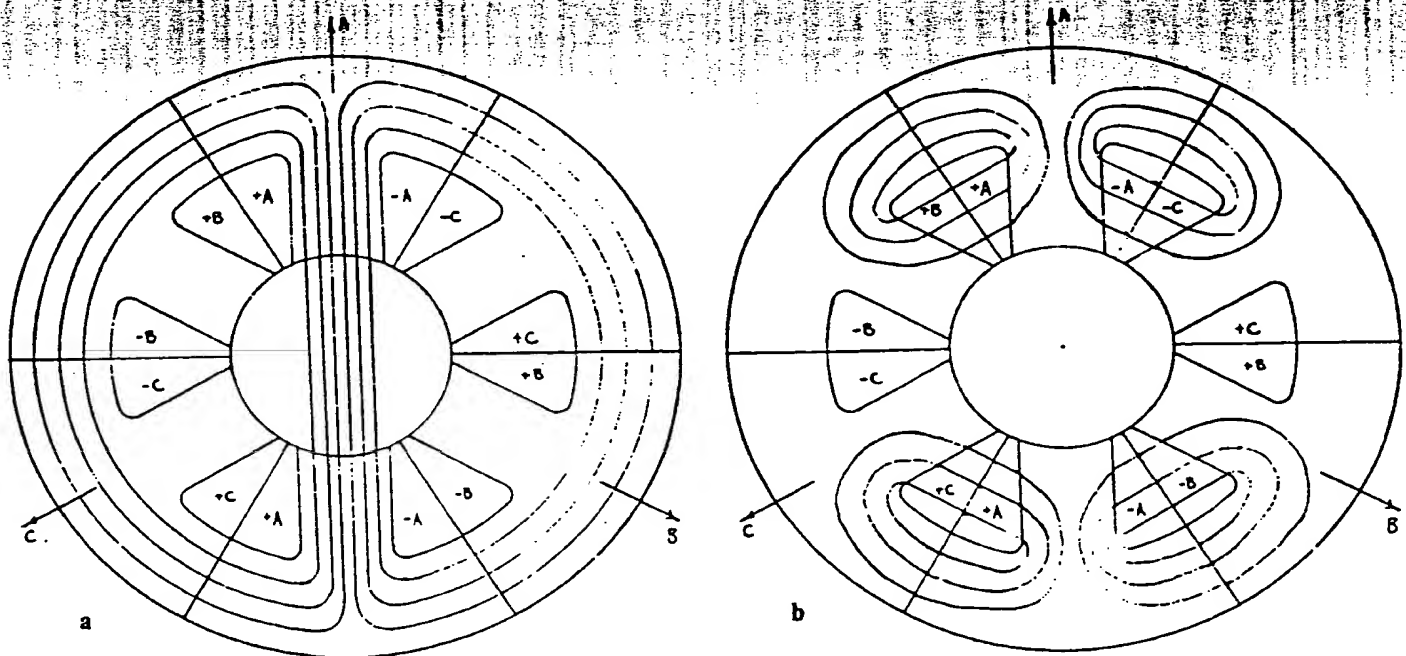


Figure 5.2-2. Division of Salient-Pole Stator Flux into Two Portions
(a) Flux Producing Gap Inductance L_g
(b) Flux Producing Leakage Inductance L_l

because of the effect on the economy of operation. Table 5.2-2 is a partial economical comparison of the six-tooth stator with a monolith cylinder stator and a conventional generator of the same rating. Included in the comparison are core and insulation costs as well as core and conductor electrical losses. It is seen that the core cost and losses of the six-tooth stator are more than three times that of the monolith cylinder stator. The extra core losses of the six-tooth stator amount to more than half the losses eliminated with the utilization of a superconducting rotor. The armature I^2R losses of the six-tooth stator are also larger than those of the monolith cylinder armature. The six-tooth stator machine would incur extra erection costs because the tooth and coil modules must be assembled at the power station by premium-priced erectors. The consensus on the six-tooth stator is that it is a bulky, expensive, and inefficient design that may be removed from consideration for mostly economic reasons.

Table 5.2-2

**ECONOMIC COMPARISON OF THE SALIENT-POLE STATOR WITH THE
MONOLITH CYLINDER STATOR AND A CONVENTIONAL GENERATOR
600 MVA**

	Core		Ground Insulation		Core Loss kW	Armature I^2R Loss
	Volume, in. ³	Material Cost	Volume, in. ³	Material Cost		
Six-Tooth Stator 345 kV	2462K	432K	491K	25K (50 V/mil pressboard)	1489	24% larger than monolith cylinder
Monolith Cylinder 345 kV	751K	131K	587K	29K (50 V/mil pressboard)	454	
Conventional 22 kV	1050K	176K	74K	52K (mica)	635	

5.3 INTEGRAL-INSULATED PHASE-BELT ARMATURE - TAPED SYSTEM

An integral-insulated phase-belt armature that uses many layers of tape in its construction is illustrated in Figure 5.3-1. The layers of tape are configured substantially orthogonally to the electric stresses, and the thickness of the tape layers is coordinated to the voltage that appears across them. Peripheral electrical creepage across the breadth of the phase-belts is eliminated by the tape configuration.

In the proposed construction, the basic unit is a half-turn braided-filament conductor, each of which is wrapped with turn insulation. Groups of conductors are formed together into a single structure, which may, for convenience, be termed a bundle. The number of conductors grouped into each bundle is the designer's choice, but the total number of conductors in the phase-belt is determined by the desired machine ratings.

A phase-belt structure is assembled from the center out. A layer of tape insulation is applied to the center bundle or pair of bundles. A bundle is placed on both sides of the structure so formed, and an additional layer of insulation is applied. Pairs of bundles and layers of insulation are alternatively added until the entire phase-belt structure has been formed.

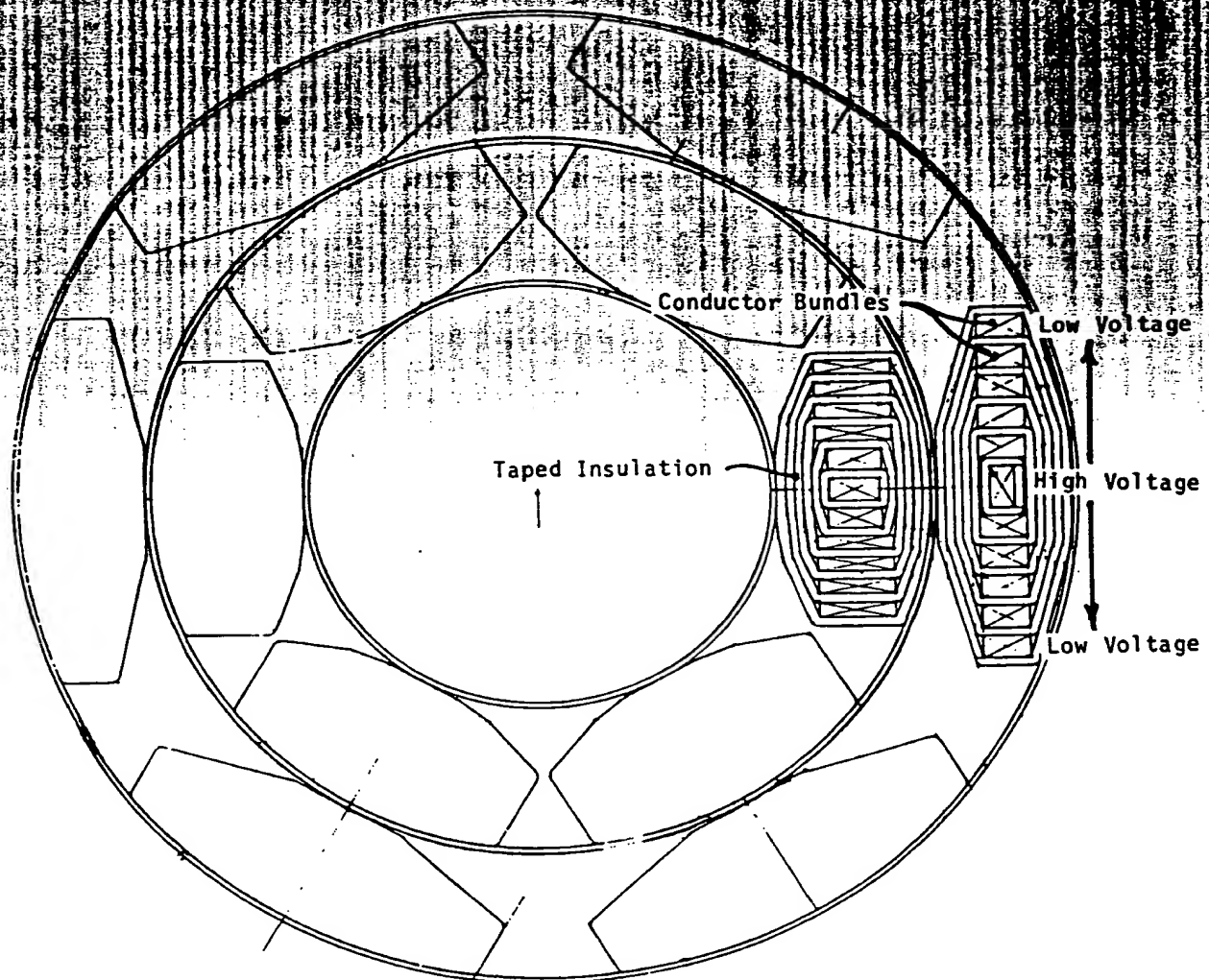


Figure 5.3-1. Cross-Section of an Integral-Insulated Phase-Belt Armature with Taped Insulation

The armature is assembled by bringing all the phase-belt structures together with appropriate mechanical structures placed between them. Interconnection of the bundles is made in such a manner that the inner bundles in each phase-belt are at the highest potential, and successive bundles (ordered from the inside out) are at progressively lower potential. The bundle connection is the same as described in Section 2.1 for the 60° phase-belt, two-circuit, graded-wye connection. The total thickness of insulation surrounding each bundle is proportional to the electrical potential of the bundle.

Figure 5.3-1 is a cross-section of this armature designed at a 600 MVA, 345 kV rating with 50 kV/in. insulation dielectric stress. The electromagnetic properties of this armature are similar to the monolith cylinder armature. The preferred coil shape is the helical coil shape, since the diamond coil shape would introduce additional taping complexities at its bends.

The conductor bundles of the phase-belt structures are configured in a flat layout, as opposed to a layout conforming to a 60° arc. This is because it is difficult to tape the concave surface of an arc layout. However, this introduces other complexities into the manufacturing process. Each conductor bundle lies on a slightly different radius and therefore lies on a slightly different helix. In addition, the faces of all but the centermost bundle do not align with the radial and peripheral coordinates. Therefore, each conductor bundle requires a separate bending form configured to an exotic shape. The conductor bundle assembly is likely to be slow and difficult.

Figure 5.3-2 illustrates a couple of end-connection layouts. Peripheral electrical creepage at the end connections is avoided by spreading the connections axially, where there is more room to lengthen the creepage paths. The connections start at the outermost pair of bundles, which are at the lowest potential. Connections are made with consecutively inward pairs of bundles, extending axially at each step. The innermost bundle, which is at the highest potential, has the greatest axial extension. In the upper design of Figure 5.3-2, there is a problem with electrical clearances between adjacent connections; in the lower design of Figure 5.3-2, the connections are bent outward. Figure 5.3-3 is a photograph of a model of the connections.

Electrical creepage studies of these connections indicate no difficulties. The physical distance consumed by the conductors and connections is greater than that required for creepage considerations. The axial distance required by this connection scheme can be in the order of 4 ft on each end. When one also considers the additional axial clearance required between the axially furthestmost connection and a grounded frame part such as the tank wall, it is realized that, while this connection scheme handles electrical creepage well, it will require considerably greater rotor bearing spans.

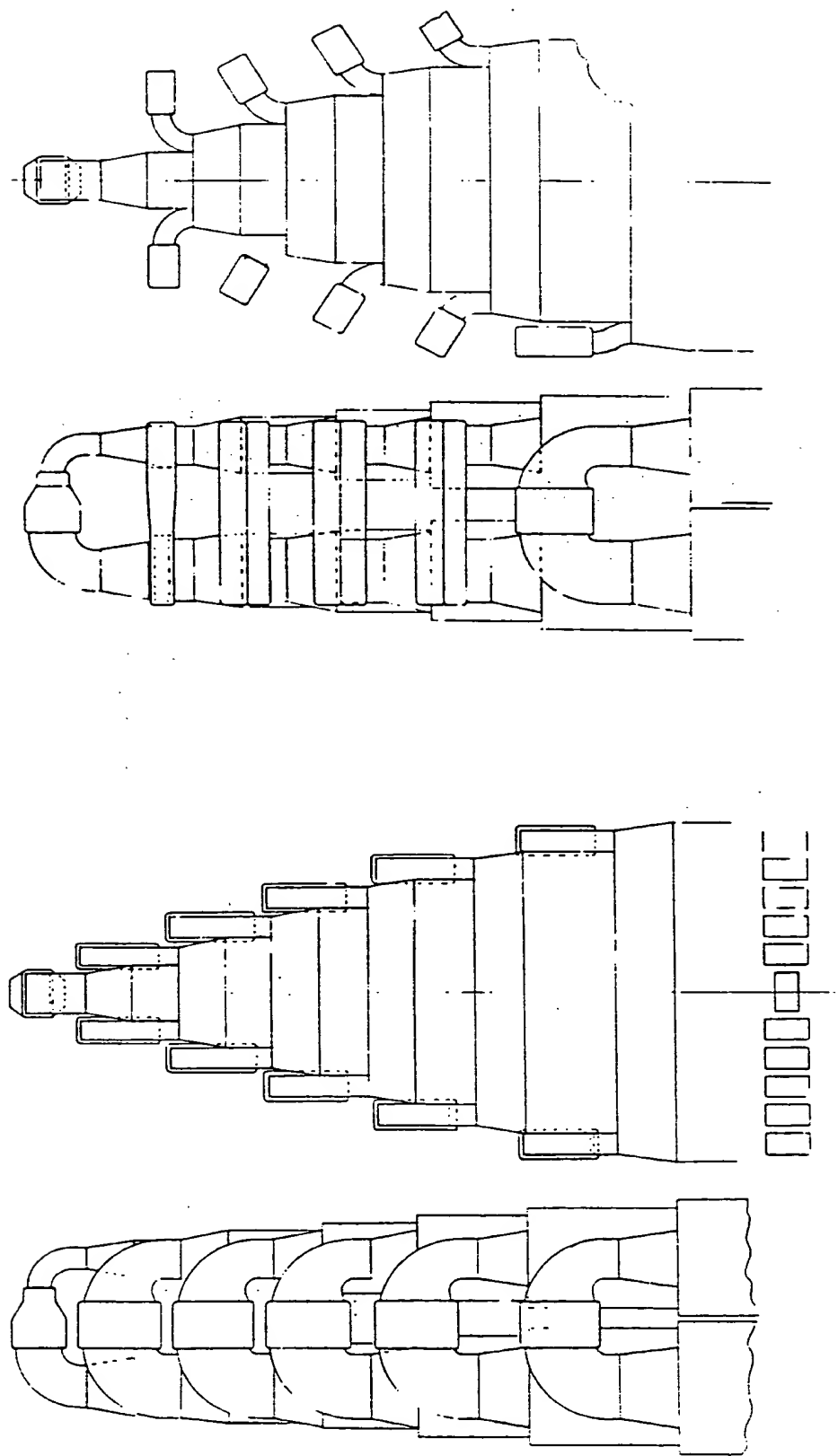


Figure 5.3-2. End Connections for the Integral-Insulated Phase-Belt Armature with Taped Insulation

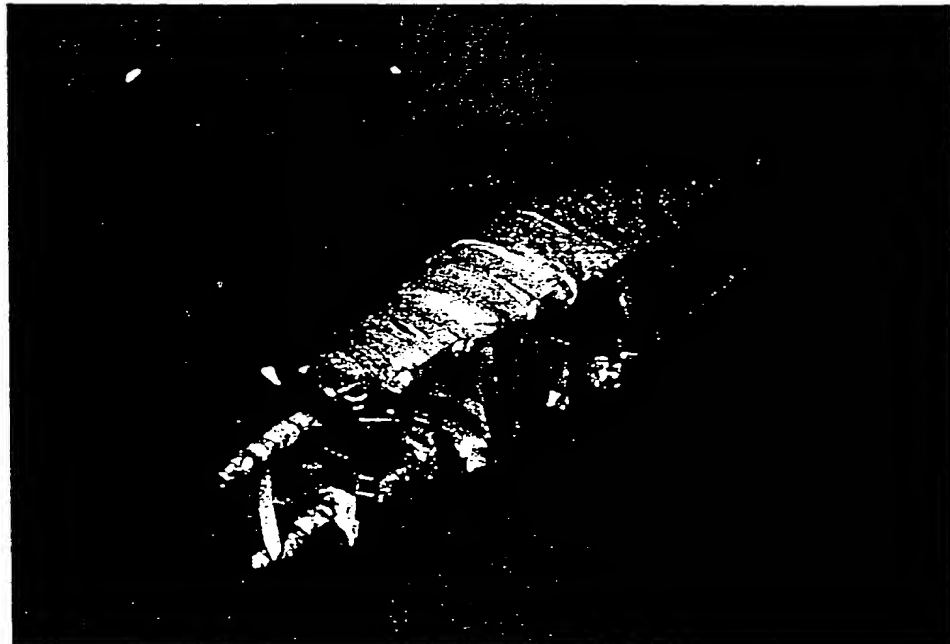


Figure 5.3-3. Model of the End Connections for the Integral-Insulated Phase-Belt Armature with Taped Insulation

5.4 INTEGRAL-INSULATED PHASE-BELT ARMATURE - COAXIAL SYSTEM

The phase-belts of a **coaxial system integral-insulated phase-belt armature** (Ref. 5-3) utilize conductors that are arranged concentrically, with each turn being surrounded by a succeeding turn. Figure 5.4-1 illustrates a cross-section of such a phase-belt. The winding would be connected in wye with the outermost coax to ground and the innermost coax at terminal. The coaxial design eliminates the need for very thick insulations, since the high voltage does not act on any single insulation thickness but is developed over the summation of the coaxial turn-to-turn insulations (each shielded from each other by the coaxial arrangement of the conductors). Thin-turn insulation materials such as fiberglass-epoxy or mica tapes could be used. The elongated shape of the coaxial phase-belt helps to equalize interturn capacitances and create a more uniform surge voltage distribution.

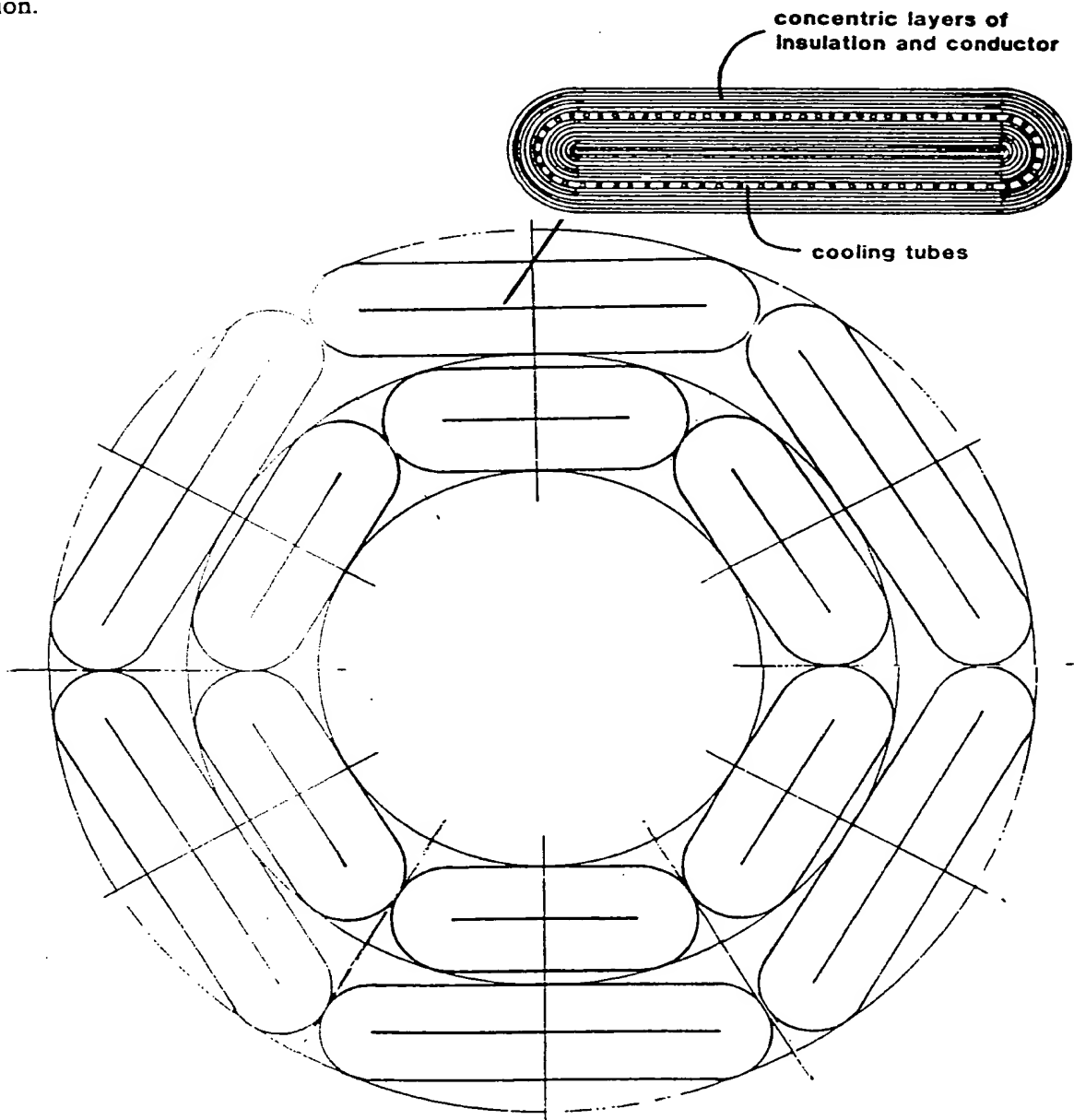


Figure 5.4-1. Cross-Section of an Integral-Insulated Phase-Belt Armature with Coaxial Phase-Belts

The coaxial arrangement of the conductors eliminates electrical creepage paths within the body of the winding. Electrical creepage at the end connections can be eliminated by a uniform axial tapering of the phase belt, as illustrated in Figure 5.4-2. This design is quite similar to the end connections for the taped system integral-insulated phase belt, illustrated in Figure 5.3-2. The coaxial system end connections suffer the same deficiencies that the taped system end connections suffer. Mechanical considerations dictate that the axial extension of the taper be much longer than the extension required for creepage considerations. This axial extension is in the order of four feet for each end. Additional axial distance is required for the clearance of grounded frame parts, and rotor bearing spans are likely to become excessive.

The coaxial phase belts may be incorporated into armatures which have either one layer or two layers. The two-layer design would be most familiar. There would be a total of 12 coaxial phase-belts formed into helical coil shapes, with inner and outer layers twisting in opposite directions, according to the usual manner for a helical winding. This winding would be connected as a double-circuit wye (as opposed to a single-circuit wye) so that the outer coax of all phase belts may be grounded. A single-layer armature would incorporate six coaxial phase-belts that run axially straight down the stator bore. Diametrically opposite phase belts would be joined through a decidedly complicated end-connection scheme that is the hallmark of single-layer windings. This winding would be a single-circuit wye.

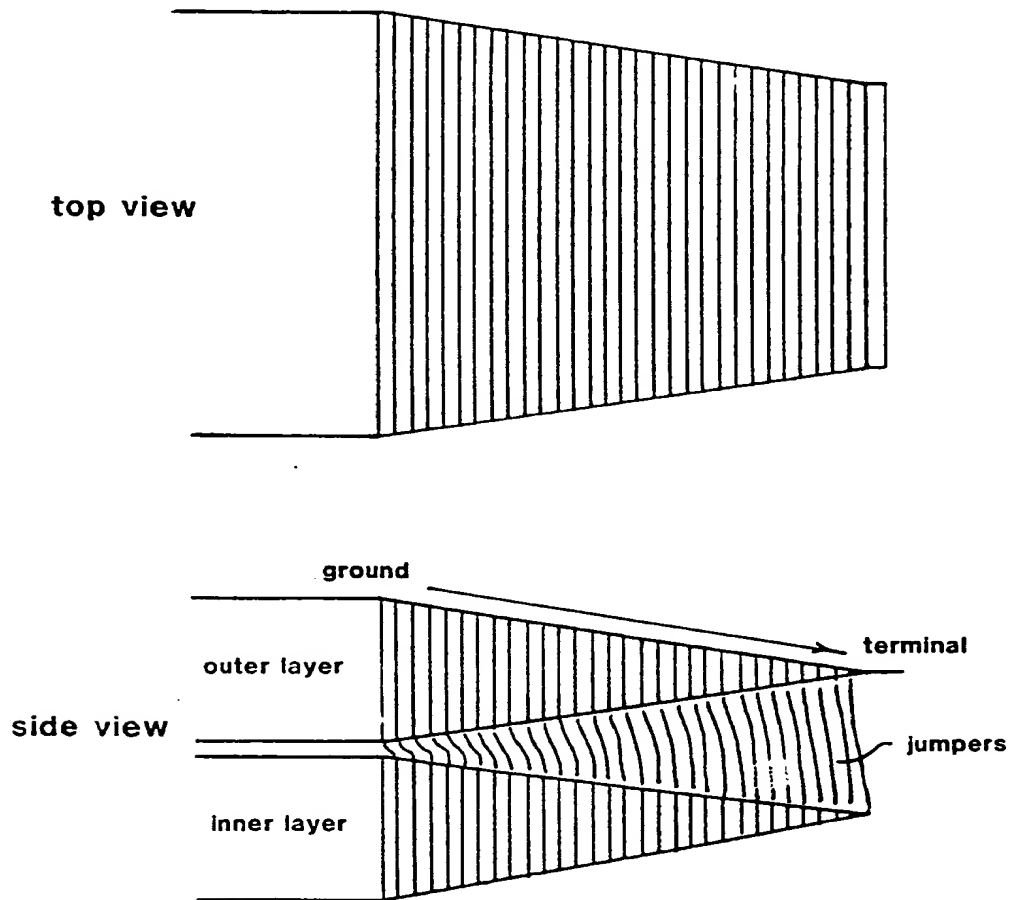


Figure 5.4-2. End-Region Connections of the Coaxial Integral-Insulated Phase-Belt Armature

The single-layer winding has a superior space utilization as compared to the two-layer winding; this is because the insulation is duplicated in the two-layer winding. Figure 5.4-3 illustrates a sizing comparison between the two windings at a 600 MVA, 345 kV rating. Both windings use insulation stressed at 50 kV/in. and a conductor-sheath current density which ranges from approximately 300 A/cm² at the inner conductors to approximately 150 A/cm² at the outer conductors. Both windings start with a 19 in. armature bore radius. The conductors and the insulation are packed tightly and the core's resultant inner radii are determined. The double-layer winding has a 42 in. core inner radius as compared to a 32.5 in. core inner radius on the single-layer winding. The single-layer winding, therefore, has a two-to-one advantage in space utilization. However, the single-layer winding's difficult end connections pose a serious impediment to its feasibility.

The conductor sheaths in the coaxial phase-belt must be extremely thin (less than 10 mils) because of the long coax perimeters. The conductor sheaths would have to be comprised of a thin, braided filament gauze and would likely resemble ladies' hosiery. It would not be practicable to provide cooling tubes for every conductor sheath, so it would be necessary to place layers of cooling tubes for every so many layers of conductor and insulation. The heat transfer through many layers of conductor sheath and insulation is not likely to be very satisfactory.

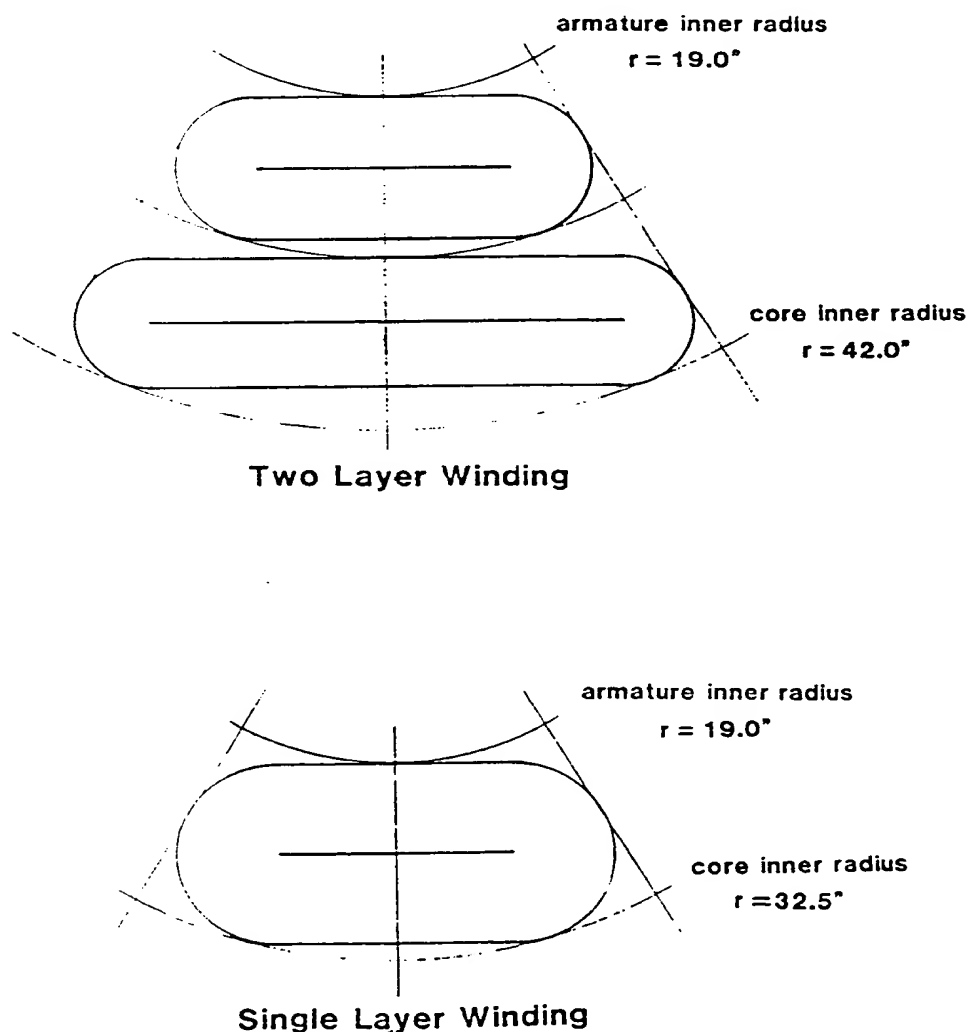


Figure 5.4-3. Comparison of Two-Layer and Single-Layer Coaxial Integral-Insulated Phase-Belt Windings

References

- 5-1. C. Flick, "New Armature Winding Concepts for EHV and High CFCT Applications of Superconducting Turbine Generators," *IEEE Transactions Power Apparatus and Systems*, Vol. PAS-98, No. 6, Nov./Dec. 1979.
- 5-2. Westinghouse Electric Co., *Superconducting Generator Design*, EPRI Research Project RP429-1, Final Report, Nov. 1977.
- 5-3. G. Aichholzer, M. Manowarda, "Approach to Development of a 230 kV Airgap Winding," *Proceedings of the International Conference of Electrical Machines*, Athens, 1980.

Section 6

ECONOMIC ANALYSIS OF SUPERCONDUCTING GENERATORS

Considering all the uncertainties associated with the new technologies required to introduce low-voltage and high-voltage superconducting generators, it is very difficult to perform a definitive economic analysis which can be used to make firm decisions for long-range development effort. A review of all past published economic studies shows that they have used only portions of a full economic study. These studies indicated significant economic advantages if the reliability and availability of superconducting generators proved to be equivalent to present-day conventional generators. Such studies had merit when the primary concern was proving the technological feasibility of superconducting generators. However, as development programs continue and as better knowledge is gained of technical feasibility, cost of manufacturing, cost of development, potential savings, and future business conditions, a more detailed economic analysis becomes necessary.

In this section, a methodology is outlined and employed to compare the potential economic advantages of low-voltage and high-voltage superconducting generators over conventional generators. The methodology identifies estimated yearly development expenses and cost savings for a 35-year period, using an estimated introduction and penetration rate of low-voltage and high-voltage superconducting generators. With these data, anticipated rates of return on industry development expenses can be calculated to provide an indication whether the effort will increase the industry's economic performance. Breakeven periods and present worth values are also calculated, and the calculations are performed for different estimate scenarios so that an understanding of the sensitivity to the various assumed estimates can be obtained.

The rationale behind the estimated values for the expenses and savings used in this analysis are described in following subsections. It is realized that many of the estimates are arrived at by a subjective process. No two persons or organizations will arrive at the same values. However, the methodology is presented so that updated data can be introduced in the future to continually improve the accuracy of the results.

The uncertainties of the results are the greatest for comparing low-voltage and high-voltage superconducting generators to conventional generators, since a number of technical problems and the effect of solving these problems on manufacturing cost and efficiency have not been fully resolved. For example, the following items were not included in the economic study:

- Modifications required in turbine design to minimize overspeed during load rejections. This potential problem results from lowered turbine-generator total rotor inertia using lower weight superconducting fields. The solution to this problem could result in increased turbine control costs and possibly a turbine efficiency reduction which would offset the improved efficiency of superconducting generators.
- Modifications required to minimize rotor torsional stresses when superconducting generator units are subjected to three-phase short circuits or fast reclosing conditions.
- Reliability and availability that is not comparable to the present-day standards of conventional generators. A small deterioration in reliability and availability would completely eliminate even the optimistic savings scenarios shown in this analysis.
- Potential savings resulting from improved steady state and transient stability associated with the lower reactances of superconducting generators. These savings could be included by speculating that superconducting generators would eliminate the need for 10 to 20 one hundred-mile-long transmission lines between the years 2000 and 2020 at a value of \$50 million per line in 1985 dollars. Since these savings would not be realized until far into the future, the effects on the economic results would not be dramatic.

The economic comparisons of high-voltage and low-voltage superconducting generators with each other should have less uncertainty than the comparisons made to conventional units. The assumptions and estimates used to calculate the results are based on similar reasoning, and the uncertainties listed above do not apply. However, the results must be tempered by the uncertainties and subjectiveness of the input data used to perform the analysis.

The monetary values used in these analyses are total domestic industry quantities. The estimated development costs assume that two or more manufacturers will participate in the development effort, since a technically competitive environment will produce optimal results.

6.1 METHODOLOGY OF ECONOMIC ANALYSIS

The economic analyses presented in this section use a straightforward textbook methodology. Table 6.1-1 displays the basic approach. Estimated total industry development expenses and potential savings (1985 dollars) per each year from 1986 through 2020 are required for the analysis, and later subsections will discuss the logic used to arrive at the development costs and savings estimates.

Table 6.1-1
ECONOMIC ANALYSIS APPROACH

Years	Dev. Cost \$ × 10 ⁶	Est. Savings \$ × 10 ⁶
1986	X ₁	—
1987	X ₂	—
1988	X ₃	—
1989	X ₄	—
1990	X ₅	—
1991	X ₆	Z ₁
1992	X ₇	Z ₂
1993	X ₈	Z ₃
1994	X ₉	Z ₄
1995	X ₁₀	Z ₅
↓	↓	↓
Present Worth Development Cost		Present Worth Savings
$\sum_n^N X_n (1+i)^n \frac{1}{(1+r_1)^n}$		$\sum_n^N Z_n (1+i)^n \frac{1}{(1+r_1)^n}$

i = Inflation rate
*r*₁ = Rate of return to cover cost of money (inc. inflation)
 Cost and savings are first period dollars.

Inflation can be removed from the equation by using an *r*₂ equivalent to:

$$\frac{(1+i)^n}{(1+r_1)^n} = \frac{1}{(1+r_2)^n}$$

In this case, an *r*₂ of 6% to 7% will define a breakeven period for a utility. This value includes 3% to 4% cost of money without inflation, plus 2% to 3% for capitalization (taxes, insurance, etc.).

The present worth of the development costs and savings can be calculated by applying interest formulas to account for inflation and the rate of return required to cover the cost of borrowing money. The present worth formula can be simplified by eliminating inflation from the formulas and using a modified rate-of-return (r_2). Computer programs which accept the yearly development costs and savings and calculate a rate of return are readily available.

To establish whether the calculated rate of return describes a scenario that will significantly improve the industry's economic performance, it is necessary to define a minimum rate of return percentage which will produce a breakeven present worth value. In the utility industry, using noninflated dollars as the input values for each year, the modified rate of return must be 6% to 7% to describe a breakeven period. This 6% to 7% accounts for a long-term average cost of borrowing money of 3% to 4% (without inflation), plus 2% to 3% for capitalization expenses such as income taxes, insurance, etc.. In this report, 7% has been used as the base criterion for each scenario.

The results of the economic analysis for each scenario can be described in a number of different manners:

- *Rate of Return Value.* This value must be greater than 7% or a breakeven period has not been achieved. The higher the rate of return over 7%, the greater the potential is for the project to improve the economic performance of the industry.
- *Breakeven Period or Year.* The present worth of the savings is calculated for each year and is summed to the year in which the savings equal the present worth of the total development costs. The present worth calculations use $r_2 = 7\%$.
- *Present Worth Value.* The present worth using $r_2 = 7\%$ is calculated for both development expenses and savings. The net present worth is calculated by subtracting the development value from the savings value.

The values described above can be considered to be qualitative indications of the merit of the project being analyzed. The decision as to whether the project should be selected for future development effort must be made by ascertaining whether other development projects, which would use the same development funds, could provide significantly greater financial benefits.

6.2 RESULTS OF ECONOMIC ANALYSES

Tables 6.2-1 and 6.2-2 contain the input data used to calculate the rate of return, breakeven period, and the present worth for a number of different business scenarios. Table 6.2-1 illustrates the economical comparison of low-voltage superconducting generators with conventional generators. Two different electrical industry growth rates are used to arrive at two different penetration rates for the low-voltage superconducting generators. The estimated yearly industry savings in 1985 dollars are shown for each year and are based on the introduction and penetration rate scenarios. The savings estimates are displayed for high, average, and low savings scenarios. An estimate of the yearly industry development cost which would apply to either introduction rate scenario is shown. The methods and judgments used to arrive at these input values are described in following subsections. Table 6.2-2 illustrates the economical comparison of high-voltage superconducting generators with conventional generators. Tables 6.2-1 and 6.2-2 allow a comparison of the merits of the high-voltage generator economic study (Table 6.2-2) with the low-voltage generator study (Table 6.2-1).

The rates of return, the breakeven years, and the present worth values are shown for each scenario. Assuming that the average estimated savings scenarios are the most likely to be realized, the results show a potential for either the low-voltage or the high-voltage superconducting generator development effort to provide the industry with improved economic performance. However, the data also suggest that the economic benefit of a major effort to develop high-voltage generators for introduction in the 1990's is little improvement on the economic benefit of the sole development of low-voltage superconducting technology. These results are of primary interest to help establish whether follow-on effort should be recommended for the high-voltage generator.

Table 6.2-1
ECONOMIC STUDY FOR LOW-VOLTAGE SUPERCONDUCTING GENERATORS
(1985 DOLLARS)

From Late 1960 to 1985	1985 Dollars Development Cost 2 Manuf. Introduced Low Voltage SCG	Growth Rate				Low Business Growth Low-Voltage SCG Introduction Scenario				Growth Rate				Medium Business Growth Low-Voltage SCG Introduction Scenario									
		1.5% 1990		2.3% 2020		2.5% 1990		2.8% 2000		3.0% 2020		2.5% 1990		2.8% 2000		3.0% 2020							
		Total Cap. Added	SCG GW	SCG Add GW	No. Units	High Est. Size MVA	Avg. Est. Savings \$x10 ⁶	Low Est. Savings \$x10 ⁶	Total Cap. Added	SCG GW	SCG Add GW	No. Units	High Est. Size MVA	Avg. Est. Savings \$x10 ⁶	Low Est. Savings \$x10 ⁶	Total Cap. Added	SCG GW	SCG Add GW	No. Units	High Est. Size MVA	Avg. Est. Savings \$x10 ⁶	Low Est. Savings \$x10 ⁶	
86	48	10.2	0.27	1	300	-	-	-	16.0	0.27	1	300	-	-	-	16.0	0.27	1	300	-	-	-	
87	12	11.0							17.4							17.4							
88	12																						
89	12																						
90	18		0.54	2	300	2.42	-1.1	-5.9		0.54	2	300	2.42	-1.1	-5.9		0.54	2	300	2.42	-1.1	-5.9	
91	18	16.8							22.0							22.0							
92	18																						
93	18																						
94	24																						
95	24																						
96	18	19.8							26.4							26.4							
97	12																						
98	12		2.0	2	1200	14.1	8.2	2.1		2.0	2	1200	14.1	8.2	2.1		2.0	2	1200	14.1	8.2	2.1	
99	6																						
2000	264		4.0	4	1200	28.2	16.4	4.2		4.0	4	1200	28.2	16.4	4.2		4.0	4	1200	28.2	16.4	4.2	
01	-48	21.4	5.0			35.2	20.5	5.2	31.8	5.0			35.2	20.5	5.2	31.8	5.0			35.2	20.5	5.2	
02	216		5.0			35.2	20.5	5.2		6.0			42.3	24.6	6.3		6.0			42.3	24.6	6.3	
03			6.0			42.3	24.6	6.3		7.0			49.3	25.7	7.3		7.0			49.3	25.7	7.3	
04			7.0			49.3	28.7	7.3		8.0			56.4	32.8	8.4		8.0			56.4	32.8	8.4	
2005			8.0			56.4	32.8	8.4		10.0			70.5	41.0	10.5		10.0			70.5	41.0	10.5	
06		24.0	10.0			70.5	41.0	10.5	36.4	12.0			84.6	49.2	12.6	36.4	12.0			84.6	49.2	12.6	
07			11.0			77.5	45.0	11.5		14.0			98.7	57.4	14.7		14.0			98.7	57.4	14.7	
08			12.0			84.6	49.2	12.6		16.0			112.8	65.6	16.8		16.0			112.8	65.6	16.8	
09			12.0							20.0			141.0	82.0	21.0		20.0			141.0	82.0	21.0	
2010			12.0							22.0			155.0	90.2	23.1		22.0			155.0	90.2	23.1	
11		28.4	18.0			127.0	73.8	18.9	43.8	25.0			176.0	102.5	26.2	43.8	25.0			176.0	102.5	26.2	
2015																							
16		31.4	22.0			155.0	90.2	23.1	50.6	35.0			247.0	143.5	36.7	50.6	35.0			247.0	143.5	36.7	
2020																							
		Rate of Return		Breakeven Year (7% ROR)		P.W. Savings - P.W. Dev. Costs		(million dollars) (7% ROR)															
		13%		2008		216		67															
		9%		2013		216		67															
		4%		>2020		216		67															
		15%		2007		350		144															
		11%		2011		350		144															
		5%		>2020		350		144															

Table 6.2-2
ECONOMIC STUDY FOR HIGH-VOLTAGE SUPERCONDUCTING GENERATORS
(1985 DOLLARS)

1985 Dollars Development Cost Introduce High-Voltage SCG		Low Business Growth High-Voltage SCG Introduction Scenario							Medium Business Growth High-Voltage SCG Introduction Scenario								
Total Dev. Funds Req'd \$x10 ⁶		Total Cap. Added GW	SCG Add GW	No. Units	Unit Size MVA	High Est. Savings \$x10 ⁶	Avg. Est. Savings \$x10 ⁶	Low Est. Savings \$x10 ⁶	Total Cap. Added GW	SCG Add GW	No. Units	Unit Size MVA	High Est. Savings \$x10 ⁶	Avg. Est. Savings \$x10 ⁶	Low Est. Savings \$x10 ⁶		
From Late 1960 To	48	10.2							16.0								
1985	1	11.0							17.4								
86	18	1							1								
87	18	1							1								
88	18	1							1								
89	18	1							1								
1990	27	16.8	0.27	1	300	3.4	0.9	-1.6	1	0.27	1	300	3.4	0.9	-1.6		
91	27	1							22.0								
92	27	1							1								
93	27	1							1								
94	36	1							1								
1995	36	19.8	0.54	2	300	6.8	1.8	-3.2	1	0.54	2	300	6.8	1.8	-3.2		
96	27	1							26.4								
97	27	1							1								
98	27	1	1.0	2	600	15.4	9.8	4.0	1	1.0	2	600	15.4	9.8	4.0		
99	27	1							1								
2000	18	21.4	2.0	2	1200	30.6	23.0	15.4	1	2.0	2	1200	30.6	23.0	15.4		
01	12	1							31.8								
02	6	1							1								
03	462	1	4.0	4	61.2	46.0	30.8		1	4.0	4	1200	62.2	46.0	30.8		
04	-48	1	5.0	5	76.5	57.0	38.5		1	6.0			91.8	69.0	46.2		
2005	414	24.0	5.0	5	76.5	57.0	38.5		1	8.0			122.4	92.0	61.6		
06		1	6	6	91.8	69.0	46.2		36.4	10.0			153.0	115.0	77.0		
07		1	7	7	107.1	80.5	53.9		1	12.0			183.6	138.0	92.4		
08		1	8	8	122.4	92.0	61.6		1	14.0			214.2	161.0	108.0		
09		1	10	10	153.0	115.0	77.0		1	16.0			244.0	184.0	123.0		
2010		1	11	11	168.3	126.5	84.7		1	18.0			275.4	207.0	138.6		
11		28.4	12	12	183.6	138.0	92.4		43.8	22.0			336.0	253.0	169.4		
2015		1	1	1	1	1	1	1	1	1	1	1	1	1	1		
16		31.4	18	18	275.4	207.0	138.6		50.6	25.0			382.0	287.0	192.0		
2020		1	1	1	1	1	1	1	1	1	1	1	1	1	1		
Rate of Return		12%							15%							10%	
Breakeven Year (7% ROR)		2011							2008							2013	
P.W. Savings - P.W. Dev. Costs (million dollars) (7% ROR)		274							586							163	

The sensitivity of the rate of return percentages to the high, average, and low cost savings estimates is shown in Tables 6.2-1 and 6.2-2. Figure 6.2-1 illustrates a sensitivity study where either development costs or savings are varied, with the other value held constant. Figure 6.2-1 demonstrates the sensitivity of the rate of return percentage to variations of the development cost estimates. The curve forms can be generally described by the analytical model shown in the figure.

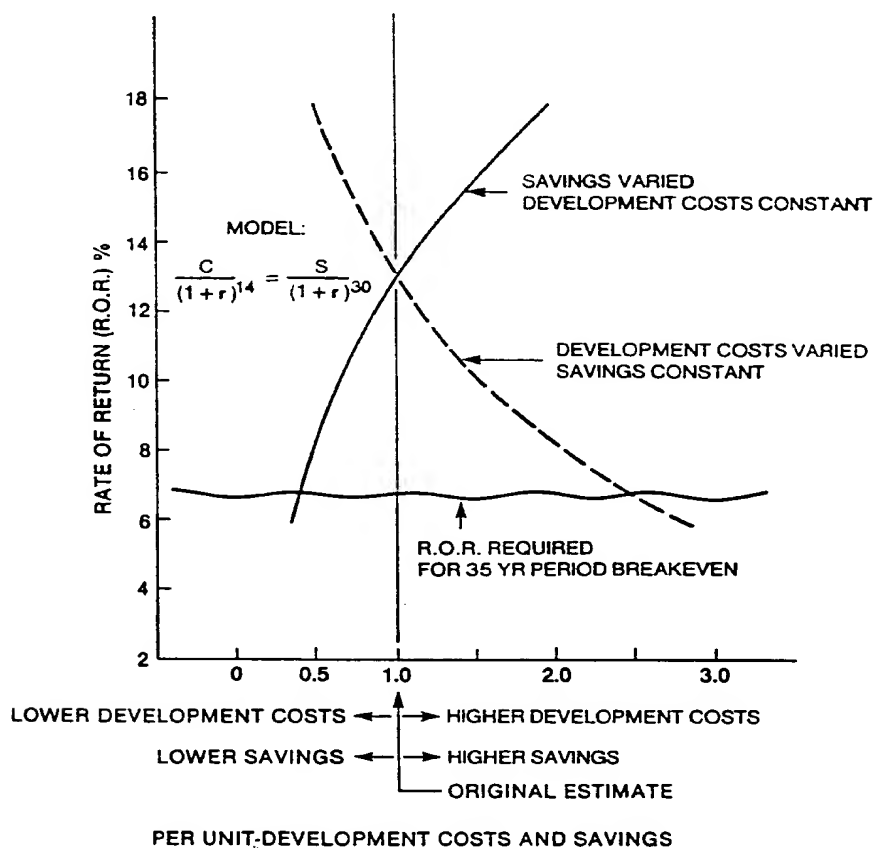


Figure 6.2-1. Typical Sensitivity Study for Variations in Development Costs and Savings Estimates

6.3 GENERATOR INTRODUCTION AND PENETRATION RATES

To arrive at the estimated yearly savings from using low-voltage and high-voltage superconducting generators, it was necessary to establish the number of units which could be expected to be added to the national grid during the study period from 1986 to 2020. This task was accomplished with the methodology outlined in Reference 6-1.

Table 6.3-1 defines two domestic utility load growth rates. Based on these growth rates, the anticipated added generator capacity for each five-year period is calculated. The low growth rate scenario is pessimistic. However, considering the 1% electrical growth rates recorded during the last two years and the large number of units shipped by manufacturers which have not been installed, this scenario represents a reasonable estimate of total new business installed capacity for at least the next 10 years. The medium or high growth rate scenario is more optimistic. However, it is still considerably below the 4.2% per year growth rate recently published in Reference 6-2. The results of the economic studies are very sensitive to the magnitude of the growth rate used. For example, the fact that present-day growth rate forecasts are significantly lower than the historical 7% per year has dramatically reduced the number of installed units and thus the potential savings during the years 2000 through 2020. The lower growth rates have also reduced the manufacturers' anticipated business level. Thus, available development funds to address new technology projects are significantly lower than in the past. The need for larger rating sizes, where superconducting generator technology appears to have a significant advantage, has virtually disappeared.

The average added equipment capacity entries in Table 6.3-1 are calculated by starting with the 615 GW total installed capacity in 1980 (from Reference 6-3). The capacities for each successive 5-year period are calculated from the percent growth rates shown. It is assumed that 90% of the total installed capacity is steam and gas turbine equipment. Five-year added capacity values are obtained by subtracting earlier period capacities from successive period capacities. Estimated 5-year equipment retirement values are added to the 5-year added capacities to obtain 5-year total added equipment capacities. A yearly average added equipment capacity is obtained by dividing a 5-year total added equipment capacity by five.

Using the yearly average added equipment capacity values and a judgment as to the introduction rate of demonstration generators during the development period, penetration scenarios can be generated for the low and high load growth rate estimates for both the low-voltage and high-voltage superconducting generator economic studies. Table 6.2-1 displays the introduction and penetration rate for the low-voltage superconducting generator using the low growth rate estimate. The introduction rate for the high growth rate estimate is the same. The demonstration or development unit sizes are rapidly escalated to 1200 MVA ratings to provide the highest estimated savings based on potential market needs. Penetrations of the low-voltage superconducting generators are escalated after the 1200 MVA generator size has been reached. The penetration, however, is limited to 70% of the total anticipated added equipment capacity during the later years. This limit reflects the possibility that not all the total added equipment capacity will be superconducting generator central stations. That is, at least 30% will be gas turbines, small cogeneration stations, or other power supplies which will not use superconducting generator technology.

The same types of judgments are used to arrive at the introduction and penetration rates for the high-voltage superconducting generator economic studies. A review of the data presented in Tables 6.2-1 and 6.2-2 will show the major differences in the estimates used. The introduction rates are delayed based on the development effort starting later. The total penetration is limited to only 50% to 57% of the total added equipment capacity per year during the later years. This judgment is based on the possibility that high-voltage superconducting generators will have additional restraints that will preclude the higher 70% penetration estimated for the low-voltage superconducting generators. For example, high-voltage generators appear to be limited to 500 kV. If 750 kV and higher voltage transmission lines are extensively used in the years 2010 through 2020, high-voltage generators may not be selected. The physically larger generator sizes required to produce the same MVA rating could also limit the use of high-voltage superconducting generators in the future.

Table 6.3-1
AVERAGE ADDED EQUIPMENT CAPACITY
Low-Growth Scenario

% Growth	Year	Total Installed Capacity GW	90% Steam-Gas Turbine GW	Added Capacity 5 Yr. Period GW	Equipment Retirement 5 Yr. Period GW	Total Added Equipment Capacity 5 Yr. Period GW	Average Added Equipment Capacity GW/Yr.
1 1.5%	1980	615	553				
	1985	662	596	45	6	51	10.2
1 2.3%	1990	717	645	49	6	55	11.0
	1995	803	723	78	6	84	16.8
	2000	900	810	89	10	99	19.8
	2005	1008	907	97	10	107	21.4
	2010	1130	1017	110	10	120	24.0
	2015	1266	1139	122	20	142	28.4
	2020	1418	1276	137	20	157	31.4

Medium- or High-Growth Scenario

% Growth	Year	Total Installed Capacity GW	90% Steam-Gas Turbine GW	Added Capacity 5 Yr. Period GW	Equipment Retirement 5 Yr. Period GW	Total Added Equipment Capacity 5 Yr. Period GW	Average Added Equipment Capacity GW/Yr.
1 2.5%	1980	615	553				
	1985	693	627	74	6	80	16.0
1 2.8%	1990	786	708	81	6	87	17.4
	1995	902	812	104	6	110	22.0
1 3.0%	2000	1037	933	121	20	131	26.4
	2005	1202	1082	149	20	159	31.8
	2010	1394	1254	172	20	182	36.4
	2015	1615	1453	199	20	219	43.8
	2020	1872	1688	233	20	253	50.6

6.4 POTENTIAL SAVINGS ESTIMATES

The yearly potential savings using high, average, and low estimates are shown in Tables 6.2-1 and 6.2-2. These values were calculated by establishing a present worth (1985 dollars) for both low-voltage and high-voltage superconducting generators compared to conventional generators. The saving estimates for the low-voltage superconducting generators account for the improved generator efficiency, which reduces fuel cost, and the estimated cost differences between superconducting generators and conventional generators. The cost savings estimated for the high-voltage generators account for the following items:

- Generator cost differences
- Generator efficiency improvements
- Transformer cost elimination
- Transformer losses elimination
- Equipment costs to ensure adequate generator grounding

It was pointed out earlier that there are a number of other factors which could either reduce or increase these savings. However, the knowledge available to assign specific dollar values to these items is limited. Thus, in this study, it has been assumed that the extra cost items will be offset by the lower cost items. Future experience and/or more detailed studies will reduce the uncertainties in these cost estimates.

The cost differences between conventional generators and superconducting generators were obtained by a cost estimating process comparing labor and material cost requirements. As a result of the uncertainties in identifying the labor and material costs involved with the new technology of superconducting generators, high, low, and average cost estimates were generated. Curves similar to Figure 6.4-1 were developed to show the estimated cost at the utility level of the different types of generators. The high, low, and average cost differences were obtained as shown in the figure.

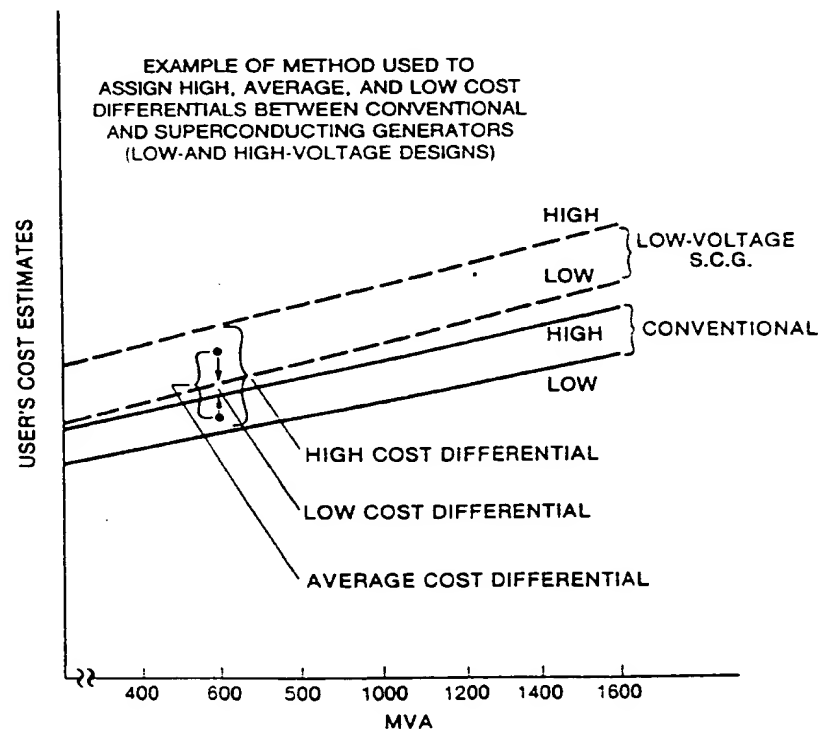


Figure 6.4-1. High, Average, and Low Cost Differentials of Superconducting Generators over Conventional Generators

Figure 6.4-1 is representative of the approach used to establish the cost differences. The cost differences obtained from the estimated cost curves are shown in Tables 6.4-1 and 6.4-2.

The improved efficiency values were arrived at by the use of a \$1270/kW value derived in Appendix J. This value of efficiency is a utility's justified investment value in 1985 dollars for the savings in fuel during the lifetime of the unit. The efficiency values and generator cost differences can be added or subtracted to arrive at a single value of savings for the economic evaluation.

Table 6.4-1
VALUE TO USERS – LOW-VOLTAGE S.C.G. OVER CONVENTIONAL GENERATORS
1985 DOLLARS – \$1270/kW EFFICIENCY EVALUATION

High Savings – Based on Low Generator Cost Differential Estimates

MW	MVA	Gen. Cost \$ × 10 ⁶	Gen. Eff. Savings \$ × 10 ⁶	Total Savings \$ × 10 ⁶
270	300	0	+1.71	+1.71
540	600	.25	3.43	3.68
1080	1200	.7	6.35	7.05

Average Savings – Based on Average Generator Cost Differential Estimates

MW	MVA	Gen. Cost \$ × 10 ⁶	Gen. Eff. Savings \$ × 10 ⁶	Total Savings \$ × 10 ⁶
270	300	–2.27	1.71	–.56
540	600	–2.14	3.43	1.29
1080	1200	–2.27	6.35	4.08

Low Savings – Based on High Generator Cost Differential Estimates

MW	MVA	Gen. Cost \$ × 10 ⁶	Gen. Eff. Savings \$ × 10 ⁶	Total Savings \$ × 10 ⁶
270	300	–4.66	1.71	–2.95
540	600	–4.66	3.43	–1.23
1080	1200	–5.29	6.35	1.06

Efficiency Evaluation = kW × .005 × \$1,270/kW
(–) = Negative Savings

Table 6.4-2

VALUE TO USERS – HIGH VOLTAGE S.C.G. OVER CONVENTIONAL GENERATORS
1985 DOLLARS – \$1270/KW EFFICIENCY EVALUATION

High Savings – Based on Low Generator Cost Differential Estimates

MW	MVA	Gen. Cost \$ × 10 ⁶	Gen. Eff. Savings \$ × 10 ⁶	Transf. Eff. Savings \$ × 10 ⁶	Est. Trans. Cost Savings \$ × 10 ⁶	Cost Grounding Equipment \$ × 10 ⁶	Total Savings \$ × 10 ⁶
270	300	-1.8	1.71	1.1	2.6	- .2	3.41
540	600	-1.2	3.43	2.17	3.6	- .3	7.70
1080	1200	-1.5	6.35	4.34	6.5	- .4	15.29

Average Savings – Based on Average Generator Cost Differential Estimates

MW	MVA	Gen. Cost \$ × 10 ⁶	Gen. Eff. Savings \$ × 10 ⁶	Transf. Eff. Savings \$ × 10 ⁶	Est. Trans. Cost Savings \$ × 10 ⁶	Cost Grounding Equipment \$ × 10 ⁶	Total Savings \$ × 10 ⁶
270	300	-4.28	1.71	1.1	2.6	- .25	.88
540	600	-3.91	3.43	2.17	3.6	- .38	4.91
1080	1200	-4.91	6.34	4.34	6.5	- .76	11.51

Low Savings – Based on High Generator Cost Differential Estimates

MW	MVA	Gen. Cost \$ × 10 ⁶	Gen. Eff. Savings \$ × 10 ⁶	Transf. Eff. Savings \$ × 10 ⁶	Est. Trans. Cost Savings \$ × 10 ⁶	Cost Grounding Equipment \$ × 10 ⁶	Total Savings \$ × 10 ⁶
270	300	-6.80	1.71	1.1	2.6	- .25	-1.64
540	600	-6.68	3.43	2.17	3.6	- .5	2.02
1080	1200	-8.44	6.34	4.34	6.5	-1.0	7.74

Generator Efficiency Evaluation = KW × .005 × \$1,270/KW

Transformer Efficiency Evaluation = KVA × .95 × .003 × \$1,270/KW

(-) = Negative Saving

Tables 6.4-1 and 6.4-2 show the calculated cost adders and savings for the low-voltage and high-voltage superconducting generators, respectively. High, low, and average estimates are displayed. The efficiency improvement evaluations used in the estimates are shown at the bottom of each table. The capital cost savings of the transformer elimination was set equal to the cost of four single-phase transformers (three active and one spare). This cost value may be somewhat high, but it is consistent with an assumption of high transformer availability potential which the high-voltage generator will have to match.

The results of the savings calculations shown in Tables 6.4-1 and 6.4-2 are plotted in Figure 6.4-2. This curve shows high evaluated first cost savings that are of the same order of magnitude that previous studies have shown. However, the values are tempered by the potential for low or medium savings if the generator cost differences are ultimately found to be higher. The potentially greater savings using high-voltage generators appear to be dramatic. However, as pointed out in Section 6.2, when a full economic analysis is performed using estimated development costs and savings, the rate of return benefits for the high-voltage generator are not significantly greater than for the low-voltage superconducting generator.

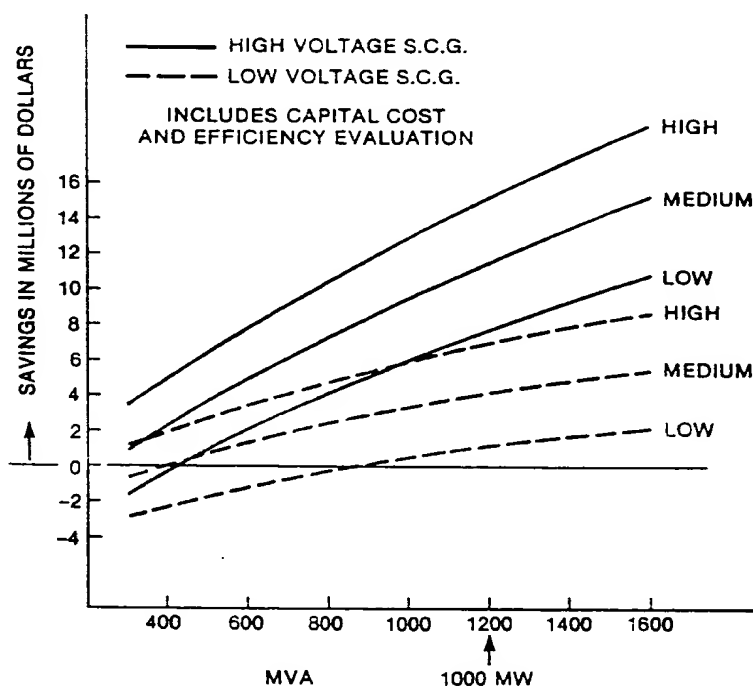


Figure 6.4-2. Potential User Savings (1985 Dollars) of Superconducting Generators over Conventional Generators

6.5 DEVELOPMENT COST ESTIMATES

The long-term costs to develop superconducting generators are required to perform the economic analyses. In previous studies, these costs were not addressed. In this report, simplistic and subjective estimates of these costs have been made. The cost values used in these analyses are based on the expenses required to develop and install the first 300 MVA low-voltage superconducting generator at the TVA Gallatin station planned for completion in 1985. It has been estimated that the development costs of this project will be \$33 million (Ref. 6-4). Additional considerations include the estimated introduction rate of superconducting generators and the participation of two or more domestic manufacturers in the development effort. Table 6.5-1 shows the assumed development effort based on the introduction rate of low-voltage superconducting generators and the yearly development funds used in the economic analyses.

Table 6.5-1
DEVELOPMENT COST ESTIMATES
LOW-VOLTAGE S.C.G.

Year	Introduction Rate	Total Dev. Cost	Yearly Dev. Expense
1985	1-300 MVA*	33×10^6	12×10^6
86			12
87			12
88			12
89			12
1990	2-300 MVA	66×10^6	18
91			18
92			18
93			18
94			24
1995	2-600 MVA	70×10^6	24
96			18
97			12
98	2-1200 MVA	80×10^6	12
99			6
2000		216×10^6	216×10^6

Development Costs Assume:

- Two domestic suppliers will participate and be supported by utility development funds.
- Participating utilities will require backup conventional generators to ensure reliability and availability until S.C.G.'s are proven, or the costs reflect the expense associated with the new product learning curve.

- * The cost of the TVA Gallatin S.C.G. (1985 shipment) has been used to gauge development costs estimates.

The development cost estimates following the introduction of the first 300 MVA superconducting generator may appear to be high. However, they address the concern for the industry's requirement to have high reliability and availability performance. It is questionable whether any individual utility could afford to accept an advance design concept such as the superconducting generator without having a backup conventional unit to cover contingencies. The development costs also reflect the following considerations:

- Two or more manufacturers will be participating and will be supported by utility development funds.
- Startup manufacturing costs will be significantly higher than the mature cost estimates used in the economic analyses.
- Expenses involved with the new product learning curve will occur.

The development expenses estimated for the high-voltage superconducting generator were arrived at using an even a less-well-defined subjective judgment. The yearly development costs are displayed in Table 6.2-2. The high-voltage generator development costs were obtained by multiplying the low-voltage generator development costs by 1.5 and extending the development effort over a longer period to reflect the delayed introduction rates. The significantly higher development costs for high-voltage superconducting generators reflect the following considerations:

- New high-voltage stator technology developments will be required.
- Low-voltage superconducting generator development effort will have to be carried on in parallel in case a critical problem with the high-voltage generator is defined during the development phases.
- New and expensive manufacturing facilities will be required to produce high-voltage generators and to test their electrical insulation integrity.

Although the development costs defined in this study were not arrived at by a rigorous analysis, they do provide a basis for a better understanding of the overall economic analysis. That is, for a project to be viable, it must have a great enough potential savings to recover the anticipated development costs.

In this study, total industry development funds spent or committed before 1986 were not used in the economic analyses. Even though these expenses amount to \$48 to \$55 million, they play no part in the decision to commit further development funds.

An examination of the estimated required yearly development costs from 1986 through 2000 for both the low-voltage and high-voltage superconducting generators reveals very high investments. These investments are much greater than the industry manufacturers can afford to make, based on the anticipated business level over those years. Thus, if the introduction rates of superconducting generators used in this report are to be realized, a large portion of the funding will have to be supported by the electrical utilities through EPRI or government agencies.

References

- 6-1. *Superconducting Generators: Current Technology and Benefits*, Arthur D. Little, Inc., Sept. 1979, C-82504.
- 6-2. *Overview and Strategy 1982-1986 Research and Development Program Plan*, EPRI Publication P-2156-SR, Nov. 1981.
- 6-3. *Statistical Year Book*, Edison Electric Institute, Number 48, Nov. 1981.
- 6-4. "Superconducting Magnets Head for Upsurge in Applications," *American Metal Market/Metal Working News*, March 1, 1982.

Section 7

FINAL DESIGN RECOMMENDATION

7.1 FINAL RECOMMENDATION

The conclusion of this study is that, although there are possibly a number of high-voltage superconducting generator conceptual designs which may prove to be technically feasible, only one conceptual design has the potential of being proven both technically and economically feasible.

The high-voltage stator winding concept which was selected as having the best characteristics and highest potential of success is the monolith cylinder armature. The design details and studies performed on the monolith cylinder armature are described in many sections of this report. A brief summary of its characteristics and limitations are listed below.

- The armature is constructed of concentric cylinders of insulation and winding conductors completely bonded together into a single module.
- Many hundreds of winding turns are required in the monolith cylinder armature, as well as in any high-voltage armature. Each conductor is insulated with only turn-voltage insulation, as compared to the full ground insulation that is applied to each of the several dozen conductors in a conventional generator.
- The stator winding uses a fully helical coil construction which provides uniform winding packing. It is believed that this feature will provide greater mechanical integrity than winding designs which have bends or discontinuities that can produce mechanical stress concentrations.
- The winding uses the two-circuit delta winding arrangement, which provides a uniform voltage grading circumferentially around the winding. Phase-break insulation therefore is not required and each turn requires only sufficient insulation to withstand local turn-voltage stresses. This feature provides as high a material utilization as any of the other high-voltage generator concepts studied, or higher.
- The uniform voltage grading provided by the two-circuit delta winding also greatly reduces local electrical creepage and puncture stress concentrations which most other high-voltage stator windings exhibit. Thus, calculated electrical creepage and puncture performance based on analytical studies should provide good correlation with actual performance.
- The insulation material proposed for the insulation cylinders is transformer high-density cellulose pressboard impregnated with a dielectric fluid such as transil oil or Freon. This material system was selected on the judgment that no other known material combination could rationally be expected to provide successful long-term performance operating at the high electrical puncture and creepage stresses identified in this study. The dielectric-fluid-impregnated system assures that all voids resulting from assembly operations or from cracks caused by winding forces or thermal expansion forces will be filled with dielectric fluid. Thus, incipient electrical insulation damage due to ionization in voids will be minimized.
- The insulation cylinder thicknesses are designed for 50 V/mil average dielectric stress. This limit as applied to the inner and outer insulation cylinders results from finite element analyses which show that surface electrical creepage stresses in the armature end region are very sensitive to the insulation cylinder thicknesses. Since the center insulation cylinder, located between the inner and outer conductor layers, is not subjected to this end region electrical creepage stress, it could be speculated that a higher dielectric stress might be used for this

cylinder. However, until test data are obtained to show that very thick impregnated press-board material will operate at higher dielectric stresses, it was considered prudent to size this cylinder at 50 V/mil.

- Cooling of the armature winding, core, and insulation cylinders is performed by a once-through dielectric fluid flow system. Cooling passages are formed into the core and insulation cylinders as they are assembled. The armature winding uses stainless steel tubes interspersed between the conductors to provide the cooling passages.
- The maximum practical voltage rating appears to be 500 kV. Higher voltages (750 kV and up) will require very thick insulation cylinders and special design features to hold the electrical creepage stresses to a level that can be controlled with present-day technology. Shipping problems and poor space utilization will render these ultra-high-voltage generator designs uneconomical.
- A methods analysis of the manufacturing operations required to assemble the monolith cylinder armature indicates that the operations can be performed. However, the operations are significantly different from present operations used on conventional generators and anticipated to be used on low-voltage superconducting generators. Completely new manufacturing facilities and processes will be required to introduce the monolith cylinder armature.
- Electrical faults occurring within the body of the winding, whether they are the result of turn-to-turn shorts, major ground insulation shorts, or phase-to-phase shorts, will force the complete winding to be scrapped. Due to the bonded module construction, it is not considered practical to attempt to repair an internal electrical fault.

7.2 JUSTIFICATION FOR SELECTION OF THE MONOLITH CYLINDER DESIGN

During the conceptual design phase of the program, a number of different design concepts were studied in sufficient detail to assess which designs had the best chance of being proven technically and economically feasible. The basic design concepts that were studied included the following:

- Monolith Cylinder Armature
- Spiral Pancake Armature
- Salient Pole Armatures
 - Three-pole (magnetic poles)
 - Six-pole (magnetic and nonmagnetic poles)
- Integral-Insulated Phase-Belt Armature - Taped System
- Integral-Insulated Phase-Belt Armature - Coaxial System
- Toroidal Winding Armature

Preliminary design evaluations eliminated the salient pole designs and the toroidal winding design for a number of technical and economical reasons. For example, the salient pole armature with three magnetic poles would produce unbalanced forces on the rotor of a magnitude that could never be tolerated. The salient pole armatures with either six magnetic or nonmagnetic poles and the toroidal winding armature were identified as having very poor space utilization, high electrical losses, and high reactances. Rough first-cost estimates of these designs indicated that they could not compete economically with conventional generators and, especially, low-voltage superconducting generators. Thus, these designs were dropped from further technical evaluations.

The major challenge of the early part of the Phase II effort was to perform the necessary evaluations to establish which of the following design concepts had the best chance of being proven technically and economically feasible:

- Monolith Cylinder Armature
- Spiral Pancake Armature

- Integral-Insulated Phase-Belt Armature - Taped System
- Integral-Insulated Phase-Belt Armature - Coaxial System

The integral-insulated phase-belt armature concepts (with either taped or coaxial systems) were generated during the contract period. These concepts were proposed for study because they appeared to drastically reduce the electrical creepage stress problems that had been previously identified in the monolith cylinder and spiral pancake designs. Drawings and models were made of each design concept to assess whether the manufacturing processes were practical and whether the final component structures would match the requirements of the high-voltage generator. From these studies, it was concluded that the manufacturing problems and the difficulties anticipated with producing the end-winding coil connections rendered these designs to be only marginally practical. Thus, these designs were eliminated from further consideration.

Based on the design elimination process described above, the final design recommendation selection was made between the monolith cylinder armature and the spiral pancake armature. Although the spiral pancake armature was judged to be the easiest to manufacture due to its continuous-winding construction, a number of problems which drastically lowered its probability of meeting the ultimate technical and economical high-voltage generator requirements were identified. The major concerns are listed below.

- Insulation volume requirements are significantly greater than for the monolith cylinder armature, producing units of considerably larger dimensions.
- The use of separate phase-belt assemblies with their dielectrically sharp edges produces very high electrical puncture and creepage stresses locally in the major insulation sections. Although special electrical creepage barrier designs which would reduce the electrical creepage stresses were identified, these designs would be difficult to implement and control. The local electrical puncture stresses on the spiral pancake design would always be significantly greater than on the monolith cylinder design.
- The use of curved, spiral phase-belt coils and insulation sections which are mechanically discontinuous raises questions as to whether the completed full winding assembly could satisfactorily support the coils against vibration during running and short circuit conditions.
- No satisfactory design concept was developed to provide liquid cooling of the stator windings. The use of continuous turns and the large number of turns required negates the possibility of using phase-end connections as inlet-outlet cooling connections. The outermost turns of the spiral pancake coils block the introduction of cooling fluid to the inner turns. Consequently, liquid coolant must be introduced through insulation or mechanical support material. All of the liquid cooling passage designs reviewed during the studies indicated that significant reduction in mechanical integrity might be expected.

After reviewing of all the advantages and disadvantages of the monolith cylinder armature and the spiral pancake armature, it was concluded that the monolith cylinder armature has the best characteristics and the highest potential of being proven successful, following an extensive development program.

Section 8

RECOMMENDATION FOR FOLLOW-ON EFFORT

8.1 INSULATION TESTING PROGRAM

It is expected that a satisfactory design for the high-voltage armature can be achieved by using cellulose pressboard and transil oil as the principal insulation system. A considerable background of high-voltage transformer technology is therefore applicable for design purposes. However, the important residual differences between the insulation systems of transformers and high-voltage armatures must be taken into consideration.

In high-voltage power transformers, the dielectric barriers surrounding the high-voltage coils are formed from concentric pressboard cylinders that encompass annular regions of transil oil. The purpose of the pressboard cylinders is to partition the oil regions into annuli that are thin enough to be dielectrically manageable. Pressboard is also used to form the walls of annular cooling ducts. In either application, the total oil thickness is usually greater than the total pressboard thickness, and the electric stress in the pressboard is about 60% less than that in the oil, due to the difference in dielectric constants.

In the monolith cylinder high-voltage armature, pressboard is laminated to form the thick insulation cylinders, and the oil annuli found in the transformer insulation system are eliminated. The pressboard must be stressed to at least 50 V/mil to obtain reasonably compact machine dimensions; this stress is perhaps two times higher than that encountered in normal transformer practice, although it is a reasonable stress for many oil-impregnated paper-tape applications. Also, the pressboard insulation cylinders are required to be from 4 to 8 in. thick each, and practically no experience exists for the application of such thick pressboard insulators at the required dielectric stresses.

Therefore, although the development of high-voltage armatures can be accomplished with reasonable confidence provided by using existing transformer technology, it would be desirable to accompany such development with a limited backup testing program. A testing program might be divided into two phases:

- Uniform field tests on thick pressboard sections at 60 Hz and impulse voltages
- Mockup winding tests

Tests to obtain electrical creepage data would not be necessary if it is assumed that transformer technology is directly transferable for electrical creepage.

A more extensive testing program would be necessary if an alternative fluid impregnant such as Freon* were proposed. Electrical creepage tests would here be necessary.

8.1.1 Dielectric Tests for Pressboard and Transil Oil

Uniform field tests can be performed by placing sheets of pressboard between large (12 in.-diameter) contoured disk electrodes. Data can be obtained by running tests at a series of thicknesses and plotting the dielectric properties of interest as a function of thickness. The dielectric properties which could be determined are:

60 Hz:	Corona inception stress Breakdown stress Loss tangent
Impulse:	Breakdown stress (both lightning and switching surges may be necessary)

* E.I. DuPont De Nemours & Co., Inc.

It would be desirable to test thicknesses over a range from 1/4 in. to 2 in. Tests of 3 to 6 samples at each point would be desirable to obtain adequate statistics. The 60 Hz breakdown strength of a 2 in.-thick sample might be as high as 500-1000 kV, so large test equipment is implied. To make the testing program cost-effective, it may be desirable to trade off the maximum voltage capability against the cost of operation of available test equipment. Whatever data are acquired can be extrapolated to thicknesses greater than those tested.

8.1.2 Dielectric Tests for Pressboard and Freon

Freon may be a more desirable dielectric fluid than transformer oil because of its better cooling properties and its nonflammability. Freon 113 is finding increasing application in vaporization-cooled transformers as a combination dielectric fluid and coolant. In the transformer application, the transformer heating boils the Freon fluid, and the Freon vapors are cooled, condensed, and returned to the transformer tank. The boiling point of Freon 113 is only 46 °C, so the Freon is pressurized at about 2 atmospheres to raise the boiling point. In an application to a high-voltage armature, vapor generation is not desired because the generated vapor bubbles must surely lower the dielectric performance of the fluid. Therefore, further pressurization would be required to raise the boiling point above the armature hot-spot temperature. If the armature hot-spot temperature is limited to 90 °C, a desirable Freon 113 boiling point might be 100 °C, and a pressurization of about 3 atmospheres would be required. If pressurization is deemed to be unattractive, other Freon formulations having boiling points above 100 °C are available, although they are considerably more expensive.

The uniform field tests described in Section 8.1.1 could be repeated for the selected Freon fluid, using identical electrodes and test voltages, and operating at a suitable combination of pressure and temperature that would simulate the generator environment. If the results of the uniform field tests are favorable, preliminary electrical creepage data in pressurized Freon should be obtained to establish its creepage capability compared to transil oil. For preliminary comparison, a standard creepage fixture consisting of two circular electrodes placed on a sheet of pressboard could be used. Creepage strength as a function of electrode spacing would be measured in the pressurized Freon, and the results would be compared to identical measurements made with transil oil.

8.1.3 Winding Mockup Tests

Additional dielectric data can be obtained by testing mockups of the monolith cylinder armature. Armature components, or mockups of components, could be constructed for testing to the limits of failure. Such tests would provide dielectric breakdown information for the dielectric configurations of the actual armature. Construction of the mockups would also provide experience in component fabrication and armature assembly. The types of tests which could be proposed follow.

1. Phase-Belt Creepage

A short section of one phase-belt could be placed between two sheets of pressboard. The pressboard sheets would be flat simulations of the insulation cylinders that encompass a conductor layer. The 60 Hz turn-to-turn voltage gradient could be established by an external capacitor ladder network and the voltage would be incrementally raised until creepage failure occurs. Similar tests could be made with impulse voltages.

2. End-Winding Creepage

A mockup of the monolith cylinder end region could be constructed for the purpose of establishing the strength of the electrical creepage paths running from the series loops along the surfaces of the insulation cylinders. The same mockup could also be used to test the type of creepage barriers described in Section 2.5.1. Similar tests could be made with impulse voltages.

3. Insulation Cylinder Breakdown

By arranging two winding mockups at an angle across opposite sides of a flat sheet of press-

board laminations, the line-to-line voltage across the center insulation cylinder can be simulated. Both 60 Hz and impulse breakdown tests could be made with this configuration.

The creepage tests are more significant than the insulation cylinder breakdown test because the dielectric strength of the pressboard should be reasonably well established from the uniform field tests proposed in Section 8.1.1.

8.2 MODEL STATOR FOR THE GENERAL ELECTRIC MODEL SUPERCONDUCTING ROTOR

After a reasonable insulation testing program has been completed, a logical continuation of this effort would be to construct a small prototype model of a high-voltage armature. The General Electric Company possesses a model superconducting rotor which is being tested in a 20 MVA low-voltage generator design. The long-range plans for this rotor are unclear, and it is possible that it may eventually become available for use in a high-voltage stator demonstration model. The high-voltage stator model would be designed to operate at 69 or 138 kV with a volt-ampere rating of 14 MVA. The reduced volt-ampere rating reflects the poorer stator flux linkage resulting from the greater insulation volume in a high-voltage armature. Figure 8.2-1 illustrates a comparison between low- and high-voltage model stators for the General Electric model superconducting rotor.

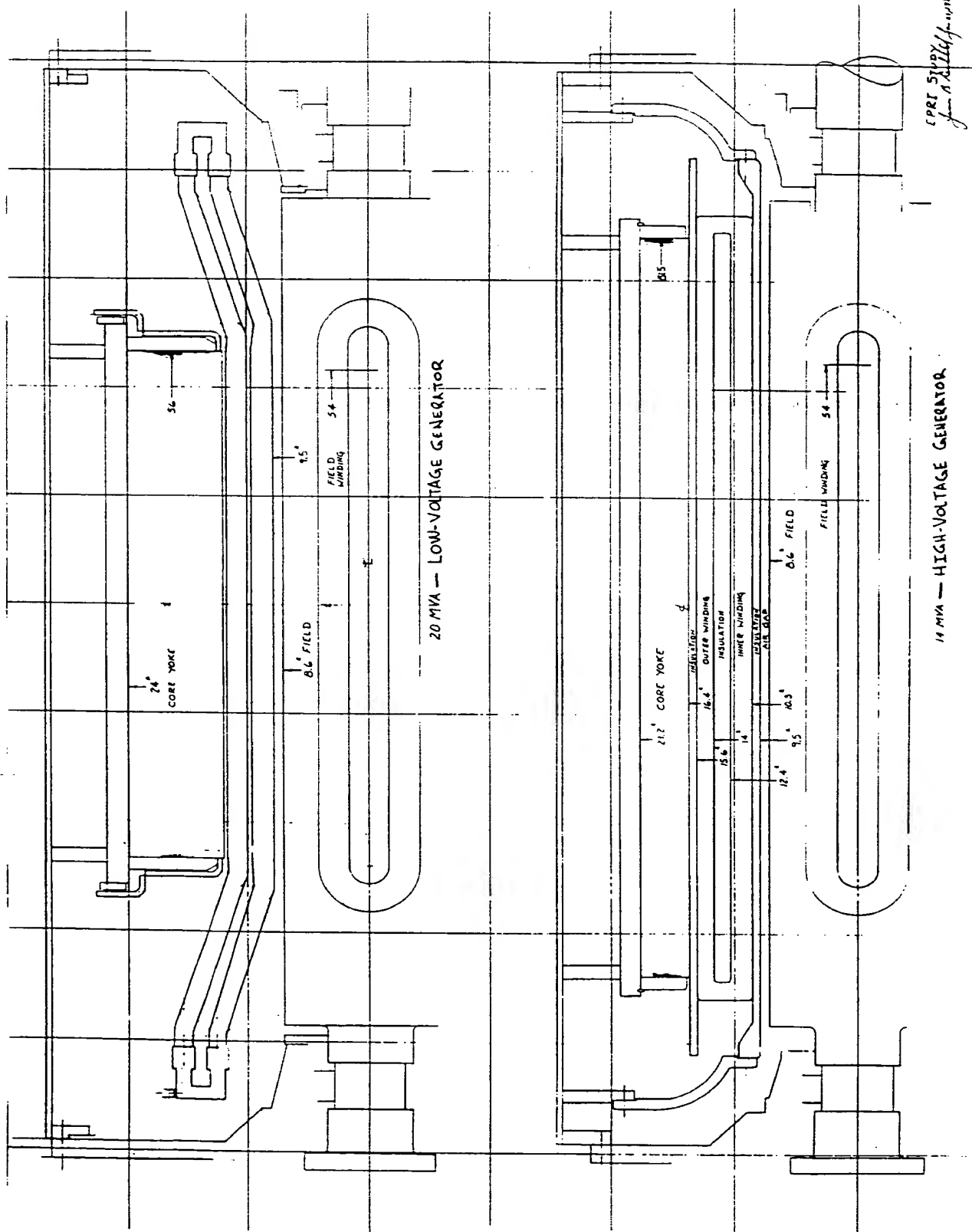


Figure 8.2-1. Low- and High-Voltage Model Superconducting Generators

Appendix A

LITERATURE SEARCH

HIGH-VOLTAGE AIR-GAP ARMATURE WINDINGS

A.I. Abramov, *Hydroalternators of 110 to 220 kV*, Elektrotech. obz., Vol. 64, No. 3, pp. 132-136, March 1975 (in Czech).

G. Aichholzer, M. Manowarda, "Approach to Development of a 230 kV Airgap Winding," International Conf. of Electrical Machines, Athens, 1980.

G.A. Beschastnov, A.V. Ivanov-Smolenski, P.Z. Nikitin, "High-Voltage Generators," *Elektrotehnika*, Vol. 48, No. 6, pp. 1-5, 1977.

C. Flick, "New Armature Winding Concepts for EHV and High CFCT Applications of Superconducting Turbine Generators," *IEEE Trans. Power Apparatus and Systems*, Vol. PAS-98, No. 6, pp. 2190-2200, Nov./Dec. 1979.

P.Z. Nikitin, A.V. Ivanov-Smolenski, J.S. Pinal, G.A. Beschastnov, "Problems in Design of the 110-500 kV High Voltage Generators," World Electrotechnical Conference, Section 1, Paper 18, June 1977, Moscow.

M.M. Steeves, J.L. Kirtley, "Toroidal Winding Geometry for High Voltage Superconducting Alternators," *IEEE Trans. Power Apparatus and Systems*, Vol. PAS-93, pp. 1902-1908, Nov./Dec. 1974.

Westinghouse Electric Corp, *Superconducting Generator Design*, EPRI Research Project 429-1, Final Report, Nov. 1977.

LOW-VOLTAGE AIR-GAP ARMATURE WINDINGS

G. Aichholzer, "New Ways of Building Two-Pole Turbogenerators up to 2 GVA 60 kV," *Elektrotechnik und Maschinenbau*, Vol. 89, No. 1, Jan. 1972.

G. Aichholzer, "New Approaches for Design of Large Turbogenerators up to 2 GVA, 60 kV," *Elektrotechnik und Maschinenbau*, Vol. 92, No. 6, pp. 249-255, June 1975.

D.R. Albright, H.F. Sage, J.B. Archibald, *Air-Gap Winding Stator Construction for Dynamoelectric Machine*, U.S. Patent 4,330,726, May 1982.

A.D. Appleton, H.O. Lorch, A.B.J. Reece, D.A. Smith, J.G. Steel, "Advanced Turbine-Generators — An Assessment," International Conference on Large High Voltage Electric Systems, Paper 11-02, Aug.-Sept. 1976.

A.D. Appleton, J.S.H. Ross, J. Bumby, A.J. Mitcham, *Superconducting A.C. Generators: Progress on the Design of a 1300 MW, 3000 Rev/Min Generator*, International Research and Development Co., LTD, 1976.

T. Bratoljic, *Delta-Connected, Two-Layer, Three-Phase Winding for an Electrical Machine*, U.S. Patent 4,200,817, April 1980.

P.L. Conley, J.L. Kirtley, W.H. Hagman, A.H. Ula, "Demonstration of a Helical Armature for a Superconducting Generator," *IEEE Transactions on Power Apparatus and Systems*, PAS-99, 4, pp. 1642-1649.

E.J. Davies, "Airgap Windings for Large Turbogenerators," *Proc. IEE*, Vol. 118, No. 3/4, March/April 1971.

- J.C. Dudley, *Fabrication of an Armature for a Generator with a Superconducting Rotating Field Winding*, S.B. and S.M. MIT Thesis, May 1969.
- C. Flick and S. Ying, *Support Structure for Dynamo-Electric Machine Stators: Spiral Pancake Winding*, U.S. Patent 4,292,558, Sept. 29, 1981.
- General Electric Co., *Superconducting Generator Design*, EPRI Research Project RP 429-2, Final Report, Dec. 1977.
- R. Gillet, J. Carlier, *Device for Fixing Winding Bars on a Stator of an Electric Rotating Machine*, U.S. Patent 4,068,142, Jan. 1978.
- J.F. Heuillard, *Structure of a Cryo-Generator Stator Winding and Environment Protection*, *Rev. Gen. Electr.*, Vol. 86, No. 1, pp. 51-56, Jan. 1977 (in French).
- M. Iwamoto, O. Ogino, T. Nomura, "A 6250 KVA Superconducting Generator," IEEE PES Winter Meeting Paper A79 013-4, New York, NY, Feb. 1979.
- T.A. Keim, S.H. Minnich, *Star Connected Armatures Having Limited Voltage Gradient*, Patent Disclosure Letter, General Electric Co., Aug. 16, 1979.
- V.S. Kil'dishev, L.N. Ruzhinskii, "Large Synchronous Generators with Smooth Stator," *Elektrichestvo*, No. 1, 11-16, 1977.
- J.L. Kirtley, *Design and Construction of an Armature for an Alternator with a Superconducting Field Winding*, Ph.D. Thesis, MIT, Aug. 1971.
- J.L. Kirtley, J.L. Smith, P. Thullen, "MIT-EEI Program on Large Superconducting Machines," *IEEE Trans. Power Apparatus and Systems*, Vol. 92, No. 4, pp. 1282-1286, July/Aug. 1973.
- J.L. Kirtley, "Armature of the MIT-EPRI Superconducting Alternator," *IEEE Trans. Power Apparatus and Systems*, Vol. PAS-96, pp. 88-96, Jan./Feb. 1977.
- O. Krenkova, "Construction of Slotless High Power Turboalternators," *Elektrotech. obz.*, Vol. 68, No. 2, pp. 95-99, Feb. 1979 (in Czech).
- Massachusetts Institute of Technology, *Demonstration of an Advanced Superconducting Generator*, Reports prepared for the U.S. Dept. of Energy, Contract No. E(49-18)-2295, Task Order No. 11.
- N. Petrenko, W. Kunze, "Mounting of the Armature Winding and Power Limit of Slotless Synchronous Machines," *Elektrie*, Vol. 32, No. 11, pp. 595-597, 1978 (in German).
- T.W. Preston, A.B.J. Reece, *Dynamo Electric Machines*, British Patent Specification #1365191, Aug 1974.
- J.S.H. Ross, A.F. Anderson, R.B. MacNab, *Alternating Current Dynamo-Electric Machine Winding*, British Patent Specification #1395152, May 21, 1975.
- J.L. Smith, *High Voltage Oil Insulated and Cooled Armature Windings*, U.S. Patent 3,743,867, July 1973.
- J.L. Smith, J.L. Kirtley, *Polyphase Synchronous Alternators Having a Controlled Voltage Gradient Armature Winding*, U.S. Patent 3,743,875, July 1973.
- E. Spooner, "Fully Slotless Turbogenerators," *Proc. IEE*, Vol. 120, No. 12, Dec. 1972.
- P. Thullen, J.C. Dudley, D.L. Greene, J.L. Smith, H.H. Woodson, "An Experimental Alternator with a Superconducting Rotating Field Winding," *IEEE Trans. Power Apparatus and Systems*, Vol. PAS-90, No. 2, pp. 611-619, March/April 1971.
- A.H. Ula, J.L. Kirtley, J.L. Smith, "Demonstration of Advanced Concepts in a 10 MVA Superconducting Generator," International Conference on Electrical Machines, Sept. 1980, Athens, Greece.

M. Watanabe, M. Takahashi, N. Takahashi, T. Tsukui, "Experimental Study of a Practical Airgap Winding Stator Arrangement for Large Turbine Generators," IEEE PES Winter Meeting, Paper F 79 190-0, New York, NY, Feb. 1979.

Westinghouse Electric Co., *Superconducting Generator Design*, EPRI Research Project RP 429-1, Final Report, Nov. 1977.

George V. Yenetchi, *Thermal and Mechanical Design of an Armature for a Superconducting Field Winding*, M.S. Thesis, Dept. of Mechanical Engineering, MIT, August 1974.

AIR-GAP ARMATURE WINDINGS, THEORETICAL TOPICS

S.R. Alwash, B.I. Hassall, P.J. Lawrenson, J.M. Stephenson, "Magnetic Fields in Superconducting A.C. Generators," International Conference on Electrical Machines, Sept 1980, Athens, Greece.

A.F. Anderson, J.R. Bumby, B.I. Hassall, "Analysis of Helical Armature Windings with Particular Reference to Superconducting A.C. Generators," *IEE Proc.*, Vol. 127, Pt.C, No. 3, pp. 129-144, May 1980.

M.R. Bailey, J.R. Bumby, B.I. Hassall, A.F. Anderson, "Magnetic Fields and Inductances of Helical Windings with 120° Phasebands," *Electric Machines and Electromechanics*, Vol. 6, No. 4, July-Aug. 1981, pp. 323-335.

M.V.K. Chari, T.R. Haller, *Steady State and Short-Circuit Force Analysis on the Stator Windings of a Superconducting Generator*, IEEE PES Summer Meeting, Paper F 79 624-8, July 1979, Vancouver, Canada.

T.A. Keim, "Fractional Pitch Coil in Air-Gap Armatures," IEEE PES Winter Meeting, Paper A 80 047-1, Feb. 1980, New York, NY.

J.L. Kirtley, "Basic Formulas for Air-Core Synchronous Machines," IEEE Winter Power Meeting, Paper CP 155-PWR, Feb. 1971, New York, NY.

J.L. Kirtley, "Per-Unit Reactances of Superconducting Synchronous Machinery," *IEEE Trans. Power Apparatus and Systems*, Vol. PAS-92, No. 4, pp. 1316-1320.

L.N. Ruzhinskii, V.P. Tolkunov, "The Electro-dynamic Forces in a Stator Winding Which Is Situated in the Air Gap of a Powerful Turbogenerator," *Power Eng. (Aca. Sci. USSR)*, Vol. 13, No. 2, pp. 110-119, 1975.

P.S. Tavner, J. Penman, R.L. Stoll, H.O. Lorch, "Influence of Winding Design on the Axial Flux in Laminated-Stator Cores," *Proc. IEE*, Vol. 125, No. 10, Oct. 1978.

Appendix B

OPTIMAL COIL SHAPE FOR MONOLITH CYLINDER WINDINGS

To design a monolith cylinder air-gap winding, it may become necessary to design the overall winding length to a shorter value than in conventional turbine-generator design practice, in order to minimize the bearing span length of the superconducting rotor. Since the coils of a monolith cylinder air-gap winding are not confined to lie in slots, there is no reason that the coils must conform to the conventional turbine-generator configuration of having straight sections over the length of the core with end arms hanging outside of the core. It will be shown that improved coil configurations are achieved by bringing the end arms inside the rotor flux producing length, allowing smaller overall winding lengths.

The terminology is illustrated in Figure B-1. Within the active length, L_s , the rotor magnetic flux is axially uniform. Outside the flux is zero. The end arm length, L_e , is the axial length from the straight section bend to the end of the coil, and the overhang length, L_o , is the axial length of coil hanging outside of the active flux region.

The open-circuit induced voltage of a fully pitched coil is

$$V_c = \sqrt{2} r B (L_s - 2L_e + 2L_o) + \frac{4\sqrt{2} L_e}{\pi} r B \cos \left(\frac{\pi}{2} \frac{L_o}{L_e} \right) \quad (B1)$$

where r is the winding radius and B is the radial flux density at that radius. For windings having inner and outer conductor layers lying at different radii, r is the average radius. The terminal voltage is proportional to the number of turns in a phase belt times the coil voltage:

$$V_t \propto NV_c \quad (B2)$$

The number of turns in a phase belt is proportional to the peripheral breadth of a phase belt, Δ , divided by the conductor pitch, p :

$$N \propto \frac{\Delta}{p} \quad (B3)$$

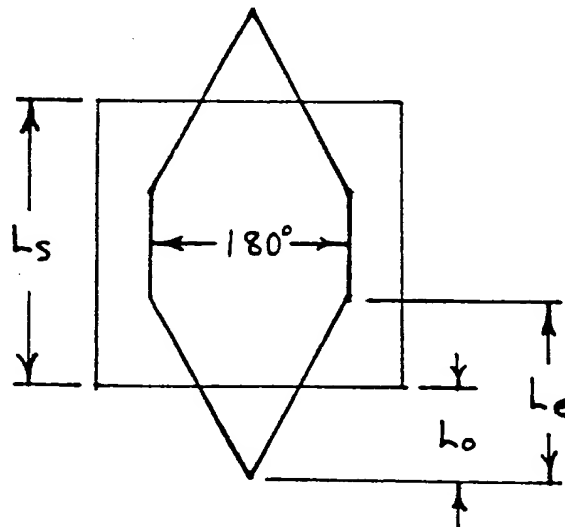


Figure B-1. Coil Shape Terminology

The conductor width, w , is related to the conductor pitch, p , by the end arm geometry. Figure B-2 illustrates an end arm geometry where the conductors are tightly packed in the end regions, and it is seen that spaces appear between the conductors in the straight section. The conductor pitch is related to the conductor width and the helix angle, γ , by

$$p = \frac{w}{\cos \gamma} \quad (B4)$$

The term $\cos \gamma$ is called the packing factor because it is a measure of how many conductors can be packed within a phase-belt periphery. The packing factor is related to the end arm geometry by

$$\cos \gamma = \frac{2L_e}{\sqrt{4L_e^2 + r^2\pi^2}} \quad (B5)$$

The terminal voltage now becomes a product of the coil voltage and the packing factor:

$$V_t \propto \frac{\Delta}{w} V_c \cos \gamma \quad (B6)$$

The machine rating is the product of the terminal voltage and the terminal current,

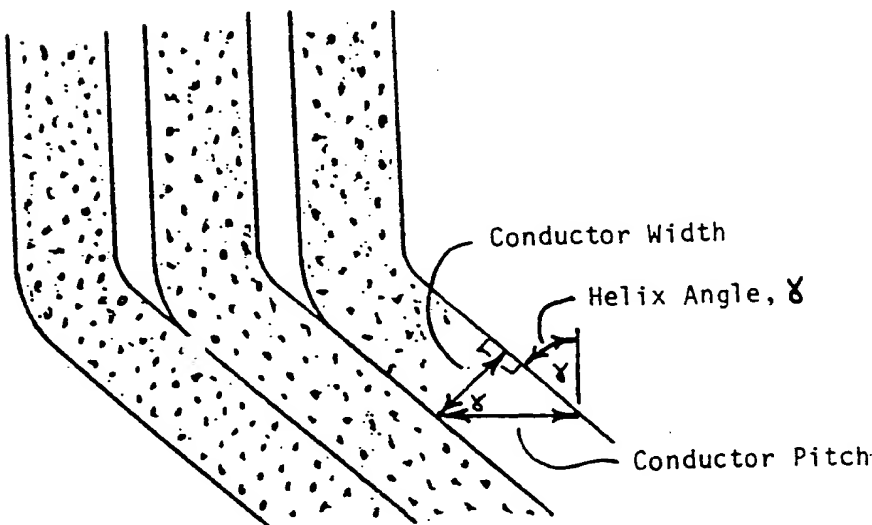
$$\text{MVA} \propto V_t I \quad (B7)$$

and the terminal current is a function of the conductor current density, J , conductor width, w , and conductor height, h , by

$$I = Jwh \quad (B8)$$

Substitution of Equations B6 and B8 into Equation B7 yields an expression for the machine rating:

$$\begin{aligned} \text{MVA} &\propto Jh\Delta V_c \cos \gamma \\ &\propto Jh\Delta \left[L_s - 2L_e + 2L_o + \frac{4}{\pi} L_e \cos \left(\frac{\pi}{2} \frac{L_o}{L_e} \right) \right] \left[\frac{L_e}{\sqrt{4L_e^2 + r^2\pi^2}} \right] \end{aligned} \quad (B9)$$



γ	Width/Pitch
30°	.866
45°	.707
60°	.500

Figure B-2. Illustration of Coil Packing

The variation of the rating with L_e and L_o is illustrated in Figure B-3, with L_e forming the abscissa and L_o forming the family of curves. The conductor current density and dimensions are assumed constant, and numerical values of $r = 25$ in. and $L_s = 100$ in. are used. The effect of increasing the end arm length is to decrease the coil voltage while increasing the packing factor. Since the rating is the product of these two counteracting effects, it might be expected that there is an optimal end arm length to produce a maximum rating, and from the curves it is seen that optimal end arm lengths produce coil shapes that have rather short straight sections. At maximum L_e , a coil shape with no straight section is achieved, and it is equivalent to a fully helical coil. The value of rating at maximum L_e is only slightly below that of the optimal L_e , suggesting that if it is constructionally advantageous to build a fully helical winding, it can be accomplished with little sacrifice. However, the rating is high over a fairly wide range of L_e , and it may be preferred to build coils having longer than optimal straight sections. The effect of increasing the overhang length, L_o , is to increase the rating, because the coil voltage is increased. However, to demonstrate the claim that shorter wind-

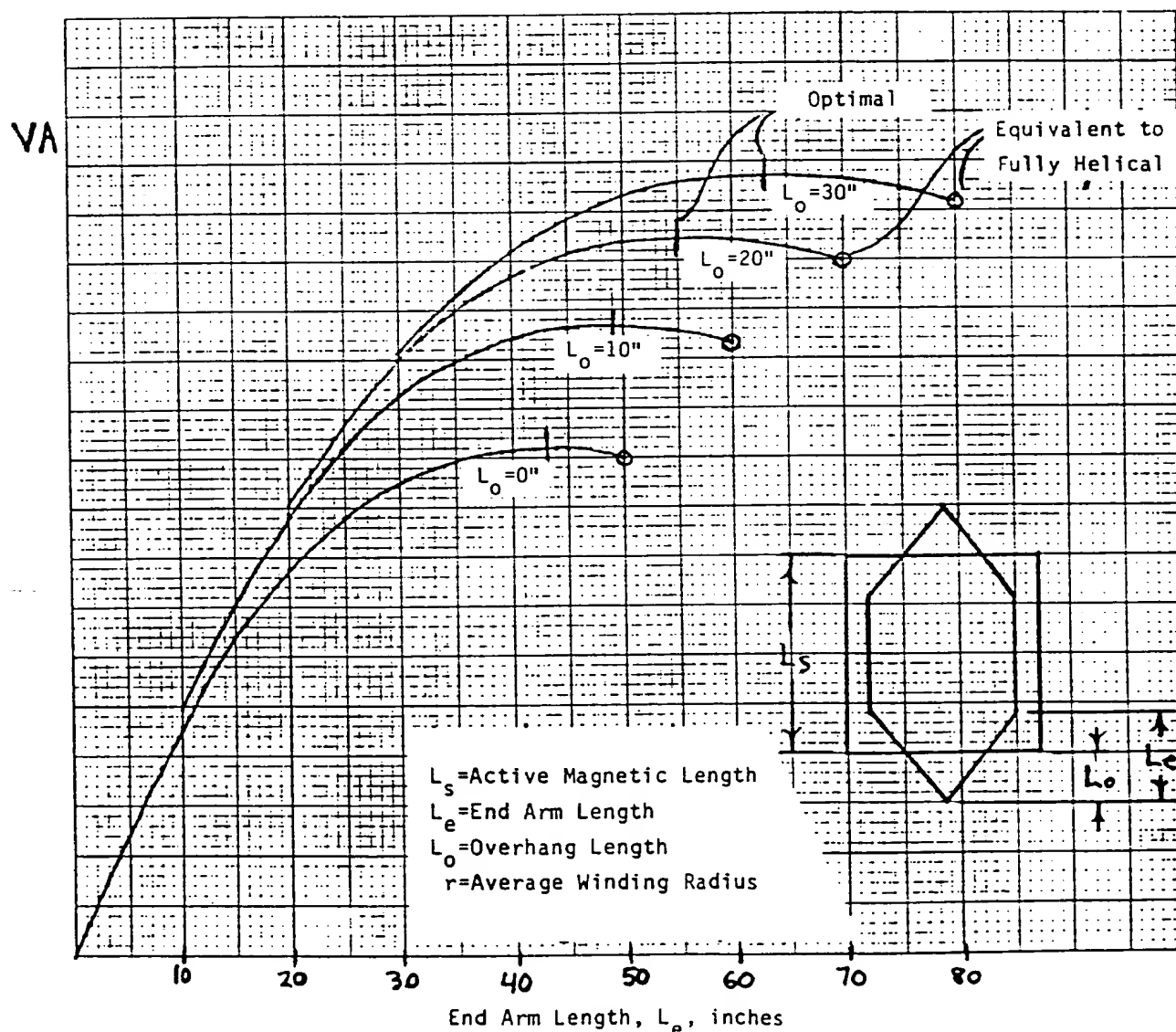


Figure B-3. Variation of Rating with End Arm Length and Overhang Length for Fully Pitched Coils with Constant Bar Dimensions and Constant Current Density; $r = 25$ in., $L_s = 100$ in.

ing lengths can be achieved by bringing the end arms inside the rotor flux region, the curves show that a winding with a 10 in. overhang and a 49 in. end arm length is superior to a winding having a 30 in. overhang and a 30 in. end arm length (a geometry conforming to conventional turbine-generator design).

The effects of variations in the end winding geometry can also be demonstrated with respect to winding space utilization. The cross-sectional area of the conductor layers, A_c , is proportional to the product of the peripheral breadth of the phase belts, Δ , and the conductor height, h :

$$A_c \propto \Delta h \quad (\text{B10})$$

By rearranging Equation B9 and substituting into Equation B10, it is seen that

$$A_c \propto \frac{\text{MVA}}{J V_c \cos \gamma} \propto \frac{\text{MVA}}{J} \frac{1}{\left[L_s - 2L_e + 2L_o + \frac{4L_e}{\pi} \cos \left(\frac{\pi}{2} \frac{L_o}{L_e} \right) \right] \left[\frac{L_e}{\sqrt{4L_e^2 + r^2 \pi^2}} \right]} \quad (\text{B11})$$

The proportionality of the conductor layer area, keeping the rating and conductor current density constant, is just the inverse of the proportionality of Equation B9. That is to say, for a constant rating, optimal coil shapes produce minimal conductor layer areas and, therefore, the most compact winding structures with respect to cross-sectional area.

Appendix C

120° PHASE-BELT WINDINGS AND ROTOR VIBRATORY FORCES

Section 2.1 describes two voltage-gradient-controlled windings that utilize 120° phase-belts (the 120° phase-belt delta and the 120° phase-belt graded wye). The greatest advantage of a 120° phase-belt is that the electrical creepage across the breadth of the phase-belt is greatly reduced because of the 120° phase-belt's greater peripheral span. Also, the 120° phase-belt windings are both single-circuit windings and require only about half as many individual conductors as the 60° phase-belt two-circuit windings. Figure C-1 illustrates the phase-belt placement of a 120° phase-belt winding.

To its detriment, a 120° phase-belt winding produces 120 Hz vibratory forces on the rotor, caused by even harmonic armature reaction flux distributions. To understand how even harmonic flux distributions are produced, it is necessary to consider the magnetic effects of each layer of the winding separately. The current distribution of the inner layer, described to the fifth harmonic is

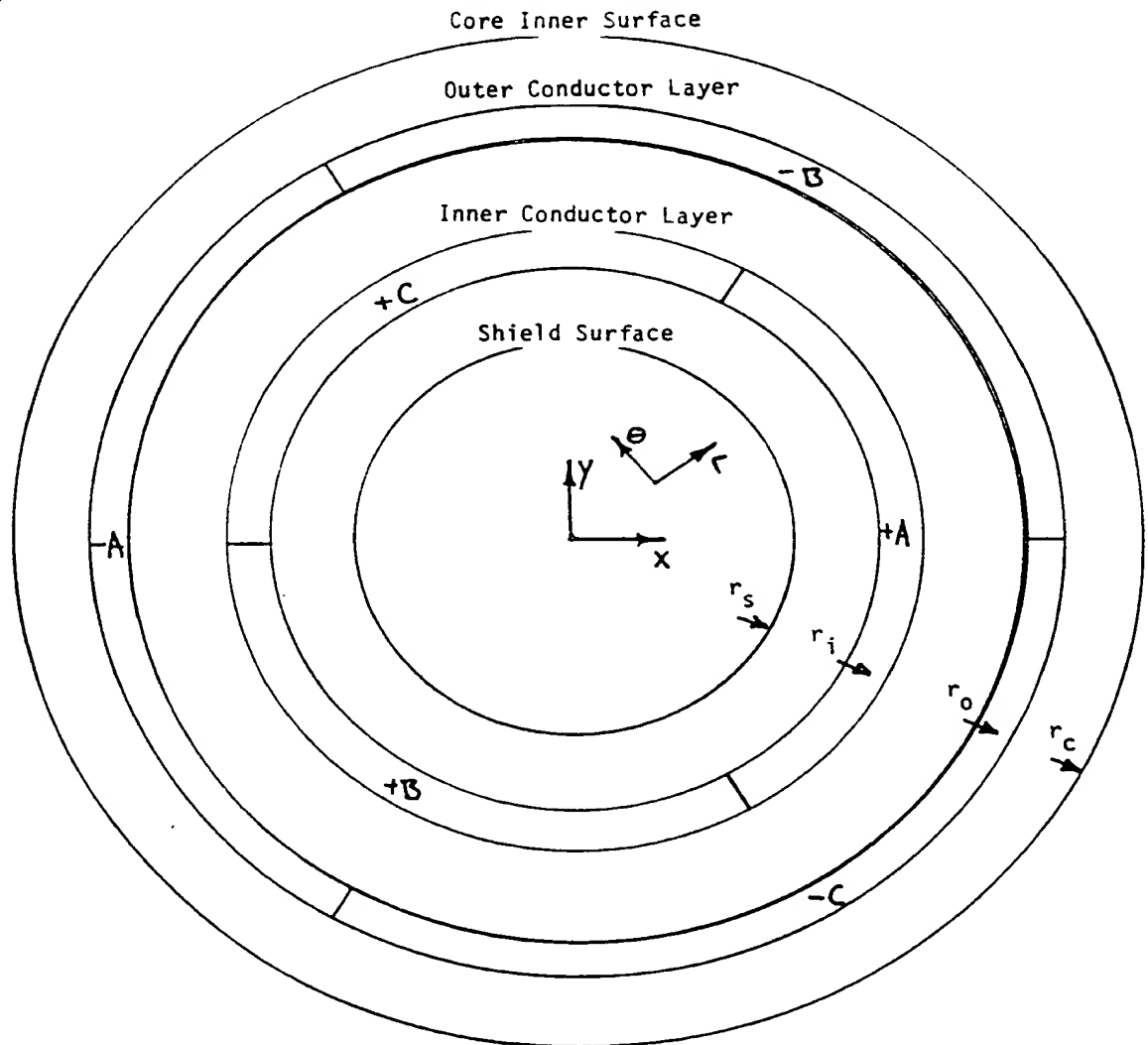


Figure C-1. Cross-Section of a 120° Phase-Belt Winding

$$\begin{aligned}
\vec{B}_{aw} = & \vec{a}_r B_1 \cos(\omega t - \theta) - \vec{a}_\theta B_1 \sin(\omega t - \theta) \\
& - \vec{a}_\theta \frac{B_{2\theta}}{2} \sin(\omega t + 2\theta) - \vec{a}_\theta \frac{B_{4\theta}}{2} \sin(\omega t - 4\theta) \\
& - \vec{a}_\theta \frac{B_{5\theta}}{2} \sin(\omega t + 5\theta)
\end{aligned} \tag{C9}$$

Substitution of Equations C7 and C9 into Equation C8 gives

$$\begin{aligned}
\vec{P} = & -\vec{a}_r \frac{(J_2 B_{2\theta} + J_4 B_{4\theta} + J_5 B_{5\theta})}{4} \\
& + \vec{a}_r \frac{J_2 B_1}{2} \cos(2\omega t + \theta) - \vec{a}_\theta \frac{J_2 B_1}{2} \sin(2\omega t + \theta) + \vec{a}_r \frac{(J_4 B_{5\theta} + J_5 B_{4\theta})}{4} \cos(2\omega t + \theta) \\
& + \vec{a}_r \frac{(J_2 B_{4\theta} + J_4 B_{2\theta})}{4} \cos(2\omega t - 2\theta) \\
& - \vec{a}_r \left(\frac{J_2 B_1 + J_4 B_1}{2} + \frac{J_2 B_{5\theta} + J_5 B_{2\theta}}{4} \right) \cos 3\theta - \vec{a}_\theta \frac{J_2 B_1}{2} \sin 3\theta \\
& + \vec{a}_r \left(\frac{J_2 B_{2\theta}}{4} + \frac{J_5 B_1}{2} \right) \cos(2\omega t + 4\theta) - \vec{a}_\theta \frac{J_5 B_1}{2} \sin(2\omega t + 4\theta) \\
& + \vec{a}_r \frac{J_4 B_1}{2} \cos(2\omega t - 5\theta) - \vec{a}_\theta \frac{J_4 B_1}{2} \sin(2\omega t - 5\theta) \\
& - \vec{a}_r \left(\frac{J_2 B_{4\theta} + J_4 B_{2\theta}}{4} + \frac{J_5 B_1}{2} \right) \cos 6\theta - \vec{a}_\theta \frac{J_5 B_1}{2} \sin 6\theta \\
& + \vec{a}_r \frac{(J_2 B_{5\theta} + J_5 B_{2\theta})}{4} \cos(2\omega t + 7\theta) \\
& + \vec{a}_r \frac{J_4 B_{4\theta}}{4} \cos(2\omega t - 8\theta) \\
& - \vec{a}_r \frac{J_4 B_{5\theta} + J_5 B_{4\theta}}{4} \cos 9\theta \\
& + \vec{a}_r \frac{J_5 B_{5\theta}}{4} \cos(2\omega t + 10\theta)
\end{aligned} \tag{C10}$$

The pressure expression is grouped into dc, fundamental, and harmonic components with respect to the peripheral angle θ . The dc component produces a compressive hoop stress on the shield. The harmonic components want to deform the shield into various harmonic noded ellipses, which should be no problem for a shield designed to withstand short circuit forces. However, the fundamental components produce an offsetting force, a force wanting to pound the rotor against its bearings. Figure C-3 illustrates the fundamental component pressure distributions that produce offsetting forces. The offsetting forces can cause potentially damaging vibration that would be transmitted to the stator and foundation, so it is necessary to investigate further. The offsetting pressure distribution is

$$\begin{aligned}\vec{P} = & \vec{a}_r \frac{J_2 B_1}{2} \cos(2\omega t + \theta) - \vec{a}_\theta \frac{J_2 B_1}{2} \sin(2\omega t + \theta) \\ & + \vec{a}_r \frac{(J_4 B_{5\theta} + J_5 B_{4\theta})}{4} \cos(2\omega t + \theta)\end{aligned}\quad (C11)$$

A change into x-y coordinates is accomplished by the transformation

$$\begin{pmatrix} P_x \\ P_y \end{pmatrix} = \begin{pmatrix} \cos \theta & -\sin \theta \\ \sin \theta & \cos \theta \end{pmatrix} \begin{pmatrix} P_r \\ P_\theta \end{pmatrix}, \quad (C12)$$

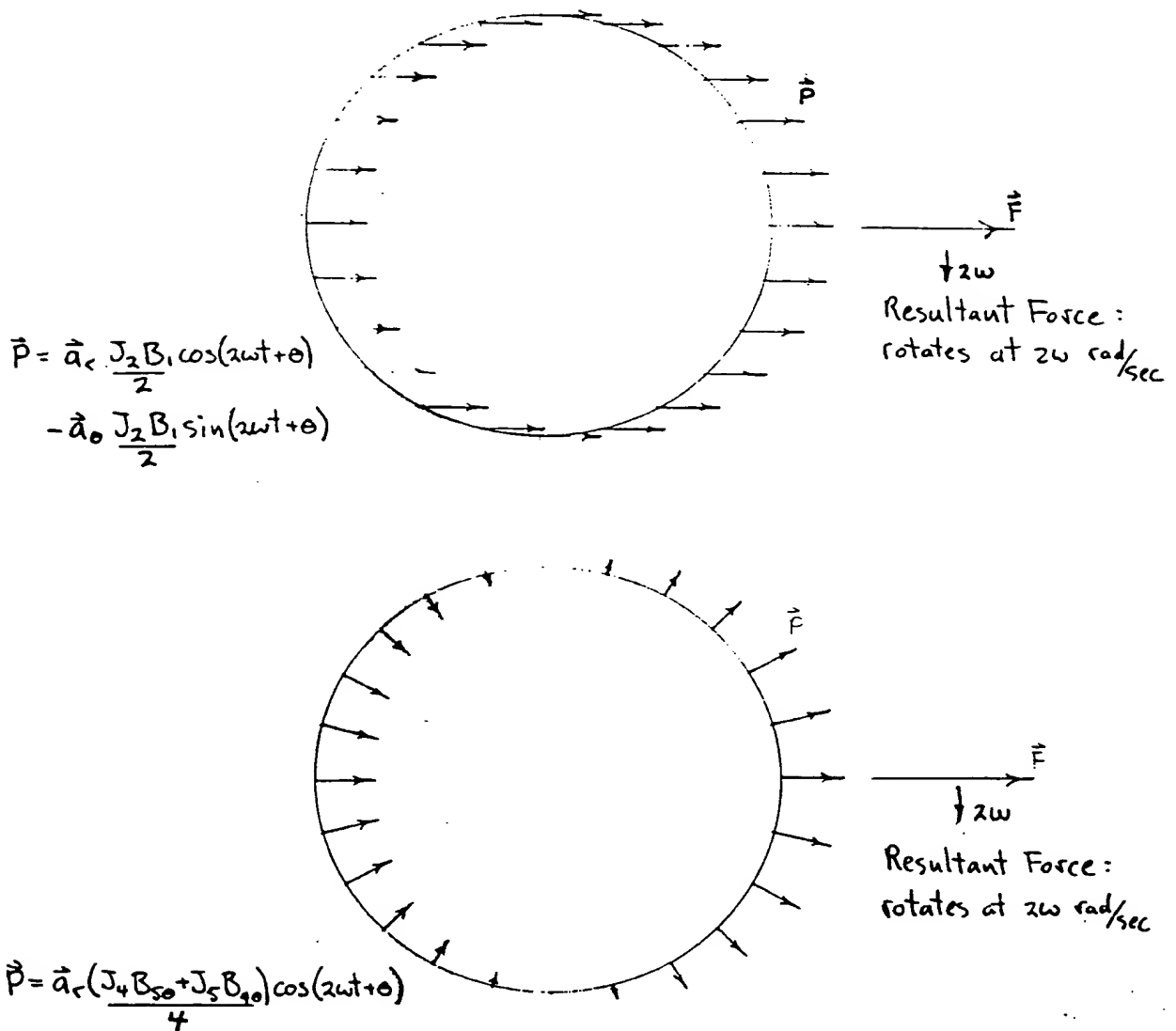


Figure C-3. Pressure Distributions Producing Offsetting Forces

which yields

$$\begin{aligned}\vec{P} = \vec{a}_x & \left[\frac{J_2 B_1}{2} \cos 2\omega t + \frac{(J_4 B_{5\theta} + J_5 B_{4\theta})}{8} \cos 2\omega t + \frac{(J_4 B_{5\theta} + J_5 B_{4\theta})}{8} \cos (2\omega t + 2\theta) \right] \\ & - \vec{a}_y \left[\frac{J_2 B_1}{2} \sin 2\omega t + \frac{(J_4 B_{5\theta} + J_5 B_{4\theta})}{8} \sin 2\omega t - \frac{(J_4 B_{5\theta} + J_5 B_{4\theta})}{8} \sin (2\omega t + 2\theta) \right] \quad (C13)\end{aligned}$$

The total force on the rotor is the integral of the pressure over the area of the shield surface:

$$\vec{F} = \int_0^L \int_0^{2\pi} \vec{P} r_s d\theta dz, \quad (C14)$$

where L is the active length and r_s is the shield surface radius. The force is therefore

$$\begin{aligned}\vec{F} = \vec{a}_x \pi r_s L & \left[J_2 B_1 + \frac{J_4 B_{5\theta} + J_5 B_{4\theta}}{4} \right] \cos 2\omega t \\ & - \vec{a}_y \pi r_s L \left[J_2 B_1 + \frac{J_4 B_{5\theta} + J_5 B_{4\theta}}{4} \right] \sin 2\omega t \quad (C15)\end{aligned}$$

Recalling that

$$J_2 = \frac{B_{2\theta}}{\mu_o} \quad J_4 = \frac{B_{4\theta}}{\mu_o} \quad J_5 = \frac{B_{5\theta}}{\mu_o}$$

gives

$$\begin{aligned}\vec{F} = \vec{a}_x \frac{\pi r_s L}{\mu_o} & \left[B_1 B_{2\theta} + \frac{B_{4\theta} B_{5\theta}}{2} \right] \cos 2\omega t \\ & - \vec{a}_y \frac{\pi r_s L}{\mu_o} \left[B_1 B_{2\theta} + \frac{B_{4\theta} B_{5\theta}}{2} \right] \sin 2\omega t \quad (C16)\end{aligned}$$

It is seen that the force rotates at twice frequency in a direction that is opposite to the rotation of the fundamental armature flux. The force is composed of two interactions: between the fundamental and second harmonic, and between the fourth and fifth harmonics.

Expressions for the magnetic flux magnitudes at the outer surface of the shield are contained in Table C-1, separated into contributions from the inner conductor layer and the outer conductor layer. These expressions were obtained from solutions of Laplace's equation in the air region between the perfectly magnetic core and the perfectly conducting rotor shield, with the armature conductor layers modeled as thin sheets.

The rotor forces will be calculated for a sample machine rated at 1200 MVA, 500 kV. The pertinent dimensions of this machine are listed in Table C-2. Numerical values of the magnetic flux magnitudes are listed in Table C-3, and calculations of the force magnitudes are listed in Table C-4. It is seen that the fundamental and second harmonic interaction contributes the largest component to the force magnitude.

The magnitude of the rotor forces could be reduced considerably if the second harmonic flux could be eliminated. Examination of Table C-3 shows that the magnitude of the second harmonic flux produced by the inner conductor layer is larger than that of the outer layer. It would be desirable to be able to raise the second harmonic flux of the outer layer to exactly cancel that of the inner layer. This can, in fact, be accomplished by inserting spacers between the phase-belts of the outer layer, as illustrated in Figure C-4. New expressions for the flux magnitudes can be written in terms of the outer layer phase-belt span, α , and are contained in Table C-5.

Table C-1
MAGNETIC FLUX MAGNITUDES
(teslas)

Flux Harmonic	Contribution from Inner Layer	Contribution from Outer Layer
B_1	$\frac{\mu_o}{2} \left(\frac{3\sqrt{3}}{\sqrt{2}\pi} J t_i \right) \frac{r_c^2 + r_i^2}{r_c^2}$	$\frac{\mu_o}{2} \left(\frac{3\sqrt{3}}{\sqrt{2}\pi} J t_o \right) \frac{r_c^2 + r_o^2}{r_c^2}$
$B_{2\theta}$	$\mu_o \left(\frac{3\sqrt{3}}{2\sqrt{2}\pi} J t_i \right) \frac{r_s}{r_i} \frac{r_i^4 + r_c^4}{r_s^4 + r_c^4}$	$\mu_o \left(\frac{-3\sqrt{3}}{2\sqrt{2}\pi} J t_o \right) \frac{r_s}{r_o} \frac{r_o^4 + r_c^4}{r_s^4 + r_c^4}$
$B_{4\theta}$	$\mu_o \left(\frac{-3\sqrt{3}}{4\sqrt{2}\pi} J t_i \right) \frac{r_s^3}{r_i^3} \frac{r_i^8 + r_c^8}{r_s^8 + r_c^8}$	$\mu_o \left(\frac{3\sqrt{3}}{4\sqrt{2}\pi} J t_o \right) \frac{r_s^3}{r_o^3} \frac{r_o^8 + r_c^8}{r_s^8 + r_c^8}$
$B_{5\theta}$	$\mu_o \left(\frac{-3\sqrt{3}}{5\sqrt{2}\pi} J t_i \right) \frac{r_s^4}{r_i^4} \frac{r_i^{10} + r_c^{10}}{r_s^{10} + r_c^{10}}$	$\mu_o \left(\frac{-3\sqrt{3}}{5\sqrt{2}\pi} J t_o \right) \frac{r_s^4}{r_o^4} \frac{r_o^{10} + r_c^{10}}{r_s^{10} + r_c^{10}}$

J = conductor layer current density, $\frac{\text{rms-A}}{\text{m}^2}$, (same for both layers)
 r_s = rotor shield surface radius, m
 r_i = average radius of inner conductor layer, m
 r_o = average radius of outer conductor layer, m
 r_c = core inner radius, m
 t_i, t_o = thickness of inner and outer conductor layers, m

Note: It is required that $r_i t_i = r_o t_o$, so that the total current in the inner layer will equal the total current in the outer layer.

Table C-2
DIMENSIONS OF A 1200 MVA – 500 kV
HIGH-VOLTAGE GENERATOR

$J = 2121 \text{ A/in.}^2 = 3.288 \times 10^6 \text{ A/m}^2$
$r_s = 22.25 \text{ in.} = 0.5652 \text{ m}$
$r_i = 27.60 \text{ in.} = 0.7010 \text{ m}$
$r_o = 35.08 \text{ in.} = 0.8910 \text{ m}$
$r_c = 38.72 \text{ in.} = 0.9835 \text{ m}$
$t_i = 1.93 \text{ in.} = 0.0490 \text{ m}$
$t_o = 1.52 \text{ in.} = 0.0386 \text{ m}$
$L = 137.0 \text{ in.} = 3.4798 \text{ m}$

Table C-3
NUMERICAL VALUES OF MAGNETIC FLUX MAGNITUDES
(teslas)

<u>Flux Harmonic</u>	<u>Contribution from Inner Layer</u>	<u>Contribution from Outer Layer</u>	<u>Total</u>
B_1	0.179	0.170	0.349
$B_{2\theta}$	0.1082	-0.0892	0.0190
$B_{4\theta}$	-0.0327	0.0171	-0.0156
$B_{5\theta}$	-0.0206	-0.0083	-0.0289

Table C-4
FORCE MAGNITUDES

Interaction of first and second harmonics	32,600 newtons = 7,330 lbs
Interaction of fourth and fifth harmonics	1,109 newtons = 249 lbs
Total	33,709 newtons = 7,579 lbs

The second harmonic flux can be eliminated by adjusting the outer layer phase-belt span, α , so that the second harmonic flux of the outer layer exactly cancels that of the inner layer. From Table C-5, the mathematical requirement for this condition is

$$\frac{3\sqrt{3}}{2\sqrt{2}\pi} J_i t_i \frac{r_i^4 + r_c^4}{r_i} = \sqrt{2} \frac{\sin \alpha}{\alpha} J_o t_o \frac{r_o^4 + r_c^4}{r_o} \quad (C17)$$

Substituting

$$J_o = J_i \frac{2\pi}{3} \frac{1}{\alpha} \text{ and } t_o = \frac{r_i}{r_o} t_i \quad (C18)$$

(the requirements detailed in the note to Table C-5), and rearranging terms, Equation C17 transforms to

$$\frac{\sin \alpha}{\alpha^2} = \frac{9\sqrt{3}}{8\pi^2} \frac{r_o^2}{r_i^2} \frac{r_i^4 + r_c^4}{r_o^4 + r_c^4} \quad (C19)$$

A value of α is easily determined by trial and error, and for the present numerical example,

$$\alpha = 112.47 \text{ degrees}$$

The spacers inserted between the phase-belts of the outer layer subtend 7.53° , which certainly requires no great sacrifice in terms of the winding's space utilization. Electrically, the spacers would be the most lightly stressed insulation in the winding structure.

Numerical values of the magnetic flux magnitudes for the modified winding are listed in Table C-6, along with force magnitudes in Table C-7. It is seen that the modification has increased the flux magnitudes of the fourth and fifth harmonics, and consequently the fourth-fifth force component. However, the total force is much lower. This force amounts to an unbalance of .004 kg, or 0.009 lbs, at the surface of shield, as determined from the relationship

$$F = m \omega^2 r \quad (C20)$$

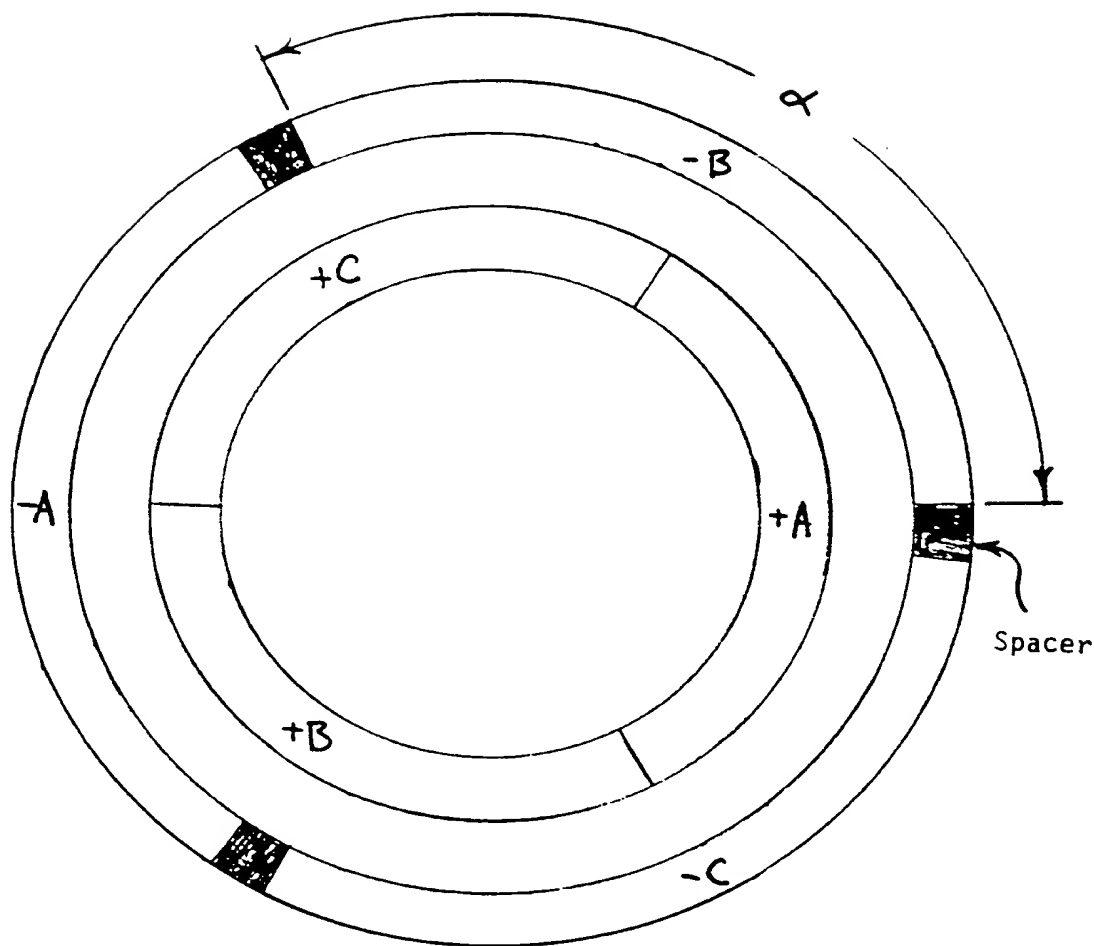


Figure C-4. Modified 120° Phase-Belt Winding

using $\omega = 2 \times 377$ rad/s. This unbalance should be of little consequence to the steady state running of a rotor weighing 60,000 lbs, unless a resonance in the rotor structure is hit.

The analysis that has been described applies only to the straight-section portions of a diamond coil winding. Second harmonic mmf distributions start to reappear in the end windings; to minimize forces it would be preferable to construct the end arms outside of the core region, where the absence of core in the magnetic circuit would reduce the magnitude of second harmonic fluxes. However, it is shown in Appendix B that optimal coil shapes are made by bringing the end arms inside of the core region. This could still be utilized to some extent, if it could be proven that the forces do not become excessive. A fully helical winding would be the most difficult to utilize, being equivalent to a winding that is nothing but end windings.

Table C-5
MAGNETIC FLUX MAGNITUDES FOR THE MODIFIED WINDING
(teslas)

<u>Flux Harmonic</u>	<u>Contribution from Inner Layer</u>	<u>Contribution from Outer Layer</u>
B_1	$\frac{\mu_o}{2} \left(\frac{3\sqrt{3}}{\sqrt{2}\pi} J_i t_i \right) \frac{r_c^2 + r_i^2}{r_c^2}$	$\frac{\mu_o}{2} \left(\frac{2\sqrt{2}}{\alpha} \sin \frac{\alpha}{2} J_o t_o \right) \frac{r_c^2 + r_i^2}{r_c^2}$
$B_{2\theta}$	$\mu_o \left(\frac{3\sqrt{3}}{2\sqrt{2}\pi} J_i t_i \right) \frac{r_s}{r_i} \frac{r_i^4 + r_c^4}{r_s^4 + r_c^4}$	$\mu_o \left(-\frac{\sqrt{2}}{\alpha} \sin \alpha J_o t_o \right) \frac{r_s}{r_o} \frac{r_o^4 + r_c^4}{r_s^4 + r_c^4}$
$B_{4\theta}$	$\mu_o \left(\frac{-3\sqrt{3}}{4\sqrt{2}\pi} J_i t_i \right) \frac{r_s^3}{r_i^3} \frac{r_i^8 + r_c^8}{r_s^8 + r_c^8}$	$\mu_o \left(\frac{-\sin 2\alpha}{\sqrt{2}\alpha} J_o t_o \right) \frac{r_s^3}{r_o^3} \frac{r_o^8 + r_c^8}{r_s^8 + r_c^8}$
$B_{5\theta}$	$\mu_o \left(\frac{-3\sqrt{3}}{5\sqrt{2}\pi} J_i t_i \right) \frac{r_s^4}{r_i^4} \frac{r_i^{10} + r_c^{10}}{r_s^{10} + r_c^{10}}$	$\mu_o \left(\frac{2\sqrt{2}}{5\alpha} \sin \frac{5}{2} \alpha J_o t_o \right) \frac{r_s^4}{r_o^4} \frac{r_o^{10} + r_c^{10}}{r_s^{10} + r_c^{10}}$

Note: It is required that $r_i t_i = r_o t_o$ and $J_o = J_i 2\pi/3 \ 1/\alpha$ so that the total current in the inner layer will equal the total current in the outer layer.

Table C-6
NUMERICAL VALUES OF MAGNETIC FLUX MAGNITUDES
FOR THE MODIFIED WINDING
(teslas)

<u>Flux Harmonic</u>	<u>Contribution from Inner Layer</u>	<u>Contribution from Outer Layer</u>	<u>Total</u>
B_1	0.179	0.171	0.350
$B_{2\theta}$	0.1082	-0.1082	0
$B_{4\theta}$	-0.0327	0.0159	-0.0168
$B_{5\theta}$	-0.0206	-0.0106	-0.0312

Table C-7
FORCE MAGNITUDES FOR THE MODIFIED WINDING

Interaction of first and second harmonics	0
Interaction of fourth and fifth harmonics	1,289 newtons = 290 lbs
Total	1,289 newtons = 290 lbs

Appendix D

LUMPED PARAMETER CIRCUIT MODEL OF A HEAT GENERATING SOLID

The integration of a heat generating solid with significant thermal resistivity into a thermal resistance circuit poses a difficulty, because the solution of the heat generating solid is essentially a field problem and not a circuit problem. However, if the heat flow is one-dimensional and if one is only interested in knowing the temperature at the center of the heat generating solid, the problem can be easily modeled as a lumped parameter circuit.

Consider a heat generating solid extending a great distance in the vertical and axial directions and having a horizontal thickness, t , as illustrated in Figure D-1. Poisson's equation for heat transfer in the horizontal direction is

$$\frac{\delta^2 T}{\delta x^2} = \frac{-Q'''}{k} \quad (D1)$$

where k = thermal conductivity
 Q''' = heat generation per unit volume
 x = horizontal coordinate
 T = temperature

The solution of Poisson's equation is

$$T = \frac{-Q'''}{2k} x^2 + C_1 x + C_2 \quad (D2)$$

where C_1, C_2 = constants of integration

If the temperatures at both edges are identical and equal to T_0 , then the temperature at the mid-line, $x = t/2$, is

$$T_{\max} = T_0 + \frac{Q'''}{2k} \left(\frac{t}{2} \right)^2 \quad (D3)$$

and the edge-to-center temperature rise is

$$\Delta T = \frac{Q'''}{2k} \left(\frac{t}{2} \right)^2 \quad (D4)$$

Now consider the lumped parameter circuit model, also illustrated in Figure D-1. There are two thermal resistances representing the two halves of the heat generating solid. The resistances connect three nodes that represent the temperatures at the edges and center of the solid. The heat input of the center node represents the heat generation of the entire solid.

The thermal resistances are

$$R = \frac{t/2}{kA} \quad (D5)$$

where A = area transverse to heat flow

and the nodal heat input is

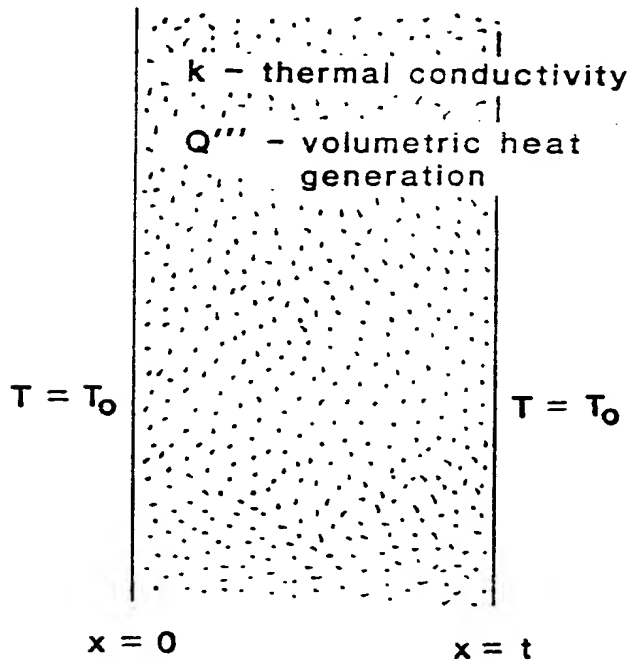
$$q = Q''' t A \quad (D6)$$

If the temperatures at both edge nodes are equal, then the heat input divides into exactly two when flowing through the resistances. The edge-to-center temperature rise is therefore

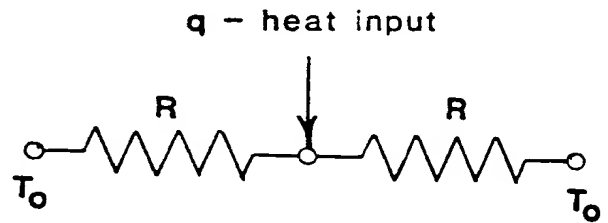
$$\Delta T = \frac{q}{2} R$$

$$= \frac{Q''' }{k} \left[\frac{t}{2} \right]^2 \quad (D7)$$

The temperature rise calculated by the circuit method is exactly twice that calculated by the field method. Therefore, the circuit model can be employed to gain exact results if the numerical values of the thermal resistances are cut in half when entered into the model.



Field Model



Circuit Model

Figure D-1. Field and Circuit Models of a Heat Generating Solid

Appendix E

SOLUTION OF THE MONOLITH CYLINDER ARMATURE WINDING THERMAL CIRCUIT MODEL

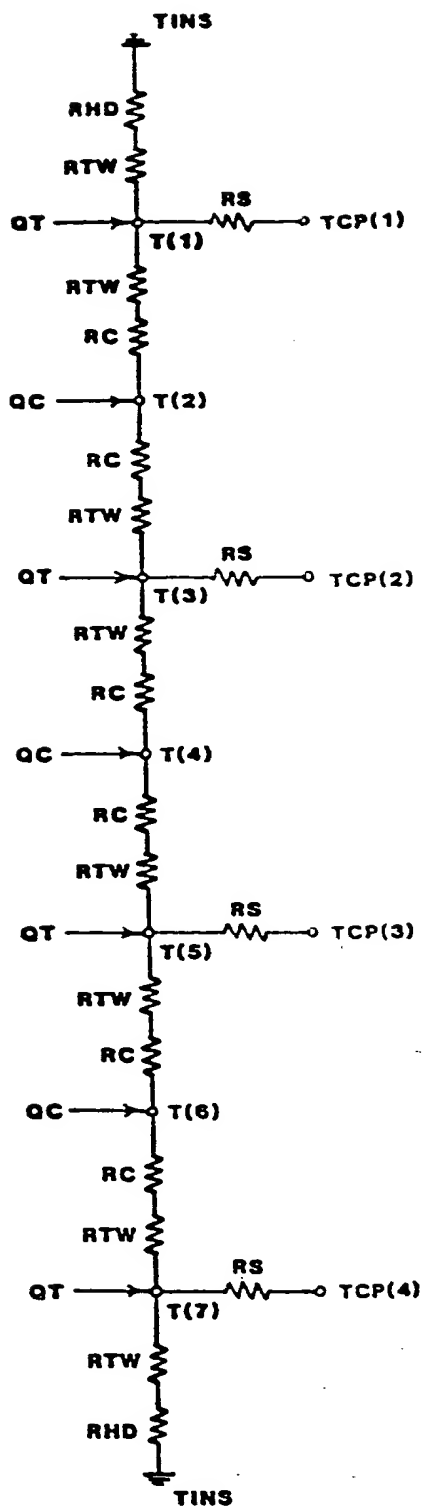
The solution of the monolith cylinder armature winding thermal circuit is described for an example containing three conductors and four cooling tubes, although the method is easily extended for systems containing any number of conductors. The only constraints are: one, there must be one more cooling tube than conductor; and two, the conductors and cooling tubes are alternatively stacked in a column with the cooling tubes top and bottommost in the stack. The thermal circuit is illustrated in Figure E-1. The inputs to the circuit are the resistor values, the cylinder insulation temperatures, marked "TINS", and the coolant stream temperatures, marked "TCP()". The circuit is solved for the cooling tube temperatures and conductor midline temperatures, marked "T()". Even arguments of T() indicate a cooling tube temperature and odd arguments of T() indicate a conductor midline temperature.

Circuit equations can be written and reduced to a set of simultaneous equations, represented here in a matrix formulation:

$\frac{1}{R_S} + \frac{1}{RCRTW} + \frac{1}{RTWRHD}$	$-\frac{1}{RCRTW}$						T(1)	$QT + \frac{TCP(1)}{R_S} + \frac{1}{RTWRHD}$
$-\frac{1}{RCRTW}$	$\frac{2}{RCRTW}$	$-\frac{1}{RCRTW}$					T(2)	QC
	$-\frac{1}{RCRTW}$	$\frac{1}{R_S} + \frac{2}{RCRTW}$	$-\frac{1}{RCRTW}$				T(3)	$QT + \frac{TCP(2)}{R_S}$
		$-\frac{1}{RCRTW}$	$\frac{2}{RCRTW}$	$-\frac{1}{RCRTW}$			T(4)	QC
			$-\frac{1}{RCRTW}$	$\frac{1}{R_S} + \frac{2}{RCRTW}$	$-\frac{1}{RCRTW}$		T(5)	$QT + \frac{TCP(3)}{R_S}$
				$-\frac{1}{RCRTW}$	$\frac{2}{RCRTW}$	$-\frac{1}{RCRTW}$	T(6)	QC
					$-\frac{1}{RCRTW}$	$\frac{1}{R_S} + \frac{1}{RCRTW} + \frac{1}{RTWRHD}$	T(7)	$QT + \frac{TCP(4)}{R_S} + \frac{1}{RTWRHD}$

The notation of the matrix equation conforms to that of the figure, except that the notations "RCRTW" and "RTWRHD" indicate the summations of RC plus RTW and RTW plus RHD, respectively. The matrix formulation is easily extended to a system of any number of conductors because of the repetitive nature of the rows in the matrix. The top and bottommost rows are the same for a system of any number of conductors. The even-numbered rows are all similar in nature, involving identical matrix elements centered around the matrix diagonal, the conductor temperature in the vector of unknowns, and the conductor heat inputs in the right-hand side vector. The odd-numbered rows, excluding the first and last rows, are also similar in form. The matrix is extended to a system of any number of conductors by merely provided enough of the similarly constructed rows.

The matrix formula is solved by substituting numerical values for the entries and applying a computer subroutine that solves large systems of simultaneous equations.



LEGEND

- RHD - RESISTANCE OF HORIZONTAL DIVIDER
- RTW - RESISTANCE OF COOLING TUBE INSULATION WRAP
- RC - RESISTANCE OF CONDUCTOR HALF
- RS - EQUIVALENT RESISTANCE OF CONVECTION SURFACE RISE
- QC - CONDUCTOR HEAT INPUT
- QT - COOLING TUBE HEAT INPUT
- T() - TEMPERATURE OF COOLING TUBE, ODD ARGUMENT
- TEMPERATURE OF CONDUCTOR CENTER, EVEN ARGUMENT
- TCP() - COOLANT TEMPERATURE
- TINS - TEMPERATURE OF CYLINDER INSULATION (45° C)

Figure E-1. Thermal Circuit Diagram

Appendix F

INDUCTIVE ELEMENT DETERMINATION BY HELICAL FIELD THEORY

The calculation of mutual inductance between two helical coils lying at different radial and peripheral locations will be described. The helical winding is assumed to have two parallel circuits for each phase. The two circuits are labeled "A" and "B", and the coils within each circuit are sequentially numbered, as illustrated in Figure F-1. Figure F-2 illustrates a developed view of four helical coils labeled "1A", "2A", "1B", and "2B", according to the convention of Figure F-1. The solid lines refer to coil sides lying on the inner conductor layer, and the dotted lines refer to coil sides lying on the outer conductor layer. Coils 1 and 2 of each circuit lie at different peripheral and radial locations. Referring to the radii terminology of Figure F-3, the coil sides of coil 1A lie on radii R_{1i} and R_{1o} and the coil sides of coil 2A lie on radii R_{2i} and R_{2o} . Coil 2 is peripherally shifted from coil 1 by the angle ϕ . The aforementioned applies to the coils 1B and 2B, which are shifted from coils 1A and 2A by 180° . The surface marked by radius R_r corresponds to the rotor shield and is considered to be diamagnetic since surges will not penetrate the rotor shield. The surface marked by radii R_c corresponds to the core and is considered to be perfectly magnetic.

To find the coil mutual inductance, it is appropriate to assume a current in one coil (say 1A) and then to calculate the flux linked by another coil (say 2A). The currents in coils 1A and 1B are the same, so coils 2A and 2B will link the same amount of flux. Note that, as far as the currents are concerned, it makes no difference to assume that coil halves solid 1A and solid 1B make up a coil and that dotted 1A and dotted 1B make up another. Similarly, the amount of flux linked by the two fictitious coils solid 2A — solid 2B and dotted 2A — dotted 2B is the same as the amount of flux linked by the actual coils solid 2A — dotted 2A and solid 2B — dotted 2B. What this means is that it is possible to compute inductances by assuming coils which are simple opposed helices with full pitch. There is no mutual inductance between the solid line coils and the dotted line coils because of the opposite helix directions.

Since the inner layer and outer layer helices are independent, it is possible to consider each separately and then combine the results. Consider, then, a situation in which equal current I appears in the solid-line (inner layer) coil halves 1A and 1B. The axial current may be expressed by a Fourier series:

$$K_z = \sum_{n=0}^{\infty} K_n \cos n \left(\theta - \frac{\pi z}{\ell} \right) \quad (F1)$$

Note that the form of Equation F1 is dictated by the spiral symmetry of the problem. Because the current is carried by single wires, the Fourier components in Equation F1 are given by

$$K_n = \frac{2}{\pi} \frac{I}{R_o} \quad (F2)$$

Total axial surface current may then be written as

$$K_z = \sum_{n=0}^{\infty} \frac{2}{\pi} \frac{I}{R_o} \cos n \left(\theta - \frac{\pi z}{\ell} \right) \quad (F3)$$

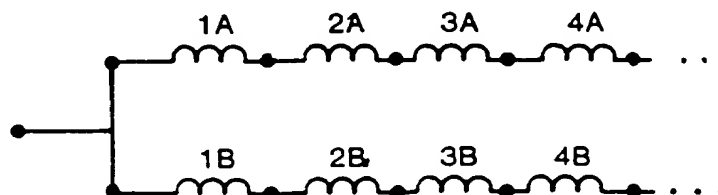


Figure F-1. Coil Labeling of a Two-Circuit Winding

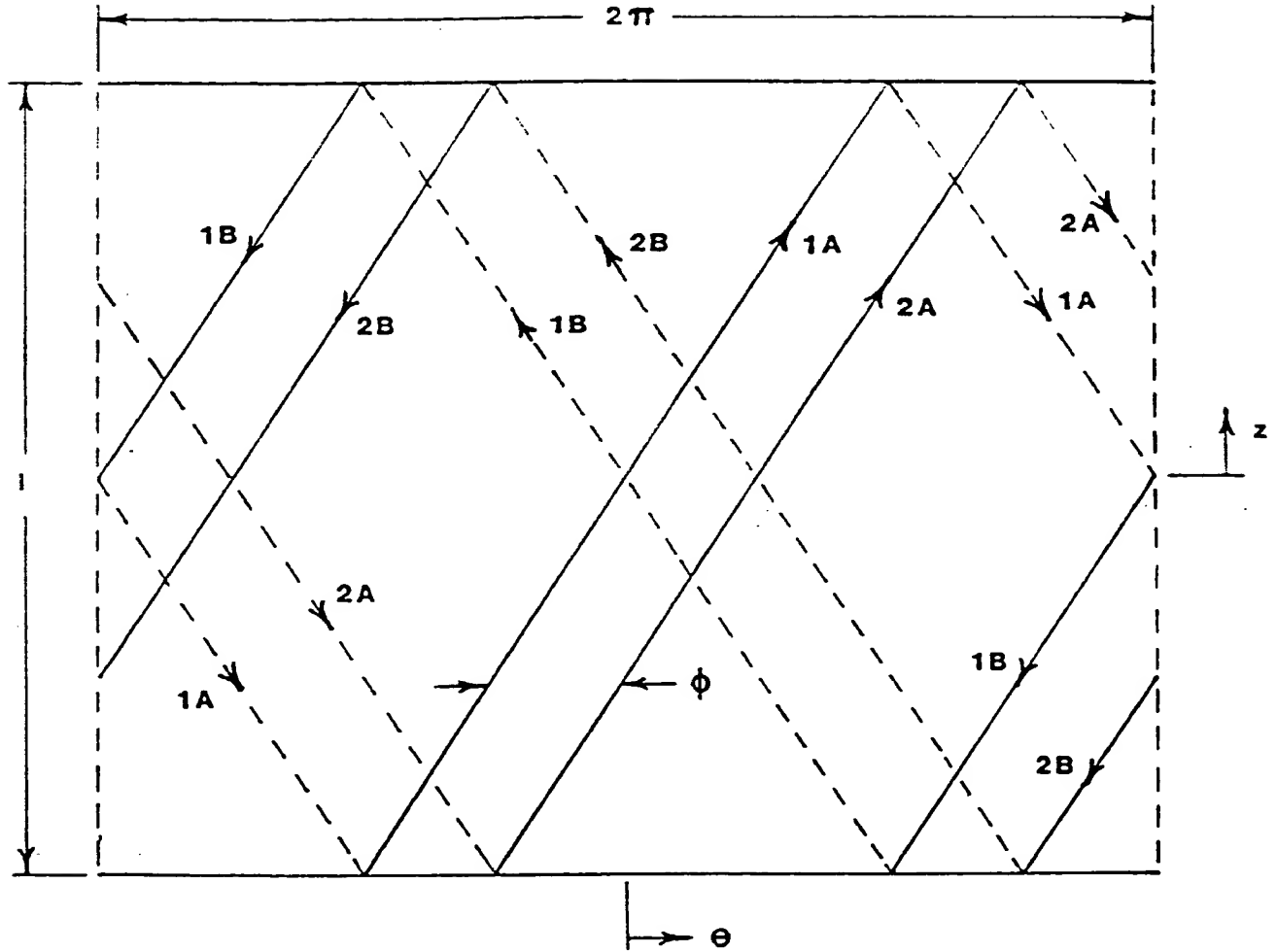


Figure F-2. Developed View of Helical Coils

Next, it is necessary to compute magnetic field produced by the currents expressed in Equation F3. Since this field analysis is well known, only an outline will be given here. The magnetic field may be found as the gradient of a scalar potential which, in turn, must obey Laplace's equation:

$$\vec{H} = -\nabla\Phi \quad (\text{F4})$$

$$\nabla^2\Phi = 0 \quad (\text{F5})$$

The magnetic field and scalar potential have a form roughly the same as the current distribution. For each space harmonic component of order n

$$\Phi(r, \theta, z) = \phi(r) \sin n(\theta - \frac{\pi z}{l}) \quad (\text{F6})$$

Equation F5 may be reduced to a form of Bessel's equation which is solved by

$$\phi(r) = A I_n(\frac{n\pi r}{l}) + B K_n(\frac{n\pi r}{l}) \quad (\text{F7})$$

where A and B are arbitrary constants and I_n and K_n are the hyperbolic or modified Bessel functions.

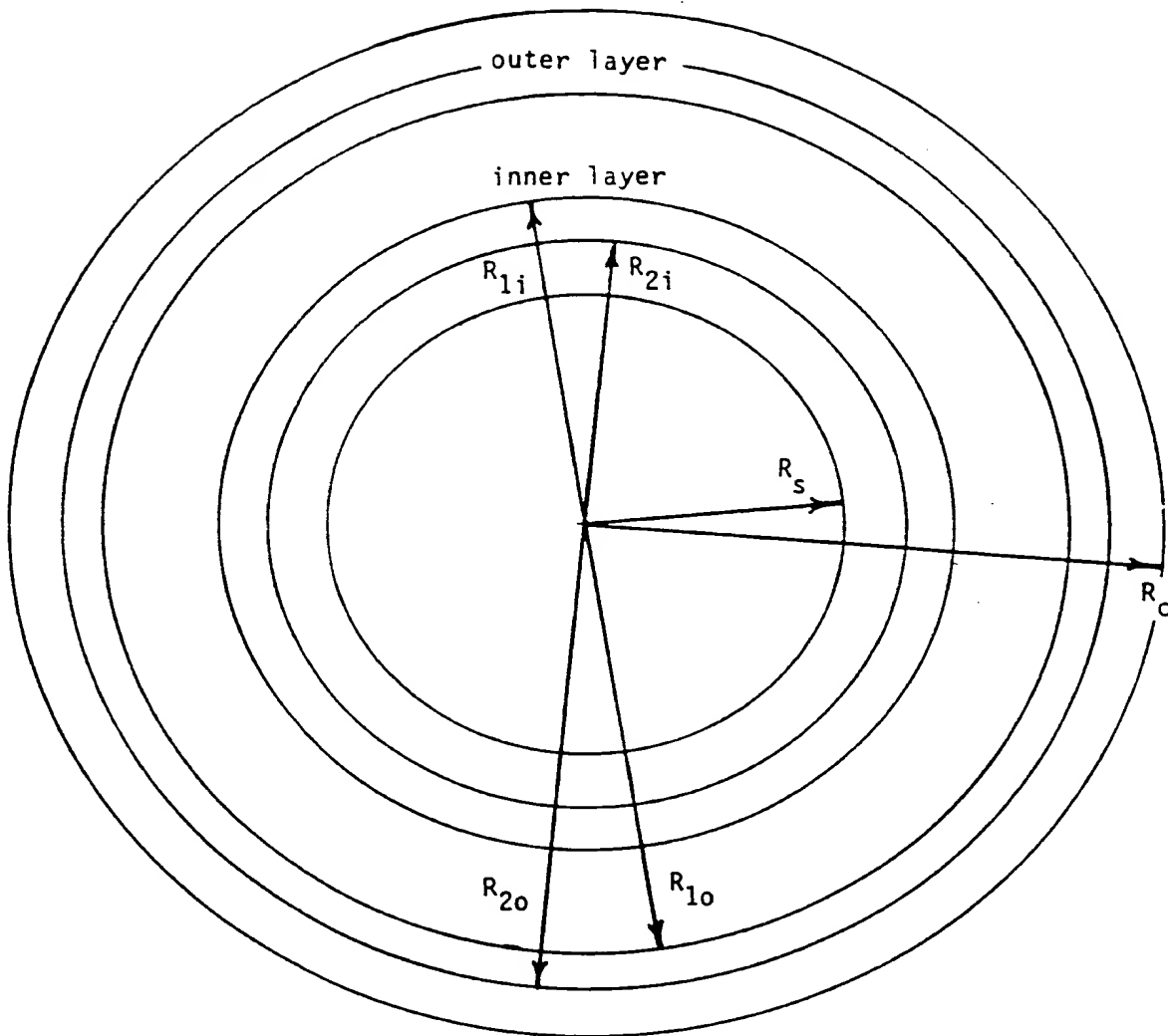


Figure F-3. Radii Terminology of the Helical Armature

Now, assuming that the current filaments are at radius R_1 , the following magnetic boundary conditions apply:

- at $r = R_s$, $H_r = 0$ (F8)

- at $r = R_1$, $H_r|_{r=R_1-} = H_r|_{r=R_1+}$ (F9)

- at $R = R_1$, $H_\theta|_{r=R_1+} - H_\theta|_{r=R_1-} = K_z$ (F10)

- at $r = R_c$, $H_\theta = 0$ (F11)

Equation F7 must be solved twice for the two regions:

- 1) $R_s < r < R_1$

- 2) $R_1 < r < R_c$

There are two sets of constants, A and B, corresponding to regions 1 and 2. Combining the boundary conditions presented in Equations F8 through F11 with Equation F7 and F4, the following expression of the constants is obtained:

$$\begin{vmatrix} I_n'(\frac{n\pi R_s}{\ell}) & K_n'(\frac{n\pi R_s}{\ell}) & 0 & 0 \\ 0 & 0 & I_n(\frac{n\pi R_c}{\ell}) & K_n(\frac{n\pi R_c}{\ell}) \\ I_n'(\frac{n\pi R_1}{\ell}) & K_n'(\frac{n\pi R_1}{\ell}) & -I_n'(\frac{n\pi R_1}{\ell}) & -K_n'(\frac{n\pi R_1}{\ell}) \\ -I_n(\frac{n\pi R_1}{\ell}) & -K_n(\frac{n\pi R_1}{\ell}) & I_n(\frac{n\pi R_1}{\ell}) & K_n(\frac{n\pi R_1}{\ell}) \end{vmatrix} \begin{vmatrix} A_i \\ B_i \\ A_o \\ B_o \end{vmatrix} = \begin{vmatrix} 0 \\ 0 \\ 0 \\ \frac{R_1}{n} K_{zn} \end{vmatrix} \quad (F12)$$

It is straightforward but tedious to solve Equation F12 using Cramer's rule. The next step is to reconstitute the magnetic field by using Equation F9 and Equation F4. Once this is done, the magnetic field is found. For radius less than R_1 , the result is

$$H_m = \frac{n\pi^2 R_1^2 K_{zn}}{2} \frac{\left[I_n(\frac{n\pi R_c}{\ell}) K_n'(\frac{n\pi R_1}{\ell}) - K_n(\frac{n\pi R_c}{\ell}) I_n'(\frac{n\pi R_1}{\ell}) \right]}{\left[I_n(\frac{n\pi R_c}{\ell}) K_n'(\frac{n\pi R_s}{\ell}) - K_n(\frac{n\pi R_c}{\ell}) I_n'(\frac{n\pi R_s}{\ell}) \right]} \times \left[K_n'(\frac{n\pi R_s}{\ell}) I_n'(\frac{n\pi r}{\ell}) - I_n'(\frac{n\pi R_s}{\ell}) K_n'(\frac{n\pi r}{\ell}) \right] \sin n(\theta - \frac{\pi z}{\ell}) \quad (F13)$$

Note that Equation F13 expresses one space harmonic component of the magnetic field produced by the inner layer spiral pseudocoil. The complete problem will involve a second set of field components for the coils of the outer layer. Flux linked by a full-pitched spiral coil at radius $R_2 < R_1$ will be given by

$$\lambda_n = \frac{2\mu_o \ell R_2}{n} H_m(R_2) \cos n\phi, \quad (F14)$$

where ϕ is the relative angle between the two coils. This is actually twice the contribution to coil inductance, since each physical coil has both inner layer and outer layer portions. Thus the contribution to inductance is

$$L_n = \frac{2\pi\mu_o R_1 R_2}{\ell} \frac{[1][2]}{[3]} \cos n\phi \quad (F15)$$

where

$$[1] = \left[K_n'(\frac{n\pi R_s}{\ell}) I_n'(\frac{n\pi R_2}{\ell}) - I_n'(\frac{n\pi R_s}{\ell}) K_n'(\frac{n\pi R_2}{\ell}) \right] \quad (F16)$$

$$[2] = \left[I_n(\frac{n\pi R_c}{\ell}) K_n'(\frac{n\pi R_1}{\ell}) - K_n(\frac{n\pi R_c}{\ell}) I_n'(\frac{n\pi R_1}{\ell}) \right] \quad (F17)$$

$$[3] = \left[I_n(\frac{n\pi R_c}{\ell}) K_n'(\frac{n\pi R_s}{\ell}) - K_n(\frac{n\pi R_c}{\ell}) I_n'(\frac{n\pi R_s}{\ell}) \right] \quad (F18)$$

The complete contribution to inductance for harmonic n includes Equation F15 evaluated for both inner and outer layers. Of course, in finding the complete inductance for a pair of coils, it is necessary to sum a number of space harmonics.

Appendix G

MATHEMATICAL ANALYSIS OF THE VERTICAL DIVIDER FABRICATION

The top and bottom edges of the vertical dividers in a helical armature describe concentric helices. These concentric helices can be formed by twisting a pair of concentric arcs, as is demonstrated in Figure 2.9-3. The mathematical foundation for this geometrical relationship is here described. Figure G-1 illustrates the geometry relevant to this analysis. The inner helix lies at radius r_1 and progresses 180° peripherally over the axial length L_s . The same is true for the outer helix, which lies at radius r_2 . The helix lengths are

$$L_1 = \sqrt{L_s^2 + \pi^2 r_1^2} \quad (G1)$$

$$L_2 = \sqrt{L_s^2 + \pi^2 r_2^2} \quad (G2)$$

Now consider a pair of concentric arcs at radii r_{a1} and r_{a2} , where

$$r_{a2} - r_{a1} = r_2 - r_1 \quad (G3)$$

a condition required to maintain the divider height. The length of the inner arc is

$$L_{a1} = \theta r_{a1} \quad (G4)$$

and the length of the outer arc is

$$L_{a2} = \theta r_{a2} = \theta (r_{a1} + r_2 - r_1) \quad (G5)$$

The ratios of the lengths are set equal:

$$\frac{L_1}{L_2} = \frac{L_{a1}}{L_{a2}} \quad (G6)$$

This condition yields the inner arc radius

$$r_{a1} = \frac{\sqrt{L_s^2 + \pi^2 r_1^2}}{\sqrt{L_s^2 + \pi^2 r_2^2} - \sqrt{L_s^2 + \pi^2 r_1^2}} (r_2 - r_1) \quad (G7)$$

The outer arc radius is then

$$r_{a2} = r_{a1} + r_2 - r_1 \quad (G8)$$

and the peripheral span of the arcs is

$$\theta = \frac{\sqrt{L_s^2 + \pi^2 r_1^2}}{r_{a1}} \quad (G9)$$

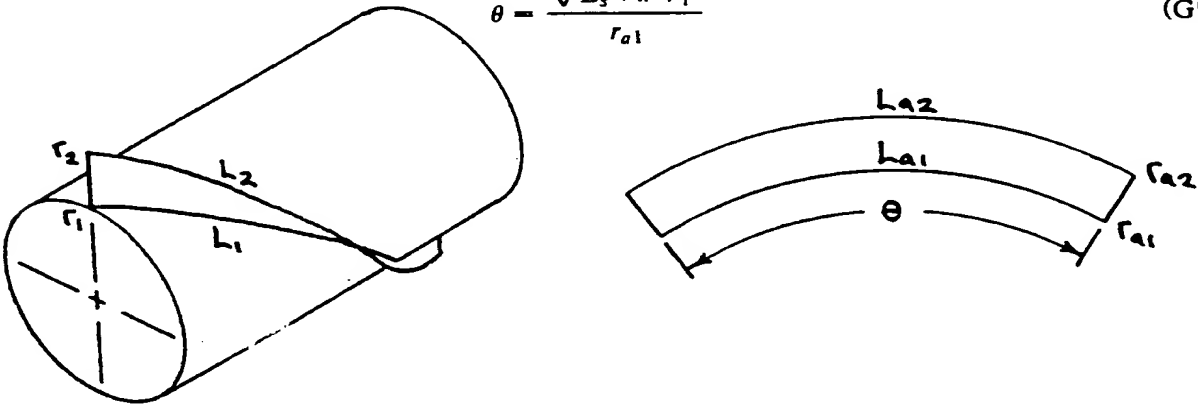


Figure G-1. Concentric Helices Formed from Concentric Arcs

Appendix H

EQUATIONS AND PARAMETERS FOR THE MATHEMATICAL MODEL OF A HIGH-VOLTAGE GENERATOR WITH A SUPERCONDUCTING ROTOR

The high-voltage superconducting generator is modeled with conventional synchronous machine theory using a single shell rotor. The per-unit model equations are as follows. The mutual inductances between the stator and rotor circuits and between the rotor circuits are, in general, unequal.

STATOR VOLTAGE EQUATIONS

$$e_d = p \Psi_d - \Psi_q \omega - R_a i_d$$

$$e_q = p \Psi_q + \Psi_d \omega - R_a i_q$$

FIELD VOLTAGE EQUATION

$$e_{fd} = p \Psi_{fd} + R_{fd} i_{fd}$$

D AND Q AXIS FLUX LINKAGE EQUATIONS

$$\begin{bmatrix} \Psi_d \\ \Psi_{fd} \\ \Psi_{ld} \end{bmatrix} = \begin{bmatrix} X_d & X_{afd} & X_{ald} \\ X_{afd} & X_{ffd} & X_{fld} \\ X_{ald} & X_{fld} & X_{lld} \end{bmatrix} \begin{bmatrix} i_d \\ i_{fd} \\ i_{ld} \end{bmatrix}$$

$$\begin{bmatrix} \Psi_q \\ \Psi_{lq} \end{bmatrix} = \begin{bmatrix} X_q & X_{alq} \\ X_{alq} & X_{llq} \end{bmatrix} \begin{bmatrix} i_q \\ i_{lq} \end{bmatrix}$$

D AND Q AXIS SHELL EQUATIONS

$$0 = p \Psi_{ld} + R_{lld} i_{ld}$$

$$0 = p \Psi_{lq} + R_{llq} i_{lq}$$

The relevant per-unit model parameters are given below for the 600 MVA, 345 kV, .9 PF, 60 Hz unit modeled.

$R_a = .00247$	$R_{fd} = 1.515 \text{ E-}8$
$X_d = .2989$	$X_{afd} = .0577$
$X_{ald} = .0577$	$X_{ffd} = .1004$
$X_{fld} = .0421$	$X_{lld} = .0479$
$X_q = .2989$	$X_{alq} = .0577$
$X_{llq} = .0474$	$R_{lld} = 9.4 \text{ E-}3$
$R_{llq} = 9.4 \text{ E-}3$	

Appendix I

TURBINE-GENERATOR MODEL DATA FOR SHAFT TORSIONAL STUDIES

PER-UNIT ELECTRICAL DATA

	690 MVA	815 MVA	892 MVA	HV Stator 588 MVA
R_a	.0044	.0032	.0018	.00247
X_l	.1711	.12	.1319	.2412
X_{ad}	1.601	1.51	1.6551	.0577
X_{aq}	1.598	1.44	1.6315	.0577
R_{fd}	.00095	.00083	.00056	1.51E-8
X_{fd}	.14755	.0571	.0889	.1004
R_{kd}	.0419	.0229	.0109	.0094
X_{kd}	.1063	.0314	.0553	.0479
R_{kql}	.00343	.00385	.0016	.0094
X_{kql}	.6563	.3025	.328	.0474
R_{kq2}	.0123	.012	.0035	
X_{kq2}	.0682	.02174	.0381	
X_d	1.7721	1.63	1.787	.2989
X'_d	.3023	.175	.19	.2657
X''_d	.2306	.14	.1653	.2287

PER-UNIT INERTIAS AND SPRING CONSTANTS

	892 MVA	815 MVA	690 MVA	HV Stator
$J1$.186	.143	NS	
$J2$.311	.230	.457	
$J3$	1.719	1.328	1.800	
$J4$	1.770	1.385	1.804	
$J5$	1.738	1.929	1.413	.46
$J6$.0685	.0226	.0267	
$K1$	19.32	12.542	NS	
$K2$	34.961	22.839	37.066	
$K3$	52.084	55.196	59.188	
$K4$	70.920	70.197	67.562	
$K5$	2.825	1.823	1.945	

NS = No shaft

Appendix J

MONETARY VALUE OF GENERATOR AND TRANSFORMER LOSSES

A methodology for calculating the value of a kilowatt of losses at the utility level is here outlined. The value of \$1270/kW is based on the savings resulting from reduced coal costs over the 35-year life of the unit. This \$/kW value was used to calculate the savings of improved generator efficiencies and of the elimination of the transformer losses when high-voltage superconducting generators were evaluated.

The method used to calculate the justified investment value of a \$/kW uses heat rate improvement formulas. The heat rate formulas and calculations provide a saving value as shown below:

Value of heat rate — in plant cost terms (1985 dollars)

$$\$12.7/\text{kW}/\% = 14\text{¢}/\text{kW}/\text{Btu}$$

These heat rate values can be converted to \$/kW by the relationships described in the example below:

Example to identify a \$/kW value for a 0.1% improvement in heat rate.

9 Btu's

$$\begin{aligned} \$12.7/\text{kW}/\% \times 1,000,000 \text{ kW unit} \times 0.1\% &= \$1,270,000 \\ \uparrow 1\% = 90 \text{ Btu's} &= \$141,000/\text{Btu}/\text{kW-Hr} \\ \frac{\$1,270,000}{\text{kW savings}} = \frac{\$1,270,000}{1,000,000 \times 0.001} &= \$1,270/\text{kW} \\ \uparrow & \\ 0.1\% \text{ Improvement in Gen. Losses} & \end{aligned}$$

METHOD USED TO CALCULATE VALUE OF HEAT RATE

A. Assumptions

1. Privately owned utility
2. 35-year life
3. Assumed economic conditions continue
4. Coal fuel, 250¢/MBTU in 1985, 7%/Yr. inflation after 1985.
5. 1985 service.
6. Plant net HR (weighted) = 9,000 Btu/kW/Hr.
7. Interest lost during construction is not included.
8. Additional assumptions as described below.

B. Rate of Return (Estimate)

	% Capital		Cost, %	Weighted Cost, %
Long Term Bonds	55	×	11.5	6.32
Preferred Stock	10	×	10.0	1.00
Common Stock	35	×	15.0	5.25
	100%			12.57

"Rate of Return" = 12.6%

C. Capitalization Ratio (Annual Fixed Charge Rate)

Rate of Return, r	=	12.57%
Depreciation (35 yrs. at 12.57%), d_1	=	0.20
Income Tax (Federal and State), T^{**}	=	5.15
Ad Valorem Tax	=	2.31
Insurance	=	0.10
General and Administration Expenses	=	1.00
CR = Capitalization Ratio	=	21.33%

..

$$T = \frac{t}{1-t} \frac{r-DB}{r} r + d_1 - d_2$$

$$\text{where } D = 55\%, B = 11.5\%, d_2 = \frac{1}{35}, \text{FTR} = 48\%, \text{STR} = 6\%$$

$$t = (\text{FTR})(1-\text{STR}) + \text{STR}$$

D. Capacity Factor (CF)

While current capacity (load) factors are depressed due to low load growth, etc., it is likely that in the lifespan of a new, large unit the capacity factor will be in the traditional 60-65% range. Therefore, assume:

Year	Capacity Factor
1-2	55%
3-10	78%
11-20	70%
21-30	60%
31-35	40%

E. Annual Fuel Cost

$$\$ = \frac{\Delta \text{HR}(8760) \text{kW}(\text{CF})(\text{FC})}{10^{10}}$$

Example — Inflated or then current dollars = 1000 kW capacity, 1986 dollars

$$\$ = 90 \text{ Btu/kW-Hr. } (8760 \text{ Hrs.}) 1000 \text{ kW} \frac{(55)}{100} \frac{267.5¢}{10^6 \text{ Btu}} \times \frac{\$1.00}{100¢}$$

$$= \$1,159.73$$

$$\text{Present worth} = 1,159.73 \times \frac{1}{(1+r)^n} = 1159.73 \times .8883 = 1030.23$$

$$r = 12.57\% = .1257$$

F. Value of Heat Rate — In Plant Cost Terms

With the above assumptions, the annual fuel cost may be calculated for each year, present worth (using the rate of return), summed, levelized (divided by the uniform series present worth factor) and capitalized. Table J-1 shows such a calculation.

The result is the value for heat rate in 1984-1985 of

$$\$12.7/\text{kW}\% \text{ or } \frac{\$12.70}{90} = 14¢/\text{kW/Btu}$$

G. Differential Kilowatt Capacity Due to Heat Rate Differences

Whether to evaluate kilowattage capacity differences resulting from heat rate differences or not, and at what rate is a controversial subject involving many factors and philosophies. It is likely that a fossil plant with the required air clean-up equipment will cost at least \$800/kW during the 1984-1985 period. However, the equipment that varies with incremental kW capacity is about 30% of the total plant and the price of incremental capacity is about 20% of the base price for such equipment.

Thus a reasonable incremental kilowattage capacity charge might be $800 (.3) (.2) = \$50/\text{kW}$.

For an 800 MW unit (880,000 capacity), the fuel cost and capacity value for a 0.1% change in heat rate (and kilowattage) would be about (at customer level):

Fuel Savings-Heat Rate	12.7 (880,000)	0.1	=	\$1,120,000
Incremental Capacity	50 (880,000)	.001	=	44,000
			Total	= \$1,164,000

Since the value of incremental kilowattage is only $\approx 4\%$ of the heat rate value, and well below the uncertainty in assumed values of many parameters, it is believed incremental kilowattage savings should not be included in this analysis.

H. References

Excellent information on utility economics is available in the following:

1. P. Leung and R.F. Durning, *Power System Economics: On Selection of Engineering Alternates*, ASME Paper No. 77-JPGC-PWR-7.
2. Paul H. Jaynes, *Profitability and Economic Choice*, The Iowa State University Press, 1968.

Table J-1

HEAT RATE JUSTIFIED INVESTMENT

Max Life 35 yrs
 Rate of Return 12.6%
 Rate of Inflation (M&L) 0%
 Rate of Inflation (FUEL) 7%
 Fuel Cost per million Btu \$2.50

kW Capacity 1000 kW
 \$/Day Out 0\$
 F/O-Risk 0.000%
 F/O-Days 0
 Capt. Ratio 21.33%

All dollars in inflated or then current dollars except summations (PW)

Yr.	PWF	Inf. M&L	Inf. Fuel	Delta hr	CF	Cents Fuel Cost	\$ Δhr	PW
1	.8883	1.00	1.07	90.0	55	268.	1160.	1030
2	.7891	1.00	1.14	90.0	55.	286.	1211.	956
3	.7010	1.00	1.23	90.0	78.	306.	1883.	1320
4	.6227	1.00	1.31	90.0	78.	388.	2015.	1255
5	.5532	1.00	1.40	90.0	78.	351.	2156.	1193
6	.4914	1.00	1.50	90.0	78.	375.	2307.	1134
7	.4366	1.00	1.61	90.0	78.	401.	2469.	1078
8	.3878	1.00	1.73	90.0	78.	430.	2612	1013
9	.3445	1.00	1.84	90.0	78.	460.	2886.	974
10	.3060	1.00	1.97	90.0	78.	492.	3034.	928
11	.2719	1.00	2.10	90.0	70.	536.	3904.	790
12	.2415	1.00	2.25	90.0	70.	563.	3107.	750
13	.2145	1.00	2.41	90.0	70.	602.	3385.	715
14	.1906	1.00	2.58	90.0	70.	645.	3558.	678
15	.1693	1.00	2.76	90.0	70.	690.	3807.	644
16	.1504	1.00	2.95	90.0	70.	738.	4073.	612
17	.1336	1.00	3.16	90.0	70.	790.	4358.	582
18	.1187	1.00	3.33	90.0	70.	815.	4663.	553
19	.1054	1.00	3.62	90.0	70.	904.	4990.	526
20	.0937	1.00	3.87	90.0	70.	967.	5339.	500
21	.0832	1.00	4.14	90.0	60.	1035.	4897.	407
22	.0739	1.00	4.43	90.0	60.	1108.	5339.	387
23	.0657	1.00	4.74	90.0	60.	1185.	5606.	368
24	.0583	1.00	5.07	90.0	60.	1268.	5999.	350
25	.0518	1.00	5.43	90.0	60.	1357.	6418.	332
26	.0460	1.00	5.81	90.0	60.	1452.	6868.	316
27	.0409	1.00	6.21	90.0	60.	1553.	7319.	300
28	.0363	1.00	6.65	90.0	60.	1662	7863.	285
29	.0323	1.00	7.11	90.0	60.	1779.	8413.	272
30	.0387	1.00	7.61	90.0	60.	1903.	9002.	258
31	.0355	1.00	8.15	90.0	40.	2036.	6423.	228
32	.0326	1.00	8.72	90.0	40.	2179.	6871.	222
33	.0201	1.00	9.33	90.0	40.	2331.	7352.	148
34	.0178	1.00	9.98	90.0	40.	2495.	7867.	131
35	.0159	1.00	10.68	90.0	40.	2668.	6417.	102

ΣPW = 21281.

$$\text{Justified Investment} = \frac{\Sigma PW \$ \Delta HR}{CR \cdot PWF \cdot KW}$$

$$JI = \frac{21281}{(.2133)(7.83)1000} = \$12.74/kW/\%$$

Note: Calculation is for 1000 kW

$$PWF = \left[\frac{(1+r)^n - 1}{r(1+r)^n} \right]$$

EPRI EL-3391

Below are five index cards that allow for filing according to the four cross-references in addition to the title of the report. A brief abstract describing the major subject area covered in the report is included on each card.

EPRI EL-3391
RP1716-1
Final Report
April 1984

High-Voltage Stator Winding Development

Contractor: General Electric Company

A new, high-voltage stator winding configuration, when used in conjunction with superconducting rotors, may permit the direct connection of turbine generators to high-voltage transmission systems. By eliminating the need for step-up transformers, utilities could save \$10-\$14 million per 1000-MVA unit. 294 pp.

EPRI Project Manager: J. S. Edmonds

Cross-References:

1. EPRI EL-3391
2. RP1716-1
3. Rotating Electrical Machinery Program
4. Superconducting Generators

ELECTRIC POWER RESEARCH INSTITUTE
Post Office Box 10412, Palo Alto, CA 94303 415-855-2000

EPRI EL-3391

High-Voltage Stator Winding Development

EPRI EL-3391
RP1716-1
Final Report
April 1984

Contractor: General Electric Company

A new, high-voltage stator winding configuration, when used in conjunction with superconducting rotors, may permit the direct connection of turbine generators to high-voltage transmission systems. By eliminating the need for step-up transformers, utilities could save \$10-\$14 million per 1000-MVA unit. 294 pp.

EPRI Project Manager: J. S. Edmonds

Cross-References:

1. EPRI EL-3391
2. RP1716-1
3. Rotating Electrical Machinery Program
4. Superconducting Generators

ELECTRIC POWER RESEARCH INSTITUTE
Post Office Box 10412, Palo Alto, CA 94303 415-855-2000

RP1716-1

High-Voltage Stator Winding Development

EPRI EL-3391
RP1716-1
Final Report
April 1984

Contractor: General Electric Company

A new, high-voltage stator winding configuration, when used in conjunction with superconducting rotors, may permit the direct connection of turbine generator high-voltage transmission systems. By eliminating the need for step-up transformers, utilities could save \$10-\$14 million per 1000-MVA unit. 294 pp.

EPRI Project Manager: J. S. Edmonds

Cross-References:

1. EPRI EL-3391
2. RP1716-1
3. Rotating Electrical Machinery Program
4. Superconducting Generators

ELECTRIC POWER RESEARCH INSTITUTE
Post Office Box 10412, Palo Alto, CA 94303 415-855-2000

ROTATING ELECTRICAL MACHINERY PROGRAM

High-Voltage Stator Winding Development

RP1716-1

Final Report
April 1984

Contractor: General Electric Company

A new, high-voltage stator winding configuration, when used in conjunction with superconducting rotors, may permit the direct connection of turbine generators to high-voltage transmission systems. By eliminating the need for step-up transformers, utilities could save \$10-\$14 million per 1000-MVA unit. 294 pp.

EPRI Project Manager: J. S. Edmonds

Cross-References:

1. EPRI EL-3391
2. RP1716-1
3. Rotating Electrical Machinery Program
4. Superconducting Generators

SUPERCONDUCTING GENERATORS

High-Voltage Stator Winding Development

EPRI EL-3391
RP1716-1
Final Report
April 1984

Contractor: General Electric Company

A new, high-voltage stator winding configuration, when used in conjunction with superconducting rotors, may permit the direct connection of turbine generators to high-voltage transmission systems. By eliminating the need for step-up transformers, utilities could save \$10-\$14 million per 1000-MVA unit. 294 pp.

EPRI Project Manager: J. S. Edmonds

Cross-References:

1. EPRI EL-3391
2. RP1716-1
3. Rotating Electrical Machinery Program
4. Superconducting Generators

ELECTRIC POWER RESEARCH INSTITUTE
Post Office Box 10412, Palo Alto, CA 94303 415-855-2000

12-1-54

30

1

APPENDIX C

**M. Clark, et al., Changing Insulation Systems – Benefits and Problems
GE Canada, April 2000**

Changing Insulation Systems – Benefits and Problems

M. Clark, J. Dymond, J. Hayward, B. Moore
D. Snopek, N. Stranges, K. Younsi

GE Canada Inc.
Peterborough, ON
Canada

Abstract: In the last decade there have been numerous advances made in insulating tapes, resins, test methods and instrumentation. The impact of the application of the newer tapes and resins has produced step surges in insulation technology. The primary emphasis has been on the reduction of the total insulation in the machines to achieve higher output density, improved heat transfer, improved efficiency and performance. The enhancements in test methods and equipment have served to increase the predictive accuracy of pending failures and to improve the integrity of the insulation system. Methods designed to find failures are now used to predict weakness and improve the insulation processes. As the demands on insulation systems are increased, failure mechanisms that were infrequent are starting to become more common.

This paper will look at one manufacturer's vision of the future of insulation technology as it applies to the design of rotating equipment. It will also discuss the use of insulation evaluation techniques in insulation design, and will review insulation failure mechanisms and problems.

PART A: – THE FUTURE CHALLENGE

Introduction:

To look at the future and gain an appreciation of the increasingly rapid growth in insulation technology, it is good to first look backward to the past.

From the turn of the century to the 1950's and 60's, the standard groundwall insulation for much of rotating equipment was a combination of asphalt and mica flakes. Mica was an excellent dielectric, was fairly inexpensive and led to heavy insulation builds and low stress levels. Many will remember dissecting old asphalt / mica coils and finding large air voids in the insulating wall, even though the coil had not failed in service.

In the 1950's and 60's, the industry saw the advent of the synthetic resin systems, primarily epoxy and polyester. Resin rich B-staged tapes appeared and became the system of choice for pressed coils and bars. As well, the asphalt compound tank of a previous generation saw a rebirth with the autoclave epoxy systems. Mica flakes gave way to mica paper, and in low binder (dry) tapes saw heavy use in the vacuum pressure impregnation (VPI) systems. The pace of insulation development began a more rapid advance as the millennium appeared on the horizon.

Industry Changes:

In the 1980's, the utility industry was undergoing profound changes. The beginnings of deregulation in some countries, and the rapid expansion of many world economies, resulted in increased power demands. However, with the 1990's came the anomaly of ever increasing demand and flat selling prices. Manufacturers looked for ways to gain the advantage needed for sales, and technology was again pushed to the fore.

On the industrial side, motors were becoming increasingly larger and more complex. Failure of a large motor would have serious and immediate consequences for its owner.

Strangely, the need for technology advancement came at a time when the equipment manufacturer, utility and industrial customers had, in many instances, just completed a downsizing in their technology functions. Laboratories had been closed, technology expenditures were often scaled back, and the academic arena often became the site of new investigations and advancement, albeit often too theoretical for manufacturing applications.

To replace the lost inhouse insulation expertise, customers began using the *insulation consultant* – a freelance third party expert working on their behalf to maintain a predetermined quality level. Except in a few instances, particularly with the larger utilities, the days of the career insulation specialist appeared to be disappearing.

Voltage Levels:

With the emphasis on the use of contractors to plan and implement projects, the selection of equipment on lowest initial cost and the use of less experienced personnel, there is a tendency to ask for products at ratings that are not consistent with either good design, manufacturing practices or operating experience. One example is the specification of high voltage on low horsepower machines. This leads to oversized machines or less reliable equipment.

Today, it is not unexpected to see the specification of power system voltages to perhaps 35 kV for machines in order to eliminate transformers and breakers. Although some work has been done to produce air cooled machines at voltage ratings above 15 kV, it is not a simple matter. Choice of clearances,

bracing, cooling method, corona suppression, winding terminations and cabling, enclosures, cooling medium, slot grounding, grading, contamination, strand, turn, ground wall insulation, etc. will have a more significant impact than at the 15 kV level. Things that were minor problems at lower voltages will become major problems on the new machines. Designers and users will require a new mind set to be able to build and maintain reliable higher voltage machines. The advantages of the higher voltage machines are not going to come without careful analysis of all the factors, some of which many of the current generation of machine designers and insulation specialists are totally unaware.

Standards and Evaluation Techniques:

It is perhaps not surprising that the decline in dialog between manufacturer and customer due to mandated downsizing, resulted in the increased use and development of international standards. Customers increasingly began to rely on the use of standard practices in their specification requirements. Manufacturers, as well, increased their participation to protect against interpretation not intended by documentation.

A case in point is IEEE 1043-1996 [1]. The standard as written does not give defined minimum hours to failure. It was generally understood between knowledgeable manufacturers and customers, however, that historical data shows that for a 13.8 kV system, 400 hours at 30 kV (or 250 hours at 35 kV) defined acceptable limits. There are, however, increasing incidences where a "ratcheting up" of the historical limits has caused problems; the notion that if 250 hrs is good, then 500 hours is twice as good. This often resulted in manufacturers designing and producing a coil or bar set to pass a test, rather than designing for acceptable life. This issue is presently being addressed in a revision to IEEE 1043.

In the 1990's, a new standard IEEE 1310 1996 [2] was developed to determine the thermal cycling characteristics of generator insulation systems. It is generally considered to be a "type" test, and this is reasonable. It is now however, occasionally demanded as a quality assurance tool *on each contract unit* with the attendant increased cost for a several week evaluation. The situation sometimes begs the question "Who wins??"

As manufacturing and customers become more global in nature, the increased use of country specific and IEC standards are becoming more common.

A recent issue that must be addressed for those manufacturers selling into the European Community, is the issue of the CE Mark. This identification must be applied to all equipment, and requires backup documentation to ensure that equipment meets appropriate domestic standards. It is, in

many ways, similar to the UL mark familiar in North America.

Understand world standardization practices. Getting an order may depend on it.

The Future:

The expanding need for power on the utility side and larger motors to feed the expanding economy, came at a time when the generators and motors of the 1950's and 60's began to falter and needed either complete replacement or at least insulation renewal. The manufacturing world of Replace, Modernize and Upgrade was born. It is a fact that, as we enter the new millennium, *the Service sector of many manufacturers may outstrip the growth of new equipment sales.*

For equipment manufacturers, the rules have suddenly changed. No longer is it acceptable to quote six months delivery on a coil or bar rewind. With power demand high, any time out of service impacts heavily on the utility bottom line. Manufacturers are now finding that the supplier with the shortest delivery is the winner and subsuppliers of copper, insulated wire and composite insulation products now feel this delivery pressure as well.

New Insulation Systems:

As stated earlier, there were essentially two major systems developed for primary coil and bar insulation in the 1900's – the asphalt mica and the synthetic resin mica systems.

Although the synthetic resin mica system is still the standard today, the 1990's saw a new variation on this theme – the introduction of filled material technology. This variant saw its genesis in a patented process, US 4760296 [3] where it was revealed that certain fillers could increase the corona resistance of insulating materials. The benefits accrued were in proportion to the composition of the filler chosen, the percentage of the filler included in the material, the filler particle size and its dispersion. Products containing improved corona resistant and thermal properties are being used today.

It is suggested that this concept has set in motion a new wave in insulation development, with variations over the next decade that may radically change the generator or motor, as we know it today.

Benefits – Generators:

On the utility generation side, the use of filled technology has already allowed for reduced or compact builds. These thinner

Optimized Machine Redesign – Compact Insulation Systems								
<u>Machine</u>	<u>Volts</u>	<u>HP</u>	<u>%Reduction</u>	<u>%Wt Reduction</u>		<u>% Wt Reduction</u>		<u>% Wt Reduction</u>
<u>Induction</u>			<u>D²L</u>	<u>Cu</u>		<u>Steel</u>	<u>Cu</u>	<u>Insulation</u>
				<u>Stator</u>	<u>Rotor</u>	<u>Stator & Rotor</u>	<u>End Ring</u>	
4 Pole	4.0 kV	5000	20%	19%	20%	20%	5%	45%
10 Pole	6.6 kV	2000	22%	24%	35%	21%	28%	34%
18 Pole	4.0 kV	4000	34%	45%	49%	33%	NC	57%
26 Pole	4.0 kV	2000	40%	39%	37%	37%	64%	56%
4 Pole	13.2 kV	7500	14%	8%	18%	13%	22%	29%
20 Pole	13.2 kV	4000	15%	20%	15%	15%	25%	12%

Table 1

builds (Fig. 1) result in increased stress in the coil and bar insulation groundwall. Therefore, for a given slot geometry, reduced build can allow for more copper, translating into increased output in some cases. At least one manufacturer is already leveraging these concepts [4].

It is cautioned that this redesigned groundwall insulation brings with it other benefits and challenges. Reduced groundwall relates to a shorter thermal copper to core path, and can benefit machine cooling. However, without modification, grading systems may become overheated, due to the increased stress. As well the mechanical properties of the bar should be evaluated when compact builds are contemplated.

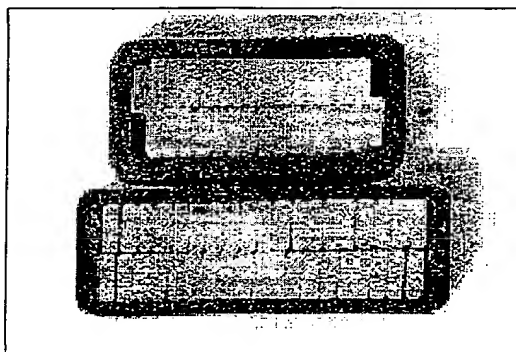


Fig. 1 – Standard and Compact Builds

Compact build is a design issue with new equipment, and early consultation between the parties can in fact result in a smaller generator for similar output. In the rewind market, an uprate may be possible where turbine capacity allows. It is recommended those utility customers and manufacturers, either OEM or service groups, discuss and understand the possible advantages of reduced build coil and bar insulation.

Benefits – Motors:

As shown above, the process of reduced build / higher stress insulation development typically began on the generation side of the business. It became apparent that the advantages of this program could migrate into the large motor arena with equally dramatic advantage [5].

To illustrate the effects of an arbitrary 30% reduction in groundwall thickness on the design of a large motor, a *theoretical* optimized design was performed. The results are shown as Table 1.

It is recognized that machine design optimization involves tradeoffs, and no insulation system is perfect, but the results of this screening suggest *some major benefits in machine size and weight can accrue with compact build technology*.

Manufacturer's development ingenuity will determine the winners and losers over the next decade.

PART B: THE ISSUES AND PROBLEMS OF TODAY

Machine Design:

Pole coil insulation:

Generally, very few field windings suffer failures due to high voltage stresses because the enameled or enameled with glass wire used in most field windings is subjected to very low voltage stress. The same holds true for strip wound field poles. The majority of pole windings see voltages less than 250 V on insulation that normally passes hi-pot levels over 3000 V. Field winding failures are related more to thermal, mechanical and chemical stresses or combinations of these three processes. Thermal aging causes delamination of the insulation leading to vibration of the turns and mechanical failure. Mechanical failure can also occur due to loose poles, loose pole collars and even loose coil brackets, as well as abrasion from air borne particles. Chemical failure comes from such things as process gases, oil contamination, moisture, and cleaning chemicals. The chemicals eat away the coatings, soften the epoxies, cause tubing of the enamels or combine with moisture and other chemicals to produce concentrated acids that attack the insulation. Strip wound fields can be shorted by contamination or conducting metals that are transported by the cooling medium. Materials and chemicals that are inert at room temperature become deadly enemies at the operating temperature of the winding.

With the move toward smaller machines, the rotor insulation system will be worked harder both thermally and mechanically. The challenge to the machine designer is to increase rotor ventilation and improve the mechanical properties of the insulation.

Bracing:

There is no bracing system that will work in all applications. The bracing requirements of a machine have to be evaluated based upon the duty cycle and starting characteristics of the machine, the copper section and arrangement in the coil, and the actual insulating materials and resins used in the insulation system. Not all resins and insulating materials will develop the same strength, flexibility and resilience when fully processed. The stress strain curve for each system will vary significantly with temperature, generally with a drastic reduction in the tensile strength and modulus of elasticity. Measurements made of several different systems (Fig 2) show the mechanical strength of the insulated coil dropping to about 25 % of the room temperature value when operating at 105° C, the normal operating point for a class B rise machine in a 25° C ambient.

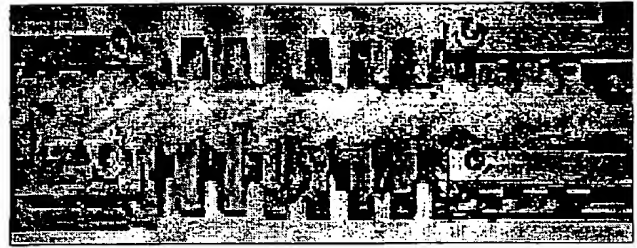


Fig. 2 – Bracing Test Assembly

Methods for calculating the forces that the insulation and its associated bracing and support rings must contain under various operating conditions go from the simple cantilever beam to the full end winding including all the instantaneous currents. Forensic analysis of end winding failures show that whenever the original insulation system is replaced by another system, the end winding bracing needs to be re-evaluated. This requirement to re-evaluate the bracing is especially true whenever a machine is up-rated or the speed changed.

Coils, Bars and Resin Impregnation:

Stator coils may be found on both generators and large motors. Coils require relatively little connection work during installation relative to bars. However, they tend to be more difficult to wind due to the fixed geometry of the coil span. When replacement of a coil is required both top and bottom legs need to be removed, making replacement of a coil with a damaged top leg more difficult than that of a damaged top bar.

Bars are primarily used on generators. They are suited to larger machines for their relatively lower weight as each leg can be handled and wound independently. For the same reason replacement of a failed top bar is considerably easier than it is in the case of coils where a span needs to be lifted.

Many machine stators utilize a global vacuum-pressure impregnation (VPI) method for epoxy penetration and cure. However, there are occasions when machines are constructed using preformed ("hard") coils, where the insulation is already fully cured and rigid prior to insertion in the stator slot. There are two principal reasons why this type of construction is used:

- The stator's design is such that it is too large for the existing VPI facilities.
- The customer specifies a hard coil stator construction.

If the size of the tank and oven facilities allow, the benefits of the VPI method of resin application are numerous. It is a proven method for effective insulation of stators, as there are well-known resin/tape combinations. The finished

system consists of a solid mass of resin and tape. This system is resistant to chemical attack and is rugged when handled. Manufacturing of the coils can be streamlined by use of lower cost tape and is less labour-intensive per coil. Winding of stators is facilitated by the use of green VPI coils because they are flexible and easier to install, even on large spans.

The VPI method does present some challenges, notably with the material handling, vacuum and baking equipment required to run the process. Very large stators may make the VPI method unfeasible, if the existing crane and tank capacities are limited. A new setup requires considerable capital investment and there is cost associated with maintenance of an existing facility. VPI facilities need dedicated staff to run them, require compliance with environmental regulations, and may present problems with disposal and rotation of old VPI resin. The process may be sensitive to taping variations arising early in the process. If vacuum tank control is not properly maintained, there exists an opportunity for formation of voids or dry pockets in the insulation, leading to increased PD activity in higher-voltage machines. Due to the very strong mechanical bond between resin and tape (the VPI resin, coils and stator form a solid mass), a complete stator rewind is required if repairs are needed at any time after the completion of the VPI process.

The principal benefit to using pre-formed coils in stator winding is that the facilities for complete immersion and subsequent baking of the stator are not required. There are fewer environmental issues associated with hard coil manufacture. For a given volume of insulation, there is a higher mica-to-resin ratio in a hard coil, resulting in an improved ability to handle voltage stress. Pressing of filled tapes around the entire profile of the coil results in fewer opportunities for voids and dry pockets to form. The resin content is known and pre-loaded into the tape before coil pressing. This improves the assurance of fresh tape and resin with each coil. Compression is excellent, resulting in a more compact coil. There is no "gluing" of the system, which allows for rewinds and repairs to take place at site, avoiding removal and transport of the stator. The stator can be split and shipped in sections, so there is no limit to its physical size. Armour-to-core contact is improved by the presence of semi-conductive centre and bottom-fillers, and various side packing methods.

The hard coil method is not without challenges. The winding process is labour-intensive, requiring more robust bracing and lashing. Due to the more expensive materials used in their construction, the coils may be costly to purchase. Large spans may present challenges to winders due to the rigidity of the coils – a considerable amount of stress is put on the coil loops when the span is lifted, which

could damage the insulation. The required side packing may need replacement before the end of motor life.

It can be seen that the two systems are not entirely interchangeable depending on convenience. There are circumstances when one system offers advantages over the other. The strength of the VPI system is in the construction of physically smaller stators, multiple (spare) stators for one machine, and tight stator bores. VPI machine maintenance is easier when the stators can easily be transported for reconditioning to a service shop or the original manufacturing facility. The non-VPI hard coil system is more suited to larger, single machines in remote locations or where removal and transfer is difficult (such as marine installations), and to machines with wide stator bores.

Variable Speed Drive Issues:

Variable speed drives (VSD) repeatedly subject a machine winding to electronic switching transients. These transients can have very fast rise-times, particularly in pulse width modulated (PWM) drives. With longer lengths of cable running between the drive and motor, voltage reflection problems may also arise. In the worst case, if no protective steps are taken, the transient voltage at the motor terminals can reach twice the line voltage. The results of a 1988 EPRI study [6] also suggest that the high frequency transient voltages tend to be unevenly distributed across the coils and turns of the winding. The effects of VSD can be mitigated by using thicker turn insulation. To compensate for the increased turn insulation thickness, the groundwall insulation thickness is reduced correspondingly. In this way, the total build from the copper to the slot is the same. Corona resistant materials will also provide a major improvement to insulation life in VSD applications.

Manufacturing:

VPI Monitoring:

The standard method of monitoring the VPI resin impregnation process is the use of sacrifice coils. This method has two important drawbacks, the first being that the sacrifice coils are not confined in the stator slot and are more freely exposed to the resin. They are also free to mechanically cycle with pressure changes increasing resin influx. The second drawback is that, due to the destructive nature of the test, the supply of sacrifice coils may become exhausted before they indicate the winding has been completely filled.

An improved method of fill monitoring involves the monitoring of slot-section capacitance. The stator is placed in the VPI tank so that it is electrically isolated from ground. All phases are tied together and $1 V_{RMS}$ is applied to

the winding during VPI. A bridge is used to measure the capacitance and DF of the slot section of the winding.

As the tank is filled the resin displaces the air in the winding, thereby raising the overall dielectric constant of the insulation. This change in dielectric constant is observed as a change in capacitance (Fig. 3). When the winding is unable to take any more resin the capacitance remains constant with time and pressure.

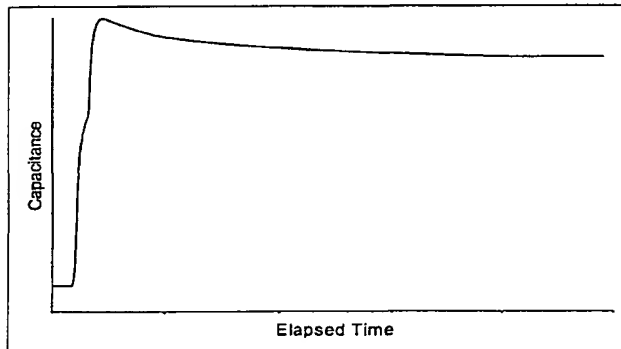


Fig. 3 – Capacitive Monitoring Trace

It is important to note that this method does not indicate the winding has been completely filled but that the winding has stopped taking in resin. For this reason sacrifice coils are often used in conjunction with capacitance monitoring. A second drawback of this system is that it uses the entire winding to give capacitance. A localized resin-poor area may not be a significant contributor to the global parameter being measured but may be significant from an electrical performance standpoint.

Quality Assurance: [7]

Dissipation Factor and Capacitance:

This test is performed on the wound stator after the VPI process. These tests provide information on the condition of the insulation, including degree of compaction, armour to core contact, and grading condition. The tests are performed on each phase with remaining phases grounded to ensure that no abnormalities (Cap & DF) exist among phases. Typically the data is collected at 10 % of rated voltage with subsequent data captured at 10 % increments up to 120 % of rated voltage. The tip-up is calculated from the difference between the DF at 20 % and 100% of line to neutral voltage.

A database correlating DF vs. voltage rating, machine geometry, type of insulation system etc., will assist in trending process quality.

Partial Discharge:

Utilizing PD instrumentation, partial discharge data is collected on the wound stator after the VPI process. Phases are tested together and independently to segregate the endwinding activity from the slot section of the machine. Data is collected at 100 % of line to neutral voltage and at 120 %. Again, a database will allow for better assessment of PD data when peculiar PD plots occur. The merits of Partial Discharge testing extend beyond the evaluation of the stator winding. Cable clearances, conduit box geometry and termination hardware are a few examples of scenarios where PD activity has been identified.

A machine's initial PD "fingerprint" can help identify sources of PD activity. As well, recent developments in UV viewing technology can complement PD instrumentation by more precisely locating sites of corona activity, often eliminating the need for "black hi-pots."

Hi-pot Testing:

There is a continuing debate on the merits of AC vs. DC hi-pot testing in searching insulation defects. Recently this debate has expanded to the use of very low frequency (0.1 Hz) voltage application.

After insertion of the stator coils, AC hi-pots are performed above rated voltage. Following connection, the test is repeated. Subsequent to impregnation and bake, a full rated hi-pot test (2E+1kV) is performed.

On VPI systems, it is strongly cautioned that repeated hi-pot testing of coils before impregnation (green state) can cause internal corona activity, weaken the groundwall structure and possibly compromise insulation life.

Surge Testing:

The turn testing of stator coils is performed during two different stages of the manufacturing process. The coils are first turn tested upon completion of coil manufacturing with the second test after the insertion of the coils into the stator. Surge testing establishes a confidence level that the turn insulation has not been compromised during the handling of the stator coil until it has reached its wedged position within the slot. Typical test equipment may include an inductive or pulse generator type with either having a known rise time of 0.1-0.2 μ s.

Cabling and Phase Leads Routing:

At any altitude and environment, particularly in a polluted one, air clearances and adequate spacing between coil / bar endarms is critical. Equally important is the routing and



Fig. 4 – Ozone Damaged Cable

clearances associated with cables and phase leads. In difficult to see and limited access locations around the stator winding and conduit box, insufficient air clearances can lead to premature cable insulation aging. This aging is caused by corona discharge and mechanical cycling due to electromagnetic forces. Ozone generated by this corona discharge activity is also known to prematurely age and make the insulation surface on PE, XLPE and various rubber insulated cables become brittle (Fig. 4). This ozone problem is particularly encountered in confined spaces, complex cable/lead arrangements and long routings through the frame.

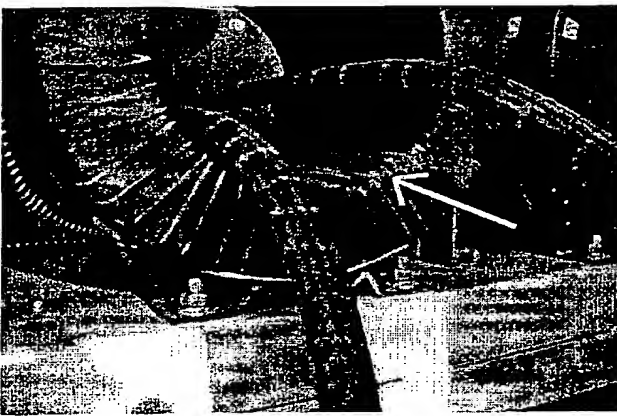


Fig. 5 – Inadequate Cable Clearances

Fig. 5 shows a conduit box on a 11,000 HP, 13.2 kV synchronous compressor motor. The cables were too long and routed with no air clearance to ground (note corona on CT). Corona activity between the cables and

ground caused a catastrophic in service failure on this unit.

In order to prevent this type of insulation damage and premature aging of the machine winding, it is necessary to use clearance gauges to ensure adequate air gaps between highly stressed parts. Gauge size should take into account voltage rating and altitude of machine installation site.

Spray and Submersion Tests:

Modern epoxies for global VPI applications provide rigid insulation systems. However, high rigidity also makes the endwinding areas prone to cracking, particularly during fast cool down steps after baking. Cracking can also develop in service during severe thermal cycling (major load swings, reversals, etc.) As well, inadequate restraining of endwindings can cause mechanical stresses capable of cracking the groundwall insulation at slot exit locations, or in the endarm regions.

A spray or submersion test is designed to check the integrity of totally sealed global VPI processed insulation systems, per NEMA MG1-20.49. This test is also referred to as Wet or Water test. The finished wound stator, after VPI treatments and baking, is sprayed or submerged in a moderately conductive solution of water and surfactant. The surfactant agent, by its low surface tension, wets the entire stator insulation surface. This increases the searching capability for cracks and weak spots. After spray or submersion, the wound stator must pass a successful meggar test, followed by a hi-pot. Failure of the meggar test means drying, repair and retest of the winding. Wet test failures occur at endarms caused by forced blocking of coils, at the lead to circuit ring connections (taps), at cable to circuit ring splices or on a damaged lead cable insulation.

To reduce the number of these failures, thermal shocks should be avoided after bake. The wound stator is cooled down from the cure temperature, typically 160° C to ambient, in no less than 12 hours. Cables should be carefully routed with no sharp bending radius during bake. Taps to circuit rings and cable splices use special resin soaked felts and silicone putties to fill the V shaped gaps between connected conductors. Adequate taping materials and methods are used to obtain a high insulation level and a fully sealed system.

Field Issues, Maintenance and Repair:

Because of maintenance budget limitations, for rotating machinery users, it is of paramount importance for users to prioritize their repair or replacement program. Machines are generally considered on a case by case basis. Although some utilities have developed their own engineering base over the years, decision making is quite often a difficult one on highly critical and strategic machines.

A wide spectrum of test standards and recommendations (IEEE and IEC) are known and used in the field. The vast majority of these tests are performed offline. The most widely accepted online high voltage test is Partial Discharge (PD) testing, which is rapidly gaining popularity among industrial users and utilities.

Contamination and Tracking:

Description of the Tracking Phenomenon Due to Contamination:

Electrical insulation tracking is described in detail by Mathes and McGowan [8]. Tracking is a surface failure phenomenon that occurs when contaminants collect on the surface of an insulating material. A moisture film on the polluted surface will conduct a leakage current and generate heat. Dry bands will form, resulting in regions of very high resistivity between the edges of the remaining wet film. Nearly the entire surface voltage will appear across this dry band, causing flashover of the gap. The temperature of the arc is sufficient to decompose and carbonize the material locally. Dry banding, arcing and the formation of conductive carbon will proceed in a relatively random manner somewhat like the branches of a tree. The arc will then tend to prefer previously carbonized spots. Eventually a continuous conducting path forms between the live parts and a flashover occurs. Fig. 6 shows an example of a phase to ground fault caused by surface tracking.

Typical Case Studies:

Instances of failures due to surface tracking are illustrated by the following case histories. A weather-protected machine, with a high voltage (13.8 kV) winding, suffered a failure in the circuit ring connections while starting during a thunderstorm. When the winding was returned for inspection and testing, it was so contaminated with a conducting material that the leakage current protection on the hi-pot set would trip at less than 4 kV. Once steam cleaned and baked, the winding withstood hi-pot levels up to 40 kV. Examination of the winding after removal from the stator core showed that extensive surface discharge had been taking place.

A finite element analysis of the circuit ring section showed that the uneven distribution of the contaminant over the surface of the circuit rings and the connection bundle increased the maximum electrical stress in the insulation [9]. Modifications to the enclosure to reduce the possibility of the conducting contaminant entering the machine, combined with more frequent contamination removal, appear to have solved the problem on this unit.

In another instance, a call from a North American consultant revealed that units that he had purchased from an unspecified supplier were failing. He asked if it would be possible to discuss mechanisms that would help him determine the cause of the failures. His units were vertical weather protected machines operating under 7 kV on a peninsula in the Philippines. The units were downwind, in an area of high sea water spray and high humidity and rain. The windings were covered with salt and failing. It was felt that the salt contamination was shorting out the grading and ground tapes causing tracking and failure.

Approximately 5 years after the first high voltage winding failure discussed previously, we were notified of a failure on a second unit. Unfortunately, the unit had been sent out and rewound before we were notified. The failure on this unit was again in the circuit ring connection area. The unit was not in a highly contaminated area but the machine had been in the same service shop within the previous year for the replacement of some cables that had been damaged.



Fig. 6 – End Bracing Surface Tracking

Investigation of the cable repair indicated that after the cables had been replaced, the endwinding had been dipped in a commercially available insulating varnish and baked. A series of tracking tests were initiated to determine if the anti-tracking characteristics of the insulation system could be affected by the varnish. Inclined plane tests were made in accordance to ASTM D2303 [10]. A polyester laminate substrate was first covered with the base resin and baked. Alternate materials were then applied on top of the resin layer. The findings for the insulating varnish were so poor that the program was expanded to look at all the different coatings that might be used on the insulation and on other systems that might be used in the future. Various combinations of materials were investigated. The track resistance of the standard resin was least affected when it was covered by epoxy paint, a polyurethane coating or an

anti-abrasive coating. The test samples became extremely vulnerable to tracking when the resin was covered with commercial filling compounds, varnish, or combinations of epoxy paint and filler or varnish. This work is described in detail by Dymond et al. [11].

The best way to avoid surface tracking in machines operating in a contaminated atmosphere is to keep the contaminated cooling air out of the machine. This requires the use of a totally enclosed machine with a heat exchanger or a purged air system. When this is not possible, the designer must have a thorough understanding of how the insulation system will perform in this contaminated environment.

Summary:

As we start the new millennium, the insulation engineer is facing many new challenges. The pace of new development has quickened. New materials, and variations of long used materials are appearing. The long established relationships between manufacturer and customer have changed. New international standards now complement domestic ones, and the manufacturers, as well as some customers, are global in their manufacturing and sourcing practices.

It is perhaps then strangely ironic that with the rapidly changing manufacturing environment, many of the same insulation problems that have plagued us for years remain. Improved material properties are being leveraged as never before, and dedication to processing detail is now more important than ever. Only through attention to manufacturing quality using appropriate testing procedures and after-market inspections, can long machine life be assured.

Authors:

Authors Clark, Dymond, and Stranges are employees of GE Motors. Authors Hayward, Moore, Snopek and Younsi are employees of GE Hydro. All are located at Peterborough, ON, Canada.

References:

[1] IEEE 1043 - (1996), Recommended Practice for Voltage Endurance Testing of Form-Wound Bars and Coils

[2] IEEE 1310 - (1996), Recommended Practice for Thermal Cycle Testing of Form-Wound Stator Bars and Coils for Large Generators.

[3] Johnston, D. R., Markovitz, M., US Patent 4760296, "Corona-Resistant Insulation, Electrical Conductors Covered Therewith and Dynamoelectric Machines and Transformers Incorporating Components of Such Insulated Conductors," - July 1988

[4] Draper, R. E., Moore, B.J., "Development of a Vertical Generator Bar Insulation System for Operation at Increased Stress" - EIC/EMCW Expo97 Sept. 1997, Chicago

[5] Moore, B.J., Rehder, R. H., Draper, R.E., - "Utilizing Reduced Build Concepts in the Development of Insulation Systems for Large Motors"- EIC/EMCW Expo99, Oct 1999, Cincinnati

[6] "Turn Insulation Capability of Large AC Motors", EPRI Report EL-5862, Vol 1, Project 2307-1, July 1988

[7] Draper, R.E., Rehder, R.H., Moore, B.J., "Insulation System Evaluation for Rotating Machinery", - IEEE Insulation Magazine, July/Aug 1995, Vol 11 No 4

[8] Mathes, K.N., McGowan, E.J., "Electrical Insulation Tracking - A Design-Engineering Problem", Electro-Technology, April 1962, pp. 146-151.

[9] Weeber, K., Stutt, M., Dymond, J., Rehder, R., "Finite Element Field Analysis Of Nonuniform Surface Contaminations On High Voltage Windings Of Electric Machines", Proceedings of Conference on Electrical Insulation and Dielectric Phenomena, October 20-23, 1996, Millbrae, California, USA.

[10] ASTM D2303 - "Standard Test Methods for Liquid - Contaminant, Inclined-Plane Tracking and Erosion of Insulating Materials", September 1990, pp. 503-512.

[11] Dymond, J., Stranges, N., Younsi, K., "Stator Winding Failures: Contamination, Surface Discharge, Tracking", Paper No. PCIC-99-32, Technical Proceedings of the Petroleum and Chemical Industry Conference, held Sept 1999, San Diego.

APPENDIX D

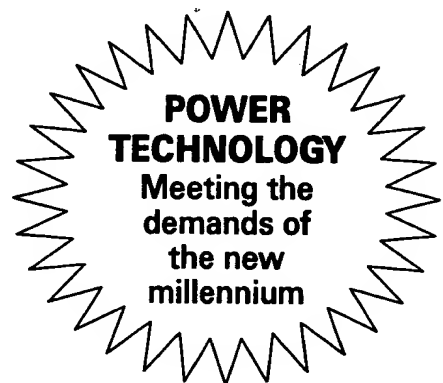
Table of Contents – Proceedings of INSUCON/ISOTEC '98

PROCEEDINGS OF

INSUCON/ISOTEC '98

**The 8th BEAMA
International Electrical Insulation
Conference and Exhibition**

Harrogate International Centre • 12 – 14 May 1998



CONTENTS

ISOTEC '98

TUESDAY 12 MAY

SURVEY PAPER		PAGE NO.
08.45	Survey of insulation technology for winding of rotating electrical machines (electric motors) based on form wound coils. J Langer – Siemens AG, Germany	1
 DETAIL PAPERS		
	DESIGN & PROCESS	
09.15	Evaluation of impregnating resins for large high voltage rotating electrical machines. J A Nurse – GEC ALSTHOM – Electrical Machines, UK	10
09.35	Modern manufacturing processes of multi-turn coils for high voltage motors. A Genhart – ABB Industrie AG, Switzerland	21
09.55	VPI Technology Plants for Rotating Machines – State of the art and its future. E W Boesch – Micafil AG, Switzerland	34
	INSULATING MATERIALS AND INSULATED CONDUCTORS	
11.10	Resin rich technology today and trends J E Neal – Jones Stroud Insulations, UK	44
11.30	VPI Technology and trends. H Brandes – Von Roll Isola, Switzerland	56
 SURVEY PAPER		
13.45	Survey of insulation technology for stator winding bars of rotating electrical machines (generators). R H Schuler – ABB Industrie, AG, Switzerland	61
 DETAIL PAPERS		
14.15	Advanced technology of stator coil insulation system for turbo-generator M Tari; N Iwata; H Hatano; H Matsumoto, Y Inoue; T Yoshimitsu Toshiba Corporation, Japan	78
14.35	New manufacturing process of indirect cooled stator winding bars for VPI post impregnation technology. N Didzun; F Stobbe – Siemens AG, Germany	87
14.55	Highly stressed generator insulations. K Scherer; F Müller – ELIN, Austria	96
	INSULATION MATERIALS AND INSULATED CONDUCTORS	
16.10	Advances in mica paper in mica tapes for high voltage generators using global impregnation. E Barrutia; N Mortier – Cogebi, Belgium	105
16.30	Mica tapes for high voltage generators; state of the art and newest trends. B Hafner – Isovolta Österreichische Isolierstoffwerke AG, Austria	114
17.10	Summary. R Schwander – Beltec Isola, Switzerland	

CONTENTS

INSUCON '98

WEDNESDAY 13 MAY

PAGE NO.

08.30-08.45	CONFERENCE OPENING AND INTRODUCTION Roger Trotman – Chairman, Electrical Insulation Association	
SESSION 1 08.45-10.15	TRANSFORMERS Session Chairman J Fyvie, Peebles Electric Ltd, UK	
	Design for cost and reliability.	125
	D Allan – GEC ALSTHOM Transformers, UK – <i>Keynote Speaker</i>	
	Polyethyle Naphthalate (PEN) Film – a rapidly developing material for electrical insulation applications.	132
	J M Mace – Dupont Polyester Films, UK	
	On-line monitoring of oil in power transformers.	140
	A J McGrail; B Pahlavanpour, A Wilson – National Grid Company, UK	
	Long-term performance of transformer insulation.	147
	A Wilson; P N Jarman – National Grid Company, UK	
SESSION 2 10.45-12.15	MATERIALS 1 Session Chairman A Whitman, Jones Stroud Insulations, UK	
	New technologies and environmental aspects.	161
	P Boss – ABB Sécheron SA, Switzerland – <i>Keynote Speaker</i>	
	New prepeg systems for reducing the production times and costs for generator bars.	168
	W Uher – August Krempel Soehne GmbH + Co. Germany	
	Stress control on stator endwindings.	175
	A E Baker; A M Gully; J C G Wheeler – GEC ALSTHOM ERC, UK	
	Evaluation of Polyethylene Naphthalate (PEN) film acting as the reinforcement for mica based insulation to insulate high voltage rotating machines.	182
	S Taylor – Jones Stroud Insulations, UK	
	Coil end corona protection studies.	194
	R Brammer, K Bengtsson, D Rudolfsson – ABB Generation; H Å Eriksson, G Andersson, J Seppas – ABB Industrial Systems; M Lindgren – ABB Corporate Research, Sweden	
SESSION 3 13.30-15.00	PARTIAL DISCHARGE Session Chairman A Wilson, National Grid Company, UK	
	The present state of in-service partial discharge testing of rotating machine stator windings.	203
	G C Stone – Iris Power Engineering, Canada – <i>Keynote Speaker</i>	
	Experience with partial discharge measurements for the evaluation of high voltage winding insulation of large and medium-sized motors.	210
	K Bauer; A Bethge; M Kaufhold; H Wang – Siemens AG, Germany	
	Condition monitoring of electrical rotating plant.	217
	J W R Smith; A J Brown – BAeSEMA Ltd, UK	
	Performance of motor windings subjected to pulse shaped voltage stress.	221
	S Lanz; T Füglistner; J Ruhe – ABB Industrie, AG, Switzerland	

CONTENTS

	PAGE NO.
SESSION 4	
15.30-17.00	
MACHINE LIFE	
Session Chairman J Langer – Siemens AG, Germany	
'The next generation' – a review of the factors influencing the output of electrical machines in the new millennium.	231
C N Glew – GEC ALSTHOM Large Machines, UK – <i>Keynote Speaker</i>	
A novel parameter for the prediction of deterioration in generator stator insulation.	243
J B Kim; D H Hwang; J W Jeon; Y J Kim – Korea Electrotechnology Research Institute, Korea	
Development of advanced techniques for life assessment of generators based on ageing tests in laboratory and diagnostic tests on field.	250
A Kortajarena; L Martinez – Labein; J Hernandez; E Sierra – Iberdrola, Spain	
High voltage motor winding insulation for high power adjustable speed drives fed by IGBT converter.	257
K Bauer; M Kaufhold; H Wang – Siemens AG, Germany	
Condition monitoring – effect of winding design and calibration.	264
J W R Smith – BAeSEMA Ltd, UK	

CONTENTS

INSUCON '98

THURSDAY 14 MAY

	PAGE NO.
08.30-08.45 INTRODUCTION Roger Trotman – Chairman, Electrical Insulation Association	
 SESSION 5A MEASUREMENT SYSTEMS	
08.45-10.15 Session Chairman G C Stone – Iris Power Engineering Inc. Canada	
Expert systems enable continuous in-service diagnostics of installed high voltage plant.	271
J Petrou; D J Kopaczynski; M F Lachman – Doble Engineering Company, USA – <i>Keynote Speaker</i>	
Partial discharge measurements on transformers: Fingerprints analysis.	278
J. Poittevin; D Uhde – GEC ALSTHOM T & D; N Foulon; J-P Lucas; G Barré – Alcatel Alsthom Recherche, France	
Experience of on-line versus off-line partial discharge testing on a hydro-generator.	291
H Zhu; V Green – Adwel International Ltd, Canada; D Huynh – Pacificorp, USA	
Test methods for direct current series wound armatures. D E Schump – Baker Instrument Company, USA	297
Operational experience of non-intrusive partial discharge measurements on high voltage switchgear. P M Brown – EA Technology Ltd, UK	304
 SESSION 5B (PARALLEL WITH 5A) – CABLES	
Session Chairman R McKinlay – EA Technology, UK	
Laser ablation studies on polymeric cable sheaths. S J Sutton – National Grid Company, UK	313
The analysis of cross linked polythene cable insulations using FTIR spectroscopy.	321
J A Bevis – Pirelli Cables Ltd, UK	
Multifactor dry ageing of cable grade XLPE. C L Griffiths; J Freestone; R N Hampton – BICC Cables Ltd, UK	328
Oil leaks – detection and remediation techniques. D Patel – National Grid Company, UK	335
Evaluation of a method for the determination of emissions during curing of impregnating resins. G Baumgarten – BASF Coating AG, Germany	342
 SESSION 6A RESINS	
10.45-12.15 Session Chairman H S McNaughton – Consultant, UK	
Lifetime reductions in epoxy resin systems. J M Cooper – National Grid Company, UK	351
A new resin system for impregnating electrical windings with low emissions during application and curing. G Hegemann – Beck Elektroisoliersysteme, Germany	359
Quantitative determination of tape resin blends. A J I Cox; D R Walton – Jones Stroud Insulations, UK	367
Thermal simulation of epoxy resin during cure. L S Pritchard; H M Ryan – University of Sunderland; J S Graham – Roll-Royce: The Bushing Company, UK	374

CONTENTS

	PAGE NO.
SESSION 6A RESINS (Continued)	
Qualification of the enhancement obtained by re-vacuum pressure impregnating machine windings. R Scollay – Calidus Von Roll Isola; M M Botha – L H Marthinusen, South Africa	380
SESSION 6B (PARALLEL WITH 6A) – POWER CAPACITORS	
Session Chairman M Smart – ABB Power T&D, UK	
High energy density capacitor development. J Connolly; M Dunn – ABB Power T&D Ltd, UK	387
Endurance of impregnated metallised power capacity systems. D S Warschawsky – Elkon Company, Kazakhstan	394
Reliability of film-based capacitors for power electronics. J P Ballard; A M Gully – GEC ALSTHOM ERC, UK	397
An improved all-synthetic dielectric arrangement for HV carrier communication equipment. R Manjunath; T P Govindon – Crompton Greaves Ltd; T S Ramu – IISc, India	405
Forecasting endurance capacitors insulation systems with influence of multi-avalanche discharges. D S Warschawsky – Elkon Company, Kazakhstan	412
SESSION 7 13.30-15.00	
TRANSFORMER FLUIDS	
Session Chairman J Poittevin – GEC ALSTHOM, France	
Ester-based insulating liquids and monitoring their behaviour in a traction transformer. P Boss – ABB Sécheron SA, Switzerland; W D Phillips – FMC Corporation (UK) Ltd	419
Assessment of transformer life from paper – oil analysis – Indian experience. P G Agashe; T S R Murthy; U Yugandhar-Bharat Heavy Electricals Ltd, India	427
Testing of high temperature insulation systems for liquid immersed transformers. R L Provost – E I DuPont de Nemours; R J Whearty – Power Engineering Consultant, USA; J C Duart – DuPont de Nemours, International SA, Switzerland	433
Dissolved gas analysis in insulating oils by controlled headspace sampling coupled with capillary gas chromatography. R Gilbert; J Jalbert – Institut de Recherche d'Hydro-Quebec, Canada	444
SESSION 8 15.30-17.00	
MATERIALS 2	
Session Chairman J C G Wheeler – GEC ALSTHOM ERC, UK	
New Trends in high performance polyimide films insulation. R G Schmidt – DuPont de Nemours, Germany	455
A comparison of the impregnation properties of PETP film backed and glass backed mica paper tapes for global impregnation applications. J A Nurse – GEC ALSTHOM Electrical Machines Ltd, UK	467
Characterisation of polymeric insulators. H M Young; A Haddad; A R Rowlands; R T Waters – School of Engineering, University of Wales, UK	472
Dinorwig Power Station generator motor 18 kv stator insulation. I Cook – First Hydro Company, UK	479
Construction and Application of MICA tapes. Their importance in VPI Insulation Technology for rotating machines. R Brüttsch; J Allison – Von Roll Isola, Switzerland	487

10

APPENDIX E

Rabinowitz, M., “Power Systems of the Future (Part 4)”, IEEE Power Engineering Review, August 2000, Vol. 20, No. 8, pp 4-

IEEE power engineering **REVIEW**

AUGUST 2000

VOLUME 20

NUMBER 8

(ISSN 0272-1724)

Construction, Operation, and Live-Line Maintenance

621.42
In7

GLOBAL

AC
2000

6-13 October, Montréal



1000

Mario Rabinowitz

Power Systems of the Future (Part 4)

The assets and working philosophy of individual electric utilities will, in large measure, be reflected by the modernization of their power systems during the next 20 years. Part 1 of this article appeared in the January 2000 issue of *IEEE Power Engineering Review* and featured transmission and distribution, comparing overhead and underground delivery, pros and cons of underground delivery, superconducting transmission, and cryoresistive delivery. It also included a table of contents for the complete article. Part 2 appeared in the March 2000 issue and featured FACTS, electrical insulation, distribution cables, and transformers. Part 3 appeared in the May 2000 issue and looked at the potential for fault current limiters, lightning and restoration preparedness, compressed-gas insulated (CGI) transmission, and advanced delivery technologies.

This part, which concludes the article, addresses dc transmission, dispersed generation, distributed automation, use of computer information technology, and other factors worthy of continued consideration in the twenty-first century.

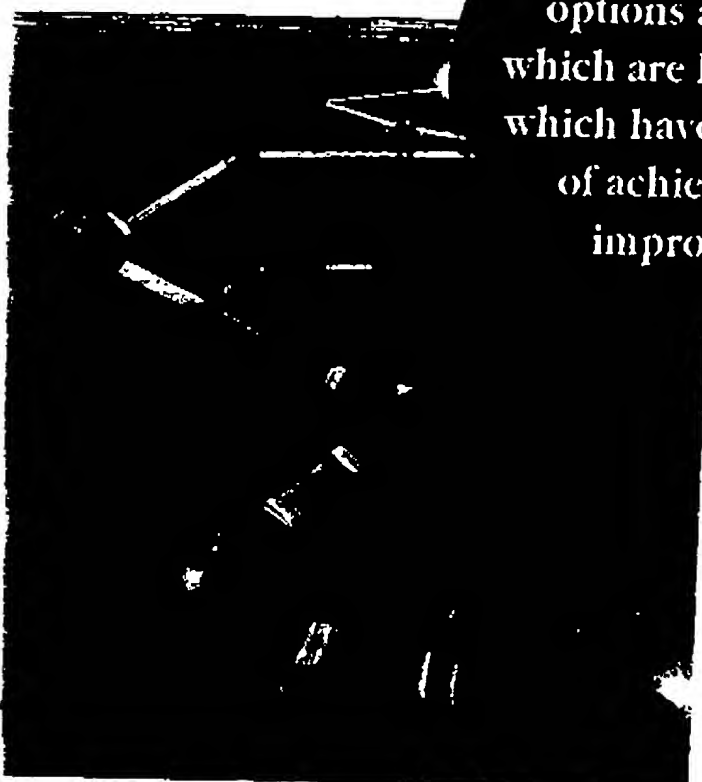
Direct Current, Grid Stability, and Superconducting Generators

For long distance transmission, dc is significantly less costly than ac. Direct current also serves an important function in tying together two large ac systems, even for short distances, thus circumventing problems related to synchronization. However, for ordinary transmission, dc is limited to long lengths because of the high cost of rectification and inversion at the two ends of the line involving high power diodes, transformers, and filters. Substantial filtering is typically required, at significant expense, to remove the ripple at the dc output. Substantial filtering is also required on the primary side of the transformer to prevent surge and harmonics from getting back to the generator.

An increase in frequency reduces the degree of ripple and of filtering required. Mere substitution of a conventional low-voltage generator that provides high frequency is unsatisfactory, since this would increase the transformer impedance and losses (especially core losses) and decrease the power transmitted. Furthermore, it is impractical to try to generate at substantially higher voltages with a conventional generator. This is because the flux density is limited by iron saturation, and the armature turns must be insulated from the grounded iron, thereby limiting the ampere-turns density and the voltage.

The amplitude of the ripple is decreased approximately inversely as the square of the number of phases. Similarly, the filtering requirement is reduced as the frequency is increased. In a conventional system utilizing a high-voltage transformer, as the number of phases are increased, the cost increases proportionately, which is substantial. Development of a high-voltage superconducting generator will entirely eliminate the transformer. This permits increases both in frequency and in the number of phases without a concurrent cost penalty, which means that less reactance will be needed in both the input and output sides of the diodes. An increase in the frequency by a factor of three can reduce the reactor requirement by a factor of three. An increase in the number of phases by a factor of two reduces the reactor requirement by a factor of four.

The per-unit synchronous reactance of a superconducting generator is about 1/4 that of a conventional generator of simi-



What power delivery options are available, which are less likely, and which have the potential of achieving major improvements?

This is the last part of a multipart article by Mario Rabinowitz: part 1 appeared in the January 2000 issue, part 2 appeared in the March 2000 issue, and part 3 appeared in the May 2000 issue of IEEE Power Engineering Review. M. Rabinowitz is with Armor Research.

lar rating. This results in an increased steady-state stability limit of the superconducting machine by as much as a factor of four when the transmission line reactance is relatively small. Superconducting power generation and superconducting magnetic energy storage (SMES) were covered in-depth in the May 2000 issue of *IEEE Power Engineering Review*, so only a little additional material is covered in this article.

Energy Storage, Voltage Sags, and Grid Stability

The increasing scarcity of the earth's primary energy resources has steadily raised their cost and, in turn, the cost of electricity production. This has led to increased interest in load-leveling energy storage systems. The procedure would be to store excess energy that is generated during off-peak periods when the load is low and later to deliver it during peak load periods. There are many energy storage methodologies such as pumped-hydro, compressed air, flywheel, thermal, magnetic, and electro-chemical storage, such as batteries and fuel cells. The interest in SMES is not only because SMES is expected to have a higher round-trip efficiency than any other large-scale storage technology but also because it can be used to help stabilize the power grid by quickly adding or removing power.

The use-capacity of an ac line may be increased by rapid regulation of a SMES unit [11]. The ac line use-capacity primarily depends on three factors: transient stability limit, voltage collapse, and electro-mechanical oscillations resulting from subsynchronous resonance of the turbine shaft and the transmission network. Of these, SMES is expected to most easily ameliorate the electro-mechanical oscillations resulting from subsynchronous resonance of the turbine shaft and the transmission network by damping the oscillations. Smaller SMES coils are contemplated, where their primary use would be in maintaining power system stability [12].

There is even a power-quality niche for what may be called microSMES (MSMES), despite the fact that it is very inefficient and very costly. The commercial viability of this technology is readily apparent in the semiconductor industry, where voltage sags of two or three cycles can ruin several single silicon crystal ingots, each worth \$15,000. Such power dips costing between \$50,000 and \$100,00 imply that the cost of a MSMES can be recovered in about 3 years. However, they would prefer to pay the utility a lot more per kWhr than normal cost, because, in the silicon wafer fabrication industry, equipment and buildings become obsolete in less than 10 years. Advocates estimate that MSMES could save U.S. industry \$12 billion per year.

More research needs to be done for better HTS in wire form before they are adequate for SMES. However, it may be possible to circumvent this problem by using HTS in a wide variety of aggregate forms such as granules, particulates, foil, and thin film in which the magnetic energy is stored in trapped form to be released as electrical energy by magnetically coupling to a normal coil as the trapped field is caused to decay [14, 15]. This trapped-field energy storage (TES) has the advantages of elevated temperature operation, so that a HTS wire coil need not be made, and the elimination of losses in leads. However, much research needs to be done to make TES a practical reality.

Power System Planning and Operations

In the future, electric utilities will find themselves in an increasingly competitive environment that will push the power system to the limits of its operability. Conflicting requirements of operating the system closer to its thermal and stability limits, re-

sponding quickly to wholesale energy transactions, and yet maintaining system security and integrity will demand well-coordinated power system planning, dispatching, and operations. As the quantity of wheeled power increases together with the rate of wheeling transactions, the system vulnerability will also increase. There is much ongoing work to develop methods, procedures, guidelines, and software products to deal with these contingencies in the operation and control of the grid.

If these programs are successful in achieving at least a modest 5% savings in power production, the overall nationwide impact is significant. With a roughly \$50 billion/year fuel cost, the potential savings amounts to \$2.5 billion/year. Goals of this work are to enable planners and dispatchers of the future to determine:

- Safe transfer limits across critical interfaces so as not to exceed stability and thermal limits
- How much margin is available on generation and delivery systems
- How best to control the delivery system
- How best to respond both judiciously and expeditiously to constantly changing transaction opportunities
- How best to predict, implement, and supervise over transaction decisions.

Biological Effects of Electromagnetic Fields

The issue of adverse biological effects of electromagnetic fields (EMF) will crucially affect power delivery of the future. At this point, it is not clear whether or not there is strong evidence for adverse effects. There are clearly some beneficial effects and a number of effects that are neither beneficial nor adverse. Electric utilities cannot afford to be complacent on this issue.

Biological systems respond to unbelievably low electric and magnetic fields. Freshwater catfish respond to electric fields as low as 10^{-6} V/cm. Marine sharks and rays are sensitive to less than 5×10^{-9} V/cm and use this sensitivity to navigate using the voltage gradients induced by ocean currents flowing in the earth's magnetic field. Magnetite was discovered in the human brain in 1992. Strands of magnetite function like compass needles to help one-celled bacteria navigate. Magnetite has been found in homing pigeons, salmon, dolphins, tuna, bats, and honeybees, and it may be part of their navigational systems.

The application of magnetic fields to broken bones has clearly been shown to speed up the mending of bones. Siskin et al. have studied the basic problems encountered in nerve injury and regeneration [16]. They find that electric and electromagnetic fields may help the healing process. They have demonstrated that pulsed electromagnetic fields accelerate nerve regeneration in the injured sciatic nerve of rats and that this has broad implications for the clinical use of these fields in the management of nerve injuries [17].

On the other hand, in 1991 Adair wrote a paper to show that normally encountered 60 Hz electromagnetic fields have no significant biological effect at the cell level [18]. More recently, Bennett came to the same conclusion [19]. These are very well-written papers that make a strong case that the electric and magnetic fields from power lines are well below the levels of natural exposure. Aside from a few inconsequential errors, their physics, calculations, and numbers appear reasonable. However, they consider only single cell response. They do not adequately address the point that an organized system of living cells is sensitive to and can respond to a much smaller signal than that of a single cell. This is analogous to digital processing in finding a signal in a situation in which there is a large noise-to-signal ratio. While

100

the work of Weaver and Astumian [20] is referenced, they do not seem to adequately respond to the point that living cells can and do react to field levels well below the thermal noise limit.

Biological molecules made of long chains of amino acids fold themselves up properly in an instant. Their dynamics can be as short as a femtosecond (10^{-15} s). Bennett focuses only on the breakup of a biological molecule, while neglecting the effects of interference with the folding process. Thus, he thinks that only much larger fields can be significant biologically.

Scientists at Sandia National Labs and the University of New Mexico claim to have observed unambiguous and reproducible nonthermal deleterious effects of pulsed magnetic fields on developing quail embryos. The exposed group had 10 times the abnormalities compared to a control group. They used larger fields than usually encountered to enable them to produce clear-cut, easily observable effects where the effect is not lost in the noise. Bennett and Adair did not cover these experiments.

Most recently, Blackman et al. claim to have unequivocally and reproducibly demonstrated that nerve growth can be inhibited by exposure to power line levels of magnetic fields as a function of either magnetic flux density or frequency [21]. These tests were *in vitro* rather than *in vivo*. Although nerve repair has been verified *in vivo*, it remains to be shown whether nerve growth inhibition can be demonstrated in living animals. Reproduction of these experiments has not yet been reported in other laboratories. If reproducible, their results should be judged independently of their "ion parametric resonance model," which is used to guide their research and to explain their results.

Straightforward ways can be implemented to minimize EMF concerns with respect to transmission lines, distribution lines, and substations. Increasing the number of phases decreases the electromagnetic field. Generally balanced three-phase underground cable has a smaller EMF than balanced three-phase overhead lines. This is simply because the solid insulation has higher dielectric strength than air, permitting closer spacing of the three phases and a faster fall-off of the fields from the lines. Unbalanced lines and ground loops for single-phase circuits produce large electromagnetic fields. Epidemiological studies indicate that, if there is a causal connection between EMF and adverse biological effects, it is very tenuous. Thus one may be optimistic that we can find reasonable corrections if we do find causal connections.

Dispersed Generation

Traditionally, both in generation and in transmission, electric utilities have pursued economies of scale with large power plants in increasing efficiency and in reducing capital and operating costs. However, both natural and artificial constraints limit such expansion. As discussed earlier, transmission line capacity is limited by a practical line voltage of 1,200 kV. Temperature and pressure limits are being approached in turbine and boiler design. Sometimes the reason for the limit is clear, but often the limit constraint is quite subtle.

When these limits are reached, new technological breakthroughs, such as the superconducting generator, can result in new greater limits or in new ways of doing business. This may be as simple as a new way of generating electricity; or, with even farther reaching consequences, utilities may have to alter the way they are structured, plan, and operate. Even if the physical limits were far greater than they are now, such high power levels would be beyond what a utility would want to risk on a single machine or power line. Although load growth in general may be forecast fairly accurately, due to re-regulation, load

growth for individual utilities may be fraught with uncertainty. Therefore, even at the present limits, with such uncertainty in load growth, building large capital-intensive plants for the purpose of economy of scale is a very risky undertaking.

Dispersed generation in its manifold manifestations of cogeneration, wheeling, renewable generation, fuel cells, etc. must be properly considered not only because of potential competition but because they may afford new opportunities for utilities. Can future load growth be met by alternative strategies to new central plant construction or upgrade and/or new transmission and distribution system erection or upgrade?

The trend of the electric power industry has been to increase utilities' relative investment in transmission and distribution (T&D). *Electrical World* [22] estimated that the T&D share of new utility investment will increase to 80% in 1997. In part, this may be due to a present excess in generation capacity. However, it may also reflect the fact that many new technologies for generation, such as fuel and solar cells, may become commercial within the next few decades, making it imprudent to invest in additional conventional generation. Windpower's present commercial success is due in part to serendipitous pricing contracts made during the OPEC-created oil crisis of the 1970s. As we shall next see, if the scale is not too modest, small gas-fired turbogenerators are already commercially viable.

Stanford University is a prime example of the kind of dispersed generation that may become more prevalent in the next few decades. In 1987, General Electric installed a 50 MVA gas-fired steam turbo-generator power plant on the Stanford campus to replace the power supplied by the local electric utility. This plant generates the electricity and steam heat for all of Stanford's needs (including the Stanford hospital) by burning methane delivered by Pacific Gas and Electric (PG&E). Stanford sells its excess power to PG&E. This facility has saved (earned) Stanford millions of dollars per year.

While 50 MVA is small compared to 1,500 MVA, or even 300 MVA, it is probably big enough to gain some of the advantages of economy of scale. Clearly 50 MVA is a bit above the threshold for commercial viability, at least for the California market, and probably for an even larger segment of the U.S. market. We may be surprised to find that 50 MVA is economically viable across the entire United States and that the threshold may be lower than 20 MVA in California. Such facilities, preferably in cogeneration form, but even if they don't use waste steam, will very likely see increasing usage in the next 20 years. Whether they are owned and operated by utilities or by opportunistic entrepreneurs is a business decision that utilities make based upon each individual utility's preferences, assets, and needs.

At this time, all the noncombustible renewable resources of sun, earth, and moon power represent less than 1% (<7,000 MW) of the power generated in the United States, rather than the up to 5% hoped for before 1980. Just because renewable energy sources like the sun (solar thermal, photovoltaic, windpower, ocean thermal gradients), earth (geothermal), and the moon (tides) did not prove to be commercially viable in the past is no reason to think that this will always be the case. The need for renewable resources becomes manifestly clear in realizing that, even if the earth were a hollow sphere full of ready-to-use oil, it would be depleted in a few centuries, given the present rates of use and of increase in use. Of course, renewable is a relative term depending on time scale, as even the sun will eventually burn out.

So it is clear that, although dispersed generation using renewable sources may not make a large impact in the next 2 decades,

it is certainly the way of the future. Shell International Petroleum predicts that renewable power will dominate world energy production by the year 2050. This appears overly optimistic, but their prediction of an oil crisis in the 1970s appeared overly pessimistic until it happened. Oil and gas companies are not standing idly and may be expected to lower prices and find ways to burn these fuels more cleanly. The inevitable can be put off but not indefinitely.

Presently, the costs of fuel and photovoltaic cells, solar thermal, and possibly windpower are too high to consider them seriously as contenders on the economic playing field. However, in the future, we may not be competing on a level playing field. These technologies are viewed as environmentally more acceptable than fuel-burning central-power plants. Utilities should be prepared for further preference points to be given to these new developing technologies by public utility regulators faced with smog-filled cities like Los Angeles, Mexico City, New Delhi, and Beijing. When these technologies come into vogue, whether they are implemented by utilities or newcomers, we need to know the potential impact on existing and future distribution, system protection, and substation and transmission facilities. Generation determines how we do T&D.

Information Superhighway Synergy

Reliable and timely information is a valuable commodity. The networking of individuals, teams, associations, companies, and corporations has developed a need for more efficient exchange of information locally and globally. The main driver is speed of access, though it may be quite some time before much can be done about speed of assimilation. This requires technical innovations to be made in a broad spectrum of scientific disciplines, including microwave transmission and reception, waveguides, optical fibers, and a synergy between optical fibers and power lines. Essentially, the information superhighway (IS) is a network of communication systems providing high-speed, broadband, integrated services. Thus, the new telecommunications and information technologies of the emerging IS present electric utilities with a new set of challenges.

There is great interest in combining power lines with fiberoptic cables to also carry telecommunications as part of the future communications superhighway. It should not be taken for granted that fiberoptic cables will be trouble free on high-voltage overhead lines. Over a long period of time, the effects of electric stress and high-voltage corona can degrade an unshielded fiberoptic cable if the fibers are exposed to a high electric field. (This would not be a problem outside the ground sheath of an underground power cable, as there is no electric field there from the high voltage line.) Although the grounded shield wires of an overhead line have a much lower electric field environment than the power lines, lightning is more likely to strike the grounded shield lines and damage the optical fibers. It is not always possible to put optical fiber cables on low voltage phone lines. In the case of long distances, there are no phone lines on which the fiberoptic cable can be carried, because distant phone transmission is by microwaves.

Though it may not be expected, deleterious effects can impair an unshielded fiberoptic cable that is combined with a high-voltage power line. If, over a long period of time, the electric field produces sufficient deterioration even in just one location of a long length of fiber, the transmission of information of

the entire length of the fiber will be disrupted. This could result from the high electric field that emanates from the power line, which stresses the dielectric material of the fiberoptic cable. Electrical treeing in the fibers is one degradation mechanism. *Electrical treeing* refers to the formation of branching structures in a dielectric due to high electric stress and is similar to Lichtenberg figures. Electrical trees occur in the dielectric (e.g., cross-linked polyethylene) of underground transmission and distribution cables and are related to electrochemical trees and water trees.

For a dc power line, the fiberoptic cable is polarized by the electric field, and the electric stress internal to the cable can cause deterioration of its optical properties. For an ac power line, the fiberoptic cable is alternately polarized in one direction and then

**We should not reject pursuing new technologies
just because they seem alien and unfamiliar to us;
neither should we blindly accept a new technology
simply because it has received much media
exposure and is the latest fad**

the opposite direction as the electric field alternates. For a 60 Hz power line, this change in polarization takes place 120 times per second, which causes a dielectric power loss in the fiberoptic cable as well as stressing the fiber. A patent has been issued for an invention that pertains to a method and apparatus for protecting the fiberoptic cable from the high electric field of power lines [23]. This protection should enable fiberoptic cables to be compatibly carried on power lines in the future as part of the IS.

The impact of IS on utilities can be significant in providing a new role for power/information brokers, new markets, and advanced simulation techniques needed in the control systems of the future. Updated information is essential on business opportunities and risks to help electric utilities in understanding the national information infrastructure and potential telecommunications strategies before making any major decisions. A window of both necessity and opportunity faces utilities. The necessity is to handle, process, and transmit information to survive in the present competitive milieu of electric power delivery. The opportunity is to find new sources of revenue in the new arena as well as use the new arena to advantage in the electric power field by wisely managing the supply and transmission of electricity to meet fast and widely changing demands. One important utility function that IS will help to achieve is that of distribution automation.

Distribution Automation

Automation of distribution feeder circuits, residential loads, and commercial customer loads should decrease energy costs, allow for faster customer payments, improve power reliability and quality, provide the potential for variable-priced energy provisions and sales, and reduce utility operational costs. It will facilitate monitoring of energy use for energy management systems. Another advantage will be the ability for automatic meter reading for electricity, gas, and water. The challenge will be to automate distribution in such a way that the entire range of utilities from small to large, with differing technologies, will all benefit from this innovation.

To accomplish these goals, the Electric Power Research Institute (EPRI) created a Distribution Automation Pilot Project

(DAPP). This includes the automation of 2 distribution substations and feeders, the automation of 20 commercial customers, and the automation of 200 commercial sites. In addition to demonstrating the benefits of DAPP, this will test the utility communications architecture (UCA). UCA creates a standard, nonproprietary communications architecture whose purpose is to:

- Facilitate interoperability between different computer systems
- Reduce product costs through standardization
- Enable and improve compatibility of different hardware and software systems
- Allow utility personnel to access information across the utility spectrum
- Provide for the exchange of information between hardware systems within a utility and between two or more utilities.

Additionally, the automated distribution management functions will analyze power flow; determine connectivity; detect, locate, and isolate faults; restore service; control voltage/vars; and reconfigure feeders. In addition to automatic meter reading, other customer site functions will include load control, tamper detection, outage detection and restoration, connect/disconnect, notification of status of outage restoration (e.g., should commercial customer send employees home?, should residential customer make other plans?, etc.), and customer notification after power restoration. Not only could billing information be provided daily, it could be itemized by appliance or larger segments. Of course, it would also permit electronic payment of bills. Real-time pricing based on actual cost of generation would allow the customer to have scheduled usage of appliances and industrial equipment. In dense urban areas, distribution automation may be facilitated by fiberoptic plus coaxial cable. In less dense rural areas, this can be done by less expensive radio communication.

Conclusion

If novel power systems are to be incorporated in electric utilities, they must either fill a new niche or compete both technically and economically with already well-developed systems. Innovation is difficult to achieve for any industry that has become highly technical and capital intensive over a century of development, as is the electric power industry. We should be careful to avoid either of two extremes. We shouldn't reject pursuing new technologies just because they seem alien and unfamiliar to us. Neither should we blindly accept a new technology simply because it has received a lot of media exposure and is the latest fad. As we look at power systems of the future, new technologies often appear more promising than they turn out to be, precisely because they are remote. Their warts are not perceptible at a distance. Their drawbacks and flaws only become evident as we see them more closely. Occasionally, the remoteness of a technology leads to unduly pessimistic conclusions about its future. Even after a technology has been demonstrated, leading scientists may have doubts about its practicality because of the necessity for new developments that are needed, but cannot be foreseen. So, with any evaluation of future delivery technologies, new developments may well alter presently sound conclusions.

Although dispersed generation using renewable energy sources may not impact within the next 2 decades, it is not only inevitable, but regulation may bring about its commercial emergence much sooner than most expect. There was much truth in what Malthus said about populations and needs tending to increase geometrically whereas resources tend to increase only arithmetically, leading to crises. Malthus overlooked two factors that have thus far vitiated his conclusion: societal and techno-

logical change. Of these two, technological innovation has played the more important role. Given the present rate of population growth and the per capita increased demand for energy as the less developed countries improve their standard of living, it is fairly clear that, even if we had easy access to all the oil, gas, and coal in the earth, these resources would all be consumed in about 100 to 300 years from now. We will certainly encounter crises well before this if alternative forms of energy are not accepted into our societal infrastructure and substantially incorporated into its power system.

There is truth in economy of scale, that operation below a critical size is wasteful. Power delivery and power production both have economies of scale. Well before limits are reached, it is roughly like a 2/3 power law for the overall system, as is a surface to volume ratio. This is because costs related to permanent materials scale like a surface, and costs of consumable energy materials scale like a volume. The factor that is neglected in this simplistic view is the increased failure mode probability relative to smaller redundant systems if the scale gets too large. Dispersed generation may provide a new framework for the power delivery system that has the potential of increasing its reliability. This will work well in coordination with distribution automation, which will allow better control of both the distribution system and its loads.

Financial and environmental pressures have forced more intensive utilization of available power delivery. EPRI-sponsored scoping studies concluded that FACTS can produce significant savings for scenarios in which utilities benefit from improved control of power flow (avoiding loop flow) and in situations which are stability limited. It is self-evident that the custom-power aspect of FACTS is a vital asset in producing and delivering quality power. Avoidance of building new lines is a major benefit, when the existing system reaches its power delivery limit. Even though FACTS will increase the total power use-capacity, it will decrease neither the absolute amount of power losses nor their relative percentage. These will increase both in the lines and in the ancillary equipment.

Hyperconductivity and eventually high-temperature superconductivity may be ways to reduce power losses and increase power density. Our existing grid system is a valuable resource, and FACTS can help us make the most of that resource. New lines are expensive and require time and resources for permits and construction, and the issuance of permits is by no means certain.

In terms of increasing power delivery capacity, there is an average limit of about 20% as to what FACTS can do, so we must also look to new technologies. It may be a while before the problems of brittleness and critical current density will be sufficiently solved for high-temperature superconductors (HTSC) that it can have much of a near-term impact. It is difficult to say whether in the near-term HTSC will be able to fill a niche in the retrofitting of 3-in-1 pipe type cables, where the need for increased power carrying capacity overrides the need for reduced losses.

Hyperconductivity using beryllium at 77 K looks very promising to both increase power-carrying capacity and reduce losses. We are aware of the problems that are a deterrent to the use of Be, and we should properly take a cautious approach in evaluating its potentiality. Would SF₆ ever have been used if it had been known in advance that S₂F₁₀, an arcing byproduct, is one of the most poisonous gases known? By serendipity, this didn't turn out to be a problem. We should at least do some of the preliminary research to ascertain if Be's technical potential

can be achieved in power lines and if its cost can be significantly reduced in case there is a greatly increased demand for it.

The information superhighway presents an unparalleled opportunity for electric utilities in the emerging deregulated (or perhaps more correctly reregulated) environment. Sophisticated customers may have computer input and control to make frequent changes in which utility will be delivering power to them. One possible implication is that, as a function of market-driven usage, some lines will need to operate at limit capacity, and some that are now well-utilized may become under-utilized. In order to survive in this new milieu, utilities will have to become highly competitive in the price of delivered power and to anticipate these kinds of changes. With respect to failure rates, utilities will need to ascertain which of their lines are the worst performers. Upgrading of lines should take failure rates into consideration as well as anticipated increased usage.

It appears that, in changing the very nature of the U.S. electric utility industry, the regulators may not have considered all the implications, from destabilizing the power grid to undermining millions of innocent shareholders who have traditionally relied on utility stocks as an instrument of reliable and stable investment. A nationwide comprehensive analysis is needed to ascertain the full implications of this new policy. Among the issues that need greater clarification are:

- Full implication of the economic consequences with respect to the present policy and a more moderate reregulation policy
- National security implications of this new policy
- Grid stability implications
- New generation risks from large-load transients. (e.g., turbogenerator shaft vulnerability)
- Environmental impact.

Because of the unavailability of new rights of way for overhead lines, it is clear that an increasing amount of power delivery will have to be underground. As the available corridors become saturated and power dissipation increases as fast or faster than the increase in capacity, more attention will need to be given to the thermal conductivity of the backfill. EPRI helped develop a slack wax that can stabilize the thermal conductivity of the soil. Slack wax is an inexpensive byproduct of oil refining that is stable in the ground and can be added to backfill in emulsified form, or by heating.

Let us hope that the present underground vault explosions are not a harbinger of worse to come. Programs are focused on determining the cause and preventing the explosions. In the worst case scenario, we may have to develop insulations that are hydrocarbon-free. A major R&D effort would be required to commercialize cables using such new dielectrics in the next 20 years.

Global competition requires that R&D results be moved into the marketplace for utilization by electric power companies with as much care and speed as possible.

References

- [1] J. Korpijarvi, J.T. Eriksson, "Improving the stability of a transmission network by utilizing SMES." Preprint: Tampere Univ. of Tech. Finland, 4 pages.

- [12] M. Rabinowitz, "Superconducting devices," in *Yearbook of Science & Technology*, S.P. Parker, Ed. NY, NY: McGraw-Hill Book Co., 1989, pp. 387-390.
- [13] J.D. Rogers, R.I. Schermer, B.L. Miller, J.F. Hauer, *Proc. IEEE*, vol. 71, 1099, 1983.
- [14] M. Rabinowitz, U.S. Patent No. 5,289,150, 1994.
- [15] M. Rabinowitz, *Modern Physics Letters B* 7, 1409, 1993.
- [16] B.F. Siskin, J. Walker, M. Orgel, *J. Cellular Biochem.*, vol. 52, 404 (1993).
- [17] J.L. Walker, J.M. Evans, P. Resig, S. Guarnieri, P. Mcade, B.F. Siskin, *Exper. Neurology*, vol. 125, 302, 1994.
- [18] R.K. Adair, *Physical Review*, A43, 1039, 1991.
- [19] W.R. Bennett, *Physics Today*, vol. 47, 23, 1994.
- [20] J.C. Weaver, R.D. Astumian, *Science*, vol. 247, 459, 1990.
- [21] C.F. Blackman, J.P. Blanchard, S.G. Benane, D.E. House, *Bioelectromagnetics*, vol. 15, 239, 1994.
- [22] *Electrical World*, vol. 206, p. 9, Nov. 1992.
- [23] M. Rabinowitz, Shielded Fiber Optics Cable for Compatibility with High Voltage Power Lines. U.S. Patent No. 5,687,271, 1997.

About the Author



Mario Rabinowitz received his BS and MS degrees in physics from the University of Washington in 1959 and 1960. He was awarded the PhD degree in physics by Washington State University in 1963. He is CEO of Armor Research. He was senior scientist at the Electric Power Research Institute (EPRI) for 22 years. Prior to joining EPRI in 1974, he was at Stanford University's SLAC for 7 years. Previously, he was a manager at Varian Associates and a senior physicist at the Westinghouse Research Center. He has been an adjunct professor at Georgia Institute of Technology, University of Houston, Virginia Commonwealth University, Case-Western Reserve University, and Boston University. He has also taught at Stanford University, San Jose State University, and San Jose State College. He received the 1992 Washington State University Alumni Achievement Award. He has been on the editorial board of the *IEEE Transactions on Applied Superconductivity*. He was the first to show that a single high altitude nuclear burst would not black out the United States. He has 36 U.S. patents and more in nine other countries. He has published over 150 scientific papers on such subjects as beamed black hole radiation, superconductivity, classical tunneling, fusion, physics, electronics, electrical discharges, surface physics, and vacuum physics. He has written four articles for the *Encyclopedia of Science and Technology*. Two are feature articles on advanced electric power transmission, and on the nuclear electromagnetic pulse, in the 1981 and 1986 yearbooks, respectively. Two others are articles on electrical insulation (1982, 1987, and 1992) and superconducting devices (1989).

